Conference Proceedings of the Society for Experimental Mechanics Series

Sez Atamturktur · Tyler Schoenherr · Babak Moaveni
Costas Papadimitriou *Editors*

Model Validation and Uncertainty Quantification, Volume 3

Proceedings of the 34th IMAC, A Conference and Exposition on Structural Dynamics 2016

Springer

Conference Proceedings of the Society for Experimental Mechanics Series

Series Editor

Kristin B. Zimmerman, Ph.D.
Society for Experimental Mechanics, Inc.,
Bethel, CT, USA

More information about this series at http://www.springer.com/series/8922

Sez Atamturktur • Tyler Schoenherr • Babak Moaveni
Costas Papadimitriou
Editors

Model Validation and Uncertainty Quantification, Volume 3

Proceedings of the 34th IMAC, A Conference and Exposition on Structural Dynamics 2016

Springer

Editors
Sez Atamturktur
Civil Engineering
Clemson University
Clemson, SC, USA

Babak Moaveni
Tufts University
Medford, MA, USA

Tyler Schoenherr
Kohler Company
Kohler, WI, USA

Costas Papadimitriou
University of Thessaly
Thessaly, Greece

ISSN 2191-5644 ISSN 2191-5652 (electronic)
Conference Proceedings of the Society for Experimental Mechanics Series
ISBN 978-3-319-29753-8 ISBN 978-3-319-29754-5 (eBook)
DOI 10.1007/978-3-319-29754-5

Library of Congress Control Number: 2014931235

Printed on acid-free paper

This Springer imprint is published by Springer Nature
The registered company is Springer International Publishing AG Switzerland

Preface

Model Validation and Uncertainty Quantification represents one of ten volumes of technical papers presented at the 34th IMAC, A Conference and Exposition on Structural Dynamics, organized by the Society for Experimental Mechanics and held in Orlando, Florida, on January 25–28, 2016. The full proceedings also include volumes on Nonlinear Dynamics; Dynamics of Civil Structures; Dynamics of Coupled Structures; Sensors and Instrumentation; Special Topics in Structural Dynamics; Structural Health Monitoring, Damage Detection and Mechatronics; Rotating Machinery, Hybrid Test Methods, Vibro-Acoustics and Laser Vibrometry; Shock and Vibration, Aircraft/Aerospace, Energy Harvesting, Acoustics and Optics, and Topics in Modal Analysis and Testing.

Each collection presents early findings from experimental and computational investigations on an important area within Structural Dynamics. Model Validation and Uncertainty Quantification (MVUQ) is one of these areas.

Modeling and simulation are routinely implemented to predict the behavior of complex dynamical systems. These tools powerfully unite theoretical foundations, numerical models, and experimental data which include associated uncertainties and errors. The field of MVUQ research entails the development of methods and metrics to test model prediction accuracy and robustness while considering all relevant sources of uncertainties and errors through systematic comparisons against experimental observations.

The organizers would like to thank the authors, presenters, session organizers, and session chairs for their participation in this track.

Clemson, SC, USA — S. Atamturktur
Kohler, WI, USA — T. Schoenherr
Medford, MA, USA — B. Moaveni
Thessaly, Greece — C. Papadimitriou

Contents

1 **Bayesian Treatment of Spatially-Varying Parameter Estimation Problems via Canonical BUS** 1
Sadegh Rahrovani, Siu-Kiu Au, and Thomas Abrahamsson

2 **Bayesian Modelling of Offshore Platforms** 15
P.L. Green, U.T. Tygesen, and N. Stevanovic

3 **Bayesian Inference and RJMCMC in Structural Dynamics: On Experimental Data** 23
D. Tiboaca, P.L. Green, R.J. Barthorpe, I. Antoniadou, and K. Worden

4 **Approximate Bayesian Computation by Subset Simulation for Parameter Inference of Dynamical Models** 37
Majid K. Vakilzadeh, Yong Huang, James L. Beck, and Thomas Abrahamsson

5 **Determining Model Form Uncertainty of Reduced Order Models** 51
Matthew S. Bonney, Daniel C. Kammer, and Matthew R.W. Brake

6 **Uncertainty Analysis of Mechanical Behavior of Functionally Graded Carbon Nanotube Composite Materials** 59
E. García-Macías, R. Castro-Triguero, Michael I. Friswell, A. Sáez-Pérez, and R. Gallego

7 **Interval Uncertainty Analysis Using CANDECOMP/PARAFAC Decomposition** 73
Jinchun Lan and Zhike Peng

8 **Uncertainty Quantification for Nonlinear Reduced-Order Elasto-Dynamics Computational Models** 83
E. Capiez-Lernout, C. Soize, and M. Mbaye

9 **Estimating Noise Spectra for Data from an Instrumented Building** 91
Bryan S. Joyce and Pablo A. Tarazaga

10 **Uncertainties in an Application of Operational Modal Analysis** 107
Lorenzo Banfi and Luigi Carassale

11 **Stochastic Finite Element Model Updating by Bootstrapping** 117
Vahid Yaghoubi, Majid K. Vakilzadeh, Anders T. Johansson, and Thomas Abrahamsson

12 **Dynamic Identification of Classically Damped Uncertain Structures** 131
E. Lofrano, A. Paolone, and M. Vasta

13 **Interval Finite Element Approach for Modal Analysis of Linear Elastic Structures Under Uncertainty** 143
Naijia Xiao, Francesco Fedele, and Rafi Muhanna

14 **Model-Based Effects Screening of Stringed Instruments** 151
R. Viala, V. Placet, S. Cogan, and E. Foltête

15 **Innovation Dilemmas, Design Optimization, and Info-Gaps** 159
Yakov Ben-Haim

16 Approach to Evaluate and to Compare Basic Structural Design Concepts of Landing Gears in Early Stage of Development Under Uncertainty 167
Roland Platz, Benedict Götz, and Tobias Melz

17 Robust Sensor and Exciter Design for Linear Structures 177
Fabien Maugan, Scott Cogan, Emmanuel Foltête, and Aurélien Hot

18 Robust Model Calibration Using Determinist and Stochastic Performance Metrics 185
P. Lépine, S. Cogan, E. Foltête, and M.-O. Parent

19 Designing a Mechanical Latch for Robust Performance 193
François Hemez and Kendra Van Buren

20 From Model Calibration and Validation to Reliable Extrapolations 205
Gabriel Terejanu

21 Application of PCA-SVD Validation Metric to Develop Calibrated and Validated Structural Dynamic Models 213
Hasan G. Pasha, Randall J. Allemang, and Manish Agarkar

22 An Enhanced Metropolis-Hastings Algorithm Based on Gaussian Processes 227
Asif Chowdhury and Gabriel Terejanu

23 The Challenge of Dynamic Similarity Assessment 235
Adam C. Moya, Julie M. Harvie, and Mike J. Starr

24 Model Based Robust Balancing Approach for Rotating Machines 243
Arinan Dourado Guerra Silva, Aldemir Ap Cavalini Jr. and Valder Steffen Jr.

25 Statistical Modeling of Wavelet-Transform-Based Features in Structural Health Monitoring 253
Aral Sarrafi and Zhu Mao

26 A Bayesian Framework for Optimal Experimental Design in Structural Dynamics 263
Costas Argyris and Costas Papadimitriou

27 Towards the Diagnosis and Simulation of Discrepancies in Dynamical Models 271
P.L. Green

28 Effects of Prediction Error Bias on Model Calibration and Response Prediction of a 10-Story Building 279
Iman Behmanesh, Seyedsina Yousefianmoghadam, Amin Nozari, Babak Moaveni, and Andreas Stavridis

29 Finite Element Model Updating Techniques of Complex Assemblies with Linear and Nonlinear Components 293
Alexandros Arailopoulos and Dimitrios Giagopoulos

30 Metamodeling of Model Evidence 307
Ramin Madarshahian and Juan M. Caicedo

31 Calibration, Validation and Uncertainty Quantification of Nominally Identical Car Subframes 315
Mladen Gibanica, Thomas J.S. Abrahamsson, and Magnus Olsson

32 Modeling and Experimental Test Study of a Multilayer Piezoelectric Actuator 327
ZhongZhe Dong, Cassio T. Faria, Wim Desmet, and Martin Hromcik

33 Study of Correlation Criteria for Spacecraft-Launch Vehicle Coupled Loads Analysis 337
J.F. Mercer, G.S. Aglietti, M. Remedia, and A.M. Kiley

34 Full-Field Strain Prediction Applied to an Offshore Wind Turbine 349
Alexandros Iliopoulos, Wout Weijtjens, Danny Van Hemelrijck, and Christof Devriendt

35 A State-Input Estimation Approach for Force Identification on an Automotive Suspension Component 359
E. Risaliti, B. Cornelis, T. Tamarozzi and W. Desmet

36 A Pretest Planning Method for Model Calibration for Nonlinear Systems 371
Yousheng Chen, Andreas Linderholt, Thomas Abrahamsson, Yuying Xia, and Michael I. Friswell

Chapter 1
Bayesian Treatment of Spatially-Varying Parameter Estimation Problems via Canonical BUS

Sadegh Rahrovani, Siu-Kiu Au, and Thomas Abrahamsson

Abstract The inverse problem of identifying spatially-varying parameters, based on indirect/incomplete experimental data, is a computationally and conceptually challenging problem. One issue of concern is that the variation of the parameter random field is not known a priori, and therefore, it is typical that inappropriate discretization of the parameter field leads to either poor modelling (due to modelling error) or ill-condition problem (due to the use of over-parameterized models). As a result, classical least square or maximum likelihood estimation typically performs poorly. Even with a proper discretization, these problems are computationally cumbersome since they are usually associated with a large vector of unknown parameters. This paper addresses these issues, through a recently proposed Bayesian method, called Canonical BUS. This algorithm is considered as a revisited formulation of the original BUS (Bayesian Updating using Structural reliability methods), that is, an enhancement of rejection approach that is used in conjunction with Subset Simulation rare-event sampler. Desirable features of CBUS to treat spatially-varying parameter inference problems have been studied and performance of the method to treat real-world applications has been investigated. The studied industrial problem originates from a railway mechanics application, where the spatial variation of ballast bed is of our particular interest.

Keywords Bayesian methodology • Bayesian updating using structural reliability methods (BUS) • Subset simulation (SS) • Stochastic simulation • Rare-event sampler

1.1 Introduction

Bayesian system identification is a promising approach that does not require the parameters to be identifiable, it is able to explicitly treat various sources of modelling uncertainties and, at the model selection level, it has a built-in penalty term against the over-parameterized model classes [1, 2]. Given measurement data, a priori distribution function over the parameters (our prior knowledge of parameters) can be updated, by using the Bayes Theorem, to obtain a *posterior* probability distribution [3]. Later on, the posterior PDF can be used for prediction of a response quantity of interest by estimating its updated expectation. Among different Bayesian approaches, Markov Chain Monte Carlo (MCMC) based methods are powerful means that are developed to efficiently draw samples from an arbitrary distribution, used for computation of statistical estimates, marginal and conditional probabilities [4]. For Bayesian updating problems, MCMC popular implementations such as Metropolis, Hybrid Monte-Carlo and simulated annealing algorithms have been developed to efficiently draw samples from the posterior distribution while circumventing the need to evaluate the normalizing factor in Bayes' formula (known as model class evidence) [5]. However, avoiding the explicit evaluation of the model evidence is not allowed for the model class selection problem whereby quite different types of MCMC-based methods, such as Transitional MCMC and Reversible Jump MCMC, have been developed for computing the model evidence [6]. While MCMC based stochastic simulation methods, in principle, provide a powerful sampling tool, many of these algorithms are not trivially applicable for computation of model evidence and posterior statistics in real-world problems. Such high-dimensional inference problems are conceptually and computationally challenging. One important issue, in these problems, is the *Curse of dimensionality*; a situation where the algorithm only works fine in low dimension but break down in problems with high dimensional parameter space [7]. Consequently, the acceptance probability in the Markov chain process tends to zero systematically, leading to high rejection of the proposed candidates, at almost all the time. Another issue, typically

S. Rahrovani (✉) • T. Abrahamsson
Department of Applied Mechanics, Chalmers University of Technology, Gothenburg, Sweden
e-mail: sadeghr@chalmers.se

S.-K. Au
School of Engineering, University of Liverpool, Liverpool, UK

S. Atamturktur et al. (eds.), *Model Validation and Uncertainty Quantification, Volume 3*, Conference Proceedings of the Society for Experimental Mechanics Series, DOI 10.1007/978-3-319-29754-5_1

arises when dealing with large amount of data (informative data), is the poor efficiency of the MCMC techniques. In such cases, the posterior PDF shrinks in a small region of the parameter space, leading to high rejection rate of the proposed candidates. This makes the choice of proposal distribution difficult, since it results in a significant bias when it is not well-treated [8]. Spatially-varying parameter estimation problems is one example that suffer from these issues, since it is typically associated with a large vector of unknown parameters, created due to the spatial discretization of parameter field, see [9] and [10]. On the other side, computational efficiency and dimension robustness issues are both well-recognized in the reliability community, whereby robust methods have been developed to tackle them [7]. In this regard, although it is not trivial, attempts have been made recently to bridge the gap between these two communities, which enable us to use the portfolio of available reliability methods and the associated softwares for the Bayesian updating problem. By establishing an analogy with the reliability problem, an enhancement of classical rejection sampling algorithms, called BUS (Bayesian Updating using Structural reliability methods), has been proposed for efficient computation of posterior statistics of uncertain model parameters, in general [11]. This formulation opens up the possibility of using subset simulation algorithm, as a robust and efficient rare-event sampler, with the capability to adaptively generate samples from the frequent/safe region to the rare/fail region, for efficient treatment of Bayesian model updating problems with high dimensional parameter space. However, one main concern in BUS is the prudent choice of a multiplier, which can considerably affect the correctness and efficiency of the method [11]. This issue has been deeply studied in [12], where the presented rigorous mathematical study provides us a fundamental understanding of the multiplier choice that leads to a revisited formulation of the original BUS, called Canonical BUS (CBUS). Briefly stated, by redefining the target failure/rare event, the new formulation allows subset simulation to be implemented independent of the choice of a predetermined multiplier [13]. Moreover, the presented analysis predicts the properties of the log-evidence function, which provides a stopping criterion for the subset simulation algorithm used under CBUS formulation. Desirable features of CBUS for treating high-dimensional inference problems, such as in spatially-varying parameter estimation problems, have been studied and performance of the method to treat real-world applications has been investigated. The studied industrial problem originates from a railway mechanics application, where the spatial variation of ballast bed is of our particular interest.

1.2 Methodology

1.2.1 Challenges in Spatially-Varying Parameter Estimation Problems

A straight forward approach in spatially-varying parameter estimation problems, as in the railway application studied in this paper, consists of two main steps: First to discretise the target field and represent the parameter field in a finite-dimensional parameter subspace, secondly to perform model calibration to infer the unknown parameters, based on measured/simulated data. However, the main concern is that the shape and variation of the parameter field is usually not known a priori, and therefore, it is typical that inappropriate discretization of the random field leads to either inaccurate approximation (due to modelling error) or ill-conditioning/unidentifiability issue (due to the use of over-parameterized models). One rational strategy, to tackle these problems, is to use a set of candidate model classes with different level of complexity and try to find the best/optimal model class after performing the calibration of different candidate models. However, if model class assessment is based purely on some measure of the model fit with respect to the data, as in least square estimation or maximum likelihood estimation, the best model class will always be the most complicated one since it covers the largest output space [2]. Although over-parameterized models might result in a lower inference error, they can lead to unreliable solutions when used for response predictions, since they depend too much on details of data and the noise contamination in the measurements [3]. Therefore, at the model class selection stage, it is necessary to penalize more complicated model classes such that the simpler models (with a reasonable consistency to data) are preferred over too-complex model classes [2]. Using a Bayesian approach is beneficial in this sense, since it does not require the parameters to be identifiable while, at model selection level, it has a built-in penalty term against the over-parameterized model classes. This approach enables us to make the calibration in a prediction setting, instead of only simulation, that enables us to reliably use the established calibrated models for future predictions.

1.2.2 Bayesian Updating and Model Class Selection

The primary target in Bayesian updating is to draw samples from the posterior distribution of the unknown parameter vector $\boldsymbol{\theta}$, which incorporates the data $\mathcal{D}$ information in the context of a model class $\mathcal{M}_i$. In this regard, the fundamental Bayes' theorem is formulated as

$$p\left(\boldsymbol{\theta}\middle|\mathcal{D},\mathcal{M}_i\right)=\frac{P\left(\mathcal{D}\middle|\boldsymbol{\theta},\mathcal{M}_i\right)p\left(\boldsymbol{\theta}\middle|\mathcal{M}_i\right)}{P\left(\mathcal{D}\middle|\mathcal{M}_i\right)} \tag{1.1}$$

where $p(\boldsymbol{\theta}\middle|\mathcal{M}_i)$ and $P(\mathcal{D}\middle|\boldsymbol{\theta},\mathcal{M}_i)$ denotes the prior probability distribution and the Likelihood function, respectively. The posterior PDF is given by normalizing the likelihood multiplied with the prior, to a unit area where normalizing constant is

$$P(\mathcal{D}\middle|\mathcal{M}_i)=\int P(\mathcal{D}\middle|\boldsymbol{\theta},\mathcal{M}_i)p(\boldsymbol{\theta}\middle|\mathcal{M}_i)\mathrm{d}\boldsymbol{\theta} \tag{1.2}$$

In a 'Bayesian updating problem' (given a model class), however, the normalizing constant $P(\mathcal{D}\middle|\mathcal{M}_i)$ is immaterial since it does not affect the shape of the posterior distribution, i.e. $p(\boldsymbol{\theta}\middle|\mathcal{D},\mathcal{M}_i)\propto P(\mathcal{D}\middle|\boldsymbol{\theta},\mathcal{M}_i)p(\boldsymbol{\theta}\middle|\mathcal{M}_i)$. In this regard, efficient sampling methods aim at drawing samples from the posterior distribution while circumventing the need to evaluate the normalizing constant (known as model evidence or marginal Likelihood in the context of Bayesian model selection). The generated samples incorporate the data information into future predictions of a response quantity of interest $r(\boldsymbol{\theta})$, by evaluating the updated posterior expectation as

$$E\left(r\left(\boldsymbol{\theta}\right)\middle|\mathcal{D},\mathcal{M}_i\right)=\int r\left(\boldsymbol{\theta}\right)p\left(\boldsymbol{\theta}\middle|\mathcal{D},\mathcal{M}_i\right)\mathrm{d}\boldsymbol{\theta} \tag{1.3}$$

On the contrary, avoiding the explicit evaluation of $P\left(\mathcal{D}\middle|\mathcal{M}_i\right)$, is not allowed in the 'Bayesian model selection problem', since it is the primary quantity of interest based on which the candidates are compared [2]. The model class evidence is then used to compare the posterior probability of different competing model classes, by evaluating the Bayes quotient.

$$\frac{P\left(\mathcal{M}_i\middle|\mathcal{D}\right)}{P\left(\mathcal{M}_j\middle|\mathcal{D}\right)}=\frac{P\left(\mathcal{D}\middle|\mathcal{M}_i\right)P\left(\mathcal{M}_i\middle|\mathbf{M}\right)}{P\left(\mathcal{D}\middle|\mathcal{M}_j\right)P\left(\mathcal{M}_j\middle|\mathbf{M}\right)} \tag{1.4}$$

Here, $P\left(\mathcal{M}_i\middle|\mathbf{M}\right)$ expresses the user judgement on the initial probability of $\mathscr{M}_i$ in the candidate models set, $\mathbf{M}=\{\mathcal{M}_1,\ \mathcal{M}_2,\ldots,\ \mathcal{M}_{N_M}\}$. Assuming the same initial probability for different model classes, i.e. $P\left(\mathcal{M}_i\middle|\mathbf{M}\right)=1/N_M$, the model class with (relatively) higher model evidence is always better; not only in a descriptive, but also in a predictive setting. Further insight about this desirable property of the Bayesian model selection approach can be obtained by looking at the *information-theoretic* interpretation of the model evidence, as it was noted in [3]. Thus, the logarithm of the model evidence $\ln\left[P\left(\mathcal{D}\middle|\mathcal{M}_i\right)\right]$ can be formulated as

$$\ln\left[P\left(\mathcal{D}\middle|\mathcal{M}_i\right)\right]=\int\ln\left(p\left(\mathcal{D}\middle|\boldsymbol{\theta},\mathcal{M}_i\right)\right)p\left(\boldsymbol{\theta}\middle|\mathcal{D},\mathcal{M}_i\right)\mathrm{d}\boldsymbol{\theta}-\int\ln\left(\frac{p\left(\boldsymbol{\theta}\middle|\mathcal{D},\mathcal{M}_i\right)}{p\left(\boldsymbol{\theta}\middle|\mathcal{M}_i\right)}\right)p\left(\boldsymbol{\theta}\middle|\mathcal{D},\mathcal{M}_i\right)\mathrm{d}\boldsymbol{\theta} \tag{1.5}$$

This formulation explicitly shows the trade-off between two competing terms; The posterior mean of the log-likelihood—i.e., first term in Eq. (1.5)—rewards models for being high fidelity meanwhile the relative entropy between the prior and the posterior—i.e., second term in Eq. (1.5)—penalises models for being too complicated. Unfortunately, evaluating the model evidence is a highly non-trivial task, primarily resulting from the complexity of the likelihood function. The most common approach is to use stochastic simulation techniques, since in typical cases the integral in Eq. (1.5) is either too complex to be analytically integrated or of too high a dimension to be treated with numerical quadrature [3]. Note that estimating the

model evidence (normalizing constant in the Bayes formulation) in a Bayesian model selection problem is analogous to estimating the probability of failure in an equivalent reliability problem, where both leading to evaluation of a multi-level integral [8]. MCMC is a powerful tool to draw random samples, from an arbitrary posterior distribution, for integration in a statistical setting. However, it often performs inefficient (due to the high rejection rate of the proposed candidates) when treating real-world problems, i.e. high-dimensional inference problems based on large amount of data samples or rare-event simulation problem in high-dimensional parameter space. To tackle these issues, typically arise in spatially-varying parameter estimation problems, a brief review of a recently proposed Bayesian Updating approach (called BUS) and its revisited formulation (called CBUS) will be presented.

1.2.3 Bayesian Updating Using Structural Reliability Methods

For reader's convenience, we briefly review the BUS formulation, given in [11]. This approach is considered as an enhancement of the classical rejection sampling algorithms that builds up an analogy between the Bayesian updating problems and the structural reliability problems, thereby allowing subset simulation (SS), as a well-known robust and efficient rare-event sampler, to be applied to the former [12]. Subset simulation is of particular interest, since it is shown to be a robust algorithm while providing us a significant saving in the number of required simulations to achieve a given estimation accuracy. Briefly stated, SS is sustainable for high-dimensional problems due to the use of independent-component MCMC algorithm, it is robust to ergodic problem due to the multi-chain strategy adopted in it, and moreover, it does not suffer from the so called 'burn in' problem that is associated to the convergence of the Markov chains. Considering these desirable features, SS is considered as a good alternative (among different reliability methods) that, when it is utilized in the context of Bayesian updating problems, it enables us to circumvent the robustness and efficiency issues that arise in high-dimensional Bayesian updating problems based on a large set of data samples. This will be followed by studying the theory of a recently proposed revisited formulation of the original BUS, called Canonical BUS, and its desirable features [12]. For notation simplicity in the Bayesian Updating, we use $q(\boldsymbol{\theta})$ to denote the prior distribution $p\left(\boldsymbol{\theta}\middle|\mathcal{M}\right)$, $L(\boldsymbol{\theta})$ to denote the likelihood function $p\left(\mathcal{D}\middle|\boldsymbol{\theta},\mathcal{M}\right)$ and $p_D(\boldsymbol{\theta})$ to denote the posterior distribution $p\left(\boldsymbol{\theta}\middle|\mathcal{D},\mathcal{M}\right)$. Also, we replace the normalizing constant (or model evidence) $p\left(\mathcal{D}\middle|\mathcal{M}\right)$ by P_D. The BUS is an enhanced rejection algorithm, for which (similar to any rejection sampling technique) the following inequality condition should be fulfilled for all values of the parameter vector $\boldsymbol{\theta}$

$$cL(\boldsymbol{\theta}) < 1 \tag{1.6}$$

c is called the *likelihood multiplier* (or multiplier). Then, samples $\boldsymbol{\Theta}$ distributed as the posterior distribution $P_D(\boldsymbol{\theta}) \propto L(\boldsymbol{\theta})\, q(\boldsymbol{\theta})$ can be generated through the conventional rejection principle, described in Table 1.1. Note that usually the prior distribution $q(\boldsymbol{\theta})$ is chosen from standard class of distributions, thus, generating i.i.d. samples from the prior PDF can be done efficiently by utilizing the available algorithms. The candidates are proposed based on the prior PDF $q(\boldsymbol{\theta})$ whereas the accept/reject decision depends on the value of likelihood function $L(\boldsymbol{\theta})$. This approach, however, typically leads to a high rejection rate and poor efficiency, since usually the main support regions of the prior are very different from that of the likelihood function [1]. Strategies, similar to simulated annealing, have been proposed in order to break down the original difficult problem into a sequence of more manageable problems, with fewer amounts of data [14].

Table 1.1 Standard rejection principle algorithm

Proposal candidate $(\boldsymbol{\Theta}, U)$
Generate U sample from uniform distribution on $[0,1]$: $u \sim \mathcal{U}(0,1)$
Generate $\boldsymbol{\Theta}$ i.i.d. samples from the prior PDF $q(\boldsymbol{\theta})$: $\theta \sim q(0,1)$
Accept the proposal
IF $cL(\boldsymbol{\theta}) - U > 0$
Reject the proposal
ELSEIF $cL(\boldsymbol{\theta}) - U < 0$

1.2.3.1 Using Subset Simulation Under BUS Formulation

Recognizing the high rejection rate when rejection principle is directly applied to typical Bayesian problems, the BUS formulation enables us to generalize the rejection principle such that the posterior samples do not require to be drawn directly from a standard rejection algorithm [12]. Instead the rejection principle can be utilized in conjunction with a rare-event sampler, such as SS, that is capable of adaptively generating samples from the frequent region (safe region in reliability context) to the rare region (failure region in reliability context). Thus, the Bayesian updating problem for parameter vector $\boldsymbol{\theta}$ inference is converted into an equivalent reliability problem (more specifically probabilistic failure analysis problem) with uncertain parameters denoted by $(\boldsymbol{\theta}, U)$. $\boldsymbol{\theta}$ and U are independent random variables drawn from prior PDF and uniform distribution, respectively. The'failure event' is defined as

$$F = \{U < cL(\boldsymbol{\theta})\} \tag{1.7}$$

Now suppose that (by the use of a rare-event sampler) we obtain a failure sample $(\boldsymbol{\Theta}', U')$ that is jointly distributed as $q(\boldsymbol{\theta}) I(0 < u < 1)$ and conditional on the failure event F, then the corresponding distribution is given by

$$p_{\boldsymbol{\Theta}', U'}(\boldsymbol{\theta}, \mathrm{u}) = \frac{q(\boldsymbol{\theta}) I(0 < u < 1) I(u < cL(\boldsymbol{\theta}))}{P_F} \tag{1.8}$$

where $I(.)$ is the indicator function, which has value of 1 if its argument is true and zero otherwise. The normalizing constant P_F (failure probability of the equivalent reliability problem), is given by

$$P_F = \int\int q(\boldsymbol{\theta}) I(0 < u < 1) I(u < cL(\boldsymbol{\theta})) \, \mathrm{d}\boldsymbol{\theta} \, \mathrm{d}u \tag{1.9}$$

Then the marginal PDF of $\boldsymbol{\Theta}$, generated by the algorithm in Table 1.1, can be obtained by integrating out the uncertainty of U,

$$p_{\boldsymbol{\Theta}'}(\boldsymbol{\theta}) = \int_0^1 p_{\boldsymbol{\Theta}', U'}(\boldsymbol{\theta}, \mathrm{u}) \; \mathrm{d}u = {P_F}^{-1} q(\boldsymbol{\theta}) \int_0^1 I(u < cL(\boldsymbol{\theta})) \, \mathrm{d}u \tag{1.10}$$

It is clear that for an admissible c value ($cL(\boldsymbol{\theta}) < 1$), the Eq. (1.10) becomes identical to the posterior PDF $p_D(\boldsymbol{\theta})$.

$$p_{\boldsymbol{\Theta}'}(\boldsymbol{\theta}) = {P_F}^{-1} q(\boldsymbol{\theta}) \; cL(\boldsymbol{\theta}) = c p_D(\boldsymbol{\theta}) \tag{1.11}$$

Therefore, to be able to generate $\boldsymbol{\Theta}$ samples that are correctly distributed as the posterior distribution, BUS requires the selection of the multiplier value c, prior to the start of the SS algorithm. According to Eq. (1.6), an admissible multiplier value needs to fulfill the following condition

$$c < c_{\max} = [\max_{\boldsymbol{\theta}} L(\boldsymbol{\theta})]^{-1} \tag{1.12}$$

However, since $c_{\max}$ is not known a priori, selection of proper value for c is not always a trivial task. As discussed in [12], an inadmissible (too large) c value introduces bias since the resulting distribution of the failure samples $\boldsymbol{\Theta}$ is truncated to the prior, in the regions of the parameter space that the inequality (1.12) is violated, $B = \{\boldsymbol{\theta} \in R^n : cL(\boldsymbol{\theta}) > 1\}$.

$$p_{\boldsymbol{\Theta}'}(\boldsymbol{\theta}) = \begin{cases} {P_F}^{-1} q(\boldsymbol{\theta}) \displaystyle\int_0^1 I(u < cL(\boldsymbol{\theta})) \, \mathrm{d}u = {P_F}^{-1} q(\boldsymbol{\theta}) \propto q(\boldsymbol{\theta}) & \boldsymbol{\theta} \in B \\ {P_F}^{-1} q(\boldsymbol{\theta}) \displaystyle\int_0^1 I(u < cL(\boldsymbol{\theta})) \, \mathrm{d}u = {P_F}^{-1} q(\boldsymbol{\theta}) \, cL(\boldsymbol{\theta}) \propto p_D(\boldsymbol{\theta}) & \boldsymbol{\theta} \notin B \end{cases} \tag{1.13}$$

On the other side, the acceptance rate of the rejection principle is proportional to the multiplier value (the proof can be shown by integrating the Eq. (1.10) and noting that the integral on the LHS is equal to one).

$$P_{\text{acc.}} = P_F = cP_D \tag{1.14}$$

Therefore, larger values of c is desirable in the sense of computational efficiency of the Monte-Carlo based rejection approaches where, on the other side, c values larger than $c_{\max}$ introduce bias. This shows how the prudent choice of the likelihood multiplier c can affect the correctness and efficiency of BUS, which is not always a trivial task.

1.2.3.2 Using Subset Simulation Under Canonical BUS Formulation

In view of the choice of the '*likelihood multiplier*', a revisited formulation of the original BUS, which isolates the effect of the multiplier in a fundamental manner, has been presented in [12]. This improved formulation is called Canonical BUS. Canonical BUS provides a fundamental understanding of the multiplier choice, see [12], despite that the modification consists of an apparently slight change in the definition of the SS driving variable. The modification is based on the reformulating of the failure/rare event, as follows,

$$F = \left\{ \ln \left[\frac{L(\boldsymbol{\theta})}{U} \right] > -\ln c \right\} \tag{1.15}$$

Then, $\mathrm{Y} = \ln \left[\frac{L(\boldsymbol{\theta})}{U} \right]$ can be considered as the new driving variable in SS and the target failure event is redefined as

$$F = \{\mathrm{Y} > b\} \tag{1.16}$$

where the new threshold level is $b = -\ln c$. According to Eq. (1.12), the maximum admissible value for the multiplier is $[\max_{\boldsymbol{\theta}} L(\boldsymbol{\theta})]^{-1}$, and correspondingly, the minimum value of b, beyond which the failure samples settle at posterior PDF, is

$$b_{\min} = -\ln c_{\max} = \ln \left[\max_{\boldsymbol{\theta}} L(\boldsymbol{\theta})\right]^{-1} \tag{1.17}$$

Considered as the distinct feature of CBUS formulation, the (unknown) likelihood multiplier does not affect the SS driving variable Y but only the target threshold $b_{\min}$, and therefore, one does not need the value of $b_{\min}$ to be able to start the SS algorithm. Instead, one can simply perform SS until the threshold level passes $b_{\min}$, where fulfillment of this condition can be verified by looking at the characteristic behaviour of the CCDF (Complementary Cumulative Distribution Function) of the driving variable Y, i.e. $P(Y > b)$.

Considering an admissible value for b, then according to Eq. (1.11), the samples conditional on the fail/rare event $\{Y > b\}$ are distributed as the posterior distribution PDF, $P_D(\boldsymbol{\theta})$. Consequently, the CCDF of the Y becomes equal to the failure probability of the equivalent reliability problem (in the context of CBUS)

$$\begin{aligned} P_F = P(Y > b) &= \int\int q(\boldsymbol{\theta})\, I(0 < u < 1)\, I\left(\ln\left[\tfrac{L(\boldsymbol{\theta})}{U}\right] < b\right) \mathrm{d}\boldsymbol{\theta}\, \mathrm{d}u \\ &= \int q(\boldsymbol{\theta}) \int_0^1 I\left(u < e^{-b} L(\boldsymbol{\theta})\right) \mathrm{d}u \mathrm{d}\boldsymbol{\theta} = e^{-b} \int q(\boldsymbol{\theta})\, L(\boldsymbol{\theta})\, \mathrm{d}\boldsymbol{\theta} \end{aligned} \tag{1.18a, b}$$

where, according to Eq. (1.2), model evidence P_D is the last integral in Eq. (1.18a, b). Consequently, P_D is obtained as a by product, $P_D = e^{-b} P(Y > b)$, when the threshold level in SS has passed $b_{\min}$ (Note that $\int_0^1 I\left(u < e^{-b} L(\boldsymbol{\theta})\right) \mathrm{d}u = e^{-b} L(\boldsymbol{\theta})$ since $b > b_{\min}$). In order to verify that $b_{\min}$ is passed, one can check the trend of $P(Y > b)$ versus b. $P(Y > b)$ is a monotonically decreasing function that experiences different characteristics on two regimes of b. When $b < b_{\min}$, it decreases smoothly, where it starts to decrease exponentially $P_D e^{-b}$ (w.r.t. b), when $b_{\min}$ is passed. With similar argument, $V(b) = \ln(P(Y > b)) + b$, start with a zero slope at the left tail of CCDF, going into a transition and then settles at $\ln P_D$ after passing $b_{\min}$. This property provides us a stopping criteria to stop the SS and collect the failure samples that are distributed

correctly as the posterior PDF. Finally, it is worth mentioning that since the sample correlation tends to increase with the simulation level, in SS, there is no need to perform more simulation levels than it is required to pass $b_{\min}$. This will be discussed more in the studied numerical example. In the following sections, the performance of CBUS has been investigated in our real-world application of interest, originated from railway mechanics.

1.3 Ballast Identification Problem in Railway Mechanics

During the last two decades, much attention has been paid to various vibration problems associated with railways—including railway bridges [15] and railway ballasted tracks, see [16–18]. Sleepers are considered as fundamental parts of the ballasted track that are used to maintain the gauge between the two rails and to transmit the wheel/rail contact loads from a passing train down to the ballast, see Fig. 1.1. Current sleeper design is based on some simplifications considered in the guidelines, such as UIC leaflet [20, 21] or European standards [21]. One example of these simplifications in the design analysis of the sleepers is how the distribution of sleeper support is accounted for. When the ballast under a sleeper is damaged, the stiffness that it should provide to support the sleeper is reduced and the dynamic behaviour of the sleeper changes. The embedding ballast conditions of railway sleepers seemingly vary randomly from site to site [22] and the sleeper-ballast interaction is neither uniformly distributed nor fixed. However, guidelines consider a uniform distribution of ballast stiffness, either along the complete length of the sleeper or limited to the rail seat.

These simplifications are used in combination with traditional safety factors that, according to [23], are more based on experience rather than on theory. This may explain the difference in results when comparing sleeper responses either calculated according to different sleeper design guidelines or from in-field studies. In this regard, the corresponding safety factors need to be calibrated based on the new conditions, including both higher axle loads and higher speeds, compared to those treated by the current guidelines. Thus, it is of particular importance to improve our knowledge about spatial variation of the ballast stiffness-within a track FE model-based on in-field experiments and to use such valid predictive models for better understanding of sleeper dynamics.

1.3.1 Finite Element Model of the Railway Track

The considered track consists of 20 bays with equal length where the sleeper in bay no. 10 is of particular interest, i.e. the one we are interested to characterize its interacting force with the underlying ballast through experimental measurement, see Fig. 1.2. The time response is simulated using an in-house MATLAB code, called DIFF, developed in CHARMEC railway centre [24], for finite element dynamic analysis of train/track systems. The input parameters of the used track model in DIFF corresponds to UIC rail and rail pad with damping $c_{\mathrm{p}} = 12$ kNs/N and stiffness $k_{\mathrm{p}} = 88$ MN/m. The rail is modelled by eight Rayleigh-Timoshenko beam elements in each of the sleeper bays and the sleepers are modelled using Euler-Bernoulli beam elements. The ballast is modelled as viscously damped Winkler foundation, with total stiffness and damping of $k_{\mathrm{b}} = 186$ [MN/m] and $\mathrm{c_b} = 165$ [kNs/m] [13].

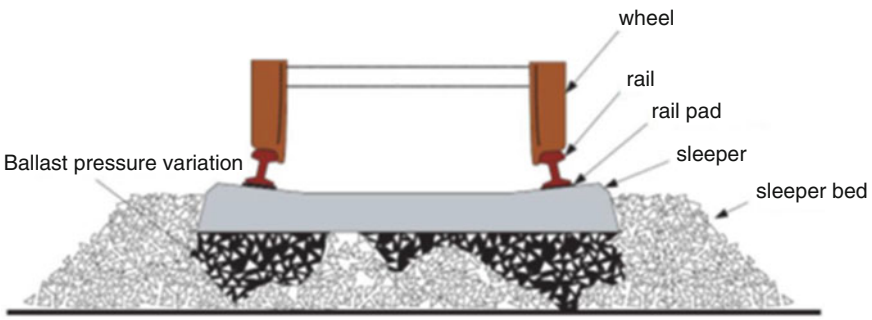

Fig. 1.1 Example of variation in stiffness under a sleeper due to ballast distribution change, Figure from [19]. Due to different loading condition, poor maintenance of sleeper or bad quality of ballast, a random load distribution along the sleeper-ballast interface may occur. This might result in a fully or partially hanging sleeper in which the sleeper hangs in the rails

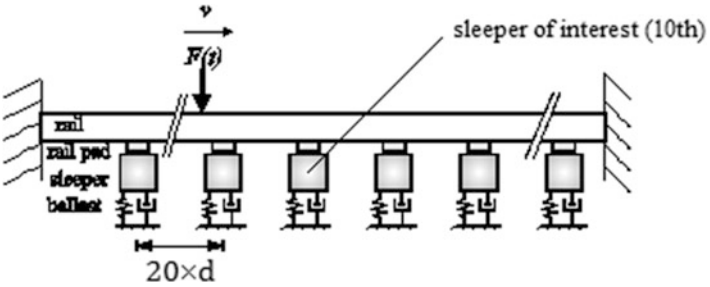

Fig. 1.2 The track consists of 20 bays with equal length. The sleeper in bay no. 10 is hanging before the train passage. The rail is modelled by eight Rayleigh-Timoshenko beam elements in each of the sleeper bays. The ballast bed, modeled as a viscously damped Winkler foundation, are described as $k_{bi} = 186$ [MN/m] and $c_{bi} = 165$ [kNs/m] while the pad is modeled as a spring and a viscous damper in parallel, i.e. indicated as $k_p = 88$ [MN/m] and $c_p = 12$ [kNs/m]. Track is subjected to a time-varying moving load

Fig. 1.3 The prescribed load time history applied to the rail at the passage of the center sleeper. At all other times $F = 125$ kN

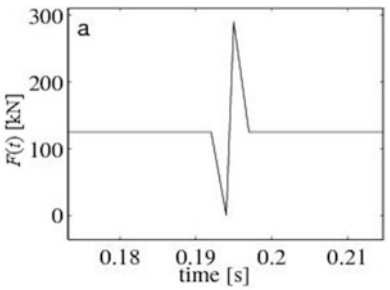

An idealized train running on a flexible railway track structure, at a constant cruising speed is considered. The selected train speed and the axle load are equal to 120 km/h and 125 kN, respectively. Input load affecting a railway sleeper depend on the traffic and the track conditions, which can be probably best seen as stochastic. However, this study focus on the stochastic properties of the embedding only and one representative deterministic load history is used for all analyses. The loading on the track is dynamic because of the moving train, but also as a consequence of irregularities present on the rails and on the wheels. To account for the influence of a wheel/rail irregularity, an impact load is superimposed on the static wheel load at the instant when the wheel load is just above the sleeper of interest. The magnitude of the impact load is set to 295 kN, chosen according to maximum wheel-flat load allowed on Swedish railway track [24], see Fig. 1.3.

1.3.2 Spatial Discretization of Ballast Bed Along the Sleeper

As mentioned before, in a spatially-varying estimation problem we first need to discretize the target field and represent the parameter field in a finite dimensional parameter subspace, before performing the model calibration. Based on a previous study, presented in [13], the minimum number of sensors required to capture the embedding stiffness field is equal to 32. According to that study, the ballast under the sleeper of interest, in bay number ten, is modelled by 32 elements and, for the rest of other 19 bays, 10 elements are considered for the ballast along the length of sleepers. Since the variation of the parameter field is not known a priori, four different conditions (model classes with different level of model complexity) are considered for the ballast bed distribution along the sleeper in bay number 10, as shown in Fig. 1.4.

A parabolic ballast bed modulus has been used as the mean value condition where the ballast is mostly distributed under the rail seats. This is the likely ballast condition when the track is either newly built or after performing the regular tamping operation on the ballast [25]. The stochastic ballast bed condition is modelled by four model classes, shown in Fig. 1.4, where their parameters are supposed to be identified based on simulated/real data.

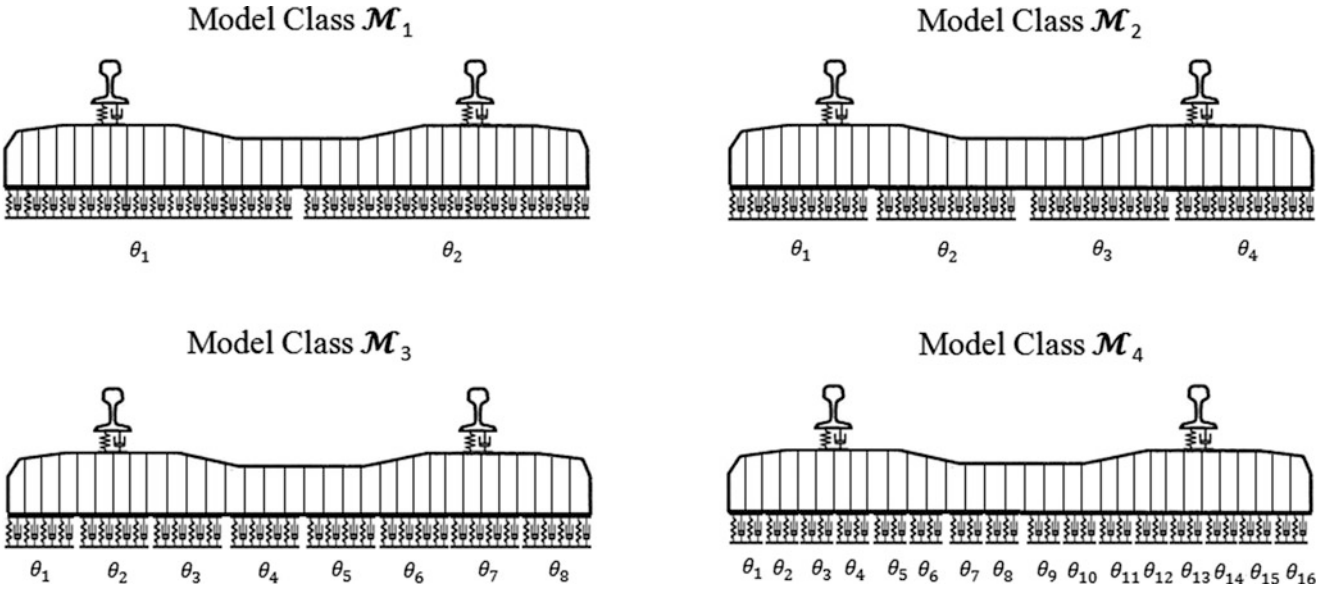

Fig. 1.4 Four candidate model classes for representing the stochastic unknown ballast bed condition under the sleeper of interest in bay number 10. The continuous Winkler foundation is discretised into 32 elements, where different model classes can capture different correlation/variation of the ballast stiffness parameter field, e.g. model class $\mathcal{M}_1$ is suitable when the ballast is smoothly distributed meanwhile model class $\mathcal{M}_4$ is capable of capturing more complex ballast bed condition. As shown above, the sleeper of interest, in bay number 10, is composed of 32 Euler-Bernoulli elements, independent of the model we use to model the ballast bed

1.4 Bayesian Updating Based on Simulated Data

1.4.1 Simulated Structure and Simulated Responses

It should be noted first that in the following sections we use normalized standard uncertain values, as suggested in [11]. In this regard, our prior knowledge about the mean value μ_k and standard deviation σ_k of the ballast, see [13], is being used to transform the stochastic random variable into the standard normal variable space, as follows

$$k_i^N = \frac{k_i - \mu_k}{\sigma_k} \tag{1.19}$$

where note that k_i's are defined in physical parameter space and the k_i^N's are the standard normal stochastic parameters. According to our prior knowledge [13], the mean and standard deviation of the ballast global stiffness are considered as $\mu = 186$ [MN/m] and $\sigma = 22$ [MN/m], respectively. Note that the viscous properties of the ballast is assumed to be statistically dependent on the stiffness stochastic parameters, therefore, only the stiffness parameters are considered as independent stochastic parameters that we aim to identify. According to [25], one likely scenario for the ballast distribution along the sleeper of interest (where the ballast is mostly distributed around the rail-seat and less in the centre of the sleeper) are considered for generating the pseudo-data $\mathcal{D}$. The DIFF code is used to simulate the described moving load problem and to obtain the response time history. The normalized ballast stiffness parameters are considered as $k_i^N = -1$ for $i = 9, \ldots, 24$ and $k_i^N = 1$ for $i = 1, \ldots, 8$ and $i = 25, \ldots, 32$. To simulate the measurement noise, a small amount of Gaussian white noise is added to each channel of generated data, for each measurement sample, which is equal to about 5 % of the root-mean-square values of the signal for each channel.

1.4.2 Measure of Data Fit

Four model classes, shown in Fig. 1.4, are considered for system identification. These are used to generate the prediction of the observables, $y_t^{(j)}, j = 1, \ldots, N_d, t = 1, \ldots, N_t$ for $N_d = 32$ channels of $N_t = 51$ time samples at a time step size of $\Delta t = 0.001$ s. The unknown parameter vector $\boldsymbol{\theta}$ is associated with the ballast bed, which is of different size in the four different model classes, shown in Fig. 1.4. The parameter space size is equal to 2, 4, 8 and 16 for $\mathscr{M}_1$, $\mathscr{M}_2$, $\mathscr{M}_3$ and $\mathscr{M}_4$, respectively. The prediction error is defined as the deviation of the predicted response (predicted by $\mathscr{M}_1$, $\mathscr{M}_2$, $\mathscr{M}_3$ and $\mathscr{M}_4$) and the pseudo-data (generated based on the parameter realizations, in Sect. 1.4.1, with a 32-parameter model). Based on the Principle of Maximum Information Entropy, the prediction error is taken as Gaussian, with zero mean and equal variance for each individual channel (equal to the noise variance of the corresponding channel). The likelihood function is

$$L(\boldsymbol{\theta}) = L\left(\boldsymbol{\theta}\middle|\mathcal{D}, \mathcal{M}\right) = \prod_{i=1}^{N_d}\prod_{t=1}^{N_t} \frac{1}{\sqrt{2\pi\sigma_j^2}} \exp\left(-\frac{1}{2}\left(\frac{y_t^{(j)} - \widehat{y}_t^{(j)}(\boldsymbol{\theta})}{\sigma_j}\right)^2\right) \tag{1.20}$$

where $\hat{y}_t^{(j)}(\boldsymbol{\theta})$ is the measured (pseudo) data in channel j at time sample t. The prior PDFs of the standard normal variables are assumed to have zero mean with standard deviation 1, for all 32 unknown variables.

1.4.3 Bayesian Updating Using Force-Cell Response Data

Results for Bayesian updating based on pseudo-data $\mathcal{D}$ is performed, using CBUS. For the subset simulation settings, the number of samples per level is considered to be equal to $N = 5000$ with level probability $p_0 = 0.1$, where the number of required levels to reach the posterior, by updating the prior, varies between 6 and 36 levels for different models ($\mathscr{M}_1$, $\mathscr{M}_2$, $\mathscr{M}_3$ and $\mathscr{M}_4$). As explained in Sect. 1.3, CBUS predicts the properties of the log-evidence function where its characteristics provides us a stopping criterion, to assure that the obtained samples are correctly distributed as the posterior PDF. It was shown theoretically by Eqs. (1.11) and (1.18a, b), that when the threshold variable of the highest level pass $b_{\min}$ value, the samples distributed as the posterior PDF and consequently the log-evidence function ($\ln(P(Y > b)) + b$ vs b) flattens out. The shape of the resulting simulated curves agrees with the characteristic trend predicted by the theory, expecting that there is a transition from a linearly increasing function to a horizontal line with zero slope. This characteristic is shown in Fig. 1.5. Then the samples of $\boldsymbol{\theta}$ becomes identical to the target posterior distribution. However, due the increase of the samples correlation (due to the mechanism behind SS), their efficiency will deteriorates as the simulation level ascends during the SS run. Those samples at higher levels ($b_0^{(i)} > b_{\min}$) can still be used for statistical estimation but with lower efficiency. In this regard, once we pass the $b_{\min}$ (characterized by flattening of the log-evidence), it is better to stop the SS for the purpose of having less correlation in the posterior samples, and therefore, higher efficiency for future statistical estimation. Given pseudo-data $\mathcal{D}$, we expect $\mathscr{M}_1$ to give an inaccurate result due to poor modelling and $\mathscr{M}_3$ and $\mathscr{M}_4$ to be both too-complex over-parameterized with respect to the process that have generated the data. On the other hand, $\mathscr{M}_2$ is the model is identical to the underlying physical model that is used for pseudo-data $\mathcal{D}$ generation. This is consistence with the obtained results, presented in Fig. 1.5 and Table 1.2, showing that $\mathscr{M}_2$ is the most probable model, given $\mathcal{D}$ response data. The log-evidence that corresponds to $\mathscr{M}_1$ is comparably the smallest, due to the low-quality measure of data fit. As shown in Fig. 1.5, the log-evidence function for this model flattens at much lower values, compared to the others. On the other side, $\mathscr{M}_3$ and $\mathscr{M}_4$ are penalized due to redundant complexity so their log-evidence are smaller than the log-evidence of the $\mathscr{M}_2$ model.

Figure 1.6 shows how the samples in the parameter space gradually move from the prior distribution to the posterior. The increase of levels in SS algorithm is shown where the highest level is the one that the samples are distributed as the posterior. Convergence to the posterior is checked by flattening of the log-evidence curve, as it was shown in Fig. 1.5. We know that there is a modelling error when using model $\mathscr{M}_1$, and as expected, the optimal value for this model is not equal to the true value (true value for the ballast stiffness under the rail on both left and right sides is equal to $+1$), see Fig. 1.6. For models $\mathscr{M}_2$, $\mathscr{M}_3$ and $\mathscr{M}_4$, however, there is no modelling error and the optimum is equal to the true value. For this case also all the models are identifiable, although due to modelling error in $\mathscr{M}_1$ the optimum is not equal to the true value.

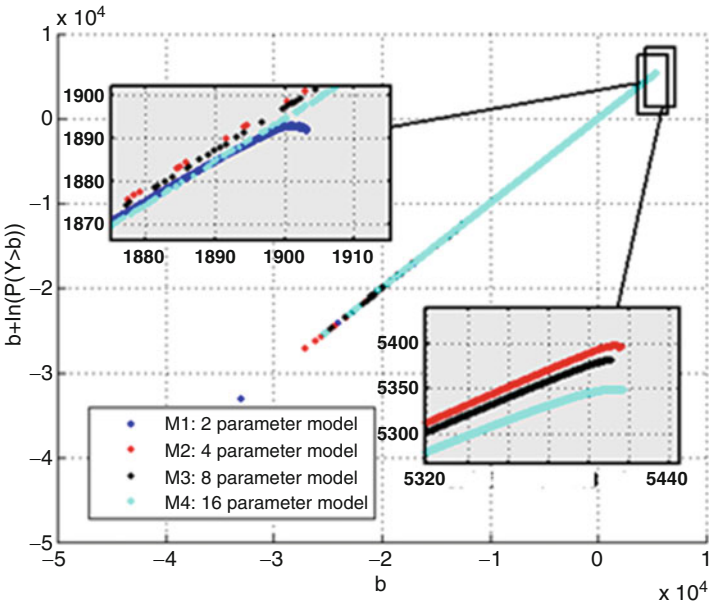

Fig. 1.5 The Log-evidence, flatten as the threshold passes $b_{\min}$. The results are shown for four the different model classes ($\mathscr{M}_1$, $\mathscr{M}_2$, $\mathscr{M}_3$ and $\mathscr{M}_4$) updating through $\mathcal{D}$ data. The CBUS algorithm stops at the level that Log-evidence starts to flatten

Table 1.2 Bayesian model selection results for force-cell data ($\mathcal{D}$). The Log-evidence is estimated CBUS algorithm stops at the level that Log-evidence starts to flatten

	Model selection given $\mathcal{D}$ data		
Model class	Log-evidence	Model probability	Model ranking
$\mathscr{M}_1$	1894	0.000	Rank 4
$\mathscr{M}_2$	**5400**	**≈0.999**	**Rank 1**
$\mathscr{M}_3$	5380	<0.001	Rank 2
$\mathscr{M}_4$	5350	<0.001	Rank 3

1.5 Concluding Remarks and Future Work

This paper addresses the computational and modelling issues that typically arise in spatially-varying parameter estimation based on indirect experimental data. Due to inappropriate discretization resolution of a parameter field, these problems typically suffer from either inaccurate approximation or ill-condition problem. Bayesian system identification approach is considered to systematically treat these problems. In such problems—with large number of uncertain parameters that are created due to discretization of the ballast random field—many of the MCMC techniques suffer from poor computational efficiency. To treat the modelling and computational issues, a recently proposed Bayesian approach (called Canonical BUS) has been utilized, its desirable features to treat FE model calibration problems with high-dimensional parameter space (such as in spatially-varying problems) has been discussed and performance of the method to treat real-world applications has been validated. The studied industrial problem originates from a railway mechanics application, where the spatial variation of ballast bed is of our particular interest.

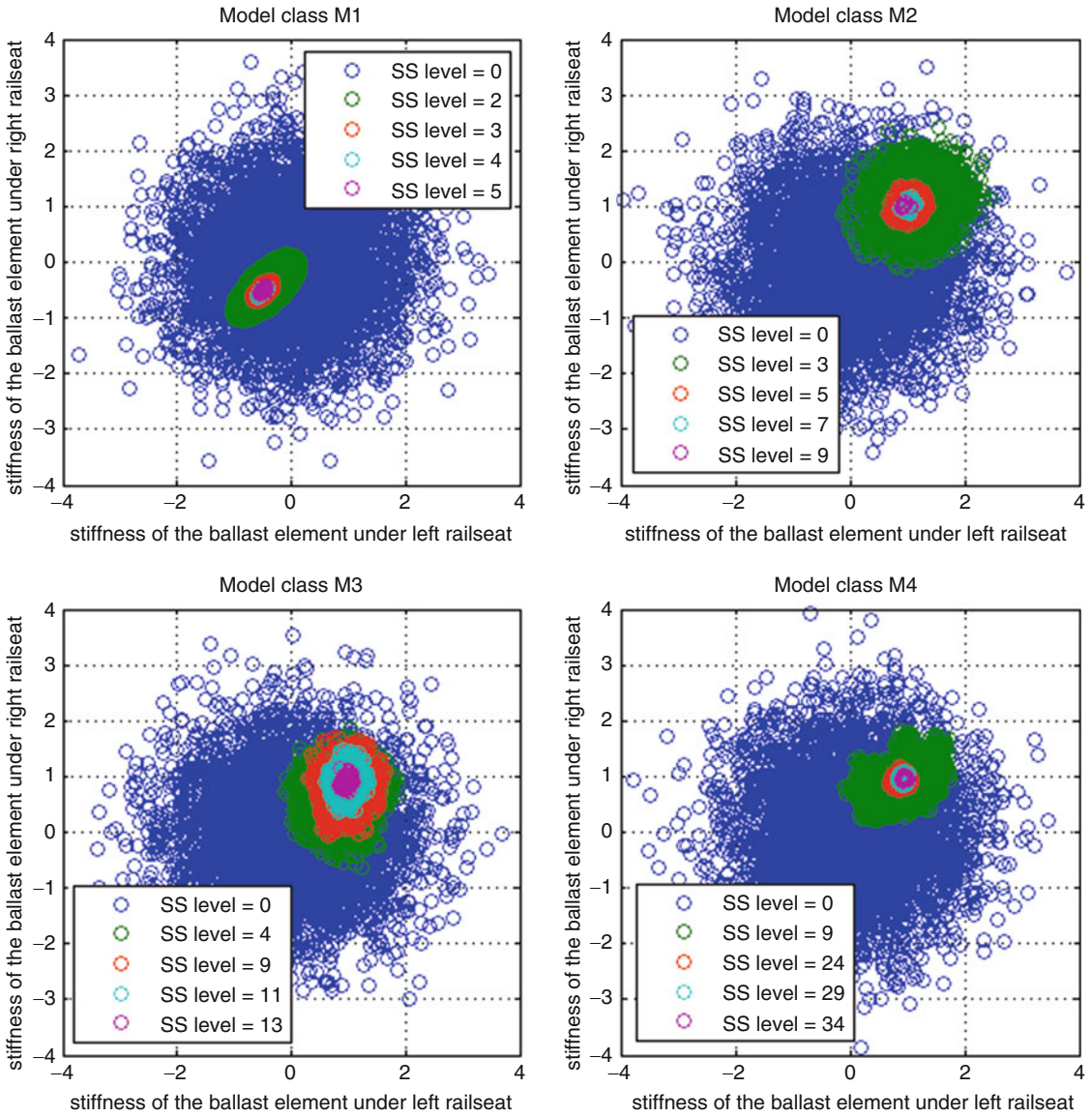

Fig. 1.6 Plots of the samples of the stiffness under the left rail seat (*horizontal axis*) and stiffness under right rail seat (*vertical axis*), in the standard normal space. The samples scattering belong to different 'levels' of the CBUS algorithm. Results, corresponding to four identification model classes based on force data $\mathcal{D}$

References

1. Beck, J.: Bayesian system identification based on probability logic. Struct. Control. Health Monit. **17**, 825–847 (2010)
2. Yuen, K.: Bayesian Methods for Structural Dynamics and Civil Engineering. Wiley, Hoboken (2010)
3. Muto, M., Beck, J.: Bayesian updating and model class Selection for hysteretic structural models using stochastic simulation. J. Vib. Control. **14**(1–2), 7–34 (2008)
4. Robert, C., Casella, G.: A short history of Markov Chain Monte Carlo subjective recollections from incomplete data. Stat. Sci. **26**(1), 102–115 (2011)
5. Spall, J.: Estimation via Markov Chain Monte Carlo. IEEE Control. Syst. **23**(2), 34–45 (2003)
6. Green, P., Worden, K.: Bayesian and MCMC methods for identifying nonlinear systems in the presence of uncertainty. Phil. Trans. R. Soc. A **373** (2015)
7. Au, S.-K., Beck, J.: Estimation of small failure probabilities in high dimensions by subset simulation. Probab. Eng. Mech. **16**(4), 263–277 (2001)
8. Au, S.-K., Wang, Y.: Engineering Risk Assessment with Subset Simulation. Wiley, Singapore (2014)
9. Webster, C., Zhang, G., Gunzburger, M.: An adaptive sparse-grid iterative ensemble Kalman filter approach for parameter field estimation. Int. J. Comput. Math. **91**(4), 798–817 (2014)

10. Koutsourelakis, P.: A multi-resolution, non-parametric, Bayesian framework for identification of spatially-varying model parameters. J. Comput. Phys. **228**, 6184–6211 (2009)
11. Straub, D., Papaioannou, I.: Bayesian updating with structural reliability methods. J. Eng. Mech. 04014134 (2015). doi:10.1061/(ASCE)EM.1943-7889.0000839
12. Au, S.-K., DiazDelaO, F.A., Yoshida, I.: Bayesian updating and model class selection with subset simulation. Probab. Eng. Mech. **16**(4), 263–277 (2016)
13. Lilja, J., Abrahamsson, T., Nielsen, J.: Experimental investigation of stochastic boundary conditions – planning a railway sleeper test. In: A Conference on Structural Dynamics (IMAC). Springer, Florida (2008)
14. Ching, J., Chen, Y.: Transitional Markov Chain Monte Carlo method for Bayesian model updating, model class selection, and model averaging. J. Eng. Mech. **133**(7), 816–832 (2007)
15. Cheng, Y., Au, F., Cheung, Y.: Vibration of railway bridges under a moving train by using bridge-track-vehicle element. Eng. Struct. **23**(12), 1597–1606 (2001)
16. Zhai, W., Wang, K., Lin, J.: Modelling and experiment of railway ballast vibrations. J. Sound Vib. **270**(4–5), 673–683 (2004)
17. Lam, H., Wong, M., Yang, Y.: A feasibility study on railway ballast damage detection utilizing measured vibration. Eng. Struct. **45**, 284–298 (2012)
18. Lam, H., Hu, Q., Wong, M.: The Bayesian methodology for the detection of railway ballast damage under a concrete sleeper. Eng. Struct. **81**, 289–301 (2014)
19. Kaewunruen, S., Remennikov, A.: Progressive failure of prestressed concrete sleepers under multiple high-intensity impact loads. Eng. Struct. **31**(10), 2460–2473 (2009)
20. Design of mono-bloc concrete sleepers. In: UIC leaflet 713 R, pp. 30 (2004)
21. European standard EN 13230:1:2002: Railway Applications-Track-Concrete Sleepers and Bearers, pp. 36 (2002)
22. Rahrovani, S.: Test data evaluation from field measurements of sleeper-ballast interface. Chalmers University of Technology, Goteborg (2010)
23. Buekett, J.: Concrete sleepers. In: Railway Industry Association, First Track Sector course, Warford, pp. 411–417 (1983)
24. Nielsen, J., Igeland, A.: Vertical dynamic interaction between train and track – influeince of wheel and track imperfections. J. Sound Vib. **187**(5), 825–839 (1995)
25. Bolmsvik, R., Nielsen, J., Singhal, A.: Guideline for design optimization and production of prestressed concrete railway sleepers, Chalmers University, Applied Mechanics, Goteborg, Research report 2011:5 (2011)

Chapter 2
Bayesian Modelling of Offshore Platforms

P.L. Green, U.T. Tygesen, and N. Stevanovic

Abstract This paper details a case study, where Bayesian methods are used to estimate the model parameters of an offshore platform. This first involves running a series of Finite Element simulations using the Ramboll Offshore Structural Analysis Programs (ROSAP)—developed by Ramboll Oil & Gas—thus establishing how the modal characteristics of an offshore structure model vary as a function of its material properties. Data based modelling techniques are then used to emulate the Finite Element model, as well as estimates of model error. The uncertainties associated with estimating the hyperparameters of the data based modelling techniques are then analysed utilising Markov chain Monte Carlo (MCMC) methods. The resulting analysis takes account of the uncertainties which arise from measurement noise, model error, model emulation and parameter estimation.

Keywords System identification • Model updating • Offshore platform • Gaussian process • Uncertainty quantification

2.1 Introduction

Ramboll Oil & Gas utilise bespoke Finite Element (FE) software [1] to estimate the fatigue damage present in offshore platforms. Before such an assessment can take place the parameters of the FE model are updated, using measurement data, in two phases. The first stage involves using measured modal data to update parameters which, for example, represent the stiffness or centre of gravity (COG) of the offshore structure. With the second stage, other key parameters are updated using measurements which relate wave loading to the stresses measured at certain points on the platform.

This paper is the starting point of a longer term project, which aims to quantify and propagate the uncertainties involved in both of these states of model updating. The current work is concerned with the situation where modal data is used to infer the COG of the platform. (This is necessary because, as a result of the accumulation of unregistered equipment and/or expansion projects, the COG is often difficult to measure accurately.) Specifically, it focuses on then scenario where a sparse set of measurements are available and, because of computational constraints, only a limited number of FE simulations are possible. It utilises the fundamental framework which, originally proposed in [2], will now be described within the context of the current problem.

The vector $\boldsymbol{x}_i$ is used to denote the ith measurement of the first ten natural frequencies of an offshore platform while z_i represents a corresponding measurement of the platform's COG (for now, in this preliminary work, only the vertical position of the COG will be considered). A total of n measurements are available. It is assumed that z_i and $\boldsymbol{x}_i$ are related by

$$z_i = y(\boldsymbol{x_i}) + \eta(\boldsymbol{x_i}) + \epsilon, \qquad \epsilon \sim \mathcal{N}(0, \lambda^{-1}), \qquad i = 1, \ldots, n \tag{2.1}$$

P.L. Green (✉)
Institute for Risk and Uncertainty, Centre for Engineering Sustainability, School of Engineering, University of Liverpool, Liverpool L69 3GQ, UK
e-mail: p.l.green@liverpool.ac.uk

U.T. Tygesen
Ramboll Oil & Gas, Willemoesgade 2, Esbjerg 6700, Denmark
e-mail: utt@ramboll.com

N. Stevanovic
Siemens Wind Power, Borupvej 16, Brande 7330, Denmark
e-mail: Nevena.stevanovic@siemens.com

S. Atamturktur et al. (eds.), *Model Validation and Uncertainty Quantification, Volume 3*, Conference Proceedings of the Society for Experimental Mechanics Series, DOI 10.1007/978-3-319-29754-5_2

where $y(\boldsymbol{x_i})$ is the output of the FE model, ϵ is measurement noise and η represents *model error*—the inevitable discrepancy between the response of the FE model and that of the real structure. The approach outlined in [2] uses data based modelling techniques—Gaussian processes (GPs) specifically[1]—to achieve two things. Firstly, they are used to interpolate between measurements of model error, thus providing an estimate of η in regions where measurements are unavailable. Secondly, they are used to emulate the expensive FE model, thus reducing the computational cost of the model updating procedure. The aim of this paper is to investigate whether, by applying the methods described in [2], it is possible to realise parameter estimates which are more accurate than those that can be realised simply by interpolating between available measurements.

The paper is organised as follows. A brief description of the FE simulations used in this paper are given in Sect. 2.2. The full model updating procedure is described in detail in Sect. 2.3 before results are presented and discussed in Sects. 2.4 and 2.5 respectively.

2.2 FE Model

The FE analysis was performed using the in-house Ramboll Oil & Gas software, ROSAP. The vast majority of all offshore jackets, topsides, offshore bridges and risers within the Danish oil and gas sector in the North Sea have been analysed and certified by use of the ROSAP. It is currently used to facilitate a large range of analyses including push-over analysis, ship impact analysis, deterministic/transient/spectral fatigue analysis as well as Risk- and Reliability based Inspection Planning software (RBI).

For the present study, a FE model of a typical offshore platform has been used as a basis for data generation. In this case the FE analysis has been used to compute the variation in the first ten natural frequencies of an offshore platform as a function of the vertical offset of its COG (Fig. 2.1). Typically, through model updating, the FE model would then be used to track how the COG changes with time (as a result of well intervention operations, for example). In the analysis described here it is shown how, through the addition of even a sparse number of measurements, this analysis can be greatly improved.

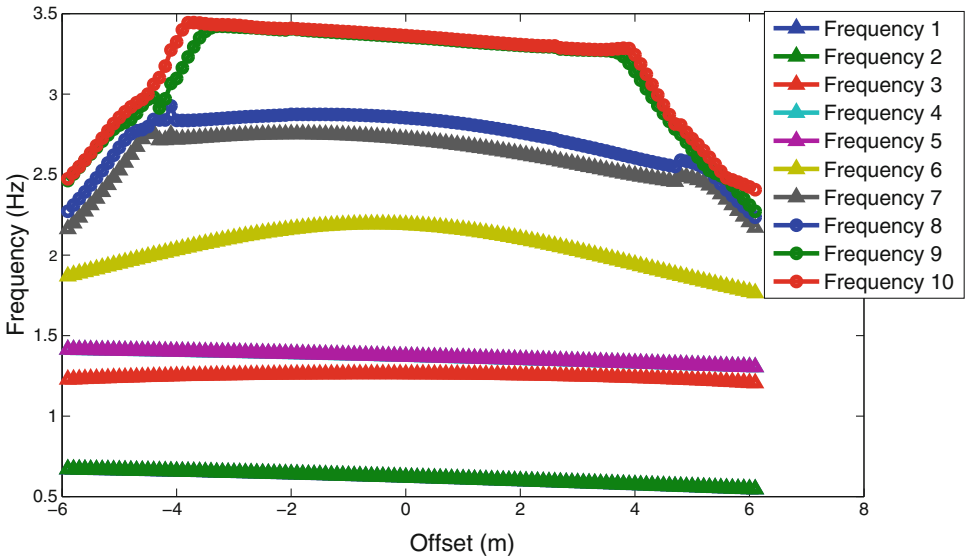

Fig. 2.1 Finite element results

[1] A detailed introduction to Gaussian processes is a little beyond the scope of this paper. For the interested reader, the books [3, 4] are recommended.

2.3 Bayesian Modelling

2.3.1 Available Data

It was found that the FE model predicted a 1–1 relationship between the first natural frequency of the platform and the offset of the COG (shown as blue dots in Fig. 2.2). As a result, for the remainder of this work, it will be assumed that measurements of the first natural frequency only are needed to predict the position of the COG. The frequencies and offset values that were investigated using the FE model are concatenated into the vectors $\boldsymbol{x'} = (x'_1 \quad \dots \quad x'_N)^T$ and $\boldsymbol{y} = (y(x'_1) \quad \dots \quad y(x'_N))^T$ respectively. This relationship between $\boldsymbol{x'}$ and $\boldsymbol{y}$ will be emulated by a GP with prior

$$p(\boldsymbol{y}) = \mathcal{N}(\boldsymbol{0}, \boldsymbol{K_1}) \tag{2.2}$$

where the ijth element of $\boldsymbol{K_1}$ is given by the kernel function

$$k_1(x'_i, x'_j) = \exp\left(-\frac{\alpha_1}{2}(x'_i - x'_j)^2\right) \tag{2.3}$$

where α_1 is a hyperparameter. The n measurements of the first natural frequency and COG offset, denoted $\boldsymbol{x} = (x_1 \quad \dots \quad x_n)^T$ and $\boldsymbol{z} = (z_1 \quad \dots \quad z_n)^T$, are shown as black circles in Fig. 2.2. These observations were created artificially, so that the true relationship between the first natural frequency of the platform and the COG offset could be observed (for validation purposes). The true relationship is shown as a red line in Fig. 2.2. The observations are samples from this true relationship, which have been corrupted with Gaussian noise whose precision, λ, was set equal to 10.

2.3.2 Model Error

With n measurements available, there are therefore n measurements of model error, denoted $\boldsymbol{\eta} = (\eta(x_1) \quad \dots \quad \eta(x_n))^T$. This relationship between input and model error will also be emulated by a GP, with prior:

$$p(\boldsymbol{\eta}) = p(\boldsymbol{0}, \boldsymbol{K_2}) \tag{2.4}$$

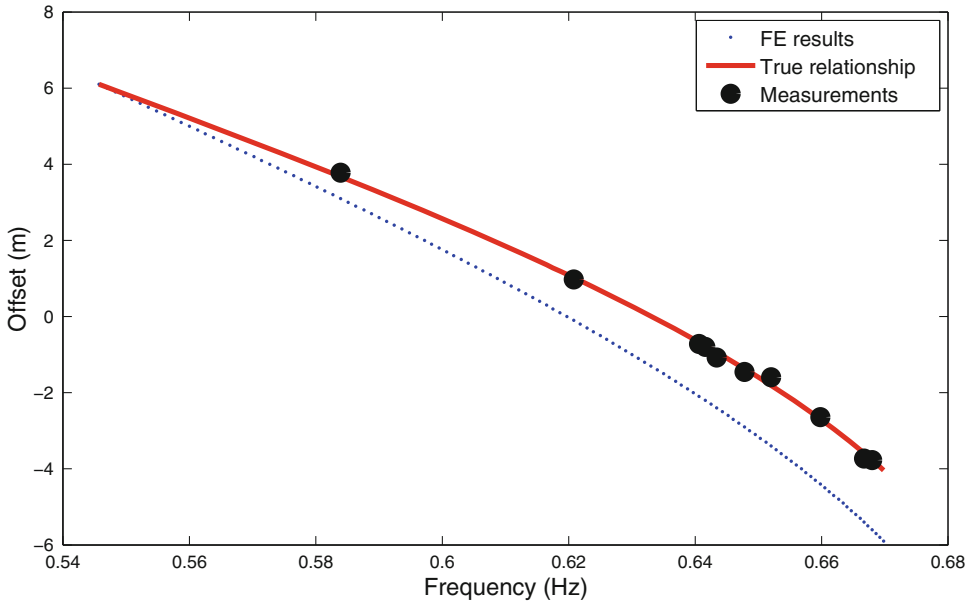

Fig. 2.2 Relation between the first natural frequency of an offshore platform and the vertical offset of its COG. *Blue dots* show results according to the FE model, *black dots* represent available measurement and the *red line* represents the true relationship

where the ijth element of $\boldsymbol{K_2}$ is given by the kernel function

$$k_2(x_i, x_j) = \exp\left(-\frac{\alpha_2}{2}(x_i - x_j)^2\right) \tag{2.5}$$

and α_2 is a second hyperparameter.

2.3.3 Predictions

Say a new frequency measurement, x^*, is obtained. The aim here is to predict the probability of

$$z^* = y(x^*) + \eta(x^*) + \epsilon, \tag{2.6}$$

given the data, $\boldsymbol{d} = (\boldsymbol{y}^T, \boldsymbol{z}^T)^T$. To do so, one can first derive the joint probability density function $p(\boldsymbol{d}, z^*)$ such that, by exploiting some useful properties of Gaussian distributions, it is then be possible to find the conditional distribution $p(z^*|\boldsymbol{d})$. Before proceeding, it is convenient to write $p(\boldsymbol{d})$ in the following form:

$$p(\boldsymbol{d}) = \mathcal{N}(\boldsymbol{0}, \boldsymbol{V_d}), \qquad \boldsymbol{V_d} = \begin{bmatrix} \boldsymbol{V}_1 & \boldsymbol{C} \\ \boldsymbol{C}^T & \boldsymbol{V_2} \end{bmatrix}. \tag{2.7}$$

The ijth element of $\boldsymbol{V_1}$ is given by

$$\mathrm{Cov}[y_i, y_j] = k_1(x_i', x_j') + \beta^{-1}\delta_{ij} \tag{2.8}$$

where β is a hyperparameter whose roll will be explained shortly. The ijth element of $\boldsymbol{C}$ is given by

$$\mathrm{Cov}\left[y_i, z_j\right] = \mathrm{Cov}\left[y(x_i'), y(x_j) + \eta(x_j) + \epsilon_j\right] = \mathrm{Cov}[y(x_i'), y(x_j)] = k_1(x_i', x_j), \tag{2.9}$$

and the ijth element of $\boldsymbol{V_2}$ is given by

$$\begin{aligned} \boldsymbol{V_2} = \mathrm{Cov}[z_i, z_j] &= \mathrm{Cov}[y(x_i) + \eta(x_i) + \epsilon_i, y(x_j) + \eta(x_j) + \epsilon_j] \\ &= \mathrm{Cov}[y(x_i), y(x_j)] + \mathrm{Cov}[\eta(x_i), \eta(x_j)] + \mathrm{Cov}[\epsilon_i, \epsilon_j] \\ &= k_1(x_i, x_j) + k_2(x_i, x_j) + \lambda^{-1}\delta_{ij}. \end{aligned} \tag{2.10}$$

Using a similar approach it can then be shown that

$$p(\boldsymbol{d}, z^*) = \mathcal{N}\left(\boldsymbol{0}, \begin{bmatrix} \boldsymbol{V_d} & \boldsymbol{a} \\ \boldsymbol{a}^T & c \end{bmatrix}\right), \qquad \boldsymbol{a} = \begin{pmatrix} \boldsymbol{a_1} \\ \boldsymbol{a_2} \end{pmatrix} \tag{2.11}$$

where the ith element of $\boldsymbol{a_1}$ is

$$\mathrm{Cov}[y_i, z^*] = k_1(x_i', x^*), \tag{2.12}$$

the ith element of $\boldsymbol{a_2}$ is

$$\mathrm{Cov}[z_i, z^*] = k_1(x_i, x^*) + k_2(x_i, x^*) \tag{2.13}$$

and

$$c = \mathrm{Var}[z^*] = k_1(x^*, x^*) + k_2(x^*, x^*) + \lambda^{-1}. \tag{2.14}$$

Table 2.1 Hyperparameter prior limits

Parameter	Lower limit	Upper limit
α_1	0	1×10^4
α_2	0	1×10^4
β	0	1×10^6

Using the generic properties of Gaussian distributions, the desired conditional distribution is then given by

$$p(z^*|\boldsymbol{d}) = \mathcal{N}(m, \sigma^2) \tag{2.15}$$

where

$$m = \boldsymbol{a}^T \boldsymbol{V_d}^{-1} \boldsymbol{d}, \qquad \sigma^2 = c - \boldsymbol{a}^T \boldsymbol{V_d}^{-1} \boldsymbol{a}. \tag{2.16}$$

2.3.4 *Hyperparameters*

The kernel functions were defined as

$$k_1(x_i, x_j) = \exp\left(-\frac{\alpha_1}{2}(x_i - x_j)^2\right), \qquad k_2(x_i, x_j) = \exp\left(-\frac{\alpha_2}{2}(x_i - x_j)^2\right) \tag{2.17}$$

where α_1 and α_2 are hyperparameters which require estimation. The third hyperparameter, β, is included in Eq. (2.8) simply because, if tuned appropriately, it can be used to avoid numerical errors when calculating the inverse of $\boldsymbol{V_d}$. The vector of hyperparameters which require estimation is therefore $\boldsymbol{\theta} = (\alpha_1 \quad \alpha_2 \quad \beta)^T$.

In the current work the authors endeavored to include hyperparameter uncertainty in the analysis. Bayes' theorem allows the probability of $\boldsymbol{\theta}$ given the data, $\boldsymbol{d}$, to be written as

$$p(\boldsymbol{\theta}|\boldsymbol{d}) \propto p(\boldsymbol{d}|\boldsymbol{\theta}) p(\boldsymbol{\theta}) \tag{2.18}$$

where $p(\boldsymbol{d}|\boldsymbol{\theta})$ is given by Eq. (2.7) and $p(\boldsymbol{\theta})$ was chosen to be a uniform distribution, whose limits are shown in Table 2.1. Samples from the posterior, $p(\boldsymbol{\theta}|\boldsymbol{d})$, were then generated using Markov chain Monte Carlo (MCMC). In this example, the authors used the Transitional MCMC algorithm [5], as it is suitable for parallelisation and can generate samples from distributions with complex geometries. A discussion of various MCMC methods, within the context of structural dynamics, can be found in [6].

2.4 Results

The resulting MCMC samples are shown in Fig. 2.3 while Fig. 2.4 shows the predictions made using the most probable estimates of the hyperparameters. It can be seen that, despite the model error present, the predicted relationship between the first natural frequency and the COG offset closely follows the true relationship.

Monte Carlo simulations were then used to propagate hyperparameter uncertainty into the offset predictions. This can be achieved using 'ancestral sampling', where one first generates a sample from $p(\boldsymbol{\theta}|\boldsymbol{d})$ before going on to generate a sample from $p(z^*|\boldsymbol{\theta}, \boldsymbol{d})$. This is possible in the current case as samples from $p(\boldsymbol{\theta}|\boldsymbol{d})$ have already been obtained using MCMC and $p(z^*|\boldsymbol{\theta}, \boldsymbol{d})$ is given by Eq. (2.15). The mean and variance of one's predictions can then be estimated using the resulting ensemble of predictions. The results of this analysis are shown in Fig. 2.5. It can be seen that, by accounting for this additional source of uncertainty, the confidence bounds have grown in the regions where little measurement data is available.

While these results are promising, one may question whether the additional complexity of this methodology is necessary—could similar results have been achieved if one simply interpolated through the available measurement data, $\boldsymbol{z}$? To that end, a GP with prior

$$p(\boldsymbol{z}) = \mathcal{N}(\boldsymbol{0}, \boldsymbol{K_3}), \tag{2.19}$$

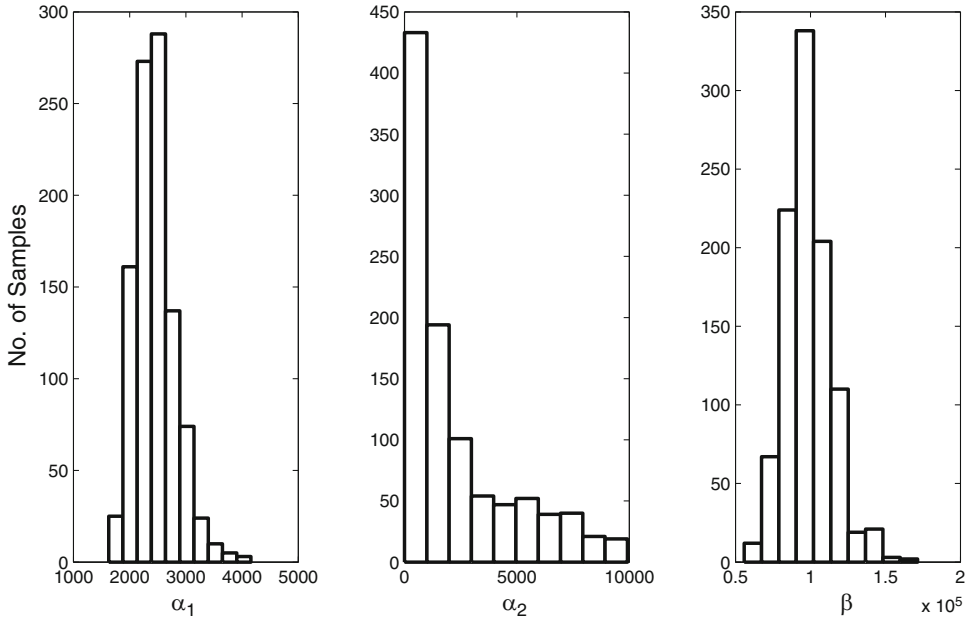

Fig. 2.3 MCMC samples from $p(\boldsymbol{\theta}|\boldsymbol{d})$

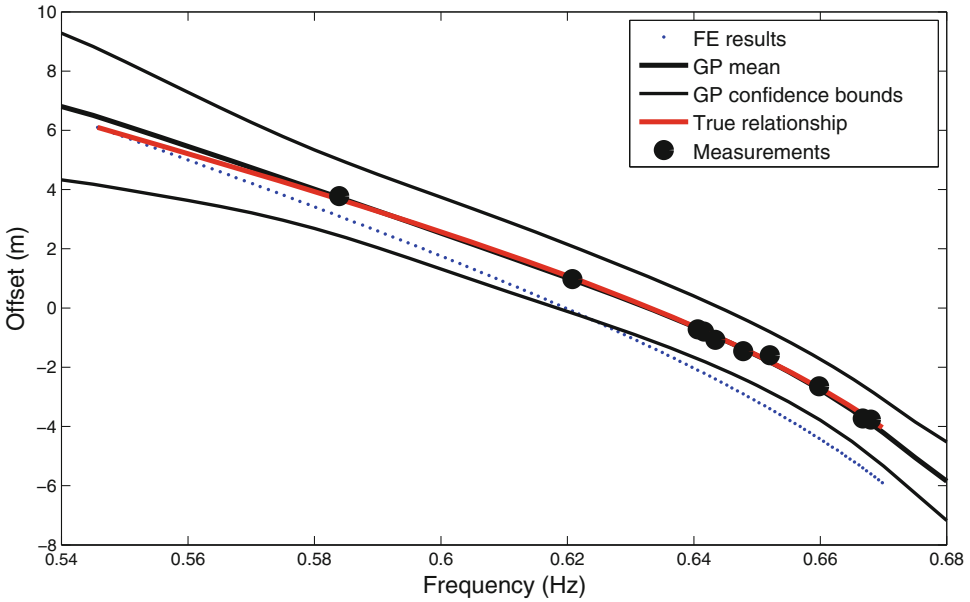

Fig. 2.4 Predictions made using the most probable hyperparameter estimates (with 3 σ confidence bounds)

where the (i,j) element of $\boldsymbol{K_3}$ is given by the kernel function

$$k_3(x_i,x_j) = \exp\left(-\frac{\alpha_3}{2}(x_i-x_j)^2\right) + \lambda^{-1}\delta_{ij}, \tag{2.20}$$

was used to interpolate between $\boldsymbol{z}$. To account for hyperparameter uncertainty, MCMC samples from $p(\alpha_3|\boldsymbol{z})$ were obtained using MCMC (Fig. 2.6). By, again, using Monte Carlo simulations to propagate the hyperparameter uncertainty into the predictions, the results shown in Fig. 2.7 were realised. It is clear that, by using the 'full' framework described in [2], far better predictions have been obtained.

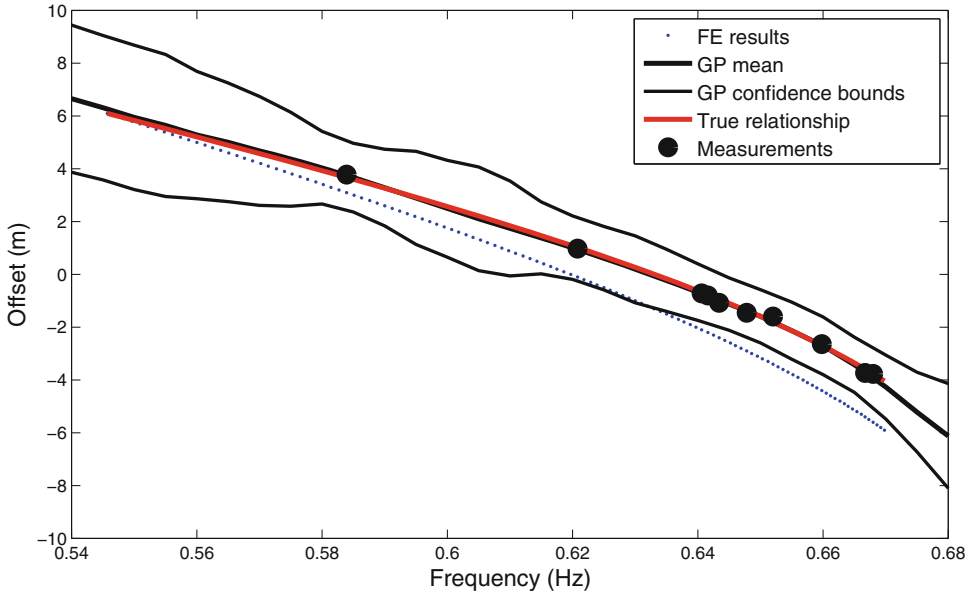

Fig. 2.5 Predictions made accounting for hyperparameter uncertainty (with 3 σ confidence bounds)

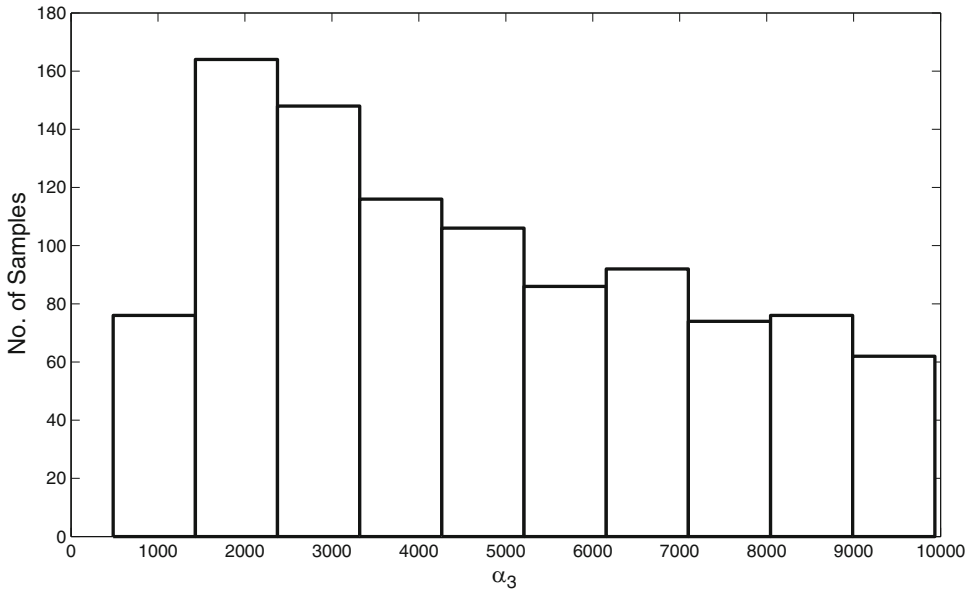

Fig. 2.6 MCMC samples from $p(\alpha_3|z)$

2.5 Conclusions

In this paper, the approach described in [2] was used to aid the model updating of a FE model of an offshore structure. This involved quantifying the uncertainties generated by model error, measurement noise and, through the use of MCMC sampling methods, hyperparameter uncertainty. It emphasises how, by utilising only a sparse set of measurements which are taken during different operational conditions, the accuracy of the updating procedure can be greatly improved.

While the current paper only addressed the updating of a single parameter of the FE model, the authors aim to use this methodology to update the full set of parameters utilised in the bespoke FE models employed by Ramboll Oil & Gas. It is hoped that, by 'compressing' the outputs of the FE model simulations using a Singular Value Decomposition (see [7] for more details), the computational cost of this approach should be kept relatively small.

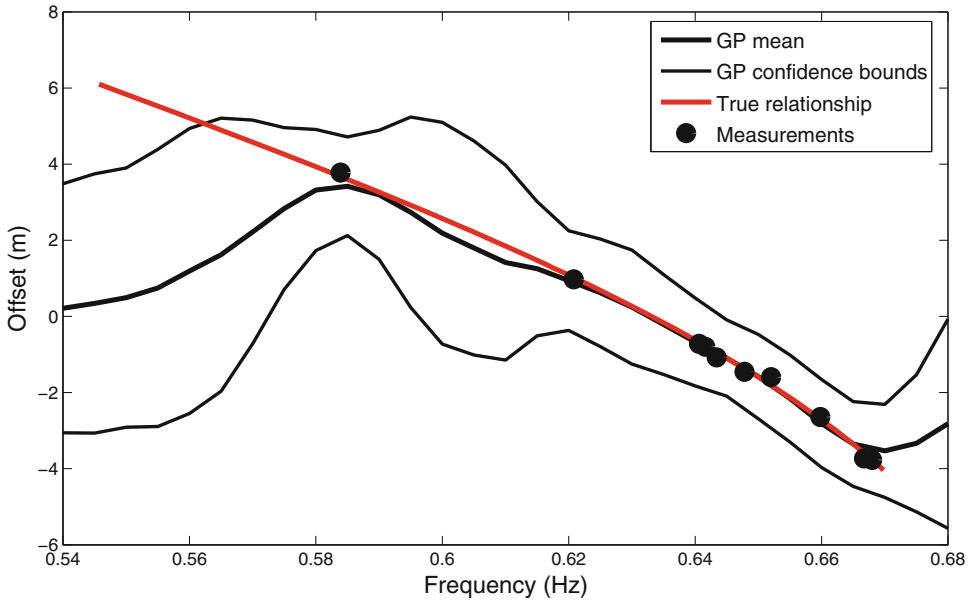

Fig. 2.7 Predictions made by simply interpolating through the available measurement data

References

1. Ramboll Oil & Gas: Ramboll Offshore Structural Analysis Programs (ROSAP). www.ramboll.com/oil-gas.
2. Kennedy, M.C., O'Hagan, A.: Bayesian calibration of computer models. J. R. Stat. Soc. **63**(3), 425–464 (2001)
3. Bishop, C.M.: Pattern Recognition and Machine Learning. Springer, Berlin (2006)
4. MacKay, D.J.C.: Information Theory, Inference and Learning Algorithms. Cambridge University Press, Cambridge (2003)
5. Ching, J., Chen, Y.C.: Transitional Markov chain Monte Carlo method for Bayesian model updating, model class selection, and model averaging. J. Eng. Mech. **133**(7), 816–832 (2007)
6. Green, P.L., Worden, K.: Bayesian and Markov chain Monte Carlo methods for identifying nonlinear systems in the presence of uncertainty. Philos. Trans. R. Soc. A **373**(2051), 20140405 (2015)
7. Higdon, D., Gattiker, J., Williams, B., Rightley, M.: Computer model calibration using high-dimensional output. J. Am. Stat. Assoc. **103**(482), 570–583 (2008)

Chapter 3
Bayesian Inference and RJMCMC in Structural Dynamics: On Experimental Data

D. Tiboaca, P.L. Green, R.J. Barthorpe, I. Antoniadou, and K. Worden

Abstract This paper is concerned with applying the Reversible Jump Markov Chain Monte Carlo (RJMCMC) algorithm on an MDOF system, within a Bayesian framework, in order to identify its parameters and do model selection simultaneously. Bayesian Inference has been widely used in the area of System Identification (SID) on issues of parameter estimation as well as model selection, due to its advantages of using prior knowledge and penalising model complexity, the Bayesian probability framework has been employed on issues of parameter estimation as well as model selection. Even though the posterior probabilities of parameters are often complex, the use of Markov Chain Monte Carlo (MCMC) sampling methods has made the application of the approach significantly more straightforward in structural dynamics. The most commonly applied MCMC sampling algorithm used within a Bayesian framework in the area of structural dynamics is probably the Metropolis-Hastings method. However, the MH algorithm cannot cover model selection in cases where competing model structures have different number of parameters, as it is not capable of moving between spaces of differing dimension. Hence, a new MCMC algorithm, the Reversible Jump Markov Chain Monte Carlo (RJMCMC), has surfaced in 1995. The RJMCMC sampling algorithm is capable of simultaneously covering both parameter estimation and model selection, while jumping between spaces in which the dimension of the parameter vector varies. Using a Bayesian approach, the RJMCMC method ensures that overfitting is prevented.

This work focuses on using the RJMCMC algorithm for System Identification (SID) on experimental time data gathered from an MDOF 'bookshelf' type structure. The major issue addressed is that of noise variance. Two models are used, the first one using a single noise variance for the entire structure and the second one employing three different noise variances for the three different levels of the structure. The results presented in the last section show the capabilities of the RJMCMC algorithm as a powerful tool in the SID of dynamical structures.

Keywords RJMCMC • Bayesian inference • Structural dynamics • MCMC • System identification

Nomenclature

$\boldsymbol{\theta}$	Vector of parameters
$\boldsymbol{\theta}'$	Proposed vector of parameters
$\boldsymbol{M}$	Vector of models
M	Model
$M^{(l)}$	Model $'l'$, $'l' = 1 \rightarrow L$
$\boldsymbol{\theta}^{(n)}$	Vector of parameters at $'n'$th iteration , $'n' = 1 \rightarrow N$ (for Metropolis-Hastings algorithm)
$\boldsymbol{\theta}^{(1)}$	Vector of parameters for model $M^{(1)}$
$\boldsymbol{\theta}^{(2)}$	Vector of parameters for model $M^{(2)}$
$\pi(\boldsymbol{\theta})$	Target PDF
$Q(\boldsymbol{\theta}'\|\boldsymbol{\theta})$	Proposal PDF
$T(\boldsymbol{\theta} \rightarrow \boldsymbol{\theta}')$	Transition function
$\alpha(\boldsymbol{\theta}'\|\boldsymbol{\theta})$	Acceptance probability
D	Measured data

D. Tiboaca (✉) • R.J. Barthorpe • I. Antoniadou • K. Worden
Dynamics Research Group, Department of Mechanical Engineering, The University of Sheffield, Mappin Street, Sheffield S1 3JD, UK
e-mail: daniela.tiboaca@sheffield.ac.uk

P.L. Green
Institute for Risk and Uncertainty, School of Engineering, University of Liverpool, Liverpool L69 3GQ, UK

S. Atamturktur et al. (eds.), *Model Validation and Uncertainty Quantification, Volume 3*, Conference Proceedings of the Society for Experimental Mechanics Series, DOI 10.1007/978-3-319-29754-5_3

$P(\boldsymbol{\theta}\,\vert D, M)$	Posterior distribution
$P(D\vert\boldsymbol{\theta}, M)$	Likelihood
$P(\boldsymbol{\theta}\,\vert M)$	Prior distribution
$P(D\vert M)$	Evidence term
m	Mass
c	Damping coefficient
k	Linear stiffness
θ	The linear stiffness parameter
$\theta_{(2)}^{(2)}$	The cubic stiffness parameter
$k_{(3)}^{(2)}$	Cubic stiffness for model $M^{(2)}$
$\boldsymbol{u}$	Vector of random numbers
$\boldsymbol{u}'$	Vector of random numbers
g	PDF from which the random numbers $\boldsymbol{u}$ are generated
g'	PDF from which the random numbers $\boldsymbol{u}'$ are generated
λ	Randomly introduced parameter in model $M^{(1)}$
μ	Constant
h	Mapping to go forward and backward between $\boldsymbol{\theta}^{(1)}$ and $\boldsymbol{\theta}^{(2)}$
$P(l)$	Prior for model $'l'$
b_l	Probability of birth move at model $'l'$
d_l	Probability of death move at model $'l'$
u_l	Probability of update move
p	Constant that adjusts the update move in relation with the birth and death moves
α_m	Acceptance probability of birth move
α'_m	Acceptance probability of death move

3.1 Introduction: System Identification

Bayesian Inference is widely used as a probabilistic framework to tackle the identification of dynamical systems (i.e. System Identification (SID)—parameter estimation and model selection). Due to the complexity of the parameter posterior probability distributions, the Bayesian framework is frequently used together with Markov chain Monte Carlo (MCMC) sampling algorithms, as they are capable of sampling from distributions with complex geometries. MCMC sampling methods are believed to be costly computational algorithms but their advantages are many. Together with algorithms such as the Metropolis-Hastings sampling algorithm, Bayesian approaches have been employed to do parameter estimation and model selection of dynamical systems [1, 2]. Between the real structure and the modelled approximation there is a degree of uncertainty. Using a probabilistic framework helps one to deal with the issue of uncertainty by estimating confidence bounds in one's findings. The Bayesian framework tends to penalise model complexity and therefore prevents overfitting.

Generally, Bayesian Inference is widely used together with the Metropolis-Hastings algorithm to do parameter estimation of both linear and nonlinear systems. As expected, the algorithms become potentially more costly once the number of parameters that need to be identified increases. The Metropolis-Hastings method may be attractive due to the fact that one does not need to know the evidence term and also due to the proposal density being whatever the user wants, but it cannot perform model selection. In order for the MH method to provide samples from the posterior distribution of parameters, the Markov chain needs to obey the principle of detailed balance (i.e. at equilibrium each processes should be balanced out by its reverse process). When it comes to model selection, because there is a need to move between spaces of varying dimension (each model might depend on a different number of parameters), detailed balance is not obeyed anymore by the Markov chain. Hence, there surfaced the need for an algorithm that could do model selection and parameter estimation whilst obeying the principle of detailed balance. In 1995, Green developed the RJMCMC algorithm, a transdimensional MCMC method (i.e. MCMC algorithm capable of moving between dimensions), based around the MH algorithm, with the added benefits of obeying detailed balance and being capable of jumping between models with vectors of parameters of varying dimension [3].

To the best of the authors' knowledge, the RJMCMC algorithm has been applied to many fields but not to SID in the context of structural dynamics. This contribution aims to prove the effectiveness of the RJMCMC algorithm in the context of SID of dynamical systems on experimental time data, with the ultimate goal of successfully applying it to SID of nonlinear systems and in Structural Health Monitoring (SHM).

Section 3.1 covers details on the need of a Bayesian framework and MCMC sampling algorithms in system identification of dynamical systems. Section 3.2 provides explanations on the experimental set-up as well as the results and Sect. 3.3 covers conclusions and a brief discussion of the results.

3.1.1 Introduction to Bayesian Inference

Employing the Bayes theorem (Eqs. (3.1) and (3.2)), the basic approach of a Bayesian framework is that it provides samples from the posterior distribution of parameters or models, making use of any prior knowledge one has about the studied structure, so that,

$$P(\boldsymbol{\theta}|D,M) = \frac{P(D|\boldsymbol{\theta},M)P(\boldsymbol{\theta}|M)}{P(D|M)} \tag{3.1}$$

and

$$P(\boldsymbol{M}|D) = \frac{P(D|\boldsymbol{M})P(\boldsymbol{M})}{P(D)} \tag{3.2}$$

where $\boldsymbol{\theta}$ is the vector of parameters, D is the available data, M is the selected model and $\boldsymbol{M}$ is the vector of possible models. $P(\boldsymbol{\theta}|D,M)$ is called the posterior parameter distribution and is the probability of the parameters $\boldsymbol{\theta}$ after one has seen D. The evidence, $P(D|M)$, acts as a normalising constant,ensuring that the posterior parameter distribution will integrate to unity. $P(\boldsymbol{\theta}|M)$, called the prior, is the probability assigned to the parameters before one has seen the data. It represents one's knowledge about the system from previous experience. The likelihood, $P(D|\boldsymbol{\theta},M)$, is the probability of seeing the data given the selected model and the parameters. $P(\boldsymbol{M}|D)$ is the posterior model distribution and it represents the probability of the models after one has seen D. The evidence in Eq. (3.1) plays the role of likelihood in Eq. (3.2). $P(\boldsymbol{M})$ is the prior of models, meaning the probability assigned to the models before one has seen the data. $P(D)$ is a normalising constant for Eq.(3.2) and it is the probability of the data, D.

3.1.2 Review of Current MCMC

The issue that arises with Bayes theorem is that the evidence term is often an intractable integral for parameter estimation. The evidence term is most important in the process of model selection as it gives one a clear indication of which model is better to choose. Even so, the use of the MCMC sampling algorithms helps one with this issue and makes a Bayesian framework a good candidate for SID of structural dynamics. MCMC sampling algorithms, as stated in Sect. 3.1, are capable of sampling from probability distributions with complex geometries as long as the Markov chain respects detailed balance.

A successful usage of MCMC sampling methods within a Bayesian framework is given in [4]. Beck et al. introduce a version of Metropolis Hasting and use it to do updating and reliability studies over a locally identifiable and unidentifiable model, provided vibration data is available. The paper discusses the difficulty in integrating the evidence term and its importance in obtaining a robust process of system identification. Even though valuable, the study does not present a general computational tool for doing model selection. The models are weighted by the probability of the parameters as data becomes available, which can become time consuming and makes the approach less efficient when not enough data is available. Advantages of using the MH algorithm include that one can use any proposal distribution and that the evidence term from Eq. (3.1) does not need to be known. For a better understanding of how the MH algorithm is used in the context of parameter estimation of dynamical systems, the interested reader is referred to a previous work by the authors, [5]; a more thorough work is presented in [6]. The contribution explains doing model selection and updating between classes of hysteretic models using a fairly new MCMC algorithm, the Transitional Markov Chain Monte Carlo method [7]. A good description is provided regarding globally identifiable, locally identifiable and unidentifiable models. The TMCMC method is illustrated using simulated seismic data. The advantage of using the TMCMC algorithm is that one can do model selection by comparing the evidence of the models considered. A drawback to the approach is that the computational cost increases considerably once one has have to consider more than two models. Also, it requires post-processing of the data.

Simulated annealing and data annealing are two often encountered algorithms in the MCMC literature, examples being [8, 9]. The purpose of Simulated Annealing is to make sure that a Markov Chain does not get stuck in a local maximum region. Reference [8] uses the Shannon entropy to gradually introduce data into the algorithm in order to provide a smooth transition from the prior probability distribution of parameters to the posterior distribution of parameters. The method is successfully applied in doing system identification on nonlinear dynamical systems and it is illustrated using simulated data. In [10], it is proposed to do system identification of nonlinear dynamical systems using what is known as 'highly informative training data'. The Shannon entropy is used to decide the amount of information the data contains. The method is employed on a simulated 3-DOF mass-spring-damper system. The paper outlines one of the issues extant in this method, the assumption that there exists only one set of parameters that is suitable. Both studies discussed above have applied the approaches proposed on experimental data.

In this study, the RJMCMC algorithm will be used on experimental data coming from a 4-story structure.

Though all methods presented in previous work have their advantages, the authors propose the RJMCMC algorithm in order to do model selection and parameter estimation simultaneously, due to the added benefits presented in Sect. 3.2.3.

3.2 Reversible Jump Markov Chain Monte Carlo: On an Experimental MDOF Structure

3.2.1 The Experimental Rig

The present work focuses on the RJMCMC algorithm applied on experimental time data from an MDOF structure, in order to do SID of a linear dynamical system.

The structure used throughout this contribution is pictured in Fig. 3.1.

The 'bookshelf' structure has four levels, with the lower level being considered the base. Each main plate/level has a weighted mass of 5.2 kg and dimensions $35 \times 25.5 \times 2.5$ cm (*LxWxh*). Each upright beam connecting the four levels has a weighted mass of 238 g and dimensions $55.5 \times 2.5 \times 0.6$ cm. Each square block used to connect the main plates and the upright beam has a weighted mass of 18 g and dimensions $2.5 \times 2.5 \times 1.3$ cm. For each block, four bolts were used with a weighted mass of 10 g and of Viraj A2–70 grade. The structure was mounted on a rail system which was bolted in and then clamped onto a testing table. In order to introduce the excitation into the structure, a shaker with a force transducer was connected to the base. The output of the structure was recorded as acceleration, using 4 accelerometers positioned, as in Fig. 3.1, at the middle of each main plate/level.

The data was gathered using a SCADAS-3 interface connected to a PC running LMS Test.Lab software. 93,184 data points were recorded at a sampling frequency of 1024 Hz in the form of time domain acceleration readings from accelerometer sensors glued on the structure at each level as pictured in Fig. 3.1.

The following model was proposed:

$$\begin{aligned} m_1\ddot{z}_1 + 2c\dot{z}_1 - c\dot{z}_2 + 2kz_1 - kz_2 &= -m_1\ddot{y}_b \\ m_2\ddot{z}_2 - c\dot{z}_1 + 2c\dot{z}_2 - c\dot{z}_3 - kz_1 + 2kz_2 - kz_3 &= -m_2\ddot{y}_b \\ m_3\ddot{z}_3 - c\dot{z}_2 + c\dot{z}_3 - kz_2 + kz_3 &= -m_3\ddot{y}_b \end{aligned} \tag{3.3}$$

where m_1, m_2, m_3 are the masses of levels 2, 3 and 4 (counting from the lowest level to the highest level), $\ddot{z}_1$, $\ddot{z}_2$ and $\ddot{z}_3$ are the relative accelerations of each corresponding level with respect to the base (for example, $\ddot{z}_1 = \ddot{y}_1 - \ddot{y}_b$), $\dot{z}_1$, $\dot{z}_2$ and $\dot{z}_3$ are the relative velocities of each corresponding level with respect to the base, z_1, z_2 and z_3 are the relative displacements of each corresponding level with respect to the base and finally $\ddot{y}_b$ is the acceleration of the base.

3.2.2 Metropolis-Hastings: On the Experimental MDOF System

For illustration purposes, the authors will further present the MH algorithm applied on the experimental MDOF system. As mentioned in Sect. 3.2, the Metropolis-Hastings algorithm is a widely used MCMC method capable of doing parameter

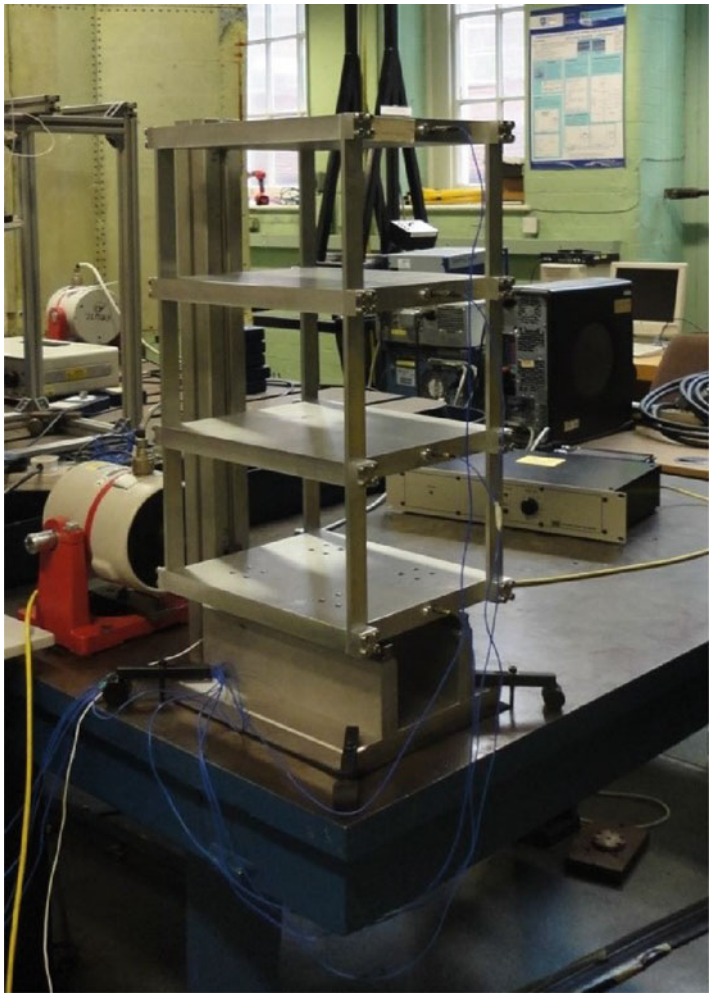

Fig. 3.1 Experimental rig

estimation in the context of structural dynamics. The MH method follows a straight-forward approach. It creates a Markov chain of samples by using a proposal probability distribution to provide one with samples from the posterior parameter distribution [11].

The MH algorithm was applied on the 3-DOF system in order to identify the parameters stiffness, k, damping coefficient, c and also σ, in order to estimate the standard deviation of the noise. For simplicity, the parameters were kept the same throughout the model. The likelihood function was chosen such that the noise is considered to be Gaussian with variance σ^2.

Accounting for the transient response, the data used was of 5000 samples, data points between 20,000 and 25,000, with a burn-in of 500 samples. The proposal probabilities used were Gaussian with respective widths of 100 for k, 0.1 for c and 0.01 for σ. The number of iterations was chosen to be 10,000. Figures 3.2 and 3.3 show the graphical results, histogram of samples of parameters and the Markov chains of the samples.

Figure 3.2 shows the frequency of the samples for all three parameters of interest, stiffness, k, damping coefficient, c and standard deviation of noise, σ. It can be observed that the most frequent values are $k = 4.481 \times 10^5$ N/m, $c = 21.5$ Ns/m and $\sigma = 0.85$. In Fig. 3.3 one can check the stationary Markov chains of the samples for all three parameters. The plots show how the Markov chains efficiently explored the space of each parameter.

As a starting point, the mathematical model identified seems like a good fit. Noise is one of the reasons for uncertainty being present in the identification process. As discussed previously, the model was simplified to a single noise variance for the entire system. A next step might be to include in the simulation for each level of the structure having its own noise standard deviation. Due to the fact that the three-noise-standard-deviation model might be overly complex, one might like to look at it in a Bayesian context; as this is not possible with the MH algorithm, the RJMCMC methods will be used. Although the mathematical approximation of the real structure is simplified,the proposed approach gives robust results still.

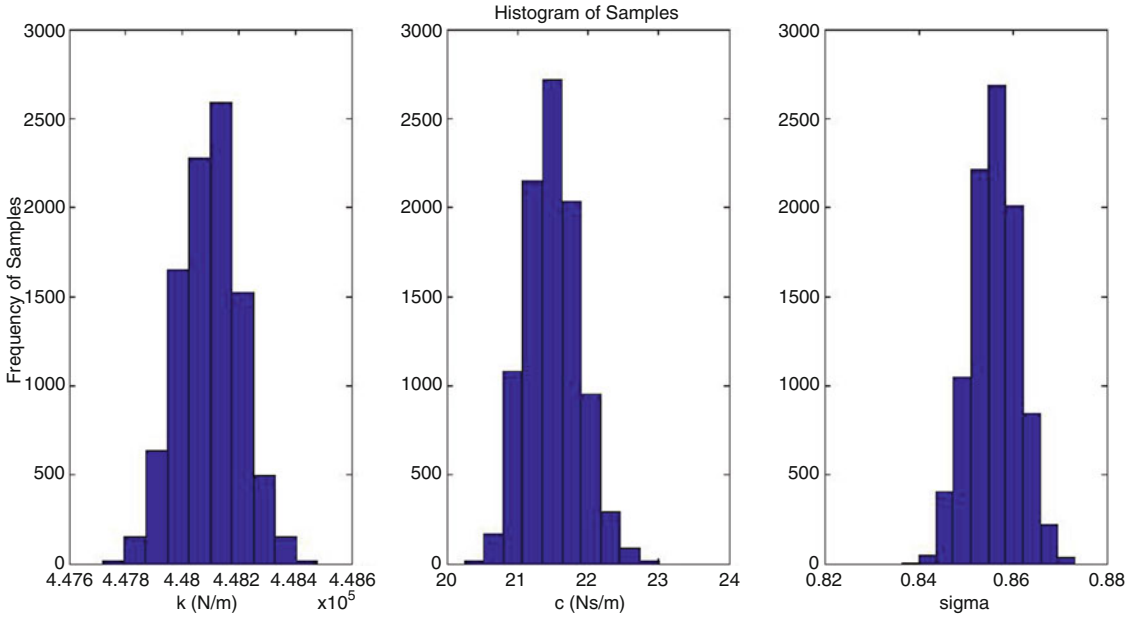

Fig. 3.2 Histogram of samples

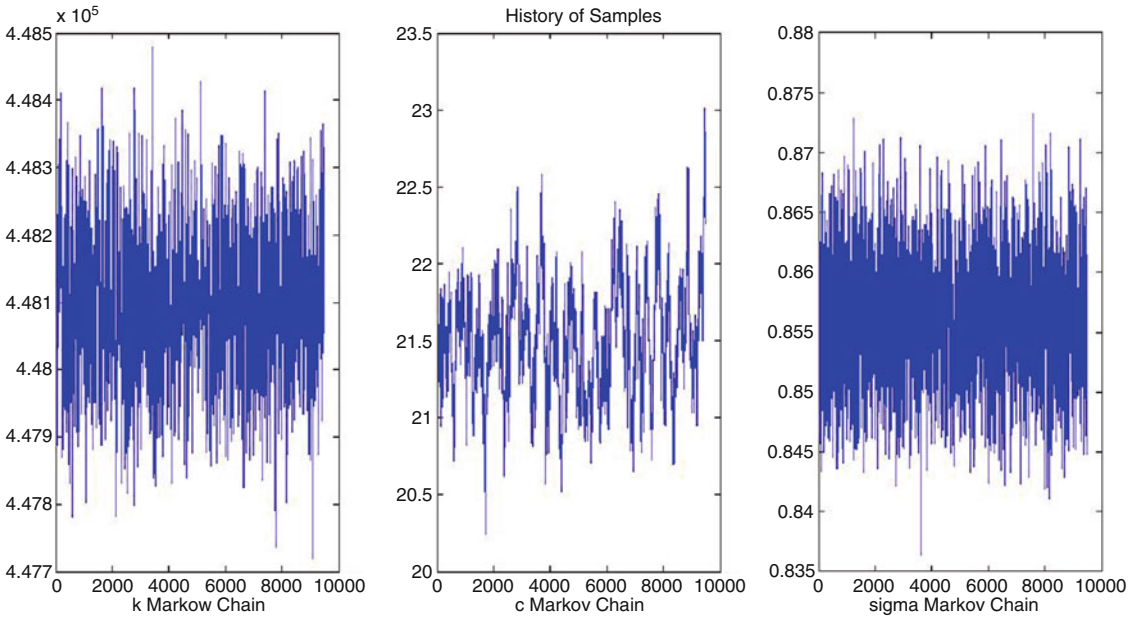

Fig. 3.3 History of samples

Motivated by this aspect, the next section introduces the Reversible Jump Markov Chain Monte Carlo algorithm applied on the 3-DOF model with one variance of noise for the whole system and a 3-DOF model with three different variances of noise for each respective level of the system.

3.2.3 Reversible Jump Markov Chain Monte Carlo

The Reversible Jump Markov Chain Monte Carlo algorithm was developed by Green in 1995 [3].

Since 1995, many works came forward to explain and demonstrate the extensive usage of the RJMCMC algorithm in numerous research areas. In the area of signal processing, Andrieu et al. analyzed the RJMCMC's capabilities in doing model selection [12] and estimation of sinusoids corrupted by noise [13]. Razul et al. demonstrated the usage of the RJMCMC algorithm in nuclear physics [14]. The RJMCMC algorithm is extensively being used in biology research fields [15], control [16] as well as computer science [17]. Lately, the authors have attempted to make use of the method in the area of structural dynamics for nonlinear system identification in [5]. Reference [5] is a good reference point for a more thorough explanation of the RJMCMC algorithm. The RJMCMC method was successfully used on a numerical case study in [18]. The study included a SDOF system with two possible representing models, the first a mass-damper-stiffness linear system and the second a mass-damper-stiffness-cubic stiffness nonlinear system, i.e. a Duffing Oscillator. The algorithm proved efficient in correctly identifying that the linear model should represent simulated linear data and the nonlinear model should represent simulated nonlinear data.

3.2.3.1 A Quick Introduction to the RJMCMC Algorithm

The RJMCMC algorithm is based on three type of moves:

- Birth move—attempt with probability b_l to move from model $M^{(l)}$ to model $M^{(l+1)}$;
- Death move—attempt with probability d_l to move from model $M^{(l+1)}$ to model $M^{(l)}$;
- Update move—remain in current model and update parameters—MH algorithm;

The constant p is used to adjust the update probability, u_l, with respect to the birth and death probabilities, b_l and d_l. The $P(l)$ and $P(l-1)$ components refer to the prior probabilities of models l and $l-1$.

The probabilities are defined as follows:

$$b_l = p\min\left\{1, \frac{P(l+1)}{P(l)}\right\} \tag{3.4}$$

If the birth move condition is not met, the algorithm attempts a death move:

$$d_l = p\min\left\{1, \frac{P(l-1)}{P(l)}\right\} \tag{3.5}$$

If neither the birth move condition or the death move condition are met, then update move is used:

$$u_l = 1 - (b_l + d_l) \tag{3.6}$$

The following pseudo code gives a brief description of how the RJMCMC method works.

The quantities α_m, α'_m, are the acceptance probabilities of the birth and death moves respectively and are obtained from the detailed balance equation (3.7). Detailed balance is introduced for the case when one is dealing with only two models. Finally, the generated random number u_m dictates the proposal.

$$\pi(\boldsymbol{\theta})q(\boldsymbol{\theta}'|\boldsymbol{\theta})\alpha(\boldsymbol{\theta} \rightarrow \boldsymbol{\theta}') = \pi(\boldsymbol{\theta}')q(\boldsymbol{\theta}|\boldsymbol{\theta}')\alpha(\boldsymbol{\theta}' \rightarrow \boldsymbol{\theta})\left|\frac{\partial\left(k^{(2)}, c^{(2)}, \sigma_1^{(2)}, \sigma_2^{(2)}, \sigma_3^{(2)}\right)}{\partial\left(k^{(1)}, c^{(1)}, \sigma^{(1)}, \lambda, \epsilon\right)}\right| \tag{3.7}$$

In the present scenario, the mapping that takes one from model $M^{(1)}$ to model $M^{(2)}$ is of the form:

$$\begin{Bmatrix} k^{(2)} \\ c^{(2)} \\ \sigma_1^{(2)} \\ \sigma_2^{(2)} \\ \sigma_3^{(2)} \end{Bmatrix} = \begin{bmatrix} 0 \\ 0 \\ 0 \\ a \\ b \end{bmatrix} + \begin{Bmatrix} k^{(1)} \\ c^{(1)} \\ \sigma^{(1)} \\ \lambda \\ \epsilon \end{Bmatrix} \tag{3.8}$$

For more details about mappings refer to [19].

The mapping's inverse is applied to go from model $M^{(2)}$ to model $M^{(1)}$.

Algorithm 1 RJMCMC Algorithm

for $n = 1 : N$ **do**
  Get u_m *from* $U[0,1]$ $-$*generates a random number from an uniform distribution*;
  if $u_m \leq b_l^{(n)}$ $-$*birth move condition*; **then**
    $-$*propose birth move*
    Generate u_b *from* $U[0,1]$ $-$*generates a random number from an uniform distribution*;
    Evaluate α_m (*detailed below*)
    if $u_b \leq \alpha_m$ **then**
      $-$*update to model* $l+1$ *and update model parameters*;
    else
      $-$*stay in model* l;
    end if
  else
    if $u_m \leq (b_l^{(n)} + d_l^{(n)})$ $-$*death move condition*; **then**
      $-$*propose death move*
      Get u_d *from* $U[0,1]$ $-$*generates a random number from an uniform distribution*;
      Evaluate α'_m (*detailed below*)
      if $u_d \leq \alpha'_m$ **then**
        $-$*go to model* $l-1$ *and update model parameters*;
      else
        $-$*stay in model* l;
      end if
    else
      normal MH algorithm, model remains at l *state, update parameters only*;
    end if
  end if
end for

$\boldsymbol{\theta}$ is the vector of parameters for model $M^{(1)}$ and it is of the form, $\boldsymbol{\theta} = \{k^{(1)}, c^{(1)}, \sigma^{(1)}, \lambda, \epsilon\}$, where λ and ϵ are randomly generated numbers used to obey dimension matching [3].

In the same form, $\boldsymbol{\theta}'$ is the vector of parameters for model $M^{(2)}$ and it is of the form, $\boldsymbol{\theta}' = \{k^{(2)}, c^{(2)}, \sigma_1^{(2)}, \sigma_2^{(2)}, \sigma_3^{(2)}\}$.

The present contribution is concerned with applying the RJMCMC algorithm for doing SID on an experimental rig. For a full description and explanation of RJMCMC and principle of detailed balance please refer to [5].

3.2.3.2 RJMCMC: On an Experimental MDOF System

As introduced in Sect. 3.2, the present study focuses on applying the RJMCMC algorithm on an experimental 4-level structure modelled as a 3-DOF dynamical system, Fig. 3.4.

Uncertainty is a big problem in SID of dynamical systems. One of the sources of uncertainty is random variability in measurement data. This comes from the process of gathering the data in a laboratory and it is generally referred to as noise. Not taking into account noise or modelling it incorrectly can lead to erroneous results and bad estimations.

In this section, one is confronted with two models for the bookshelf or the 3-DOF system. The first model has a noise variance for the entire system and the second model is defined with three different noise variances, one for each of the 3-DOF's respectively.

In order to approximate the best model that fits the data and also to estimate the parameters characterising the models, the RJMCMC algorithm was employed.

The RJMCMC algorithm was used to do model selection and parameter estimation on the 3-DOF experimental dynamical system. Equal prior probabilities of 0.5 were given to the first model, $M^{(1)}$, characterised by parameters $\boldsymbol{\theta} = \{k^{(1)}, c^{(1)}, \sigma^{(1)}, \lambda, \epsilon\}$ and the second model, $M^{(2)}$, characterised by the vector of parameters $\boldsymbol{\theta}' = \{k^{(2)}, c^{(2)}, \sigma_1^{(2)}, \sigma_2^{(2)}, \sigma_3^{(2)}\}$.

A number of $25,000$ data points were necessary to account for the effects of the transient response. The RJMCMC employed $10,000$ iterations. The proposals used were of Gaussian type with widths 100, 0.1 and 0.01 for k, c and σ of $M^{(1)}$ and of widths 100, 0.1, 0.01, 0.01 and 0.01 for $k, c, \sigma_1^{(2)}, \sigma_2^{(2)}$ and $\sigma_3^{(2)}$ of $M^{(2)}$, respectively. Starting values for the Markov chains were approximated through numerical calculations from the information gathered about the structure in the laboratory.

Figures 3.5 and 3.6 illustrate the histograms and Markov chains for $M^{(2)}$, which was the model selected by the RJMCMC algorithm as being more appropriate to represent the studied data.

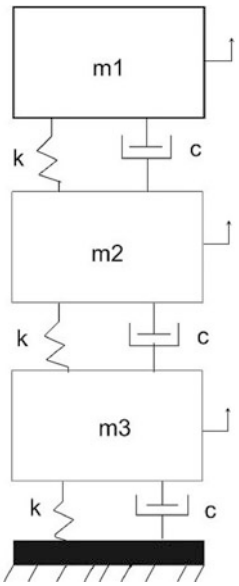

Fig. 3.4 MDOF experimental structure

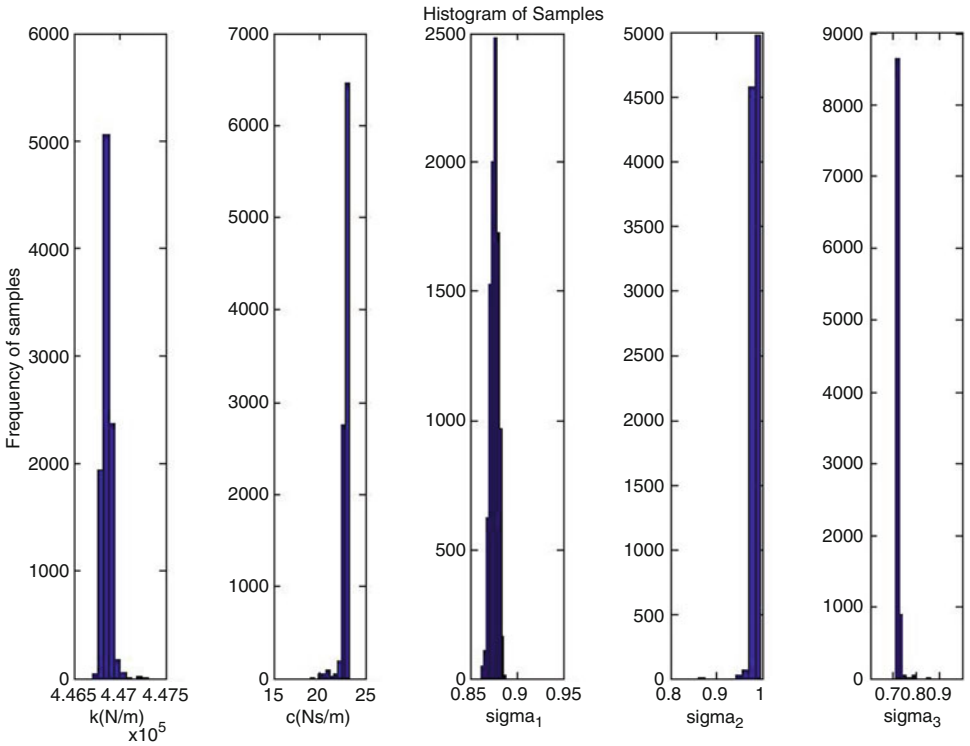

Fig. 3.5 Histogram of samples model 2

For comparison reasons, the results for $M^{(1)}$ are illustrated below, Figs. 3.7 and 3.8. It is straightforward to see that the RJMCMC algorithm did not spend enough time in $M^{(1)}$ which lead to non-stationary Markov chains, in the sense that little credibility could be given to the parameter estimates.

In order to check the RJMCMC algorithm, Monte Carlo simulations were run using samples of parameters of both models. Confidence bounds of 97 % were used. The following figures, Figs. 3.9, 3.10 and 3.11, represent the bounds for each of the three levels,respectively. In order to visualise the results better, zoomed-in versions of the plots are provided due to the large number of data points. What this particular study revealed was that there existed little to no difference between the two models representing the data. However, in order to further explain the results obtained, another MCMC algorithm, the TMCMC [7],

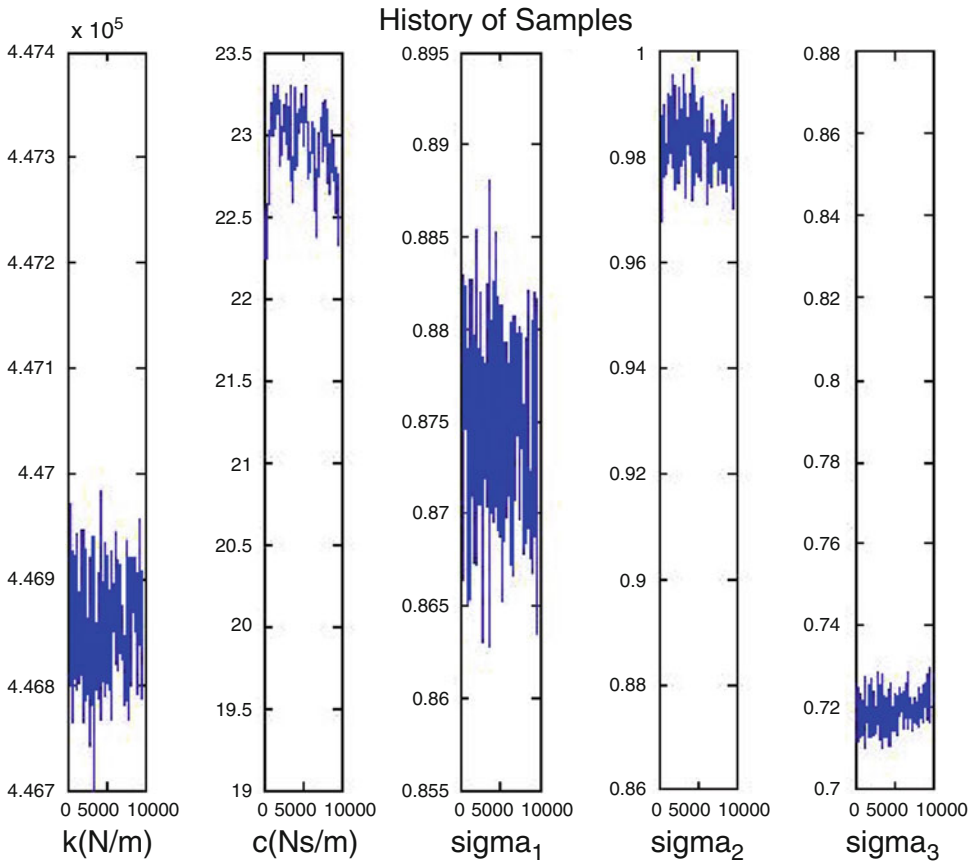

Fig. 3.6 History of samples model 2

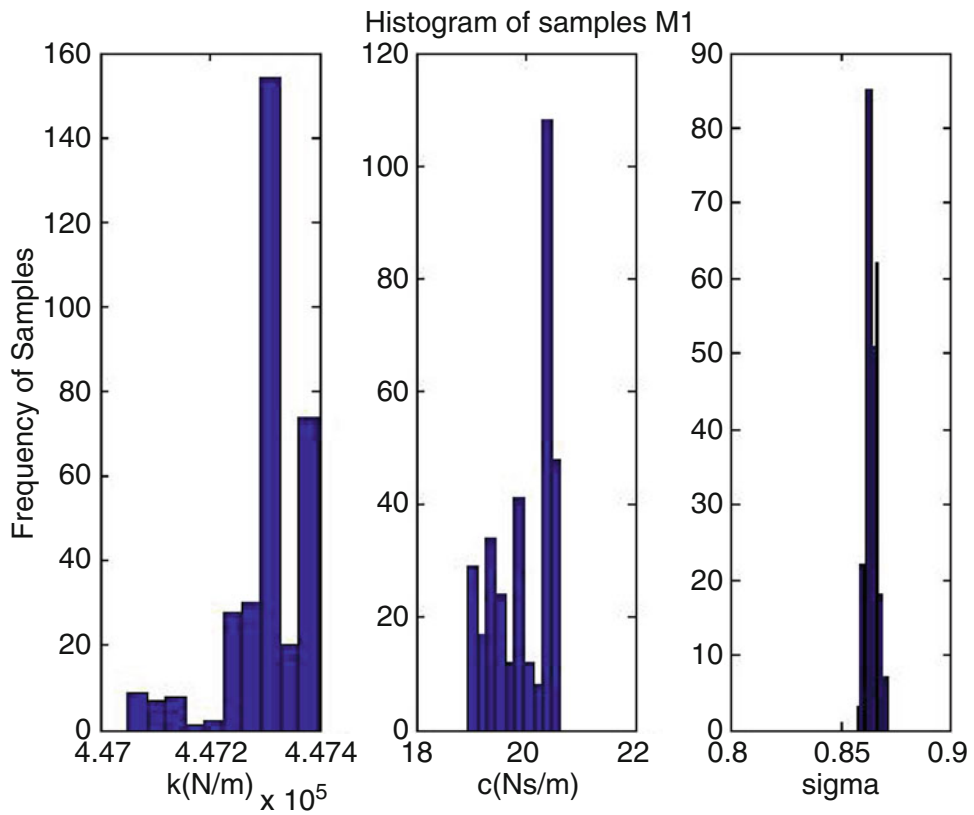

Fig. 3.7 Histogram of samples model 1

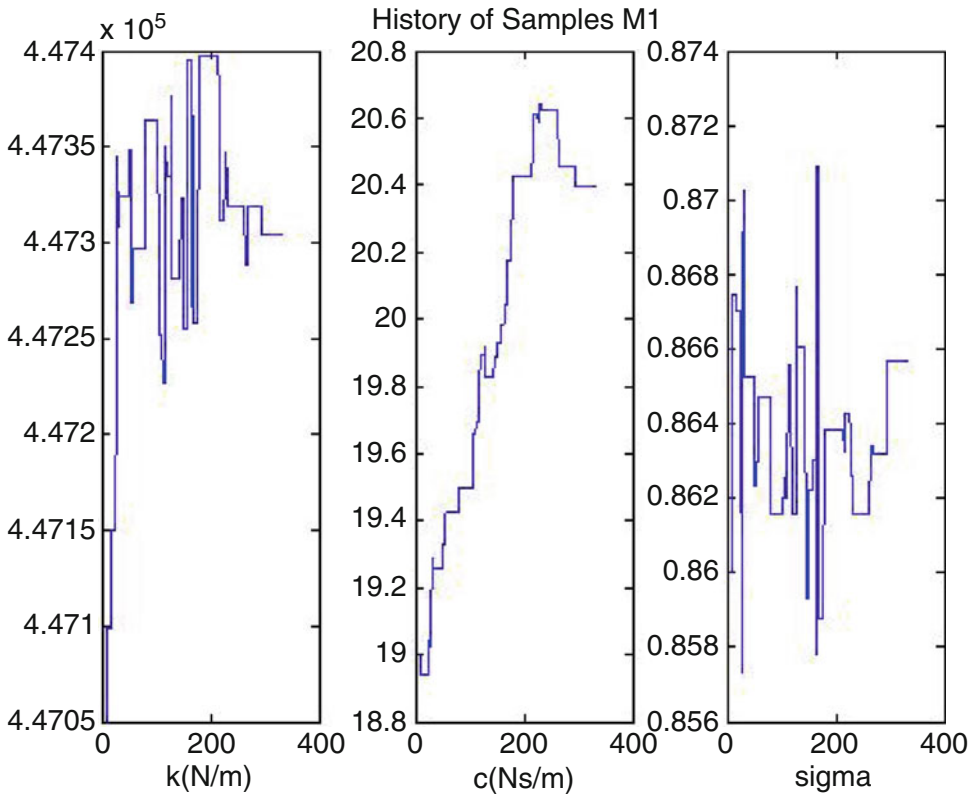

Fig. 3.8 History of samples model 1

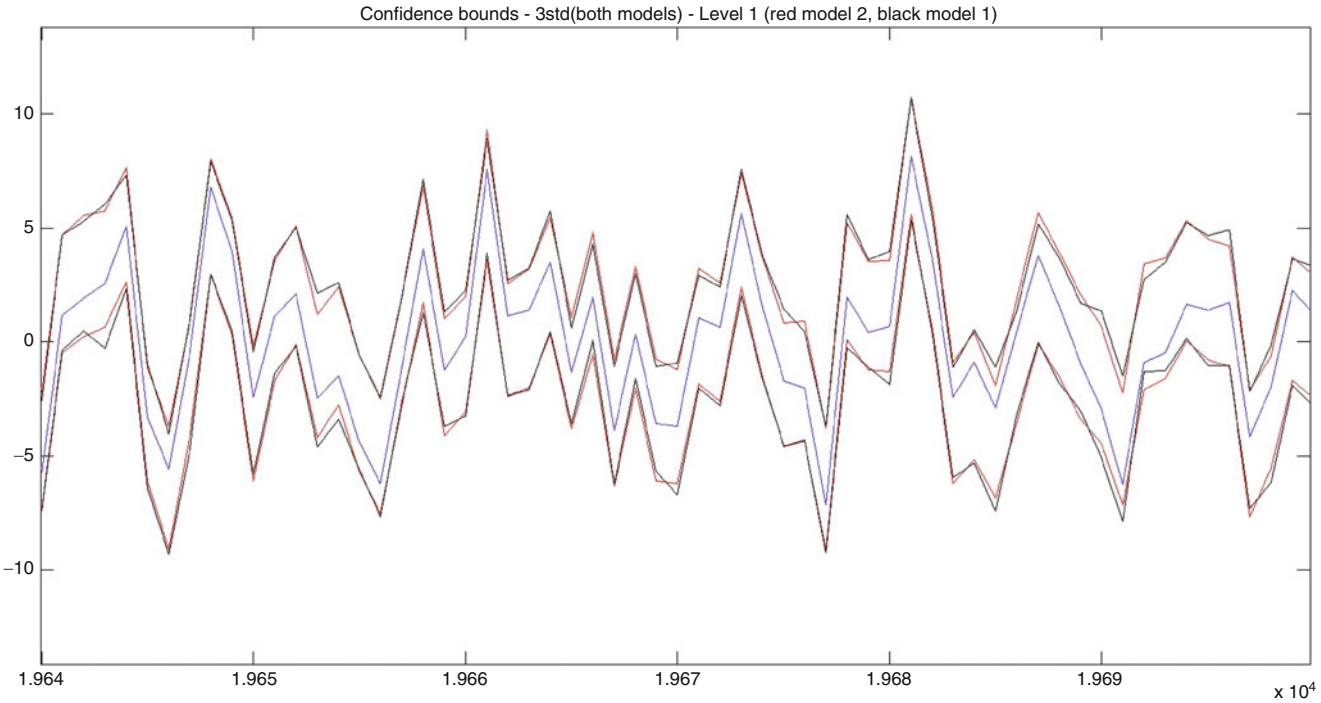

Fig. 3.9 MC simulation results level 1, *red line* $M^{(2)}$, *black line* $M^{(1)}$

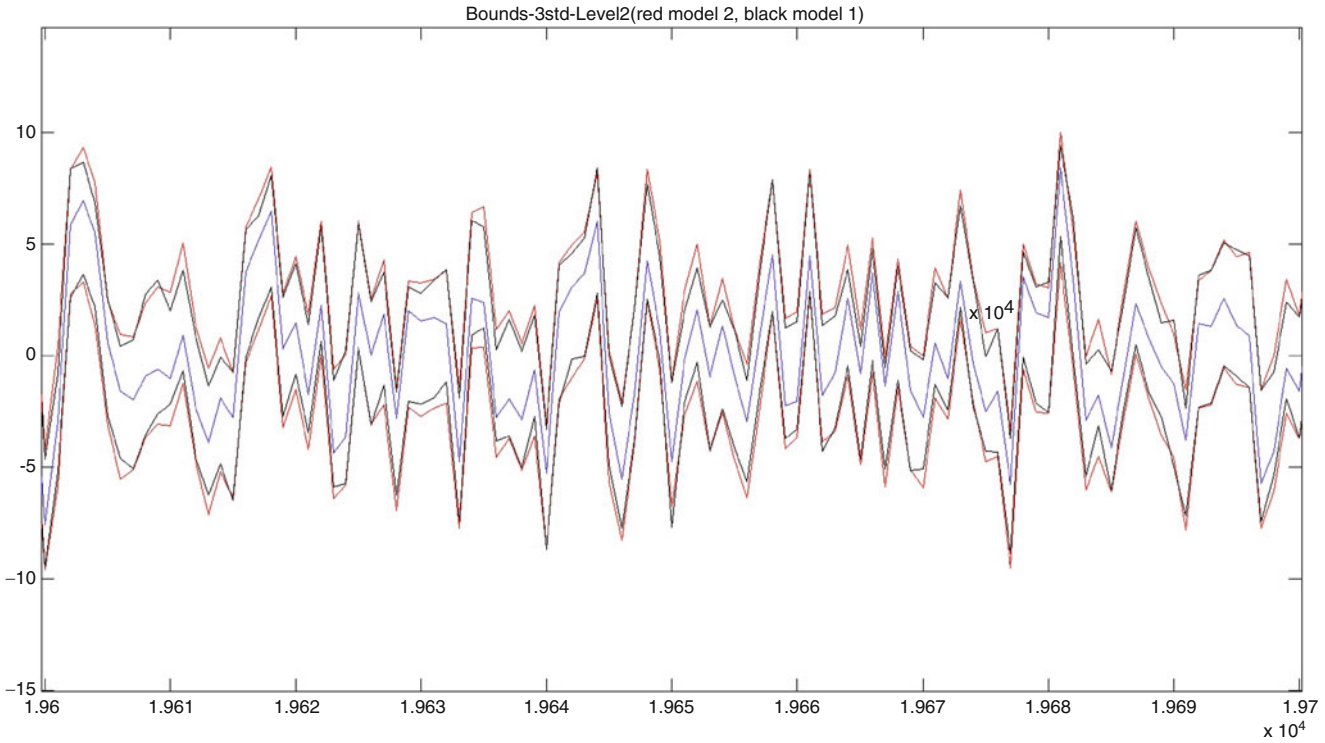

Fig. 3.10 MC simulation results level 2, *red line* $M^{(2)}$, *black line* $M^{(1)}$

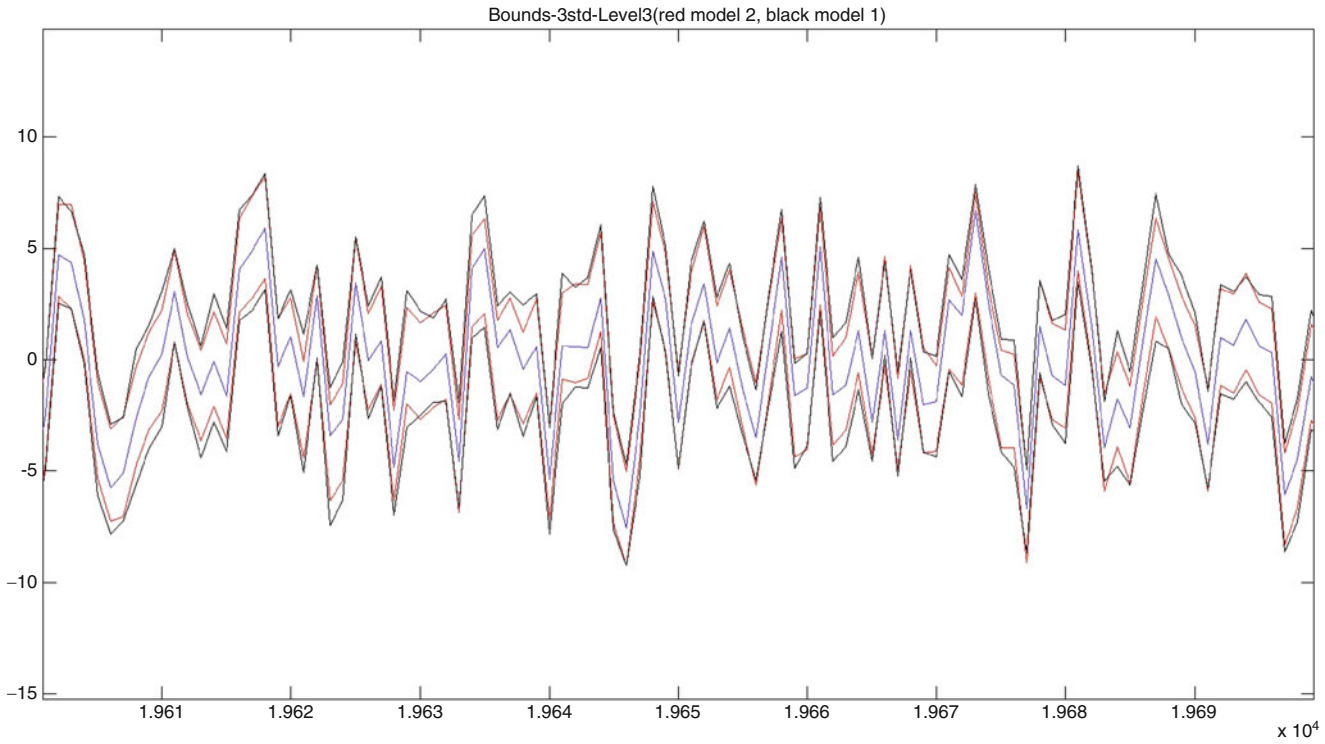

Fig. 3.11 MC simulation results level 3, *red line* $M^{(2)}$, *black line* $M^{(1)}$

was applied on the two models, making use of the same set of data. Even though the approximations and estimations of the parameters were almost identical, the evidence terms of the posterior distributions for the two models suggested that $M^{(1)}$ rather than $M^{(2)}$ is the model preferred.

The following section will present some concluding remarks regarding the results of the present contribution as well as a few points on why they might be the case.

3.3 Conclusions and Discussion

The RJMCMC algorithm is part of a bigger family of MCMC algorithms commonly known as transdimensional MCMC algorithms. Evidently, the mentioned informal class of MCMC methods is concerned with algorithms capable of moving between spaces of varying dimension. One of the most encountered issues with this type of algorithms is the construction of the Markov chain that is supposed to go between spaces. Once detailed balance is respected and such a Markov chain exists, one has to deal with its efficiency. As presented in [20], efficient Markov chains are difficult to construct when it comes to transdimensional moves. The ratio between accepted and rejected moves needs to be balanced. In this present work, what one encounters is that when using the RJMCMC algorithm, once the algorithm reaches a model it prefers, it tends to stay in that model for a long period of time. What the authors discovered was that from all the samples of $M^{(1)}$ only 36 were unique out of 333, while for $M^{(2)}$ only 305 samples were unique out of 9669, proving that the Markov chain tends to spend more time in the current model rather than moving between models. These type of issues are dealt with by tuning the proposal widths so that one gets better acceptance ratios. So far this is done manually, which brings up another problem dealt with in [20], automation of the transdimensional algorithms.

As mentioned in Sect. 3.2, the authors used two MCMC algorithms, RJMCMC and TMCMC, and compared the results. It was found that even though the parameter estimations are similar, the RJMCMC algorithm approximated $M^{(2)}$ to be a better fit for the data while TMCMC estimated that $M^{(1)}$ would be a better fit for the data. Considering the little difference there was between the two models, this fact is not worrying. This only indicates that the RJMCMC is more sensitive to slight changes. In computational time, the RJMCMC algorithm is also more efficient than TMCMC.

The purpose of this contribution was to apply the RJMCMC algorithm on an MDOF experimental structure within a dynamical context. The algorithm was used on experimentally gathered data to jump between two models, one with a single model of noise variance for all DOF and the second one with different models of noise variance for each individual DOF. The results of the research showed that the model to best represent the data should be the slightly more complex one, $M^{(2)}$. As future work, the authors plan to look into applying the RJMCMC algorithm on MDOF system approximated by models with more significant differences, for example choice of multiple nonlinear models.

Acknowledgements The authors would like to acknowledge 'Engineering Nonlinearity' EP/K003836/1, an EPSRC funded Programme Grant, for supporting their research (http://www.engineeringnonlinearity.ac.uk/).

References

1. Beck, L.J.: Bayesian updating, model selection and robust stochastic predictions of structural response. In: Proceedings of the 8th International Conference on Structural Dynamics, EURODYN, Leuven (2011)
2. Worden, K., Hensman, J.J.: Parameter estimation and model selection for a class of hysteretic systems using Bayesian inference. Mech. Syst. Signal Process. **32**, 153–169 (2012)
3. Green, P.J.: Reversible jump Markov chain Monte Carlo computation and Bayesian model determination. Biometrika **82**, 711–732 (1995)
4. Beck, L.J., Au, S-K.: Bayesian updating of structural models and reliability using Markov chain Monte Carlo simulation. J. Eng. Mech. **391**, 128–380 (2002)
5. Tiboaca, D., Green, P.L., Barthorpe, R.J.: Bayesian system identification of dynamical systems using reversible jump Markov chain Monte Carlo. In: Proceedings of IMAC XXXII, Conference and Exposition on Structural Dynamics, Orlando (2014)
6. Beck, L.J., Muto, M.: Bayesian updating and model class selection for Hysteretic structural models using stochastic simulation. J. Vib. Control **14**, 7–34 (2008)
7. Ching, J., Chen, Y.: Transitional Markov Chain Monte Carlo method for Bayesian model updating, model class selection, and model averaging. J. Eng. Mech. **133**, 816–832 (2007)
8. Green, P.L.: Bayesian system identification of nonlinear dynamical systems using a fast MCMC algorithm. In: Proceedings of 8th European Nonlinear Dynamics Conference, ENOC, Vienna (2014)
9. Green, P.L.: Bayesian system identification of a nonlinear dynamical system using a novel variant of simulated annealing. J. Mech. Syst. Signal Process. **52–53**, 133–146 (2015)

10. Green, P.L., Cross, E.J., Worden, K. Bayesian system identification of dynamical systems using highly informative training data. J. Mech. Syst. Signal Process. **56–57**, 109–122 (2014)
11. MacKay, D.J.C.: Information Theory, Inference, and Learning Algorithms. Cambridge University Press, Cambridge (2003)
12. Doucet, A., Andrieu, C.: Joint Bayesian model selection and estimation of noisy sinusoids via reversible jump MCMC. IEEE Trans. Signal Process. (1999)
13. Doucet, A., Djuric, P.M., Andrieu, C.: Model selection by MCMC computation. J. Signal Process. **81**, 19–37
14. Razul, S.G., Fitzgerald, W.J., Andrieu, C.: Bayesian model selection and parameter estimation of nuclear emission spectra using RJMCMC. J. Nucl. Instrum. Methods Phys. Res. **497**, 492–510 (2003)
15. Liu, R.Y., Tao, J., Shi, N.Z., He, X.: Bayesian analysis of the patterns of biological susceptibility via reversible jump MCMC sampling. Comput. Stat. Data Anal. **55**, 1498–1508 (2011)
16. Baldacchino, T., Anderson, S.R., Kadirkamanathan, V.: Computational system identification for Bayesian NARMAX modelling. Automatica **49**, 2641–2651 (2013)
17. Damen, D., Hogg, S.: Recognizing linked events: searching the space of feasible explanations. In: Proceedings of IEEE Computer Science and Pattern Recognition, Miami, pp. 927–934 (2009)
18. Tiboaca, D., Green, P.L., Barthorpe, R.J.: Bayesian parameter estimation and model selection of a nonlinear dynamical system using reversible jump Markov chain Monte Carlo. In: Proceedings of ISMA International Conference on Noise and Vibration Engineering, Leuven (2014)
19. Schutz, B.: Geometrical Methods of Mathematical Physics. Cambridge University Press, Cambridge (1980)
20. Sisson, S.A.: Transdimensional Markov Chains: A decade of progress and future perspectives. J. Am. Stat. Assoc. **100**(471), 1077–1089 (2005)

Chapter 4
Approximate Bayesian Computation by Subset Simulation for Parameter Inference of Dynamical Models

Majid K. Vakilzadeh, Yong Huang, James L. Beck, and Thomas Abrahamsson

Abstract A new multi-level Markov chain Monte Carlo algorithm for Bayesian inference, ABC-SubSim, has recently appeared that combines the principles of Approximate Bayesian Computation (ABC) with the method of subset simulation for efficient rare-event simulation. ABC-SubSim adaptively creates a nested decreasing sequence of data-approximating regions in the output space. This sequence corresponds to increasingly closer approximations of the observed output vector in this output space. At each stage, the approximate likelihood function at a given value of the model parameter vector is defined as the probability that the predicted output corresponding to that parameter value falls in the current data-approximating region. If continued to the limit, the sequence of the data-approximating regions would converge on to the observed output vector and the approximate likelihood function would become exact, but this is not computationally feasible. At the heart of this paper is the interpretation of the resulting approximate likelihood function. We show that under the assumption of the existence of uniformly-distributed measurement errors, ABC gives exact Bayesian inference. Moreover, we present a new optimal proposal variance scaling strategy which enables ABC-SubSim to efficiently explore the posterior PDF. The algorithm is applied to the model updating of a two degree-of-freedom linear structure to illustrate its ability to handle model classes with various degrees of identifiability.

Keywords Approximate Bayesian computation • Subset simulation • Adaptive modified Metropolis algorithm • Dynamical systems • Optimal proposal variance scaling

4.1 Introduction

In the Bayesian updating framework, the likelihood function of a model parameter vector expresses the probability of getting measured data based on a particular predictive model, and it is essential since the data affects the posterior through it via Bayes' Theorem. However, for some complex models, e.g., hidden Markov models, an analytical formula for the likelihood function might be difficult, or even impossible to establish [1]. Approximate Bayesian Computation (ABC) was conceived to bypass the explicit evaluation of the likelihood function [2, 3] by sampling from a posterior probability distribution conditional on model predicted outputs that are acceptably close under some metric in the output space to the observed data vector, rather than using this observed data vector directly in Bayes' Theorem. Thus, an approximate likelihood function is defined for use in Bayes' theorem to be the probability that the predicted output corresponding to a value of the model parameter vector falls in the data-approximating region of the observed data vector where the accuracy of the approximation is determined by a tolerance level ε on the chosen metric.

M.K. Vakilzadeh (✉)
Division of Engineering and Applied Science, California Institute of Technology, Pasadena, CA 91125, USA

Department of Applied Mechanics, Chalmers University of Technology, Gothenburg, Sweden
e-mail: khorsand@chalmers.se

Y. Huang
Division of Engineering and Applied Science, California Institute of Technology, Pasadena, CA 91125, USA

Key Lab of Structural Dynamic Behavior and Control of the Ministry of Education, Harbin Institute of Technology, Harbin, China

J.L. Beck
Division of Engineering and Applied Science, California Institute of Technology, Pasadena, CA 91125, USA

T. Abrahamsson
Department of Applied Mechanics, Chalmers University of Technology, Gothenburg, Sweden

S. Atamturktur et al. (eds.), *Model Validation and Uncertainty Quantification, Volume 3*, Conference Proceedings of the Society for Experimental Mechanics Series, DOI 10.1007/978-3-319-29754-5_4

The ABC method can be utilized for any model for which forward simulation is available and it broadens the realm of models for which Bayesian statistical inference can be accessed. Numerous new ABC methods have been proposed over the last decade or so with the goal of improving the approximation accuracy and computational efficiency, e.g., ABC-MCMC [4–6], ABC-PRC [7, 8], ABC-SMC [9–11] and ABC-PMC [12] and, very recently, ABC-SubSim [13].

For a good approximation of the posterior distribution in the ABC approach, we want the tolerance parameter ε to be sufficiently small so that only the predicted outputs falling in a close neighborhood centered on the observed data vector are accepted. However, this leads to a problem of rare-event simulation and so if Monte Carlo simulation is used, the model output must be computed for a huge number of candidate samples in order to produce an acceptable sample size in the specified data-approximating region. The computational cost can be reduced by using Markov Chain Monte Carlo (MCMC) sampling directly, but it is still not very efficient due to difficulty in initializing the chain and in achieving fast convergence in order to sample from the stationary distribution. To address this problem, Chiachio et al. [13] recently proposed a new ABC algorithm, named ABC-SubSim, by incorporating the Subset Simulation technique [14] in the ABC algorithm to achieve computational efficiency for the rare event sampling. In Subset Simulation, rare-event simulation is converted into sampling from a sequence of nested subsets that corresponds to large conditional probabilities. This is automatically accomplished by ABC-SubSim adaptively selecting a sequence of intermediate tolerance parameters ε that control the conditional probabilities at each level. In this way, ABC-SubSim automatically creates a nested decreasing sequence of regions in the output space that corresponds to increasingly closer approximations of the observed data vector. As the procedure continues, the sequence of data-approximating regions becomes more concentrated around the actual data vector so that a good approximation of the posterior distribution is achieved.

The most important contributions of this paper are; (1) Based on previous studies of adaptive proposal PDFs for MCMC algorithms [15–17], we propose an improved strategy to find the optimal variance for the proposal distributions of the MCMC algorithm, i.e. modified Metropolis algorithm (MMA), used in Subset Simulation [14] to explore the conditional probability distributions, (2) we show that the basic ABC approximation with an infinity norm as the metric in output space can be interpreted as performing exact Bayesian updating with independent uniformly-distributed combined measurement and modeling errors and this can be generalized to any norm on the output space, although in general the errors will be dependent, and (3) we also find that the variance for any Gaussian prediction error in the forward prediction that is included as a model parameter will be suppressed by the original ABC algorithm as the tolerance level ε decreases. To get around this problem, we marginalize over any prediction error variance parameters to account for their prior uncertainty and the corresponding new forward model for generating simulated data is then updated.

The structure of this paper is as follows. First, the hierarchical stochastic model class for a state-space model of a dynamic system is defined and the ABC-SubSim approach is introduced for approximate Bayesian model updating. Second, the interpretation of the exactness of the ABC-SubSim approximation under certain conditions is discussed and two improvements for the ABC-SubSim method are presented. Third, we present experimental results with synthetic data to demonstrate the effectiveness of the ABC-SubSim approach for Bayesian model updating of a two degree-of-freedom linear structure with various topologies of the posterior distributions that corresponds to globally, locally and unidentifiable model classes. Finally, conclusions are drawn.

4.2 Formulation

This section begins with the formulation of a hierarchical state-space model class for dynamical systems and then explains the application of a recently-introduced algorithm, ABC-SubSim [13], to sample from the posterior PDF of the general state-space model. Finally, the proposed enhancements for ABC-SubSim are presented.

4.2.1 Formulation of Hierarchical Stochastic Model Class

We treat the general case of a discrete-time finite-dimensional state-space model of a real dynamic system:

$$\begin{aligned} \forall n \in \mathbb{Z}^+,\ \mathbf{x}_n &= \mathbf{f}_n\left(\mathbf{x}_{n-1}, \mathbf{u}_{n-1}, \boldsymbol{\theta}_s\right) \in \mathbb{R}^{N_s} \ \text{(State evolution)} \\ \mathbf{y}_n &= \mathbf{g}_n\left(\mathbf{x}_n, \mathbf{u}_n, \boldsymbol{\theta}_s\right) \in \mathbb{R}^{N_o} \ \text{(Output)} \end{aligned} \tag{4.1}$$

where $\mathbf{u}_n \in \mathbb{R}^{N_I}$, $\mathbf{x}_n \in \mathbb{R}^{N_s}$ and $\mathbf{y}_n \in \mathbb{R}^{N_o}$ denote the (external) input, model state and output vector at time t_n and $\boldsymbol{\theta}_s \in \mathbb{R}^{N_p}$ is a vector of uncertain-valued model parameters that includes the initial state $\mathbf{x}_0$ if is unknown.

We embed this deterministic model in a stochastic state-space model [18]:

$$\begin{aligned} \forall\, n \in \mathbb{Z}^+,\ \mathbf{x}_n &= \mathbf{f}_n\left(\mathbf{x}_{n-1}, \mathbf{u}_{n-1}, \boldsymbol{\theta}_s\right) + \mathbf{w}_n \\ \mathbf{y}_n &= \mathbf{g}_n\left(\mathbf{x}_n, \mathbf{u}_n, \boldsymbol{\theta}_s\right) + \mathbf{v}_n \end{aligned} \tag{4.2}$$

where we now re-define $\mathbf{x}_n$ and $\mathbf{y}_n$ to be the dynamic system state and output vectors at time t_n, not the model state and output, and so uncertain state and output prediction errors, $\mathbf{w}_n$ and $\mathbf{v}_n$, must be introduced to account for the model being only an approximation of the real system and for possible unknown disturbances on the system. Their prior distributions, $\mathcal{N}\left(\mathbf{w}_n \middle| 0,\ \mathbf{Q}_n\left(\boldsymbol{\theta}_w\right)\right)$ and $\mathcal{N}\left(\mathbf{v}_n \middle| 0,\ \mathbf{R}_n\left(\boldsymbol{\theta}_v\right)\right)$, $\forall n \in \mathbb{Z}^+$, are chosen based on the Principle of Maximum (Information) Entropy [19] under first and second moment constraints, where $\{\mathbf{w}_n\}_{n=1}^N$ and $\{\mathbf{v}_n\}_{n=1}^N$ are sequences of independent stochastic variables [18]. We add the uncertain parameters that specify these priors to the model parameters and use $\boldsymbol{\theta} = \left[\boldsymbol{\theta}_s^{\mathrm{T}}, \boldsymbol{\theta}_w^{\mathrm{T}}, \boldsymbol{\theta}_v^{\mathrm{T}}\right]^{\mathrm{T}}$ to denote the uncertain parameter vector for the stochastic state-space model.

The defined stochastic state-space model defines a "hidden" Markov chain for the state time history $\{\mathbf{x}_n\}_{n=1}^N$ (which will also be denoted by the vector $\mathbf{x}_{1:N} = \left[\mathbf{x}_1^T, \ldots, \mathbf{x}_N^T\right]^T \in \mathbb{R}^{NN_s}$) by implying a state transition PDF (probability density function):

$$\forall\, n \in \mathbb{Z}^+,\ p\left(\mathbf{x}_n \middle| \mathbf{x}_{n-1}, \mathbf{u}_{n-1}, \boldsymbol{\theta}\right) = \mathcal{N}\left(\mathbf{x}_n \middle| \mathbf{f}_n\left(\mathbf{x}_{n-1}, \mathbf{u}_{n-1}, \boldsymbol{\theta}\right), \mathbf{Q}_n\left(\boldsymbol{\theta}\right)\right) \tag{4.3}$$

along with a state-to-output PDF:

$$\forall n \in \mathbb{Z}^+,\ p\left(\mathbf{y}_n \middle| \mathbf{x}_n, \mathbf{u}_n, \boldsymbol{\theta}\right) = \mathcal{N}\left(\mathbf{y}_n \middle| \mathbf{g}_n\left(\mathbf{x}_n, \mathbf{u}_n, \boldsymbol{\theta}\right), \mathbf{R}_n\left(\boldsymbol{\theta}\right)\right) \tag{4.4}$$

These, in turn, imply the following two probability models connecting the input, state and output discrete-time histories:

$$p\left(\mathbf{x}_{1:N} \middle| \mathbf{u}_{0:N}, \boldsymbol{\theta}\right) = \prod_{n=1}^{N} p\left(\mathbf{x}_n \middle| \mathbf{x}_{n-1}, \mathbf{u}_{n-1}, \boldsymbol{\theta}\right) \tag{4.5}$$

$$p\left(\mathbf{y}_{1:N} \middle| \mathbf{x}_{1:N}, \mathbf{u}_{0:N}, \boldsymbol{\theta}\right) = \prod_{n=1}^{N} p\left(\mathbf{y}_n \middle| \mathbf{x}_n, \mathbf{u}_n, \boldsymbol{\theta}\right) \tag{4.6}$$

The stochastic input–output model (or forward model) for given parameter vector $\boldsymbol{\theta}$ is then:

$$p\left(\mathbf{y}_{1:N} \middle| \mathbf{u}_{0:N}, \boldsymbol{\theta}\right) = \int p\left(\mathbf{y}_{1:N} \middle| \mathbf{x}_{1:N}, \mathbf{u}_{0:N}, \boldsymbol{\theta}\right) p\left(\mathbf{x}_{1:N} \middle| \mathbf{u}_{0:N}, \boldsymbol{\theta}\right) \mathrm{d}\mathbf{x}_{1:N} \tag{4.7}$$

This high-dimensional integral usually cannot be done analytically. We will therefore structure the stochastic input–output model using a Bayesian hierarchical model to avoid the integration in Eq. (4.7).

For Bayesian updating using sensor data, we extend the stochastic model to predict the measured system output $\mathbf{z}_n$ at time t_n:

$$\mathbf{z}_n = \mathbf{y}_n + \mathbf{e}_n = \mathbf{g}_n\left(\mathbf{x}_n, \mathbf{u}_n, \boldsymbol{\theta}\right) + \mathbf{v}_n + \mathbf{e}_n \tag{4.8}$$

where $\mathbf{e}_n$ denotes the uncertain measurement error at time t_n. Unlike $\{\mathbf{w}_n\}_{n=1}^N$ and $\{\mathbf{v}_n\}_{n=1}^N$, the stochastic sequence $\{\mathbf{e}_n\}_{n=1}^N$ will not necessarily be modeled as a set of independent stochastic variables; rather, we allow for dependence by specifying a joint PDF for $\mathbf{e}_{1:n}$ for any $n \in \mathbb{Z}^+$. Thus, the PDF for predicting the observed system output (sensor output) $\mathbf{z}_{1:n}$, given the actual system output $\mathbf{y}_{1:n}$, is:

$$p\left(\mathbf{z}_{1:n} \middle| \mathbf{y}_{1:n}, \varepsilon\right) = p\left(\mathbf{e}_{1:n} \middle| \varepsilon\right)\Big|_{\mathbf{e}_{1:n}=\mathbf{z}_{1:n}-\mathbf{y}_{1:n}} \tag{4.9}$$

where ε is a scalar or vector that parameterizes the chosen prior PDF for $\mathbf{e}_{1:n},\ \forall n \in \mathbb{Z}^+$.If measured system input and output data:

$$\mathcal{D}_N = \{\hat{\mathbf{u}}_{0:N}, \hat{\mathbf{z}}_{1:N}\}$$

are available from the dynamic system, then the PDF in Eq. (4.9) gives a likelihood function $p\left(\hat{\mathbf{z}}_{1:N}\middle|\mathbf{y}_{1:N}, \varepsilon\right)$ with corresponding hierarchical prior PDF that is readily sampled:

$$p\left(\mathbf{y}_{1:N}, \mathbf{x}_{1:N}, \boldsymbol{\theta}\middle|\hat{\mathbf{u}}_{0:N}\right) = p\left(\mathbf{y}_{1:N}\middle|\mathbf{x}_{1:N}, \hat{\mathbf{u}}_{0:N}, \boldsymbol{\theta}\right) p\left(\mathbf{x}_{1:N}\middle|\hat{\mathbf{u}}_{0:N}, \boldsymbol{\theta}\right) p\left(\boldsymbol{\theta}\right) \tag{4.10}$$

where $p(\boldsymbol{\theta})$ is taken to be independent of $\hat{\mathbf{u}}_{0:N}$. The PDFs in Eqs. (4.9) and (4.10) define a hierarchical stochastic model class [18] for each value of ε. The posterior PDF for this stochastic model class is then given by Bayes' Theorem:

$$p\left(\mathbf{y}_{1:N}, \mathbf{x}_{1:N}, \boldsymbol{\theta}\middle|\mathcal{D}_N, \varepsilon\right) = E^{-1} p\left(\hat{\mathbf{z}}_{1:N}\middle|\mathbf{y}_{1:N}, \varepsilon\right) p\left(\mathbf{y}_{1:N}, \mathbf{x}_{1:N}, \boldsymbol{\theta}\middle|\hat{\mathbf{u}}_{0:N}\right) \tag{4.11}$$

where the evidence for the stochastic model class is:

$$\begin{aligned} E = p\left(\hat{\mathbf{z}}_{1:N}\middle|\hat{\mathbf{u}}_{0:N}, \varepsilon\right) &= \int p\left(\hat{\mathbf{z}}_{0:N}\middle|\mathbf{y}_{1:N}, \varepsilon\right) p\left(\mathbf{y}_{1:N}\middle|\hat{\mathbf{u}}_{0:N}\right) \mathrm{d}\mathbf{y}_{1:N} \\ &= \int p\left(\hat{\mathbf{z}}_{1:N}\middle|\mathbf{y}_{1:N}, \varepsilon\right) p\left(\mathbf{y}_{1:N}, \mathbf{x}_{1:N}, \boldsymbol{\theta}\middle|\hat{\mathbf{u}}_{0:N}\right) \mathrm{d}\mathbf{y}_{1:N}\mathrm{d}\mathbf{x}_{1:N}\mathrm{d}\boldsymbol{\theta} \end{aligned} \tag{4.12}$$

Remark 1. To characterize the posterior PDF in Eq. (4.11), we need to draw samples from it. In this case, we automatically get samples from its marginal PDFs $p\left(\mathbf{y}_{1:N}\middle|\mathcal{D}_N, \varepsilon\right)$, $p\left(\mathbf{x}_{1:N}\middle|\mathcal{D}_N, \varepsilon\right)$ and $p\left(\boldsymbol{\theta}\middle|\mathcal{D}_N, \varepsilon\right)$ corresponding to the robust posterior predictive PDFs for the system output history and state history corresponding to the measured input, and the posterior PDF for the model parameters. Therefore, it provides a signal smoothing distribution not only for state estimation but also for the system output. This benefit is a result of the choice of a hierarchical model where the likelihood function $p\left(\hat{\mathbf{z}}_{1:N}\middle|\mathbf{y}_{1:N},\ \varepsilon\right)$ is expressed in terms of $\mathbf{y}_{1:N}$, rather than the more common $p\left(\hat{\mathbf{y}}_{1:N}\middle|\hat{\mathbf{u}}_{0:N}, \boldsymbol{\theta}\right)$ given in Eq. (4.7) where the $\mathbf{v}_n$ in Eq. (4.2) are usually taken as measurement errors (sometimes modeling errors as well).

4.2.2 Approximate Bayesian Computation

ABC (Approximate Bayesian computation) is an approach where the likelihood function ($p\left(\hat{\mathbf{z}}_{1:N}\middle|\mathbf{y}_{1:N}, \varepsilon\right)$ in the formulation here) is replaced by an approximation, $P\left(\mathbf{z}_{1:N} \in \mathcal{D}(\delta)\middle|\mathbf{y}_{1:N}, \varepsilon\right)$ where $\mathcal{D}(\delta)$ is a small neighborhood of the data vector $\hat{\mathbf{z}}_{1:N} \in \mathbb{R}^{NN_o}$ of "radius" δ. Then only sampling from the stochastic forward model is needed if an accept/reject algorithm is used to generate K approximate posterior samples:

Algorithm 1. Basic ABC algorithm

For $k = 1$ to K

1. Repeatedly draw a candidate sample $\left(\widetilde{\mathbf{z}}_{1:N}, \widetilde{\mathbf{y}}_{1:N}, \widetilde{\mathbf{x}}_{1:N}, \widetilde{\boldsymbol{\theta}}\right)$ from $p\left(\mathbf{z}_{1:N}\middle|\mathbf{y}_{1:N}, \varepsilon\right) p\left(\mathbf{y}_{1:N}, \mathbf{x}_{1:N}, \mathbf{y}_{1:N}\middle|\hat{\mathbf{u}}_{0:N}\right)$ until $\widetilde{\mathbf{z}}_{1:N} \in \mathcal{D}(\delta)$;
2. Set $\left(\mathbf{y}_{1:N}^{(k)}, \mathbf{x}_{1:N}^{(k)}, \boldsymbol{\theta}^{(k)}\right) = \left(\widetilde{\mathbf{y}}_{1:N}, \widetilde{\mathbf{x}}_{1:N}, \widetilde{\boldsymbol{\theta}}\right)$

End for

For a good approximation, we want $\mathcal{D}(\delta)$ to be a small neighborhood centered on the data vector $\hat{\mathbf{z}}_{1:N}$ in $\mathbb{R}^{NN_o}$, e.g., $\mathcal{D}(\delta) = \left\{\mathbf{z}_{1:N} \in \mathbb{R}^{NN_o} :\ \|\mathbf{z}_{1:N} - \widehat{\mathbf{z}}_{1:N}\| \le \delta\right\}$ where $\|.\|$ is some vector norm on $\mathbb{R}^{NN_o}$ and δ is a suitably small "radius". The probability $P\left(\mathbf{z}_{1:N} \in \mathcal{D}(\delta)\middle|\varepsilon\right)$ will then be small and so, on average, many candidate samples will be required to generate an acceptable sample having $\widetilde{\mathbf{z}}_{1:N} \in \mathcal{D}(\delta)$ (on average, $1/P\left(\mathbf{z}_{1:N} \in \mathcal{D}(\delta)\middle|\varepsilon\right)$ candidate samples will be required). We therefore need to replace the basic ABC algorithm by one that is more efficient for sampling rare events. The same problem arises in the estimation of small failure probabilities for highly-reliable systems by Monte Carlo simulation where a sample falling in the failure region is a rare event. Subset Simulation [14] was originally developed to address this problem, but the algorithm can be readily adapted for the ABC approach and for this application it is called ABC-SubSim [13]. The reader is referred to these two papers for a detailed explanation of how Subset Simulation and ABC-SubSim work.

ABC-SubSim adaptively creates a nested decreasing sequence of data-approximating regions, $\mathcal{D}\left(\delta_j\right)$ of "radius" δ_j, as defined above, where $\delta_{j+1} < \delta_j$. At each stage j, the approximate likelihood function is defined as the conditional probability that the predicted sensor output history $\mathbf{z}_{1:N}$ falls in $\mathcal{D}\left(\delta_j\right)$:

$$\begin{aligned} P\left(\mathbf{z}_{1:N} \in \mathcal{D}\left(\delta_j\right) \middle| \mathbf{y}_{1:N}, \varepsilon\right) &= \int_{\mathcal{D}\left(\delta_j\right)} p\left(\mathbf{z}_{1:N} \middle| \mathbf{y}_{1:N}, \varepsilon\right) \mathrm{d}\mathbf{z}_{1:N} \\ &= \int \mathbb{I}_{\mathcal{D}\left(\delta_j\right)}\left(\mathbf{z}_{1:N}\right) p\left(\mathbf{z}_{1:N} \middle| \mathbf{y}_{1:N}, \varepsilon\right) \mathrm{d}\mathbf{z}_{1:N} \end{aligned} \tag{4.13}$$

where the indicator function for set $\mathcal{D}\left(\delta_j\right)$ is used. If $\delta_j \to 0$ with increasing j, then the $\mathcal{D}\left(\delta_j\right)$ will converge onto $\hat{\mathbf{z}}_{1:N}$ and the approximate likelihood function will be proportional to $p\left(\hat{\mathbf{z}}_{1:N} \middle| \mathbf{y}_{1:N}, \varepsilon\right)$, the exact likelihood function, in the limit.

Now, for reasons which will become clearer in the next sub-section, we neglect temporarily the measurement error so that $\mathbf{z}_{1:N} = \mathbf{y}_{1:N}$ but we still denote the measured output history by $\hat{\mathbf{z}}_{1:N}$. The approximate likelihood function is now:

$$P\left(\mathbf{y}_{1:N} \in \mathcal{D}\left(\delta_j\right) \middle| \mathbf{y}_{1:N}, \delta_j\right) = \mathbb{I}_{\mathcal{D}\left(\delta_j\right)}\left(\mathbf{y}_{1:N}\right) \tag{4.14}$$

where $\mathcal{D}\left(\delta_j\right) = \left\{\mathbf{y}_{1:N} \in \mathbb{R}^{NN_o} : \left\|\mathbf{y}_{1:N} - \hat{\mathbf{z}}_{1:N}\right\| \le \delta_j\right\}$. The approximate posterior from ABC is then given by Bayes' theorem as:

$$p\left(\mathbf{y}_{1:N}, \mathbf{x}_{1:N}, \boldsymbol{\theta} \middle| \mathbf{y}_{1:N} \in \mathcal{D}\left(\delta_j\right), \hat{\mathbf{u}}_{0:N}\right) \propto \mathbb{I}_{\mathcal{D}\left(\delta_j\right)}\left(\mathbf{y}_{1:N}\right) p\left(\mathbf{y}_{1:N}, \mathbf{x}_{1:N}, \boldsymbol{\theta} \middle| \hat{\mathbf{u}}_{0:N}\right) \tag{4.15}$$

4.2.3 Bayesian Updating with a Uniform PDF on the Measurement Error

We now choose a uniform prior on the measurement errors $\mathbf{e}_{1:n}$ in the original formulation:

$$p\left(\mathbf{e}_{1:n} \middle| \varepsilon\right) = \frac{\mathbb{I}_\varepsilon\left(\mathbf{e}_{1:n}\right)}{V_n\left(\varepsilon\right)}, \quad \forall \mathbf{e}_{1:n} \in \mathbb{R}^{N_o n} \tag{4.16}$$

where $\mathbb{I}_\varepsilon\left(\mathbf{e}_{1:n}\right)$ is the indicator function for the set $S\left(\varepsilon\right) = \left\{\mathbf{e}_{1:n} \in \mathbb{R}^{N_o n} : \left\|\mathbf{e}_{1:n}\right\| \le \varepsilon\right\}$ for some vector norm (e.g., $\|.\|_\infty$ or $\|.\|_2$) on $\mathbb{R}^{N_o n}$, and $V_n\left(\varepsilon\right) = \int_{\mathbb{R}^{N_o n}} \mathbb{I}_\varepsilon\left(\mathbf{e}_{1:n}\right) \mathrm{d}\mathbf{e}_{1:n}$ is the volume of region $S(\varepsilon)$. One choice of norm on $\mathbb{R}^{N_o n}$ is $\left\|\mathbf{e}_{1:n}\right\| = \max_{1 \le m \le n} \left\|\mathbf{e}_m\right\|$ using some vector norm on $\mathbb{R}^{N_o}$; in this case, it can be shown that the $\mathbf{e}_n$, $n \in \mathbb{Z}^+$, are all independent. We use this norm with $\|.\|_\infty$ on $\mathbb{R}^{N_o}$ in the examples later in Sect. 4.3.

The predictive PDF for the observed system output (sensor output) $\mathbf{z}_{1:n}$, given the actual system output $\mathbf{y}_{1:n}$ is then:

$$p\left(\mathbf{z}_{1:n} \middle| \mathbf{y}_{1:n}, \varepsilon\right) = p\left(\mathbf{e}_{1:n} \middle| \varepsilon\right)\Big|_{\mathbf{e}_{1:n} = \mathbf{z}_{1:n} - \mathbf{y}_{1:n}} = \begin{cases} V_n(\varepsilon)^{-1}, & \text{if } \left\|\mathbf{z}_{1:n} - \mathbf{y}_{1:n}\right\| \le \varepsilon \\ 0, & \text{otherwise.} \end{cases} \tag{4.17}$$

For data $\mathcal{D}_N = \{\hat{\mathbf{u}}_{0:N}, \hat{\mathbf{z}}_{1:N}\}$, this gives the likelihood function:

$$p\left(\hat{\mathbf{z}}_{1:N} \middle| \mathbf{y}_{1:N}, \varepsilon\right) = V_N(\varepsilon)^{-1} \mathbb{I}_{\mathcal{D}(\varepsilon)}\left(\mathbf{y}_{1:N}\right) \tag{4.18}$$

using the indicator function for the set $\mathcal{D}\left(\varepsilon\right) = \left\{\mathbf{y}_{1:N} \in \mathbb{R}^{NN_0} : \left\|\mathbf{y}_{1:N} - \hat{\mathbf{z}}_{1:N}\right\| \le \varepsilon\right\}$.

The posterior PDF in Eq. (4.11) is therefore now:

$$\begin{aligned} p\left(\mathbf{y}_{1:N}, \mathbf{x}_{1:N}, \boldsymbol{\theta} \middle| \mathcal{D}_N, \varepsilon\right) &= E^{-1} V_n(\varepsilon)^{-1} \mathbb{I}_{\mathcal{D}(\varepsilon)}\left(\mathbf{y}_{1:N}\right) p\left(\mathbf{y}_{1:N}, \mathbf{x}_{1:N}, \boldsymbol{\theta} \middle| \hat{\mathbf{u}}_{0:N}\right) \\ &\propto \mathbb{I}_{\mathcal{D}(\varepsilon)}\left(\mathbf{y}_{1:N}\right) p\left(\mathbf{y}_{1:N}, \mathbf{x}_{1:N}, \boldsymbol{\theta} \middle| \hat{\mathbf{u}}_{0:N}\right) \end{aligned} \tag{4.19}$$

where the evidence E is now:

$$E = V_n(\varepsilon)^{-1} \int \mathbb{I}_{\mathcal{D}(\varepsilon)}\left(\mathbf{y}_{1:N}\right) p\left(\mathbf{y}_{1:N}, \mathbf{x}_{1:N}, \boldsymbol{\theta} \middle| \hat{\mathbf{u}}_{0:N}\right) \mathrm{d}\mathbf{y}_{1:N} \mathrm{d}\mathbf{x}_{1:N} \mathrm{d}\boldsymbol{\theta} \tag{4.20}$$

Thus, setting $\varepsilon = \delta_j$, the exact posterior PDF in Eq. (4.19) using a uniform measurement error PDF is identical to the ABC posterior PDF given in Eq. (4.15) for no measurement errors. Thus, ABC-SubSim applied to the Bayesian updating problem with zero measurement error (but possibly with prediction errors from the modeling as in Eq. (4.2)) will give samples from the exact posterior PDF for a uniform measurement error (this connection between an ABC posterior and an exact posterior was noted by Wilkinson [20, 21]). In the remainder of the paper, we will use the exact interpretation of ABC-SubSim, keeping in mind that: $p\left(\mathbf{y}_{1:N}, \mathbf{x}_{1:N}, \boldsymbol{\theta} \middle| \mathcal{D}_N, \varepsilon\right) = p\left(\mathbf{y}_{1:N}, \mathbf{x}_{1:N}, \boldsymbol{\theta} \middle| \mathbf{y}_{1:N} \in \mathcal{D}\left(\delta_j\right), \hat{\mathbf{u}}_{0:N}\right)$ from Eqs. (4.15) and (4.19).

4.2.4 Proposed Improvements

4.2.4.1 Adaptive Modified Metropolis Algorithm in ABC-SubSim

Au and Beck [14] reported that the efficiency of the MMA algorithm used in Subset Simulation depends on the spread of the local proposal PDFs but not their type (uniform, Gaussian, etc.). In case of Gaussian proposal PDFs, if the variances are too large, then the proposed moves are rejected too often and if they are too small, then chain moves too slowly. Consequently, the proposal variance should be optimally selected to make the resulting Markov chain converge to stationarity as fast as possible. In this section, we briefly explain what is meant by optimal variance selection and then an algorithm is presented to adaptively adjust the proposal variance during simulation.

Since the reason behind drawing samples from the posterior PDF is most often to compute the posterior expectation of a quantity of interest of the form $h: \boldsymbol{\theta} \to \mathbb{R}$, it seems natural to consider the statistical performance of the estimate of its expectation as an efficiency criterion for adaptive adjustment of the proposal variance. To this end, let $\boldsymbol{\theta}_j^{(k),n}$ be the nth sample vector in the kth Markov chain at the jth conditional level and $\boldsymbol{\theta}_{j,i}^{(k),n}$ be its ith component. The posterior expectation of the function h at the jth level is then estimated as follows:

$$\overline{h}_j = \mathbb{E}_{p\left(\boldsymbol{\theta} \middle| \mathcal{D}_N, \varepsilon\right)}\left[h\left(\boldsymbol{\theta}\right)\right] \approx \frac{1}{N} \sum_{k=1}^{N_c} \sum_{n=1}^{N_s} h\left(\boldsymbol{\theta}_j^{(k),n}\right) = \widetilde{h}_j \tag{4.21}$$

where $p\left(\boldsymbol{\theta} \middle| \mathcal{D}_N, \varepsilon\right)$ is a marginal of the posterior PDF in Eq. (4.19), $N_s = 1/P_0$ is the number of samples simulated from each Markov chain, and N_c is the number of Markov chains and thus $N = N_c N_s$ is the total number of samples at level j. The variance of the estimator $\widetilde{h}_j$ can be expressed in the form [14]:

$$\mathrm{Var}\left(\widetilde{h}_j\right) = \frac{R_j^0}{N}\left(1 + \gamma_j\right) \tag{4.22}$$

where

$$\gamma_j = 2 \sum_{\tau=1}^{N_s - 1} \left(1 - \frac{\tau}{N_s}\right) \frac{R_j^{(\tau)}}{R_j^0} \tag{4.23}$$

Here, $R_j^{(\tau)}$ is the autocovariance of $h(\boldsymbol{\theta})$ at lag τ, $R_j^{(\tau)} = \mathbb{E}\left[h\left(\boldsymbol{\theta}_j^{(1)}\right) h\left(\boldsymbol{\theta}_j^{(1+\tau)}\right)\right] - \overline{h}_j^2$, which can be estimated using the Markov chain samples at the jth level by (see Eq. (4.21) for the distinction between $\overline{h}_j$ and $\widetilde{h}_j$):

$$R_j^{(\tau)} \approx \widetilde{R}_j^{(\tau)} = \left[\frac{1}{N - \tau N_c} \sum_{k=1}^{N_c} \sum_{n=1}^{N_s - \tau} h\left(\boldsymbol{\theta}_j^{(k),n}\right) h\left(\boldsymbol{\theta}_j^{(k),n+\tau}\right)\right] - \widetilde{h}_j^2 \tag{4.24}$$

Given that the statistical efficiency of the estimator using dependent samples $(\gamma_j > 0)$ is reduced compared with that of independent samples ($\gamma_j = 0$) (the effective number of independent samples is $N/(1+\gamma_j)$), one can minimize γ_j to select the optimal variance at the jth simulation level. In the context of Subset Simulation, Zuev et al. [22] reported the following heuristic variance selection strategy: *set the proposal standard deviation σ_j at the jth simulation level such that the expected acceptance rate is in the range of 30–50 %*. Unfortunately, the implementation of this strategy is often an art requiring user experience or sometimes a brute force search, which is inefficient. Thus, there is a great appeal for adaptive adjustment of the proposal variance within ABC-SubSim to facilitate more efficient sampling from the posterior PDF. Here, we propose to learn the proposal variance on-the-fly in order to coerce the mean acceptance probability to a desirable value.

In the jth intermediate simulation level, the ABC-SubSim algorithm starts different Markov chains in parallel from $N_c = P_0 N$ seeds to simulate N samples that lie in $\mathcal{D}(\varepsilon_j)$. The adaptation algorithm generates these chains in an iterative manner by randomly dividing the N_c seeds into N_c/N_a groups. In each iteration, N_a Markov chains are generated using the same proposal variance where their seeds are selected randomly, without replacement, from the N_c seeds. Then, the proposal variance to generate the next group of N_a Markov chains is adaptively adjusted based on the acceptance rate of the N_a Markov chains in the previous group. We start the adaptation algorithm by running the first N_a chains with the same proposal standard deviations that are chosen by scaling a reference value $\hat{\sigma}_{j,i}$ for each of the d components θ_i of the parameter vector $\boldsymbol{\theta}$, i.e. $\sigma_{j,i}(1) = \lambda_j(1)\hat{\sigma}_{j,i}$ for $i = 1, \ldots, d$. One can obtain an initial guess for the reference value based on the sample standard deviation of the components of the seeds as follows [23]:

$$\hat{\sigma}_{j,i} = \sqrt{\frac{1}{N_c - 1}\sum_{k=1}^{N_c}\left(\theta_{j,i}^{(k),1} - \hat{\mu}_{j,i}\right)^2}, \quad i = 1, \ldots, d \tag{4.25}$$

where the sample mean of the components of the seeds is evaluated as

$$\hat{\mu}_{j,i} = \frac{1}{N_c}\sum_{k=1}^{N_c}\theta_{j,i}^{(k),1}, \quad i = 1, \ldots, d \tag{4.26}$$

Based on these N_a chains, we calculate the average acceptance rate, $\hat{\alpha}_{iter}$, which is the average number of accepted samples provided by all N_a chains. Then, the revised proposal variance is $\sigma_{j,i}(iter) = \lambda_j(iter)\hat{\sigma}_{j,i}$ where the scaling factor $\lambda_j(iter)$ can be revised by the standard Robbins-Monro recursion expression as follows [15]:

$$\log\left[\lambda_j(iter+1)\right] = \log\left[\lambda_j(iter)\right] + \xi_{iter}\left[\hat{\alpha}_{iter} - \alpha^*\right] \tag{4.27}$$

where α^* is the desired acceptance rate, which can be selected in the interval [0.4, 0.5] (the optimal value in this context is 0.44 [22]), and $\{\xi_{iter} \geq 0,\ iter = 1, \ldots, N_c/N_a - 1\}$ is the sequence of stepsizes. The above recursive relation guarantees that if the average acceptance rate is low (i.e. $\hat{\alpha}_{iter} - \alpha^* < 0$), λ_j will decrease, while on the other hand, if the average acceptance rate is high, λ_j will increase. Consequently, one can expect the ABC-SubSim algorithm to more efficiently explore the posterior PDF.

The choice of the stepsize sequence in Eq. (4.27) has a significant influence on the number of iterations required to attain the optimal value for λ_j. Here, we take up the idea in [17] and use the following relation in order to adaptively select the stepsize sequence:

$$\xi_{iter+1} = \max\left\{0, \xi_{iter} + s\left(\Delta\alpha_{iter}\Delta\alpha_{iter-1}\right)\right\} \tag{4.28}$$

where the initial stepsize ξ_1 and $\Delta\alpha_0$ are chosen a priori and $s(\alpha)$ is a sigmoid function with range $[-1, 1]$ given by $s(\alpha) = (1 - e^{-m\alpha})/(1 + e^{-m\alpha})$. Our experience is that m = 100 is a good choice, which is shown in Fig. 4.1.

The proposed adaptive MMA algorithm is briefly presented in Algorithm 2 below. For the number of seeds in each iteration, we set up $N_a = P_a N_c = P_a P_0 N$, so the number of iterations is $1/P_a$ within each simulation level. Papaioannou et al. [16] suggest that a choice of $P_a \in [0.1,\ 0.2]$ leads to good results. Regarding the scaling factor $\lambda_1(1)$, one only needs to select the initial value in the first simulation level, $j = 1$, of the ABC-SubSim. We found $\lambda_1(1) = 0.6$ to be a good choice. For $j \geq 2$, the scaling factor takes its value from the last iteration in the previous simulation level. For the initial stepsize at each simulation level, the choice of $\xi_1 = 1$ was found to be satisfactory.

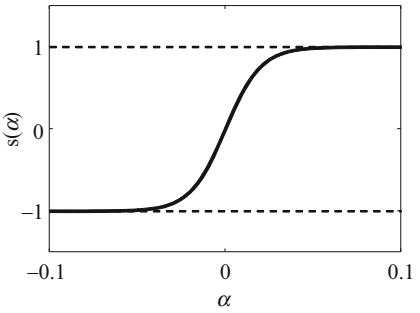

Fig. 4.1 Plot of sigmoid function for $\mathbf{m} = 100$

4.2.4.2 Treatment of Uncertain Prediction-Error Model Parameters

In reality, the parameters specifying the covariance matrix ($\boldsymbol{\theta}_w$ and $\boldsymbol{\theta}_v$) for each of the Gaussian distributions modeling the uncertain prediction errors $\mathbf{v}_n$ and $\mathbf{w}_n$, are unknown and they therefore should be learned from the data $\mathcal{D}_N$ within the ABC framework. However, when this was tried, we found that shrinking the data-approximation region, $\mathcal{D}(\varepsilon)$ ($\varepsilon \to 0$), drives the covariance matrices of the state and output prediction errors to zero. We speculate that it is due to the almost zero probability of drawing sequences of random numbers $\{\mathbf{w}_n\}_{n=1}^N$ and $\{\mathbf{v}_n\}_{n=1}^N$ such that the actual system output $\mathbf{y}_{1:N}$ exactly matches the measured system output $\hat{\mathbf{z}}_{1:N}$. Therefore, the closest approximation to the data vector $\hat{\mathbf{z}}_{1:N}$ for a given value of the structural model parameters $\hat{\boldsymbol{\theta}}_s$ is attained by the output of the underlying deterministic state-space model where all the $\mathbf{w}_n$ and $\mathbf{v}_n$ are zero. From this observation, we conclude that not only are the parameters specifying the uncertain prediction errors unidentifiable based on the likelihood function $p\left(\hat{\mathbf{z}}_{1:N}\middle|\mathbf{y}_{1:N}, \varepsilon\right)$ constructed from the entire data, but also that when $\varepsilon \to 0$, the stochastic state-space model reduces to the underlying deterministic model and, hence, one cannot properly describe the posterior uncertainty in the state and output predictions. To the authors' knowledge, this problem has not been addressed within the existing literature on ABC methods where error variances are typically assigned "a priori" in examples but are highly uncertain in real applications. In the rest of this section we therefore present a theoretical framework which allows us to get around this problem and facilitates the construction of the robust posterior predictive PDFs, see Remark 1, for a stochastic state-space model with unknown covariance matrices for the prediction errors.

Since the ABC formulation of the approximate posterior distribution in Eq. (4.15), or its equivalent exact posterior in Eq. (4.19), hinders the inference about the parameters $\boldsymbol{\theta}_w$ and $\boldsymbol{\theta}_v$ specifying the uncertain state and output prediction errors, we propose to treat them as "nuisance" parameters and integrate them out from the posterior distribution. The marginal posterior distribution of the model parameters $\boldsymbol{\theta}_s$ can be computed from:

$$p\left(\mathbf{y}_{1:N}, \mathbf{x}_{1:N}, \boldsymbol{\theta}_s\middle|\mathcal{D}_N, \varepsilon\right) = \int p\left(\mathbf{y}_{1:N}, \mathbf{x}_{1:N}, \boldsymbol{\theta}_s, \boldsymbol{\theta}_w, \boldsymbol{\theta}_v\middle|\mathcal{D}_N, \varepsilon\right) \mathrm{d}\boldsymbol{\theta}_w \mathrm{d}\boldsymbol{\theta}_v \tag{4.29}$$

Substituting Eq. (4.19) into Eq. (4.29):

$$\begin{aligned} p\left(\mathbf{y}_{1:N}, \mathbf{x}_{1:N}, \boldsymbol{\theta}_s\middle|\mathcal{D}_N, \varepsilon\right) &= E^{-1} V_N(\varepsilon)^{-1} \mathbb{I}_{\mathcal{D}(\varepsilon)}(\mathbf{y}_{1:N}) \int p\left(\mathbf{y}_{1:N}, \mathbf{x}_{1:N}, \boldsymbol{\theta}_s, \boldsymbol{\theta}_w, \boldsymbol{\theta}_v\middle|\hat{\mathbf{u}}_{0:N}\right) \mathrm{d}\boldsymbol{\theta}_w \mathrm{d}\boldsymbol{\theta}_v \\ &= E^{-1} V_N(\varepsilon)^{-1} \mathbb{I}_{\mathcal{D}(\varepsilon)}(\mathbf{y}_{1:N})\, p\left(\mathbf{y}_{1:N}, \mathbf{x}_{1:N}, \boldsymbol{\theta}_s\middle|\hat{\mathbf{u}}_{0:N}\right) \end{aligned} \tag{4.30}$$

Let $p(\boldsymbol{\theta}_s)$, $p(\boldsymbol{\theta}_w)$ and $p(\boldsymbol{\theta}_v)$ denote the prior PDFs for $\boldsymbol{\theta}_s$, $\boldsymbol{\theta}_w$ and $\boldsymbol{\theta}_v$ where the two prediction-error parameter vectors are taken to be independent a priori of each other and of the model parameters $\boldsymbol{\theta}_s$ in Eq. (4.1), then the hierarchical prior PDF in Eq. (4.10) gives for the prior in Eq. (4.30):

$$\begin{aligned} p\left(\mathbf{y}_{1:N}, \mathbf{x}_{1:N}, \boldsymbol{\theta}_s\middle|\hat{\mathbf{u}}_{0:N}\right) &= \int p\left(\mathbf{y}_{1:N}\middle|\mathbf{x}_{1:N}, \boldsymbol{\theta}_s, \boldsymbol{\theta}_v, \hat{\mathbf{u}}_{0:N}\right) p\left(\mathbf{x}_{1:N}\middle|\boldsymbol{\theta}_s, \boldsymbol{\theta}_w, \hat{\mathbf{u}}_{0:N}\right) p(\boldsymbol{\theta}_w)\, p(\boldsymbol{\theta}_v)\, p(\boldsymbol{\theta}_s)\, d\boldsymbol{\theta}_w d\boldsymbol{\theta}_v \\ &= p\left(\mathbf{y}_{1:N}\middle|\mathbf{x}_{1:N}, \boldsymbol{\theta}_s, \hat{\mathbf{u}}_{0:N}\right) p\left(\mathbf{x}_{1:N}\middle|\boldsymbol{\theta}_s, \hat{\mathbf{u}}_{0:N}\right) p(\boldsymbol{\theta}_s) \end{aligned} \tag{4.31}$$

where $p\left(\mathbf{y}_{1:N}\middle|\mathbf{x}_{1:N}, \boldsymbol{\theta}_s, \hat{\mathbf{u}}_{0:N}\right)$ and $p\left(\mathbf{x}_{1:N}\middle|\boldsymbol{\theta}_s, \hat{\mathbf{u}}_{0:N}\right)$ are the probability models connecting the input, state and output time histories with the prediction-error parameters integrated out. Notice that the marginal hierarchical *prior* PDF given in

Algorithm 2. Pseudo implementation of adaptation in simulation level j of ABC-SubSim

Inputs:

N (total number of samples to be generated at level j)

$N_c = P_0 N$ (number of seeds at level j from samples at level $j-1$; e.g. $P_0 = 0.2$)

$N_a = P_a N_c$ (number of seeds in each iteration for adaptation; e.g. $P_a = 0.1$)

ξ_1 (initial value of the stepsize sequence for $\log \lambda$ in Eq. (4.27); e.g. $\xi_1 = 1$)

α^* (desired acceptance rate; e.g. $\alpha^* = 0.44$)

$\lambda_1(1)$ (initial value for the scale factor in the first iteration of the first simulation level; e.g. $\lambda_1(1) = 0.6$)

$\lambda_j(1) = \lambda_{j-1}\,(1/P_a)$ for $j \geq 2$

Algorithm:

Permute randomly the seeds $\left\{\left(\boldsymbol{\theta}_j^{(k),1}, \mathbf{x}_j^{(k),1}, \mathbf{y}_j^{(k),1}\right) : k = 1, \ldots, N_c\right\}$ at simulation level j that were generated from $p\left(\boldsymbol{\theta}, \mathbf{x}, \mathbf{y} \middle| \mathcal{D}\left(\varepsilon_{j-1}\right)\right)$ at the previous level and lie in $\mathcal{D}\left(\varepsilon_j\right)$.

Compute the sample mean $\hat{\mu}_{j,i}$ and standard deviation $\hat{\sigma}_{j,i}$ of each component i of the seeds $\left\{\theta_{j,i}^{(k),1} : k = 1, \ldots, N_c\right\}$ using Eqs. (4.26) and (4.25).

Set $\Delta\alpha_0 = 1$.

For $iter = 1, \ldots, 1/P_a$

Set the proposal standard deviation $\sigma_{j,i}(iter) = \lambda_j(iter)\hat{\sigma}_{j,i}$

For $k = (iter-1)\,N_a + 1, \ldots, iter \cdot N_a$

Starting from $\boldsymbol{\theta}_j^{k,(1)}$, run MMA to generate an additional $1/P_0 - 1$ states of a Markov chain lying in $\mathcal{D}\left(\varepsilon_j\right)$ with the proposal standard deviation $\sigma_{j,i}(iter)$ for the ith component.

End for

Using all of the N_a/P_0 samples provided by the last N_a chains, calculate the average acceptance rate $\hat{\alpha}_{iter}$.

Update

$\Delta\alpha_{iter} = [\hat{\alpha}_{iter} - \alpha^*]$

$\log \lambda_j\,(iter+1) = \log \lambda_j(iter) + \xi_{iter}\Delta\alpha_{iter}$

$\xi_{iter+1} = \max\{0, \xi_{iter} + s\,(\Delta\alpha_{iter}\Delta\alpha_{iter-1})\}$

End for

Eq. (4.31) actually accounts for the *posterior* uncertainty induced by the nuisance parameters $\boldsymbol{\theta}_w$ and $\boldsymbol{\theta}_v$ in the inference for the model parameters $\boldsymbol{\theta}_s$, as seen in Eq. (4.30). This result is due to the hierarchical structure of the model class.

To compute the marginal probability models in Eq. (4.31), we choose the covariance matrices for the output prediction error $\mathbf{v}_n$ and the state prediction error $\mathbf{w}_n$ as time-invariant isotropic diagonal matrices, $\mathbf{Q}\left(\boldsymbol{\theta}_w\right) = \beta_w^{-1}\mathbf{I}_{N_s}$ and $\mathbf{R}\left(\boldsymbol{\theta}_v\right) = \beta_v^{-1}\mathbf{I}_{N_o}$, that is, $\boldsymbol{\theta}_w = \beta_w$ and $\boldsymbol{\theta}_v = \beta_v$, where the scalar parameters β_w and β_v define the precision in the Gaussian PDFs for the state transition PDF Eq. (4.3) and the state-to-output PDF Eq. (4.4), respectively. We take Gamma conjugate priors:

$$p\left(\beta_w \middle| a_w, b_w\right) = \mathrm{Gam}\left(\beta_w \middle| a_w, b_w\right) = \frac{b_w^{a_w}}{\Gamma\left(a_w\right)}\beta_w^{a_w-1}e^{-b_w\beta_w} \tag{4.32}$$

and $p\left(\beta_v \middle| a_v, b_v\right) = \mathrm{Gam}\left(\beta_v \middle| a_v, b_v\right)$. Thus, the marginal probability models in Eq. (4.31) can be computed using Eqs. (4.3)–(4.6) as:

$$\begin{aligned} p\left(\mathbf{x}_{1:N} \middle| \boldsymbol{\theta}_s, \hat{\mathbf{u}}_{0:N}, a_w, b_w\right) &= \int \prod_{n=1}^{N} \mathcal{N}\left(\mathbf{x}_n \middle| \mathbf{f}_n\left(\mathbf{x}_{n-1}, \mathbf{u}_{n-1}, \boldsymbol{\theta}_s\right), \beta_w^{-1}\mathbf{I}_{N_s}\right) \mathrm{Gam}\left(\beta_w \middle| a_w, b_w\right) d\beta_w \\ p\left(\mathbf{y}_{1:N} \middle| \mathbf{x}_{1:N}, \boldsymbol{\theta}_s, \hat{\mathbf{u}}_{0:N}, a_v, b_v\right) &= \int \prod_{n=1}^{N} \mathcal{N}\left(\mathbf{y}_n \middle| \mathbf{g}_n\left(\mathbf{x}_n, \mathbf{u}_n, \boldsymbol{\theta}_s\right), \beta_v^{-1}\mathbf{I}_{N_o}\right) \mathrm{Gam}\left(\beta_v \middle| a_v, b_v\right) d\beta_v \end{aligned} \tag{4.33}$$

One can readily evaluate these integrals to obtain the following marginal probability models for the state and output time histories:

$$
\begin{aligned}
p\left(\mathbf{x}_{1:N}\middle|\boldsymbol{\theta}_s, \hat{\mathbf{u}}_{0:N}, a_w, b_w\right) &= \mathrm{St}\left(\mathbf{x}_{1:N}\middle|\mathbf{f}_{1:N}, \tfrac{a_w}{b_w}\mathbf{I}_{NN_s}, 2a_w\right)\\
p\left(\mathbf{y}_{1:N}\middle|\mathbf{x}_{1:N}, \boldsymbol{\theta}_s, \hat{\mathbf{u}}_{0:N}, a_v, b_v\right) &= \mathrm{St}\left(\mathbf{y}_{1:N}\middle|\mathbf{g}_{1:N}, \tfrac{a_v}{b_v}\mathbf{I}_{NN_o}, 2a_v\right)
\end{aligned}
\tag{4.34}
$$

where $\mathbf{g}_{1:N} = \left[\mathbf{g}_1^{\mathrm{T}}, \mathbf{g}_2^{\mathrm{T}}, \ldots, \mathbf{g}_N^{\mathrm{T}}\right]^{\mathrm{T}}$ and $\mathbf{f}_{1:N} = \left[\mathbf{f}_1^{\mathrm{T}}, \mathbf{f}_2^{\mathrm{T}}, \ldots, \mathbf{f}_N^{\mathrm{T}}\right]^{\mathrm{T}}$ and

$$
\mathrm{St}\left(\boldsymbol{\varphi}\middle|\boldsymbol{\mu}, \Lambda, \kappa\right) = \frac{\Gamma\left(n_\varphi/2 + \kappa/2\right)}{\Gamma\left(\kappa/2\right)} \frac{|\Lambda|^{n_\varphi/2}}{(\pi\kappa)^{n_\varphi/2}} \left[1 + \frac{(\boldsymbol{\varphi} - \boldsymbol{\mu})^{\mathrm{T}} \Lambda\, (\boldsymbol{\varphi} - \boldsymbol{\mu})}{\kappa}\right]^{-n_\varphi/2-\kappa/2} \tag{4.35}
$$

is a multivariate Student's t-distribution with mean $\boldsymbol{\mu}$ and precision matrix Λ. Here, n_φ is the dimensionality of φ and κ is known as the degrees of freedom.

4.3 Illustrative Example

This example follows the spirit of the first example used in Ching and Chen [24]. The goal of this example is to draw samples from parameter posterior PDFs with different topologies that corresponds to globally identifiable, locally identifiable and unidentifiable model classes [25]. In this example, a two degree-of-freedom shear building is used to model a moment-resisting frame structure in order to identify the interstory stiffnesses and modal damping coefficients based on the measured acceleration data from the structure.

The shear building has known story masses $m_1 = m_2 = 1000$ kg and known ground acceleration giving the excitation. We parameterize the unknown interstory stiffnesses as $k_1 = \bar{k}_1\theta_1$ and $k_2 = \bar{k}_2\theta_2$ where $\bar{k}_1 = \bar{k}_2 = 1000$ kN/m are the actual interstory stiffnesses for the first and second stories. A similar approach is used to parameterize the damping coefficient of the first, $\xi_1 = \bar{\xi}_1\theta_3$ and the second, $\xi_2 = \bar{\xi}_2\theta_4$, vibrational modes of the shear building, where the actual modal damping coefficients are $\bar{\xi}_1 = \bar{\xi}_2 = 3\%$ for the two vibrational modes which have the natural periods of $\mathrm{T}_1 = 0.32$ s and $\mathrm{T}_2 = 0.12$ s. Thus, the uncertain parameter vector $\boldsymbol{\theta}_{\mathrm{s}} = [\theta_1\ \theta_2\ \theta_3\ \theta_4]^{\mathrm{T}}$ for the structural model is to be identified.

The equation of motion for this model can be represented by

$$
\mathbf{M}\ddot{\mathbf{z}}\,(\mathrm{t}) + \mathbf{V}\,(\boldsymbol{\theta}_{\mathrm{s}})\,\dot{\mathbf{z}}\,(\mathrm{t}) + \mathbf{K}\,(\boldsymbol{\theta}_{\mathrm{s}})\,\mathbf{z}\,(\mathrm{t}) = -\mathbf{M}1\mathrm{u}(t) \tag{4.36}
$$

where $\mathbf{z}(t) \in \mathbb{R}^2$ is the displacement vector, u(t) is the ground acceleration and $\mathbf{1} = [1, 1]^{\mathrm{T}}$. Real positive-definite symmetric matrices $\mathbf{M},\ \mathbf{V},\ \mathbf{K} \in \mathbb{R}^{2\times2}$ are mass, damping and stiffness matrices, respectively. Following the algorithm presented in Beck [18] and defining the state vector as $\mathbf{x}\,(\mathrm{t}) = \left[\mathbf{z}(\mathrm{t})^{\mathrm{T}}\ \dot{\mathbf{z}}(\mathrm{t})^{\mathrm{T}}\right]^{\mathrm{T}} \in \mathbb{R}^4$, for a given discrete-time history of the ground acceleration $\mathrm{u}_{0:\mathrm{N}}$ and model parameters $\boldsymbol{\theta}$, samples of the dynamic system state $\mathbf{x}_n$ and output $\mathbf{y}_n$ at time $t_n = n\Delta t$ can be readily generated by the following stochastic discrete state-space system

$$
\begin{aligned}
\mathbf{x}_n &= \mathbf{A}\mathbf{x}_{n-1} + \mathbf{B}\mathrm{u}_{n-1} + \mathbf{w}_n,\\
\mathbf{y}_n &= \mathbf{C}\mathbf{x}_{n-1} + \mathbf{D}\mathrm{u}_{n-1} + \mathbf{v}_n
\end{aligned}
\tag{4.37}
$$

where $\mathbf{x}_n \equiv \mathbf{x}\,(n\Delta t)$, $\mathbf{u}_n \equiv \mathbf{u}\,(n\Delta t)$ for $n = 0, 1, 2, \ldots, N$, $\mathbf{C} \in \mathbb{R}^{N_o\times4}$ is the output matrix, and $\mathbf{D} \in \mathbb{R}^{N_o}$ is the feedthrough matrix where N_o is the number of the outputs. The prior distributions $\mathcal{N}\,(0, \mathbf{Q}\,(\beta_w))$ and $\mathcal{N}\,(0, \mathbf{R}\,(\beta_v))$ are specified for the state and output prediction errors, $\mathbf{w}_n$ and $\mathbf{v}_n$, respectively, where the covariance matrices are modeled as diagonal matrices:

$$
\mathbf{Q}\,(\beta_w) = \begin{bmatrix} 0 & 0 \\ 0 & \beta_w^{-1}\mathbf{I}_2 \end{bmatrix}, \text{ and } \mathbf{R}\,(\beta_v) = \beta_v^{-1}\mathbf{I}_{N_o} \tag{4.38}
$$

Here we consider various levels of identifiability [26]: (1) Case I (Unidentifiable): there are infinitely many MLEs (Maximum Likelihood Estimates) because only the ground and roof accelerations are measured for 2 s and the ground excitation is chosen such that it only excites the first mode of the shear building; (2) Case II (Locally identifiable): there are finitely many MLEs because only the ground and roof accelerations are measured but the ground excitation is chosen such that both

Table 4.1 Parameter configuration of the ABC-SubSim algorithm

ABC-SubSim		Adaptation algorithm		Simulation levels (m)		
Sample size (N)	Conditional probability (P_0)	Adaptation probability (P_a)	Optimal acceptance rate (α^*)	Case I	Case II	Case III
2000	0.2	0.1	0.5	3	5	6

vibrational modes of the building are excited; (3) Case III (Globally identifiable): there is a unique MLE because the ground, roof and second floor accelerations are measured and the excitation is again selected such that it excites both modes of the structure.

For all cases, our objective is to draw samples from the posterior $p\left(\mathbf{y}_{1:N}, \mathbf{x}_{1:N}, \boldsymbol{\theta} \middle| \mathcal{D}_N, \varepsilon\right)$ where $\mathbf{y}_{1:N}$ is constrained to lie in a small neighborhood, $\mathcal{D}(\varepsilon)$, of the data vector defined by

$$\mathcal{D}(\varepsilon) = \left\{ \mathbf{y}_{1:N} \in \mathbb{R}^{NN_o} : \max_{1 \le n \le N} \|\hat{\mathbf{z}}_n - \mathbf{y}_n\|_\infty \le \varepsilon \right\} \tag{4.39}$$

the infinity norm on $\mathbb{R}^{N_o}$.

The synthetic ground acceleration is a discrete time history $\mathrm{u}_{0:\mathrm{N}}$ with $N = 200$ time steps of $\Delta t = 0.01$ s s to give 2 s of data. To exclusively excite the frequency bands of interest in each case, the ground acceleration is designed using random phase multisine excitation [27]. The excited frequencies are chosen on the equidistant frequency grids kf_0, $f_0 = 0.5$ Hz, where $k \in \{5, 6\}$ for Case I and $k \in \{2, 3, \ldots, 20\}$ for Cases II and III. The ground acceleration is normalized to give a RMS value equal to 1 ms^{-2}.

For the given excitation time history and the actual value of the model parameters, the noisy measurements at the observed DOFs (roof only, or roof and the second floor) are synthetically generated from Eq. (4.37) with $\beta_w = 10^6$ $\mathrm{m}^{-2}\mathrm{s}^2$ and $\beta_v = 25$ $\mathrm{m}^{-2}\mathrm{s}^4$ and using $\Delta t = 0.01$ s, $N = 200$, where β_w is selected such that state prediction error $\{\mathbf{w}_n\}_{n=1}^N$ gives about 1 % RMS noise-to-signal ratio over the velocity states of the actual state-space model, and β_v is selected such that output prediction error $\{\mathbf{v}_n\}_{n=1}^N$ gives approximately 10 % RMS noise-to-signal ratio over the acceleration data from the actual state-space model for all cases. In this example we treat the parameters β_w and β_v as nuisance parameters and adopt the prior distributions $\mathrm{Gam}\left(\beta_w \middle| 5, 5 \times 10^6\right)$ and $\mathrm{Gam}\left(\beta_v \middle| 5, 125\right)$. Thus, following the marginalization algorithm explained in Sect. 4.2.2, we compute the marginal posterior PDF of the uncertain structural model parameters $\boldsymbol{\theta}_\mathrm{s}$. The prior PDF for the parameter vector $\boldsymbol{\theta}_\mathrm{s}$ is selected as the product of uniform distributions for each component $\theta_i \in [0, 3]$, for $i = 1, .., 4$. Table 4.1 presents the information used to configure the ABC-SubSim algorithm.

Figure 4.2 plots 2000 samples of the parameter vector drawn from the marginal posterior distribution $p\left(\boldsymbol{\theta}_\mathrm{s} \middle|_N, \varepsilon\right)$. The four components of the ABC-SubSim samples are shown in two groups, the interstory stiffness parameters in the top row and the modal damping coefficients in the bottom row. For Case I, the distribution of the samples drawn from the joint posterior PDF of the interstory stiffness parameters shows that there is a continuum of most probable values lying around a manifold in the parameter space. This means that the lack of sufficient information in the given data in Case I causes the interstory stiffness parameters to be unidentifiable [25]. For Case II, the posterior samples for the stiffness parameters are clustered around two optimal models that are roughly equally plausible based on the data, meaning that the model class in this case is only locally identifiable. For Case III, the stiffness parameter samples obtained from ABC-SubSim are clustered around a single optimal model at the true parameter values, i.e. model class is globally identifiable, at least with respect to the two stiffness parameters. The posterior distribution of the damping parameters reveals higher uncertainty than the stiffness parameters.

Figure 4.3 shows the ability of the proposed adaptive algorithm to adjust automatically the proposal variance such that the average acceptance rate remains around the desired value, which is set to 50 % in this example. It is worth mentioning that drawing samples from posterior PDFs where the parameters exhibit nonlinear correlations, e.g. the posterior distribution in Case I, has been addressed as a challenging problem in the literature for adaptive MCMCs [28, 29]. Here, we have shown that ABC-SubSim with the proposed adaptive algorithm works well for this type of posterior distributions.

Figure 4.4 shows the sequence of the tolerance levels obtained by ABC-SubSim using $P_0 = 0.2$ for all cases. Here, we stopped the ABC-SubSim algorithm when the average acceptance rate drops significantly to a value much less than the desired optimal acceptance rate.

Figure 4.5 illustrates the predictive (smoothing) capability of the Bayesian model updating using ABC-SubSim, where the time history of the responses from the roof and the second floor for the exact state-space model in different cases are compared with the corresponding predictions from the marginal robust posterior predictive PDF of the response using Eq. (4.30). The black solid curve shows the response from the exact model, the blue solid curve shows the mean response

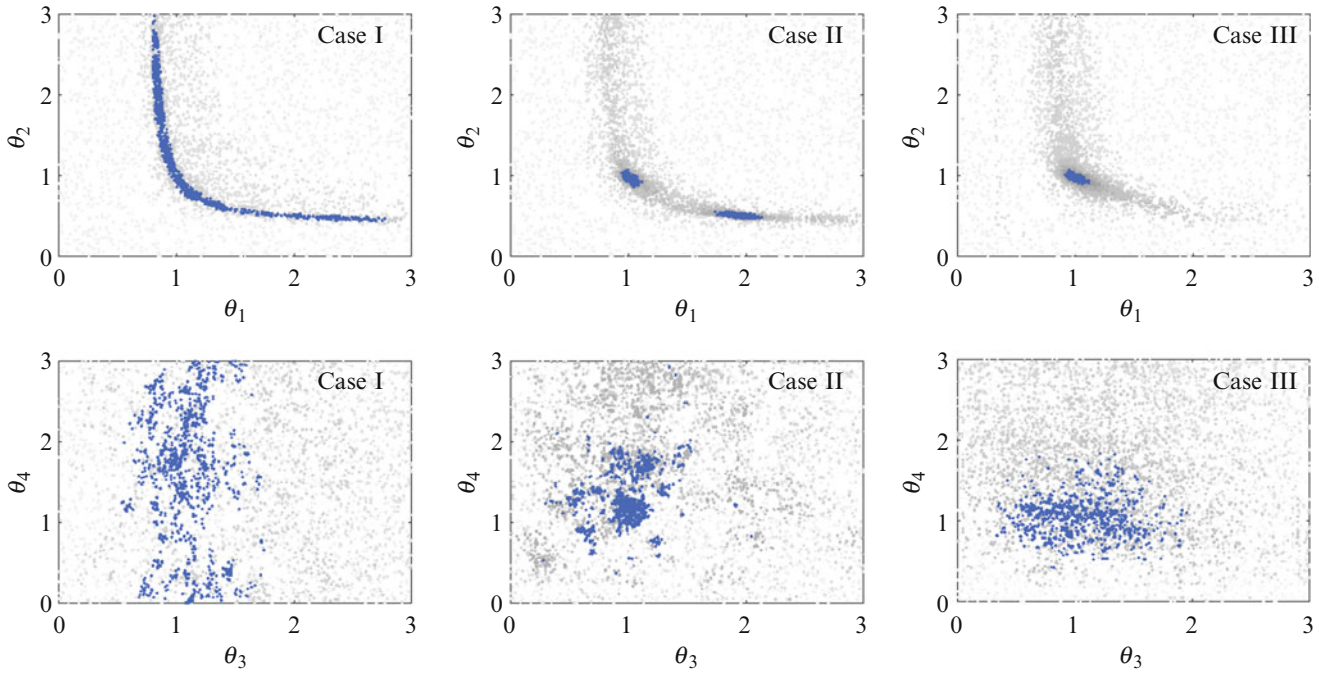

Fig. 4.2 Scatter plot of 2000 posterior samples of the model parameters, $\boldsymbol{\theta}_s$, of the linear two DOF structure for the intermediate levels (*in gray*) and the final level (*in blue*) and for different cases; Case I (unidentifiable), Case II (locally identifiable), Case III (globally identifiable)

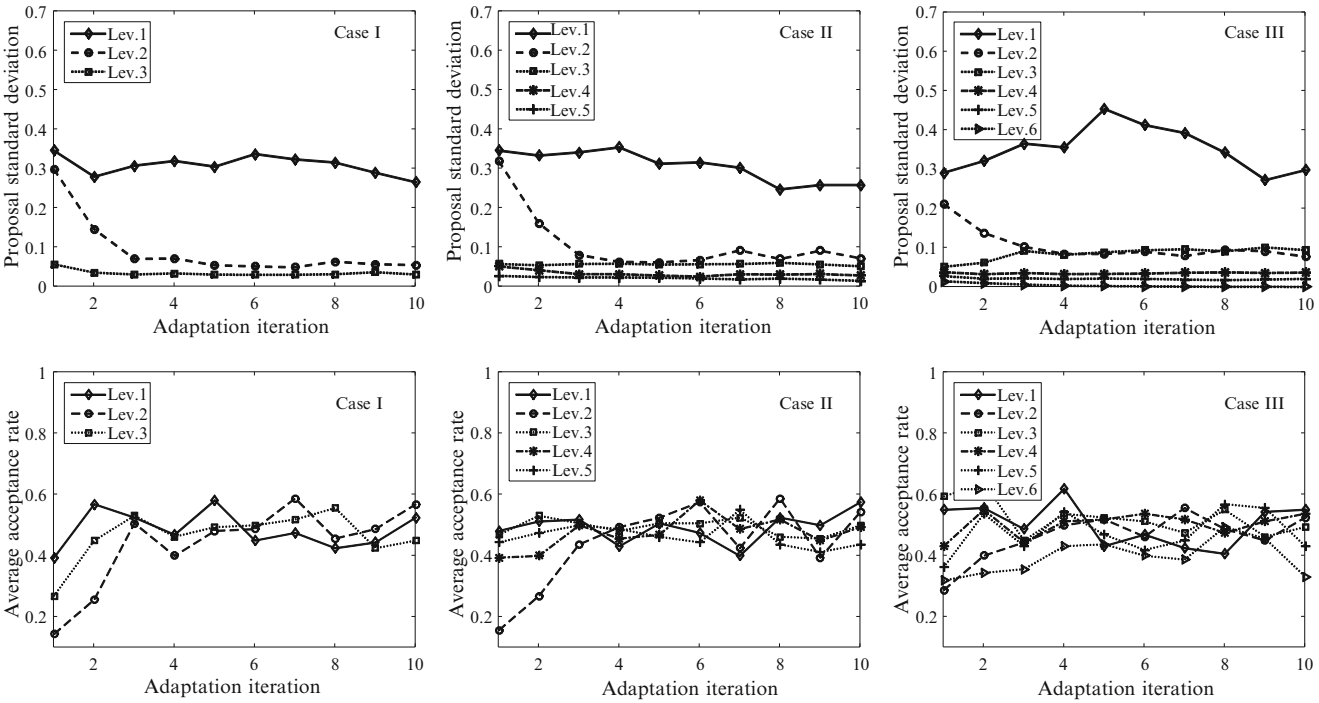

Fig. 4.3 The proposal standard deviation for θ_1 and the average acceptance rate of the MMA algorithm within different levels of the ABC-SubSim for different cases; Case I (*first column*), Case II (*second column*), and Case III (*third column*)

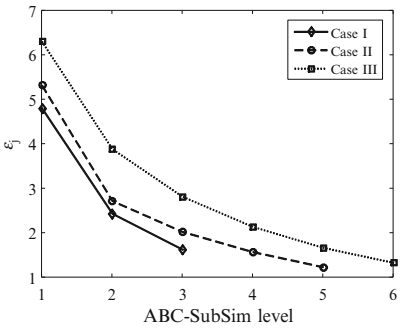

Fig. 4.4 The sequence of tolerance levels, ε_j, using $P_0 = 0.2$ for Cases I, II and III

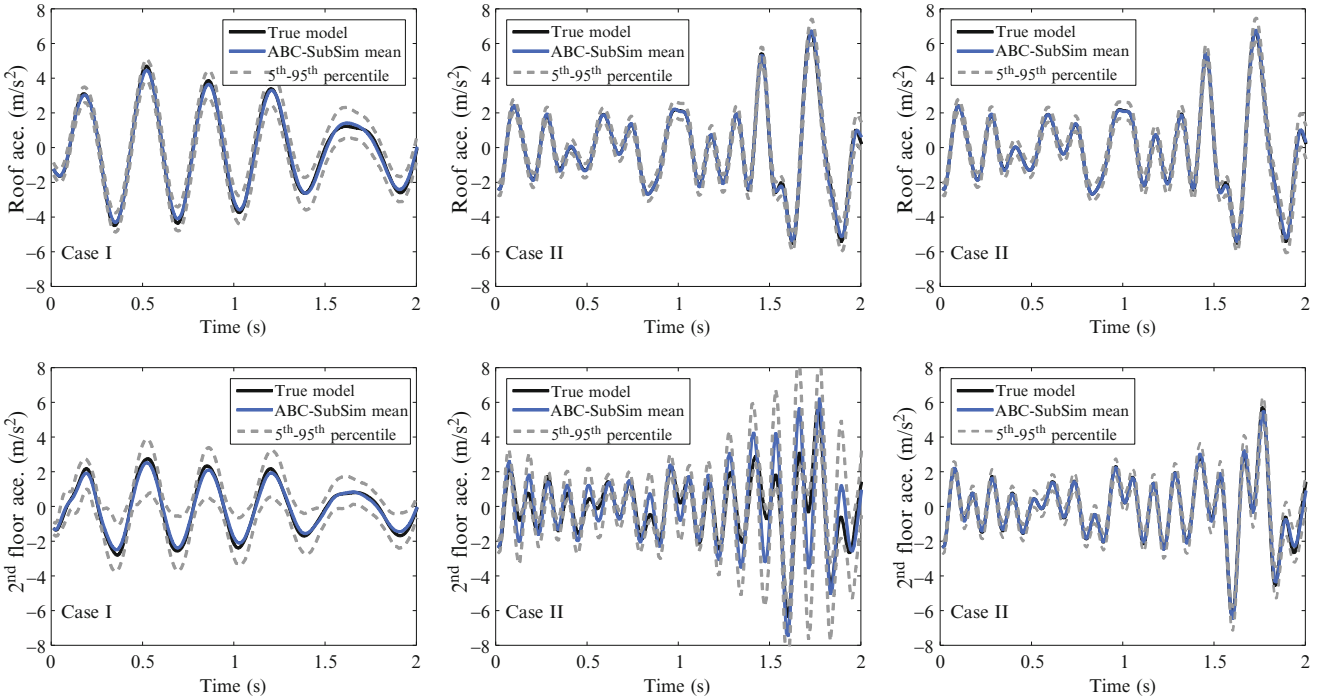

Fig. 4.5 The exact time histories of acceleration for the roof (*top row*) and second floor (*bottom row*) together with the mean estimate from the ABC-SubSim approximation and the 5th and 95th percentiles, predicted based on the marginal robust posterior predictive PDF of the response in Eq. (4.30) for Case I, II and III

estimated by averaging over the samples from the robust posterior predictive PDF and the two dashed curves correspond to 5th and 95th percentiles of the responses sampled from the robust posterior predictive PDF. In all cases, the exact response at the roof and the second floor lies between the two percentiles. This indicates the ability of the Bayesian robust predictive analysis to give informative predictions even at the unobserved floors and despite the fact that the model class has various degrees of identifiability based on the measured data in different cases.

4.4 Conclusion

This paper presented the potential of the ABC-SubSim algorithm, a recently developed multi-level MCMC algorithm, for solving the Bayesian model updating problems for a general hierarchical state-space model. It was shown that under the assumption of the existence of uniformly-distributed measurement errors, ABC is equivalent to solving the exact Bayesian inference. This interpretation gives a better understanding of the approximations made in the ABC algorithms. We developed a new adaptive strategy for selection of the proposal variance for MMA in ABC-SubSim. This strategy adjusts the proposal variance in each simulation level of ABC-SubSim such that the mean acceptance probability is forced to remain close to a desirable target value. Besides, we reported a fundamental difficulty in using ABC algorithms to estimate the

parameters of the uncertain state and output prediction errors in a stochastic state-space model; when shrinking the data approximation region towards their data, ABC based on the entire data drives the covariance matrices of the uncertain prediction errors towards zero. To circumvent this behavior, these parameters were treated as nuisance parameters and eliminated by analytically integrating them out of the posterior. The results showed the ABC-SubSim is able to explore posterior distributions with challenging topologies, such as well-separated regions of high probability or a continuum of highly probable parameter values with nonlinear correlation among the parameters.

Acknowledgment The first author of this paper wants to express his gratitude to the California Institute of Technology (Caltech) for kindly hosting him during the course of this work.

References

1. Madarshahian, R., Caicedo, J.M.: Reducing MCMC computational cost with a two layered Bayesian approach. In: Model Validation and Uncertainty Quantification, vol. 3, pp. 291–297. Springer International Publishing (2015)
2. Marin, J.M., Pudlo, P., Robert, C.P., Ryder, R.J.: Approximate Bayesian computational methods. Stat. Comput. **22**(6), 1167–1180 (2012)
3. Pritchard, J.K., Seielstad, M.T., Perez-Lezaun, A., Feldman, M.W.: Population growth of human Y chromosomes: a study of Y chromosome microsatellites. Mol. Biol. Evol. **16**(12), 1791–1798 (1999)
4. Bortot, P., Coles, S.G., Sisson, S.A.: Inference for stereological extremes. J. Am. Stat. Assoc. **102**(477), 84–92 (2007)
5. Marjoram, P., Molitor, J., Plagnol, V., Tavaré, S.: Markov chain Monte Carlo without likelihoods. Proc. Natl. Acad. Sci. **100**(26), 15324–15328 (2003)
6. Sisson, S.A., Fan, Y.: Likelihood-free Markov chain Monte Carlo. In: Handbook of Markov Chain Monte Carlo, pp. 319–341. Chapman and Hall/CRC Press, Boca Raton (2011)
7. Sisson, S., Fan, Y., Tanaka, M.: A note on backward kernel choice for sequential Monte Carlo without likelihoods. Technical report, University of New South Wales (2008)
8. Sisson, S.A., Fan, Y., Tanaka, M.M.: Sequential Monte Carlo without likelihoods. Proc. Natl. Acad. Sci. **104**(6), 1760–1765 (2007)
9. Del Moral, P., Doucet, A., Jasra, A.: An adaptive sequential Monte Carlo method for approximate Bayesian computation. Stat. Comput. **22**(5), 1009–1020 (2012)
10. Drovandi, C.C., Pettitt, A.N.: Estimation of parameters for macroparasite population evolution using approximate Bayesian computation. Biometrics **67**(1), 225–233 (2011)
11. Toni, T., Welch, D., Strelkowa, N., Ipsen, A., Stumpf, M.P.: Approximate Bayesian computation scheme for parameter inference and model selection in dynamical systems. J. R. Soc. Interface **6**(31), 187–202 (2009)
12. Beaumont, M.A., Cornuet, J.M., Marin, J.M., Robert, C.P.: Adaptive approximate Bayesian computation. Biometrika **96**, 983–990 (2009)
13. Chiachio, M., Beck, J.L., Chiachio, J., Rus, G.: Approximate Bayesian computation by Subset Simulation. SIAM J. Sci. Comput. **36**(3), A1339–A1358 (2014)
14. Au, S.K., Beck, J.L.: Estimation of small failure probabilities in high dimensions by Subset Simulation. Probab. Eng. Mech. **16**(4), 263–277 (2001)
15. Andrieu, C., Thoms, J.: A tutorial on adaptive MCMC. Stat. Comput. **18**(4), 343–373 (2008)
16. Papaioannou, I., Betz, W., Zwirglmaier, K., Straub, D.: MCMC algorithms for Subset Simulation, Manuscript, Engineering Risk Analysis Group, Technische Universität München (2014)
17. Plakhov, A., Cruz, P.: A stochastic approximation algorithm with step-size adaptation. J. Math. Sci. **120**(1), 964–973 (2004)
18. Beck, J.L.: Bayesian system identification based on probability logic. Struct. Control. Health Monit. **17**(7), 825–847 (2010)
19. Jaynes, E.T.: Information theory and statistical mechanics. Phys. Rev. **106**(4), 620 (1957)
20. Wilkinson, R.D.: Approximate Bayesian computation (ABC) gives exact results under the assumption of model error. Stat. Appl. Genet. Mol. Biol. **12**(2), 129–141 (2013)
21. Wilkinson, R.D.: Bayesian inference of primate divergence times. University of Cambridge (2007)
22. Zuev, K.M., Beck, J.L., Au, S.K., Katafygiotis, L.S.: Bayesian post-processor and other enhancements of Subset Simulation for estimating failure probabilities in high dimensions. Comput. Struct. **92**, 283–296 (2012)
23. Au, S.K., Cao, Z.J., Wang, Y.: Implementing advanced Monte Carlo simulation under spreadsheet environment. Struct. Saf. **32**(5), 281–292 (2010)
24. Ching, J., Chen, Y.C.: Transitional Markov chain Monte Carlo method for Bayesian model updating, model class selection, and model averaging. J. Eng. Mech. **133**(7), 816–832 (2007)
25. Beck, J.L., Katafygiotis, L.S.: Updating models and their uncertainties. I: Bayesian statistical framework. J. Eng. Mech. **124**(4), 455–461 (1998)
26. Katafygiotis, L.S., Beck, J.L.: Updating models and their uncertainties. II: model identifiability. J. Eng. Mech. **124**(4), 463–467 (1998)
27. Pintelon, R., Schoukens, J.: System identification: a frequency domain approach. Wiley-IEEE Press, United States (2012)
28. Roberts, G.O., Rosenthal, J.S.: Examples of adaptive MCMC. J. Comput. Graph. Stat. **18**(2), 349–367 (2009)
29. Solonen, A., Ollinaho, P., Laine, M., Haario, H., Tamminen, J., Järvinen, H.: Efficient MCMC for climate model parameter estimation: parallel adaptive chains and early rejection. Bayesian Anal. **7**(3), 715–736 (2012)

Chapter 5
Determining Model Form Uncertainty of Reduced Order Models

Matthew S. Bonney, Daniel C. Kammer, and Matthew R.W. Brake

Abstract The quantification of model form uncertainty is very important for engineers to understand when using a reduced order model. This quantification requires multiple numerical simulations which can be computationally expensive. Different sampling techniques, including Monte Carlo and Latin Hypercube, are explored while using the maximum entropy method to quantify the uncertainty. The maximum entropy method implements random matrices that maintain essential properties. This is explored on a planar frame using different types of substructure representations, such as Craig-Bampton. Along with the model form uncertainty of the substructure representation, the effect of component mode synthesis for each type of substructure representation on the model form uncertainty is studied.

Keywords Model-form uncertainty • Uncertainty quantification • Maximum entropy • Sub-structuring

5.1 Introduction

Model form uncertainty is a very important research topic in the study of computational mechanics. Depending on how the analyst choses to represent the material or structure, the results from the simulations may differ. One major cause of this difference is model reduction. High-fidelity models can give high accuracy results although the computational time and resources is expensive. To reduce the cost of this computational requirement, a model reduction is typically used. This reduction induces some model form error, which can be difficult to quantify.

The study of model reduction uncertainty due to truncation has typically been done by calculating a percent difference in the natural frequency individually. This gives first order uncertainty information that cannot be propagated into assembled system if sub-structuring is used. In order to perform an uncertainty propagation, information about the model itself is required on a physical level, such as mass and stiffness matrices. The method used to describe the uncertainty in the system matrices is the maximum entropy approach [2, 4–7]. This method, primarily developed by Soize, incorporates the use of random matrix theory. The maximum entropy approach is able to characterize the uncertainty of the physical matrices in terms of a scalar value for each system matrix. This scalar value is used to characterize the randomness of the system matrix which is simple to propagate to a desired result using sampling methods such as Monte-Carlo (MC). Maximum entropy uses the probability from the MC analysis instead of a percentage difference of deterministic frequencies. This technique is used on a Craig-Bampton (CB) [3] reduced order model (ROM).

Sandia National Laboratories is a multi-program laboratory managed and operated by Sandia Corporation, a wholly owned subsidiary of Lockheed Martin Corporations, for the U.S. Department of Energy's National Nuclear Security Administration under Contract DE-AC04-94AL85000.

M.S. Bonney (✉)
University of Wisconsin-Madison, Madison, WI, USA
e-mail: msbonney@wisc.edu

D.C. Kammer
Engineering Physics, University of Wisconsin-Madison, Madison, WI, USA
e-mail: kammer@engr.wisc.edu

M.R.W. Brake
Sandia National Laboratories, Albuquerque, NM, USA
e-mail: mrbrake@sandia.gov

S. Atamturktur et al. (eds.), *Model Validation and Uncertainty Quantification, Volume 3*, Conference Proceedings of the Society for Experimental Mechanics Series, DOI 10.1007/978-3-319-29754-5_5

5.2 Theory

This research combines a model reduction technique, CB, and a method for determining the uncertainty of the physical system matrices, maximum entropy. Craig-Bampton is a technique that have been thoroughly studies and understood for the past 40 years [3]. The maximum entropy approach used in this paper is a relatively new technique for quantifying the error associated with the system matrices first described in [5] and further in [7]. The exact method used in this paper is described in detailed in [2]. Each of these techniques are explained in the next sections.

5.2.1 Craig-Bampton/Fixed Interface

Craig-Bampton is a model reduction technique that uses fixed interface modes along with physical interface DOF. The fixed interface modes are truncated typically based on frequency. The reduction can be written as

$$\begin{pmatrix} u_i \\ u_j \end{pmatrix} = \begin{bmatrix} \Phi_k & \Psi \\ 0 & I \end{bmatrix} \begin{pmatrix} \eta_k \\ u_j \end{pmatrix}, \tag{5.1}$$

where u are the physical DOF, Φ are the fixed-interface modes, Ψ are the constraint modes that describe how the interior DOF deflect due to a unit displacement in a single interface DOF, and η are the fixed-interface modal DOF. 0 is a matrix of zeros, I is the identity matrix, the subscript i is the interior DOF, subscript j is the interface DOF, and the subscript k is the kept fixed-interface mode. The fixed-interface modes are typically truncated at frequencies greater than 1.5 or 2 times the highest desired frequency. This reduction is done for each substructure. Once this reduction is performed, the system matrices are combined and synthesized. The system DOF are organized for two substructures, as is the form of this investigation's problem, as

$$u_{cb} = \begin{pmatrix} \eta_k^\alpha \\ u_j^\alpha \\ \eta_k^\beta \\ u_j^\beta \end{pmatrix}, \tag{5.2}$$

where the superscript α refers to the first substructure and the superscript β refers to the second substructure. This partitioning of the DOF for this synthesis yields system matrices in the form of

$$[M_{cb}] = \begin{bmatrix} [M]^\alpha & 0 \\ 0 & [M]^\beta \end{bmatrix} \quad [K_{cb}] = \begin{bmatrix} [K]^\alpha & 0 \\ 0 & [K]^\beta \end{bmatrix}. \tag{5.3}$$

The individual substructure matrices are already reduced by using the CB method. These system matrices form the equations of motion for an undamped and unforced system as

$$[M_{cb}]\ddot{u}_{cb} + [K_{cb}]u_{cb} = 0. \tag{5.4}$$

These subsystems are still independent and are not constrained together. The interface DOF are constrained to be equal. This is written as

$$u_j^\alpha = u_j^\beta = u_j. \tag{5.5}$$

This constraint reduces the DOF vector to

$$u = \begin{pmatrix} \eta_k^\alpha \\ \eta_k^\beta \\ u_j \end{pmatrix}. \tag{5.6}$$

The advantage of using this reduction is that the interface DOF are preserved in the substructure allowing for easy connection. The synthesized system contains the fixed interface modes from both substructures and the physical DOF at the interface. One disadvantage of using this ROM is for systems with highly connected interfaces. This type of system produces a relatively large ROM, which decreases the utility of this technique.

5.2.2 Maximum Entropy

The equations of motion of the system is based on linear mass and stiffness. The mass matrix is positive definite while the stiffness matrix is either positive definite or semi-positive definite depending if the system is constrained or contains rigid body motion. Due to the definiteness of the matrices, these can decomposed using a Cholesky decomposition similar to

$$[M] = [L_M]^T [L_M], \tag{5.7}$$

with $[L_M]$ is an upper triangular matrix that is the Cholesky decomposition of the mass matrix $[M]$. For a non-singular matrix, $[L_M]$ is a square matrix, and for a singular matrix, $[L_M]$ is a rectangular matrix. The Cholesky decomposition is a function of the input parameters to the finite element model. To incorporate model form error, a random germ is added which is also generated to be positive definite so that the resulting matrix is still positive definite or positive semi-definite. The germ is incorporated using the relation

$$[M] = [L_M]^T [G(\delta_M)][L_M], \tag{5.8}$$

where $[G]$ is a random germ with an expected value of I and δ_M is the dispersion parameter for the mass matrix. The variance of the random germ is a function of δ scaled by the size of the matrix. More detail of how to formulate this germ is given in [1, 2, 4, 5]. The dispersion parameter is chosen to best fit the truth data, which corresponds to having the highest probability in the probability density function. Truth data can be given as many things such as the frequency response function, mode shapes, or natural frequencies. This research uses the first 11 elastic natural frequencies as the truth data. The probability is best given as the likelihood function, which is the objective function for the dispersion variable. The main calculation is the likelihood value for each dispersion variable which controls the variance of the random matrices. The likelihood value is defined as the joint probability that the truth data exists within the model. This is shown as

$$L(\delta) = \Pr(TruthData|\delta), \tag{5.9}$$

where $L(\delta)$ is the likelihood value and $Pr()$ is the probability value that the truth data exists in the model. For the simplicity of calculations, each natural frequency is treated as independent. Due to the independence, the joint probability can be rewritten as

$$\Pr(TruthData|\delta) = \Pi_i \Pr(\omega_i|\delta). \tag{5.10}$$

This calculation yields a value on the range of $[0, 1]$. The optimal dispersion value is defined as the argument maximum of the likelihood function. Since this calculation has a very small range, the differences between each dispersion value can be small which can be affected by the computer resolution error. In order to reduce this error, the log-likelihood function is used. For this calculations, the negative log-likelihood function is used in order to possibly use optimization techniques. The negative log-likelihood is calculated by computing $\ell = \sum_i -log(\Pr(\omega_i|\delta))$. The reason this works is because $-log$ is a monotonically decreasing function, which means that the argument minimum of the negative log-likelihood is the same as the argument maximum of the likelihood function.

The calculation of the likelihood is based on the probability measure. There are two ways to compute this probability: analytically or numerically. In order to calculate the probability analytically, the distribution of the natural frequency must be known which is very hard to generate. This simulation calculates the probability numerically based on a MC simulation. In order to calculate the probability, a histogram is used. For these calculations the tolerance band is based on 0.1 % of the natural frequency. The probability is calculated as the percentage of the number of times a natural frequency lands within this tolerance band. The determination of the band is very critical in the execution of this analysis. A band that is too small will result in very large variability, while a band that is too large will not be able to differentiate between different dispersion values. The argument minimum of this negative log-likelihood function is the statistical estimate of the dispersion variable.

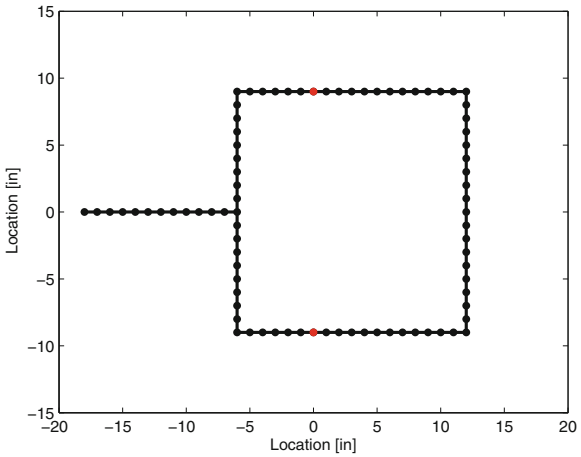

Fig. 5.1 Planar frame example system

In this paper, the likelihood is computed with 5000 samples from a distribution and is run 50 times to show randomness of the likelihood. This permits the calculation of the empirical negative log-likelihood using the expression

$$EL(\delta) = \sup_i \ell_i(\delta), \tag{5.11}$$

in which, i is the independent evaluation of the negative log-likelihood, ℓ_i. This empirical formulation accounts for the randomness in the Monte-Carlo sampling technique. The optimal dispersion parameter is then chosen based on

$$\delta^{optimal} = \arg min\ EL(\delta). \tag{5.12}$$

The optimal dispersion parameter is used in a forward propagation of the matrices to determine the distribution of the desired output, such as reliability measure or dynamic characteristics.

5.3 Example System

The system used to illustrate these techniques is a planar fame with an appendage. This system is shown in Fig. 5.1.

Figure 5.1 contains two subsystems that are combine to form the full system separated by the red nodes. The subsystem to the right is called system "B" and the subsystem to the left with the appendage is called system "D". These subsystems are reduced using the desired ROM technique, then are combined using component mode synthesis. Due to time constraints, only the synthesis of CB to CB is examined. The red connection nodes are shared between the two subsystems and are defined as the interface. The nodes shown in Fig. 5.1 are connected using simple Euler beam elements. Each of the two subsystems has 129 degrees of freedom. This system is relatively small but large enough to show the complexity of the techniques and how they can be applied to larger systems.

The simulations are based on matching both the substructure and system frequencies for the first 11 elastic free-free modes. For subsystem B, the 11th natural frequency is 4656.4 Hz and subsystem D has an eleventh natural frequency at 5511.5 Hz. The full system has an 11th natural frequency of 1864.3 Hz. This selection of the first 11 elastic free-free modes was due to the idea that the higher frequency modes are more subject to model form error.

5.4 Results

5.4.1 Craig-Bampton Substructure

The first result is the analysis of a single substructure. This analysis took the first 11 elastic free-free modes for each substructure as the truth data. For both of the subsystems, the eleventh free-free frequency occurs at approximately the eleventh fixed-interface frequency. Typically, the modes kept in the reduction are any modes that have a frequency less than

Table 5.1 Optimal substructure dispersion parameter

# of Elastic fixed-interface modes	δ_k for system B (%)	δ_k for system D (%)
11	0.85	1.44
12	0.82	1.93
13	0.56	1.23
14	0.47	1.04
15	**0.35**	**0.96**
16	0.25	0.52
17	0.25	*0.45*
18	**0.00**	**0.35**
19	0.00	0.32
20	0.00	0.31

one and half to two times the highest desired frequency. For system B, the largest desired frequency is 4656.4 Hz so typically all the fixed-interface modes with frequency less than 7000 or 9300 Hz are kept. This would involve 15 or 18 fixed-interface modes. A sweep of the number of fixed-interface modes from 11 to 20 is performed to analyze the convergence of the dispersion parameter. This dispersion parameter has a maximum value of one when the size of the matrix goes to infinity. Due to this bound, the dispersion parameter is typically represented as a percentage. The Monte-Carlo analysis is performed on both systems for this range of kept fixed-interface modes with 5000 samples and performed 50 times to evaluate the empirical likelihood. In order to produce a single value for the dispersion parameter, only the stiffness of the system is chosen to be stochastic and the mass matrix is chosen to be deterministic. This goes under the assumption that the mass and moments of inertia are accurately represented by Euler beam elements. These optimal parameters are shown in Table 5.1. The values in Table 5.1 highlighted in bold represent keeping all modes less than one and a half times the eleventh free-free frequency and the values highlighted in italic represent keeping all modes less than twice the eleventh free-free frequency.

Some differences between the two substructures can be seen in Table 5.1. The first difference is that system D has a larger dispersion parameter for each case tested. This is believed to be due to the appendage on system D. The appendage creates modes that are harder to express in terms of fixed-interface modes. The general trend of these dispersion parameters follows the expected trend. The dispersion parameter goes to zero as more modes are included. One abnormality found was for system D. As the number of fixed-interface modes increases from 11 to 12, the dispersion parameter increases. These values are evaluated several times to verify that this is not caused by numerical issues and is uncertain as to the cause of this increase.

5.4.2 Craig-Bampton Combined System

The combination of the substructure into one system is a very typical utilization of this reduced order model technique. One major problem with doing a component mode synthesis on a system is that the uncertainty of the combined system is difficult to determine based on the uncertainty of the substructures. One difficulty is that the truth data for each system is different. Even if the frequencies used are similar, the mode shapes are different and are more difficult to express. The first result from the combined system is to try to find a relationship between the dispersion parameter of the substructures and the dispersion parameter of the combine system. This is expressed as taking the data from the previous section and finding the dispersion parameter of the system for the prescribed number of modes kept. The results of the dispersion parameter are shown in Fig. 5.2.

The same basic trend that is found in Table 5.1 is found in Fig. 5.2. As more modes are added, the dispersion parameter decreases. One interesting aspect is when 11 fixed-interface modes are kept for both of the substructures. The synthesized system has a dispersion parameter less than the dispersion parameter of either substructure. System B has a dispersion parameter of 0.85 %, system D has a dispersion parameter of 1.44 % and the synthesized system E has a dispersion parameter of 0.49 %.

The number of modes shown in Fig. 5.2 is not typical for a substructuring analysis. As mentioned, typical analysis uses one and a half or two times the highest frequency of the full system. System E has a highest frequency of interest of 1864.3 Hz so each substructure modes up to 2800 or 3700 Hz are kept. For the case of one and a half times, substructure B keeps 8 fixed-interface modes and substructure D keeps 6 fixed-interface modes. Using these modes, system E has a dispersion

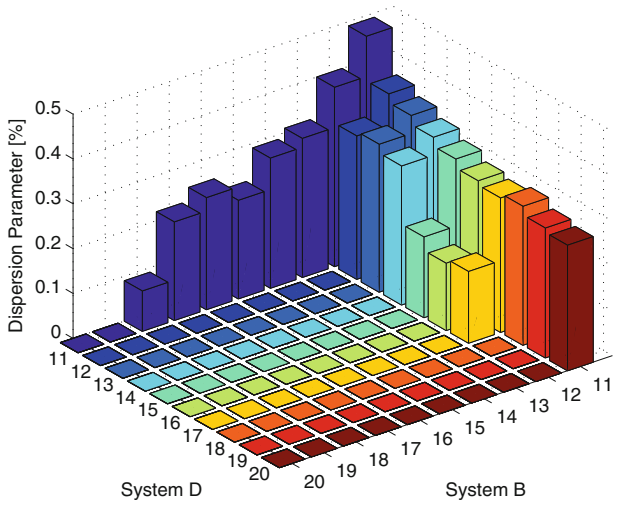

Fig. 5.2 Synthesized system dispersion parameters

parameter of 1.97 %. If twice the highest frequency is kept, substructure B keeps 9 modes and substructure D keeps 7 modes. This results in a dispersion parameter of 1.56 % for system E. This shows increasing the amount of modes by one for each substructure creates a decrease in the dispersion parameter by 20 %.

The determination of the dispersion of a synthesized system from the dispersion parameters of the substructures is a difficult analysis. One major difficulty is a theoretical issue that the truth data for the substructure and full structure are different. The chosen fact that eleven elastic free-free modes for both the substructure and full structure still contains different modes of vibration and do not represent the same information. The other difficulty is the piece-wise results. In Fig. 5.2, it is seen that if system B has at least 13 and system D has at least 12 fixed-interface modes, system E has a dispersion parameter of 0.00 %. The cause of this is unknown and is currently being studied.

5.5 Conclusions

Uncertainty of a substructure can be quantified by many different methods. Using a dispersion parameter for a random matrix allows for a physical representation that encompasses the model form error. This formulation of model form error is developed by Soize. These random matrices are propagated using a Monte-Carlo analysis along with truth data to select an optimal dispersion parameter to contain the truth data with the highest probability. This was performed on a Craig-Bampton ROM. The expected trend for the CB ROM is that as more modes are included in the ROM, the uncertainty decreases is verified using a Monte-Carlo simulation. Two CB ROMs are also combined together to get a grasp on how the substructure uncertainty propagates into the assembled system. This research shows that using the rule of thumb gives the dispersion value of 2–1.5 %. This research is a preliminary analysis on characterizing different ROMs. The use of dispersion parameters to describe the model form error allows for a single value to represent an entire system.

References

1. Batou, A., Soize, C., Audebert, S.: Model identification in computational stochastic dynamics using experimental modal data. Mech. Syst. Signal Process. **50–51**, 307–322 (2014)
2. Bonney, M.S., Brake, M.R.W.: Utilizing soize's approach to idetify parameter and model uncertainties. Technical Report SAND2014-19209, Sandia National Laboratories, Albuquerque (2014)
3. Craig, R.R., Bampton, M.C.C.: Coupling of substructures for dynamic analysis. AIAA J. **6**, 1313–1319 (1968)
4. Robertson, B.A., Bonney, M.S., Gastaldi, C., Brake, M.R.W.: Quantifying epistemic and aleatoric uncertainty in the ampair 600 wind turbine. In: Proceedings of the 33rd International Modal Analysis Conference (2014)

5. Soize, C.: Maximum entropy approach for modeling random uncertainties in transient elastodynamics. J. Acoust. Soc. Am. **5**, 1979–1994 (2001)
6. Soize, C.: Random matrix theory for modeling uncertainties in computational mechanics. Comput. Methods Appl. Mech. Eng. **194**, 1333–1366 (2004)
7. Soize, C.: Generalized probabilistic approach of uncertainties in computational dynamics using random matrices and polynomial chaos decompositions. Int. J. Numer. Methods Eng. **81**(8), 939–970 (2010)

Chapter 6
Uncertainty Analysis of Mechanical Behavior of Functionally Graded Carbon Nanotube Composite Materials

E. García-Macías, R. Castro-Triguero, Michael I. Friswell, A. Sáez-Pérez, and R. Gallego

Abstract The remarkable mechanical and sensing properties of carbon nanotubes (CNTs) suggest that they are ideal candidates for high performance and self-sensing cementitious composites. However, there is still a lack of deeper knowledge of the uncertainty associated with their incorporation, concretely in functionally graded composite materials (FGM). The influence of these uncertainties can be critical for future applications in the field of Structural Health Monitoring (SHM), techniques that usually require high accuracy modeling. Most researches restrict the aim of their studies to the analysis of composite materials with uniform or linear grading profiles. This study throws light on the basis of stochastic representation of the grading profiles and analyzes the propagation of its uncertainty into the response of some structural elements. The finite element method (FEM) is employed to study the individual and interactive effects of the mechanical properties (Young's modulus, density, Poisson's ratio and CNT's waviness) and grading profiles. The effects of stochastic uncertainties on the overall properties of the composite material are represented using the probability theory. Numerical results show the influence of these variables in several benchmark cases such as cylindrical, spherical and doubly curved shells, in terms of their static and dynamic characteristics by performing modal analysis.

Keywords Stochastic analysis • Kriging metamodel • RS-HDMR metamodel • Carbon nanotube composites • Hu-Washizu principle

6.1 Introduction

Since the discovery of carbon nanotubes (CNTs) by Ijima [1] in 1991, many researchers have got interested in their unique capabilities as reinforcements in composite materials. Due to their remarkable mechanical, electrical and thermal properties, carbon nanotubes are considered ideal reinforcing fibers for advanced high strength materials and smart materials with self-sensing capabilities [2, 3]. Functionally graded materials (FGMs) belong to a branch of advanced materials characterized by spatially varying properties. This concept has promoted the development of a wide range of applications of functionally graded composite materials since its origin in 1984 (see e.g. [4]). Inspired by this idea, Shen [5] proposed non-uniform distributions of CNTs within an isotropic matrix. The forecast of the behavior of these sorts of composites involves a high number of variables and several scales of analysis. Uncertainty in material properties is propagated along the while process, thus the properties of FG-CNTRC composite materials should be quantified probabilistically.

In order to probabilistically asses the behavior of FG-CNTRCs, the material parameters either matrix and CNTs can be considered as random. The probabilistic response of FG-CNTRCs can be processed computationally through composite mechanics and probability method. In particular, the uncertainties in mass and stiffness matrices induce the statistical

E. García-Macías (✉) • A. Sáez-Pérez
University of Seville, Sevilla, Spain
e-mail: egarcia28@us.es; andres@us.es

R. Castro-Triguero
University of Cordoba, Córdoba, Spain
e-mail: me1catrr@uco.es

M.I. Friswell
University of Swansea, Swansea, Wales, UK
e-mail: m.i.friswell@swansea.ac.uk

R. Gallego
University of Granada, Granada, Spain
e-mail: gallego@ugr.es

S. Atamturktur et al. (eds.), *Model Validation and Uncertainty Quantification, Volume 3*, Conference Proceedings of the Society for Experimental Mechanics Series, DOI 10.1007/978-3-319-29754-5_6

variation natural frequencies. In general, Monte Carlo simulation technique is popularly utilized to generate the randomized output frequency to deal with large number of samples. However MCS method is inefficient and expensive. To mitigate this lacuna, two surrogate models, Kriging technique [6] and random sampling high-dimensional model representations (RS-HDMR) [7] were proposed for quantitative model assessment and analysis tool of high-dimensional input-output system relationship very efficiently. In this problem the actual finite element model is replaced by a response surface metamodel, making the process computationally efficient and cost effective.

In the present analysis, random samples are drawn uniformly over the entire domain ensuring good prediction capability of the constructed metamodel in the whole design space including the tail regions. The present work aims to develop an algorithm for uncertainty quantification of natural frequencies of several shells using Kriging and RS-HDRM and its efficacy compared to direct Monte Carlo simulation (MCS) technique. For this purpose, two open access software developed by [8] Ziehn and Tomlin [9] for Kriging and RS-HDMR metamodeling respectively. An efficient finite element formulation based on Hu-Washizu principle to model FG-CNTRC shell elements. The shell theory is formulated in non-orthogonal general curvilinear coordinates and includes the effects of transverse shear strains by first-order shear deformation theory (FSDT). An invariant definition of the elastic transversely isotropic tensor based on the representation theorem is also defined

6.2 Finite Element Formulation

The midsurface of the shell to be considered in this paper is given in terms of general non-orthogonal curvilinear coordinates $(\theta^1;\theta^2)$ and a unity normal vector θ^3, tangents and normal to the midsurface respectively. Depending on the geometry, a basis of covariant and contravariant vectors are defined. The following relationships are formulated in a completely general way. Hence, the analyses can be carried out for different geometries just by changing this basis. The theoretical formulation is set up by a variational formulation. Denoting by U(γ) the strain energy and by γ and σ the vectors containing the strain and stress components, respectively, a modified potential of Hu-Washizu assumes the form [10]

$$\Pi_{HW}\left[v,\gamma,\sigma\right]=\int_{V}\left[U\left(\gamma\right)-\sigma^{T}\left(\gamma-Dv\right)-\Pi_{b}\right]dV-\int_{S_{\hat{v}}}\left[v-\hat{v}\right]\sigma ndV-\int_{S_{t}}\Pi_{t}dV \tag{6.1}$$

where v and the index b represent the displacement vector and the body forces, respectively, whereas $\hat{v}$ are prescribed displacements on the part of the boundary in which displacements are prescribed $(S_{\hat{v}})$. The displacement field is constructed by first-order shear deformation. The definition of non-orthogonal coordinates requires a coherent definition of the stress-strain relationships. On the basis of the representation theorems of transversely isotropic tensors developed by Spencer [11], Lumbarda and Chen [12] obtained the constitutive tensor of linear elastic transversely isotropic materials in a general coordinates system as follows

$$C_{ijkl}=\sum_{r=1}^{6}c_{r}I_{ijkl}^{r} \tag{6.2}$$

with I^r a set of linearly independent fourth order tensors that form a basis of an algebra of order 6 and c_r six elastic parameters. In component form, the fourth-order tensors I^r are defined in Eq. (6.15).

$$\begin{aligned}&I_{ijkl}^{1}=\tfrac{1}{2}\left(a^{ik}a^{jl}+a^{il}a^{jk}\right);\quad I_{ijkl}^{2}=a^{ij}a^{kl};\quad I_{ijkl}^{3}=n_{i}n_{j}a^{kl};\quad I_{ijkl}^{4}=a^{ij}n_{k}n_{l}\\&I_{ijkl}^{6}=n_{i}n_{j}n_{k}n_{l};\qquad I_{ijkl}^{5}=\tfrac{1}{2}\left(a^{ik}n_{j}n_{l}+a^{il}n_{j}n_{k}+a^{jk}n_{i}n_{l}+a^{jl}n_{i}n_{k}\right)\end{aligned}$$

where n_i are the rectangular components of an unit vector parallel to the axis of the transverse isotropy and a_{ij} are the components of the contravariant basis. The material parameters c_r depend on five elastic constants: μ and λ, shear modulus within the plane of isotropy and the Lamé constant, the out-of-plane elastic shear modulus μ_o, α and β. The constitutive equations are written in Voigt's notation in the form

$$\begin{bmatrix} s_{11} \\ s_{22} \\ s_{12} \\ s_{23} \\ s_{13} \end{bmatrix} = \begin{bmatrix} Q_{11}(z) & Q_{12}(z) & 0 & 0 & 0 \\ Q_{12}(z) & Q_{22}(z) & 0 & 0 & 0 \\ 0 & 0 & Q_{66}(z) & 0 & 0 \\ 0 & 0 & 0 & Q_{44}(z) & 0 \\ 0 & 0 & 0 & 0 & Q_{55}(z) \end{bmatrix} \cdot \begin{bmatrix} \gamma_{11} \\ \gamma_{22} \\ \gamma_{12} \\ \gamma_{23} \\ \gamma_{13} \end{bmatrix} \tag{6.3}$$

Note that Q_{ij} varies with z according to the grading profile of the CNTRC along thickness. The shell stiffness matrices, membrane, bending, shear and coupling, can be computed by the following integrals along the shell's thickness h:

$$\begin{aligned} \left(C_E^{ij}, C_C^{ij}, C_B^{ij}\right) &= \int_{-h/2}^{h/2} Q_{ij}(z) \cdot \left(1, z, z^2\right) dz \qquad (i,j = 1,2,6) \\ C_S^{ij} &= \tfrac{1}{ks} \int_{-h/2}^{h/2} Q_{ij}(z) dz \qquad (i,j = 4,5) \end{aligned} \tag{6.4}$$

where ks denotes the transverse shear correction factor for FGM, given by [13] as $ks = (6 - (V_i \nu_i + V_m \nu_m))/5$. The shell element derived in the present study is a four-noded element with five degrees of freedom at each node: three physical components of the displacements u_1; u_2; u_3 and two components of the rotations φ_1, φ_2. Bilinear shape functions are chosen for the physical components of the displacements and rotations. A linear variation of the strains and stresses by piecewise constant approximations leads to computational advantages of especial importance in repetitive computations. This outline leads to the following final expression of stiffness and mass matrices:

$$\begin{aligned} &\left[K_{Extension} + K_{Bending} + K_{Coupling} + K_{Shear}\right]_{20x20} \Delta = p \\ &K_{Extension} = A_N^{-1} \overline{D}_E A_N^{-1} E; \qquad K_{Bending} = B^T A_M^{-1} \overline{D}_F A_M^{-1} B \\ &K_{Coupling} = B^T A_M^{-1} \overline{D}_C A_N^{-1} E + E^T A_N^{-1} \overline{D}_C A_M^{-1} B \qquad K_{Shear} = G^T A_Q^{-1} \overline{D}_S A_Q^{-1} G \end{aligned} \tag{6.5}$$

$$M = \begin{bmatrix} M_{11} & M_{12} & M_{13} & M_{14} \\ & M_{22} & M_{23} & M_{24} \\ & & M_{33} & M_{34} \\ sym & & & M_{44} \end{bmatrix} \; with \; M_{ij} = \begin{bmatrix} \int_A I_1 N_i N_j dA & \int_A \mathcal{A} I_1 N_i N_j dA & 0 & \int_A I_2 N_i N_j dA & \int_A \mathcal{A} I_2 N_i N_j dA \\ & \int_A I_1 N_i N_j dA & 0 & \int_A \mathcal{A} I_2 N_i N_j dA & \int_A I_2 N_i N_j dA \\ & & \int_A I_1 N_i N_j dA & 0 & 0 \\ & & & \int_A I_3 N_i N_j dA & \int_A \mathcal{A} I_3 N_i N_j dA \\ & sym & & & \int_A I_3 N_i N_j dA \end{bmatrix} \tag{6.6}$$

Where I_1; I_2; I_3 and $\mathcal{A}$ (the contravariant components relationship) are defined by:

$$I_1 = \int_{-h/2}^{h/2} \rho(z) dz; \quad I_2 = \int_{-h/2}^{h/2} z\rho(z) dz; \quad I_3 = \int_{-h/2}^{h/2} z^2 \rho(z) dz; \quad \mathcal{A} = \frac{a^{12}}{\sqrt{a^{11} a^{22}}} \tag{6.7}$$

6.3 Kriging Metamodel

In general, surrogate models are an approximation of the Input/Output of a main model. The main idea of surrogate models is to fit the data obtained by a large model in a compact and cost effective way for computation. There are a set of m observations, so called design sites $\mathrm{x} = [\mathrm{x}_1 \ldots \mathrm{x}_m]^T$ with $\mathrm{x}_i \in \mathbb{R}^n$ and a set of outputs $Y = [y_1 \ldots y_m]^T$ with $y_i \in \mathbb{R}^q$. The Kriging model expresses the unknown function of interest $y(x) \in \mathbb{R}^q$ for an n dimensional input $x \subseteq D \subseteq \mathbb{R}^n$, as the sum of a regression model $\mathcal{F}(\mathrm{x})$ and a stochastic function Z(x) as follows

$$y(x) = \mathcal{F}(x) + Z(x), \quad l = 1 \ldots q \tag{6.8}$$

the function Z(x) is the realization of a stochastic process with mean zero, variance and non-zero covariance, \mathcal{F}(x) is a known regression function dependent on k regression parameters $\{\beta_{k,l}\}$ and defined functions $f_j : \mathbb{R}^n \to \mathbb{R}$

$$\mathcal{F}\left(\beta_{:,l}, x\right) = f(x)^T \cdot \beta_{:,l} \tag{6.9}$$

It can be understood that \mathcal{F}(x) globally approximates the design space, meanwhile Z(x) creates the localized deviations so that the Kriging model interpolates the p-sampled data points. The covariance matrix of Z(x)

$$E\left[Z\left(x^i\right) \cdot Z\left(x^j\right)\right] = \sigma^2 \cdot R\left(\theta, x^i, x^j\right) \tag{6.10}$$

between any two of the p-sampled data points x^i and x^j, where R is a $(p \times p)$ correlation matrix and $R(\theta, x^i, x^j)$ is the correlation function between, R is an $(p \times p)$ symmetric matrix with ones along its diagonal. The user can specify a wide variety of correlation functions dependent on θ parameters. The predicted estimates, $\hat{y}(x)$ of the response $y(x)$ at random values x are defined as Kriging predictor.

$$\hat{y}(x) = f(x)^T \cdot \beta^* + r(x)^T \cdot \left(Y - F \cdot \beta^*\right) \tag{6.11}$$

Where Y is the column vector of length p that contains the sample values of the frequency responses and F is the observability matrix:

$$F = \left[f\left(x_1\right), \ldots, f\left(x_p\right)\right]^T \tag{6.12}$$

$$\beta^* = \left(F^T \cdot R^{-1} \cdot F\right)^{-1} \cdot \ F^T \cdot R^{-1} \cdot Y \tag{6.13}$$

$r(x)$ is a vector with the correlations between design sites and x:

$$r(x) = \left[R\left(\theta, x_1, x\right) \ldots R\left(\theta, x_m, x\right)\right]^T \tag{6.14}$$

The mean squared error (MSE) of the predictor

$$MSE = E\left[\left(\hat{y}(x) - y(x)\right)^2\right] \tag{6.15}$$

Now the model fitting is accomplished by maximum likelihood (i.e. best guesses) for θ. Note that for a given set of design data the matrices β^* and are fixed. For every new x we just have to compute the vectors $f(x) \in \mathbb{R}^p$ and $(x) \in \mathbb{R}^m$ and add to simple products.

6.4 Random Sampling HDMR

A second surrogate model is also employed and compared to the Kriging metamodel, this is the high dimensional model representation. Random sampling high dimensional model representation (RS-HDMR) method provides a straight forward approach in exploring the input-output mapping of a high dimensional model with a reduced number of samples. The relationship between the input (x) and output variables $y = f(x)$, is expressed as:

$$\mathrm{f}\left(\mathrm{X}\right) = \mathrm{f}_0 + \sum_{\mathrm{i}=1}^{\mathrm{n}} \mathrm{f}_{\mathrm{i}}\left(\mathrm{x}_{\mathrm{i}}\right) + \sum_{1 \le \mathrm{i} \le \mathrm{j} \le \mathrm{n}} \mathrm{f}_{\mathrm{ij}}\left(\mathrm{x}_{\mathrm{i}}, \mathrm{x}_{\mathrm{j}}\right) + \cdots + \mathrm{f}_{1,2,\ldots,\mathrm{n}}\left(\mathrm{x}_1, \mathrm{x}_2, \ldots, \mathrm{x}_{\mathrm{n}}\right) \tag{6.16}$$

Each term in the expression represents the independent and cooperative contributions of the inputs upon the output. Here f_0 is a constant (zeroth order) stands for the average contribution of all inputs to the outputs. The function $\mathrm{f}_{\mathrm{i}}(\mathrm{x}_{\mathrm{i}})$ is a first order term giving the effect of variable x_{i} acting independently upon the output f(X). The function $\mathrm{f}_{\mathrm{ij}}(\mathrm{x}_{\mathrm{i}}, \mathrm{x}_{\mathrm{j}})$ is a second order term describing the cooperative effects of the x_{i} and x_{j} upon the output f(X). The higher order terms reflect the cooperative effects

of increasing numbers of input variables acting together to influence the output f(X). The last term, $f_{1,2,\ldots,n}(x_1, x_2, \ldots, x_n)$, reflects any residual nth order correlated contribution of all input variables. In most cases, terms up to second order are enough to provide accurate results. The component functions of the RS-HDMR have the following form:

$$f_0 = \int_{K^n} f(x)\, dx \tag{6.17}$$

$$f_i(x_i) = \int_{K^{n-2}} f(x)\, dx^i - f_0 \tag{6.18}$$

$$f_{ij}(x_i, x_j) = \int_{K^{n-2}} f(x)\, dx^{ij} - f_i(x_i) - f_0 \tag{6.19}$$

All the input variables are rescaled in the range [0,1]. Hence, the output response function is defined in the domain of a unit hypercube $K^n = \{(x_1, x_2, \ldots, x_n),\ i = 1, \ldots, n\}$. Generation of random sample points govern the convergence rate of MCs which is used in formulation of the component functions of RS-HDMR. The Sobol's quasi-random sequences have been employed to generate random sample points. This technique provides uniform distribution of sample points in the input domain resulting in faster convergence.

The zeroth order term f_0 is calculated by the average value of all f(X). Higher order component functions involve high-dimensional integrals that can be approximately calculated by Monte-Carlo integration. Because Monte Carlo integration is expensive, analytical basis functions, such as orthonormal polynomials provide the best accuracy among the different analytical basis functions. Thus the first and second order component functions are expressed in the following form:

$$f_i(x_i) \approx \sum_{r=1}^{k} \alpha_r^i \varphi_r(x_i) \tag{6.20}$$

$$f_{ij}(x_i, x_j) \approx \sum_{p=1}^{l} \sum_{q=1}^{l'} \beta_{pq}^{ij} \varphi_p(x_i)\, \varphi_q(x_j) \tag{6.21}$$

where k, l and l′ represent the order of the polynomial expansión, α_r^i and β_{pq}^{ij} are the constant coefficients which are determined by a minimization process and MC integration. $\varphi_r(x_i^{(s)})$, $\varphi_p(x_i^{(s)})$ y $\varphi_q(x_j^{(s)})$ are the orthonormal basis functions. The final equation of RS-HDMR up to second order component functions are expressed as:

$$f(X) = f_0 + \sum_{i=1}^{n} \sum_{r=1}^{k} \alpha_r^i \varphi_r(x_i) + \sum_{1 \le i \le j \le n} \sum_{p=1}^{l} \sum_{q=1}^{l'} \beta_{pq}^{ij} \varphi_p(x_i)\, \varphi_q(x_j) \tag{6.22}$$

The MC integration for calculating the expansion coefficients α and β controls the accuracy of RS-HDMR. Variance reduction method is utilized to improve the accuracy of Monte Carlo integration without increasing the sample size. As the HDMR component functions are independent, the order of the polynomial approximation can be chosen separately for each component function to improve the accuracy of the final surrogate model. An optimization method developed by Ziehn and Tomlin [14] chooses the best polynomial order for each of the component functions,

6.5 Stochastic Approach Using Surrogate Models

The stochasticity in material properties of carbon nanotube reinforced composites is considered for free vibration analysis of FG-CNTRC shells. In the present study, the first three natural frequencies are considered as output. It is assumed that ±10 %variation is randomness of symmetrically distributed input parameters for FG-CNTRC plate is considered. Firstly a

sensitivity analysis of the natural frequencies was carried out to detect the target parameters to be taken into consideration within the probabilistic analysis. This sort of studies lets us discern which variables are more likely to considerably alter the output. Thus, the cases wherein the random variables are investigated for:

(a) Variation of density of constituents: $\{\rho^m, \rho^{CNT}\}$
(b) Young's modulus of constituents: $\{E_{11}^{CNT}, E_{22}^{CNT}, E^m\}$

6.6 Results and Discussion

In this section, the proposed methodology is applied to several benchmark tests. Because of paucity of space we only show some results about their uncertainty analysis.

6.6.1 Flat Shells: Square Flat Shell and Skew Shell

In these first tests the aforementioned uncertainty analysis is applied to plane geometries, flat square shell (Fig. 6.1a) and skew shells (Fig. 6.1b). For these geometries, the formulation significantly simplifies as the curvature terms vanish.

The effective material properties of the two-phase nanocomposites, mixture of uniaxially aligned CNTs reinforcements can be estimated according to the Mori-Tanaka scheme [15] or the rule of mixture [3, 16]. In order to account for the scale-dependent material properties, the so called extended rule of mixtures (EROM) introduces the CNT efficiency parameters, η_j (j = 1, 2, 3). These parameters can be calculated by matching the effective properties of CNTRC obtained from a molecular dynamics (MD) or multi-scale simulations with those from the rule of mixtures. The accuracy of the EROM has been widely discussed and shown a remarkable synergism with the Mori-Tanaka scheme for functionally graded materials [17]. Due to the simplicity and convenience, in the present study the EROM was employed with two types of reinforcement grading profiles, UD and FG-V. UD-CNTRC represents the uniform distribution and FG-V a functionally graded distribution of carbon nanotubes in the thickness direction of the composite as

$$\begin{aligned} V_{CNT} &= V_{CNT}^{*} \qquad (UD\ CNTRC) \\ V_{CNT} &= \left(1 + \tfrac{2z}{h}\right) \cdot V_{CNT}^{*} \qquad (FG - V\ CNTRC) \end{aligned} \tag{6.23}$$

where V_{CNT} and $V_m = 1 - V_{CNT}$ are the volume fractions of the carbon nanotubes and matrix, respectively. The selected matrix is Poly (methyl methacrylate), referred to as PMMA. The armchair (10,10) SWCNTs are selected as reinforcements

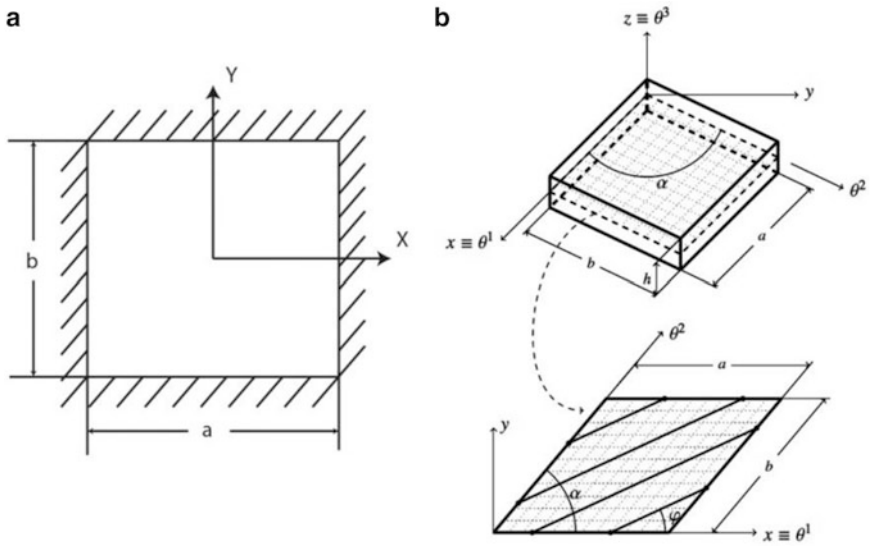

Fig. 6.1 (**a**) Geometry of fully clamped flat square shell ($\boldsymbol{a} \times \boldsymbol{b} \times \boldsymbol{h}$). (**b**) Geometry of Skew shell (Skew angle $\boldsymbol{\alpha}$)

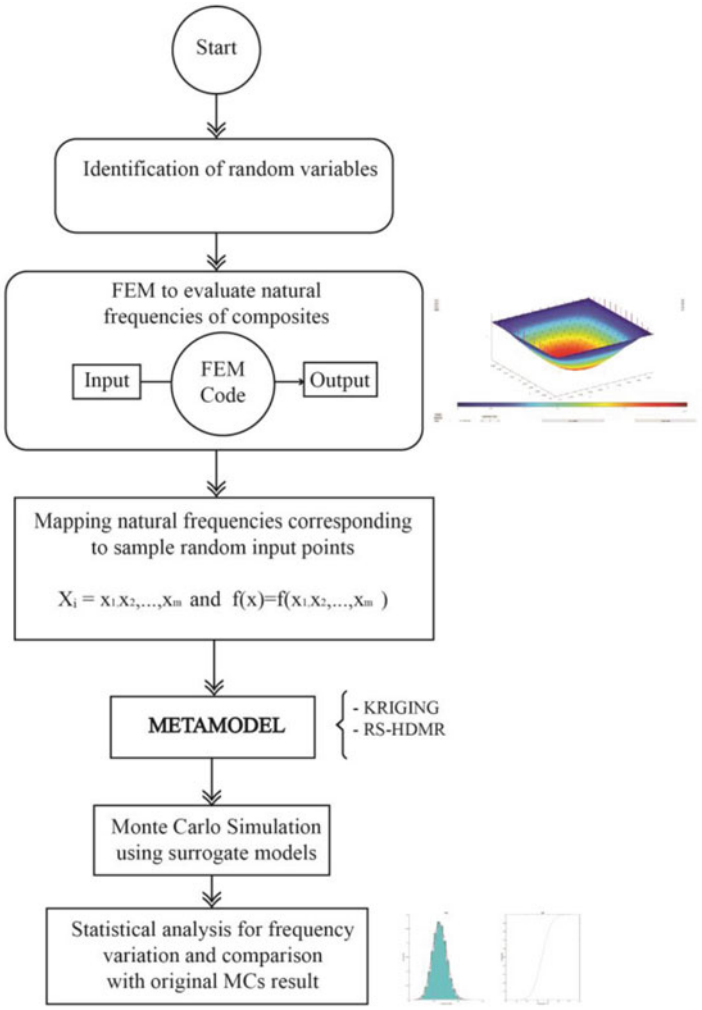

Fig. 6.2 Flowchart of stochastic free vibration analysis using Kriging and RS-HDMR metamodels

with properties taken from the MD simulation carried out by Shen and Zhang [17]. The detailed material properties of PMMA/CNT of the FG-CNTRCs are selected from the MD results reported by Han and Elliot [18], with CNT efficiency parameters defined by Shen and Zhang [19].

In the present method, MCS is conducted in conjunction with Kriging and RS-HDMR metamodels (see Fig. 6.2). Here, although the same sampling size as in direct MCS is considered, the number of FE analysis is much less compared to original MCS and is equal to number representative sample required to construct the metamodels. Hence, the computational time and effort is drastically reduced. The computational time required in the present approach is observed to be around 1/36–1/37, for Kriging and RS-HDMR respectively, of direct Monte Carlo simulation. All the cumulative distribution functions are compared with the results provided by direct Monte Carlo simulation with 10,000 samples. In order to define the number of samples to be employed in the metamodels, convergence study is carried out to determine the coefficient of determination R^2 (second order) of the RS-HDMR expansions for different samples sizes as furnished in Table 6.1. A sample size of 256 provides values close to 100 % indicating high accuracy of the fitted models. In terms of mesh size, convergence analyses by comparing with existing bibliography resulted in a mesh size of 24×24 elements. The Kriging metamodel is defined with a regression function of second order polynomial and a Gaussian correlation model. Meanwhile, the RS-HDMR metamodels are developed using first and second order component functions with orthonormal polynomials up to third order.

Figures 6.3 and 6.4 depict a sample scatter plot describing the relationship between the original FE model and the constructed Kriging metamodel for natural frequencies for square and skew plates respectively. The low scatterness of the points around the diagonal line and the close fitting between the PDF estimations of original and RS-HDMR responses verifies that Kriging metamodels are formed with accuracy. Figure 6.5 shows the PDF and CDF estimation of the first three natural frequencies of the square plate.

Table 6.1 Convergence study for coefficient of determination R^2 (second order) of the RS-HDMR expansions with different sample sizes of fully clamped UD CNTRC square plate (a = b = 1, h = a/50, $V^*_{CNT} = 0.11$, $\alpha = 30°$)

N. samples	Mode 1	Mode 2	Mode 3
128	98.55	97.86	49.76
256	98.55	97.85	05.05

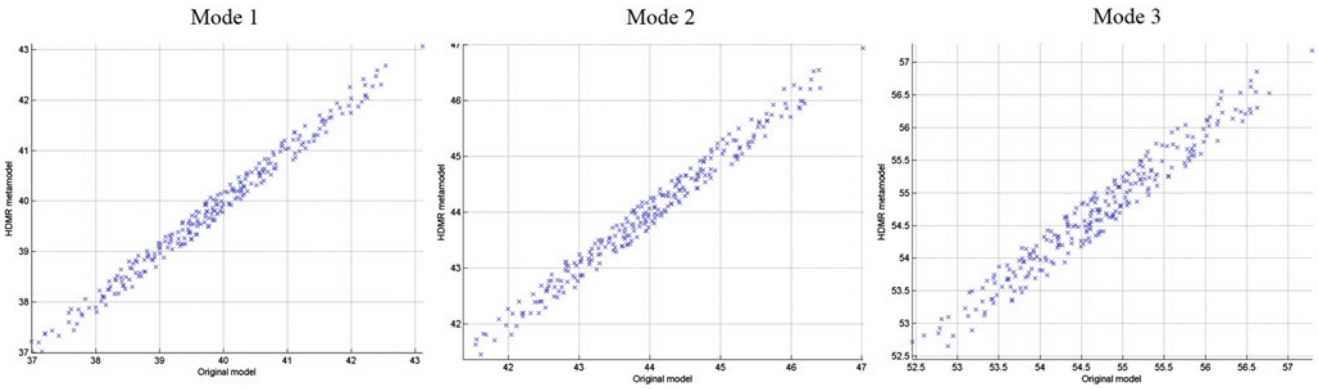

Fig. 6.3 Scatter plot for Kriging metamodel with respect to original model of first three natural frequencies for fully clamped square UD-CNTRC plate (a = b = 1, h = a/50, $\mathbf{V^*_{CNT}} = 0.11$)

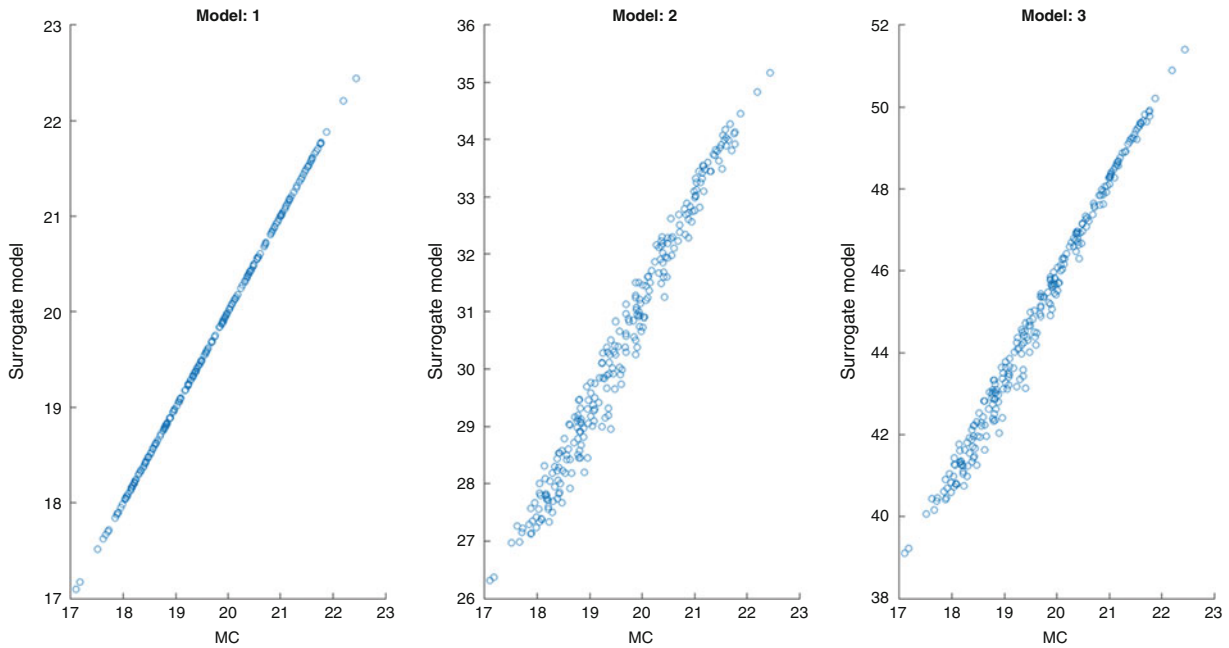

Fig. 6.4 Scatter plot for Kriging metamodel with respect to original model of first three natural frequencies for fully clamped skew plate (a = b = 1 m, h = a/50 m, $V^*_{CNT} = 0.11$, $\alpha = 30°$)

Similar good results are obtained with the RS-HDMR metamodel for both cases. Global sensitivity analysis using RS-HDMR is performed for significant input parameter screening. The sensitivity indices for each input parameters corresponding to different output responses are show in Fig. 6.7b, while a typical interaction effect between ρ^m and ρ^{CNT} is furnished in Fig. 6.7a. Table 6.2 presents the comparative study between MCS and metamodels for maximum values,

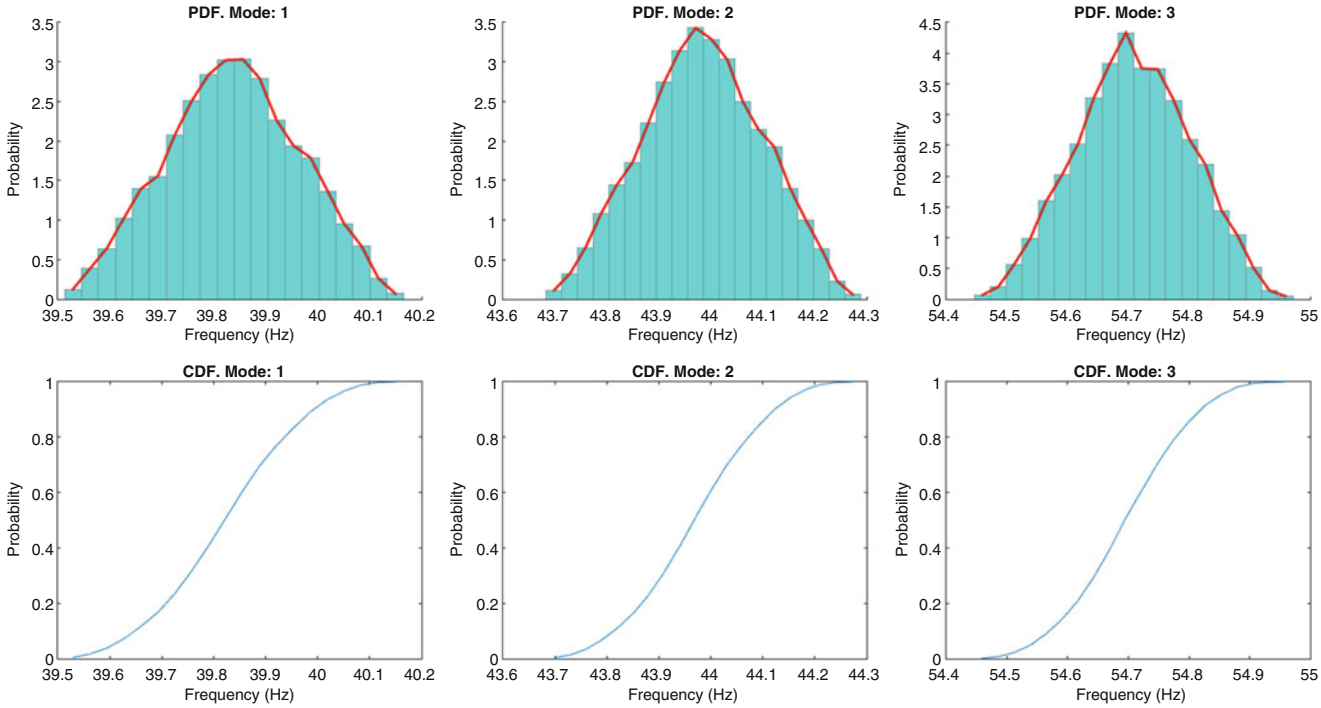

Fig. 6.5 Probability distribution functions (PDF) and Cumulative distribution function (CDF) with respect to model response of first three natural frequencies for UD-CNTRC plate considering a = b = 1, h = a/50, $V^*_{CNT} = 0.11$

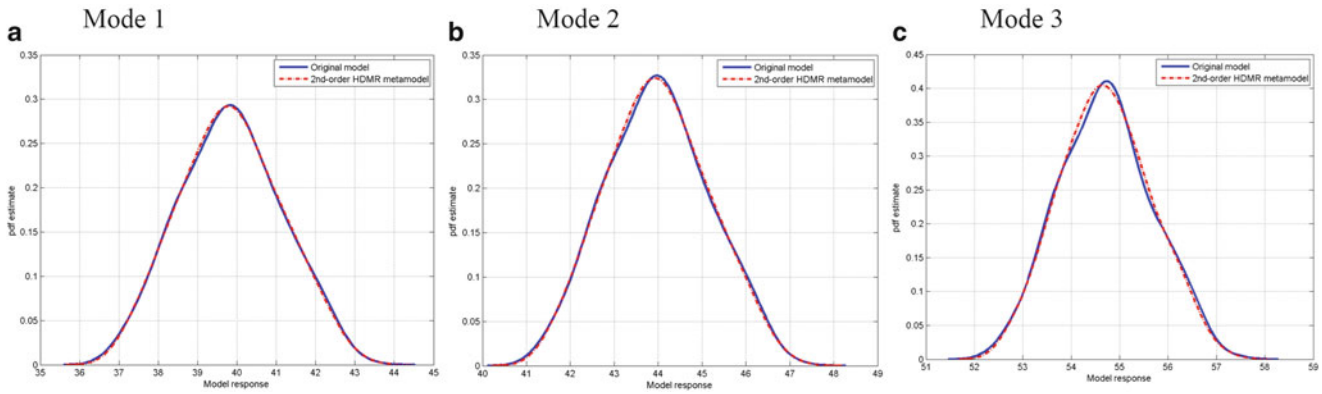

Fig. 6.6 Probability distribution function (PDF) with respect to model response of first three natural frequencies fully clamped UD-CNTRC skew plate (a = b = 1, h = a/50, $\mathbf{V^*_{CNT}} = 0.11$). (**a**) $\mathbf{R}^2D = 99.98$, (**b**) $\mathbf{R}^2D = 99.64$, (**c**) $\mathbf{R}^2D = 99.54$

minimum values and percentage of difference for first three natural frequencies. Good agreements with full MCs are found for both metamodels ensuring their efficiency and accuracy (Fig. 6.8).

6.6.2 Curved Shells: Cylindrical and Hypar Shells

Finally, in order to remark the versatility of the proposed methodology in terms of geometry, it is applied to two curved geometries. Particularly it is analyzed the probabilistic frequencies of fully clamped cylinder (see Fig. 6.9a) and a fully clamped doubly curved shell (Fig. 6.9b). In Table 6.2 it can be seen the good agreement between MCS and the two metamodels for these geometries. In Fig. 6.10 it can be seen the evolution of the first three natural frequencies together with the mean value and the 95 % confidence band (Table 6.3).

Table 6.2 Comparative study between MCS (10,000 samples) and Kriging and RS-HDMR (256 samples) for maximum values, minimum values and percentage of difference for first three natural frequencies for fully clamped UD-CNTRC square plate (R = 5.175 m, L = 2*R, h = a/1000, $V^*_{CNT} = 0.11$) and skew plate (a = b = 1 m, h = a/50 m, $V^*_{CNT} = 0.11$, $\alpha = 30°$)

	Parameter	Fundamental frequency						Second natural frequency						Third natural frequency					
		MC	Kriging	RS-HDMR	Diff. (%)			MC	Kriging	RS-HDMR	Diff. (%)			MC	Kriging	RS-HDMR	Diff. (%)		
Square Shell	Max. val.	40.1	40.2	40.1	0.1	–	0.0	44.3	44.3	44.3	0.1	–	0.0	54.9	55.0	55.0	0.1	–	0.0
	Min. val.	39.6	39.5	39.5	0.1	–	0.1	43.7	43.7	43.7	0.1	–	0.1	54.5	54.4	54.5	0.1	–	0.1
	Mean val.	39.9	39.8	39.8	0.1	–	0.0	44.0	44.0	44.0	0.0	–	0.0	54.7	54.7	54.7	0.0	–	0.0
	Standard deviation	0.1	0.1	0.1	3.8	–	1.9	0.1	0.1	0.1	3.3	–	1.7	0.1	0.1	0.1	0.6	–	0.3
Skew shell	Max. val.	20.0	20.2	20.1	0.7	–	0.4	30.9	31.1	31.2	0.6	–	0.9	43.4	45.2	44.3	4.2	–	2.1
	Min. val.	18.6	18.8	18.7	1.3	–	0.5	29.0	29.4	28.8	1.5	–	0.7	44.1	44.0	44.0	0.2	–	0.1
	Mean val.	19.9	19.6	18.0	1.4	–	9.5	29.5	30.4	28.2	3.1	–	4.4	44.6	44.8	44.7	0.5	–	0.3
	Standard deviation	0.0	0.0	0.0	25.0	–	50.0	0.0	0.0	0.0	36.6	–	18.3	0.0	0.0	0.0	2.9	–	1.5

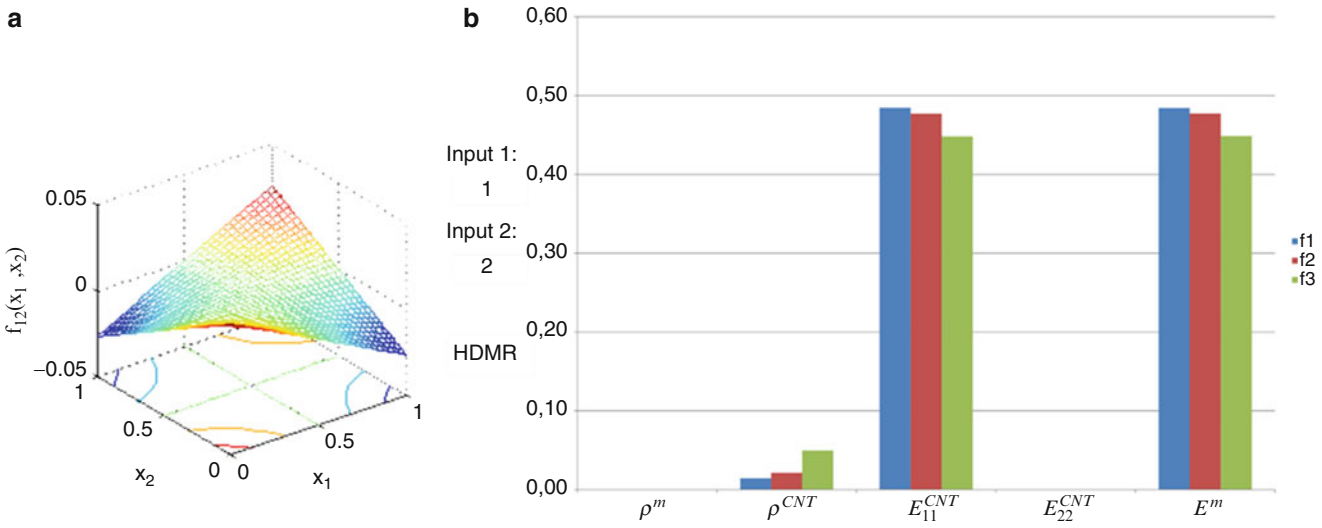

Fig. 6.7 (**a**) Interaction effect between ρ^m and ρ^{CNT} corresponding to the second order component function of the fundamental frequency. (**b**) Sensitivity indices of fully clamped square UD-CNTRC plate (a = b = 1, h = a/50, $V^*_{CNT} = 0.11$)

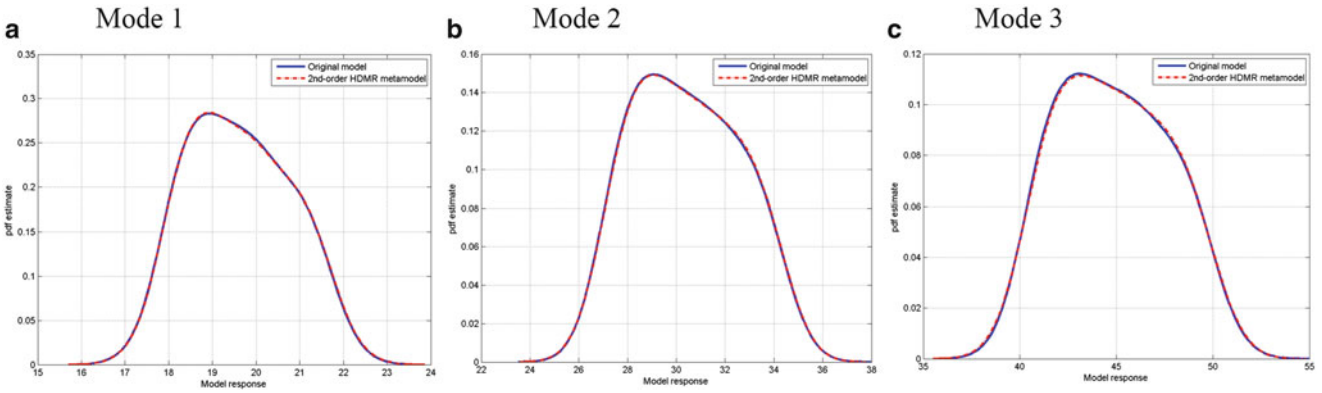

Fig. 6.8 Probability distribution function (PDF) with respect to model response of first three natural frequencies of fully clamped square UD-CNTRC plate (a = b = 1, h = a/50, $\mathbf{V^*_{CNT}} = 0.11$). (**a**) $\mathbf{R}^2 = 99.98$, (**b**) $\mathbf{R}^2 = 99.64$, (**c**) $\mathbf{R}^2 = 99.54$

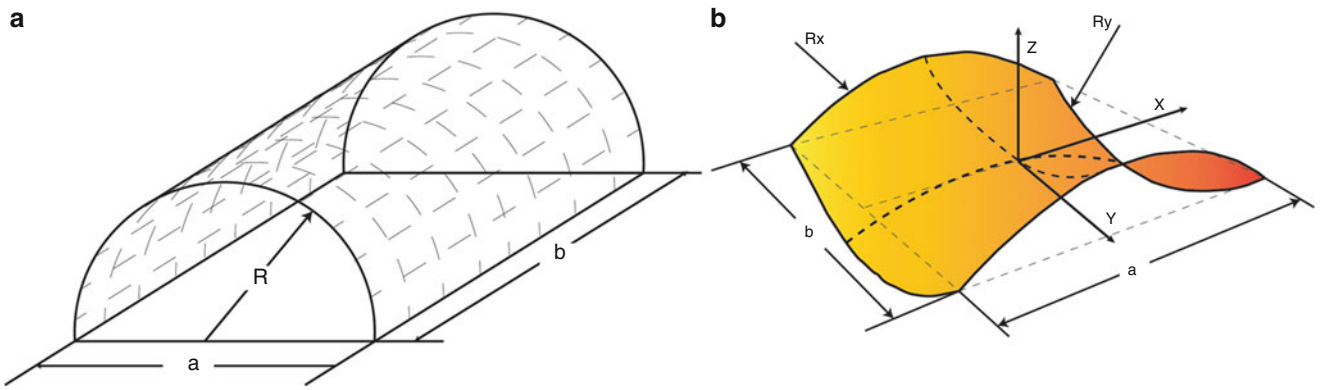

Fig. 6.9 (**a**) Geometry of cylinder (R = 5.175 m, L = 2*R, h = a/1000). (**b**) Geometry doubly curved shell (a = b = 1 m, Rx = b/0.1, Ry = −Rx, h = a/100)

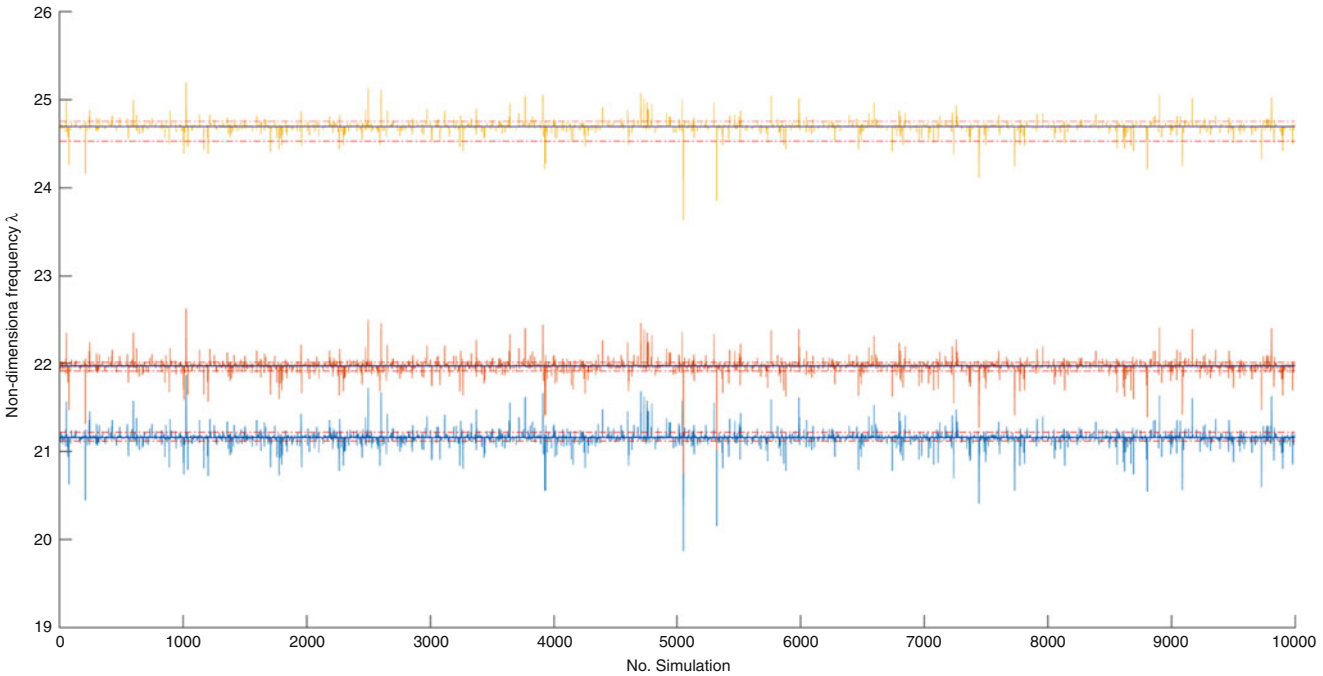

Fig. 6.10 Stochastic definition of the first three natural frequencies of fully clamped cylindrical shell (a = b = 1 m, Rx = b/0.1, Ry = −Rx, h = a/100, $V^*_{CNT} = 0.11$)

6.7 Conclusions

In the present study, a right-side-up approach is proposed for the propagation of uncertainty in the natural frequencies of general FG-CNTRC shells. Two metamodels, Kriging and RS-HDMR, are shown to be computationally effective for stochastic analysis. A FEM formulation based on Hu-Washizu and invariant constitutive definition is shown to be suitable for the dynamic analysis of plain and curved FG-CNTRC shells. The number of finite element analysis is highly reduced compared to original Monte Carlo simulation. It is observed that both approaches can handle large number of input parameters. The maximum effect on sensitivity is observed for E_{11}^{CNT} and E^m while the least sensitivity effect is identified for ρ^m, ρ^{CNT} and E_{22}^{CNT}.

Acknowledgements This research was supported by Spanish ministry of economy and competitively under the Project Ref: **DPI2014-53947-R**. E. G-M was also supported by a FPU contract-fellowship from the Spanish Ministry of Education Ref: **FPU13/04892**.

Table 6.3 Comparative study between MCS (10,000 samples) and Kriging and RS-HDMR (256 samples) for maximum values, minimum values and percentage of difference for first three natural frequencies for fully clamped UD-CNTRC cylinder (a = b = 1, h = a/50, $V^*_{CNT} = 0.11$) and hypar shell (a = b = 1 m, Rx = b/0.1, Ry = −Rx, h = a/100, $V^*_{CNT} = 0.11$)

	Parameter	Fundamental frequency						Second natural frequency						Third natural frequency					
		MC	Kriging	RS-HDMR	Diff. (%)			MC	Kriging	RS-HDMR	Diff. (%)			MC	Kriging	RS-HDMR	Diff. (%)		
Cylinder	Max. val.	254.5	255.3	254.8	0.3	–	0.1	245.2	255.4	250.3	−4.2	–	−2.1	247.9	258.2	253.0	4.2	–	2.1
	Min. val.	246.4	246.0	245.2	0.2	–	0.5	246.4	246.0	246.2	0.2	–	0.1	249.2	248.8	249.0	0.2	–	0.1
	Mean val.	250.4	250.8	251.0	0.2	–	0.2	249.6	250.9	250.3	−0.5	–	−0.3	252.4	253.7	253.1	0.5	–	0.3
	Standard deviation	1.4	1.6	1.2	19.2	–	11.1	1.7	1.6	1.6	2.9	–	1.5	1.7	1.6	1.7	2.9	–	1.5
Hypar	Max. Val.	23.4	22.1	22.7	5.56	–	2.78	24.0	22.8	23.4	5.1	–	2.5	26.6	25.7	26.1	3.5	–	1.8
	Min. val.	23	20.0	21.5	13.13	–	6.57	23.6	20.8	22.2	11.9	–	5.9	26.3	24.0	25.2	8.6	–	4.3
	Mean val.	23.2	21.2	22.2	8.62	–	4.31	23.8	22.0	22.9	7.5	–	3.7	26.4	25.1	25.7	5.1	–	2.5
	Standard deviation	0.1	0.0	0.1	71.93	–	35.96	0.0	0.0	0.0	47.6	–	23.8	0.0	0.0	0.0	53.6	–	26.8

References

1. Iijima, S.: Helical microtubules of graphitic carbon. Nature **354**(6348), 56–58 (1991)
2. Gibson, R.F.: A review of recent research on mechanics of multifunctional composite materials and structures. Compos. Struct. **92**(12), 2793–2810 (2010). ISSN: 0263-8223
3. Esawi, A.M.K., Farag, M.M.: Carbon nanotube reinforced composites: potential and current challenges. Mater. Des. **28**(9), 2394–2401 (2007). ISSN: 0261-3069
4. Udupa, G., Shrikantha Rao, S., Gangadharan, K.V.: Functionally graded composite materials: an overview. Proc. Mater. Sci. **5**, 1291–1299 (2014). ISSN: 2211-8128
5. Shen, H.-S.: Nonlinear bending of functionally graded carbon nanotube-reinforced composite plates in thermal environments. Compos. Struct. **91**(1), 9–19 (2009). ISSN: 0263-8223
6. Cressie, N.: The origins of Kriging. Math. Geol. **22**(3), 239–252 (1990)
7. Rabitz, H., Aliç, Ö.F.: General foundations of high-dimensional model representations. J. Math. Chem. **25**(2–3), 197–233 (1999)
8. Lophaven, S.N., Nielsen H.B., Søndergaard, J.: DACE-A Matlab Kriging toolbox, version 2.0, Technical Report (2002)
9. Ziehn, T., Tomlin, A.S.: GUI-HDMR. A software tool for global sensitivity analysis of complex models. Environ. Model Softw. **24**(7), 775–785 (2009). ISSN: 1364-8152
10. Wempner, G., Talaslidis, D.: Mechanics of Solids and Shells. CRC Press, Boca Raton (2003). ISBN 0-8493-9654-9
11. Spencer, A.J.M.: The formulation of constitutive equation for anisotropic solids. In: Mechanical Behavior of Anisotropic Solids/Comportment Méchanique des Solides Anisotropes, pp. 3–26. Springer, Netherlands (1982)
12. Lubarda, V., Chen, M.: On the elastic moduli and compliances of transversely isotropic and orthotropic materials. J. Mech. Mater. Struct. **3**(1), 153–171 (2008). ISSN: 1559-3959
13. Efraim, E., Eisenberger, M.: Exact vibration analysis of variable thickness thick annular isotropic and FGM plates. J. Sound Vib. **299**(4), 720–738 (2007). ISSN: 0022-460X
14. Ziehn, T., Tomlin, A.S.: A global sensitivity study of sulfur chemistry in a premixed methane flame model using HDMR. In. J. Chem. Kinet. **40**(11), 742–753 (2008). ISSN: 1097-4601
15. Shi, D.-L., et al.: The effect of nanotube waviness and agglomeration on the elastic property of carbon nanotube-reinforced composites. J. Eng. Mater. Technol. **126**(3), 250–257 (2004). ISSN: 0094-4289
16. Fidelus, J.D., et al.: Thermo-mechanical properties of randomly oriented carbon/epoxy nanocomposites. Compos. A: Appl. Sci. Manuf. **36**(11), 1555–1561 (2005). ISSN: 1359-835X
17. Sobhani Aragh, B., Nasrollah Barati, A.H., Hedayati, H.: Eshelby-Mori-Tanaka approach for vibrational behavior of continuously graded carbon nanotube-reinforced cylindrical panels. Compos. Part B **43**(4), 1943–1954 (2012). ISSN: 1359-8368
18. Shen, H.-S., Zhang, C.-L.: Thermal buckling and postbuckling behavior of functionally graded carbon nanotube-reinforced composite plates. Mater. Des. **31**(7), 3403–3411 (2010). ISSN: 0261-3069
19. Han, Y., Elliott, J.: Molecular dynamics simulations of the elastic properties of polymer/carbon nanotube composites. Comput. Mater. Sci. **39**(2), 315–323 (2007). ISSN: 0927-0256

Chapter 7
Interval Uncertainty Analysis Using CANDECOMP/PARAFAC Decomposition

Jinchun Lan and Zhike Peng

Abstract A new interval uncertain analysis method is proposed based on CANDECOMP/PARAFAC (CP) decomposition. In interval uncertain analysis of structural dynamics, we need to evaluate the lower and upper bounds of uncertain responses. To avoid the overestimation of the lower and upper bounds caused by the wrapping effect, the CP decomposition is used to approximate the interval functions. In CP decomposition, the interval functions are represented with only a few terms, and the energy of each term usually decays fast. In this way, we can achieve shaper and tighter bounds of the interval functions. CP decomposition can be obtained using different methods. Some numerical examples are demonstrated to compare the method with other methods and illustrate the effectiveness of this method.

Keywords Interval uncertainty quantification • Dynamical response • CANDECOMP/PARAFAC decomposition • Tensor decomposition • Low-rank decomposition

7.1 Introduction

In engineering problems, there exists a variety of uncertainties in geometrical parameters [1], material properties [2, 3], boundary and initial conditions [4], and so on [5–8]. It's usually impossible to obtain the distribution of uncertain parameters. In these situations, the interval method can be used as an alternative to describe uncertain parameters. In interval uncertainty analysis, uncertain parameters are represented by interval parameters which valued in intervals. These intervals can be determined from only a small set of experiments. In this way, it offers a way to represent and evaluate uncertainties for bounded parameters without knowing the complete information of the system.

In this paper we will concern on interval uncertainty based analysis of dynamical system governed by ordinary differential equations. There are many interval methods developed to analyze engineering problems [9–11]. In structural dynamical analysis, the mostly used interval uncertainty analysis methods are intrusive methods. In these methods, the stochastic responses are assumed to be represented in Taylor series, then the equations of motion can be derived. For example, Qiu and Wang [12] used first-order perturbation method to evaluate the dynamic response of structures with interval uncertainties. Qiu and Ma [13] developed Taylor series based non-probabilistic interval analysis method for nonlinear dynamical systems. In these methods, the problem of overestimation should be concerned. With time progresses, the overestimation of the bounds will increase. The results of these method may be useless in long time evaluation of structural dynamics. To overcome this problem, Wu [14, 15] has proposed Chebyshev inclusion method to solve structural dynamical systems with large interval uncertainties. In Chebyshev method, the uncertain responses are approximated using collocation method where the Mehler integral method is applied to evaluate the coefficients of the Chebyshev inclusion function. Then the Chebyshev inclusion method is used to estimate the bounds of response. In this method, we only need to solve some deterministic problems which make it easy to be implemented. The bounds estimated by Chebyshev inclusion method are shaper than that of Taylor method.

In this paper, we develop an interval estimation method using the CANDECOMP/PARAFAC (CP) decomposition. Similar to Chebyshev inclusion method, we firstly approximate the uncertain response using stochastic collocation method. Then we use the CP decomposition to approximate the interpolation polynomials with a few terms. Finally, the bounds are estimated from the CP decomposition. Using CP decomposition, we can approximate the stochastic response with only a few terms which will significantly decrease the warping effect.

J. Lan • Z. Peng (✉)
State Key Laboratory of Mechanical System and Vibration, School of Mechanical Engineering, Shanghai Jiao Tong University, 200240 Shanghai, China
e-mail: z.peng@sjtu.edu.cn

S. Atamturktur et al. (eds.), *Model Validation and Uncertainty Quantification, Volume 3*, Conference Proceedings of the Society for Experimental Mechanics Series, DOI 10.1007/978-3-319-29754-5_7

In the following parts of this paper, we will firstly describe the problem considered in this paper. Then the basic procedure of stochastic collocation method is introduced. Using the SCM a surrogate model can be constructed. Following that, we will describe how to convert the interpolation polynomials to tensor format. Then the CP decomposition will be used to approximate the tensor and estimate the bounds of the results. Finally, an example is presented to illustrate the effectiveness of this method.

7.2 Problem Statement

In many engineering applications, we can use a set of ordinary differential equations to describe dynamical behaviors we are interested in. Without loss of generality, most dynamical systems can be represented by first-order differential equations as follows

$$\begin{cases} \dot{u}(t,\boldsymbol{\xi}) = Lu(t,\boldsymbol{\xi});\ \xi \in [\xi], \quad t \in [0,T], \\ u(0,\boldsymbol{\xi}) = u_0(\boldsymbol{\xi}), \end{cases} \tag{7.1}$$

where $\mathcal{L}$ is differential operator of the problem, t denotes time, $\boldsymbol{\xi} = [\xi_1, \xi_2, \ldots, \xi_n]^T$ is a n-dimensional vector of uncertain parameters, and $u_0(\xi)$ is the initial condition of the system.

Assuming that we have little information of the uncertain parameters $\boldsymbol{\xi}$, and only the bounds of the uncertain parameters are available, we can describe the uncertain parameters using lower and upper bounds

$$\underline{\boldsymbol{\xi}} \le \boldsymbol{\xi} \le \overline{\boldsymbol{\xi}} \tag{7.2}$$

where $\underline{\boldsymbol{\xi}} = \left[\underline{\xi}_1, \underline{\xi}_2, \ldots, \underline{\xi}_n\right]^T$ and $\overline{\boldsymbol{\xi}} = \left[\overline{\xi}_1, \overline{\xi}_2, \ldots, \overline{\xi}_n\right]^T$ are vectors of lower and upper bounds of these parameters. Using the interval notation, uncertain parameters can be represented using interval vector $[\boldsymbol{\xi}]$, where interval vector $[\boldsymbol{\xi}]$ is defined to be

$$[\boldsymbol{\xi}] = \left[\underline{\boldsymbol{\xi}}, \overline{\boldsymbol{\xi}}\right] = \left\{\xi_i : \underline{\xi}_i \le \xi_i \le \overline{\xi}_i,\ i = 1, 2, \ldots n\right\} \tag{7.3}$$

When uncertain parameters ξ_is vary in $[\boldsymbol{\xi}]$, the solution of Eq. (7.1) will also change respectively in a certain set $[u]$ given by

$$\Gamma = \left\{u :\ \dot{u}(t,\boldsymbol{\xi}) = \mathcal{L}u(t,\boldsymbol{\xi});\quad \boldsymbol{\xi} \in [\boldsymbol{\xi}]\right\} \tag{7.4}$$

In interval methods, we aim at computing the lower and upper bounds of the solution

$$\underline{u}(t) = \min_{\boldsymbol{\xi} \in [\boldsymbol{\xi}]} \left\{\dot{u}(t,\boldsymbol{\xi}) = \mathcal{L}u(t,\boldsymbol{\xi});\ u(0) = u_0(\boldsymbol{\xi})\right\} \tag{7.5}$$

$$\overline{u}(t) = \max_{\boldsymbol{\xi} \in [\boldsymbol{\xi}]} \left\{\dot{u}(t,\boldsymbol{\xi}) = \mathcal{L}u(t,\boldsymbol{\xi});\ u(0) = u_0(\boldsymbol{\xi})\right\} \tag{7.6}$$

It's obvious that the exact solutions of $\underline{u}(t)$ and $\bar{u}(t)$ rely on global searching of the set Γ, which will need much computational effort and is even impossible for problems with many uncertain parameters. As it's difficult to evaluate the exact bounds $[u]$ of the solution, researchers have developed many methods to approximate the lower and upper bounds of the solution as is described in the introduction.

7.3 Interval Analysis Using CANDECOMP/PARAFAC (CP) Decomposition

7.3.1 Approximating Uncertain Functions Using Collocation Method

Before we use the CP decomposition to represent uncertain function $u(t, \boldsymbol{\xi})$, we need to build a surrogate model of $u(t, \boldsymbol{\xi})$. In this paper, stochastic collocation method will be used as an alternative to construct a surrogate model of $u(t, \boldsymbol{\xi})$. Stochastic collocation method is based on the idea of functional interpolation. In stochastic collocation method, we need to compute deterministic solutions at some pre-selected points in uncertain domain, then we can construct a polynomial to approximate the target function.

Starting from one-dimensional stochastic collocation, denoted by $\Theta_M = \{\xi_i \in \Omega, i = 1, 2, \ldots, M\}$ the predetermined point set in uncertain space Ω. Then the uncertain function $u(\xi)$ can be approximated by Lagrange interpolation polynomials, which can be expressed as follows

$$u_p(\xi) = \sum_{k=1}^{M} u(\xi_k) L_k(\xi), \tag{7.7}$$

where

$$L_k(\xi) = \prod_{\substack{j=1 \\ j \neq k}}^{M} \frac{(\xi - \xi_j)}{(\xi_k - \xi_j)}, \; k = 1, 2, \ldots, M \tag{7.8}$$

are the Lagrange polynomial basis functions and they satisfy $\mathrm{L_k}\left(\xi_\mathrm{j}\right) = \delta_{\mathrm{jk}}$. The predetermined point set Θ_M is important in stochastic collocation. The Gaussian points and Chebyshev points [16] are widely used as they can achieve good approximation of the target function with only a few points. In this paper, the Chebyshev points will be used. Assumed that we need m collocation points on interval [0, 1], then we can construct points set Θ_m using the following points

$$\xi_i = \begin{cases} 0.5 \times \left[1 - \cos\left(\frac{\pi(i-1)}{m-1}\right)\right], \; \text{for } j = 1, \ldots, m, \quad \text{if } m > 1 \\ \\ 0.5, \qquad \text{for } j = 1, \; \textit{if } m = 1 \end{cases}. \tag{7.9}$$

As to the multi-dimensional stochastic collocation, it's straightforward to extend the one-dimensional interpolation functions to multi-dimension functions using tensor products.

Consider an n-dimensional case, where $\boldsymbol{\xi} = [\xi_1, \xi_2, \ldots, \xi_n]^T$, $u(\boldsymbol{\xi})$ is the function needed to be approximated. For each variable ξ_i, i $= 1, 2, \ldots, n$, a nodal set $\Theta^i = \left\{\xi_1^{(i)}, \xi_2^{(i)}, \ldots, \xi_{m_i}^{(i)}\right\}$ is determined. Then the full tensor product interpolation formula of n-dimensional function $u(\boldsymbol{\xi})$ can be written by

$$u_p(\boldsymbol{\xi}) = \sum_{j_1=1}^{m_1} \cdots \sum_{j_n=1}^{m_n} f\left(\xi_{j_1}^{(1)}, \ldots, \xi_{j_n}^{(n)}\right) \cdot \left(L_{j_1}^{(1)} \otimes \cdots \otimes L_{j_n}^{(n)}\right) \tag{7.10}$$

7.3.2 Tensor Format Representation of Uncertain Function

In recent years, tensor numerical methods have been developed as a new tool in scientific computing [17–19]. There are many methods developed to solve large-scale linear and multi-linear algebra problems. To take advantage of recent developments in tensor numerical methods, we firstly need to convert the interpolation polynomial to tensors. There are different strategies to convert the polynomials to tensors.

In this paper we will only consider the simplest way. We convert the polynomials construct in the previous section by sampling the polynomials with a uniform grid.

We will first start from two dimensional function $f(x, y)$. In the previous section, we construct the interpolation function of $f(x, y)$

$$f_p(x, y) = \sum_{i=1}^{m_1}\sum_{j=1}^{m_2} f\left(x_i, y_j\right) L_i^{(1)}(x) L_j^{(2)}(y). \tag{7.11}$$

Denoted by $C = \left[f\left(x_i, y_j\right)\right]_{ij}$ the coefficient matrix of the above expansion, the above expression can be written by

$$f_p(x, y) = L_1^T(x) \times C \times L_2(y) \tag{7.12}$$

where

$$L_1(x) = \left[L_1^{(1)}(x), L_2^{(1)}(x), \ldots, L_{m_1}^{(1)}(x)\right]^T \tag{7.13}$$

$$L_2(x) = \left[L_1^{(2)}(x), L_2^{(2)}(x), \ldots, L_{m_1}^{(2)}(x)\right]^T \tag{7.14}$$

are basis function vectors of Lagrange interpolation polynomials. Then we can apply singular value decomposition (SVD) on the matrix C. It's obvious that the function $f(x, y)$ can be determined from coefficient matrix C. In this way, we convert the polynomial $f_p(x, y)$ to matrix format C.

Similarly, for a multivariate function $u(\boldsymbol{\xi})$, its interpolation polynomial

$$u_p(\boldsymbol{\xi}) = \sum_{j_1=1}^{m_1} \cdots \sum_{j_n=1}^{m_n} f\left(\xi_{j_1}^{(1)}, \ldots, \xi_{j_n}^{(n)}\right) \cdot \left(L_{j_1}^{(1)} \otimes \cdots \otimes L_{j_n}^{(n)}\right) \tag{7.15}$$

can be written in tensor format

$$u_p(\boldsymbol{\xi}) = \boldsymbol{T} \times_1 L_1(x_1) \times_2 L_2(x_2) \times_3 \cdots \times_n L_n(x_n) \tag{7.16}$$

where $\boldsymbol{T}$ is a tensor with entry

$$T_{i_1, i_2, \ldots, i_n} = f\left(\xi_{i_1}^{(1)}, \ldots, \xi_{i_n}^{(n)}\right), \tag{7.17}$$

and $L_j(x_j)$ is the vector of basis function corresponding to the variable x_j

$$L_j\left(x_j\right) = \left[L_1^{(j)}\left(x_j\right), L_2^{(j)}\left(x_j\right), \ldots, L_{m_j}^{(j)}\left(x_j\right)\right]^T. \tag{7.18}$$

In this way, multivariate function $u(\boldsymbol{\xi})$ has been converted to tensor $\boldsymbol{T}$.

7.3.3 Interval Computation Using CANDECOMP/PARAFAC (CP) Decomposition

Low rank tensor decomposition has attracted much attention in recent years. Among low rank tensor decomposition methods, CANDECOMP/PARAFAC (CP) decomposition has been well studied. For high-order tensors, CP decomposition can achieve much reduction in both storage and computation.

For a multivariate function $f(x_1, x_2, \ldots, x_n)$, it's CP decomposition is defined to be

$$f(x_1, x_2, \ldots, x_n) = \sum_{i=1}^{N} \lambda_i g_i^1(x_1) g_i^2(x_2) \cdots g_i^n(x_n) \tag{7.19}$$

where N is the rank of CP decomposition, λ_i is the ith eigenvalue of the decomposition, $g_i^1(x_j)$ is a basis function corresponding to variable x_j. For $n = 2$, CP decomposition degenerates to the well-known Karhunen–Loève (KL) decomposition, i.e.

$$f(x_1, x_2) = \sum_{i=1}^{N} \lambda_i g_i^1(x_1)\, g_i^2(x_2) \tag{7.20}$$

In KL decomposition, eigenvalues λ_is decay fast so that we can achieve good approximation with only a few terms.

The CP decomposition of a tensor $\boldsymbol{T}$ is the sum of rank-one tensors

$$\boldsymbol{T}_{cp} = u_1^{(1)} \otimes u_1^{(2)} \otimes \cdots \otimes u_1^{(d)} + u_2^{(1)} \otimes u_2^{(2)} \otimes \cdots \otimes u_2^{(d)} + \cdots + u_R^{(1)} \otimes u_R^{(2)} \otimes \cdots \otimes u_R^{(d)}, \tag{7.21}$$

where R is the rank of CP decomposition. Using this CP decomposition, $u_p(\boldsymbol{\xi})$ can be rewritten by

$$\begin{aligned} u_{p,cp}(\boldsymbol{\xi}) &= \boldsymbol{T}_{cp} \times_1 L_1(x_1) \times_2 L_2(x_2) \times_3 \cdots \times_n L_n(x_n) \\ &= \sum_{i=1}^{R} \left[u_i^{(1)} \otimes u_i^{(2)} \otimes \cdots \otimes u_i^{(d)} \right] \times_1 L_1(x_1) \times_2 L_2(x_2) \times_3 \cdots \times_n L_n(x_n) \\ &= \sum_{i=1}^{R} \left(L_1^T(x_1)\, u_i^{(1)} \right) \times \left(L_2^T(x_2)\, u_i^{(2)} \right) \times \cdots \times \left(L_n^T(x_n)\, u_i^{(n)} \right) \\ &= \sum_{i=1}^{R} g_i^{(1)}(x_1)\, g_i^{(2)}(x_2) \cdots g_i^{(n)}(x_n) \end{aligned} \tag{7.22}$$

where

$$g_i^{(j)}(x_j) = L_j^T(x_j)\, u_i^{(j)} \tag{7.23}$$

is the basis function of CP decomposition.

After we have obtain the CP decomposition $u_{p,cp}(\boldsymbol{\xi})$ of the function $u(\boldsymbol{\xi})$, we can estimate the upper and lower bounds of $u(\boldsymbol{\xi})$ by

$$\overline{u}(\boldsymbol{\xi}) = \sum_{i=1}^{R} \left[g_i^{(1)}(x_1)\, g_i^{(2)}(x_2) \cdots g_i^{(n)}(x_n) \right] \tag{7.24}$$

$$\underline{u}(\boldsymbol{\xi}) = \sum_{i=1}^{R} \left\lfloor g_i^{(1)}(x_1)\, g_i^{(2)}(x_2) \cdots g_i^{(n)}(x_n) \right\rfloor . \tag{7.25}$$

Example 1. As a simple example, we will illustrate how to use CP decomposition to improve the interval estimation. The results are compared with those of the Chebyshev inclusion method.

Consider

$$f(x, y) = sin(5x) + cos(6y) + sin\left(3.8x^2\right) + e^{x^2+y^2}, \qquad x, y \in [-1, 1]. \tag{7.26}$$

The figure of this function is plotted in Fig. 7.1.

In this figure, we can see that there are many local optimum points. The exact bounds of this function is $[-1.3074, 4.5015]$. We estimate the bounds of this function with different methods and plot the results in Fig. 7.2.

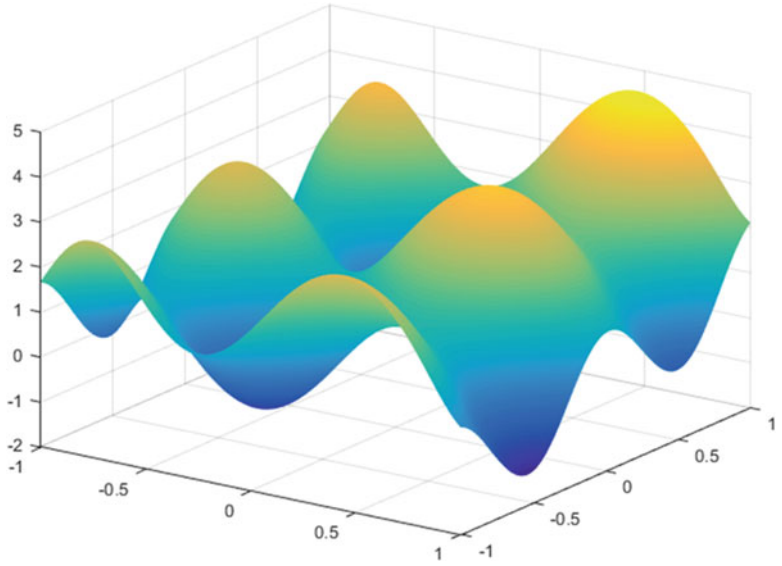

Fig. 7.1 Figure of the function in Example 1

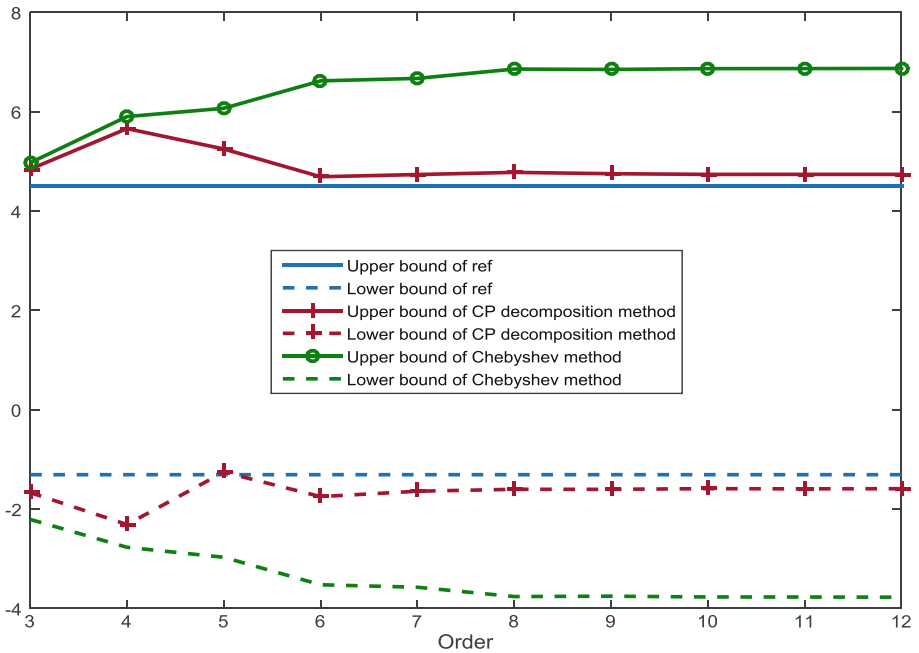

Fig. 7.2 Bounds estimated with different expansion orders

From Fig. 7.2, we can see that when the number of expansion order increase the bounds estimated by CP decomposition will converge. Compared with Chebyshev inclusion method, CP decomposition will achieve much shaper bounds.

7.4 Numerical Example: Double Pendulum Problem

Consider a double pendulum [14, 15] as shown in Fig. 7.3, where m_1 and m_2 are the masses of the two pendulums, and l_1 and l_2 are the lengths of the two pendulum rods.

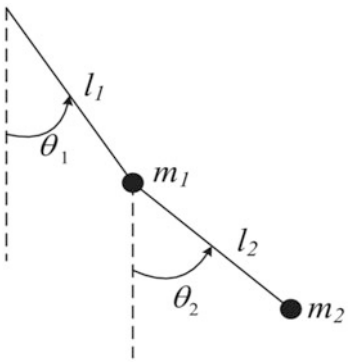

Fig. 7.3 Schematic of a double pendulum

The equations of motion of this system can be written by

$$\begin{cases} \dot{\theta}_1 = \omega_1 \\ \dot{\theta}_2 = \omega_2 \\ \dot{\omega}_1 = \dfrac{-g\,(2m_1 + m_2)\sin\theta_1 - m_2 g \sin(\theta_1 - 2\theta_2) - 2m_2 \sin(\theta_1 - \theta_2)\left(\omega_2^2 l_2 - \omega_1^2 l_1 \cos(\theta_1 - \theta_2)\right)}{l_1\,(2m_1 + m_2 - m_2 \cos(2\theta_1 - 2\theta_2))} \\ \dot{\omega}_1 = \dfrac{2\sin(\theta_1 - \theta_2)\left(\omega_1^2 l_1\,(m_1 + m_2) + g\,(m_1 + m_2)\cos\theta_1 + \omega_2^2 l_2 m_2 \cos(\theta_1 - \theta_2)\right)}{l_2\,(2m_1 + m_2 - m_2 \cos(2\theta_1 - 2\theta_2))} \end{cases} \tag{7.27}$$

where θ_1 and θ_2 are the angles of the rods, ω_1 and ω_2 denote the angle velocities respectively, and $g = 9.8\ \mathrm{m/s^2}$ is the gravity acceleration. In this example, we will consider two uncertain parameters. The lengths of the two rods are assumed to be interval parameters with 10 % uncertainty

$$\begin{cases} l_1 = [0.18, 0.22]\,m \\ l_2 = [0.27, 0.33]\,m \end{cases}. \tag{7.28}$$

The initial condition is assumed

$$\theta_1 = \frac{\pi}{3}, \quad \theta_2 = \frac{2\pi}{3}, \quad \omega_1 = \omega_1 = 0. \tag{7.29}$$

In Figs. 7.4 and 7.5, we compare the bounds estimated by different methods. In these figures, we can see that the bounds estimated by the Taylor method will enlarge with time increase. When time progresses, the bounds estimated by the Taylor method may be meaningless. What's more, we can see that the bounds estimated by CP decomposition are much better than those of the Chebyshev method.

7.5 Conclusion

In this paper, a new interval uncertain analysis method is proposed based on CANDECOMP/PARAFAC (CP) decomposition to avoid the overestimation of the lower and upper bounds caused by the wrapping effect. In this method, the stochastic responses are approximated using stochastic collocation method. The stochastic collocation method can be implemented with little modification of the deterministic program. Then the CP decomposition is applied to represent the polynomial. In most cases, we only need a few terms to approximate the stochastic response as the energy of each term usually decays fast. After that the bounds of the responses can be estimated using the interval arithmetic. From the numerical example presented in this paper, we can see that CP decomposition can achieve shaper bounds of stochastic responses than the Taylor method and Chebyshev inclusion method. The example implies that proposed method can be used to evaluate the dynamical systems with large uncertainties.

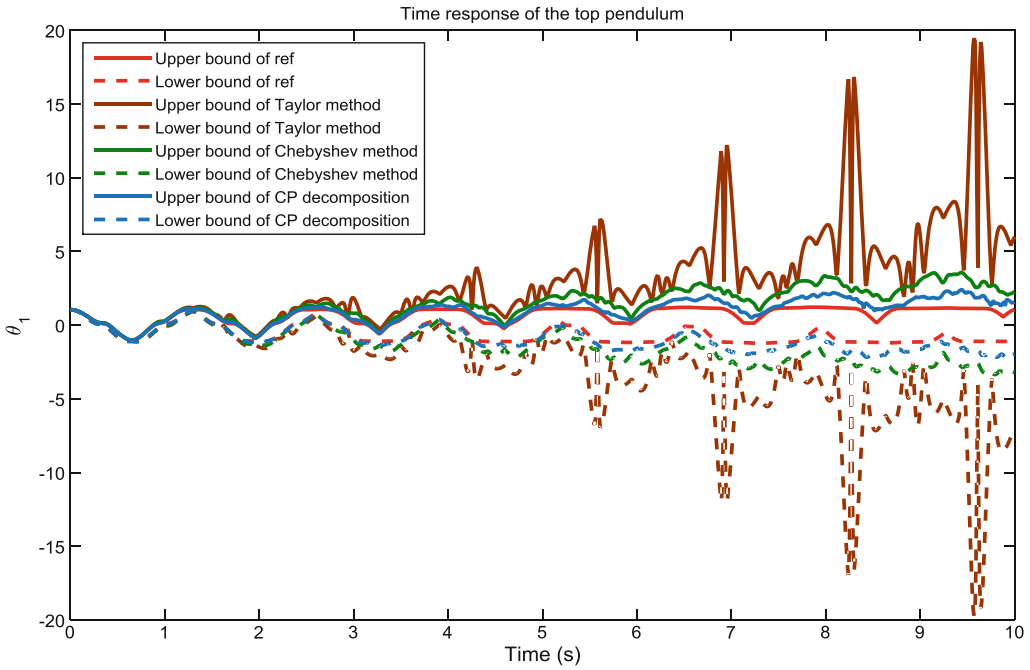

Fig. 7.4 Bounds of the *top pendulum* evaluated by different methods

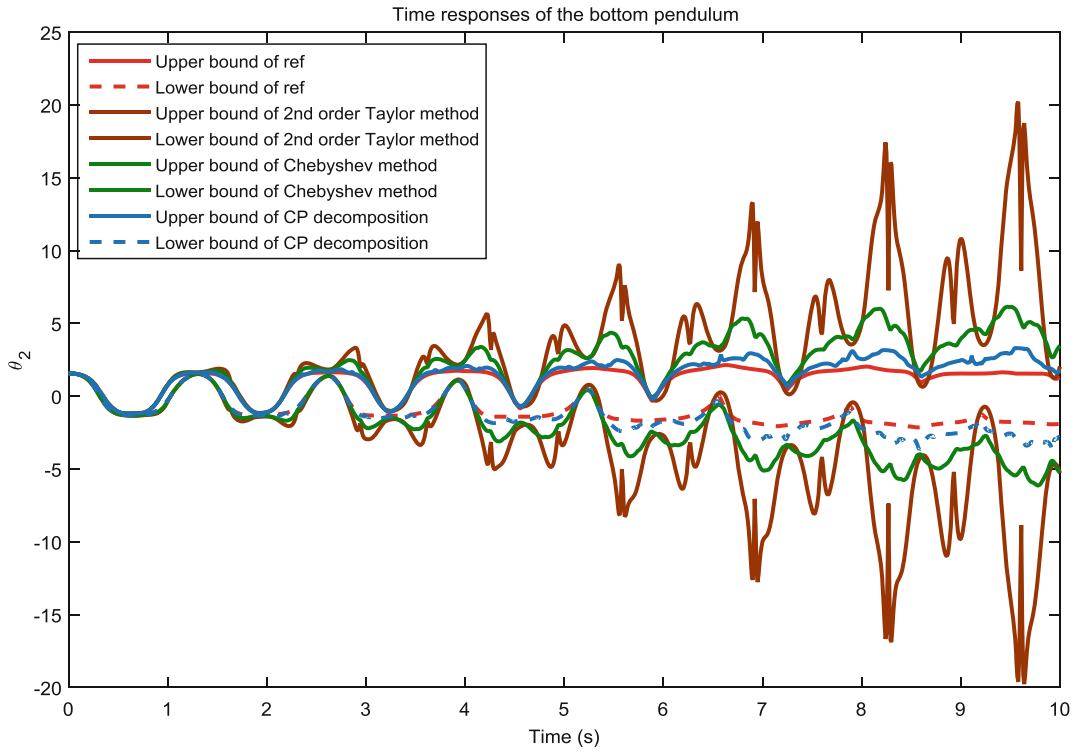

Fig. 7.5 Bounds of the *bottom pendulum* evaluated by different methods

References

1. Chandrashekhar, M., Ganguli, R.: Damage assessment of structures with uncertainty by using mode-shape curvatures and fuzzy logic. J. Sound Vib. **326**, 939–957 (2009)
2. Zhang, X.-M., Ding, H.: Design optimization for dynamic response of vibration mechanical system with uncertain parameters using convex model. J. Sound Vib. **318**, 406–415 (2008)
3. Qiu, Z.P., Lihong, M., Xiaojun, W.: Interval analysis for dynamic response of nonlinear structures with uncertainties (in Chinese). Chin. J. Theor. Appl. Mech. **38**, 645–651 (2006)
4. Kaminski Jr., J., Riera, J., de Menezes, R., Miguel, L.F.: Model uncertainty in the assessment of transmission line towers subjected to cable rupture. Eng. Struct. **30**, 2935–2944 (2008)
5. Ding, C.-T., Yang, S.-X., Gan, C.-B.: Input torque sensitivity to uncertain parameters in biped robot. Acta Mech. Sinica **29**, 452–461 (2013)
6. Guo, S.-X., Li, Y.: Non-probabilistic reliability method and reliability-based optimal LQR design for vibration control of structures with uncertain-but-bounded parameters. Acta Mech. Sinica **29**, 864–874 (2013)
7. Wang, J., Qiu, Z.-P.: Fatigue reliability based on residual strength model with hybrid uncertain parameters. Acta Mech. Sinica **28**, 112–117 (2012)
8. Jia, Y.-H., Hu, Q., Xu, S.-J.: Dynamics and adaptive control of a dual-arm space robot with closed-loop constraints and uncertain inertial parameters, Acta Mech. Sinica 112–124 (2014)
9. Moens, D., Vandepitte, D.: Interval sensitivity theory and its application to frequency response envelope analysis of uncertain structures. Comput. Methods Appl. Mech. Eng. **196**, 2486–2496 (2007)
10. Impollonia, N., Muscolino, G.: Interval analysis of structures with uncertain-but-bounded axial stiffness. Comput. Methods Appl. Mech. Eng. **200**, 1945–1962 (2011)
11. Qiu, Z.: Convex models and interval analysis method to predict the effect of uncertain-but-bounded parameters on the buckling of composite structures. Comput. Methods Appl. Mech. Eng. **194**, 2175–2189 (2005)
12. Qiu, Z., Wang, X.: Parameter perturbation method for dynamic responses of structures with uncertain-but-bounded parameters based on interval analysis. Int. J. Solids Struct. **42**, 4958–4970 (2005)
13. Qiu, Z., Ma, L., Wang, X.: Non-probabilistic interval analysis method for dynamic response analysis of nonlinear systems with uncertainty. J. Sound Vib. **319**, 531–540 (2009)
14. Wu, J., Zhang, Y., Chen, L., Luo, Z.: A Chebyshev interval method for nonlinear dynamic systems under uncertainty. Appl. Math. Model. **37**, 4578–4591 (2013)
15. Wu, J., Luo, Z., Zhang, Y., Zhang, N.: An interval uncertain optimization method for vehicle suspensions using Chebyshev metamodels. Appl. Math. Model. **38**, 3706–3723 (2014)
16. Ganapathysubramanian, B., Zabaras, N.: Sparse grid collocation schemes for stochastic natural convection problems. J. Comput. Phys. **225**, 652–685 (2007)
17. Lars, G., Daniel, K., Christine, T.: A literature survey of low-rank tensor approximation techniques. GAMM-Mitteilungen **36**, 53–78 (2013)
18. Kolda, T.G., Bader, B.W.: Tensor decompositions and applications. SIAM Rev. **51**, 455–500 (2009)
19. Khoromskij, B.N.: Tensor numerical methods for multidimensional PDES: theoretical analysis and initial applications. ESAIM Proc. Surv. **48**, 1–28 (2015)

Chapter 8
Uncertainty Quantification for Nonlinear Reduced-Order Elasto-Dynamics Computational Models

E. Capiez-Lernout, C. Soize, and M. Mbaye

Abstract The present work presents an improvement of a computational methodology for the uncertainty quantification of structures in presence of geometric nonlinearities. The implementation of random uncertainties is carried out through the nonparametric probabilistic framework from a nonlinear reduced-order model. With such usual modeling, it is difficult to analyze the influence of uncertainties on the nonlinear part of the operators with respect to its linear counterpart. In order to address this problem, an approach is proposed to take into account uncertainties for both the linear and the nonlinear operators. The methodology is then validated in the context of the linear and nonlinear mistuning of an industrial integrated bladed-disk.

Keywords Mistuning • Geometric nonlinearities • Uncertainties • Reduced-order model • Structural dynamics

8.1 Introduction

Nowadays, an essential challenge consists in considering the geometric nonlinear effects in the computational dynamical models of structures. Such situations become realistic when the considered structures are slender or/and submitted to consequent loads. For exceptional operating regimes, the large strains and the large displacements cannot be neglected anymore (see for instance [1–3] in the turbomachinery context or [4, 5] for thin or slender structures). Moreover, in many industrial applications, for which the investigated structures present a high complexity level, deterministic nonlinear computational models are in general not sufficient to accurately predict its dynamical behavior. Uncertainties have then to be taken into account in the computational models by using probabilistic models as soon as the probability theory can be used. Recently, a computational methodology adapted to the uncertainty quantification of structures in presence of geometric nonlinearities has been proposed and validated in the context of structural dynamics [6–8]. The implementation of random uncertainties is carried out through the nonparametric probabilistic framework from a nonlinear reduced-order model. It has been shown that such approach was adapted to the geometrical nonlinear case, by introducing a dedicated stiffness positive-definite operator self-containing the integrality of the information concerning the nonlinear geometric stiffness contributions. Nevertheless, its dimension increases with the square of the dimension of the nonlinear-reduced order model, requiring a large number of uncertain random germs. Consequently, establishing criteria for analyzing the influence of uncertainties on the nonlinear part of the operators with respect to its linear counterpart is difficult. The main idea for reducing the size of the random germ is to use a second reduction method before implementing the model of uncertainties. It is then possible to coherently take into account uncertainties on both the linear operator and the nonlinear operator. The paper is organized as follows. In Sect. 8.1, the main steps of the complete methodology is shortly summarized in order to give a global overview. This work is then focussed on the implementation of the random uncertainties. After recalling the usual way to implement uncertainties on the linear or nonlinear operators in the context of the nonparametric probabilistic method, it is pointed out that both situations do not appear to be compatible since no meaningful comparison can be made. A reasonable and logical requirement consists in using the same random germ for both situations, with a feasibility constraint controlled by the size of the random germ. This is achieved by replacing the Cholesky factorization of the dedicated stiffness positive-definite

E. Capiez-Lernout (✉) • C. Soize
Laboratoire Modélisation et Simulation Multi-Echelle (MSME), UMR 8208 CNRS, Université Paris-Est, Marne-La-Vallée, France
e-mail: evangeline.capiez-lernout@u-pem.fr

M. Mbaye
Turbomeca, SAFRAN Group, Bordes, France

S. Atamturktur et al. (eds.), *Model Validation and Uncertainty Quantification, Volume 3*, Conference Proceedings of the Society for Experimental Mechanics Series, DOI 10.1007/978-3-319-29754-5_8

operator by another factorization obtained from a usual eigenvalue problem for which only the contributions related to the most contributing eigenvalues are kept. In Sect. 8.2, the methodology is applied on a large finite element model of a mistuned industrial centrifugal compressor.

8.2 Computational Modeling of Mistuning Uncertainties

Recently, a complete methodology has been proposed for the geometric nonlinear analysis of mistuned bladed disks [8], for which all the terms including the rotational motion of the bladed-disk are taken into account. Below, the main steps of such methodology are briefly summarized.

1. Construction of the finite element model for the linear tuned case.
2. Solving the linear eigenvalue problem of the tuned structure for choosing the excitation frequency band known to yield drastic mistuning effects [9].
3. Construction of the external load in the time domain corresponding to a uniform sweep of the frequency band of excitation [8]
4. Choosing the projection basis as the linear eigenmodes of the tuned structure [10]
5. Direct construction of the mean nonlinear reduced-order model (MEAN-NL-ROM) by projection of the finite element operators on the chosen projection basis [6, 7]
6. Implementing the mistuning through the nonparametric probabilistic framework [11] and controlling the mistuning level by dispersion parameter $\boldsymbol{\delta} = (\delta_M, \delta_D, \delta_C, \delta_{K_c}, \delta_K)$, each scalar controlling the dispersion of the random mass, damping, gyroscopic coupling, centrifugal stiffness, elastic stiffness matrices.
7. Solving the stochastic nonlinear equations in the time-domain with efficient algorithms based on the arc-length methods [7, 8]

All the details concerning the theoretical construction of such methodology and its application to a large finite element model of an industrial bladed-disk can be found in [8].

From now on, the work is more particularly focussed on point (6), which concerns the numerical modeling of stiffness mistuning uncertainties.

8.2.1 Linear Mistuning with Deterministic Geometric Nonlinearities

Until now, it has been assumed in the industrial application [8] that the mistuning only affects the linear operators. In this case, that means that linear mistuning in presence of deterministic geometric nonlinearities is considered. Concerning the operators involved by the linear elastic constitutive equations, only the elastic linear stiffness operator issued from the MEAN-NL-ROM is uncertain, the quadratic and cubic terms remaining deterministic. Let $[\mathcal{K}^{(e)}]$ be the $(N \times N)$ elastic stiffness matrix issued from the MEAN-NL-ROM with positive-definite property. The corresponding random matrix $[\mathcal{K}^{(e)}]$ is then written as in which $[\mathcal{K}^{(e)}]$ is the $(N \times N)$ upper triangular matrix issued from the Cholesky

$$[\mathcal{K}^{(e)}] = [L_{K^{(e)}}]^{\mathrm{T}} [\mathbf{G}_{K^{(e)}}(\delta_{K^{(e)}})] [L_{K^{(e)}}], \tag{8.1}$$

factorization of $[\mathcal{K}^{(e)}]$, and where $[\mathbf{G}_{K^{(e)}}(\delta_{K^{(e)}})]$ is a full random matrix with values in the set of all the positive-definite symmetric $(N \times N)$ matrices.

8.2.2 Nonlinear Mistuning

From now on, we are interested in considering the case for which uncertainties affect all the operators issued from the elastic constitutive equations. This will be called nonlinear mistuning, that is to say both the linear and nonlinear stiffness operators are affected by uncertainties.

8.2.2.1 Definition of a Positive-Definite Stiffness Operator

In [12], the extension of the nonparametric probabilistic approach to the case of geometric nonlinearities has been considered. In such case, the $(P \times P)$ real matrix $[\mathcal{K}]$ with $P = N(N+1)$ is introduced as

$$[\mathcal{K}] = \begin{bmatrix} [\mathcal{K}^{(e)}] & [\widehat{\mathcal{K}}^{(-2)}] \\ [\widehat{\mathcal{K}}^{(-2)}]^T & 2\,[\mathcal{K}^{(3)}] \end{bmatrix}, \tag{8.2}$$

in which the matrix blocks $[\widehat{\mathcal{K}}^{(-2)}]$ and $[\mathcal{K}^{(3)}]$ are the $(N \times N^2)$ and the $(N^2 \times N^2)$ real matrices resulting from the following reshaping operation

$$[\widehat{\mathcal{K}}^{(-2)}]_{\alpha J} = \widehat{\mathcal{K}}^{(-2)}_{\alpha\beta\gamma}\,,\; J = (\beta-1)N + \gamma\,, \tag{8.3}$$

$$[\mathcal{K}^{(3)}]_{IJ} = \mathcal{K}^{(3)}_{\alpha\beta\gamma\delta}\,,\; I = (\alpha-1)N + \beta\,,\; J = (\gamma-1)N + \delta\,. \tag{8.4}$$

It has been shown in [12] that matrix $[\mathcal{K}]$ is a symmetric and positive-definite matrix and can then be written as $[\mathcal{K}] = [L_K]^T\,[L_K]$. Consequently, the nonparametric probabilistic approach initially introduced in the linear context for positive-definite symmetric operators can easily be extended to the geometrically nonlinear context and the construction of random matrix $[\mathcal{K}] = [L_K]^T\,[\mathbf{G}_K(\delta_K^{NL})]\,[L_K]$ is straightforward. Random matrix $[\mathcal{K}]$ can be block-decomposed similarly to Eq. (8.2) so that the random linear elastic, quadratic and cubic random stiffness terms $\mathcal{K}^{(e)}_{\alpha\beta}$, $\widehat{\mathcal{K}}^{(-2)}_{\alpha\beta\gamma}$ and $\mathcal{K}^{(3)}_{\alpha\beta\gamma\delta}$ can easily be deduced from Eqs. (8.2)–(8.4). Note that again, one scalar dispersion parameter controls the uncertainty level in the structure.

8.2.2.2 Difficulties About Quantifying Nonlinear Mistuning with Respect to Linear Mistuning

The main objective is to characterize the effects of the nonlinear mistuning with respect to the effects of the linear mistuning in presence of geometric nonlinearities. The nonlinear mistuning corresponds to the case for which all the linear and nonlinear operators are uncertain, in contrary to the linear mistuning where only the linear operators are uncertain. Both cases correspond to geometric nonlinear computations.

1. The case for which linear mistuning would be considered by generating random germ $[\mathbf{G}_{K^{(e)}}(\delta_{K^{(e)}})]$ whereas the nonlinear mistuning would be treated by constructing $[\mathbf{G}_K(\delta_K^{NL})]$ cannot be reasonably investigated. Indeed, the sizes of the random germs are thoroughly different and the input dispersion parameter would have to be characterized with respect to the other one.
2. The case for which the same random germ $[\mathbf{G}_K(\delta_K^{NL})]$ would have to be considered for both nonlinear and linear mistuning cases seems to be more coherent. This would imply that the linear mistuning would be considered by extracting the random linear part from random matrix $[\mathcal{K}]$, keeping the nonlinear quadratic and cubic terms as deterministic terms for the nonlinear calculations. Nevertheless, this case has been investigated in [7] in the context of the post-buckling nonlinear dynamical analysis of an uncertain cylindrical shell. With such method, a strong nonlinear level of uncertainty $\delta_K^{NL} = 0.45$ yielded an equivalent linear uncertainty level $\delta_K^{L} = 0.025$ for the linear part of the structure, yielding a subsequent scale effect, preventing to distinguish any differences between the linear and nonlinear uncertainty cases. Moreover, with such method, the nonlinear mistuning case would be involved with $N^2\,(N+1)\,(N+2)/2 \ggg N(N+1)/2$ independent random variables. This makes the feasibility of generating $[\mathbf{G}_K(\delta_K^{NL})]$ questionable as N increases.

   Consequently, the following section proposes an improvement of the methodology, allowing both linear and nonlinear mistuning cases to be coherently considered.

8.2.2.3 Strategy for Modeling and Quantifying the Nonlinear Mistuning

In the present context, one wishes to obtain a coherent germ from matrix $[\mathcal{K}]$ for both linear and nonlinear mistuning cases. The idea is to perform a second reduced-order model of matrix $[\mathcal{K}]$ by solving first the single eigenvalue problem

$$[\mathcal{K}]\,\boldsymbol{\psi}_\alpha = \lambda'_\alpha\,\boldsymbol{\psi}_\alpha. \tag{8.5}$$

Matrix $[\mathcal{K}]$ can then be approximated by the $(P \times P)$ matrix $[\tilde{\mathcal{K}}]$ such that

$$[\tilde{\mathcal{K}}] \;=\; [\tilde{L}_K]^T\,[\tilde{L}_K], \tag{8.6}$$

in which $[\tilde{L}_K]$ is the $(N' \times P)$ matrix defined by

$$[\tilde{L}_K] \;=\; [\Lambda^{N'}]^{\frac{1}{2}}\,[\Psi^{N'}]^T, \tag{8.7}$$

where $[\Lambda^{N'}]$ is the $(N' \times N')$ diagonal matrix such that $[\Lambda^{N'}]_{\alpha\alpha} \;=\; \lambda'_\alpha$, where $\lambda'_1 \geq \lambda'_2 \geq \cdots \geq \lambda'_{N'}$ and where the columns of the $(P \times N')$ matrix $[\Psi^{N'}]$ are the eigenvector $\boldsymbol{\psi}_\alpha$, $\alpha \in \{1, \ldots, N'\}$ related to eigenvalues λ'_α. Random matrix $[\tilde{\mathcal{K}}]$ is then replaced by the random matrix $[\tilde{\mathcal{K}}]$ such that

$$[\tilde{\mathcal{K}}] \;=\; [\tilde{L}_K]^T\,[\tilde{\mathbf{G}}_K(\delta_K^{NL})]\,[\tilde{L}_K], \tag{8.8}$$

in which $[\tilde{\mathbf{G}}_K(\delta_K^{NL})]$ is a $(N' \times N')$ random matrix with values in the set of the symmetric positive-definite matrices. It should be noted that one naturally expects to obtain $N \leq N' \lll N(N+1)$ in order to propose a coherent quantification of the nonlinear mistuning with respect to the linear mistuning.

8.2.3 Stochastic Nonlinear Reduced-Order Model

Once all the operators of the MEAN-NL-ROM have been replaced by the properly random operators, including the strategy explained above concerning the nonlinear stiffness reduced operators, the stochastic nonlinear reduced-order model is given by the random field $\mathbf{U}^N(\cdot, t)$ that is written, for all $\mathbf{x} \in \boldsymbol{\Omega}$, as

$$\mathbf{U}^N(\mathbf{x}, t) \;=\; \sum_{\beta=1}^{N} \boldsymbol{\varphi}^\beta(\mathbf{x})\,\mathbf{Q}_\beta(t), \tag{8.9}$$

in which the $\mathbb{R}^N$-valued random variable $\mathbf{Q}(t) \;=\; (\mathbf{Q}_1(t), \cdots, \mathbf{Q}_N(t))$ is solution of the following set of stochastic nonlinear differential equations,

$$\begin{aligned} &\mathcal{M}_{\alpha\beta}\,\ddot{\mathbf{Q}}_\beta \;+\; (\mathcal{D}_{\alpha\beta} + \mathcal{C}(\Omega)_{\alpha\beta})\,\dot{\mathbf{Q}}_\beta \;+\; (\mathcal{K}^{(e)}_{\alpha\beta} + \mathcal{K}^{(c)}(\Omega)_{\alpha\beta} + \mathcal{K}^{(g)}_{\alpha\beta})\,\mathbf{Q}_\beta \\ &+ \mathcal{K}^{(-2)}_{\alpha\beta\gamma}\,\mathbf{Q}_\beta\,\mathbf{Q}_\gamma + \mathcal{K}^{(3)}_{\alpha\beta\gamma\delta}\,\mathbf{Q}_\beta\,\mathbf{Q}_\gamma\,\mathbf{Q}_\delta \;=\; \mathcal{F}_\alpha \end{aligned} \tag{8.10}$$

The solution of such a stochastic nonlinear reduced-order model is calculated using the Monte Carlo numerical simulation, using an implicit and unconditionally stable integration scheme (Newmark method with the averaging acceleration scheme) combined with either the fixed point method or the Crisfield arc-length based algorithm [8, 13], depending on the nonlinearity rate.

8.3 Results and Discussion

8.3.1 Description of the Numerical Model

The structure under consideration is an industrial centrifugal compressor belonging to the class of integrated bladed disks. Due to proprietary reasons, the number M of blades characterizing the order of the cyclic symmetry of the structure cannot be given. The finite element model of the structure is constructed with solid finite elements and is constituted of about 2,000,000 degrees of freedom (Fig. 8.1). The structure is in rotation around its revolution axis with a constant velocity $\Omega \;=\; 30{,}750\,rpm$. Since the dynamic analysis is carried out in the rotating frame of the structure, the rigid body motion due to the rotation of the structure corresponds to a fixed boundary condition at the inner radius of the structure. The bladed disk is made up of a homogeneous isotropic material. A modal damping model is added for the bladed disk.

Fig. 8.1 Part of the finite element mesh of the bladed disk

Fig. 8.2 Convergence analysis concerning the second reduction method: graph of function $N \mapsto \text{Conv}(N)$

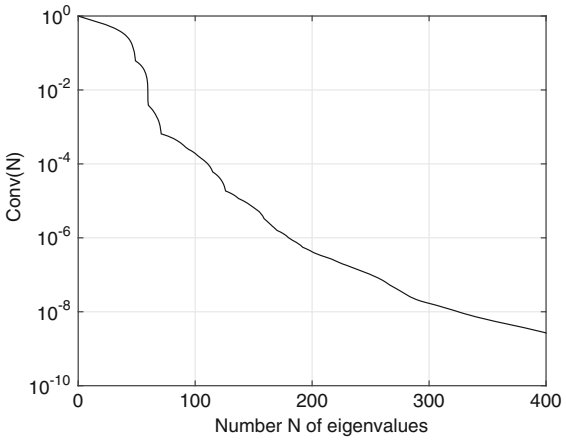

8.3.2 *Convergence of the Stiffness Operator Issued from the MEAN-NL-ROM*

The numerical MEAN-NL-ROM related to the industrial bladed-disk is constructed using $N = 60$ eigenmodes of vibration. Consequently, the matrix $[\mathcal{K}]$ defined by Eq. (8.2) has dimension $(P \times P)$ with $P = 3660$. The second reduction method is carried out as described in Section 1.2.3 and let $[\tilde{\mathcal{K}}^{N'}]$ be the approximation of matrix $[\mathcal{K}]$ obtained with the N' most important eigenvalues. Figure 8.2 displays the graph $N' \mapsto \text{Conv}(N')$ in which

$$\text{Conv}(N) = \sqrt{\frac{||[\tilde{\mathcal{K}}^{N}] - [\mathcal{K}]||_F^2}{||[\mathcal{K}]||_F^2}} \tag{8.11}$$

It can be shown that the convergence is fastly obtained. From now on, we choose $N' = 400$.

8.3.3 *Convergence of the Random Response Calculated with the Second Reduction Method*

Let ν_0 be the first eigenfrequency of the structure. From now on, all the quantities defined in the frequency domain are expressed with respect to ν/ν_0 in which ν is the physical frequency. The external load is a 5-th engine-order excitation expressed in the time domain for which the corresponding dimensionless frequency excitation band is $\mathbb{B}_{\text{exc}} = [1.78\,,\,2.34]$ with an intensity load taken as 2.5 N. It is located at the tip of each blade [14]. The random observation $W(2\pi\nu)$ related to the STOCH-NL-ROM concerns the random displacement located at the tip of the most responding blade.

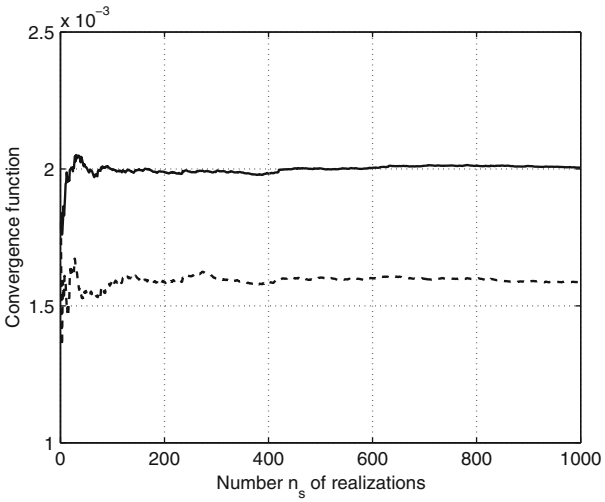

Fig. 8.3 Stochastic convergence analysis of the random response: graph $N' \mapsto \mathrm{Conv}^i_\infty(N', 1000)$ (1) main resonance (*solid line*) (2) secondary resonance (*dotted line*)

As shown in [8], it is seen that the geometric nonlinearities propagate the random response of the blade outside $\mathbb{B}_{\mathrm{exc}}$. More particularly, it is seen that the resonance located outside $\mathbb{B}_{\mathrm{exc}}$ has not only a non-negligible contribution but also is particularly sensitive to uncertainties. Such complex dynamical behavior yields to introduce the two random observations W^1_∞ and W^2_∞ such that

$$W^1_\infty = \max_{\mathbb{B}_{\mathrm{exc}}} W(2\pi\nu) \qquad W^2_\infty = \max_{\mathbb{B}_{\mathrm{sub}}} W(2\pi\nu), \tag{8.12}$$

in which $\mathbb{B}_{\mathrm{sub}} = [1\,;\,1.6]$ is a part of the frequency band of observation located below $\mathbb{B}_{\mathrm{exc}}$. The convergence of the random solution is then analyzed with respect to the number n_s of realizations required by the Monte Carlo numerical simulation and the size N' of the second-order reduction method by introducing the following quantity

$$\mathrm{Conv}^i_\infty(N', n_s) = \sqrt{\frac{1}{n_s}\sum_{j=1}^{n_s}\left(\widetilde{W}^{N',i}_\infty(\theta_j)\right)^2}, \tag{8.13}$$

in which $\widetilde{W}^{N',i}_\infty(\theta_j)$ is the realization number j of the approximation of random observation W^i_∞ obtained with the second reduction method of size N'. Figures 8.3 and 8.4 display the graphs $N' \mapsto \mathrm{Conv}^i_\infty(N', 1000)$ and $n_s \mapsto \mathrm{Conv}^i_\infty(200, n_s)$. It can be concluded that a good approximation is obtained with $N' = 200$ and $n_s = 600$.

8.3.4 Quantification of the Nonlinear Mistuning with Respect to the Linear Mistuning

Figures 8.5 and 8.6 compare the random observation for the cases of nonlinear and linear mistuning respectively. There are slight differences between the two cases. It can be observed that the presence of uncertainties on the nonlinear part of the stiffness operator yield narrower confidence region. This means that the nonlinear random observation is more robust to uncertainties when uncertainties are taken into account on both the linear and nonlinear operators.

8.4 Conclusions

In the context of structural dynamics with geometric nonlinearities, a method has been presented for quantifying the propagation of uncertainties whether only the linear operators or both linear and nonlinear operators do have uncertainties.

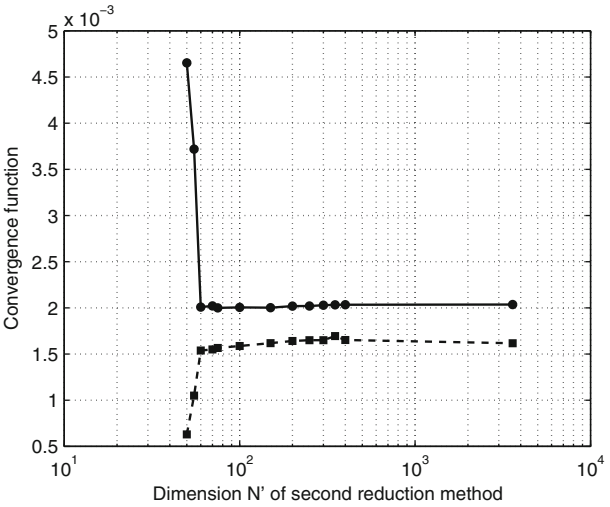

Fig. 8.4 Stochastic convergence analysis of the random response: graph $n_s \mapsto \mathrm{Conv}^i_{\infty}(200, n_s)$ (1) main resonance (*solid line*) (2) secondary resonance (*dotted line*)

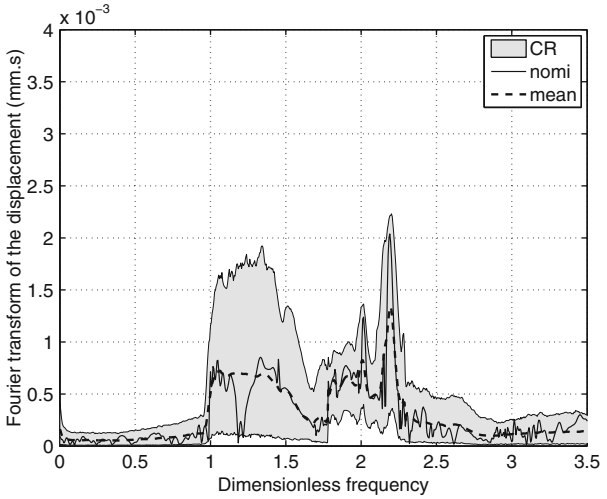

Fig. 8.5 Stochastic analysis for the nonlinear mistuning: random observation $W(2\pi\nu)$ (1) mean model (*thick line*), mean of the stochastic model (*thin dashed line*), and confidence region (*gray region*)

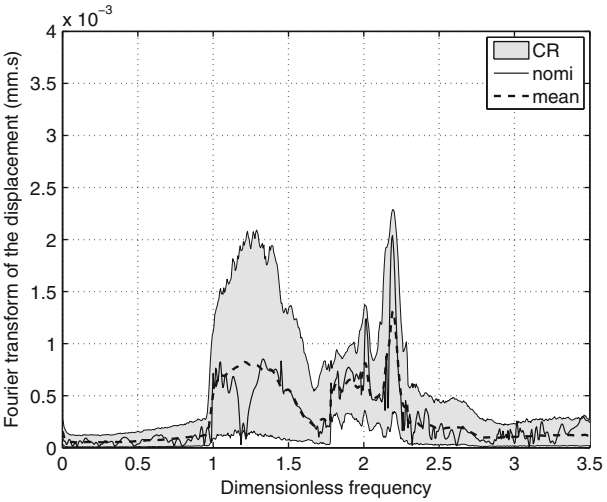

Fig. 8.6 Stochastic analysis for the linear mistuning: random observation $W(2\pi\nu)$ (1) mean model (*thick line*), mean of the stochastic model (*thin dashed line*), and confidence region (*gray region*)

The methodology has been applied in the context of both the linear and nonlinear mistuning of an industrial integrated bladed-disk. It is shown that the presence of uncertainties on the nonlinear operators increase slightly the robustness of the random dynamical response.

Acknowledgements This work was supported by the DGA (French defence procurement agency) in the context of the TURBODYNA project (project number ANR-13-ASTR-0008-01) related to the ANR ASTRID research program (specific support scheme for research works and innovation defence). SAFRAN Turbomeca is also acknowledged for giving permission to publish this work.

References

1. Pai, P.F., Nayfeh, A.H.: A fully nonlinear-theory of curved and twisted composite rotor blades accounting for warpings and 3-dimensional stress effects. Int. J. Solids Struct. **31**(9), 1309–1340 (1994)
2. Tang, D.-M., Dowell, E.H.: Nonlinear response of a non-rotating rotor blade to a periodic gust. J. Fluids Struct. **10**(7), 721–742 (1996)
3. Grolet, A., Thouverez, F.: Free and forced vibration analysis of a nonlinear system with cyclic symmetry: application to a simplified model. J. Sound Vib. **331**(12), 2911–2928 (2012)
4. Hodges, D.-H., Shang, X.-Y., Cesnik, C.E.S.: Finite element solution of nonlinear intrinsic equations for curved composite beams. J. Am. Helicopter Soc. **41**(4), 313–321 (1996)
5. Huang, H., Han, Q.: Research on nonlinear postbuckling of functionally graded cylindrical shells under radial loads. Compos. Struct. **92**(6), 1352–1357 (2010)
6. Capiez-Lernout, E., Soize, C., Mignolet, M.-P.: Computational stochastic statics of an uncertain curved structure with geometrical nonlinearity in three-dimensional elasticity. Comput. Mech. **49**(1), 87–97 (2012)
7. Capiez-Lernout, E., Soize, C., Mignolet, M.-P.: Post-buckling nonlinear static and dynamical analyses of uncertain cylindrical shells and experimental validation. Comput. Methods Appl. Mech. Eng. **271**, 210–230 (2014)
8. Capiez-Lernout, E., Soize, C., Mbaye, M.: Mistuning analysis and uncertainty quantification of an industrial bladed disk with geometrical nonlinearity. J. Sound Vib. **356**(10), 124–143 (2015)
9. Wei, S.-T., Pierre, C.: Localization phenomena in mistuned assemblies with cyclic symmetry part ii: forced vibrations. ASME J. Vib. Acoust. Stress. Reliab. Des. **110**(4), 439–449 (1988)
10. Mignolet, M.-P., Przekop, A., Rizzi, S.A., Spottswood, M.S.: review of indirect/non-intrusive reduced-order modeling of nonlinear geometric structures. J. Sound Vib. **332**(10), 2437–2460 (2013)
11. Soize, C.: Stochastic Models of Uncertainties in Computational Mechanics. Lecture Notes in Engineering Mechanics, vol. 2. American Society of Civil Engineers (ASCE), Reston (2012)
12. Mignolet, M.-P., Soize, C.: Stochastic reduced-order models for uncertain geometrically nonlinear dynamical systems. Comput. Methods Appl. Mech. Eng. **197**, 3951–3963 (2008)
13. Crisfield, M.A.: Non-Linear Finite Element Analysis of Solids and Structures, vol. 1: Essentials. Wiley, Chichester (1997)
14. Capiez-Lernout, E., Soize, C., Mbaye, M.: Uncertainty quantification for an industrial mistuned bladed disk with geometrical nonlinearities. In: Paper GT2015-42471, Proceedings of the ASME Turbo Expo 2015: Turbine Technical Conference and Exposition GT2015, Montréal, 15–19 June 2015

Chapter 9
Estimating Noise Spectra for Data from an Instrumented Building

Bryan S. Joyce and Pablo A. Tarazaga

Abstract Virginia Tech's Goodwin Hall is instrumented with over 200 highly sensitive, seismic accelerometers. These sensors detect motion from vibration sources inside the building (e.g. footsteps, HVAC equipment, and closing doors) and external (seismic motion and wind loading). The later sources produce much weaker excitations for the sensors and result in lower signal-to-noise ratios. Therefore, it is important to estimate the inherent noise present in the accelerometer signals in order to determine and analyze the actual building vibrations from seismic motion and wind loading. Sources of noise include electrical interference and self-noise in the instrumentation system including the accelerometers, cables, and signal conditioning amplifiers. This paper will examine several techniques for using collocated sensors for estimating the power spectral densities of the noise present in accelerometer measurements. First these estimation techniques are applied to simulated signals corrupted by noise. Then these methods are applied to laboratory data from several accelerometers placed on a vibration isolation table.

Keywords Noise estimation • Signal estimation • Signal-to-noise ratio • Collocated sensors • Common signal noise estimation

9.1 Introduction

Obtaining high quality data is an obvious priority in most experiments. Having a high signal-to-noise ratio (SNR) in all experimental measurements is important for reliable analysis [1, 2]. Here the signal from a sensor is defined as the portion of the measurement due to the physical input of interest. For accelerometers, the signal would be the portion of the output voltage due solely to the actual acceleration experienced by the proof mass. We define the term "noise" to mean any undesired contribution to the measurement, such as electrical interference in the transmission cables or self-noise from the sensor and data acquisition system [3]. Assuming the noise is additive to the signal, then the measurement $y(t)$ is the sum of the noise $n(t)$ and the signal $s(t)$, i.e.

$$y(t) = s(t) + n(t). \tag{9.1}$$

Ideally the noise amplitude should be small compared to that of the signal. However, this is not always possible, particularly in applications with small motions and thus small signals.

The Virginia Tech Smart Infrastructure Laboratory (VTSIL) has instrumented Goodwin Hall with over 200 high-sensitivity accelerometers. This highly instrumented building allows VTSIL to study the building's dynamics and activity of occupants among other topics. Work into localization and identification of people in the building has shown sufficiently large signals for analysis [4, 5]. As VTSIL begins analysis on building dynamics, obtaining good measurements from such weak oscillations becomes a concern. Seismic motion and wind loads on the building cause small excitations and thus small accelerations. While our accelerometers have a high sensitivity, it is still important to estimate the noise floor of these measurements. The noise floor needs to be estimated in terms of the overall noise power (for use in calculating a SNR) but also in terms of the power spectral density of the noise. It will be more difficult to estimate modal parameters in frequency bands with high noise power. Knowing the bands of high noise levels will aid later analysis. In addition, estimates of the noise spectra for the sensors can be used in simulations of building dynamics for studying data analyses techniques.

B.S. Joyce (✉) • P.A. Tarazaga
Department of Mechanical Engineering, Virginia Tech, Virginia Tech Smart Infrastructure Laboratory (VTSIL),
310 Goodwin Hall (MC 0238), 635 Prices Fork Road, Blacksburg, VA 24061, USA
e-mail: bsj@vt.edu

S. Atamturktur et al. (eds.), *Model Validation and Uncertainty Quantification, Volume 3*, Conference Proceedings
of the Society for Experimental Mechanics Series, DOI 10.1007/978-3-319-29754-5_9

There has been some work into estimating the noise levels in measured signals, particularly in the seismology community. These methods can broadly be organized into in situ and ex situ estimation techniques. For all of these methods, the accelerometer is connected to the same instrumentation equipment (cabling, signal conditioners, and data acquisition systems) that will be used in application. The ex situ noise estimation methods take the sensor out of operation. In some cases the accelerometer either in a "quiet" location with little excitation [6]. In this case, the signal is ideally close to zero and the measurement is assumed to be purely noise (see Eq. 9.1). However, this method is not feasible for high sensitivity accelerometers designed to detect the slightest ground motions. Other techniques will place the accelerometer on a shaker that applies a known excitation (often a sine wave) [7]. In this case, the uncorrupted signal $s(t)$ is known and the measured acceleration $y(t)$ is measured. Equation (9.1) leads to an estimation of the noise signal $n(t)$ or its power spectral density.

However, these methods often do not test the data acquisition system, cabling, and sensor *as installed for application*. Issues can be introduced in operation such as "misalignment noise" from improper sensor installation, electromagnetic interference in the sensors or cables, and acoustic effects [8]. Analysis of the sensor in situ provides a better estimate of the noise the sensor actually experiences in operation (because the estimation occurs while the sensor is in operation). If the accelerometer is also subject to normal operational conditions, then the in situ noise estimation techniques can also yield estimates of the signal spectrum.

The physical input to a seismic accelerometer (e.g. ground motion or wind motion) is often considered stochastic [1, 9]. Since the noise signal is often also stochastic, this makes separation of the signal from the noise more challenging. One solution to this problem is to use a set of collocated sensors. Several accelerometers in close proximity will experience nearly the same base motion. If the noise on each accelerometer is uncorrelated to each other or to the base motion (the signal), then the cross-correlation of the accelerometer measurements can lead to an estimate of the true, shared input signal, $s(t)$.

This paper will examine several noise estimation methods that use this multi-sensor approach. This paper will first present some terminology for use in later sections. Next some noise spectra estimation techniques are discussed. These are divided into two categories: methods that use two sensors and methods that use three sensors. These methods could be extended to included more than three sensors, but this is made more challenging in practice due to limits on the number of available sensors and available data acquisition channels. These methods are then applied to simulation data. Finally, these techniques are used to estimate noise spectra from sensors placed on a granite table.

9.2 Power Spectral Density (PSD) and Signal-to-Noise Ratio (SNR)

It is important to first define a few terms and state some necessary assumptions. Let the cross-correlation between the measurements from two accelerometers, $y_i(t)$ and $y_j(t)$, be denoted as $E[y_i(t)\ y_j(t+\tau)]$ where E is the expectation operator and τ is an arbitrary time delay. Then the cross-power spectral density (CPSD) is simply the Fourier transform of the cross-correlation, denoted as

$$G_{ij}(\omega) = G\left[y_i(t), y_j(t)\right] = F\left[E\left[y_i(t)\ y_j(t+\tau)\right]\right], \tag{9.2}$$

where F denotes the Fourier transform and $G[\bullet, \bullet]$ is defined here as the cross power spectral density operator [10, 11]. The result will be a function of frequency ω. The power spectral density (PSD) is calculated by applying the CPSD operator using the same signal for both operands, i.e.

$$G_{ii}(\omega) = G\left[y_i(t), y_i(t)\right] = F\left[E\left[y_i(t)\ y_i(t+\tau)\right]\right]. \tag{9.3}$$

In simulations and in experiments, the CPSDs and PSDs will be calculated using a pwelch method in MATLAB [12]. Note that because the accelerometer measurements are real-valued, only positive frequencies are considered, and one-sided PSDs will be used here.

The estimation methods in the next sections rely on a few assumptions. First assume we have collocated sensors measuring the same signal, $s(t)$. Also assume the signal and noise for each sensor (and consequently the measurement $y_i(t)$) have a zero mean value. This is justified as we will use IEPE accelerometers with AC coupling. Next assume the signal is uncorrelated to the noise. Also assume the noise on all of the sensors are uncorrelated to each other. Mathematically, these statements can be written as

$$E\left[s(t)n_i(t)\right] \quad and \quad E\left[n_i(t)n_j(t)\right] \quad for \ i \neq j \tag{9.4}$$

where $n_i(t)$ is the noise for accelerometer i. Note that no subscript is used for the signal as it is assumed the collocated accelerometers experience the same physical input and thus the same signal, $s(t)$. From this, the CPSD between the signal and noise on any channel is zero. Note that in practice the finite length of real signals will lead to a non-zero CPSD [13].

From Eq. (9.1) and the above assumptions, one can conclude that for any sensor i, the PSD of the measurement, $G_{ii}(\omega)$, can be written as

$$G_{ii}(\omega) = G_{ss}(\omega) + G_{n_i n_i}(\omega). \tag{9.5}$$

where $G_{ii}(\omega)$ is the PSD of the signal, $s(t)$ and $G_{n_i n_i}(\omega)$ is the PSD of the noise on sensor i, $n_i(t)$. If the PSD of the signal is known, then the noise PSD could be estimated easily from this equation. If the signal spectrum is known and the PSD of the measurement can be calculated from the measured data, then Eq. (9.5) will lead to an estimation of the noise spectrum. In application, the true signal is unknown and would also need to be extracted. In Sect. 9.5, "Estimator 1A" will use this method for comparison.

The power, or variance, of the signal is

$$\sigma_s^2 = \int_0^\infty (s(t))^2 \, dt = \int_0^\infty G_{ss}(\omega) \, df, \tag{9.6}$$

where the second equality comes from Parseval's theorem. A similar definition holds for the power of the noise $n_i(t)$ and the total measurement $y_i(t)$. Finally, we will take the signal-to-noise ratio for sensor i (SNR_i) as the variance of the signal divided by the variance of the noise, i.e.

$$SNR_i = \frac{\sigma_s^2}{\sigma_{n_i}^2} = \frac{\int_0^\infty (s(t))^2 \, dt}{\int_0^\infty (n_i(t))^2 \, dt} = \frac{\int_0^\infty G_{ss}(\omega) \, df}{\int_0^\infty G_{n_i n_i}(\omega) \, df}. \tag{9.7}$$

9.3 Two-Channel Estimation Methods

Several researchers have developed techniques for estimating the noise spectrum and the signal-to-noise ratio using two collocated accelerometers. This section discusses some of these methods. For all of them, it is assumed the accelerometers experience the same acceleration (common signal), but their noise spectra are independent and uncorrelated.

9.3.1 Estimator 2A: Holcomb 1989

Holmcomb is one of the first to develop a method for calculating instrument noise using collocated seismometers [2, 14, 15]. Because the noise contributions for the sensors are assumed to be independent of each other and the signal (Eq. 9.4), the cross power spectral density between measurements from the two sensors will simplify to be the signal spectrum, i.e.

$$G_{ss} = |G_{12}|, \tag{9.8}$$

where G_{12} is the cross power spectral density between measurements from two accelerometer, $y_1(t)$ and $y_2(t)$. The magnitude of the CPSD is used as this calculation may yield a complex-value while the true signal PSD is purely real. Note that the argument is dropped from the PSD for ease of notation. From this and Eq. (9.5), the noise PSD for sensor i is simply

$$G_{n_i n_i} = G_{ii} - |G_{12}| \quad for \;\; i = 1 \text{ or } 2. \tag{9.9}$$

9.3.2 Estimator 2B: Tasič 2012

Tasič and Runovc use a method which uses a reference accelerometer with a known noise spectra [8]. However, this method can be extended to a reference sensor with an unknown noise spectra by assuming both sensors have the same self-noise. In this case, the authors derive an expression for the mean noise PSD of the two sensors,

$$G_{nn} = \frac{G_{11} + G_{22}}{2} - |G_{12}|\,, \tag{9.10}$$

where G_{nn} is the average noise spectrum between the two sensors, G_{11} is the PSD of $y_1(t)$, G_{22} is the PSD of $y_2(t)$, and G_{12} is the CPSD between $y_1(t)$ and $y_2(t)$. The signal spectrum is assumed to be the same as Eq. (9.8).

9.3.3 Estimator 2C: Brincker 2007

Brincker and Larsen derive a similar common noise spectrum between two identical, collocated sensors as Tasič and Runovc [16]. However, their method uses a geometric mean in place of the arithmetic average of the two measurement PSDs, i.e.

$$G_{nn} = \sqrt{G_{11}G_{22}} - |G_{12}|\,, \tag{9.11}$$

where here G_{nn} is the geometric average of the noise spectrum between the two sensors. Equation (9.8) is used to estimate the signal PSD.

9.3.4 Estimator 2D: Rainieri 2014

Rainieri and Fabbrocino develop an alternative method for calculating the noise and signal spectra [9]. Expanding on their method, calculate the PSD of the difference between the two measurements, i.e.

$$G_{1-2,\ 1-2} = G\left[y_1(t) - y_2(t), y_1(t) - y_2(t)\right]. \tag{9.12}$$

From Eq. (9.1) and the assumptions of uncorrelated noise spectra, this reduces to

$$G_{1-2,\ 1-2} = G_{n_1n_1} + G_{n_2n_2}. \tag{9.13}$$

Note that the difference of the original measurement PSDs is

$$G_{11} - G_{22} = G_{n_1n_1} - G_{n_2n_2}. \tag{9.14}$$

Combining Eqs. (9.13) and (9.14) leads to estimates for the noise PSDs for each sensor,

$$G_{n_1n_1} = \frac{G_{1-2,\ 1-2} + (G_{11} - G_{22})}{2}, \tag{9.15}$$

$$G_{n_2n_2} = \frac{G_{1-2,\ 1-2} - (G_{11} - G_{22})}{2}. \tag{9.16}$$

Similarly, the PSD of the sum of the two accelerometer measurements is

$$G_{1+2,\ 1+2} = G\left[y_1(t) + y_2(t), y_1(t) + y_2(t)\right] = 4G_{ss} + G_{n_1n_1} + G_{n_2n_2}. \tag{9.17}$$

This leads to an estimate of the signal PSD as

$$G_{ss} = \frac{G_{1+2,\ 1+2} - (G_{n_1 n_1} + G_{n_2 n_2})}{4} = \frac{G_{1+2,\ 1+2} - G_{1-2,\ 1-2}}{4}. \tag{9.18}$$

9.4 Three-Channel Estimation Methods

Including a third, collocated sensor allows for redundancy and potentially improved accuracy. This section examines a few methods using three sensors.

9.4.1 Estimator 3A: Sleeman 2006

Sleeman et al. develop a noise spectra estimation method using three sensors [17]. Their method is similar to that of Holcomb (Estimator 2A). However, by using a third sensor, the authors can define a relative frequency response function (FRF) between any two of the sensors. Thus this method can compensate for any differences in the characteristics of the sensors.

In this method the improved estimate of the signal PSD is

$$G_{ss} = \left| h_{ij} G_{ij} \right|, \tag{9.19}$$

where h_{ij} is the relative frequency response function between sensors i and j using sensor k as a reference, i.e.

$$h_{ij} = \frac{G_{ik}}{G_{jk}}. \tag{9.20}$$

This is the same as the "H_3" formulation of the frequency response function from Ewins [10]. The noise spectra are estimated as

$$G_{n_i n_i} = G_{ii} - |G_{ss}| \ for \ \ i = 1,\ 2,\ 3. \tag{9.21}$$

9.4.2 Estimator 3B: Tasič 2012 Extended

In this work, we will also introduce an extension of the Tasič and Runovc method (Estimator 2B). We can compute averages of the PSD estimates from different pairs of the three sensors, i.e.

$$G_{ss} = \frac{|G_{12}| + |G_{13}| + |G_{23}|}{3}, \tag{9.22}$$

and

$$G_{nn} = \frac{G_{nn}^{12} + G_{nn}^{13} + G_{nn}^{23}}{3}, \tag{9.23}$$

where G_{nn}^{ij} is the noise PSD estimate from Estimator 2B using sensors i and j. Averaging the Estimator 2B results over all possible sensor pairings should yield more accurate signal and noise PSD estimates.

9.4.3 Estimator 3C: Brincker 2007 Extended

Similar to Estimator 3B, we introduce an extension to the Brincker and Larsen method (Estimator 2C) to include geometric averages of the original signal and noise estimations for two sensors, i.e.

$$G_{ss} = \left(|G_{12}|\,|G_{13}|\,|G_{23}|\right)^{1/3}, \tag{9.24}$$

and

$$G_{nn} = \left(G_{nn}^{12} G_{nn}^{13} G_{nn}^{23}\right)^{1/3}. \tag{9.25}$$

where here G_{nn}^{ij} is the noise PSD estimate from Estimator 2C using sensors i and j.

9.5 Simulation Results

These estimators are next tested on simulation data. Three types of common signals are examined: a sine wave, a low-pass filtered white noise input, and a white noise signal filtered by a dynamic system. The noise contributions to the measurements, $n_i(t)$, are constructed from filtered white noise. Each simulated channel has a different instance of noise, but the noise is derived from the same characteristics: white noise filtered by a second order, low pass Butterworth filter with a corner frequency of 200 Hz. The signal variance held constant at unity while the variance of the noise is altered for each condition.

For each simulation, the simulation time is 10 min and the sampling rate is 1000 Hz. The PSDs are calculated using MATLAB's pwelch function with a window size of 1/8th of the number of samples and an overlap of 7/8th of a window [12]. The 7/8th overlap was chosen based on analysis by Evans et al. to help smooth the spectra estimates [6]. The noise spectra are only computed for the first sensor. Finally, an additional estimator, Estimator 1A, is derived from Eq. (9.5) assuming the signal spectrum is known. While the signal spectrum will not be known in real world experiments, this method is useful for comparison to the other methods.

9.5.1 Sinusoidal Input

First a sine wave input is used with an amplitude of $\sqrt{2}$ (a variance of one) and a frequency of 100 Hz. Figure 9.1 shows the true and estimated PSDs for a case with a SNR of 20 dB. The PSD of the measured signal, G_{yy}, is composed of the sum of the noise and signal spectra. Estimator 3A and 2D show the most variation in the signal and noise PSDs while the other methods shows smoother calculations. Figure 9.2 plots the relative errors of the signal power estimation, the noise power estimation, and the signal-to-noise ratio. The relative errors are calculated as the estimated value over the true value. For all of the estimators, the error in the signal power estimation is low for high SNR (low noise power). This is intuitive as the measurement is dominated by the signal at high SNR, making estimation easier. For Estimators 1A and 2D show good prediction of noise power at low SNR. The error in noise estimation increases with SNR for Estimators 1A, 2A and 2D. For Estimators 2B, 2C, 3B, and 3C, the noise power estimation improves with increasing SNR, but these methods show larger errors at low SNR.

9.5.2 Filtered White Noise Input

Next a more broadband signal is used. The signal is constructed by filtering white noise by a third order Butterworth filter with a corner frequency of 100 Hz. Figures 9.3 and 9.4 show simulation results using the filtered white noise input case. The trends in the relative errors are similar to those seen for the sinusoidal input.

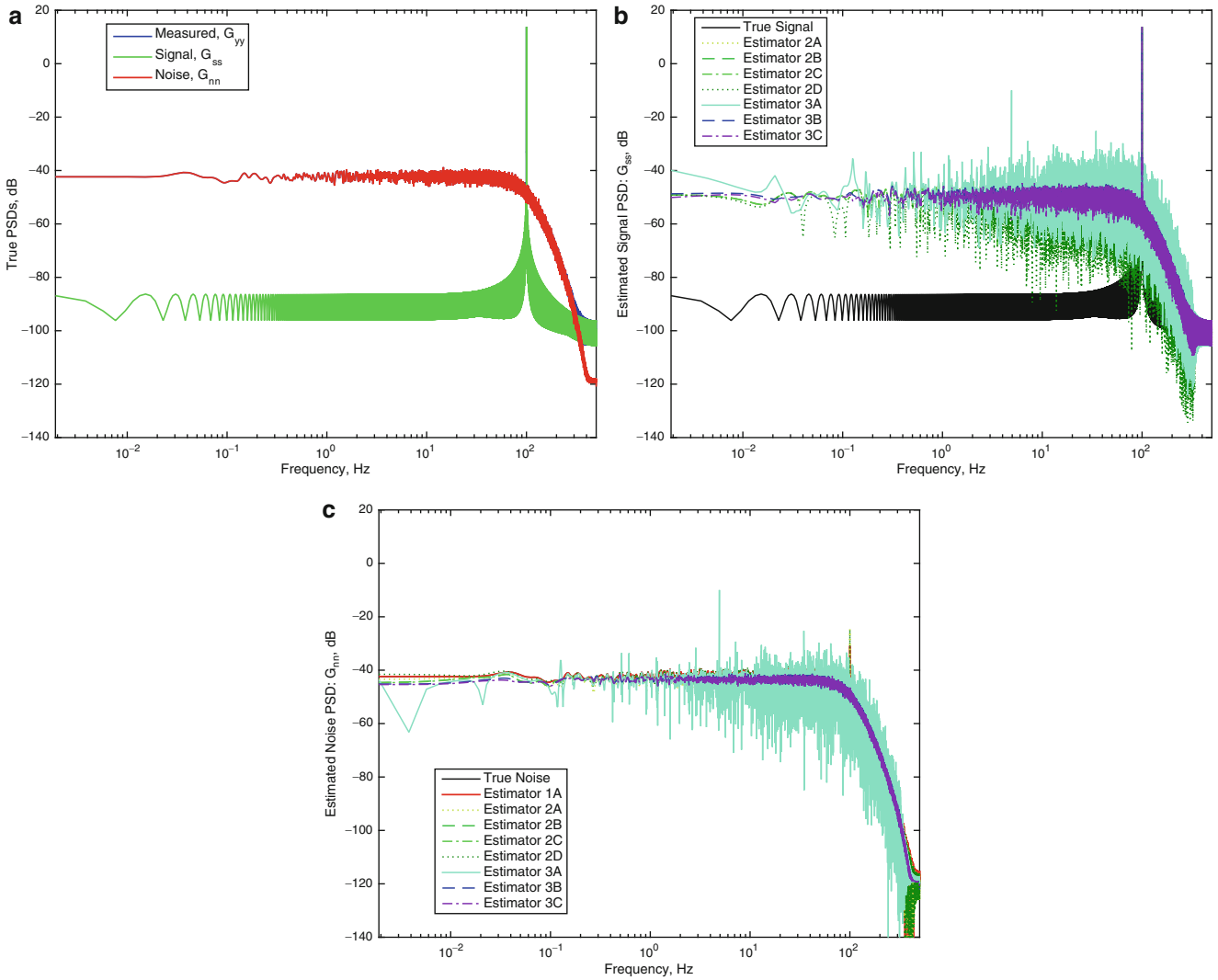

Fig. 9.1 PSDs and estimates for the measurement, signal, and noise with sine wave input at 100 Hz. Here the signal-to-noise ratio (SNR) is set to 20 dB. (**a**) The true PSDs, (**b**) estimated signal PSDs, and (**c**) estimated noise PSDs. In (**a**), the measurement PSD, G_{yy}, is behind the other PSDs

9.5.3 Dynamic Input

For the sensors in Goodwin Hall, a more realistic signal would be the acceleration of the building in response to a stochastic input. To simulated this, the low-pass filtered white noise signal used in Sect. 9.5.2 is used as input to a dynamic system. The output of this dynamic system is treated as the signal to the accelerometers, i.e. the signal $s(t)$ is constructed as

$$s(t) = \int_{\tau=0}^{t} h(t-\tau)\, w(\tau)\, d\tau, \tag{9.26}$$

where $w(t)$ is the filtered white noise from Sect. 9.5.2 and $h(t)$ is impulse response function of a dynamic system. The dynamic system is constructed using the Fourier transform of impulse response function, $H(\omega)$, in the form

$$H(\omega) = \sum_{i=1}^{5} \frac{A_i}{\omega_i^2 - \omega^2 + j2\zeta_i\omega\ \omega_i}, \tag{9.27}$$

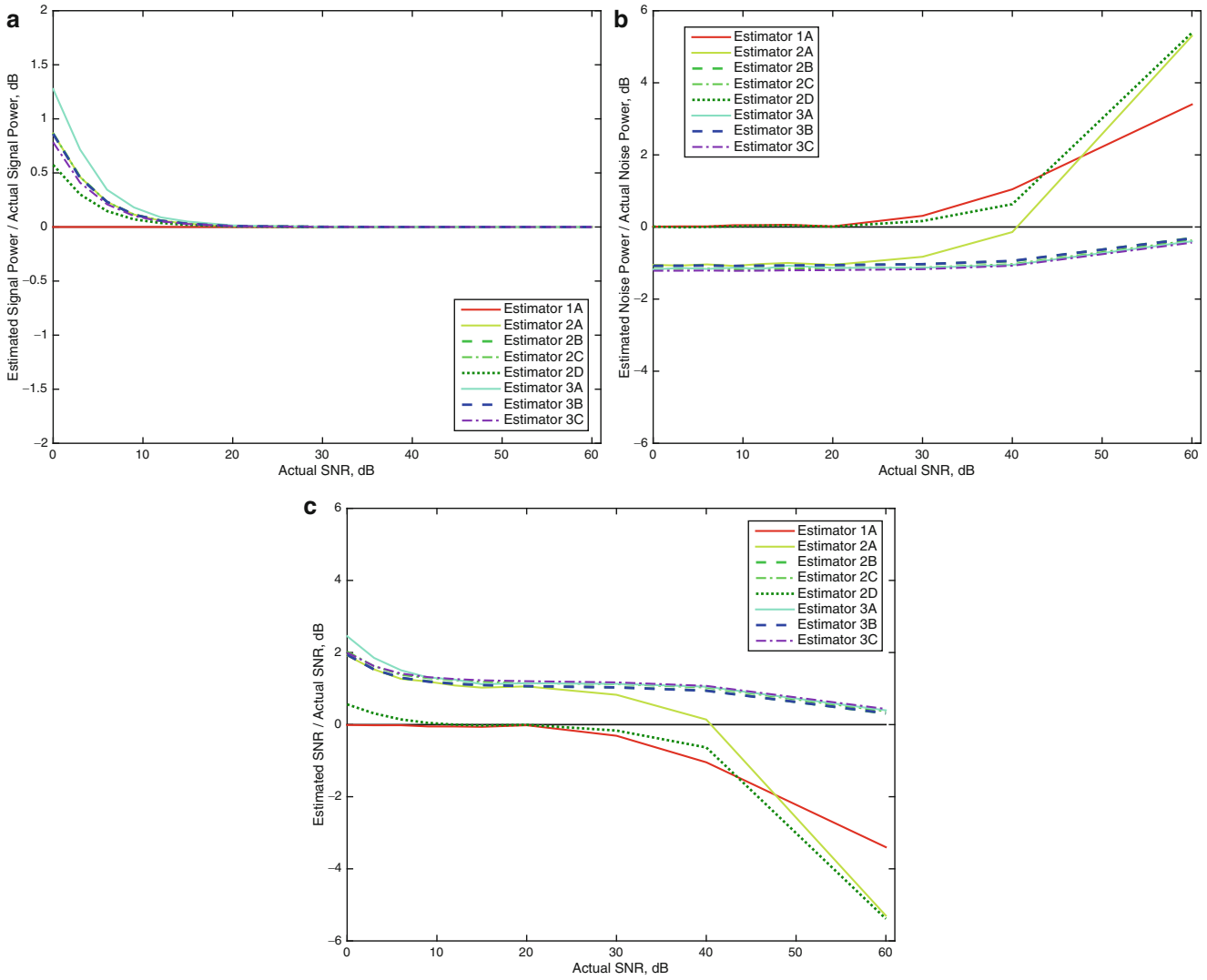

Fig. 9.2 Relative errors in (**a**) the signal power, (**b**) the noise power, and (**c**) the SNR estimations for a sinusoidal input

where ω_i is the natural frequency of mode i, ζ_i is the damping ratio, and A_i is the residue. Here five modes are used with natural frequencies of 0.1, 1, 3, 10, and 40 Hz. The damping ratios for all of the modes are 0.01. The residues (A_i) are 1 for first, third, and fourth modes and -1 for the second and fifth modes. Keeping the sign of the residue the same for the third and fourth modes produces an anti-resonance between the third and fourth modes. The final signal is then scaled to give a variance of one. Figures 9.5 and 9.6 show the simulation results for this case. The results show similar trends as the sine and random excitation case. Estimators 1A, 2A, and 2D show artificial increases in the noise power for frequencies where the signal power is large. This trend also appears for the sine wave input but is more evident here.

9.5.4 Summary of Simulation Results

For all of the inputs tested and for all of the estimation methods, the error in signal power is small for small noise levels. This follows from the measurement being dominated by the signal at low noise levels (making it more difficult to estimate the noise spectra). Estimators 3B and 3C show the smallest errors, and Estimators 2B and 2C also produce good results. This indicates that the averaging processes involved in these methods can improve the signal and noise estimations. Estimator 2D produces more accurate estimates of the overall noise power at low SNR, but produces noise and signal PSD estimates

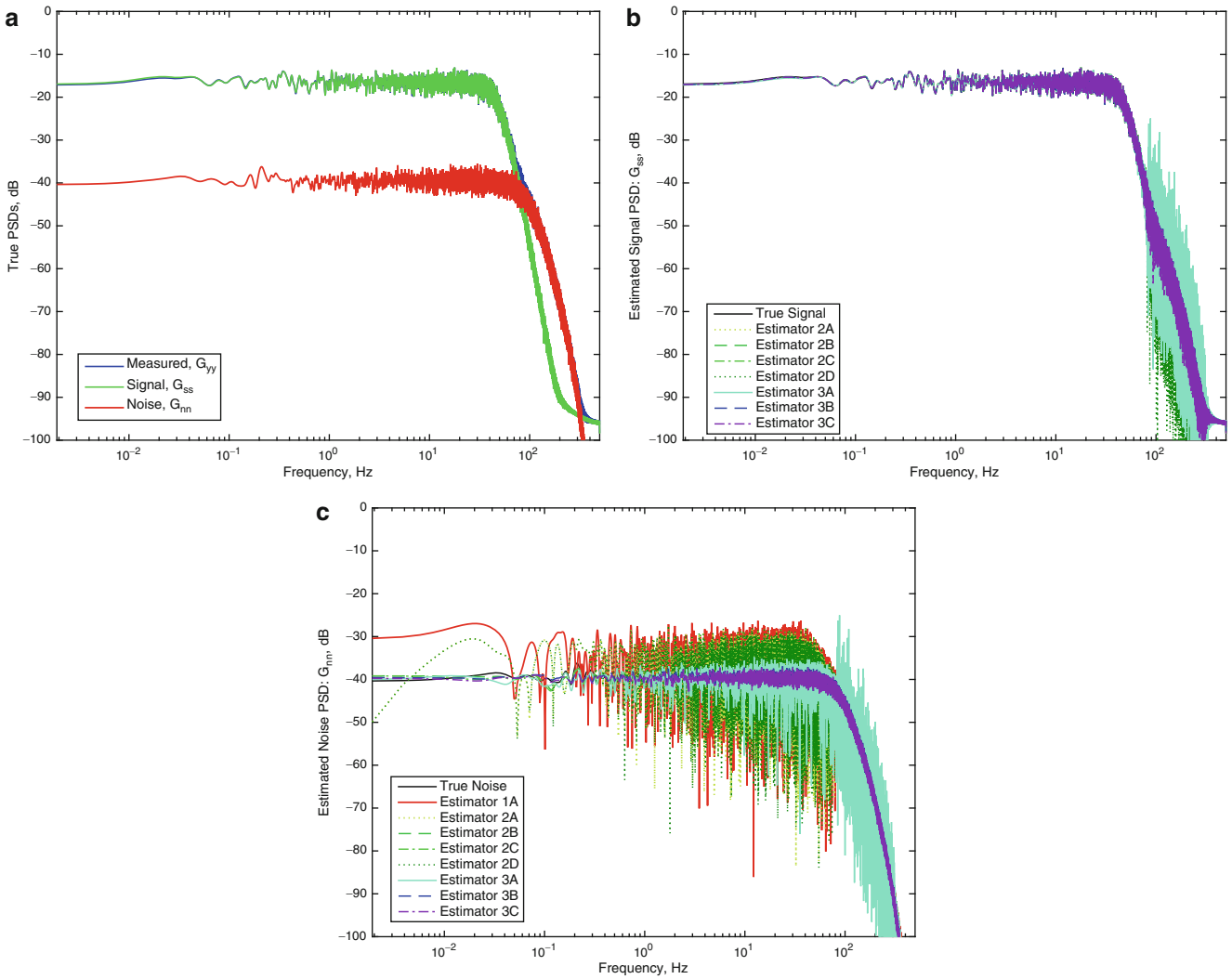

Fig. 9.3 PSDs and estimates for the measurement, signal, and noise with a filtered white noise input. The signal-to-noise ratio (SNR) is 20 dB. (**a**) The true PSDs, (**b**) estimated signal PSDs, and (**c**) estimated noise PSDs

with much larger variations than the other methods. Estimators 1A and 3A also show high variation with frequency in PSD estimations. Estimators 1A, 2A, and 2D produce noise power estimations which are too high for frequencies with high signal power.

9.6 Results from Lab Experiments

Next these noise estimators are applied to data from three collocated accelerometers on a granite table. Figure 9.7 shows the test setup. Four PCB 393B04 high sensitivity accelerometers are connected to small mounting pieces and then attached with wax to a granite table. Data is collected for all four sensors, but only three of the sensors will be used in this analysis. Each sensor is connected to a PCB 480C02 signal conditioner. Data is collected using a National Instruments NI 9215 with a 16 bit analog-to-digital convert (ADC). The voltage data from the accelerometers is scaled by each accelerometer's sensitivity (nominally 1000 mV/g). The channels are sampled at 1000 Hz for 10 min.

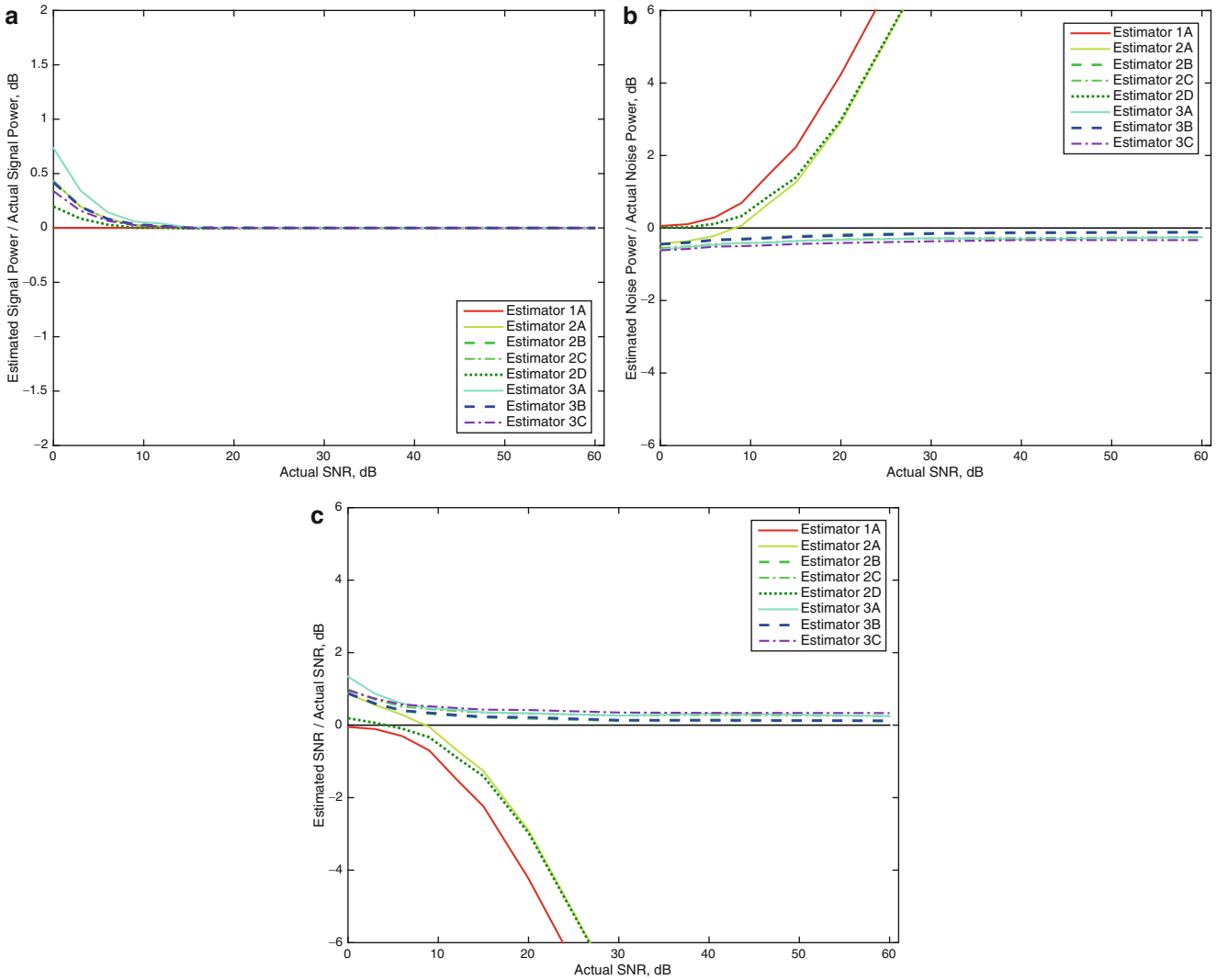

Fig. 9.4 Relative errors in (**a**) the signal power, (**b**) the noise power, and (**c**) the SNR estimations for a filtered white noise input

Figure 9.8a shows the time history of the acceleration signals, and Fig. 9.8b shows the computed power spectral densities. The PSDs show several large peaks. These peaks may be due to dynamics of the granite table or may be characteristic of the building's motion. For comparison, the plots also show the quantization noise expected from the analog-to-digital conversion. This forms a lower bound on the noise estimate. The power spectral density of the quantization noise (PSD_q) can be calculated as

$$PSD_q(\omega) = \frac{S^2 \Delta^2}{24 f_s}, \tag{9.28}$$

where f_s is the sampling rate of the data acquisition system, Δ is the least significant bit (or quantization interval), and S is the sensitivity of the first accelerometer (used to compare the quantization PSD to that of the accelerometers) [17]. The sensitivity of the accelerometer is used to convert the quantization PSD from voltage to units of acceleration for ease of comparison. The quantization PSD for this accelerometer is about 1.7×10^{-11} g^2/Hz (-108 dB). In addition, the power spectral densities are also calculated with the data acquisition channel short-circuited and with the channel short-circuited after a 10 foot length of cable. These short circuit PSDs are shown in Fig. 9.8c. The short circuit noise is clearly above the quantization noise, however much of the PSD of the accelerometer signal is around the short-circuit PSD. Together, this analysis shows that much of the signal is dominated by the short circuit noise from the data acquisition system.

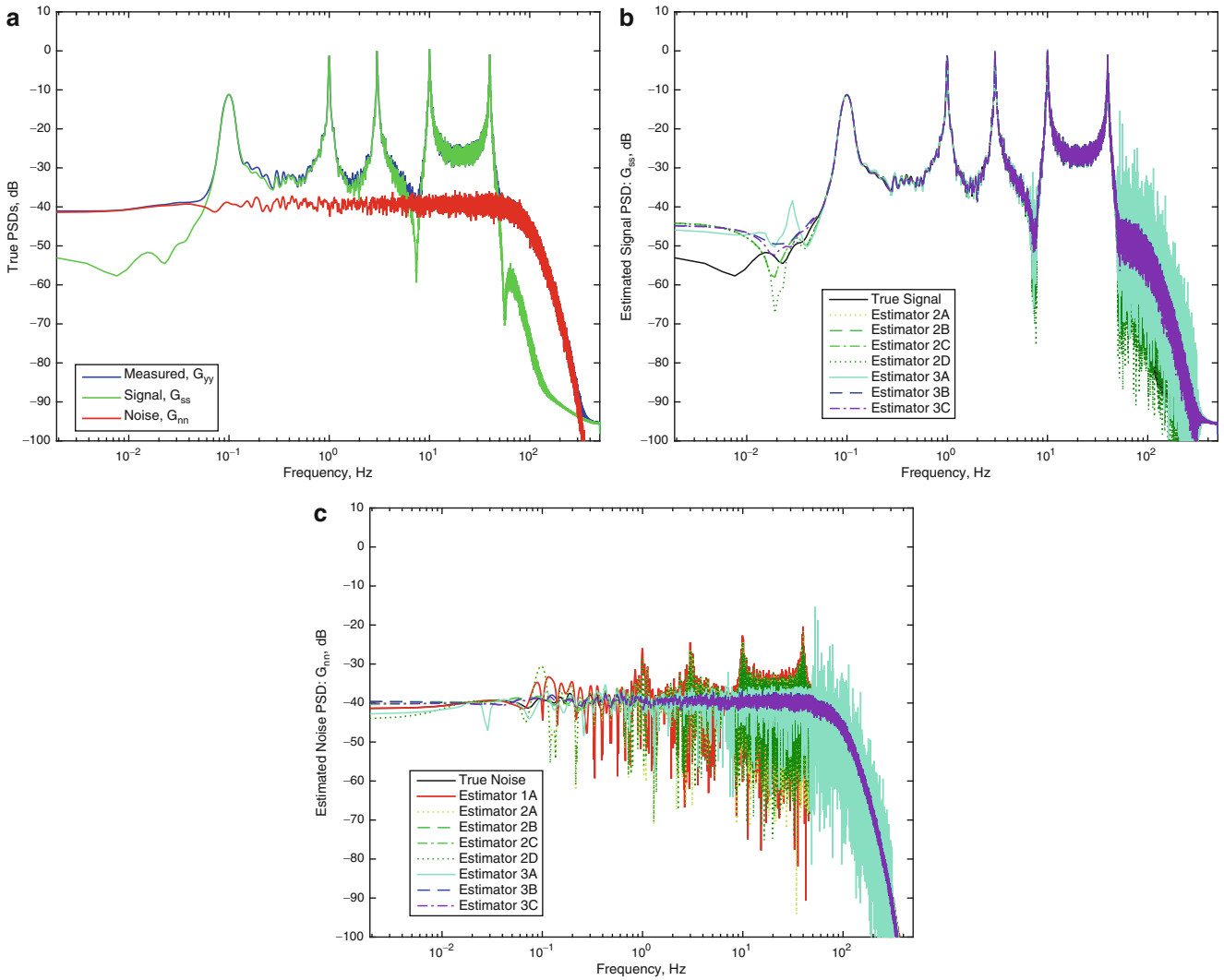

Fig. 9.5 PSDs and estimates for the measurement, signal, and noise with a dynamic input. The signal-to-noise ratio (SNR) is 20 dB. (**a**) The true PSDs, (**b**) estimated signal PSDs, and (**c**) estimated noise PSDs

Figure 9.9 plots the signal and noise PSD estimations. The noise PSDs are comparable to the short circuit PSD. The signal PSDs show features below the short circuit PSD (see between 1 and 5 Hz). Both of these show good promise that these methods are able to extract accurate signal and noise PSDs from real data. Table 9.1 summarizes the signal and noise powers from the different estimators. The powers and signal-to-noise ratios are calculated over a band from 0.1 Hz (the lowest frequency rating of the accelerometers) to the Nyquist frequency (500 Hz). The measurement power can also be calculated from the Estimators as the sum of the signal and noise power (second column in Table 9.1). For comparison, the variance of the first, second, and third accelerometer measurements is 2.36×10^{-7} g^2, 2.58×10^{-7} g^2, and 2.54×10^{-7} g^2, respectively, between 0.1 and 500 Hz. The variance in the short circuit condition was 1.14×10^{-7} g^2. Finally, the average SNR value over all of the estimators is 2.7 dB.

9.7 Conclusions and Future Work

This paper compares several methods for calculating the noise spectra in accelerometers using multiple, collocated sensors. Based on simulation and experimental data, the estimation methods using more accelerometers and using averaging techniques (Estimators 3B and 3C) yield the most accurate results at high to moderate signal-to-noise ratios. Experimental data for three accelerometers on a granite table shows low signal-to-noise ratio (around 2.7 dB).

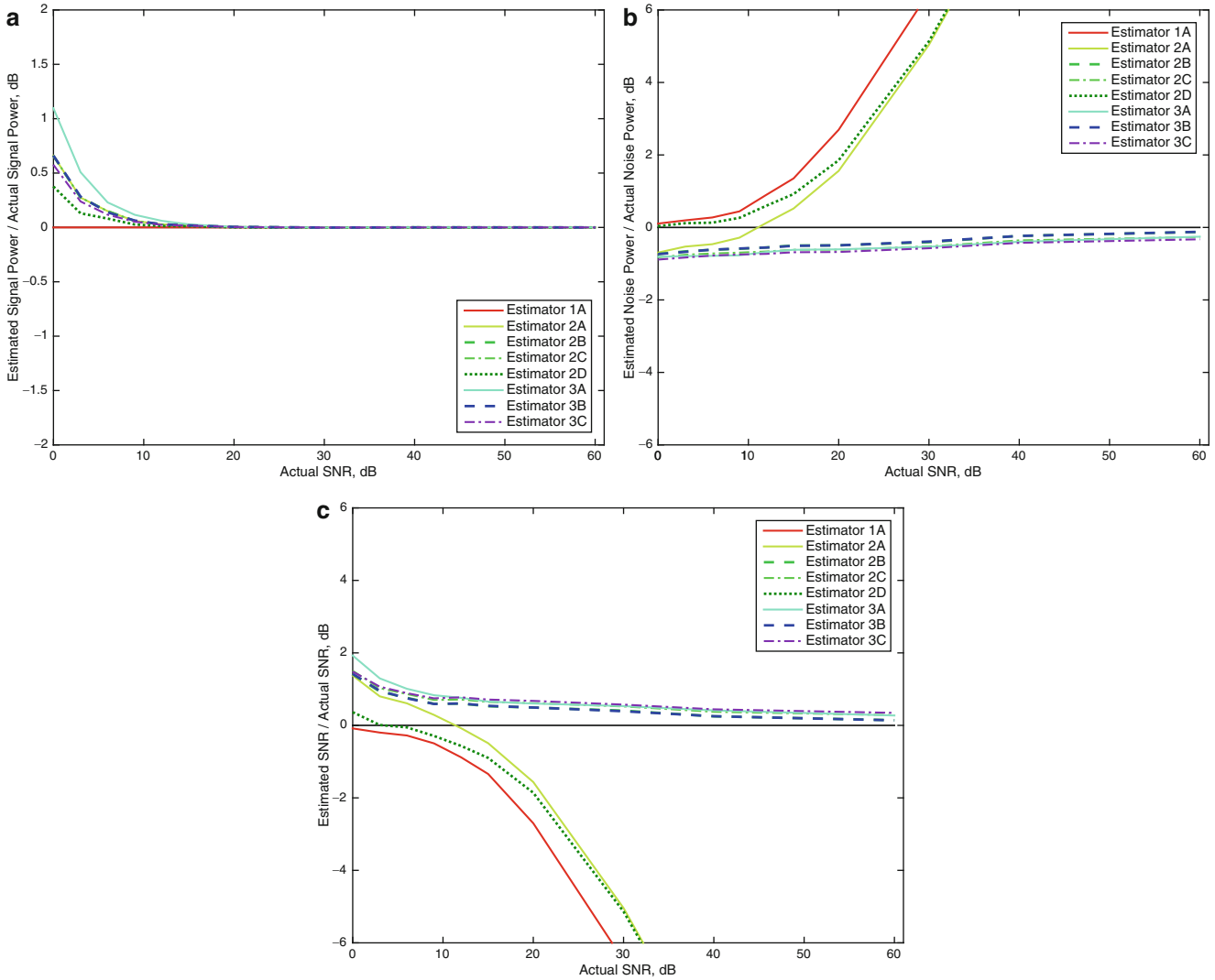

Fig. 9.6 Relative errors in (**a**) the signal power, (**b**) the noise power, and (**c**) the SNR estimations for a dynamic input

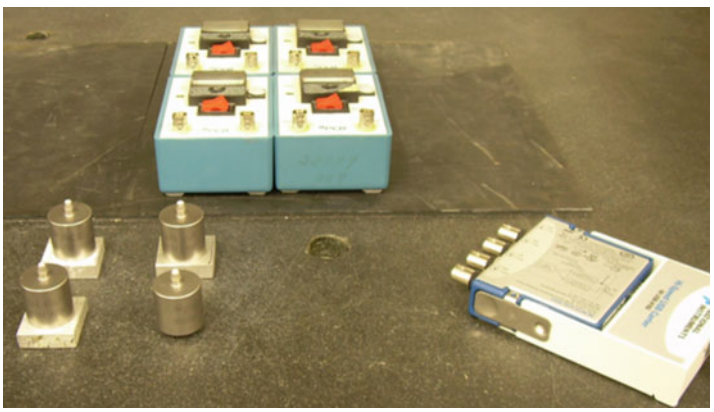

Fig. 9.7 Test setup for noise estimation. Data is recorded for four accelerometers, however data from the forth sensor is not used here

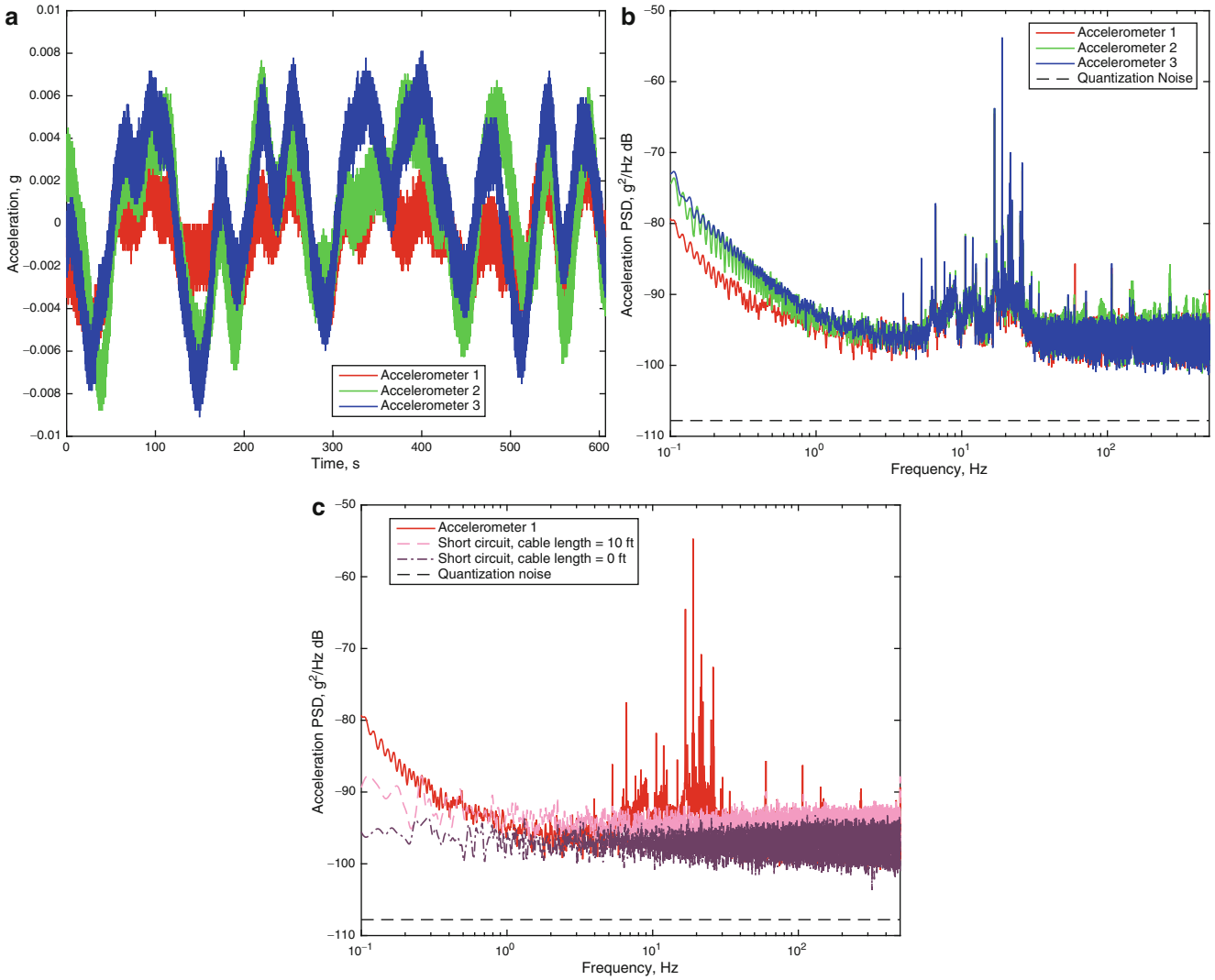

Fig. 9.8 (**a**) Time signals and (**b**) PSDs for the three accelerometers. (**c**) PSD of the first accelerometer compared to PSDs using a short circuit channel and a short circuit channel after a 10 foot cable

Future work will examine methods for improving these results as well as other algorithms for estimating the noise floor of a measurement. Using a different data acquisition system, oversampling, filtering, and altering parameters in the pwelch algorithm may improve these results. These techniques will also be applied to sample locations inside Goodwin Hall. The design of the mounts allows us to install multiple sensors in one location using an additional mounting piece. This data will lead to estimates of the acceleration in different locations, the noise spectra for different sensors with different cable lengths as installed in the building, and estimated signal-to-noise ratios for sensors throughout the instrumented building.

Acknowledgements The authors are thankful for the support and collaborative efforts provided by our sponsors VTI Instruments; PCB Piezotronics, Inc.; Dytran Instruments, Inc.; and Oregano Systems. The authors would also like to recognize the support from the College of Engineering at Virginia Tech, collaboration efforts with Gilbane, Inc., and financial support from the Student Engineering Council at Virginia Tech.

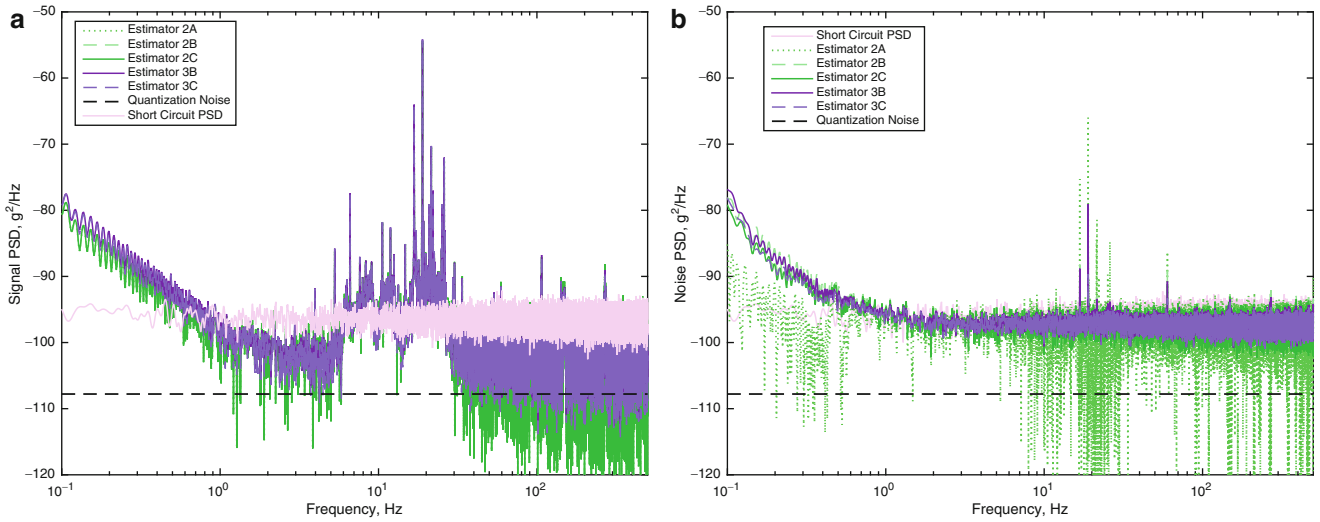

Fig. 9.9 Estimates of the (**a**) signal and (**b**) noise spectra for the first accelerometer signal. Estimators 2D and 3A show large variation and are omitted here for visual clarity

Table 9.1 Signal power, noise power, and signal-to-noise ratio (SNR) estimates for the lab experiment data

Estimator	Measurement power (g^2)	Signal power (g^2)	Noise power (g^2)	SNR (dB)
Estimator 2A	2.36×10^{-7}	1.62×10^{-7}	7.45×10^{-8}	3.4
Estimator 2B	2.58×10^{-7}	1.62×10^{-7}	9.61×10^{-8}	2.3
Estimator 2C	2.54×10^{-7}	1.62×10^{-7}	9.22×10^{-8}	2.4
Estimator 2D	2.37×10^{-7}	1.53×10^{-7}	8.37×10^{-8}	2.6
Estimator 3A	2.36×10^{-7}	1.64×10^{-7}	7.21×10^{-8}	3.6
Estimator 3B	2.58×10^{-7}	1.61×10^{-7}	9.65×10^{-8}	2.2
Estimator 3C	2.49×10^{-7}	1.58×10^{-7}	9.17×10^{-8}	2.4

Values are calculated from data between 0.1 Hz and the Nyquist frequency (500 Hz)

References

1. Brincker, R.: Some elements of operational modal analysis. Shock Vib. **2014**, 11 (2014)
2. Ringler, A.T., Hutt, C.R., Evans, J.R., Sandoval, L.D.: A comparison of seismic instrument noise coherence analysis techniques. Bull. Seismol. Soc. Am. **101**, 558–567 (2011)
3. Piersol, A.G.: Harris' Shock and Vibration Handbook, 6th edn. McGraw-Hill, New York (2010)
4. Poston, J.D., Schloemann, J., Buehrer, R.M., Sriram Malladi, V.V.N., Woolard, A.G., Tarazaga, P.A.: Towards indoor localization of pedestrians via smart building vibration sensing. In: 2015 International Conference on Localization and GNSS (ICL-GNSS), pp. 1–6 (2015)
5. Schloemann, J., Malladi, V.V.N.S., Woolard, A.G., Hamilton, J.M., Buehrer, R.M, Tarazaga, P.A.: Vibration event localization in an instrumented building. In: International Modal Analysis Conference (IMAC) XXXIII, Orlando, 2–5 February (2015)
6. Evans, J.R., Followill, F., Hutt, C.R., Kromer, R.P., Nigbor, R.L., Ringler, A.T., Steim, J.M., Wielandt, E.: Method for calculating self-noise spectra and operating ranges for seismographic inertial sensors and recorders. Seismol. Res. Lett. **81**, 640–646 (2010)
7. Payne, B.F., Serbyn, M.R.: An application of parameter estimation theory in low frequency accelerometer calibrations. Presented at the fourteenth transducer workshop, Colorado Springs, CO (1987)
8. Tasic, I., Runovc, F.: Seismometer self-noise estimation using a single reference instrument. J. Seismol. **16**(2), 183–194 (2012)
9. Rainieri, C., Fabbrocino, G.: Operational Modal Analysis of Civil Engineering Structures: An Introduction and Guide for Applications, 1st edn. Springer-Verlag, New York (2014)
10. Ewins, D.J.: Modal Testing: Theory, Practice, and Application, 2nd edn. Research Studies Press Ltd., Hertfordshire, England (2000)
11. Wirsching, P.H., Paez, T., Ortiz, K.: Random Vibrations: Theory and Practice. Wiley, New York (1995)
12. Welch, P.D.: The use of fast Fourier transform for the estimation of power spectra: a method based on time averaging over short, modified periodograms. IEEE Trans. Audio Electroacoust **15**(2), 70–73 (1967)
13. Steinhardt, A., Makhoul, J.: On the autocorrelation of finite-length sequences. IEEE Trans. Acoust. Speech Signal Process **33**(6), 1516–1520 (1985)
14. Holcomb, L.G.: A Direct Method for Calculating Instrument Noise Levels in Side-by-Side Seismometer Evaluations, pp. 89–214. U.S. Geological Survey, Albuquerque, New Mexico (1989)

15. Holcomb, L.G: A Numerical Study of Some Potential Sources of Error in Side-by-Side Seismometer Evaluations, pp. 90–406. U.S. Geological Survey, Albuquerque, New Mexico (1990)
16. Brincker, R., Larsen, J.A.: Obtaining and estimating low noise floors in vibration sensors. Presented at the 2007 IMAC-XXV: conference & exposition on structural dynamics (2007)
17. Sleeman, R., van Wettum, A., Trampert, J.: Three-channel correlation analysis: a new technique to measure instrumental noise of digitizers and seismic sensors. Bull. Seismol. Soc. Am. **96**(1), 258–271 (2006)

Chapter 10
Uncertainties in an Application of Operational Modal Analysis

Lorenzo Banfi and Luigi Carassale

Abstract Operational modal analysis is widely used to estimate the mechanical properties of vibrating systems. The several available mathematical techniques, based upon different mathematical formulations, have the common feature that the unmeasured excitation is modeled as a random process specified by some probabilistic model. In practical applications, the length of the measurement is necessarily limited and the probabilistic model adopted to represent the excitation does not necessarily apply. This, together with measurement errors, leads to uncertainties of different nature that affect the estimation of the modal parameters. We discuss the effect of these uncertainty through the assistance of a wide numerical simulation in which a realistic identification process is reproduced isolating different sources of uncertainty. Besides, the identification activity of the experimentalist (e.g. rejection of clearly unphysical results) is mimed by an automated software. The conclusions derived from the simulations are verified by applying the same procedures to a real case study for which a large measurement database is available.

Keywords Operational modal analysis • Uncertainty quantification • Monte Carlo simulations • Frequency domain decomposition • Stochastic subspace identification

10.1 Introduction

In many civil and mechanical engineering applications, Output-Only Modal Identification or Operational Modal Analysis (OMA) has become a popular activity. This is due to the general incapability of producing a controlled excitation on a mechanical system to overpass, in adequate measure, the environmental noise. Due to this deficiency, the problem must be formulated in stochastic terms and the unknown excitation is generally modeled as a multivariate random process, with Gaussian probability density function (PDF) with constant, but unknown power spectral density (PSD) matrix.

Under these hypotheses, in addition to the general assumptions for the applicability of the classical modal analysis, several mathematical formulations exist in both frequency and time domain for the identification of modal parameters.

Nevertheless, these fundamental hypotheses are rarely completely fulfilled. Besides, the necessary finite measurement time, the presence of noise and the intrinsic incapability of the mathematical models to reproduce the physical reality represent sources of different types of uncertainties, which directly affect the identification process.

The main purpose of this work is to critically investigate the effects of some of the most common experimental conditions on some well-known identification algorithms: Frequency Domain Decomposition (FDD, [1]), the Stochastic Realization Algorithm (SRA, [2]) and Stochastic Subspace Identification (SSI, [3]). Contributions to this topic have been presented in [4–6].

We consider a simple case study in which the mentioned techniques are applied to identify the modal parameters of a still tubular tower. First, a large numerical experimentation has been carried out by recreating, within a Monte Carlo framework, several realistic experimental conditions including limited measurement time, presence of noise and non-white excitation.

Second, a long-term monitoring measurement on the real tower under ambient induced vibrations involving accelerometer sensors and anemometers has been processed with the same algorithms. The uncertainties of modal parameters have been qualitatively discussed as functions of the simulated and real measurement conditions.

L. Banfi • L. Carassale (✉)
Department of Civil, Chemical and Environmental Engineering, University of Genova, Via Montallegro 1, 16145 Genova, Italy
e-mail: lorenzo.banfi@dicca.unige.it; luigi.carassale@unige.it

S. Atamturktur et al. (eds.), *Model Validation and Uncertainty Quantification, Volume 3*, Conference Proceedings of the Society for Experimental Mechanics Series, DOI 10.1007/978-3-319-29754-5_10

10.2 Frequency Domain Identification

FDD is a widely applied algorithm, in particular in the civil engineering community (e.g. [1, 4]). It is based on the local fitting of the measurement PSD matrix in a range around the resonance peaks.

Let $\mathbf{y}(t) \in \mathbb{R}^{Ns}$ be the measurement vector (function of the time t) and $\mathbf{S_{yy}}(\omega)$ its Power Spectral Density (PSD) matrix. Assuming that $\mathbf{y}$ can be idealized as a stationary random process, it can be decomposed through the Proper Orthogonal Decomposition (POD) representing $\mathbf{y}$ as a sum of Ns terms, called Principal Components (PC), that are mutually uncorrelated. According to this principle, the measurement PSD matrix is expanded as:

$$\mathbf{S_{yy}}(\omega) = \sum_{k=1}^{Ns} \boldsymbol{\theta}_k(\omega)\, \boldsymbol{\theta}_k^*(\omega)\, \gamma_k(\omega) \tag{10.1}$$

where γ_k and $\boldsymbol{\theta}_k$ are, respectively, the eigenvalues and eigenvectors of $\mathbf{S_{yy}}$. The POD eigenvalues $\gamma_k(\omega)$ are the PSD on the PCs; the POD eigenvectors $\boldsymbol{\theta}_k(\omega)$ represent the Frequency-Response Function (FRF) of linear transformations mapping the PCs into the measurement space. Since the POD eigenvalues are sorted in decreasing order, the summation in Eq. (10.1) can be reduced considering only the first or the first few terms.

On the other hand, if the (unmeasured) modal forces are mutually uncorrelated, and the measurement noise is uncorrelated from the structural response, then $\mathbf{S_{yy}}(\omega)$ can be represented through the modal expansion:

$$\mathbf{S_{yy}}(\omega) = \omega^{2r} \sum_{j=1}^{N} \boldsymbol{\phi}_j \boldsymbol{\phi}_j^T \left|H_j(\omega)\right|^2 S_{w_j w_j}(\omega) + S_{\boldsymbol{\eta}\boldsymbol{\eta}}(\omega) \tag{10.2}$$

where S_{wjwj} is the PSD of the jth modal forces, $\mathbf{S_{\eta\eta}}$ is the PSD matrix of the measurement noise $\boldsymbol{\eta}(t)$ and $\boldsymbol{\phi}_j \in \mathbb{R}^{Ns}$ is the observed part of the jth vibration mode shape. The index r is related to the type of sensors used (i.e. displacement $r = 0$, velocity $r = 1$, acceleration $r = 2$). $H_j(\omega)$ is the FRF of the jth mode

$$H_j(\omega) = \frac{1}{\omega_j^2 - \omega^2 + 2i\xi_j\omega_j\omega} \tag{10.3}$$

which is parametrized in terms of natural circular frequency ω_j and damping ratio ξ_j.

If the natural frequencies of the structure are well separated, the jth term of the Eq. (10.2) is dominant in a frequency band $I(\omega_j)$ around the jth natural frequency. On the other hand, in the same frequency band, the measurement vector tends to be fully coherent and therefore represented by a singly (the first one) PC mapped by $\boldsymbol{\theta}_1(\omega)$. This consideration justifies the assumption:

$$\begin{aligned} \boldsymbol{\phi}_j &= \boldsymbol{\theta}_1(\omega) \\ \omega^{2r}\left|H_j(\omega)\right|^2 S_{w_j w_j}(\omega) &= \gamma_1(\omega) \end{aligned} \qquad \text{with} \quad \omega \in I(\omega_j) \tag{10.4}$$

If the PSD of the excitation is locally regular, e.g. $S_{wjwj} = S_0\omega^{-\alpha}$ for $\omega \in I(\omega_j)$, then the FRF of the jth mode can be estimated minimizing the error measure:

$$J(\omega_j, \xi_j, S_0, \alpha) = \int_{I(\omega_j)} \gamma_1(\omega) \left|\gamma_1(\omega) - S_0\omega^{2r-\alpha}\left|H(\omega; \omega_j, \xi_j)\right|^2\right|^2 d\omega \tag{10.5}$$

in which the Euclidean distance is weighted by the eigenvalue γ_1. In the following, the identification procedure developed assuming $\alpha = 0$, i.e. consistent with the traditional FDD method, is denoted as FDD3. The implementation including the estimation of α is called FDD4.

10.3 Time Domain Identification

Time domain identification tools are generally based upon the discrete-time stochastic subspace representation:

$$\begin{aligned} \mathbf{x}_{k+1} &= \mathbf{A}\mathbf{x}_k + \mathbf{w}_k \\ \mathbf{y}_k &= \mathbf{C}\mathbf{x}_k + \mathbf{v}_k \end{aligned} \tag{10.6}$$

where $\mathbf{y}_k = \mathbf{y}(t_k)$ is the time-discrete measurement vector, while $\mathbf{w}_k$ and $\mathbf{v}_k$ are two random processes representing the unmeasured excitation and the measurement noise. The vector $\mathbf{x}_k \in \mathbb{R}^{2N}$ is the system state vector. The eigenvalues of the matrix $\mathbf{A}$ are related to the natural frequencies and damping ratios of the continue time state-space model by the relationships:

$$\omega_j = \left|\ln\left(\lambda_j\right)/\Delta t\right|; \xi_j = -\frac{\text{Real}\left(\ln\left(\lambda_j\right)/\Delta t\right)}{\left|\ln\left(\lambda_j\right)/\Delta t\right|} \tag{10.7}$$

where Δt is the sampling time. The observed part of the vibration modes is obtained as:

$$\boldsymbol{\phi}_j = \mathbf{C}\boldsymbol{\psi}_j \tag{10.8}$$

where $\boldsymbol{\psi}_j \in \mathbb{C}^{2N}$ are the eigenvectors of $\mathbf{A}$.

10.3.1 Stochastic Realization Algorithm (SRA)

The Stochastic Realization Algorithm, commonly referred to as Covariance-driven SSI in civil engineering applications, identifies the state matrices by decomposing a Toeplitz matrix:

$$\mathbf{T}_{1|i} = \begin{bmatrix} \boldsymbol{\Lambda}_i & \boldsymbol{\Lambda}_{i-1} & \dots & \boldsymbol{\Lambda}_1 \\ \boldsymbol{\Lambda}_{i+1} & \boldsymbol{\Lambda}_i & \dots & \boldsymbol{\Lambda}_2 \\ \dots & \dots & \ddots & \dots \\ \boldsymbol{\Lambda}_{2i-1} & \boldsymbol{\Lambda}_{2i-2} & \dots & \boldsymbol{\Lambda}_i \end{bmatrix} \in \mathbb{R}^{iN_s \times iN_s}, \qquad \boldsymbol{\Lambda}_i = \mathrm{E}\left[\mathbf{y}_{k+i}\,\mathbf{y}_k^T\right] \simeq \frac{1}{N_t - i}\sum_{k=1}^{N_t - i}\mathbf{y}_{k+i}\,\mathbf{y}_k^T \tag{10.9}$$

where $\boldsymbol{\Lambda}_i$ is the output covariance matrix and i is a user-defined quantity representing a time shift. The state matrix $\mathbf{A}$ can be estimated as:

$$\mathbf{A} = \mathbf{O}_i^{\dagger}\mathbf{T}_{2|i+1}\mathbf{C}_i^{\dagger} = \mathbf{S}_1^{-1/2}\mathbf{U}_1^T\mathbf{T}_{2|i+1}\mathbf{V}_1\mathbf{S}_1^{-1/2} \tag{10.10}$$

where $(\cdot)^{\dagger}$ represents the Moore-Penrose pseudo-inverse, $\mathbf{T}_{2|i+1}$ is a translated version of $\mathbf{T}_{1|i}$ obtained removing the first line and adding at the bottom the line $\left[\,\boldsymbol{\Lambda}_{2i}\;\boldsymbol{\Lambda}_{2i-1}\;\dots\;\boldsymbol{\Lambda}_{i+1}\,\right]$, $\mathbf{O}_i$ and $\mathbf{C}_i$ are the observability and controllability matrices of the system given by:

$$\begin{aligned} \mathbf{O}_i &= \mathbf{U}_1\mathbf{S}_1^{1/2} \\ \mathbf{C}_i &= \mathbf{S}_1^{1/2}\mathbf{V}_1^T \end{aligned} \tag{10.11}$$

where $\mathbf{S}_1 \in \mathbb{R}^{n\times n}$, with $n \leq N$, is the diagonal matrix containing the non-zero singular values of $\mathbf{T}_{1|i}$, while $\mathbf{U}_1$ and $\mathbf{V}_1 \in \mathbb{R}^{iNs\times n}$ contain the corresponding left and right singular vectors, respectively. The output matrix $\mathbf{C}$ is obtained from the first Ns rows of $\mathbf{O}_i$ ([2, 7]).

10.3.2 Stochastic Subspace Identification (SSI)

The SSI identification algorithm identifies the system matrices by solving in a least-square sense the system:

$$\begin{bmatrix} \widehat{\mathbf{X}}_{i+1} \\ \mathbf{Y}_{i|i} \end{bmatrix} = \begin{bmatrix} \mathbf{A} \\ \mathbf{C} \end{bmatrix} \widehat{\mathbf{X}}_i + \begin{bmatrix} \rho_w \\ \rho_v \end{bmatrix} \tag{10.12}$$

where ρ_w and ρ_v are residuals, while $\widehat{\mathbf{X}}_i = \left[\widehat{\mathbf{x}}_i \; \widehat{\mathbf{x}}_{i+1} \cdots \widehat{\mathbf{x}}_{i+j-1} \right] \in \mathbb{R}^{n \times j}$ is a matrix collecting the Kalman-filter estimates of state vector. These matrices may be estimated by the manipulation of the Hankel matrix obtained directly from the measured data and defined as:

$$\mathbf{Y}_{h|k} = \begin{bmatrix} \mathbf{y}_h & \cdots & \mathbf{y}_{h+j-1} \\ \vdots & & \vdots \\ \mathbf{y}_k & \cdots & \mathbf{y}_{k+j-1} \end{bmatrix} \in \mathbb{R}^{(k-h+1) \times j} \tag{10.13}$$

where j is a user-defined quantity such that $j \leq N_t - 2i + 1$, i as a user-defined quantity representing a time shift and N_t is the number of time steps available in the measurements.

The key step of the method is the projection of the future output $\mathbf{Y}_f$ subspace onto the past output subspace $\mathbf{Y}_p$ [3], from which the Kalman-filter estimates at different time steps can be identified.

10.4 A Simple Case Study

The uncertainties in the estimation of the modal parameters from a real experiment depends on a large number of factors. These include insufficient sampling (measurement have a finite length), presence of measurement noise, and modeling errors (the structure is not perfectly linear and visco-elastic, the load is not stationary, non-Gaussian nor white).

A comparative analysis of the different identification techniques and a qualitative discussion of their reliability may be carried out focusing the attention on a simple case study, drawing some general considerations.

To this purpose, the identification tools described in the previous section have been used for the modal identification of a 40 m-high tubular lighting pole (Fig. 10.1a). The structure is located in the Savona dock area in Italy, in a zone far from buildings or major obstacles. The shaft is composed by four steel telescoping tapered sections, its cross-section is a 16-sided polygon with diameter ranging from by 840 mm (at the base) and 160 mm (at the top), the width of the shaft wall ranges from 6 to 4 mm. A service ladder with safety cage is fixed at one side of the shaft.

For simulation purpose, the same structure has been modeled as a cantilever beam by the Finite Element (FE) method, using 16 Euler-Bernoulli beam elements. The order of the dynamical model is reduced by considering only the first four vibration modes representing the deflection in a specified plane. A perfect symmetry condition is assumed. Modal parameters assumed for the FEM model are reported in Table 10.1, while mode shapes are shown in Fig. 10.1b.

10.5 Monte Carlo Simulation

The availability of the numerical model gives the opportunity of simulating the identification process as it may be carried out in different realistic conditions. The external actions are generated as realizations of a stationary random process [8] applied to all the 16 FE nodes. The dynamical system is integrated in the time domain removing the transient effects due to initial conditions and $N_s = 4$ acceleration measurements are extracted for the levels ($z = 10{,}20{,}30{,}40\,m$).

To reproduce the presence of measurement noise, a random white noise $\mathbf{v}(t)$ with Gaussian distribution and with no spatial correlation has been added to the response $\mathbf{y}(t)$. The spectrum of $\mathbf{v}(t)$ is constant over the whole observed frequency range, and its amplitude is evaluated as a fraction of the measurement standard deviation.

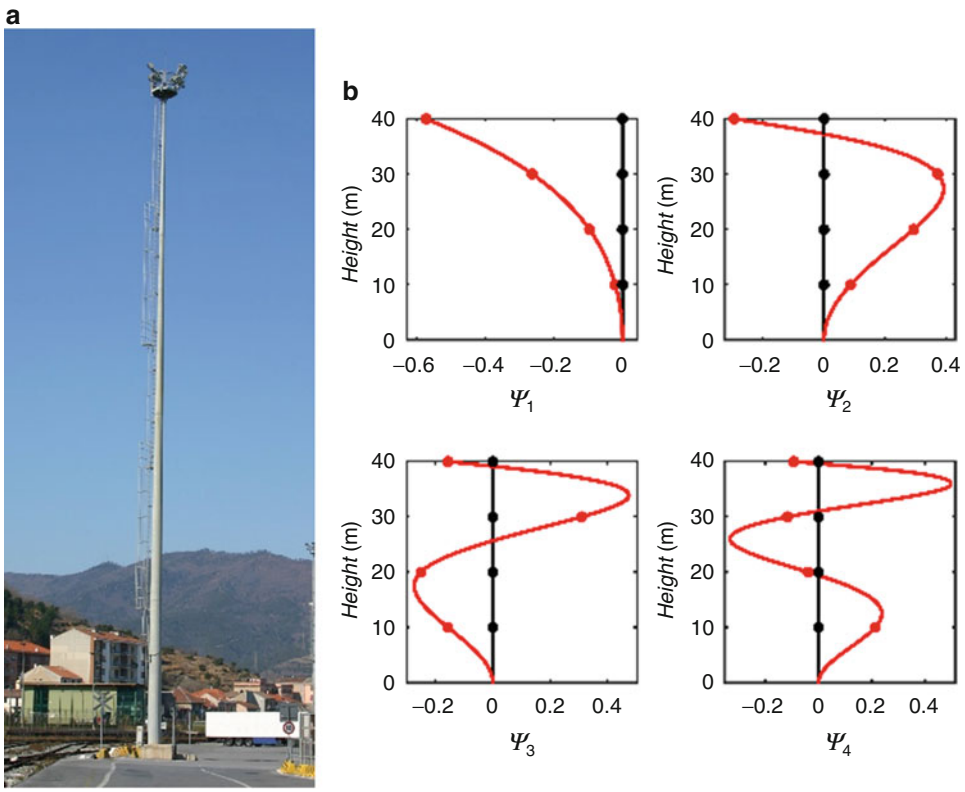

Fig. 10.1 Case study (**a**); modal shapes FE model (**b**)

Table 10.1 Modal parameters of the FE model

Mode	Frequency (Hz)	White noise excitation Damping ratio (%)	Wind excitation
1	0.35	0.42	3.00
2	1.32	0.27	3.00
3	3.35	1.05	3.00
4	6.69	2.78	3.00

10.6 Discussion of the Simulation Results

Figure 10.2 shows the mean estimation error of natural frequency and damping ratio of mode 2 as a function of the measurement time in terms of number of observed cycles (*number of cycles* $= N_t \times \Delta t \times f_j$, f_j being the natural frequency of the jth mode and $\Delta t = 0.02s$), for white noise and wind excitation with no measurement noise. The statistical analysis has been carried out on the base of 1000 simulations for each value of N_t. The dashed lines represent the mean error, while the error bars provide the standard deviation. It appears that time domain techniques have a faster convergence to the exact modal parameters and that their prediction is less spread. As a general tendency, frequency domain techniques produce predictions of damping ratio converging to the exact value from above. Moreover, it is appreciable that natural frequency estimations have errors lower than 0.2 % even for 100 cycles; on the other hand, damping ratio estimation errors are significantly higher, e.g. >10 % even for 1000 cycles.

In the case of wind excitation, time domain techniques still have a faster convergence with respect to frequency domain ones. In particular, FDD3 provides results affected by a systematic error that is independent from the measurement time, particularly evident for the natural frequency estimation.

Figures 10.3 and 10.4 shows, respectively, the PDF of the estimated natural frequency and damping ratio for mode 1 for the structure excited by the wind action. The intensity of the measurement noise is 0 (a), 2.5 % (b), 5 % (c) and 10 % (d). Dots represent the empirical PDFs while solid lines are normal PDFs having the same mean and variance of the actual data. The exact modal parameter is displayed as a dashed black line.

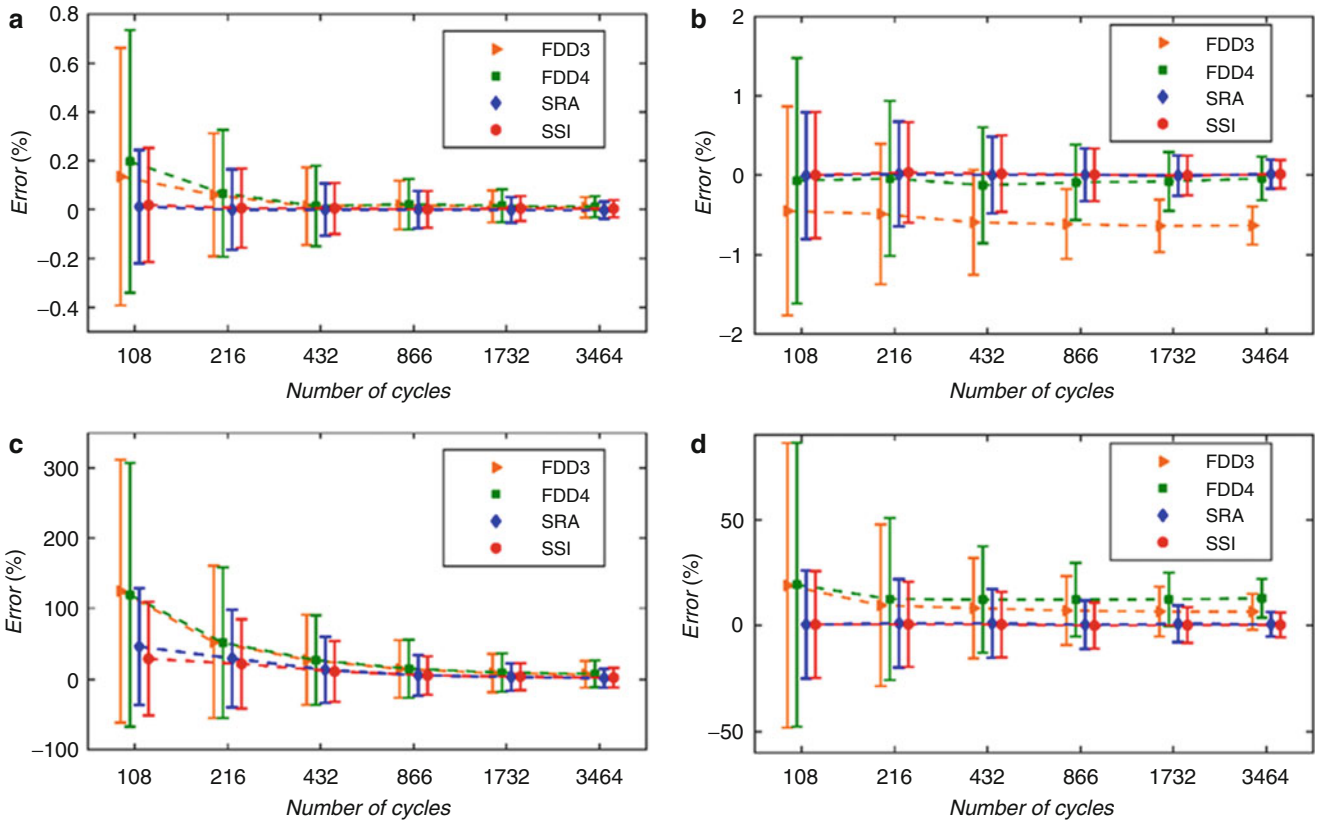

Fig. 10.2 Estimation error for mode 2. Natural frequency for white noise excitation (**a**) and wind excitation (**b**); damping ratio for white noise excitation (**c**) and wind excitation (**d**)

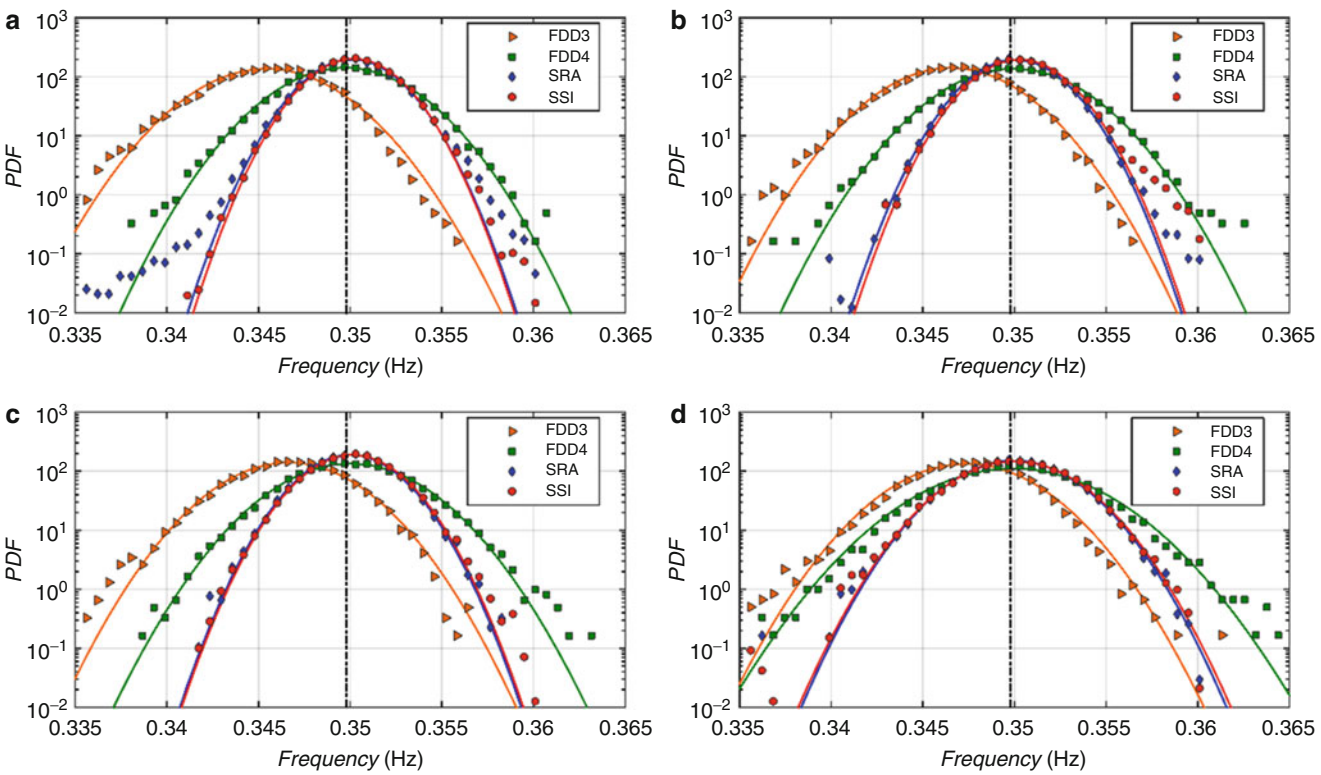

Fig. 10.3 PDF of identified natural frequency of mode 1 for wind excitation; noise level 0 (**a**), 2.5 % (**b**), 5 % (**c**), 10 % (**d**)

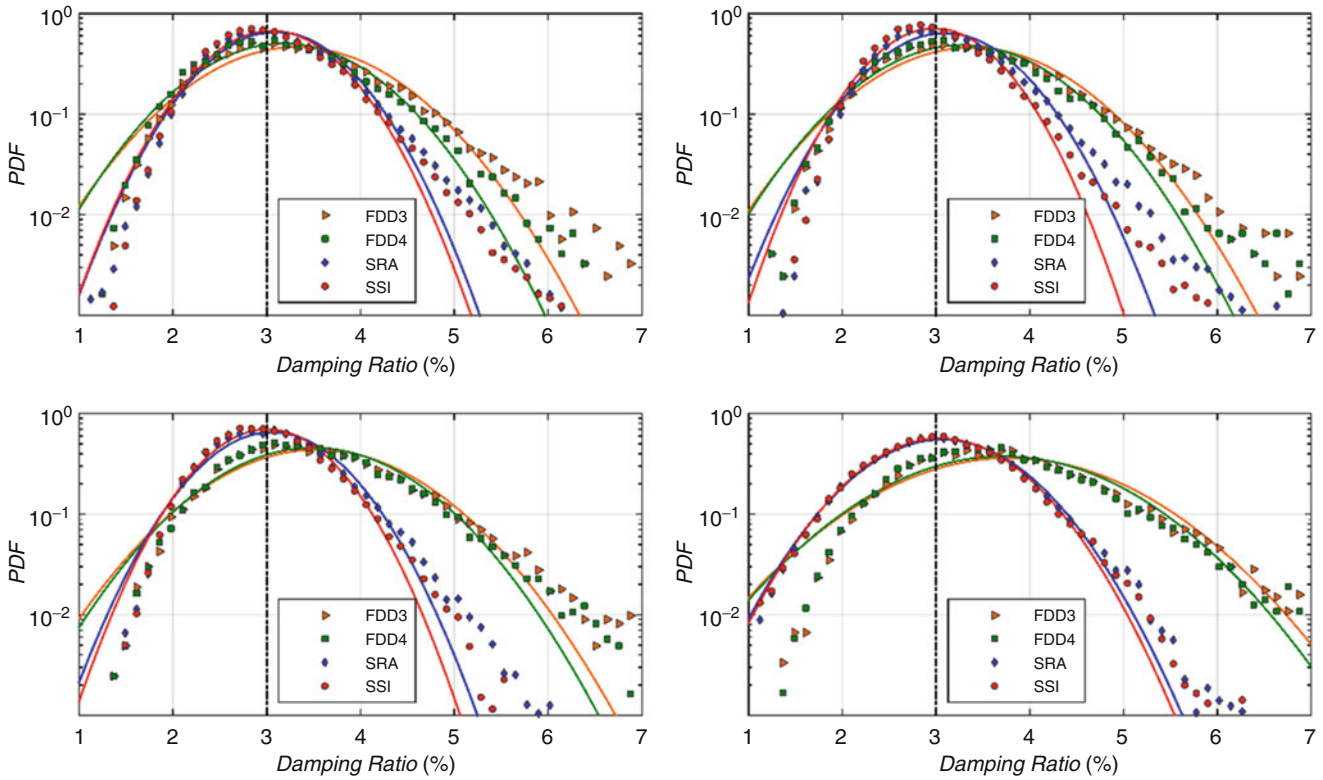

Fig. 10.4 PDF of identified damping ratio of mode 1 for wind excitation; noise level 0 (**a**), 2.5 % (**b**), 5 % (**c**), 10 % (**d**)

The analysis of the PDFs confirms a superior accuracy of time domain techniques. The presence of measurement noise has an influence on the dispersion of the results, in terms of standard deviation, for intensity greater than 5 %. The PDFs of the damping ratio are significantly asymmetric with positive skewness.

Figure 10.3a highlights the bias error in FDD3. This error gradually disappears as the noise level gets higher, i.e. as the PSD of the response becomes more flat. This phenomenon can be explained by an insufficient number of model parameters used for representing the physical behavior showed by the measured response. In the case of wind excitation, the harmonic content in the low frequency range has a preponderant importance. As a direct consequence, the first POD eigenvalue is not symmetric, as well as it is not flat for high frequency.

On the other hand, stochastic errors may rise in the time domain techniques for the opposite reason, i.e. when model order adopted is too large.

10.7 Uncertainties in a Real Experiment

In order to verify in a real case the considerations drawn from the Monte Carlo simulation, the four identification algorithms have been applied to the long term monitoring data collected on the real structure described in the previous sections.

The pole has been equipped with two couples of force-balance accelerometers, located at the top and at 2/3 height and an ultrasonic anemometer installed on a 2 m-high support fixed at the top of the pole. Data acquired from the sensors are digitalized at 100 Hz, transferred to a computer through a wireless LAN connection and recorded continuously.

Due to the topography of the zone, the pole is subjected to two main wind conditions: a typical summer condition with the sea-wind coming from south-east and a typical winter condition with wind arriving from north-west channeled into a valley. The maximum value of the 10-min-averaged wind velocity during the observation period was about 18 m/s from both the mentioned directions.

Figure 10.5 shows the first three POD eigenvalues and the stabilization diagram obtained from the analysis of a single 600 s long record with a mean wind velocity $U = 6$ m/s. Differently from the FE model, in the frequency ranges between 0.32 and 0.33 Hz, as well as between 1.22 and 1.28 Hz, two pairs of closely-spaced modes are clearly detectable. The slight

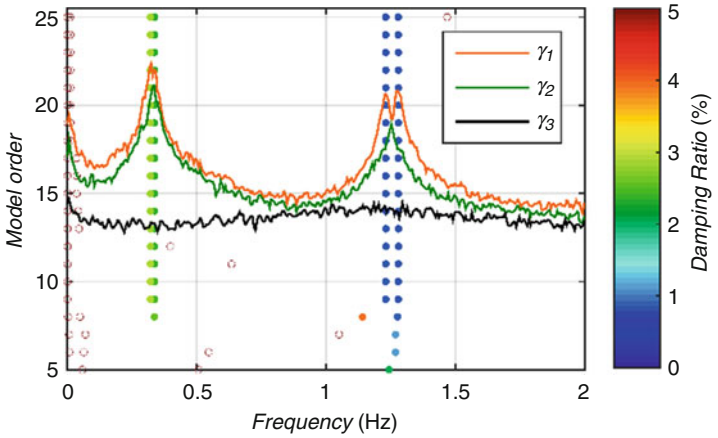

Fig. 10.5 PSD matrix eigenvalues and stabilization diagram for a sample real measurement

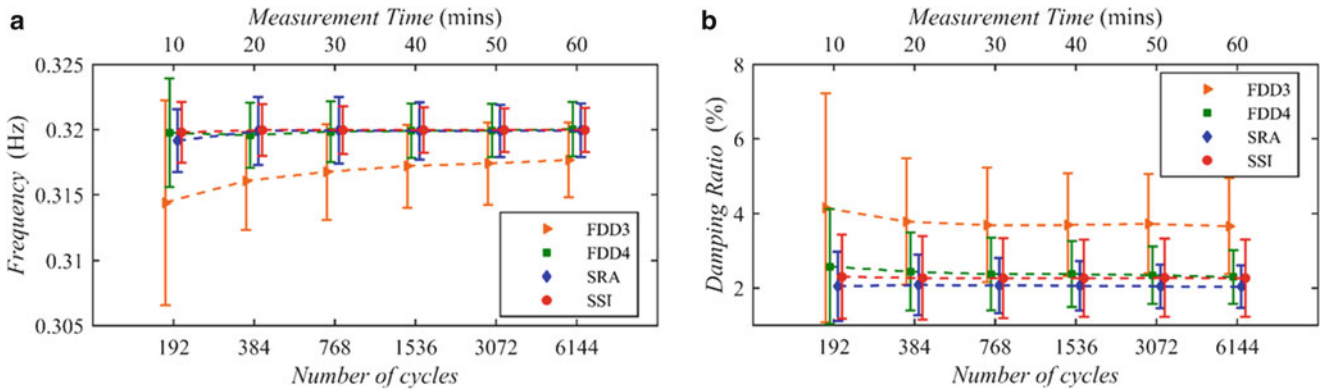

Fig. 10.6 Natural frequency (**a**) and damping ratio (**b**) of mode 1 estimated with different measurement length

difference between the modes in each pair is due to the presence of the maintenance ladder that slightly brakes the polar symmetry of the pole. All the techniques are able to distinguish between the two modes in each pair. For FDD3 and FDD4 this require including in the fitting also the second POD eigenvalue γ_2.

Figure 10.6 shows the natural frequency and damping ratio of mode 1 estimated for different measurement length. The markers represent the mean value of the estimators, the error bars identify the standard deviation. FDD3 confirms the bias affecting the estimation of natural frequency that has been discussed above. In this case, also the estimation of the damping ratio seems to be biased with respect to the other algorithms. The superior quality of FDD4 with respect to FDD3 appears evident even in this real application, as it often provides a general estimation uncertainty comparable to those of SRA and SSI.

10.8 Conclusions

A simple case study has been developed to investigate the uncertainties of the modal parameters identified by some well-known techniques. The large survey included a large numerical investigation and the analysis of a real structure monitored under ambient induced vibrations.

From the presented results some general considerations can be drawn:

- In ideal conditions, the estimation error strictly depends on the statistical information present in the measurements. In particular, it has been highlighted qualitatively that an acceptable evaluation of damping ratio in terms of mean error and standard deviation requires significantly long records.
- If the excitation is colored some systematic errors may appear due the inability of the identification algorithm to cope with the additional information in the records. FDD3 is particularly sensitive to his problem.

- The presence of measurement noise affects the quality of the identification procedures by increasing the dispersion of the results only above a certain threshold.
- Model errors depend on the number of parameters used for fitting the system response. In some cases, these errors appear mitigated by the addition of some quantity of measurement noise or by the violation of the white-noise-excitation hypothesis.

References

1. Brincker, L., Zhang, L., Andersem, P.: Modal identification from ambient responses using frequency domain decomposition. In: Proceedings of the 18th International Modal Analysis Conference, pp. 625–630 (2000)
2. Peeters, B., De Roeck, G.: Reference-based stochastic subspace identification for output-only modal analysis. Int. J. Mech. Syst. Signal Process. **13**, 855–878 (1999)
3. Overschee, P.V.: Subspace Identification for the Linear Systems: Theory Implementation. Kluwer Academic Publishers, Boston (1996)
4. Bajric, A., Georgakis, C.T., Brincker, R.: Evaluation of damping using frequency domain operational modal analysis techniques. In: Proceedings of the XXXIII IMAC Conference, Orlando, FL (2015)
5. Reynders, E.: System identification methods for (operational) modal analysis: review and comparison. Arch. Comput. Meth. Eng. **19**, 51–124 (2012)
6. Reynders, E., Pintelon, R., De Roeck, G.: Uncertainty bounds on modal parameters obtained from stochastic subspace identification. Mech. Syst. Signal Process. **22**, 948–969 (2008)
7. Banfi, L.: Modal identification in frequency and time domains: assessment of uncertainties. Master Thesis (2013)
8. Carassale, L., Solari, G.: Monte Carlo simulation ofwind velocity fields on complex structures. J. Wind Eng. Ind. Aerodyn. **94**, 323–339 (2006)
9. Carassale, L., Percivale, F.: POD-based modal identification of wind-excited structures. In: Proceedings of the 12th International Conference of Wind Engineering, Cairns, 1–6 July 2007

Chapter 11
Stochastic Finite Element Model Updating by Bootstrapping

Vahid Yaghoubi, Majid K. Vakilzadeh, Anders T. Johansson, and Thomas Abrahamsson

Abstract This paper presents a new stochastic finite element model calibration framework for estimation of the uncertainty in model parameters, which combines the principles of bootstrapping with the technique of FE model calibration with damping equalization. The bootstrapping allows to quantify the uncertainty bounds on the model parameters by constructing a number of resamples, with replacement, of the experimental data and solving the FE model calibration problem on the resampled datasets. To a great extent, the success of the calibration problem depends on the starting value for the parameters. The formulation of FE model calibration with damping equalization gives a smooth metric with a large radius of convergence to the global minimum and its solution can be viewed as the initial estimate for the model parameters. In this study, practical suggestions are made to improve the performance of this algorithm in dealing with noisy measurements. The performance of the proposed stochastic calibration algorithm is illustrated using simulated data for a six degree-of-freedom mass-spring model.

Keywords Stochastic FE model calibration • Frequency response • Experiment design • 0.632 Bootstrap • Uncertainty quantification

11.1 Introduction

Due to the high cost of doing experiments, finite element analysis (FEA) is used extensively in order to predict the dynamic behavior of engineering structures. Therefore, a credible FE model is important in complex structural design, dynamics response computation and safety assessment [1]. However, a nominal FE model is often not fully valid for the purpose of model prediction and simulation. Therefore, model calibration and validation is adopted to reduce the differences between model prediction and test data. The calibration of the FE model using noisy frequency response function (FRF) and estimation of uncertainty bounds on the model parameters and prediction is the subject of this paper.

Over the past two decades a number of techniques for deterministic FE model calibration have been proposed, either based on modal analysis or based on frequency response function (FRF). Direct use of FRFs data for FE model calibration has several advantages over using modal data. First of all no modal analysis is required in the calibration procedure. Thus the error induced in modal extraction can be avoided. Besides that, the information can be collected in wide frequency range and the calibration problem become overdetermined due to the availability of FRF data at numerous excitation and observation points [2]. Imregun and Ewins [3, 4] introduced the basic theory of model calibration using frequency response data. Balmès [5] minimized the least-squares or log-least-squares deviation in the frequency response functions. Nevertheless, the FRFs are very sensitive to the damping of structures at resonance peaks that can be considered as an advantage of using FRF since the damping must be included in an accurate finite element model [1] and also as a major challenge associated with using FRFs since damping is one of the least well-understood properties in vibration theory [2, 6].

Model calibration of damped system is the focus of some researchers, e.g., [7, 8]. Arora et al. [9] extended the Response Function method and updated the FE model's stiffness, mass, and non-proportional structural damping matrices. García-Palencia and Santini-Bell [2] presented a two-step algorithm to identify stiffness, mass, and viscous damping matrices by minimizing the difference between the experimental and analytical FRFs. Due to the challenges associated to damping treatment, in most of the work on model calibration of damped systems, the damping model is simplified by assuming constant or Rayleigh damping. The main drawback of these models lies in the fact that they do not reflect the variation of modal damping ratios with natural frequencies. A better choice for modeling the damping is modal damping. In this case,

V. Yaghoubi (✉) • M.K. Vakilzadeh • A.T. Johansson • T. Abrahamsson
Department of Applied Mechanics, Chalmers University of Technology, 412 96 Göteborg, Sweden
e-mail: khorsand@chalmers.se

S. Atamturktur et al. (eds.), *Model Validation and Uncertainty Quantification, Volume 3*, Conference Proceedings of the Society for Experimental Mechanics Series, DOI 10.1007/978-3-319-29754-5_11

the modal damping found as an outcome of experimental modal analysis (EMA) of a modal test of the structure under investigation is mapped into FE model without further attempts to understand their physical background; the difficulty of this mapping relies on mode shape pairing. Abrahamsson and Kammer [10] proposed a method called damping equalization to overcome the problem of mode pairing that can be applied to large scale problems. The damping equalization is achieved by imposing the same modal damping on all experimentally found system modes in an intermediate step.

Regardless of the deviation metrics, the above mentioned methods achieve fairly good results in point estimation of the parameters. Since the test data are often corrupted by measurement noise, this estimation can be affected and are often subjected to bias and variance. Therefore, finding uncertainty bound for the estimated parameters attracts more attention in both modal analysis-based methods [11] and FRF-based methods [12]. Bootstrapping is a general tool for assessing the statistical accuracy. By the use of bootstrapping methods, the statistical description of the parameters can be obtained. Besides that, it can be used to assess the quality of the calibrated model in predicting the intended response of the model. It is called prediction error and is the main topic of cross-validation. In cross-validation, a FE model is calibrated with some part of data, called a calibration set or a training set, and the rest of data, called a validation set is used to assess the quality of the prediction model. K-fold, leave-one-out and Monte-Carlo cross-validations are other examples of the cross-validation methods that are used extensively in the literature [13, 14].

The organization of the text is as follows. In Sect. 11.2, the required mathematical background is presented together with the problem that is addressed in this paper. The proposed framework for stochastic FE model calibration including the design of experiment, the point estimation of the parameters and the bootstrapping to estimate the statistics for the parameters and prediction error of the model are studied in detail in Sect. 11.3. In Sect. 11.4, the method is used to calibrate a six degree-of-freedom mass-spring model using simulated data.

11.2 Preliminaries

11.2.1 Mathematical Background

Using the FE method the governing partial differential equations of motion are transformed into the set of ordinary differential equations of motion as

$$\boldsymbol{M}\ddot{\boldsymbol{q}}(t) + \boldsymbol{V}\dot{\boldsymbol{q}}(t) + \boldsymbol{K}\boldsymbol{q}(t) = \boldsymbol{f}(t) \tag{11.1}$$

where $\boldsymbol{q}(t) \in \mathbb{R}^n$ is the displacement vector, $\boldsymbol{f}(t)$ is the external load vector which is governed by a Boolean transformation of stimuli vector $\boldsymbol{f}(t) = \boldsymbol{P}_{\mathrm{u}}\boldsymbol{u}(t)$; with $\boldsymbol{u}(t) \in \mathbb{R}^{n_{\mathrm{u}}}$. Real positive-definite symmetric matrices $\boldsymbol{M}, \boldsymbol{V}, \boldsymbol{K} \in \mathbb{R}^{n\times n}$ are mass, damping and stiffness matrices, respectively. The FE model can be parameterized, with physical property parameters collected in vector $\boldsymbol{p} \in \mathbb{R}^{n_{\mathrm{p}}}$, such that mass and stiffness matrices are depending on these, i.e., $\boldsymbol{M}(\boldsymbol{p})$ and $\boldsymbol{K}(\boldsymbol{p})$. The state-space realization of the equation of motion in (11.1) can be written as

$$\dot{\boldsymbol{x}}(t) = \boldsymbol{A}\boldsymbol{x}(t) + \boldsymbol{B}\boldsymbol{u}(t), \qquad \boldsymbol{y}(t) = \boldsymbol{C}\boldsymbol{x}(t) + \boldsymbol{D}\boldsymbol{u}(t) \tag{11.2}$$

where $\boldsymbol{A} \in \mathbb{R}^{2n\times 2n}$, $\boldsymbol{B} \in \mathbb{R}^{2n\times n_{\mathrm{u}}}$, $\boldsymbol{C} \in \mathbb{R}^{n_{\mathrm{y}}\times 2n}$, and $\boldsymbol{D} \in \mathbb{R}^{n_{\mathrm{y}}\times n_{\mathrm{u}}}$. The state vector is $\boldsymbol{x}^{\mathrm{T}}(t) = \left[\boldsymbol{q}(t)^{\mathrm{T}}\ \dot{\boldsymbol{q}}(t)^{\mathrm{T}}\right] \in \mathbb{R}^{2n}$ and $\boldsymbol{y}(t) \in \mathbb{R}^{n_{\mathrm{y}}}$ is the system output. Coefficient matrices $\boldsymbol{A}$ and $\boldsymbol{B}$ are related to mass, damping and stiffness as follows

$$\boldsymbol{A} = \begin{bmatrix} 0 & \boldsymbol{I} \\ -\boldsymbol{M}^{-1}\boldsymbol{V} & -\boldsymbol{M}^{-1}\boldsymbol{K} \end{bmatrix}, \quad \boldsymbol{B} = \begin{bmatrix} 0 \\ \boldsymbol{M}^{-1}\boldsymbol{P}_{\boldsymbol{u}} \end{bmatrix} \tag{11.3}$$

The frequency response of model (11.2) can be written as

$$\boldsymbol{G}(\mathrm{j}\omega) = \boldsymbol{C}(\mathrm{j}\omega\boldsymbol{I} - \boldsymbol{A})^{-1}\boldsymbol{B} + \boldsymbol{D} \tag{11.4}$$

However, the model (11.2) can be converted into a model in the discrete-time domain as

$$\boldsymbol{x}(k+1) = \boldsymbol{A}^{\mathrm{d}}\boldsymbol{x}(k) + \boldsymbol{B}^{\mathrm{d}}\boldsymbol{u}(k), \quad \boldsymbol{y}(k) = \boldsymbol{C}^{\mathrm{d}}\boldsymbol{x}(k) + \boldsymbol{D}^{\mathrm{d}}\boldsymbol{u}(k) \tag{11.5}$$

where its transfer function can be calculated as

$$\boldsymbol{G}^{\mathrm{d}}\left(e^{\mathrm{j}\omega^{\mathrm{d}}}\right)=\boldsymbol{C}^{\mathrm{d}}\left(e^{\mathrm{j}\omega^{\mathrm{d}}}\boldsymbol{I}-\boldsymbol{A}^{\mathrm{d}}\right)^{-1}\boldsymbol{B}^{\mathrm{d}}+\boldsymbol{D}^{\mathrm{d}} \tag{11.6}$$

Here, ω^{d} denotes frequency in the discrete-time domain. One option to convert a continuous-time model to its counterpart in the discrete-time domain is to employ a bilinear transformation. The bilinear transformation maps the values on the $\mathrm{j}\omega$ axis, to values on the unit circle, $e^{\mathrm{j}\omega^{\mathrm{d}}}$ using

$$\mathrm{j}\omega=\frac{2\left(e^{\mathrm{j}\omega^{\mathrm{d}}}-1\right)}{T\left(e^{\mathrm{j}\omega^{\mathrm{d}}}+1\right)} \tag{11.7}$$

where T is a free parameter under the circumstance that $2/T$ is not a pole of the continuous-time system. A significant characteristic of the bilinear transformation is that the frequency response remains invariant if the frequency scale is prewarped. This means that the continuous-time transfer function evaluated at $j\omega$ is equal to the bilinear transformed discrete-time transfer function evaluated at $e^{\mathrm{j}\omega^{\mathrm{d}}}$,

$$\boldsymbol{G}\left(\mathrm{j}\omega\right)=\boldsymbol{G}^{\mathrm{d}}\left(e^{\mathrm{j}\omega^{\mathrm{d}}}\right) \tag{11.8}$$

if $\tan\left(\omega^{\mathrm{d}}/2\right)=\omega T/2$.

11.2.2 Problem Statement

Given noise-corrupted samples of the continuous-time transfer function, $\boldsymbol{G}_i^{\mathrm{X}}\in\mathbb{C}^{n_{\mathrm{y}}\times n_u}$, at n_{f} frequency lines ω_i,

$$\boldsymbol{G}_i^{\mathrm{X}}=\boldsymbol{G}_i^{\mathrm{A}}\left(\boldsymbol{p}\right)+\boldsymbol{N}_i^{\mathrm{G}},\quad i=1,\ \ldots,n_{\mathrm{f}} \tag{11.9}$$

The FE model calibration attempts to estimate the parameter setting $\boldsymbol{p}$ such that minimizes the deviation between $\boldsymbol{G}^{\mathrm{X}}$ and $\boldsymbol{G}^{\mathrm{A}}$. Here, $\boldsymbol{G}^{\mathrm{A}}$ denotes the transfer function established by the analytical FE model and $[\boldsymbol{N}_i^{\mathrm{G}}]_{\mathrm{r,s}}$, for $\mathrm{r}=1,\ldots,n_{\mathrm{y}}$ and $\mathrm{s}=1,\ldots,n_{\mathrm{u}}$ are modeled as independent, zero mean, circular complex distributed random variables with known variances. However, our interest is not to just try to find the point estimate of the parameters but to develop a FE model calibration framework which (a) provides the statistical description of the uncertain parameters, (b) is robust with respect to noisy measurements and (c) eliminates the need for mode matching algorithms, and (d) is well-suited to problems with many inputs and outputs. In this paper we propose a stochastic FE model updating algorithm that fulfills all of these conditions.

11.3 Method

The proposed FE model calibration algorithm consists of three main steps, which will be discussed in detail in the next sections.

11.3.1 Test Data Model

To circumvent the problem of mode matching in FE model updating using frequency-domain data, Abrahamsson and Kammer [15] proposed the technique of damping equalization. In this approach, a mathematical model, TD model, is found for the experimental data using a system identification method. Then, the same level of modal damping as found in the test is imposed to all modes of the TD model. They employed the frequency-domain subspace identification method presented in [16] to identify a state-space model from experimental data. The reason for this choice is that it is a noniterative algorithm which offers numerically reliable state-space models for complex dynamical systems even when the number

of input and outputs is large. However, when the experimental data is noisy the aforementioned algorithm may lose its consistency properties, see [10] for a detailed discussion. Here, we take up the same idea to find the TD model from test data. In the next section, we propose a solution to improve the consistency of this identification algorithm by designing a dedicated frequency sampling strategy.

11.3.1.1 Frequency-Domain Subspace Identification

Given noise-corrupted samples of continuous-time transfer function $\boldsymbol{G}_i^{\mathrm{X}}$ at frequencies $\omega_i,\ i = 1, \ldots,\ n_{\mathrm{f}}$, obtained from vibration testing, the aim of frequency-domain subspace system identification is to estimate a TD model of form (11.2), such that its transfer function satisfies,

$$\lim_{n_{\mathrm{f}} \to \infty} \left\| \boldsymbol{G}^{\mathrm{X}} - \boldsymbol{G}^{\mathrm{TD}} \right\|_{\infty} = 0 \tag{11.10}$$

with probability one. The subspace algorithm is better conditioned in the discrete-time domain [16]. Therefore, the continuous-time domain identification problem can be solved in discrete-time domain using the bilinear transformation in (11.7) without introducing any approximation errors due to invariance property of $\|.\|_{\infty}$ under the bilinear transformation [16].

Let us use (11.6) to reformulate the identification problem in the discrete-time domain. Given samples of continuous-time transfer function one can obtain samples of the associated bilinear transformed transfer function in the discrete-time domain as

$$\boldsymbol{G}_i^{\mathrm{X_d}} = \boldsymbol{G}_i^{\mathrm{X}}, i = 1, \ldots,\ n_{\mathrm{f}} \tag{11.11}$$

$$\omega_i^{\mathrm{d}} = 2\tan^{-1}\left(\frac{\omega_i T}{2}\right),\ i = 1, \ldots, n_{\mathrm{f}} \tag{11.12}$$

The aim of the identification algorithm is to map data, $\boldsymbol{G}_i^{\mathrm{X_d}}$, to a transfer function of form (11.6) such that $\lim_{n_{\mathrm{f}} \to \infty} \left\| \boldsymbol{G}^{\mathrm{X_d}} - \boldsymbol{G}^{\mathrm{d}} \right\|_{\infty} = 0$. The frequency mapping in (11.12) warps the frequency scale in a nonlinear fashion and, hence, often results in nonequidistantly spaced frequency samples in the discrete-time domain. This suggests to employ the second algorithm in [16] which is applicable to data with arbitrary frequency spacing. The technical details of this algorithm are beyond the scope of the present paper, we refer an interested reader to [16]. They investigated the consistency of the aforementioned algorithm and showed that for the noise with the same covariance matrix, $E\left[\boldsymbol{N}_i^{\mathrm{G}} \boldsymbol{N}_i^{\mathrm{G^H}}\right] = \beta I$, at each frequency, the sufficient condition to guarantee the consistency is to sample data equidistantly in frequency covering the full unite circle, i.e., $\omega_k^{\mathrm{d}} = 2\pi k / n_{\mathrm{f}},\ k = 0, \ldots, n_{\mathrm{f}} - 1$, called the DFT grid from now on. The DFT grid in the discrete-time domain maps to a specific set of frequencies, $\mathbb{F}$, between $(-\infty, \infty)$ in the continuous-time domain. If the experimental frequency response is measured at this set of frequency lines the aforementioned identification algorithm would be strongly consistent. Nevertheless, in the experimental modal analysis we neither are able to cover the entire frequency range $(-\infty, \infty)$, nor need we select the sampled frequencies that match the frequency lines in the set $\mathbb{F}$. In this scenario the identification algorithm becomes inconsistent. This problem has been addressed by McKelvey et al. [16] where they designed a weighting matrix which is a function of the powers of $e^{\mathrm{j}\omega_i^{\mathrm{d}}}$. However, in many scenarios, especially when the number of samples in the frequency-domain is high or the estimation is based on a narrow frequency interval, the weighting matrix becomes ill-conditioned. To circumvent this problem, we propose a dedicated frequency sampling strategy where the frequency components, $\omega_i,\ i = 1, \ldots, n_{\mathrm{f}}$, for the continuous-time model are selected such that they are mapped into an equidistant frequency grid for the discrete-time model. Moreover, by selecting a proper T in the frequency mapping (11.12), it is even possible to use the maximum feasible range between $[0,\ 2\pi]$ for the discrete-time model. The following algorithm explains the proposed frequency sampling technique:

1. Given the frequency range of interest in the continuous-time domain $[\omega_1, \omega_{n_{\mathrm{f}}}]$, and the desired number of frequency lines, n_{f}.
2. Determine T in (11.12) such that

$$T_o = \underset{T}{\mathrm{argmax}} \left| \tan^{-1}\left(\frac{\omega_1 T}{2}\right) - \tan^{-1}\left(\frac{\omega_{n_{\mathrm{f}}} T}{2}\right) \right| \tag{11.13}$$

3. Calculate the corresponding lower and upper bound of the frequency range for the discrete-time model using T_o;

$$\omega_{\mathrm{l}}^{\mathrm{d}} = 2\tan^{-1}\left(\frac{\omega_{\mathrm{l}} T_o}{2}\right), \quad \omega_{n_f}^{\mathrm{d}} = 2\tan^{-1}\left(\frac{\omega_{n_{\mathrm{f}}} T_o}{2}\right), \tag{11.14}$$

4. Design an equidistant frequencies at the DFT grid covering the full unit circle $\Omega_k = 2\pi k/n_{\mathrm{DFT}}, k = 0, \ldots, n_{\mathrm{DFT}}$ where

$$n_{\mathrm{DFT}} = \left[\frac{2\pi n_{\mathrm{f}}}{\omega_{n_{\mathrm{f}}}^{\mathrm{d}} - \omega_{\mathrm{l}}^{\mathrm{d}}}\right] \tag{11.15}$$

Here, $[x]$ rounds x towards the nearest integer number.

5. Select the set of n_{f} first frequencies, $\Omega_l,\ \Omega_{l+1}, \ldots,\ \Omega_{l+n_{\mathrm{f}}}$, larger than $\omega_{\mathrm{l}}^{\mathrm{d}}$.

6. Map $\Omega_l,\ \Omega_{l+1}, \ldots,\ \Omega_{l+n_{\mathrm{f}}}$ back to the continuous-time domain using

$$\omega_i = \frac{2}{T_o}\tan\left(\frac{\Omega_{l+i}}{2}\right), i = 1, \ldots, n_{\mathrm{f}} \tag{11.16}$$

Therefore, this study suggests to use this algorithm in the experiment design stage in order to take the samples of the continuous-time transfer functions $\boldsymbol{G}_i^{\mathrm{X}}$ at frequencies ω_i. To summarize, given noisy samples of continuous-time transfer function at the designed frequency lines in (11.16), using the frequency-domain subspace algorithm in [16] one can estimate a state-space model in the discrete-time domain. Using the bilinear transformation this model can be transformed to the continuous-time domain as [16]

$$\begin{aligned} \tilde{A} &= \tfrac{2}{T_{\mathrm{o}}}\left(\boldsymbol{I} + \boldsymbol{A}^{\mathrm{d}}\right)^{-1}\left(\boldsymbol{A}^{\mathrm{d}} - \boldsymbol{I}\right), \quad \tilde{\boldsymbol{B}} = \tfrac{2}{\sqrt{T_{\mathrm{o}}}}\left(\boldsymbol{I} + \boldsymbol{A}^{\mathrm{d}}\right)^{-1}\boldsymbol{B}^{\mathrm{d}} \\ \tilde{\boldsymbol{C}} &= \tfrac{2}{\sqrt{T_{\mathrm{o}}}}\boldsymbol{C}^{\mathrm{d}}\left(\boldsymbol{I} + \boldsymbol{A}^{\mathrm{d}}\right)^{-1}, \quad \tilde{\boldsymbol{D}} = \boldsymbol{D}^{\mathrm{d}} - \boldsymbol{C}^{\mathrm{d}}\left(\boldsymbol{I} + \boldsymbol{A}^{\mathrm{d}}\right)^{-1}\boldsymbol{B}^{\mathrm{d}} \end{aligned} \tag{11.17}$$

The quadruple $\boldsymbol{\Sigma}^{\mathrm{TD}} = \left(\tilde{\boldsymbol{A}}, \tilde{\boldsymbol{B}}, \tilde{\boldsymbol{C}}, \tilde{\boldsymbol{D}}\right)$ is then the TD model with the transfer function $\boldsymbol{G}^{\mathrm{TD}}(\mathrm{j}\omega) = \tilde{\boldsymbol{C}}\left(\mathrm{j}\omega\boldsymbol{I} - \tilde{\boldsymbol{A}}\right)^{-1}\tilde{\boldsymbol{B}} + \tilde{\boldsymbol{D}}$. At this point, we are able to replace the experimental data by the TD model and do the model calibration of the FE model towards the frequency response of this model. In the next section this is used to find an initial estimate of the uncertain parameters.

11.3.1.2 Deterministic Calibration Towards TD Model

In this section, a deterministic FE model calibration is made by minimizing the weighted norm of the difference between the logarithm of frequency response of the analytical model $\boldsymbol{G}^{\mathrm{A}}$ and TD model $\boldsymbol{G}^{\mathrm{TD}}$ at selected frequencies. This calibration is made to find an initial estimate of the parameters.

11.3.1.3 FRF-Based Objective Function

The FE model parameter estimation problem can be cast as

$$\boldsymbol{p}^* = \arg\ \min_{\boldsymbol{p}} \sum_{i=1}^{n_{\mathrm{f}}} L^{\mathrm{c}}\left(\boldsymbol{G}_i^{\mathrm{TD}}, \boldsymbol{G}_i^{\mathrm{A}}(\boldsymbol{p})\right) = \arg\ \min_{\boldsymbol{p}} \left(\sum_{i=1}^{nf} \boldsymbol{\varepsilon}_i^{\mathrm{H}} \boldsymbol{W}_{\boldsymbol{\varepsilon}_i} \boldsymbol{\varepsilon}_i\right) \tag{11.18}$$

in which $\boldsymbol{\varepsilon}_i$ is the deviation vector defined by

$$\boldsymbol{\varepsilon}_i = \log_{10}\mathrm{vect}\left(\boldsymbol{G}_i^{\mathrm{A}}(\boldsymbol{p}) \,./ \boldsymbol{G}_i^{\mathrm{TD}}\right) \tag{11.19}$$

here the ./ operator denotes the element-by-element division and vect(.) is the vectorizing operation that makes all frequency response function elements of the $n_{\mathrm{y}} \times n_{\mathrm{u}}$ transfer function at ith frequency into an $n_{\mathrm{y}} n_{\mathrm{u}} \times 1$ column vector. Due to the

presence of noise and errors in the test data, the quality of the TD model varies over the frequency range; therefore, a diagonal weighting matrix, $\boldsymbol{W}_{\varepsilon_i} \epsilon \mathbb{R}^{n_y n_u \times n_y n_u}$, is used to adjust the importance and confidence of minimizing error at one sensor location and one frequency versus another ones. The weighting matrix is given by the signal-to-noise ratio for each frequency defined by

$$[\boldsymbol{W}_{\boldsymbol{\varepsilon}_i}]_{\alpha,\alpha} = \frac{\left[\left|\boldsymbol{G}_i^{\mathrm{TD}}\right|^2\right]_{\mathrm{r,s}}}{\left[\mathrm{var}\left(\boldsymbol{N}_i^{\mathrm{G}}\right)\right]_{\mathrm{r,s}}}, \qquad \mathrm{r} = 1, 2, \ldots, n_{\mathrm{y}},\ \mathrm{s} = 1, 2, \ldots, n_{\mathrm{u}} \tag{11.20}$$

where $\alpha = (\mathrm{r} - 1)\, n_{\mathrm{u}} \times \mathrm{s}$. This objective function can be referred to as a weighted logarithmic least square [17].

Since the most information of the system is present at one half-band-width of damped resonance frequencies, one should use the same number of samples per each mode of the system in (11.20). That is to take steps such that the logarithm of the frequency steps over the frequency range is constant, i.e.,

$$\log_{10}(\omega_{i+1}) - \log_{10}(\omega_i) = \log_{10}(\omega_i) - \log_{10}(\omega_{i-1}) \qquad \forall i \tag{11.21}$$

That sampling strategy seems reasonable, provided that relative damping of all modes in the range is equal, which rarely happens for experimentally found eigenmodes. However, the damping can be equalized by a procedure that is the topic of the following subchapter.

11.3.1.4 Damping Equalization Method

In order to have the same modal damping on all modes, the real parts of the poles of the TD model, the quadruple $\boldsymbol{\Sigma}^{\mathrm{TD}} = \left(\tilde{\boldsymbol{A}}, \tilde{\boldsymbol{B}}, \tilde{\boldsymbol{C}}, \tilde{\boldsymbol{D}}\right)$ obtained in (11.17), has to be altered. To this end, the TD model is brought to diagonal form using the mode matrix $\boldsymbol{X}$ pertinent to the eigenvalue problem $\boldsymbol{AX} = \boldsymbol{X\Lambda}$ such that

$$\dot{\boldsymbol{z}} = \overline{\boldsymbol{A}}\boldsymbol{z} + \boldsymbol{X}^{-1}\tilde{\boldsymbol{B}}\boldsymbol{u}, \qquad \boldsymbol{y} = \tilde{\boldsymbol{C}}\boldsymbol{X}\boldsymbol{z} + \tilde{\boldsymbol{D}}\boldsymbol{u} \tag{11.22}$$

with

$$\overline{\boldsymbol{A}} = \boldsymbol{X}^{-1}\tilde{\boldsymbol{A}}\boldsymbol{X} = \mathrm{diag}\,(\boldsymbol{\lambda}_n) \tag{11.23}$$

which $\boldsymbol{\lambda}_n$ are system's poles that for a physical system occur in complex conjugate pair. For a relative damping $\ll 1$, the relative modal damping ζ_n, estimated from these poles are

$$\widehat{\zeta}_n = -\Re(\lambda_n) \,/\, |\Im(\lambda_n)| \tag{11.24}$$

As the next step, these modal dampings are set to a single fixed value ζ_0, i.e.,

$$\zeta_n = \zeta_0 \qquad \forall n \tag{11.25}$$

Hence, the perturbed system is

$$\dot{\boldsymbol{z}} = \tilde{\tilde{\boldsymbol{A}}}\boldsymbol{z} + \boldsymbol{X}^{-1}\tilde{\boldsymbol{B}}\boldsymbol{u}, \quad \boldsymbol{y} = \tilde{\boldsymbol{C}}\boldsymbol{X}\boldsymbol{z} + \tilde{\boldsymbol{D}}\boldsymbol{u} \ \text{ with } \ \tilde{\tilde{\boldsymbol{A}}} = \mathrm{diag}\left(\tilde{\tilde{\boldsymbol{\lambda}}}_n\right) \tag{11.26}$$

and in turn the transfer function of the modified test data (MTD) model is

$$\boldsymbol{G}^{\mathrm{MTD}}(\mathrm{j}\omega) = \tilde{\boldsymbol{C}}\left(\mathrm{j}\omega\boldsymbol{I} - \tilde{\tilde{\boldsymbol{A}}}\right)^{-1}\tilde{\boldsymbol{B}} + \tilde{\boldsymbol{D}}. \tag{11.27}$$

which will replace the frequency response of the TD model, $\boldsymbol{G}^{\mathrm{TD}} = \boldsymbol{G}^{\mathrm{MTD}}$, and the FE model will be calibrated toward it instead.

For the FE model with given mass and stiffness matrices $\boldsymbol{M}$ and $\boldsymbol{K}$ we have the viscous damping matrix $\boldsymbol{V}$ to be [18]

$$\boldsymbol{V} = \boldsymbol{M}\boldsymbol{T}\mathrm{diag}(m_n)^{-1}\mathrm{diag}\left(2\zeta_n m_n \omega_n\right)\mathrm{diag}\left(m_n^{-1}\right)\boldsymbol{T}^{\mathrm{T}}\boldsymbol{M} \tag{11.28}$$

with eigenfrequencies ω_n, modal masses m_n, modal damping $\zeta_n = \zeta_0 \quad \forall n$ and the modal matrix $\boldsymbol{T}$ given by the undamped system's eigenvalue problem

$$\boldsymbol{K}\boldsymbol{T} = \boldsymbol{M}\boldsymbol{T}\mathrm{diag}\left(\omega_n\right), \qquad \mathrm{diag}\left(m_n\right) = \boldsymbol{T}^{\mathrm{T}}\boldsymbol{M}\boldsymbol{T} \tag{11.29}$$

In a calibration procedure we are then able to search for the mass and stiffness related parameters $\boldsymbol{p}$ of the FE model $\{\boldsymbol{K}(\boldsymbol{p}), \boldsymbol{M}(\boldsymbol{p})\}$ that render the transfer function $\boldsymbol{G}^{\mathrm{A}}(\boldsymbol{p})$ given by Eqs. (11.3), (11.4), and (11.28) and that let the criterion function of Eqs. (11.18) and (11.19) to be minimal. Because of using TD model, the frequencies used to evaluate Eq. (11.18) do not have to match the frequencies for which test results are available.

11.3.2 Uncertainty Quantification

The deterministic FE model calibration against the frequency response of the TD model, stated in (11.18) and (11.19), provides a point estimation of the physical parameters, $\boldsymbol{p}^*$. For the point estimator, no statistical spread in the test data is carried over to the estimator. Making predictions based on the point estimator model is not best practice since it does not represent our confidence in the predictions. Thus, our interest is to extract the statistical description of the model parameters from the available information in the experimental data and to quantify the predictive capability of the calibrated model.

Bootstrapping is a statistical tool for assessing different estimator measures of accuracy. In this approach, the basic idea is to repeatedly draw random datasets with replacement from the original dataset. This would be repeated $\mathfrak{B}$ times to generate $\mathfrak{B}$ datasets of the same size as the original dataset. Then the FE model is calibrated against each bootstrap dataset and the behavior of the calibrated models would be examined over the $\mathfrak{B}$ bootstrap datasets.

To this end, suppose that we represent the deviation vector

$$\boldsymbol{\gamma}_i = \mathrm{vect}\left(\boldsymbol{G}_i^{\mathrm{A}}(\boldsymbol{p})\right) - \mathrm{vect}\left(\boldsymbol{G}_i^{\mathrm{X}}\right), \quad i = 1, \ldots, n_{\mathrm{f}} \tag{11.30}$$

In analogy to the calibration metric of $\boldsymbol{\varepsilon}_i$ in (11.17), but here the test data are taken from the raw frequency response and not the frequency response computed from the TD model and $\boldsymbol{G}^{\mathrm{A}}$ is the transfer function of the FE model in which its modal damping coefficients are fixed to the values estimated from the poles of the TD model, see (11.24). We also introduce the metric

$$\boldsymbol{J} = \sum\nolimits_{i=1}^{n_{\mathrm{f}}} L^{\mathrm{bs}}\left(\boldsymbol{G}_i^{\mathrm{X}}, \boldsymbol{G}_i^{\mathrm{A}}(\boldsymbol{p})\right) = \sum\nolimits_{i=1}^{n_{\mathrm{f}}} \boldsymbol{\gamma}_i^{\mathrm{H}} \boldsymbol{W}_{\boldsymbol{\gamma}_i} \boldsymbol{\gamma}_i, \qquad i = 1, \ldots, n_f \tag{11.31}$$

where $\left[\boldsymbol{W}_{\boldsymbol{\gamma}_i}\right]_{\alpha,\alpha} = \left[\mathrm{var}\left(\left[N_i^{\mathrm{G}}\right]_{\mathrm{r,s}}\right)\right]^{-1}$ for $\mathrm{r} = 1, 2, \ldots, n_{\mathrm{y}}$ and $\mathrm{s} = 1, 2, \ldots, n_{\mathrm{u}}$, and $\alpha = (\mathrm{r}-1)\, n_{\mathrm{u}} \times \mathrm{s}$. In this study, we denote the original dataset for bootstrapping by $\mathfrak{D} = (d_1, d_2, \ldots, d_{n_{\mathrm{f}}})$ where $d_1 = \left(\omega_i, \boldsymbol{G}_i^{\mathrm{X}}\right)$. $\mathfrak{B}$ bootstrap datasets, $\mathfrak{D}^b, b = 1, \ldots, \mathfrak{B}$, from the original data set, $\mathfrak{D}$, are produced and then the FE model is calibrated towards the bootstrap datasets based on the deviation metric (11.31). Here, the calibration minimizer starts from the parameter setting found in the previous step. From bootstrap sampling we can estimate any aspect of the distribution of the estimated parameters. For instance, the variance of the estimated parameters can be computed by

$$\widehat{\boldsymbol{Var}}\left[\boldsymbol{p}^{*b}\right] = \frac{1}{\mathfrak{B}-1}\sum\nolimits_{b=1}^{\mathfrak{B}}\left(\boldsymbol{p}^{*b} - \bar{\boldsymbol{p}}^*\right)^2 \tag{11.32}$$

where $\boldsymbol{p}^{*b}$ denotes the estimated parameter setting from the bth bootstrap dataset, $\mathfrak{D}^b$, and $\bar{\boldsymbol{p}}^*$ denotes the estimated expected value of the uncertain parameters which can be represented as

$$\bar{\boldsymbol{p}}^* = \frac{1}{\mathfrak{B}}\sum_{b=1}^{\mathfrak{B}} \boldsymbol{p}^{*b} \tag{11.33}$$

To validate the prediction capability of the calibrated FE model, it is essential to use experimental data that were not considered during calibration. One approach is to calibrate the FE model towards a set of bootstrap samples, and then keep track of how well it predicts the frequency response at the frequency lines not involved in this bootstrap dataset. This means that to quantify prediction error at each frequency line we only keep track of predictions made by the FE models calibrated using bootstrap datasets not containing this frequency line. This approach is called the leave-one-out bootstrap estimator of prediction error [19] and is defined as

$$\widehat{\mathrm{Err}}^{(1)} = \frac{1}{n_\mathrm{f}} \sum_{i=1}^{n_\mathrm{f}} \frac{1}{|N^{-i}|} \sum_{b \in N^{-i}} L^{\mathrm{bs}} \left(\boldsymbol{G}_i^{\mathrm{X}}, \boldsymbol{G}_i^{\mathrm{A}} \left(\boldsymbol{p}^{*b} \right) \right) = \frac{1}{n_\mathrm{f}} \sum_{i=1}^{n_\mathrm{f}} \widehat{E}_i \tag{11.34}$$

Here N^{-i} is the set of indices of the bootstrap datasets that do not involve the ith discrete frequency, and $\left|N^{-i}\right|$ is the number of such samples. It should be noted that $\left|N^{-i}\right|$ can be equal to zero for some of frequency lines. Such frequency lines would be left out from (11.34). The leave-one-out bootstrap estimate of prediction error reflects the overfitting problem, but is a biased estimation of the prediction error due to non-distinct frequency lines in the bootstrap datasets, see [13] for further information. Efron and Tibshirani [19] designed the "0.632 estimator" to alleviate the bias problem as

$$\widehat{\mathrm{Err}}^{(.632)} = .368 \ \overline{err} + .632 \ \widehat{\mathrm{Err}}^{(1)} \tag{11.35}$$

where

$$\overline{err} = \frac{1}{n_\mathrm{f}} \sum_{i=1}^{n_\mathrm{f}} L^{\mathrm{bs}} \left(\boldsymbol{G}_i^{\mathrm{X}}, \boldsymbol{G}_i^{\mathrm{A}} \left(\boldsymbol{p}^{*} \right) \right) \tag{11.36}$$

is the training error, i.e., the deviation of the samples used for calibrations.

11.4 Numerical Examples

In this section the proposed stochastic FE model calibration is applied to a small six degree-of-freedom system. This example is taken from Kozak et al. [20]. As shown in Fig. 11.1, it consists of six masses connected by ten springs. All masses and springs are assessed as possible source of error, resulting in 16 uncertain parameters. Assume that all the masses possess sensors and the system is excited by a force through mass 6. The reason for studying this example here is twofold. First, it consists of three close eigenfrequencies, a situation which implies difficulties to the mode matching based calibration algorithms. Second, two modes with close eigenfrequencies are poorly controllable through the single excitation force Q_6, a situation which poses difficulties to the frequency-domain subspace identification algorithm [10]. All modes are in range [3–23] Hz. The test data is obtained by simulation of accelerance frequency responses of the system when the parameters are set to their true value and 1.1, 1.2, 1.3, 1.4, 1.5, and 1.6 % modal damping is assigned to the six modes in increasing eigenfrequency order. The output noise added to this synthetic data is assumed to be white noise with the same intensity in all channels. In order to trace the effect of noise on the proposed calibration algorithm, three sets of data with different levels of rms Noise-to-Signal Ratio (NSR) are considered here; 0.05, 0.5 and 5 %. To assess the bootstrap estimate for the predictive power of the calibrated model, the experimental data is divided into two datasets; calibration dataset consisting

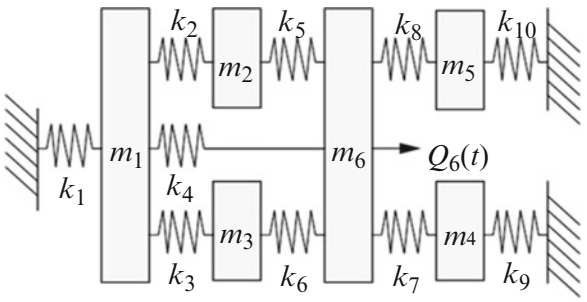

Fig. 11.1 A 6-dof mass-spring system with 16 uncertain parameters, m_i, for $i = 1, .., 6$, and k_i, for $i = 1, \ldots, 10$

of accelerance of mass 2 to mass 6 and left-out dataset which is the accelerance of mass number 1. It is emphasized that the left-out dataset is not considered during any steps of the calibration process and provides an independent dataset for validation of the model.

The model calibration procedure presented in the previous section is applied to this example to demonstrate the validity of the algorithm. The starting step in this algorithm is the identification of the TD model from experimental data using the frequency-domain subspace algorithm. The impact of the proposed frequency sampling strategy on the consistency of this identification algorithm is studied using a Monte-Carlo simulation, with 1000 realizations of noise at each NSR level. The aforementioned identification algorithm is used to produce 1000 state-space models of order 14 for each noise level and for two different scenarios of frequency sampling. In the first scenario, the fictitious frequency response test data are simulated in the frequency range [3–23] Hz with fixed frequency resolution 0.02 Hz, called ordinary frequency sampling. This scenario resembles the most often used sampling technique in experimental modal analysis, the second scenario, the test data are produced at the frequency lines proposed by (11.16), called dedicated frequency sampling. It should be emphasized that the order of 14, which is higher than the order of the system, is selected for the realized state-space models since for higher level of noise the appearance of spurious modes were inevitable. This, in turn, made some system modes to vanish in the system identified models of order 12. This choice would improve the performance of the calibration process since it ensures that the frequency response of the TD model imitate the behavior of the true model in the frequency range of interest. To assess the identified models for bias and variance of the estimated system poles, mode pairing of the realized models and true model is made through MAC analysis. Tables 11.1 and 11.2 present the statistics for bias and variance of the estimated physical poles. It is seen that the bias is less than 1 % even for the highest level of noise when frequency lines are selected using the dedicated frequency sampling. In the case of ordinary sampling the bias is much larger, especially for the two poles (#3 and #4) at around 8 Hz. Therefore, the frequency lines suggested by (11.16) are used in this study for simulation of fictitious frequency response test data.

The next step is to find a point estimate for the parameter setting, the so-called starting values, by minimizing the deviation metric in (11.18). This calibration step, with the TD model as a basis, is performed using one state-space model realization of order 14 at each noise level. A relative modal damping of 1 % was assigned to all modes of the TD and FE models. Figure 11.2 demonstrates a comparison between the experimental test data, the TD model's and nominal FE model's frequency response summed over sensors for the noise level of 5 %. The deviation between the frequency response of the TD model and other models, especially around eigenfrequencies #5 and #6, demonstrated in this figure is due to the fact that for the TD model the damping level of all modes is equalized to 1 % while the for other models is set to the true higher level of modal damping.

Table 11.1 Eigenvalue bias statistics of oscillating part $\Im(\lambda)$ of system physical poles

		Ordinary frequency sampling			Dedicated frequency sampling		
Pole #	$\Im(\lambda)$	Bias 0.05 %	Bias 0.5 %	Bias 5 %	Bias 0.05 %	Bias 0.5 %	Bias 5 %
1	3.8495	0.0033e−3	0.0105e−2	0.0100	0.0002e−3	0.004e−2	0.0028
2	7.0390	0.0118e−3	0.1126e−2	0.1177	0.0054e−3	0.010e−2	0.0035
3	7.3542	2.3940e−3	27.3927e−2	122.9739	0.3671e−3	0.868e−2	0.8329
4	7.6822	1.2899e−3	14.6870e−2	141.9072	0.1497e−3	0.241e−2	0.1499
5	14.8655	0.0033e−3	0.0038e−2	0.0013	0.0009e−3	0.001e−2	0.0032
6	19.4392	0.0011e−3	0.0002e−2	0.0003	0.0007e−3	0.002e−2	0.0007

Estimated bias for 1000 realizations of order 14 at noise levels 0.05, 0.5 and 5 % with and without using the proposed frequency sampling strategy. Bias is in relation to oracle model parameters and is given in percent (%)

Table 11.2 Eigenvalue c.o.v statistics of oscillating part $\Im(\lambda)$ of system physical poles

		Ordinary frequency sampling			Dedicated frequency sampling		
Pole #	$\Im(\lambda)$	c.o.v 0.05 %	c.o.v 0.5 %	c.o.v 5 %	c.o.v 0.05 %	c.o.v 0.5 %	c.o.v 5 %
1	3.8495	0.0139e−2	0.1303e−2	0.0135	0.0060e−2	0.059e−2	0.0064
2	7.0390	0.0457e−2	0.4368e−2	0.0397	0.0247e−2	0.254e−2	0.0446
3	7.3542	0.6218e−2	7.2469e−2	29.5708	0.3643e−2	3.919e−2	3.6026
4	7.6822	0.4897e−2	5.1792e−2	10.5556	0.2923e−2	2.913e−2	1.3210
5	14.8655	0.0099e−2	0.0959e−2	0.0100	0.0084e−2	0.089e−2	0.0086
6	19.4392	0.0029e−2	0.0300e−2	0.0034	0.0028e−2	0.029e−2	0.0030

Estimated c.o.v for 1000 realizations of order 14 at noise levels 0.05, 0.5 and 5 % with and without using the proposed frequency sampling strategy. C.o.v. is given in percent (%)

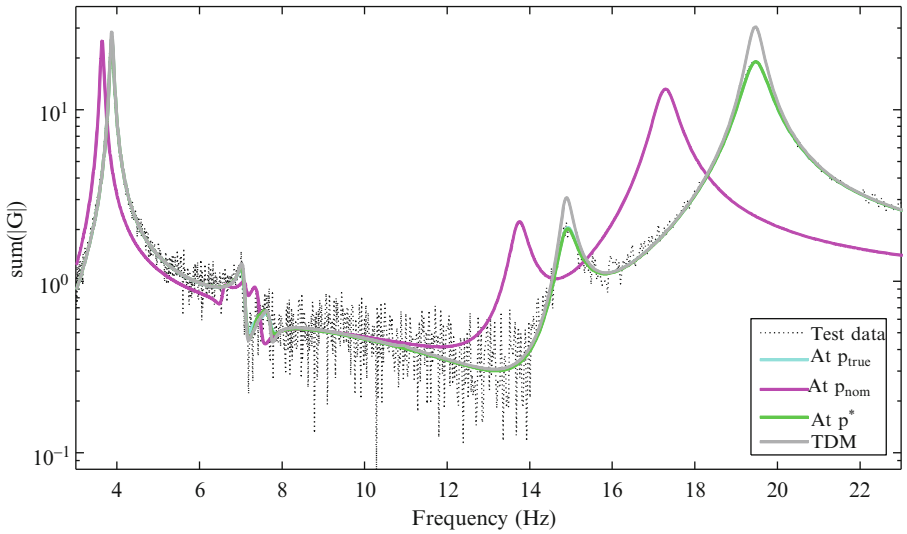

Fig. 11.2 Deviation between FE model and test data accelerances over the calibration dataset for 5 % NSR. Curves are magnitude of sum of five accelerances used as test data (*Black dashed line*) and calculated at, *Green*: the calibrated parameter setting; *Cyan*: the oracle parameter setting, hardly distinguishable due to its overlaying with calibrated model. *Magenta*: before calibration at nominal parameter setting. *Gray*: the model estimated from noisy test data using subspace algorithm, TDM adjusted to 1 % damping

Table 11.3 Parameter values for nominal model, oracle model and the initial estimates, $\boldsymbol{p}^*$, for different noise levels

Parameter	Type	Nominal $\boldsymbol{p}$	Oracle $\boldsymbol{p}$	$\boldsymbol{p}^*$ for 0.05 % NSR	$\boldsymbol{p}^*$ for 0.5 % NSR	$\boldsymbol{p}^*$ for 5 % NSR
p_1	k_1	3000	3600	3556.50	3564.28	3599.42
p_2	k_2	1500	1725	1698.10	1699.00	1436.53
p_3	k_3	1000	1200	1216.04	1214.01	1378.57
p_4	k_4	2000	2200	2187.13	2199.40	2164.89
p_5	k_5	1100	1320	1301.95	1304.50	1106.46
p_6	k_6	1400	1330	1351.76	1351.09	1585.00
p_7	k_7	1250	1500	1541.74	1541.01	1555.99
p_8	k_8	5000	5250	5234.33	5232.00	5178.11
p_9	k_9	3000	3600	3693.28	3692.04	3702.80
p_{10}	k_{10}	1000	850	839.69	837.74	822.12
p_{11}	m_1	1	1	0.99	0.99	0.98
p_{12}	m_2	1.5	1.4	1.38	1.38	1.18
p_{13}	m_3	1.2	1.2	1.22	1.22	1.42
p_{14}	m_4	2.0	2.2	2.25	2.26	2.28
p_{15}	m_5	2.5	2.5	2.49	2.49	2.45
p_{16}	m_6	1.1	0.9	0.90	0.90	0.89

To achieve a good initial point this step is started with 100 Latin Hypercube samplings, assuming a uniform distribution for the parameters centered at the nominal setting and ± 30 % from nominal as upper and lower limits. Figure 11.2 demonstrates how well the resulting calibrated model evaluated at the estimated parameter setting captures the behavior of the true model. As a result of this step, the initial values for the uncertain parameters are estimated and listed in Table 11.3.

The last step of the algorithm is to quantify the uncertainty in the model parameters based on the uncertainty in the test data using the method of bootstrapping. To this end, the raw test data and not the data computed from the TD model. The experimentally found modal damping in (11.24) is mapped to FE modes by MAC correlation analysis for the calibrated model. Then, 100 bootstrap datasets are produced from the calibration dataset. The calibration against each bootstrap dataset is formulated as the minimization of the deviation metric presented in (11.31). This problem is solved using an undamped Gauss–Newton minimizer starting from the point estimates of the parameters, presented in Table 11.3. Our hypothesis is that there is no need for damping equalization or mode-pairing for the calibration problem in this step as the variation from the point estimator will be small. This relies on the assumption that within the radius of convergence to the minimum point,

Table 11.4 Parameter statistics of calibrated models

Parameter	Oracle $\boldsymbol{p}$	Mean0.05 %	Mean0.5 %	Mean5 %	Bias0.05 %	Bias0.5 %	Bias5 %	c.o.v0.05 %	c.o.v0.5 %	c.o.v5 %
k_1	3600	3599.4	3600.1	3557.1	0.02	0.002	1.19	0.01	0.15	1.60
k_2	1725	1723.1	1725.8	1691.6	0.11	0.05	1.94	0.05	0.52	5.08
k_3	1200	1201.3	1197.8	1231.8	0.11	0.18	2.65	0.05	0.55	4.87
k_4	2200	2199.7	2199.4	2191.7	0.01	0.03	0.38	6.1e−3	0.06	0.60
k_5	1320	1318.5	1322.1	1271.9	0.11	0.16	3.65	0.05	0.49	4.86
k_6	1330	1331.5	1329.2	1367.4	0.11	0.06	2.81	0.05	0.56	5.12
k_7	1500	1500.3	1503.8	1524.7	0.02	0.25	1.64	0.04	0.32	3.60
k_8	5250	5249.6	5245.8	5227.4	0.01	0.08	0.43	9.3e−3	0.08	0.96
k_9	3600	3600.7	3608.7	3672.6	0.02	0.24	2.02	0.04	0.32	3.58
k_{10}	850	850.0	847.5	837.96	0.002	0.29	1.42	0.03	0.25	2.82
m_1	1	0.99	0.99	0.99	0.02	0.03	0.51	0.01	0.10	1.06
m_2	1.4	1.40	1.40	1.36	0.11	0.10	3.11	0.05	0.49	4.82
m_3	1.2	1.20	1.19	1.23	0.11	0.07	2.69	0.05	0.56	5.09
m_4	2.2	2.20	2.20	2.25	0.02	0.22	2.33	0.04	0.32	3.62
m_5	2.5	2.50	2.49	2.49	0.005	0.09	0.60	0.01	0.09	1.10
m_6	0.9	0.90	0.89	0.90	0.004	0.001	0.16	7.4e−4	6.2e−3	0.06

Mean, estimated coefficient of variation (c.o.v) and bias for 1000 realizations at noise levels 0.05, 0.5 and 5 %. Coefficient of variation and bias are given in percent (%). Bias is in relation to oracle model parameters

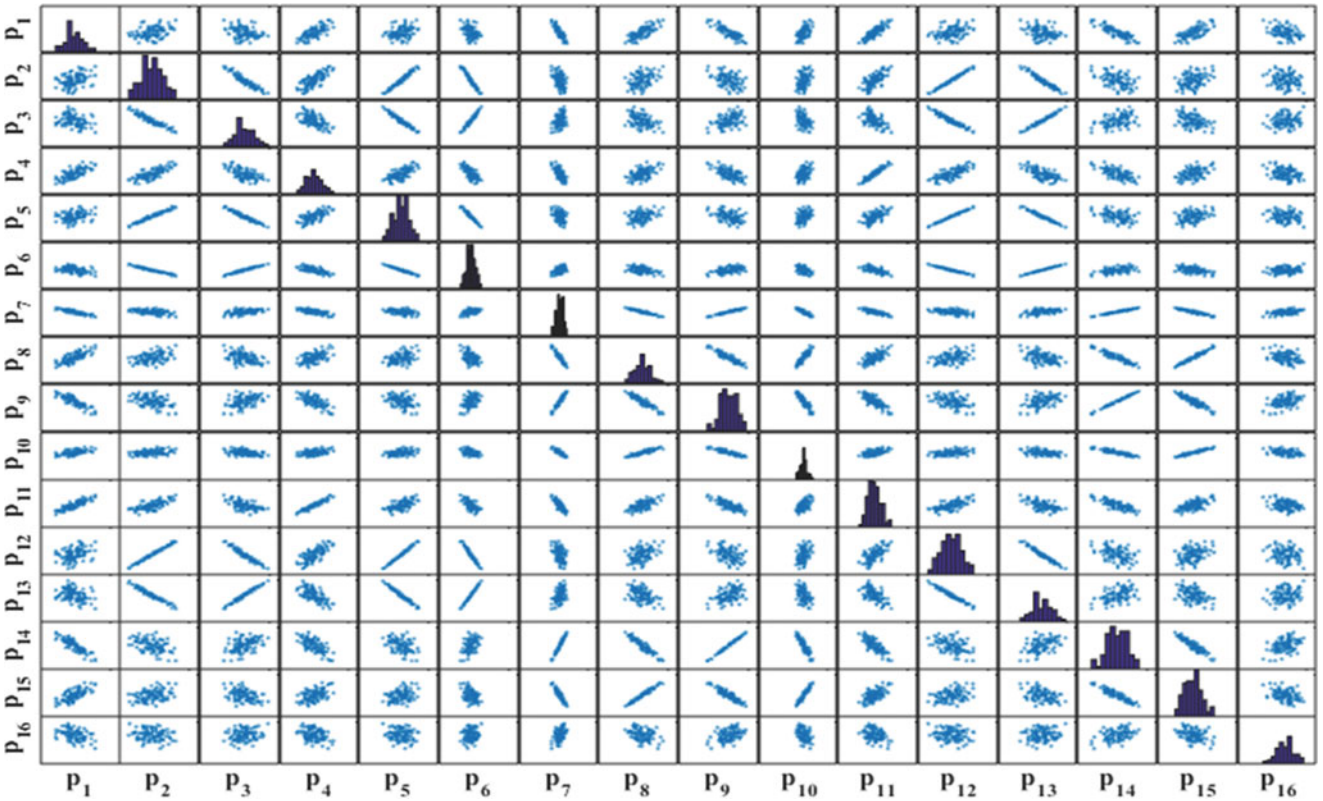

Fig. 11.3 Marginal and joint distribution of the estimated parameters corresponding to Table 11.4 for 5 % NSR

mode switching will not take place. The coefficient of variation and bias of the 16 uncertain parameters were evaluated and reported in Table 11.4. It can be seen that the parameter bias amounts to less than 4 % at a 5 % NSR for the least identifiable parameters, i.e., those that also shows the larger variance. Figure 11.3 demonstrates the marginal and joint distributions of the parameters. This figure also reveals the correlation between the parameters.

For the calibration dataset, Fig. 11.4 shows a comparison between the frequency responses obtained from experiment and computed at the oracle parameter setting and mean value of the bootstrap estimates of the uncertain parameters. This figure

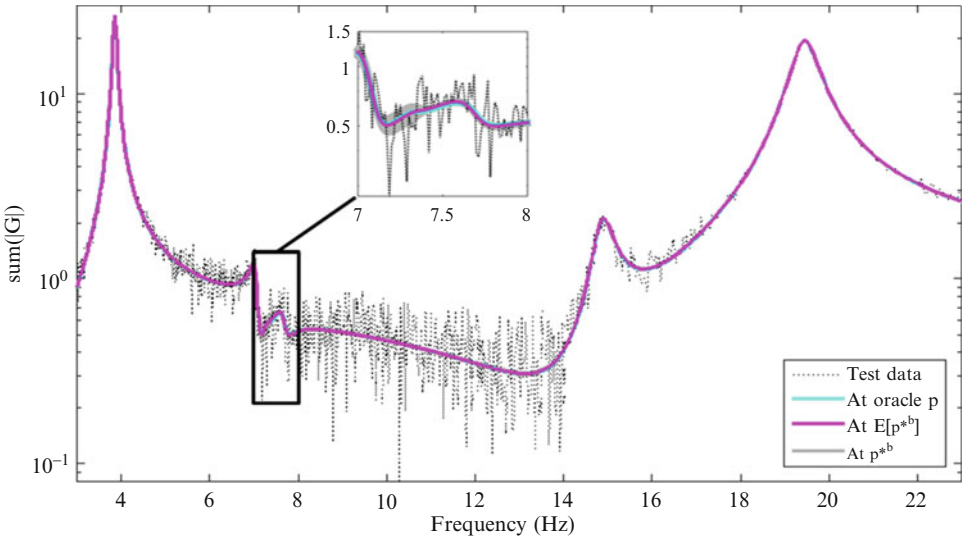

Fig. 11.4 Deviation between FE model and test data accelerances over the calibration dataset for 5 % NSR. Curves are magnitude of sum of 5 accelerances used as test data (*Black dashed line*) and calculated at, *Magenta*: the mean value of parameters estimated from bootstrapping; *Cyan*: the oracle parameter setting hardly distinguishable from the model realized at mean value of the bootstrap estimates of the parameters; *Gray*: all the parameter settings estimated from each bootstrap dataset mostly visible in the zoom-in. The magnified part of the plot show the variation resulted from propagation of distribution of estimated uncertain parameters

Table 11.5 Deviation metric per data sample evaluated for both the calibration and the left-out (LO) dataset, and calculated at nominal, mean value of the bootstrap estimates and oracle parameter setting, along with 95 % confidence interval (CI) for the 0.632 bootstrap estimator of prediction error

	Nominal $\boldsymbol{p}$		$\bar{\boldsymbol{p}}^*$				Oracle $\boldsymbol{p}$	
NSR	$\overline{err}_{LO}$	$\overline{err}$	$\overline{err}_{LO}$	$\overline{err}$	95 % CI of $\widehat{\text{Err}}^{(1)}$	95 % CI of $\widehat{\text{Err}}^{(.632)}$	$\overline{err}_{LO}$	$\overline{err}$
0.05 %	3.43e+6	3.82e+6	0.98	0.98	1.00 ± 1.41	0.98 ± 0.88	0.98	1
0.5 %	4.44e+4	4.60e+4	1.02	1.00	1.00 ± 1.42	1.02 ± 0.88	1.02	1
5 %	607.84	640.84	1.00	0.98	0.98 ± 1.37	0.98 ± 0.86	0.98	1

indicates that the model evaluated at the mean value of the bootstrap estimates closely mimics the frequency response of the true model. This figure also illustrates the frequency response corresponding to the models evaluated at parameter settings, $\boldsymbol{p}^{*b}$, estimated from bootstrap datasets. The magnified part of the figure reveals the prediction variability resulted from the inferred distribution for the parameters. This variability takes place mostly around the third mode of the system which is hardly controllable through the excitation at mass 6.

The bootstrapping allows for the estimation of the prediction error from the calibration dataset. The training error, $\overline{err}$, the 95 % confidence interval of leave-out $\widehat{\text{Err}}^{(1)}$, and the 0.632 bootstrap estimator of prediction error $\widehat{\text{Err}}^{(.632)}$, and the left-out error,

$\overline{err}_{LO}$, are reported in Table 11.5. The training error is the deviation metric (11.31) evaluated for the calibration dataset and the left-out error is the deviation metric (11.31) evaluated for the independent validation dataset, i.e., the accelerance of mass 1. The errors in this table are normalized based on the training error computed at oracle parameter setting. The table indicates that after calibration the error is due to the measurement noise and the modelling errors are insignificant since the errors of the calibrated model and the oracle are the same.

Figure 11.5 illustrates the left-out frequency responses of experimental data and computed from models evaluated at the nominal, the oracle, the initial point obtained from the second step, the mean value of bootstrap estimates, and the parameter settings found from bootstrap datasets. This figure shows the closeness of the frequency response of the true model and the model evaluated at the mean value of the estimated parameters for the independent validation dataset. This is a welcomed observation that shows the prediction capability of the model at dofs not used in the calibration procedure.

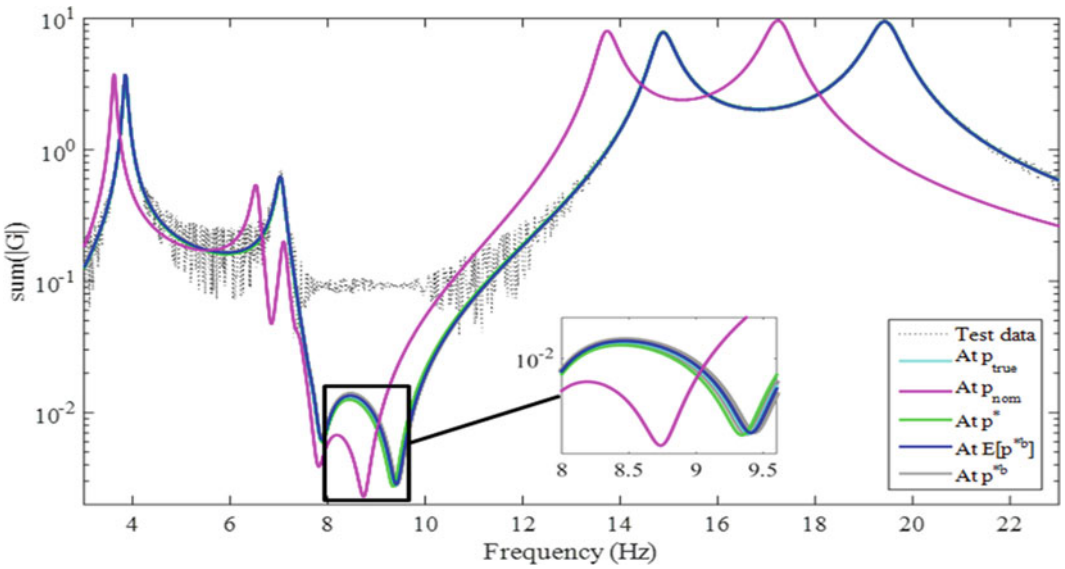

Fig. 11.5 Deviation between FE model and test data (Lab) accelerance left out for standard validation for 5 % NSR. Curves are magnitude of accelerance at mass number 1 used for the test data (*Black dashed line*) and calculated at, *Blue*: the mean value of bootstrap estimates of the parameters. *Cyan*: the true parameter setting, hardly distinguishable from the model realized at mean value of the estimated parameters; *Green*: the calibrated parameter setting; *Gray*: all the parameter settings estimated from each bootstrap dataset; *Magenta*: nominal parameter setting

11.5 Conclusion

A stochastic FE model updating procedure is presented that provides the uncertainty bounds on the unknown parameters. The procedure is demonstrated to find initial points reasonably close to the global minimum for which many researchers has been addressed this issue as a challenge in FE model updating problem. The procedure owes its success for finding good initial points to two key items: dedicated frequency sampling strategy which helps to keep the consistency of the test data model in the presence of noise and the weighted frequency based metric used.

The uncertainty level in the model parameters and the prediction error are evaluated using bootstrapping technique for which its feasibility relies on the quality of the estimated initial points and the modal damping coefficients obtained from test data model.

This procedure has been applied to a mass-spring problem with closely spaced eigenfrequencies and poorly controllable modes. Results showed that the modeling errors are substantially decreased and the measurement noise is the only source of deviation.

Acknowledgment The authors would like to express their gratitude to Prof. Tomas McKelvey for the discussions.

References

1. Jiang, D., Zhang, P., Fei, Q., Wu, S.: Comparative study of model updating methods using frequency response function data. J. Vibroeng. **16**(5), 2305–2318 (2014)
2. García-Palencia, A.J., Santini-Bell, E.: A two-step model updating algorithm for parameter identification of linear elastic damped structures. Comput. Aided Civ. Infrastruct. Eng. **28**(7), 509–521 (2013)
3. Imregun, M., Sanliturk, K.Y., Ewins, D.J.: Finite element model updating using frequency response function data: II case study on a medium-size finite element model. Mech. Syst. Signal Process. **9**(2), 203–213 (1995)
4. Imregun, M., Visser, W.J., Ewins, D.J.: Finite element model updating using frequency response function data: I theory and initial investigation. Mech. Syst. Signal Process. **9**(2), 187–202 (1995)
5. Balmès, E.: A finite element updating procedure using frequency response functions—applications to the MIT/SERC interferometer testbed. In: Proceedings of the IMAC XI, Kissimmee, FL (1993)
6. Arora, V., Singh, S.P., Kundra, T.K.: Finite element model updating with damping identification. J. Sound Vib. **324**(3–5), 1111–1123 (2009)
7. Lin, R.M., Zhu, J.: Model updating of damped structures using FRF data. Mech. Syst. Signal Process. **20**, 2200–2218 (2006)
8. Lu, Y., Tu, Z.: A two-level neural network approach for dynamic FE model updating including damping. J. Sound Vib. **275**, 931–952 (2004)

9. Arora, V., Singh, S.P., Kundra, T.K.: Further experience with model updating incorporating damping matrices. Mech. Syst. Signal Process. **24**(5), 1383–1390 (2010)
10. Khorsand Vakilzadeh, M., Yaghoubi, V., Mckelvey, T., Abrahamsson, J.S.T., Ljung, L.: Experiment design for improved frequency domain subspace system identification of continuous-time systems. In: Proceedings of the 17th IFAC Symposium on System Identification, Beijing (2015)
11. Govers, Y., Link, M.: Stochastic model updating—covariance matrix adjustment from uncertain experimental modal data. Mech. Syst. Signal Process. **24**(3), 696–706 (2010)
12. Sipple, J.D., Sanayei, M.: Full-scale bridge finite-element model calibration using measured frequency-response functions. J. Bridge Eng. **20**, 04014103, (2014)
13. Hastie, T., Tibshirani, R., Friedman, J.: The Elements of Statistical Learning. Springer, New York (2009)
14. Abrahamsson, T.J.S., Bartholdsson, F., Hallqvist, M., Olsson, K.H.A., Olsson, M., Sällström, Å.: Calibration and validation of a car subframe finite element model using frequency responses. In: Proceedings of the 33rd IMAC, Orlando, FL (2015)
15. Abrahamsson, T.J.S., Kammer, D.C.: Finite element model calibration using frequency responses with damping equalization. Mech. Syst. Signal Process. **62**, 218–234 (2015)
16. Mckelvey, T., Akçay, H., Ljung, L.: Subspace-based multivariable system identification from frequency response data. IEEE Trans. Automat. Contr. **41**(7), 960–979 (1996)
17. El-Kafafy, M., Guillaume, P., Peeters, B.: Modal parameter estimation by combining stochastic and deterministic frequency-domain approaches. Mech. Syst. Signal Process. **35**(1), 52–68 (2013)
18. Craig, R.R., Kurdila, A.J.: Fundamentals of Structural Dynamics. John Wiley & Sons, Hoboken, NJ (2006)
19. Efron, B., Tibshirani, R.: Improvements on cross-validation: the 632+ bootstrap method. J. Am. Stat. Assoc. **92**(438), 548–560 (1997)
20. Kozak, M.T., Cömert, M.D., Özgüven, H.N.: A model updating routine based on the minimization of a new frequency response based index for error localization. In: Proceedings of the 25th International Modal Analysis Conference, pp. 84–95. Orlando, FL (2007)

Chapter 12
Dynamic Identification of Classically Damped Uncertain Structures

E. Lofrano, A. Paolone, and M. Vasta

Abstract The detection of structural damping is a crucial point in structural identification. Classic techniques usually refer to deterministic systems, since the assumption of randomness in the mechanical quantities implies non-trivial analytical difficulties in the development of both the direct and the inverse problem.

In some recent works, starting from the statistics of mode-shapes and (undamped) frequencies, a perturbative approach has been introduced by the authors for the estimation of mean and variance of uncertain mass and stiffness. Here dissipative structures are considered; in detail, the method is applied for the stochastic structural identification of classically damped linear dynamic systems, dependent on a random parameter, assumed to be Gaussian. A numerical validation of the technique is then presented and discussed.

Keywords Structural identification • Dynamic techniques • Structural damping • Uncertain structures • Perturbative approach

12.1 Introduction

Structural monitoring is a key issue in many engineering fields. In this research area, dynamic identification techniques have proven very fruitful [6, 7, 16, 18]. In the case of structures with uncertain parameters, however, literary studies are mainly focused on the statistics of the dynamic system eigensolution, that is, on the statistics of the direct problem [1, 8, 17, 21]. Otherwise, structural identification techniques are usually developed neglecting the randomness of the systems, primarily for the inverse nature of such approach, which often returns ill-conditioned and indeterminate problems, as well as to the lack of closed-form solutions. Nevertheless, it seems clear that, like what happens in the direct problem, the randomness of the various properties of a structure can be a crucial factor, especially when one deals with the safety evaluation of civil, mechanical and aerospace engineering structures [2, 4]. Since for systems characterized by random parameters, also the dynamic identification must be stochastic, it turns out the need to refer to a global structural model able of considering the probabilistic information, and then to develop an approach identifying the distributions (or statistics) of the parameters.

A stochastic dynamic identification technique has been recently proposed by the authors. In [12, 14] linear dynamic discrete systems with a random parameter are considered, and an approach able to estimate mean and variance of the parameter is proposed. In [13, 15] the same solution strategy is successfully applied to vibrating 1-D continua: beam- and cable-like elements, respectively. In all these works, assuming undamped systems, the estimation of mean and variance of the uncertain parameter is gathered adopting an objective function minimizing the difference among analytical and experimental statistics of the eigenvalues, where the analytical relationships are the ones provided by a perturbative approach [9, 10, 19]. A comparison among the proposed strategy and the existing ones reveals how: respect to the non perturbative approaches (e.g., [5, 18]) the proposed one provides a low computational effort, since the statistic of the parameter are searched through closed form solutions; differently from other perturbative schemes (e.g., [3, 20]), the proposed one does not require an updating of the sensitivity matrix to find more precise solutions.

In this paper dissipative structures are considered; in detail, the work focuses on the stochastic structural dynamic identification of classically damped linear discrete dynamic systems, dependent on a random parameter, assumed to be Gaussian. Using a perturbation approach, the eigensolution of the undamped system (Sect. 12.2.2) and the damping ratios

E. Lofrano (✉) • A. Paolone
Department of Structural and Geotechnical Engineering, Sapienza University of Rome, 18, Eudossiana St., 00184 Rome, Italy
e-mail: egidio.lofrano@uniroma1.it

M. Vasta
Department of Engineering and Geology, University G. D'Annunzio of Chieti-Pescara, 42, Pindaro St., 65127 Pescara, Italy

S. Atamturktur et al. (eds.), *Model Validation and Uncertainty Quantification, Volume 3*, Conference Proceedings of the Society for Experimental Mechanics Series, DOI 10.1007/978-3-319-29754-5_12

of the dissipative one (Sect. 12.2.2) are analytically evaluated by a Taylor series expansion. These asymptotic solutions (evaluated up to the first two terms) are then used in order to recognize the expressions of mean and variance of eigenvalues and damping ratios. Lastly, a technique able to identify the mean and the variance of the random parameter is proposed (Sect. 12.3). As numerical validation, the technique is applied to a four-storey shear frame structure (Sect. 12.4), where the random parameter is a damage parameter, linearly reducing the stiffness of the third column, hence modifying also the damping matrix.

12.2 Perturbative Approximation

12.2.1 Undamped Vibrations

Given a linear (discrete or discretized) uncertain structure, the free undamped vibrations are ruled by a matrix equation

$$\mathbf{M}(\varepsilon)\ddot{\mathbf{u}}(t) + \mathbf{K}(\varepsilon)\mathbf{u}(t) = \mathbf{0} \tag{12.1}$$

where $\mathbf{M}(\varepsilon)$ and $\mathbf{K}(\varepsilon)$ are the mass and stiffness matrices, respectively, $\mathbf{u}(t)$ is the displacement vector, and ε is a Gaussian distributed random parameter $\mathcal{N}(\mu_\varepsilon, \sigma_\varepsilon^2)$, being μ_ε the mean and σ_ε^2 the variance.

The assumption of Gaussian parameter, which means that the mean and standard deviation provide a complete statistical description of its PDF, will be simplify the manipulations operated in the inverse problem (Sect. 12.3). If other distributions are required, isoprobabilistic transformations can be used, i.e., transformations which are able to map non Gaussian and dependent random variables in Gaussian and independent ones [11].

If n is the number of degree of freedom, the solution is searched adopting the usual projection on the modal space (ρ_i and θ_i are real coefficients that can be fixed imposing the initial conditions)

$$\mathbf{u}(t) = \sum_{i=1}^{n} \boldsymbol{\phi}_i \underbrace{\rho_i \sin(\omega_i t + \theta_i)}_{q_i(t)} = \boldsymbol{\Phi}\mathbf{q}(t) \tag{12.2}$$

with $\boldsymbol{q}(t)$ the modal coordinate vector and $\boldsymbol{\Phi} = [\boldsymbol{\phi}_1 \cdots \boldsymbol{\phi}_n]$ the modal matrix. Substituting Eq. (12.2) in Eq. (12.1), the following eigenvalue problem is obtained

$$(\mathbf{K}(\varepsilon) - \lambda_i \mathbf{M}(\varepsilon))\boldsymbol{\phi}_i = \mathbf{0} \qquad \lambda_i = \omega_i^2 = (2\pi f_i)^2 \qquad i = 1, \ldots, n \tag{12.3}$$

with λ_i the eigenvalues and $\boldsymbol{\phi}_i$ the eigenvectors of the system, and f_i the corresponding frequencies.

The relevant (nonlinear) random characteristic equation

$$\det(\mathbf{K}(\varepsilon) - \lambda_i \mathbf{M}(\varepsilon)) = 0 \qquad i = 1, \ldots, n \tag{12.4}$$

is approached via a perturbative scheme [9, 10, 19]. Assuming a non defective systems, i.e., n distinct eigenvalues, a Taylor expansion around $\varepsilon = 0$ can be adopted (otherwise, fractional series expansions are needed for defective system)

$$\begin{cases} \mathbf{M}(\varepsilon) = \mathbf{M}_0 + \varepsilon\mathbf{M}_1 + \varepsilon^2\mathbf{M}_2 + \ldots \\ \mathbf{K}(\varepsilon) = \mathbf{K}_0 + \varepsilon\mathbf{K}_1 + \varepsilon^2\mathbf{K}_2 + \ldots \end{cases} \qquad \|\varepsilon\| \ll 1 \tag{12.5}$$

with

$$\mathbf{M}_j = \frac{1}{j!}\frac{\mathrm{d}^j\mathbf{M}(\varepsilon)}{\mathrm{d}\varepsilon^j}\bigg|_{\varepsilon=0} \qquad \mathbf{K}_j = \frac{1}{j!}\frac{\mathrm{d}^j\mathbf{K}(\varepsilon)}{\mathrm{d}\varepsilon^j}\bigg|_{\varepsilon=0} \tag{12.6}$$

and analogously for the eigensolution

$$\begin{cases} \lambda_i = \lambda_{0i} + \varepsilon\lambda_{1i} + \varepsilon^2\lambda_{2i} + \ldots \\ \boldsymbol{\phi}_i = \boldsymbol{\phi}_{0i} + \varepsilon\boldsymbol{\phi}_{1i} + \varepsilon^2\boldsymbol{\phi}_{2i} + \ldots \end{cases} \tag{12.7}$$

with

$$\lambda_{ji} = \frac{1}{j!}\frac{\mathrm{d}^j \lambda_i(\varepsilon)}{\mathrm{d}\varepsilon^j}\bigg|_{\varepsilon=0} \qquad \boldsymbol{\phi}_{ji} = \frac{1}{j!}\frac{\mathrm{d}^j \boldsymbol{\phi}_i(\varepsilon)}{\mathrm{d}\varepsilon^j}\bigg|_{\varepsilon=0} \tag{12.8}$$

Substituting Eqs. (12.5) and (12.7) in Eq. (12.3), the balance of the powers in ε leads to

$$\begin{cases} \varepsilon^0 : (\mathbf{K}_0 - \lambda_{0i}\mathbf{M}_0)\boldsymbol{\phi}_{0i} = \mathbf{0} \\ \varepsilon^1 : (\mathbf{K}_0 - \lambda_{0i}\mathbf{M}_0)\boldsymbol{\phi}_{1i} = (\lambda_{0i}\mathbf{M}_1 + \lambda_{1i}\mathbf{M}_0 - \mathbf{K}_1)\boldsymbol{\phi}_{0i} \\ \varepsilon^2 : (\mathbf{K}_0 - \lambda_{0i}\mathbf{M}_0)\boldsymbol{\phi}_{2i} = (\lambda_{0i}\mathbf{M}_1 + \lambda_{1i}\mathbf{M}_0 - \mathbf{K}_1)\boldsymbol{\phi}_{1i} + (\lambda_{0i}\mathbf{M}_2 + \lambda_{1i}\mathbf{M}_1 + \lambda_{2i}\mathbf{M}_0 - \mathbf{K}_2)\boldsymbol{\phi}_{0i} \\ \dots \end{cases} \tag{12.9}$$

from which the zero order solution $(\lambda_{0i}, \boldsymbol{\phi}_{0i})$, that is, the solution of the eigenvalue problem Eq. (12.9_a), the so called *generating equation*, and then the perturbative terms [12, 14] (α_{ii} and β_{ii} are real coefficients that can be fixed imposing a normalization conditions)

$$\begin{cases} \lambda_{1i} = \dfrac{\boldsymbol{\phi}_{0i}^\top(\mathbf{K}_1 - \lambda_{0i}\mathbf{M}_1)\boldsymbol{\phi}_{0i}}{\boldsymbol{\phi}_{0i}^\top\mathbf{M}_0\boldsymbol{\phi}_{0i}} \\ \lambda_{2i} = \dfrac{\boldsymbol{\phi}_{0i}^\top(\mathbf{K}_1 - \lambda_{0i}\mathbf{M}_1 - \lambda_{1i}\mathbf{M}_0)\boldsymbol{\phi}_{1i}}{\boldsymbol{\phi}_{0i}^\top\mathbf{M}_0\boldsymbol{\phi}_{0i}} + \dfrac{\boldsymbol{\phi}_{0i}^\top(\mathbf{K}_2 - \lambda_{0i}\mathbf{M}_2 - \lambda_{1i}\mathbf{M}_1)\boldsymbol{\phi}_{0i}}{\boldsymbol{\phi}_{0i}^\top\mathbf{M}_0\boldsymbol{\phi}_{0i}} \\ \boldsymbol{\phi}_{1i} = \alpha_{ii}\boldsymbol{\phi}_{0i} + \displaystyle\sum_{\substack{j=1 \\ j\neq i}}^{n} \frac{\boldsymbol{\phi}_{0j}^\top(\mathbf{K}_1 - \lambda_{0i}\mathbf{M}_1)\boldsymbol{\phi}_{0i}}{(\lambda_{0i} - \lambda_{0j})\boldsymbol{\phi}_{0j}^\top\mathbf{M}_0\boldsymbol{\phi}_{0j}}\boldsymbol{\phi}_{0j} \\ \boldsymbol{\phi}_{2i} = \beta_{ii}\boldsymbol{\phi}_{0i} + \displaystyle\sum_{\substack{j=1 \\ j\neq i}}^{n} \left(\frac{\boldsymbol{\phi}_{0j}^\top(\mathbf{K}_1 - \lambda_{0i}\mathbf{M}_1 - \lambda_{1i}\mathbf{M}_0)\boldsymbol{\phi}_{1i}}{(\lambda_{0i} - \lambda_{0j})\boldsymbol{\phi}_{0j}^\top\mathbf{M}_0\boldsymbol{\phi}_{0j}} + \frac{\boldsymbol{\phi}_{0j}^\top(\mathbf{K}_2 - \lambda_{0i}\mathbf{M}_2 - \lambda_{1i}\mathbf{M}_1)\boldsymbol{\phi}_{0i}}{(\lambda_{0i} - \lambda_{0j})\boldsymbol{\phi}_{0j}^\top\mathbf{M}_0\boldsymbol{\phi}_{0j}} \right)\boldsymbol{\phi}_{0j} \\ \dots \end{cases} \tag{12.10}$$

where only one eigenvalue problem must be solved and where all these quantities $(\lambda_{0i}, \lambda_{1i}, \lambda_{2i}, \dots)$ and $(\boldsymbol{\phi}_{0i}, \boldsymbol{\phi}_{1i}, \boldsymbol{\phi}_{2i}, \dots)$ are deterministic (since these are independent on the random parameter ε).

12.2.2 Damped Vibrations

When the damping is considered, the free vibrations equations of the linear uncertain structure, Eq. (12.1), must be modified in

$$\mathbf{M}(\varepsilon)\ddot{\mathbf{u}}(t) + \mathbf{C}(\varepsilon)\dot{\mathbf{u}}(t) + \mathbf{K}(\varepsilon)\mathbf{u}(t) = \mathbf{0} \tag{12.11}$$

being $\mathbf{C}(\varepsilon)$ the damping matrix. However, if classically damped systems are of interest, i.e., systems having a damping matrix of the form

$$\mathbf{C}(\varepsilon) = \mathbf{M}(\varepsilon)\sum_{p=0}^{n-1} a_p(\varepsilon)(\mathbf{M}(\varepsilon)^{-1}\mathbf{K}(\varepsilon))^p \tag{12.12}$$

the eigensolution of the system still remains the one showed in Eqs. (12.9)–(12.10).

In order to evaluate the dissipation properties of the system, the damping ratios are computed. Following the traditional design practice, in what follows a less general expression of the damping is adopted: only the first two terms of the sum (12.12) are retained (obtaining an uncertain version of the so called *Rayleigh damping matrix*)

$$\mathbf{C}(\varepsilon) = a_0(\varepsilon)\mathbf{M}(\varepsilon) + a_1(\varepsilon)\mathbf{K}(\varepsilon) \tag{12.13}$$

from which the Taylor expansion

$$\mathbf{C}(\varepsilon) = \mathbf{C}_0 + \varepsilon\mathbf{C}_1 + \varepsilon^2\mathbf{C}_2 + \dots \tag{12.14}$$

where

$$\begin{cases} \mathbf{C}_l = \displaystyle\sum_{j=0}^{l} a_{j0}\mathbf{M}_{l-j} + a_{j1}\mathbf{K}_{l-j} \\ a_{ji} = \dfrac{1}{j!}\dfrac{\mathrm{d}^j a_i(\varepsilon)}{\mathrm{d}\varepsilon^j}\Big|_{\varepsilon=0} \qquad i = 0, 1 \end{cases} \Longrightarrow \begin{cases} \mathbf{C}_0 = a_{00}\mathbf{M}_0 + a_{01}\mathbf{K}_0 \\ \mathbf{C}_1 = a_{10}\mathbf{M}_0 + a_{11}\mathbf{K}_0 + a_{00}\mathbf{M}_1 + a_{01}\mathbf{K}_1 \\ \mathbf{C}_2 = a_{20}\mathbf{M}_0 + a_{21}\mathbf{K}_0 + a_{10}\mathbf{M}_1 + a_{11}\mathbf{K}_1 + a_{00}\mathbf{M}_2 + a_{01}\mathbf{K}_2 \\ \dots \end{cases} \tag{12.15}$$

From modal solution of damped equations of motion, the damping ratios are expressed as

$$\xi_i(\varepsilon) = \frac{\boldsymbol{\phi}_i^\top(\varepsilon)\mathbf{C}(\varepsilon)\boldsymbol{\phi}_i(\varepsilon)}{2\sqrt{\boldsymbol{\phi}_i^\top(\varepsilon)\mathbf{M}(\varepsilon)\boldsymbol{\phi}_i(\varepsilon)\ \boldsymbol{\phi}_i^\top(\varepsilon)\mathbf{K}(\varepsilon)\boldsymbol{\phi}_i(\varepsilon)}} \tag{12.16}$$

If in the Eq. (12.16) both the numerator and the terms under the square root at the denominator are developed with a Taylor series expansion, Eqs. (12.5), $(12.7)_2$, (12.14), it turns out

$$\xi_i(\varepsilon) = \frac{A_0 + A_1\varepsilon + A_2\varepsilon^2 + \dots}{2\sqrt{B_0 + B_1\varepsilon + B_2\varepsilon^2 + \dots}} \tag{12.17}$$

where

$$\begin{cases} A_0 = c_{0i} \qquad A_1 = 2\alpha_{ii}c_{0i} + c_{1i} \qquad A_2 = 2\beta_{ii}c_{0i} + c_{2i} + \gamma_{2i} \\ B_0 = m_{0i}k_{0i} \qquad B_1 = 4\alpha_{ii}m_{0i}k_{0i} + m_{1i}k_{0i} + m_{0i}k_{1i} \\ \qquad B_2 = 4\beta_{ii}m_{0i}k_{0i} + m_{2i}k_{0i} + m_{0i}k_{2i} + m_{1i}k_{1i} + 2\alpha_{ii}m_{0i}k_{1i} + 2\alpha_{ii}m_{1i}k_{0i} + 4\alpha_{ii}^2 m_{0i}k_{0i} + \delta_{2i} \end{cases} \tag{12.18}$$

being

$$\begin{cases} m_{ji} = \boldsymbol{\phi}_{0i}^\top\mathbf{M}_j\boldsymbol{\phi}_{0i} \qquad k_{ji} = \boldsymbol{\phi}_{0i}^\top\mathbf{K}_j\boldsymbol{\phi}_{0i} \qquad c_{ji} = \boldsymbol{\phi}_{0i}^\top\mathbf{C}_j\boldsymbol{\phi}_{0i} \\ \gamma_{2i} = 2\Phi_{1i}^T\mathbf{C}_1\Phi_{0i} + \Phi_{1i}^T\mathbf{C}_0\Phi_{1i} \\ \delta_{2i} = +2m_{0i}\boldsymbol{\phi}_{1i}^\top\mathbf{K}_1\boldsymbol{\phi}_{0i} + m_{0i}\boldsymbol{\phi}_{1i}^\top\mathbf{K}_0\boldsymbol{\phi}_{1i} + 2\boldsymbol{\phi}_{1i}^\top\mathbf{M}_1\boldsymbol{\phi}_{0i}k_{0i} + \boldsymbol{\phi}_{1i}^\top\mathbf{M}_0\boldsymbol{\phi}_{1i}k_{0i} \end{cases} \tag{12.19}$$

Lastly, a Taylor expansion around $\varepsilon = 0$ for both sides of the Eq. (12.16) leads to

$$\xi_i(\varepsilon) = \xi_{0i} + \varepsilon\xi_{1i} + \varepsilon^2\xi_{2i} + \dots \tag{12.20}$$

where

$$\begin{cases} \xi_{0i} = \dfrac{A_0}{2B_0^{1/2}} \\ \xi_{1i} = \dfrac{-A_0B_1 + 2A_1B_0}{4B_0^{3/2}} \\ \xi_{2i} = \dfrac{-4A_0B_0B_2 + 3A_0B_1^2 - 4A_1B_0B_1 + 8A_2B_0^2}{16B_0^{5/2}} \end{cases} \tag{12.21}$$

Although these relationships are fairly complicated, their implementation in a computer code is easy, and, it is worth remembering, the terms $(\xi_{0i}, \xi_{1i}, \xi_{2i}, \dots)$ must be evaluated only once, since these do not depend on ε.

12.3 Identification of the Uncertain Parameter

In the previous section, the modal model has been gathered starting from the mass, stiffness and damping structural properties. In detail, a perturbative scheme with integer powers has been used for the eigensolution of the undamped system and for the damping ratios of the relevant classically damped one. The idea behind the identification technique proposed here is to estimate the mean and the variance of the uncertain parameter ε adopting an objective function minimizing the difference among analytical and experimental fractiles of eigenvalues and damping ratios. It is worth pointing out that here the mode-shapes are not used in the inverse problem because in real life applications there are often difficulties in detecting with accuracy these quantities, while frequencies and damping ratios are more easily evaluable.

From Eq. (12.7)$_a$, the first and second order statistics of eigenvalues are furnished by (being $E[\bullet]$ the stochastic average operator)

$$\begin{cases} E[\lambda_i] = \lambda_{0i} + E[\varepsilon]\lambda_{1i} + E[\varepsilon^2]\lambda_{2i} \\ E[\lambda_i\lambda_j] = \lambda_{0i}\left(\lambda_{0j} + \lambda_{1j}E[\varepsilon] + \lambda_{2j}E[\varepsilon^2]\right) + \lambda_{1i}\left(\lambda_{0j}E[\varepsilon] + \lambda_{1j}E[\varepsilon^2] + \lambda_{2j}E[\varepsilon^3]\right) \\ \qquad\qquad +\lambda_{2i}\left(\lambda_{0j}E[\varepsilon^2] + \lambda_{1j}E[\varepsilon^3] + \lambda_{2j}E[\varepsilon^4]\right) \end{cases} \tag{12.22}$$

relationships that manipulated and simplified lead to [14]

$$\begin{cases} \mu_{\lambda_i} = \lambda_{0i} + \mu_\varepsilon\lambda_{1i} + \left(\mu_\varepsilon^2 + \sigma_\varepsilon^2\right)\lambda_{2i} + o(\varepsilon^2) \\ \sigma_{\lambda_i\lambda_j} = \sigma_\varepsilon^2\lambda_{1i}\lambda_{1j} + 2\sigma_\varepsilon^2\mu_\varepsilon(\lambda_{1i}\lambda_{2j} + \lambda_{1j}\lambda_{2i}) + (2\sigma_\varepsilon^4 + 4\sigma_\varepsilon^2\mu_\varepsilon^2)\lambda_{2i}\lambda_{2j} + o(\varepsilon^2) \end{cases} \tag{12.23}$$

where if the $\lambda_{2i}, \lambda_{2j}$ terms are neglected, a first order solution is employed and, because of the linear relationship among eigensolution and the parameter, also the eigenvalues are Gaussian.

In a completely analogous way, for the damping ratios is obtained

$$\begin{cases} \mu_{\xi_i} = \xi_{0i} + \mu_\varepsilon\xi_{1i} + \left(\mu_\varepsilon^2 + \sigma_\varepsilon^2\right)\xi_{2i} + o(\varepsilon^2) \\ \sigma_{\xi_i\xi_j} = \sigma_\varepsilon^2\xi_{1i}\xi_{1j} + 2\sigma_\varepsilon^2\mu_\varepsilon(\xi_{1i}\xi_{2j} + \xi_{1j}\xi_{2i}) + (2\sigma_\varepsilon^4 + 4\sigma_\varepsilon^2\mu_\varepsilon^2)\xi_{2i}\xi_{2j} + o(\varepsilon^2) \end{cases} \tag{12.24}$$

Equations (12.23) and (12.24) can be used to quantify the uncertain parameter. To this aim, one needs to know the mass and stiffness matrices $(\mathbf{M}_i, \mathbf{K}_i)$, and also the coefficients (a_{i0}, a_{i1}) that rules the dissipative properties, with $i = 0, 1, 2, \ldots$. In this way, the eigenvalues λ_i and the damping ratios ξ_i are just dependent on the random parameter ε, and a suitable comparison among the statistics of these analytical terms and the experimental counterparts, allows to identify the statistics of ε.

When a first experimental campaign has been developed, the zero-order quantities $(\mathbf{M}_0, \mathbf{K}_0, a_{00}, a_{01})$ must be initialized, and then, once fixed the dependence on ε, that is, the perturbative terms $(\mathbf{M}_i, \mathbf{K}_i, a_{i0}, a_{i1})$, $i = 1, 2, \ldots$, one can proceed with the evaluation of the uncertain parameter; in other words, the first experimental campaign allows to develop a stochastic model updating.

If a successive campaign is available, the zero-order quantities $(\mathbf{M}_0, \mathbf{K}_0, a_{00}, a_{01})$ must be just updated (basing on the results of the first tests), hence, once fixed again the dependence on ε, the evaluation of the uncertain parameter can be developed; in other words, a successive campaign allows to develop a stochastic identification of a structural change.

In both cases one should know how the structural properties of mass, stiffness and damping depend on ε, i.e., where the uncertain parameter acts. If during the stochastic model updating it can be done with a trial and error technique, for a stochastic identification of a structural change one can start from the physical meaning of the parameter. For a change in mass matrix (that appears, neglecting the variations for mass degradation and/or damage, when a structure is interested by a change of use or a structural reinforcement), an increase in stiffness matrix (a structural reinforcement), and a change in damping coefficients (inserting/removing of viscous devices), it turns out that the dependence of $(\mathbf{M}(\varepsilon), \mathbf{K}(\varepsilon), a_0(\varepsilon), a_1(\varepsilon))$ on the random parameter can certainly be considered known *a priori*. Only for a damage uncertain parameter, since the damage is in general not visible, one must employ at upstream an *ad hoc* technique able to locate the damage, one of the so called level two damage identification technique [6], or proceed with a trial and error technique.

A problem of this kind, with two unknowns, the couple $(\mu_\varepsilon, \sigma_\varepsilon)$, and a number of equations equals to $2(n_\lambda + n_\xi)$ (see (12.23) and (12.24)), being n_λ and n_ξ the number of eigenvalues and damping ratios effectively measured (usually both less than n), may be approached computing an objective function. Here the following functional of the least square methods class is used (a sum of the squared normalized discrepancies)

$$\mathcal{E}(\mu_\varepsilon, \sigma_\varepsilon) = \sum_{i=1}^{n_\lambda} \left(1 - \frac{{}^K\lambda_i}{{}^K\tilde{\lambda}_i}\right)^2 + \sum_{i=1}^{n_\xi} \left(1 - \frac{{}^K\xi_i}{{}^K\tilde{\xi}_i}\right)^2 \tag{12.25}$$

being ^{K} a fractile measure, $({}^K\lambda_i, {}^K\xi_i)$ analytic quantities, depending only on $(\mu_\varepsilon, \sigma_\varepsilon)$, and $({}^K\tilde{\lambda}_i, {}^K\tilde{\xi}_i)$ the relevant experimental counterparts.

Here fractile measures must be intended as an upper limit of the response (independent on the exact value of the relevant probability, which calculation is, in general, not straightforward) [2, 14]

$${}^K\lambda_i = \mu_{\lambda_i} + 3\,\sigma_{\lambda_i} \tag{12.26}$$

and similar for the damping ratios and the measured quantities. The choice of the value 3 comes from an analogy with Gaussian variables $x = \mathcal{N}(\mu_\varepsilon, \sigma_\varepsilon^2)$, for which the fractile ${}^K x = \mu_x + c\,\sigma_x$ has a probability of not exceeding equal (approximately) to 99.9 % when $c = 3$.

The solving equation can then be written as

$$(\tilde{\mu}_\varepsilon, \tilde{\sigma}_\varepsilon) = \arg\min \mathcal{E}(\mu_\varepsilon, \sigma_\varepsilon) \qquad \sigma_\varepsilon \geq 0 \tag{12.27}$$

where the couple of identified mean and variance of the parameter $(\tilde{\mu}_\varepsilon, \tilde{\sigma}_\varepsilon)$ minimizes the objective function with the constrain $\sigma_\varepsilon \geq 0$, plus other constraints related to the system physics. It is worth noting that this strategy solution remains the same regardless of the chosen order of approximation.

The following section shows an application of the proposed technique, where the first two terms of the series expansions are used.

12.4 Application

The technique is applied to a four degrees of freedom planar structure, a four-storey shear frame (Fig. 12.1a), which dissipative properties are assumed consistent with a Rayleigh-like damping matrix.

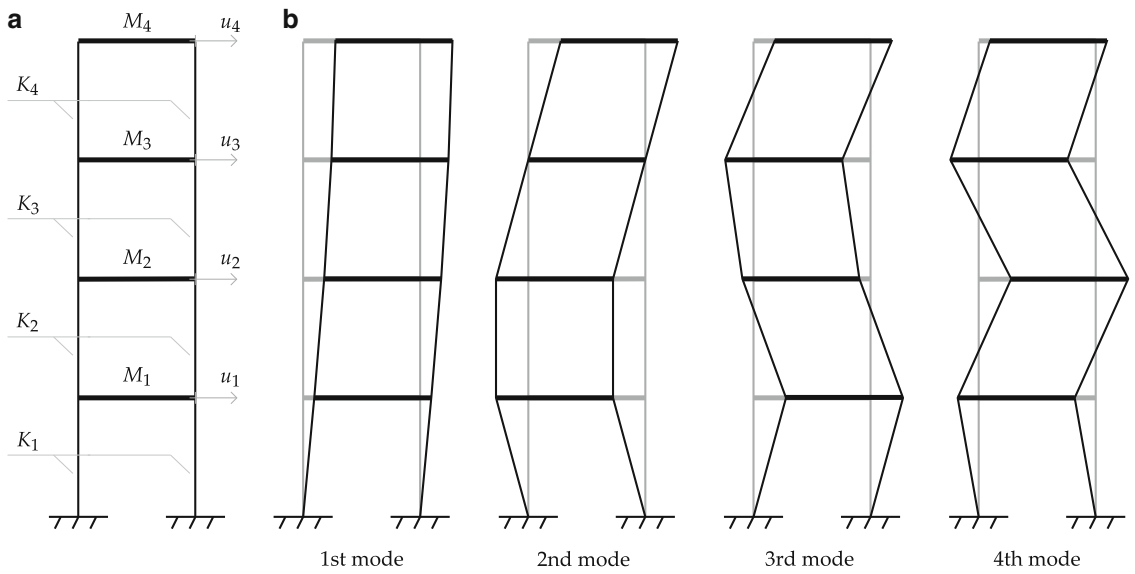

Fig. 12.1 Numerical example: (**a**) structural model, (**b**) unperturbed mode-shapes

Starting from the direct problem, the equation of motion (12.11) can be written in terms of [4]

$$\mathbf{M}(\varepsilon) = \begin{bmatrix} M_1 & 0 & 0 & 0 \\ 0 & M_2 & 0 & 0 \\ 0 & 0 & M_3 & 0 \\ 0 & 0 & 0 & M_4 \end{bmatrix} \qquad \mathbf{K}(\varepsilon) = \begin{bmatrix} K_1+K_2 & -K_2 & 0 & 0 \\ -K_2 & K_2+K_3 & -K_3 & 0 \\ 0 & -K_3 & K_3+K_4 & -K_4 \\ 0 & 0 & -K_4 & K_4 \end{bmatrix} \qquad \mathbf{u}(t) = \begin{Bmatrix} u_1 \\ u_2 \\ u_3 \\ u_4 \end{Bmatrix} \tag{12.28}$$

plus the relevant damping coefficients $a_0(\varepsilon)$ and $a_1(\varepsilon)$, see Eq. (12.13).

Adopting the following values of mass, stiffness and damping coefficients

$$\begin{cases} M_i = 1\text{kg} & i = 1,2,3,4 \\ K_i = 1800\text{N/m} & i = 1,2,4 \\ K_3 = 1800\,(1-\varepsilon)\text{N/m} & \varepsilon \approx \mathcal{N}(\mu_\varepsilon,\, \sigma_\varepsilon^2) \\ a_0 = 0.8749, a_1 = 0.0014 & \end{cases} \tag{12.29}$$

the perturbative terms are (see Eqs. (12.6) and (12.15))

$$\mathbf{M}_0 = \begin{bmatrix} 1&0&0&0 \\ 0&1&0&0 \\ 0&0&1&0 \\ 0&0&0&1 \end{bmatrix} \qquad \mathbf{K}_0 = \begin{bmatrix} 3600 & -1800 & 0 & 0 \\ -1800 & 3600 & -1800 & 0 \\ 0 & -1800 & 3600 & -1800 \\ 0 & 0 & -1800 & 1800 \end{bmatrix} \qquad a_{00} = 0.8749 \qquad a_{01} = 0.0014 \tag{12.30}$$

for the 0th-order,

$$\mathbf{M}_1 = \mathbf{0} \qquad \mathbf{K}_1 = \begin{bmatrix} 0 & 0 & 0 & 0 \\ 0 & -1800 & 1800 & 0 \\ 0 & 1800 & -1800 & 0 \\ 0 & 0 & 0 & 0 \end{bmatrix} \qquad a_{10} = a_{11} = 0$$
$$\mathbf{M}_2 = \mathbf{K}_2 = \mathbf{0} \qquad a_{20} = a_{21} = 0 \tag{12.31}$$

for the first- and second-order. Hence, for the damping matrix the Eqs. (12.15) lead to

$$\mathbf{C}_0 = a_{00}\mathbf{M}_0 + a_{01}\mathbf{K}_0 \qquad \mathbf{C}_1 = a_{01}\mathbf{K}_1 \qquad \mathbf{C}_2 = \mathbf{0} \tag{12.32}$$

Table 12.1 shows the solution for the unperturbed system $(\mathbf{M}_0, \mathbf{K}_0, \mathbf{C}_0)$: the eigenvalues λ_{0i} and the corresponding (undamped) angular frequencies ω_{0i}, cyclic frequencies f_{0i} and periods T_{0i}, the components of the eigenvectors $\boldsymbol{\phi}_{0i}$ (that are also sketched in Fig. 12.1b), and the damping ratios ξ_{0i}.

Two cases are considered for the perturbed system

- case 1—deterministic: $\mu_\varepsilon \in (0, 0.5]$, $\sigma_\varepsilon^2 = 0$;
- case 2—stochastic: $\mu_\varepsilon \in (0, 0.5]$, $\sigma_\varepsilon^2 = (0.05\,\mu_\varepsilon)^2$.

In other words, in this numerical application the uncertain parameter rules the damage evolution of the third column, linearly reducing the relevant stiffness, hence modifying also the damping matrix, that is, the relevant dissipative properties of the

Table 12.1 Modal characteristics of the unperturbed system

Mode	λ_{0i} (rad/s)^2	ω_{0i} (rad/s)	f_{0i} (Hz)	T_{0i} (s)	1st DoF	2nd DoF	3rd DoF	4th DoF	ξ_{0i} (%)
1	217.1	14.735	2.345	0.426	0.347	0.653	0.879	1.000	4.0
2	1800.0	42.426	6.752	0.148	1.000	1.000	0.000	−1.000	4.0
3	4225.1	65.001	10.345	0.097	1.000	−0.347	−0.879	0.653	5.2
4	6357.8	79.736	12.690	0.079	−0.653	1.000	−0.879	0.347	6.1

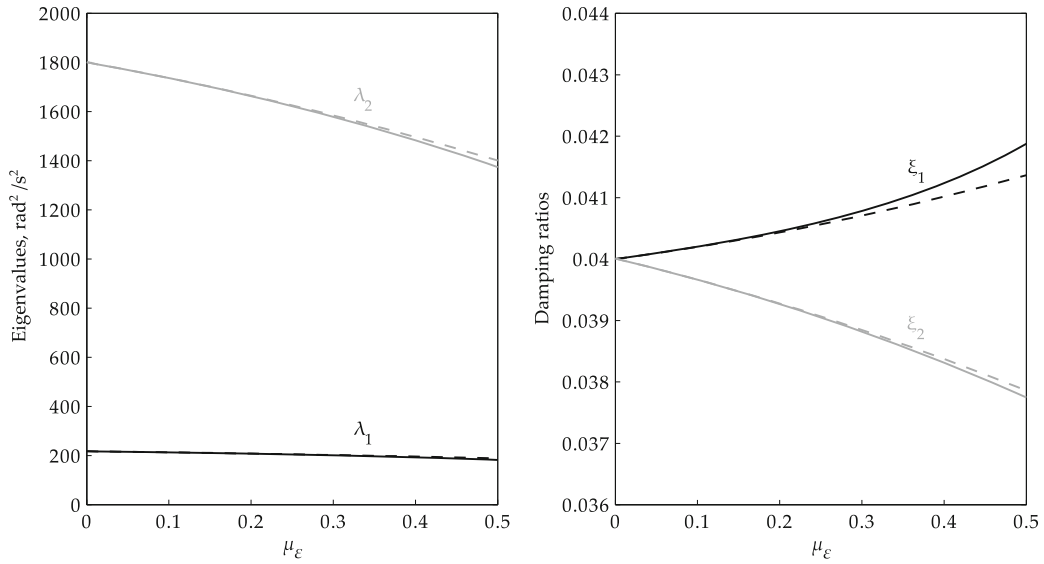

Fig. 12.2 Sensitivity of eigenvalues and damping ratios, case 1

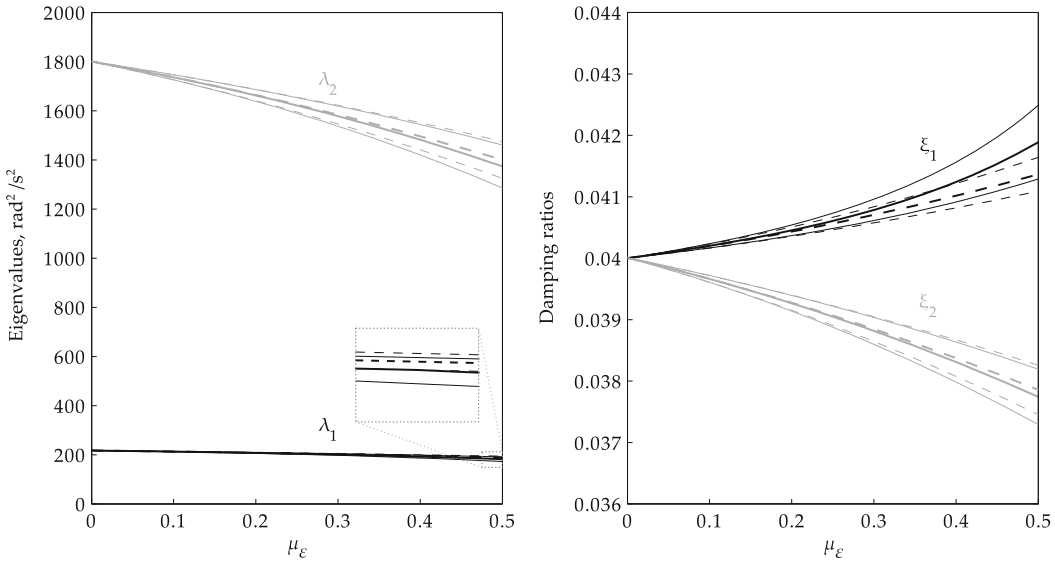

Fig. 12.3 Sensitivity of eigenvalues and damping ratios, case 2

system. The mean value of ε is increased up to 0.5 (50 % reduction of the third stiffness), and for the second case, the stochastic one, a constant coefficient of variation of the 5 % is considered (the dispersion increases when the damage increases).

Assuming that the first two eigenvalues and the first two damping ratios have been detected during the tests ($n_\lambda = n_\xi = 2$), the sensitivity of these quantities with respect of the random parameter ε is employed. In detail, the perturbative approach (PA) (see Eqs. (12.10), (12.21), (12.23), and (12.24)) is compared with the solution furnished by the eigenvalue problem (12.1) and by the damping ratios rule (12.16): for the deterministic case the current value of μ_ε (ES) is used; for the stochastic case a Monte Carlo (MC) analysis of 5000 simulations is developed for each couple of (μ_ε, σ_ε^2).

The results are shown in Fig. 12.2, for case 1, and in Fig. 12.3, for case 2

- case 1—deterministic: continuous line ES, dashed line PA;
- case 2—stochastic: continuous line MC, dashed line PA; thick and thin lines refer to mean and mean plus/minus three standard deviations values, respectively.

Consistently with the use of a perturbative approach, the discrepancy increases when the intensity of the sensitivity parameter ε increases; in order to evaluate the relevant error, the following comparisons are developed

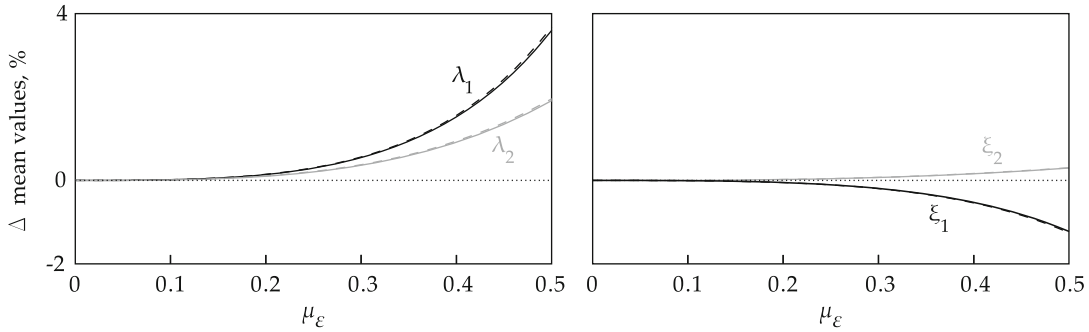

Fig. 12.4 Percentage error for the mean values, cases 1 and 2

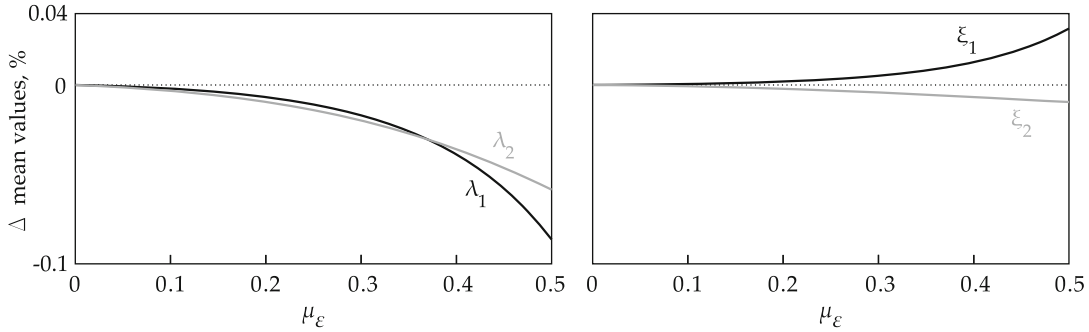

Fig. 12.5 Percentage error for the mean values, ES vs MC

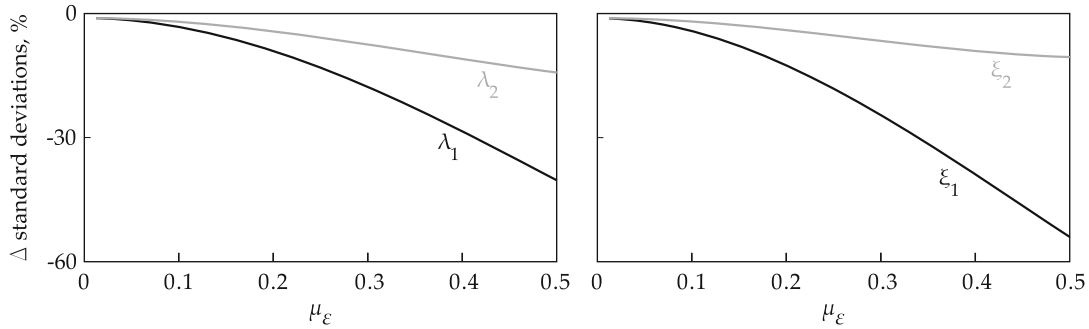

Fig. 12.6 Percentage error for the standard deviations, case 2

- case 1—deterministic: comparison between the deterministic (ES) and the perturbative (PA) solutions;
- case 1 vs case 2: comparison among the mean values obtained by the deterministic solution (ES) and the ones obtained in the stochastic case via the Monte Carlo simulation (MC);
- case 2—stochastic: comparison between the mean values and the standard deviations given by Monte Carlo simulation (MC) with those obtained by the perturbative approach (PA);

and the relevant results lead to the following comments

- the continuous curves, for the case 1 (ES vs PA), and the dashed lines, for the case 2 (MC vs PA), of Fig. 12.4 show that the percentage error for the mean values evaluation is (in absolute value) always less than the 4 %, for the eigenvalues, and the 2 %, for the damping ratios;
- the overlaps among the previous continuous and dashed curves are due to the low influence of the variance σ_ε^2 of the parameter on the means. Indeed, comparing the mean values obtained by the deterministic solution (ES) and via the Monte Carlo simulation (MC), Fig. 12.5, vanishing percentage discrepancies appear: the error is (in absolute value) always less than the 0.1 %, for the eigenvalues, and the 0.04 %, for the damping ratios;
- in the stochastic case, Fig. 12.6 shows the error for the standard deviations evaluation (MC vs PA): the maximum error (in absolute value) is of about 40 and 60 %, for the eigenvalues and the damping ratios, respectively.

Summarizing, this study on the direct problem highlights how a second order expansion leads to a good approximation of the mean values, but a rough approximation of the standard deviations.

Moving toward the inverse problem, the experimental quantities of the first two eigenvalues ${}^{K}\widetilde{\lambda}_i$ and the first two damping ratios ${}^{K}\widetilde{\xi}_i$ are here numerically simulated, starting from the solution of the eigenvalue problem (12.1) and the damping ratios rule (12.16). Again, for the deterministic case the current value of μ_ε (ES) is used, for the stochastic case a Monte Carlo (MC) analysis of 5000 simulations is developed for each couple of $(\mu_\varepsilon, \sigma_\varepsilon^2)$. Then, the identification of the uncertain parameter ε is developed applying the relationships (12.25)–(12.27).

In order to focus on the effectiveness of the proposed technique to identify the uncertain parameter, following the comments listed in the Sect. 12.3, here it is assumed that the zero-order quantities $(\mathbf{M}_0, \mathbf{K}_0, a_{00}, a_{01})$ are known from a first experimental campaign and that also the perturbative terms $(\mathbf{M}_i, \mathbf{K}_i, a_{i0}, a_{i1})$, $i = 1, 2$, can be considered known (visible damage or upstream localization of the damage via a level two damage identification technique). For the case 1, deterministic, the results obtained for the parameter identification are those of Fig. 12.7: on the left the identification obtained using only the eigenvalues, on the right the ones obtained using also the damping ratios. In these graphs the dashed line, the bisector of the first quadrant of the effective-identified plane of the parameter, indicates the ideal (perfect) path of minimum of the objective function (identified parameter equal to actual parameter). In other words, the deviation of the obtained path (continues line) from the ideal one is a direct measure of the effectiveness of the proposed technique. With the same conventions, Figs. 12.8 and 12.9 show, respectively, the identification of the mean value and the standard deviation for the case 2, stochastic.

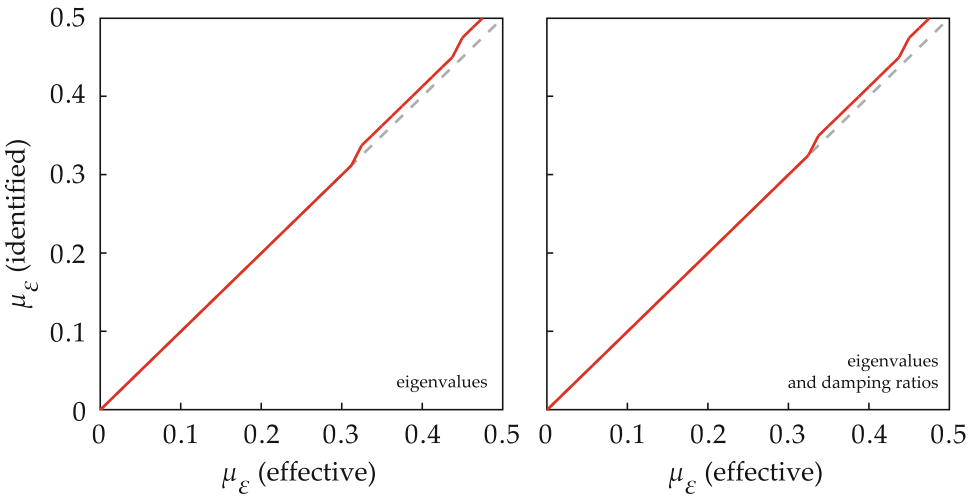

Fig. 12.7 Identification of the mean value μ_ε, case 1

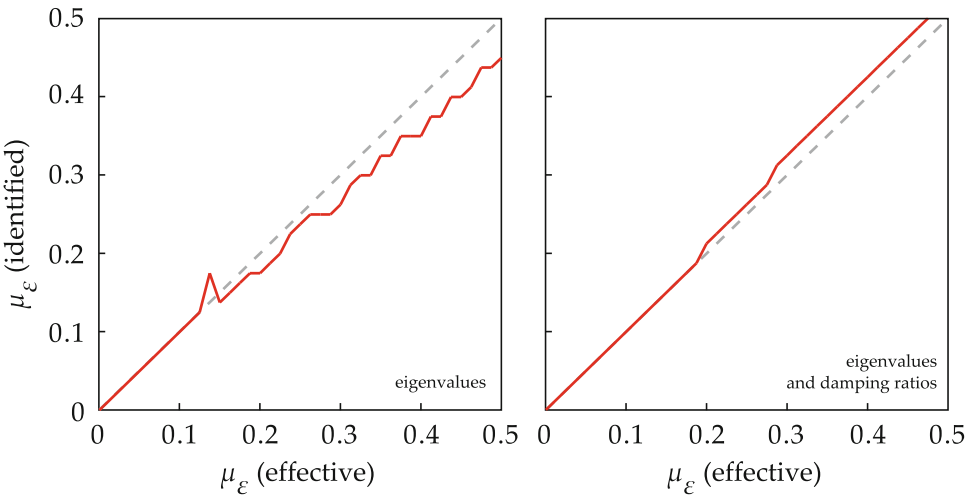

Fig. 12.8 Identification of the mean value μ_ε, case 2

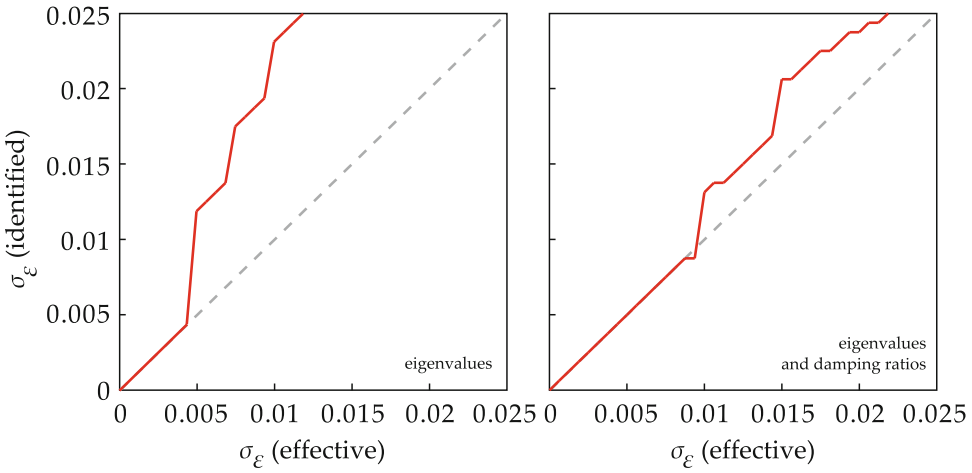

Fig. 12.9 Identification of the standard deviation σ_ε, case 2

The analysis of these results allows to conclude

- deterministic damage: if the stiffness reduction is smaller than about the 35 %, the parameter is properly identified, regardless of the use of also the damping ratios in the technique. For larger values of the reduction, the identification is anyway reasonably good;
- stochastic damage: the mean of the parameter is properly identified when the average stiffness reduction is smaller than about the 15 %, for eigenvalues based technique, and the 20 %, when also the damping ratios are considered. Again, for larger values of the reduction, the identification of the mean values is reasonably good. For the standard deviation (reminding that a constant coefficient of variation of 5 % has been assumed), it appears that a proper identification requires an average stiffness reduction smaller than about the 10 %, for eigenvalues based technique, and the 20 %, when also the damping ratios are included.

These comments, consistently with the results of the direct problem, confirm that the neighborhood properly identifiable is smaller moving from the deterministic to the stochastic damage. About the use of the damping ratios in the inverse problem, it appears that these quantities can enlarge this neighborhood, becoming also essential in order to avoid a rapid divergence of the minimum path in the standard deviation evaluation (Fig. 12.9). These new encouraging results paved the way to more general issues, mainly related to the multiparametric extension: dissipative properties evolving independently by the damage, noise corruption, multiple damages, ...

12.5 Conclusions

In this work the identification of classically damped linear dynamic systems with a random parameter has been performed. The system is assumed discrete (or discretized) and the random parameter is set as Gaussian distributed, while the damping matrix is fixed as an uncertain Rayleigh damping matrix.

Hypothesizing a non defective system, the modal model is gathered via a perturbative scheme based on a Taylor expansion: first the eigensolution of the undamped system is approached, then the damping ratios are evaluated. These asymptotic solutions are explicitly estimated up to the second order of the Taylor expansion, then, the evaluation of the analytical expressions of mean and variance of eigenvalues and damping ratios is performed. Once completed the study of the direct problem, a stochastic identification technique is proposed for the inverse one: the mean and the variance of the random parameter are assessed minimizing the difference among analytical and experimental statistics of eigenvalues and damping ratios.

The effectiveness of the technique is shown choosing as application a four-storey shear frame structure. The random parameter rules the damage evolution of the third column, linearly reducing the relevant stiffness, hence modifying also the damping matrix. The results of this numerical validation (obtained considering the first two eigenvalues and the first two damping ratios of the structural system) have proved that the technique properly identifies the mean and the variance of the random parameter, and that the stochastic dynamic identification can be improved if also the dissipative properties are considered in the objective function.

As further developments, the main questions are related to the non Gaussianity of the modal properties and to the dependence on the parameters by a random vector (i.e., the multiparametric extension, that allows to take into account: multiple damages, dissipative properties evolving independently by the damage evolution, noise corruption, ...).

References

1. Adhikari, S., Friswell, M.I.: Random eigenvalue problems in structural dynamics. In: 45th AIAA/ASME/ASCE/AHS/ASC Structures, Structural Dynamics & Materials Conference (2004)
2. Apley, D.W., Liu, J., Chen, W.: Understanding the effects of model uncertainty in robust design with computer experiments. J. Mech. Des. **128**(1), 946–958 (2006)
3. Cawley, P., Adams, R.D.: The location of defects in structures from measurements of natural frequencies. J. Strain Anal. **14**(2), 49–57 (1979)
4. Chopra, A.K.: Dynamics of Structures, 1st edn. Engineering Monographs on Earthquake Criteria, Structural Design, and Strong Motion Records, vol. 2. Earthquake Engineering Research Institute (1980)
5. Collins, J.D., Hart, G.C., Hasselmann, T.K., Kennedy, B.: Statistical identification of structures. AIAA J. **12**(2), 185–190 (1974)
6. Doebling, S.W., Farrar, C.R., Prime, M.B., Shevitz, D.W.: Damage identification and health monitoring of structural and mechanical systems from changes in their vibration characteristics: a literature review. Technical Report Los Alamos National Laboratory, LA-13070-MS (1996)
7. Ewins, D.J.: Modal Testing: Theory and Practice, 1st edn. Engineering Dynamics Series, vol. 2. Research Studies Press, Baldock (1984)
8. Ibrahim, R.A.: Structural dynamics with parameter uncertainties. Appl. Mech. Rev. **40**(3), 309–328 (1987)
9. Kaminski, M.: Generalized stochastic perturbation technique in engineering computations. Math. Comput. Model. **51**(3–4), 272–285 (2010)
10. Kato, T.: Perturbation Theory for Linear Operators, 2nd edn. Springer, Berlin (1995)
11. Lebrun, R., Dutfoy, A.: Do Rosenblatt and Nataf isoprobabilistic transformations really differ? Probab. Eng. Mech. **24**(4), 172–178 (2009)
12. Lofrano, E., Paolone, A., Vasta, M.: A perturbation approach for the identification of uncertain structures. In: 8th European Nonlinear Dynamics Conferences (ENOC) (2014)
13. Lofrano, A., Paolone, A., Vasta, M.: Identification of uncertain vibrating beams through a perturbation approach. ASCE-ASME J. Risk Uncertain. Eng. Syst. A Civil Eng. (2015)
14. Lofrano, E., Paolone, A., Vasta, M.: A perturbation approach for the identification of uncertain structures. Int. J. Dyn. Control (2015)
15. Lofrano, E., Ruta, G., Vasta, M.: Stochastic dynamic identification of damaged cables by a perturbation approach (in Italian). In: Proceedings of the 22nd the Italian Association of Theoretical and Applied Mechanics, AIMETA (2015)
16. Maia, N.M.M., Silva, J.M.M.: Theoretical and Experimental Modal Analysis, 1st edn. Engineering Dynamics Series, vol. 9. Research Studies Press, Taunton (1997)
17. Manohar, C.S., Ibrahim, R.A.: Progress in structural dynamics with stochastic parameter variations: 1987 to 1996. Appl. Mech. Rev. **52**(5), 177–197 (1999)
18. Morassi, A., Vestroni, F.: Dynamic Methods for Damage Detection in Structures, 1st edn. CISM International Centre for Mechanical Sciences, vol. 499. Springer Wien, NewYork (2008)
19. Murdock, J.A.: Perturbations: Theory and Methods, 1st edn. Wiley, New York (1991)
20. Papadopoulos, L., Garcia, E.: Structural damage identification: a probabilistic approach. AIAA J. **36**(11), 2137–2145 (1998)
21. Qiu, Z., Wang, X.: Parameter perturbation method for dynamic responses of structures with uncertain-but-bounded parameters based on interval analysis. Int. J. Solids Struct. **42**(18–19), 4958–4970 (2005)

Chapter 13
Interval Finite Element Approach for Modal Analysis of Linear Elastic Structures Under Uncertainty

Naijia Xiao, Francesco Fedele, and Rafi Muhanna

Abstract We present a new Interval Finite Element (IFEM) approach for modal analysis of linear elastic structures with uncertain geometric and material properties. Uncertain parameters are modeled as intervals. Guaranteed interval lower and upper bounds for natural frequencies and modal shapes are attained using a new decomposition strategy of the IFEM matrices that drastically reduces overestimation due to interval dependency. The associated interval generalized eigenvalue problem is solved efficiently by way of a new variant of the iterative enclosure method. Several numerical examples show the accuracy and efficiency of the proposed method.

Keywords Interval • Finite element method • Modal analysis • Iterative enclosure method • Matrix decomposition • Generalized eigenvalue problem

13.1 Introduction

Conventional probability approaches that model uncertain parameters as random variables [1–3] requires a prior knowledge on the nature of random variables, i.e. their probabilistic distribution. However, in real life situations only partial information about uncertain parameters is available, and the validity of above-mentioned probabilistic approaches is still under debate [4, 5]. Non-probabilistic approaches have been developed to handle situations of epistemic uncertainty or when only limited data is available. These include fuzzy sets [6, 7], evidence theory [8, 9], and intervals [10–12].

In this work, we model uncertain variables as intervals [13–16], and exploit Interval Finite Element Method (IFEM) to obtain a guaranteed enclosure of the exact solution [17–20]. Given an elastic structural system with uncertain material properties, we compute its natural frequencies and associated modal shapes by way of an interval generalized eigenvalue problem (IGEP) [21–23]. To reduce overestimation due to interval dependency, we present a new decomposition strategy for the interval stiffness and mass matrices associated with IFEM [24], which avoids multiple occurrences of the same interval variables and yields minimal overestimation. Further, the IGEP is solved by means of a new variant of the iterative enclosure method, which exploits the new proposed IFEM matrix decomposition.

N. Xiao (✉)
School of Civil and Environmental Engineering, Georgia Institute of Technology, Mason Building, 4132, 790 Atlantic Drive, NW, Atlanta, GA 30308, USA
e-mail: nxiao6@gatech.edu

F. Fedele
School of Civil and Environmental Engineering and School of Electrical and Computer Engineering, Georgia Institute of Technology, Technology Square Research Building (TSRB), 415, 85 5th Street, NW, Atlanta, GA 30308, USA
e-mail: fedele@gatech.edu

R. Muhanna
School of Civil and Environmental Engineering, Georgia Institute of Technology, Mason Building, 4165, 790 Atlantic Drive, NW, Atlanta, GA 30308, USA
e-mail: rafi.muhanna@gatech.edu

S. Atamturktur et al. (eds.), *Model Validation and Uncertainty Quantification, Volume 3*, Conference Proceedings of the Society for Experimental Mechanics Series, DOI 10.1007/978-3-319-29754-5_13

13.2 IFEM Matrix Decomposition

Intervals are extension of real numbers. Instead of representing one single point in the real axis, an interval represents set of real numbers, which are most suitably described by its endpoints,

$$\mathbf{x} = [\underline{x}, \overline{x}] = \left\{ x \middle| \underline{x} \leq x \leq \overline{x}, x \in \Re \right\}, \tag{13.1}$$

where $\mathbf{x}$ is the interval, $\underline{x}$ and $\overline{x}$ represent its lower and upper bounds, respectively, and *bold non-italic font is used for interval variables*. Alternatively, an interval can be represented by its midpoint $\text{mid}\,\mathbf{x} = (\underline{x} + \overline{x})/2$ and radius $\text{rad}\,\mathbf{x} = (\overline{x} - \underline{x})/2$. In this paper, we aim at computing interval enclosures of the natural frequencies and modal shapes of a given elastic structure with uncertain material and geometric properties. The following interval generalized eigenvalue problem (IGEP) is used for that purpose

$$\left(\mathbf{K} - \boldsymbol{\omega}^2 \mathbf{M}\right)\ \mathbf{u} = \mathbf{0}, \tag{13.2}$$

where $\mathbf{K}$ and $\mathbf{M}$ are given interval stiffness and mass matrices, respectively, $\boldsymbol{\omega}$ is the unknown natural frequency (measured in rad/s), and $\mathbf{u}$ is the corresponding unknown modal shape. Here $\boldsymbol{\omega}^2$ is treated as a single variable.

To obtain the tightest possible bounds when solving the IGEP equation (13.2), we propose to decompose the interval matrices $\mathbf{K}$ and $\mathbf{M}$ in a way that multiple occurrences of the same interval variables are avoided [15, 25]. In particular, we propose to decompose the interval stiffness matrix $\mathbf{K}$ into

$$\mathbf{K} = A\ \text{diag}\,(\Lambda\boldsymbol{\alpha})\, A^T, \tag{13.3}$$

where A, Λ are scalar matrices, and $\boldsymbol{\alpha}$ is the interval parameter vector accounting for uncertainties in stiffness [24]. The diagonal term $(\Lambda\boldsymbol{\alpha})$ represents Young's modulus at element integration points. Similarly, for the interval mass matrix

$$\mathbf{M} = A_m \text{diag}\,(\Lambda_m \boldsymbol{\alpha}_m)\, A_m^T, \tag{13.4}$$

where A_m, Λ_m are scalar matrices, and $\boldsymbol{\alpha}_m$ is the interval parameter vector accounting for uncertainties in mass. The diagonal term $(\Lambda_m \boldsymbol{\alpha}_m)$ represents mass density at element integration points. In practice, we first decompose element stiffness matrix $\mathbf{K}_e$ and element mass matrix $\mathbf{M}_e$. Afterward we assemble $\mathbf{K}_e$ and $\mathbf{M}_e$ into their global counter parts $\mathbf{K}$ and $\mathbf{M}$, which are compatible with the decomposition in Eqs. (13.3) and (13.4). The formulation is not limited to specific finite elements.

Following the static IFEM formulation of Rama Rao et al. [25], essential boundary conditions are applied by enforcing the additional constraint $C\mathbf{u} = \mathbf{0}$ on the nodal displacement vector $\mathbf{u}$. Here, each row of the matrix C represents one boundary condition, and the corresponding entry is set equal to 1, leaving the rest of the row null. For static problems, the IFEM equations are obtained by minimizing the augmented total potential energy functional $\boldsymbol{\Pi}$

$$\boldsymbol{\Pi} = \frac{1}{2}\mathbf{u}^T\mathbf{K}\mathbf{u} - \mathbf{u}^T\mathbf{f} + \boldsymbol{\lambda}^T (C\mathbf{u})\,. \tag{13.5}$$

Lagrangian multiplier $\boldsymbol{\lambda}$ has been introduced to enforce $C\mathbf{u} = \mathbf{0}$ in order for the essential boundary conditions to be imposed without modifying the stiffness matrix $\mathbf{K}$. The introduction of Lagrangian multipliers takes advantage of the proposed decomposition of $\mathbf{K}$ [see Eq. (13.3)] and it minimizes the number of occurrences of the same variables. As a result, overestimation in the system response is reduced. The IFEM equations follow from the first variation of $\boldsymbol{\Pi}$ as

$$\begin{Bmatrix} \mathbf{K} & C^T \\ C & 0 \end{Bmatrix} \begin{Bmatrix} \mathbf{u} \\ \boldsymbol{\lambda} \end{Bmatrix} = \begin{Bmatrix} \mathbf{f} \\ \mathbf{0} \end{Bmatrix}. \tag{13.6}$$

Note that $\boldsymbol{\lambda}$ represents negative support reactions of the structure. Following the same strategy as in the static case, the natural frequency and modal shapes can be obtained as detailed in the following section.

13.3 Interval Enclosure of Natural Frequencies and Modal Shapes

In order to explain the solution strategy of Eq. (13.2), $(\mathbf{K}-\boldsymbol{\omega}^2\mathbf{M})\mathbf{u}=\mathbf{0}$, and how each natural frequency and associated eigenmode are obtained simultaneously, we first consider the deterministic formulation and later we extend it to the interval case. Consider the mid-point values of the uncertain parameters and deterministic stiffness and mass matrices, i.e. $K_0 = \text{mid}\,\mathbf{K}$, $M_0 = \text{mid}\,\mathbf{M}$, and $\alpha_0 = \text{mid}\,\boldsymbol{\alpha}$, $\alpha_{m0} = \text{mid}\,\boldsymbol{\alpha}_m$. The corresponding deterministic generalized eigenvalue problem is given by

$$\left(K_0 - \omega_0^2 M_0\right)\ u_0 = 0. \tag{13.7}$$

Similarly to the static case of Eq. (13.6), essential boundary conditions can be imposed by means of the constraint equation $Cu_0 = 0$. The dynamical case given in Eq. (13.7) can be reintroduced in the same structure of Eq. (13.6) as

$$\left(\begin{Bmatrix} K_0 & C^T \\ C & 0 \end{Bmatrix} - \omega_0^2 \begin{Bmatrix} M_0 & 0 \\ 0 & 0 \end{Bmatrix}\right) \begin{Bmatrix} u_0 \\ \lambda_0 \end{Bmatrix} = \begin{Bmatrix} 0 \\ 0 \end{Bmatrix}. \tag{13.8}$$

More compactly

$$\left(K_{b0} - \omega_0^2 M_{b0}\right)\ u_{b0} = 0, \tag{13.9}$$

Where

$$K_{b0} = \begin{Bmatrix} K_0 & C^T \\ C & 0 \end{Bmatrix}, M_{b0} = \begin{Bmatrix} M_0 & 0 \\ 0 & 0 \end{Bmatrix}, u_{b0} = \begin{Bmatrix} u_0 \\ \boldsymbol{\lambda} \end{Bmatrix}. \tag{13.10}$$

Finally, to uniquely determine the modal shape u_0, we impose the normalization $u_0^T M_0 u_0 = 1$.

The interval extension of Eq. (13.8) yields the following governing equation for the IGEP

$$\left(\begin{Bmatrix} \mathbf{K} & C^T \\ C & 0 \end{Bmatrix} - \boldsymbol{\omega}^2 \begin{Bmatrix} \mathbf{M} & 0 \\ 0 & 0 \end{Bmatrix}\right) \begin{Bmatrix} \mathbf{u} \\ \boldsymbol{\lambda} \end{Bmatrix} = \begin{Bmatrix} \mathbf{0} \\ \mathbf{0} \end{Bmatrix}. \tag{13.11}$$

From Eq. (13.11), this can be reduced to the compact form

$$\left(\mathbf{K}_b - \boldsymbol{\omega}^2 \mathbf{M}_b\right)\ \mathbf{u}_b = \mathbf{0}, \tag{13.12}$$

and we impose the normalization $\mathbf{u}_b^T \mathbf{M}_b \mathbf{u}_b = 1$.

Now we denote the corresponding modal shape as u_0 and the support reaction as λ_0. To obtain a form that is equivalent and easier to handle, we subtract Eq. (13.8) from Eq. (13.11):

$$\begin{aligned} &-M_{b0}u_{b0}\left(\boldsymbol{\omega}^2 - \omega_0^2\right) + \left(K_{b0} - \omega_0^2 M_{b0}\right)\ \left(\mathbf{u}_b - u_{b0}\right) \\ &= \begin{Bmatrix} A & A_m \\ 0 & 0 \end{Bmatrix} \text{diag}\left(\begin{Bmatrix} -A^T\mathbf{u} \\ \boldsymbol{\omega}^2 A_m^T \mathbf{u} \end{Bmatrix}\right) \begin{Bmatrix} \Lambda & 0 \\ 0 & \Lambda_m \end{Bmatrix} \begin{Bmatrix} \boldsymbol{\alpha} - \alpha_0 \\ \boldsymbol{\alpha}_m - \alpha_{m0} \end{Bmatrix} + M_{b0}\left(\mathbf{u}_b - u_{b0}\right)\left(\boldsymbol{\omega}^2 - \omega_0^2\right), \end{aligned} \tag{13.13}$$

where we have used the matrix decompositions of $\mathbf{K}$ and $\mathbf{M}$ in Eqs. (13.3) and (13.4). Equation (13.13) takes the final form of

$$\left\{-M_{b0}u_{b0}\ K_{b0} - \omega_0^2 M_{b0}\right\} \begin{Bmatrix} \Delta\boldsymbol{\omega}^2 \\ \Delta\mathbf{u}_b \end{Bmatrix} = A_b \text{diag}\left(\begin{Bmatrix} -A^T\mathbf{u} \\ \boldsymbol{\omega}^2 A_m^T \mathbf{u} \end{Bmatrix}\right) \Lambda_b \Delta\boldsymbol{\alpha}_b + M_{b0}\Delta\mathbf{u}_b\Delta\boldsymbol{\omega}^2, \tag{13.14}$$

where $\Delta\boldsymbol{\omega}^2 = \boldsymbol{\omega}^2 - \omega_0^2$, $\Delta\mathbf{u}_b = \mathbf{u}_b - u_{b0}$, $\Delta\boldsymbol{\alpha} = \boldsymbol{\alpha} - \alpha_0$, $\Delta\boldsymbol{\alpha}_m = \boldsymbol{\alpha}_m - \alpha_{m0}$, and

$$A_b = \begin{Bmatrix} A & A_m \\ 0 & 0 \end{Bmatrix},\ \Lambda_b = \begin{Bmatrix} \Lambda & 0 \\ 0 & \Lambda_m \end{Bmatrix},\ \Delta\boldsymbol{\alpha}_b = \begin{Bmatrix} \Delta\boldsymbol{\alpha} \\ \Delta\boldsymbol{\alpha}_m \end{Bmatrix}. \tag{13.15}$$

Equation (13.14) will be solved by means of fixed-point iterations [24] as discussed below.

13.3.1 Fixed-Point Formulation

From Eq. (13.14), we solve for $\Delta\boldsymbol{\omega}^2$ and $\Delta\mathbf{u}_b$ and obtain

$$\Delta\boldsymbol{\omega}^2 = (G_\omega A_b)\,\mathrm{diag}\left(\begin{Bmatrix} -A^T\mathbf{u} \\ \boldsymbol{\omega}^2 A_m^T\mathbf{u}\end{Bmatrix}\right)\Lambda_b\Delta\boldsymbol{\alpha}_b + (G_\omega M_{b0})\,\Delta\mathbf{u}_b\Delta\boldsymbol{\omega}^2. \tag{13.16}$$

and

$$\Delta\mathrm{u}_b = (G_u A_b)\,\mathrm{diag}\left(\begin{Bmatrix} -A^T & \mathbf{u} \\ \boldsymbol{\omega}^2 & A_m^T\mathbf{u}\end{Bmatrix}\right)\Lambda_b\Delta\boldsymbol{\alpha}_b + (G_u M_{b0})\,\Delta\mathbf{u}_b\Delta\boldsymbol{\omega}^2 \tag{13.17}$$

where $G_\omega = -\left\{u_0^T\ \lambda_0^T\right\} = -u_{b0}^T$ and $G_u = \left(K_{b0} - \omega_0^2 M_{b0} + \gamma u_{b0}u_{b0}^T M_{b0}\right)^{-1}\left(I - M_{b0}u_{b0}u_{b0}^T\right)$. To further reduce overestimation, we introduce the auxiliary variables

$$\Delta\mathbf{v} = \begin{Bmatrix} A^T\Delta\mathbf{u} \\ A_m^T\Delta\mathbf{u}\end{Bmatrix} = \begin{Bmatrix} A^T & 0 \\ A_m^T & 0\end{Bmatrix}\begin{Bmatrix}\Delta\mathbf{u} \\ \Delta\boldsymbol{\lambda}\end{Bmatrix} = A_b^T\Delta\mathbf{u}_b, \tag{13.18}$$

and from Eq. (13.17)

$$\Delta\mathbf{v} = \left(A_b^T G_u A_b\right)\ \mathrm{diag}\left(\begin{Bmatrix} -A^T\mathbf{u} \\ \boldsymbol{\omega}^2 A_m^T\mathbf{u}\end{Bmatrix}\right)\Lambda_b\Delta\boldsymbol{\alpha}_b + \left(A_b^T G_u M_{b0}\right)\Delta\mathbf{u}_b\Delta\boldsymbol{\omega}^2. \tag{13.19}$$

As a result, we have minimized the number of multiple occurrences of the same interval variables, the essential key step to reduce overestimation due to interval dependency [15]. From Eqs. (13.16), (13.17), and (13.19), the final fixed-point form equations are given by

$$\Delta\mathbf{u}_g = \left(GA_g\right)\mathrm{diag}\left(\begin{Bmatrix} -A^T\mathbf{u} \\ \boldsymbol{\omega}^2 A_m^T\mathbf{u}\end{Bmatrix}\right)\Lambda_b\Delta\boldsymbol{\alpha}_b + \left(GM_g\right)\Delta\mathbf{u}_b\Delta\boldsymbol{\omega}^2. \tag{13.20}$$

where

$$\Delta\mathbf{u}_g = \begin{Bmatrix}\Delta\boldsymbol{\omega}^2 \\ \Delta\mathbf{u}_b \\ \Delta\mathbf{v}\end{Bmatrix},\quad GA_g = \begin{Bmatrix} G_\omega A_b \\ G_u A_b \\ A_b^T G_u A_b\end{Bmatrix},\quad GM_g = \begin{Bmatrix} G_\omega M_{b0} \\ G_u M_{b0} \\ A_b^T G_u M_{b0}\end{Bmatrix}. \tag{13.21}$$

In the following, we introduce a new variant of the iterative enclosure method [26] to solve for the fixed-point equation (13.20).

13.3.2 Iterative Enclosure Method

From Eq. (13.20), we define the following iterative scheme

$$\Delta\mathbf{u}_g^{i+1} = \left(GA_g\right)\mathrm{diag}\left(\begin{Bmatrix} -A^T\mathbf{u}^i \\ \left(\boldsymbol{\omega}^2\right)^i A_m^T\mathbf{u}^i\end{Bmatrix}\right)\Lambda_b\Delta\boldsymbol{\alpha}_b + \left(GM_g\right)\Delta\mathbf{u}_b^i\left(\Delta\boldsymbol{\omega}^2\right)^i, \tag{13.22}$$

where $\Delta\mathbf{u}_g^{i+1}$ is the interval solution at iteration $i+1$, and $\Delta\mathbf{u}_b^i$ and $(\Delta\boldsymbol{\omega}^2)^i$ are entries of $\Delta\mathbf{u}_g^i$ at iteration i. Moreover,

$$\begin{Bmatrix} A^T\mathbf{u}^i \\ A_m^T\mathbf{u}^i\end{Bmatrix} = \begin{Bmatrix} A^T u_0 \\ A_m^T u_0\end{Bmatrix} + \Delta\mathbf{v},\ \left(\boldsymbol{\omega}^2\right)^i = \omega_0^2 + \left(\Delta\boldsymbol{\omega}^2\right)^i. \tag{13.23}$$

The initial guess at $i = 0$ is set as

$$\Delta \mathbf{u}_g^0 = \left(GA_g\right) \operatorname{diag}\left(\begin{Bmatrix} -A^T u_0 \\ \omega_0^2 A_m^T u_0 \end{Bmatrix}\right) \Lambda_b \Delta \boldsymbol{\alpha}_b, \tag{13.24}$$

and the iterations stop when there is no solution improvement in two consecutive steps, viz. when $\Delta \mathbf{u}_g^{i+1} = \Delta \mathbf{u}_g^i$. Now, denote the corresponding converged solution as $\Delta \mathbf{u}_g^*$. Due to isotonic inclusion of interval arithmetic [15], $\Delta \mathbf{u}_g^*$ guarantees to enclose the exact interval solution set and the outer solution can be obtained as $\mathbf{u}_g^{out} = \Delta \mathbf{u}_g^* + u_{g0}$ where $\mathbf{u}_g^{out}$ includes the squared frequency $\boldsymbol{\omega}^2$ and the associated modal shape $\mathbf{u}$.

13.4 Numerical Examples

The proposed IGEP formulation is implemented in INTLAB [27], which is an interval arithmetic extension package developed for the MATLAB environment. We test the performance of the proposed method, and apply interval modal analysis to a cantilever beam and a gable frame. The Interval solutions (IS) for the natural frequency and associated modal shapes are compared against those obtained from Monte Carlo predictions (MC) and nonlinear programming (NLP). We consider material uncertainties in both stiffness and mass. Numerical results show that IS guarantees to enclose the exact solution (NLP), and the corresponding computation time is negligible when compared with other methods.

13.4.1 Cantilever Beam

Consider now a uniform cantilever beam as shown in Fig. 13.1. The length of the beam is $L = 1$ m, and the cross section area and moment of inertia are $A = 6 \times 10^{-4}$ m^2 and $I = 1.8 \times 10^{-7}$ m^4 respectively. We use 10 equal-length two-node Bernoulli-Euler beam elements. For each element, we consider 5 % uncertainties in material properties, viz. mass density $\boldsymbol{\rho}_i = [7.605, 7.995] \times 10^3$ kg/m^3, and Young's modulus $\mathbf{E}_i = [195, 205]$ GPa ($i = 1, \ldots, 10$). Figure 13.2 reports the interval solutions for the lowest natural frequency $\mathbf{f}_1$ as function of the uncertainty level β (up to 30 %) in mass density $\boldsymbol{\rho}_i$ and Young's modulus $\mathbf{E}_i$ for each element. Note that the interval solution (IS) obtained from the proposed method always contains the reference NLP solution and MC predictions from an ensemble of 10,000 simulations. Figure 13.3 shows that IS guarantees to enclose both NLP and MC solutions, regardless of the type of probability distribution used to model uncertainties.

13.4.2 Gable Frame

Consider the gable frame whose overall geometry is shown in Fig. 13.4. We assume standard rolled steel sections [28]. In particular, W21 × 44 is used for the rafters, W21 × 50 is used for the columns, and HSS7 × 7 × 1/4 is used for the HSS column. Geometric and material properties, such as the cross section area A, moment of inertia I, Young's modulus $\mathbf{E}$, and mass density $\boldsymbol{\rho}$, are listed in Table 13.1. We consider 20 % uncertainty in $\mathbf{E}$ and 5 % uncertainty in $\boldsymbol{\rho}$. In addition, since we use two beam elements to model each haunch, we list two different cross section properties for the haunches in Table 13.1.

The IFEM model for the gable frame consists of 37 two-node Euler-Bernoulli beam elements. We use 6 elements to model each column, 12 elements for each rafter (including the two used for each haunch), and one element for the HSS column. We assume that the gable frame is hinged to the ground, and the HSS column is subject to axial deformation only. For the

Fig. 13.1 A cantilever beam

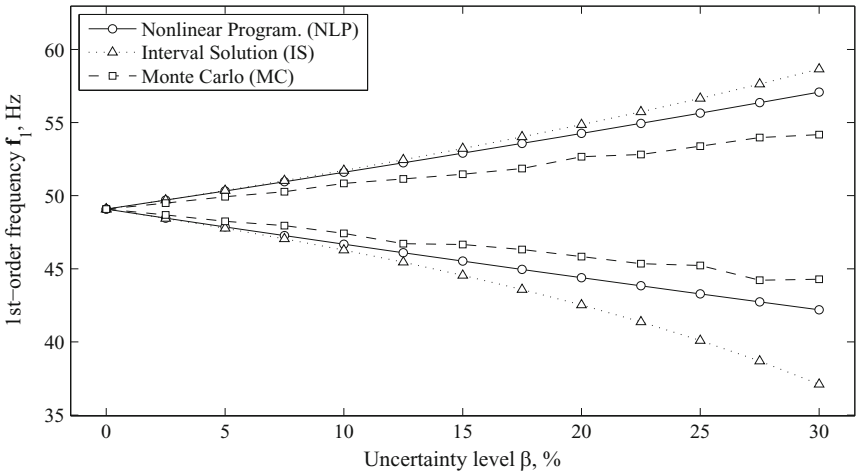

Fig. 13.2 Cantilever beam of Fig. 13.1: enclosure of the 1st-order frequency $\mathbf{f}_1$ as a function of the uncertainty level β (up to 30 %) in element mass density $\boldsymbol{\rho}_i$ and Young's modulus $\mathbf{E}_i$. *IS* interval solution, *MC* Monte Carlo solution from an ensemble of 10,000 simulations and *NLP* nonlinear programming reference solution

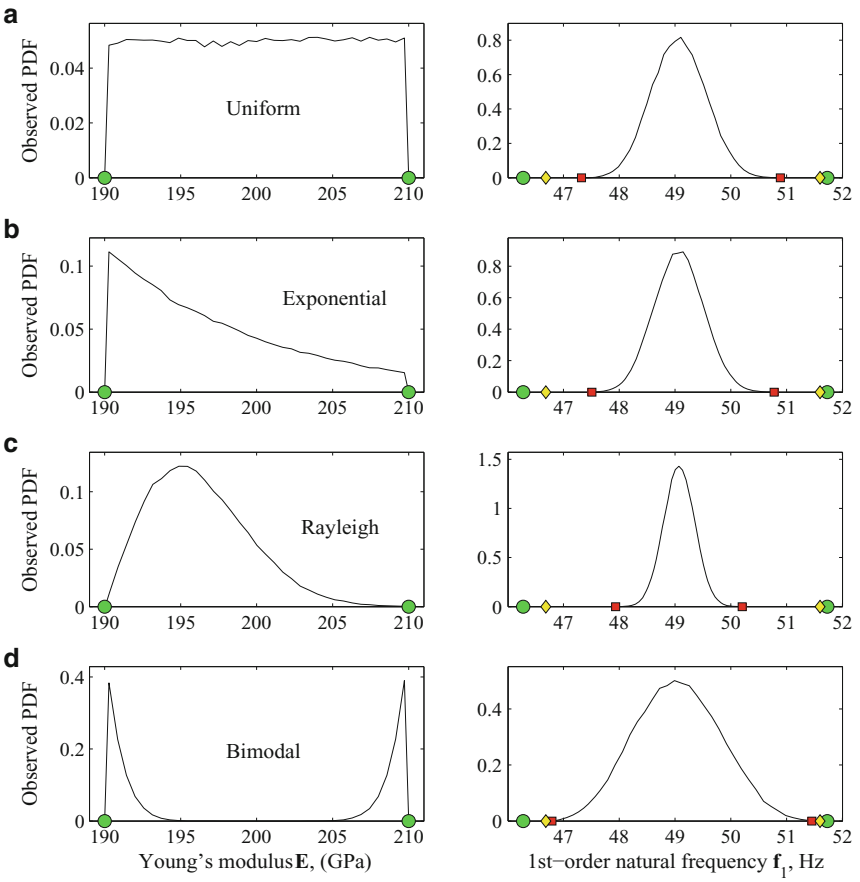

Fig. 13.3 Cantilever beam of Fig. 13.1: (*Left*) observed probability density function (PDF) of the Young's modulus $\mathbf{E} = [195, 205]$ GPa (5 % uncertainty) sampled from (**a**) uniform, (**b**) exponential, (**c**) Rayleigh, and (**d**) bimodal probability distributions (interval endpoints denoted by *circular markers*); (*right*) observed PDF of the first-order natural frequency $\mathbf{f}_1$ of the Interval solution (IS, endpoints denoted by *circular markers*), nonlinear programming (NLP, endpoints denoted by *diamond markers*) and Monte Carlo predicted interval $[\min(f_1)\ \max(f_1)]$ from an ensemble of 100,000 simulations (MC, *square markers*)

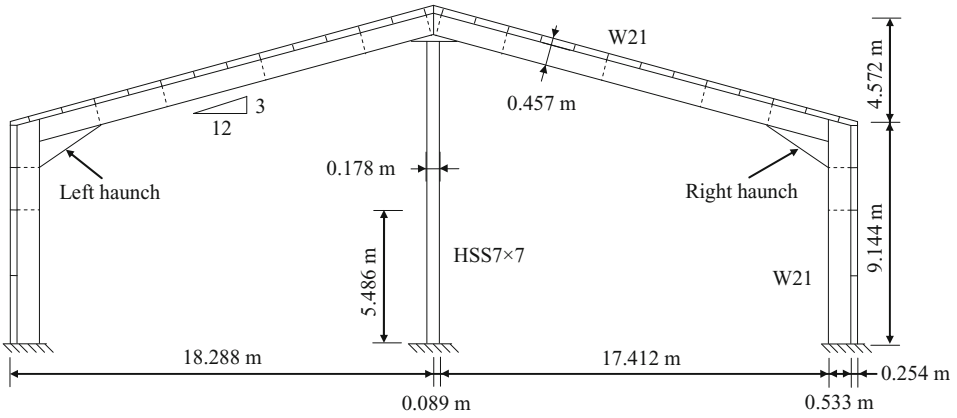

Fig. 13.4 A gable frame with a hollow structural section (HSS) column at the mid-span

Table 13.1 Gable frame of Fig. 13.4: geometric and material properties

	A (10^{-3} m^2)	I (10^{-4} m^4)	**E** (GPa)	$\boldsymbol{\rho}$ (10^3 kg/m^3)
Rafters	8.387	3.509	[180, 220]	[7.605, 7.995]
Columns	9.484	4.096	[180, 220]	[7.605, 7.995]
HSS column	3.980	0.193	[180, 220]	[7.605, 7.995]
Haunch Section 1	14.88	28.45	[180, 220]	[7.605, 7.995]
Haunch Section 2	10.55	8.573	[180, 220]	[7.605, 7.995]

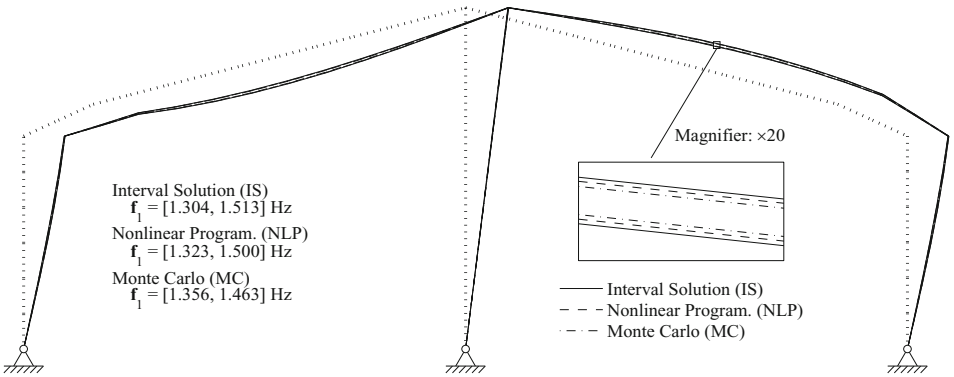

Fig. 13.5 Gable frame of Fig. 13.4: enclosure of the natural frequency $\mathbf{f}_1$, and corresponding modal shapes. Mass density $\boldsymbol{\rho}_i$ and Young's modulus $\mathbf{E}_i$ under 5 and 20 % uncertainties respectively. *IS* interval solution (*solid line*), *NLP* nonlinear programming (*dashed line*) and *MC* Monte Carlo prediction from an ensemble of 100,000 simulations (*dash-dotted line*)

columns and rafters (including the haunch), the corresponding Young's moduli and mass densities at the integration points are linearly interpolated from 13 material mesh nodes. For the HSS column, the corresponding Young's modulus and mass density are $\mathbf{E}_{14}$ and $\boldsymbol{\rho}_{14}$, respectively.

We compute the lowest four natural frequency $\mathbf{f}_1$, and display the corresponding modal shapes of the gable frame in Fig. 13.5. The undeformed frame configuration is also displayed (dotted lines). In addition, the interval solution (IS, solid lines) from the proposed method is compared against solutions obtained from the nonlinear programming approach (NLP, dashed lines) and Monte Carlo predictions (MC, dash-dotted lines) from an ensemble of 100,000 simulations. We observe that IS guarantees to enclose the exact solution NLP, which encloses MC. Further, the overestimation of IS is smaller than the underestimation of MC. Finally, we point out that the computational time for IS is 1.2 s, which is several order of magnitude less than that required by NLP (993 s) and MC methods (2889 s for 100,000 simulations).

13.5 Conclusions

We have presented a new interval approach for the analysis of natural frequencies and modal shapes of elastic structures with uncertain geometric and material properties. The method is based on the Interval Finite Element Method (IFEM). Numerical examples show that the proposed method (1) guarantees to sharply enclose the exact reference solution obtained via nonlinear programming techniques and that (2) its efficiency is superior to that of other available methods in the literature. Further, our numerical results provide strong evidence that the new decomposition strategy for the interval matrices **K** and **M** successfully reduces overestimation due to interval dependency. In addition, the iterative enclosure method can be applied to solve interval generalized eigenvalue problem associated with the modal analysis.

References

1. Ellingwood, B.R., Kinali, K.: Quantifying and communicating uncertainty in seismic risk assessment. Struct. Saf. **31**, 179–87 (2009)
2. Lutes, L.D., Sarkani, S.: Analysis of stochastic processes. In: Lutes, L.D., Sarkani, S. (eds.) Random Vibrations: Analysis of Structural and Mechanical Systems. Butterworth-Heinemann, Burlington (2004)
3. Wan, H., Mao, Z., Todd, M.D., Ren, W.: Analytical uncertainty quantification for modal frequencies with structural parameter uncertainty using a Gaussian process metamodel. Eng. Struct. **75**, 577–589 (2014)
4. Moens, D., Hanss, M.: Non-probabilistic finite element analysis for parametric uncertainty treatment in applied mechanics: recent advances. Finite Elem. Anal. Des. **47**, 4–16 (2011)
5. Zhang, M.Q., Beer, M., Quek, S.T., Choo, Y.S.: Comparison of uncertainty models in reliability analysis of offshore structures under marine corrosion. Struct. Saf. **32**, 425–432 (2010)
6. Adhikari, S., Khodaparast, H.H.: A spectral approach for fuzzy uncertainty propagation in finite element analysis. Fuzzy Set. Syst. **243**, 1–24 (2014)
7. Klir, G.J., Wierman, M.J.: Uncertainty-Based Information - Elements of Generalized Information Theory. Physica-Verlag, Heidelberg (1999)
8. Dempster, A.P.: Upper and lower probabilities induced by a multi-valued mapping. Ann. Math. Stat. **38**, 325–339 (1967)
9. Shafer, G.: A Mathematical Theory of Evidence. Princeton University Press, Princeton (1968)
10. Corliss, G., Foley, C., Kearfott, R.B.: Formulation for reliable analysis of structural frames. Reliab. Comput. **13**(2), 125–147 (2007)
11. Impollonia, N., Muscolino, G.: Interval analysis of structures with uncertain-but-bounded axial stiffness. Comput. Methods Appl. Mech. Eng. **220**(21–22), 1945–1962 (2011)
12. Muhanna, R.L., Zhang, H., Mullen, R.L.: Combined axial and bending stiffness in interval finite-element methods. J. Struct. Eng. **133**(12), 1700–1709 (2007)
13. Alefeld, G., Herzberger, J.: Introduction to Interval Computation. Academic, San Diego (1983)
14. Kulisch, U.W., Miranker, W.L.: Computer Arithmetic in Theory and Practice. Academic, New York (1981)
15. Moore, R.E., Kearfott, R.B., Cloud, M.J.: Introduction to Interval Analysis. Society for Industrial and Applied Mathematics, Philadelphia (2009)
16. Neumaier, A.: Interval Methods for Systems of Equations. Cambridge University Press, New York (1990)
17. Muhanna, R.L., Mullen, R.L.: Uncertainty in mechanics problems – interval-based approach. J. Eng. Mech. ASCE **127**(6), 557–566 (2001)
18. Muhanna, R.L., Zhang, H.: Interval finite elements as a basis for generalized models of uncertainty in engineering mechanics. Reliab. Comput. **13**, 173–194 (2007)
19. Pownuk, A. Calculation of the extreme values of displacements in truss structures with interval parameters. Available online at: http://andrzej.pownuk.com/php/ansys2interval/ (2004)
20. Yang, Y., Cai, Z., Liu, Y.: Interval analysis of frequency response functions of structures with uncertain parameters. Mech. Res. Commun. **47**, 24–31 (2013)
21. Leng, H.: Real eigenvalue bounds of standard and generalized real interval eigenvalue problems. Appl. Math. Comput. **232**, 164–171 (2014)
22. Sofi, A., Muscolino, G., Elishakoff, I.: Natural frequencies of structures with interval parameters. J. Sound Vib. **347**, 79–95 (2015)
23. Wang, C., Gao, W., Song, C., Zhang, N.: Stochastic interval analysis of natural frequency and mode shape of structures with uncertainties. J. Sound Vib. **333**, 2483–2503 (2014)
24. Xiao, N., Muhanna, R. L., Fedele, F., Mullen, R. L.: Interval finite elements for uncertainty in frame structures. 11th International Conference on Structural Safety & Reliability, New York, 16–20 June 2013
25. Rama Rao, M.V., Mullen, R.L., Muhanna, R.L.: A new interval finite element formulation with the same accuracy in primary and derived variables. Int. J. Reliab. Saf. **5**(3/4), 336–367 (2011)
26. Neumaier, A., Pownuk, A.: Linear systems with large uncertainties, with applications to truss structures. Reliab. Comput. **13**(2), 149–172 (2007)
27. Rump, S.M.: INTLAB - INTerval LABoratory. In: Csendes, T. (ed.) Developments in Reliable Computing, pp. 77–104. Kluwer Academic Publishers, Dordrecht (1999). http://www.ti3.tu-harburg.de/rump/intlab/
28. American Institute of Steel Construction, Inc.: Steel construction manual, 13th edn. ISBN 1-56424-055-X (2005)

Chapter 14
Model-Based Effects Screening of Stringed Instruments

R. Viala, V. Placet, S. Cogan, and E. Foltête

Abstract Luthiery is a secular art of craftsmanship, consisting in the selection of the best pieces of wood chosen for their texture, tone, and appearance. These pieces are then carved and assembled according to traditional methods, transmitted from master to apprentice. Instrument makers, as well as scientists, have always been interested in the complex vibratory and acoustic behavior of these assemblies and have sought to understand the physical interactions between the bow and the strings of violins. Nowadays, virtual prototyping enables researchers to study complex structures in aerospace, industry, automotive domains, and is used since the late 1970s to study musical instruments, either to predict their behavior or to explore new shapes and materials for their construction. In this study, we have modeled an unmounted violin composed of numerous solids. As violins are made of wood, the inherent orthotropic properties have been implemented for the principle parts of the instrument. The modal behavior of the assembly has been computed and an effects screening analysis performed to rank the influence of the different material properties of each part with respect to their impact on the modal behavior of the whole instrument.

Keywords Effects screening • Violin • Modal analysis • Orthotropic material • Wood

Nomenclature

$[S]$	Compliance tensor
S_{ij}	Component of compliance tensor in i,j directions
$\{\sigma\}$	Stress tensor
$\{\varepsilon\}$	Strain tensor
σ_{ij}	Stress component in i,j directions
ε_{ij}	Strain component in i,j directions
E_i	Young's modulus in i direction
ν_{ij}	Poisson's ration in i,j directions
G_{ij}	Shear modulus in i,j directions
ρ	Density
MC	Moisture content
RH	Relative humidity
$[Y^i]$	Modal matrix of i set of mode
$\{y^i_j\}$	Eigenvector j of i set of mode
L	Longitudinal
R	Radial
T	Tangential

R. Viala (✉) • V. Placet • S. Cogan • E. Foltête
Department of Applied Mechanics, University of Bourgogne Franche-Comté, FEMTO-ST Institute, 24, rue de l'Epitaphe, 25000 Besançon, France
e-mail: romain.viala@univ-fcomte.fr

S. Atamturktur et al. (eds.), *Model Validation and Uncertainty Quantification, Volume 3*, Conference Proceedings of the Society for Experimental Mechanics Series, DOI 10.1007/978-3-319-29754-5_14

14.1 Introduction

Physics-based numerical models are used in a wide range of engineering applications to guide analysts through the complex design and certification process. This paradigm is used extensively to analyze the static and dynamic behaviors of structures where analytical definitions are insufficient to describe their geometric, mechanical, and material complexity. Numerical models of guitar soundboards were first implemented by Schwab in 1976 [1] and in 1978, Knott used the Nastran finite element software to compute the modal basis of a violin and compared it to the experimental modal basis acquired from a holographic fringe pattern technique [2]. Numerous models have since been created and compared with experiments to study either parts of instruments, such as bars by Bretos in 1999 [3], or complete instruments, such as the detailed vibroacoustic study on a violin by Pyrkosz in 2014 [4]. Analytical methods have been used to investigate the sensitivity of instrument components to their geometry and material properties, for example Davis in 2013 who studied a violin top and back under free boundary conditions [5].

In 2014, the FEMTO-ST Institute has promoted a research activity focused on the virtual prototyping of stringed musical instruments which has lead to the installation of a dedicated luthier workshop with vibration testing and numerical modeling capabilities. The objective is to gain insight into the subtle physics involved in the vibroacoustics of stringed instruments, such as the bridge hill effect [6, 7] that corresponds to an amplification of the admittance of the bridge of the violin between 2000 and 3000 Hz and is curiously not observed in all the violins. This paper takes a first step toward a better understanding the bridge hill effect by ranking the relative impact of the different orthotropic material properties for the numerous components of a violin on its modal behavior.

14.2 Material Modelling

Both hardwoods and softwoods are used for all the parts of the violin.

- Maple *(acer pseudoplatanus)* is used for the neck, sides, bridge
- Ebony *(diospyros crassiflora)* is used for the fingerboard, tailpiece, chinrest, button and tuning pegs
- Rosewood *(dalbergia nigra)* is used for accessories, such as tailpiece, chinrest, button and tuning pegs
- Spruce *(picea abies)* is used for the soundboard, bass bar, corners, top and bottom end blocks and ribs

The wood will be defined as a homogeneous, orthotropic, elastic, and hygroscopic material. The question of non-homogeneous density and stiffness will not be taken into account in this study. Basically, wood can be described as extruded honeycombs created by cell walls, whose alveoli are in the RT plane. The Fig. 14.1 displays the main directions and plane of wood along a trunk.

An orthotropic definition of wood properties is convenient for the implementation of the parameters in the FEM code, defined in Cartesian system of coordinates, where the different directions L,R,T (respectively longitudinal, radial, tangential) reflect the different directions of anisotropy of wood. In the violin, pieces of wood are oriented in different ways. Material

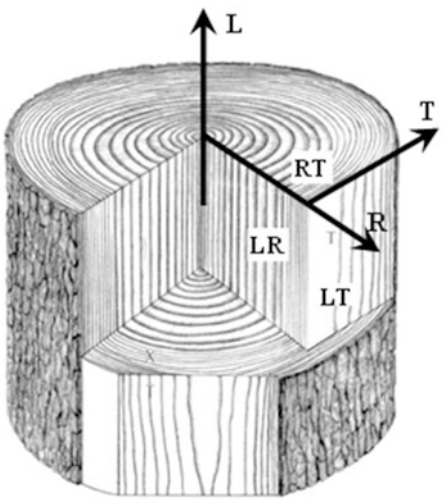

Fig. 14.1 Wood directions in the trunk, from Moutee [8]

properties are defined in local reference frames for each solid. Then this local reference frame is oriented to match the global reference coordinate system of the model. For clarity, the orientation of wood for each component will be described with respect to the trunk direction.

The material behavior laws implemented in this study follow the orthotropic elastic law given by (14.1):

$$\begin{Bmatrix} \sigma_L \\ \sigma_R \\ \sigma_T \\ \sigma_{LR} \\ \sigma_{RT} \\ \sigma_{TL} \end{Bmatrix} = [S]^{-1} \begin{Bmatrix} \varepsilon_L \\ \varepsilon_R \\ \varepsilon_T \\ 2\varepsilon_{LR} \\ 2\varepsilon_{RT} \\ 2\varepsilon_{TL} \end{Bmatrix} \tag{14.1}$$

The matrix $[S]$ is the compliance matrix, whose components are given by physical parameters of elasticity (at least 9 in the case of orthotropic elasticity since ν_{ij} is related to ν_{ji}. The compliance matrix is then given by (14.2):

$$[S] = \begin{bmatrix} S_{11=\frac{1}{E_L}} & S_{12} = -\frac{\nu_{LR}}{E_L} & S_{13} = -\frac{\nu_{TL}}{E_T} & & & \\ S_{21} = S_{12} = -\frac{\nu_{LR}}{E_L} & S_{22} = \frac{1}{E_R} & S_{23} = -\frac{\nu_{RT}}{E_R} & & 0 & \\ S_{31} = S_{13} = -\frac{\nu_{TL}}{E_T} & S_{32} = S_{23} = -\frac{\nu_{RT}}{E_R} & S_{33} = \frac{1}{E_T} & & & \\ & & & S_{44} = \frac{1}{G_{LR}} & & \\ & 0 & & & S_{55} = \frac{1}{G_{RT}} & \\ & & & & & S_{66} = \frac{1}{G_{TL}} \end{bmatrix} \tag{14.2}$$

The mechanical properties of wood are related to its density, or in other words, to the proportion of cell wall in the sample. In 1987, D. Guitard defined empirical laws that describe the variation of the stiffness parameters, as a function of its density, for both hardwoods and softwoods [9]. Those laws are a common way to obtain the order of magnitude of the compliance matrix parameters when studying wood where density is the only known parameter. These components are given as a function of density in Table 14.1. Reference densities for hardwoods and softwoods are respectively 0.65 and 0.45.

The density of the studied wood varies between −20 % and +10 % about the reference value for both hardwoods and softwoods, and this corresponds to the densities measured for samples of tonewood.[1] As mechanical properties are linked to density, this modifications of density affects the stiffness parameters. Their own variations are defined between −15 % and +15 % around references values for each parameter, which correspond to the variability at isodensity. Hygroscopicity of wood has to be taken into account, since variations of relative humidity (RH) drive the variation of moisture content (MC). Indeed, recent studies have quantified the impact of playing on the relative humidity [10] and the MC, by measuring the mass gained and lost during sorption cycle in standard utilization [11].

Table 14.1 Wood model used (values are given in MPa), from Guitard [9]

(−)	Hardwoods		Softwoods	
(−)	$\rho = 0.65$MC = 12 %	Correction	$\rho = 0.45$MC = 12 %	Correction
E_L	14,400	$\times\left(\frac{\rho}{0.65}\right)^{1.03}$	13,100	$+41,700\,(\rho - 0.45)$
E_R	1810	$\times\left(\frac{\rho}{0.65}\right)^{1.30}$	1000	$+2370\,(\rho - 0.45)$
E_T	1030	$\times\left(\frac{\rho}{0.65}\right)^{1.70}$	636	$+1910\,(\rho - 0.45)$
$\frac{E_L}{\nu_{LR}} = \frac{E_R}{\nu_{RL}} = -S_{LR}^{-1} = -S_{RL}^{-1}$	37,300	$\times\left(\frac{\rho}{0.65}\right)^{0.913}$	34,200	$+117,000\,(\rho - 0.45)$
$\frac{E_R}{\nu_{RT}} = \frac{E_T}{\nu_{TR}} = -S_{RT}^{-1} = -S_{TR}^{-1}$	2680	$\times\left(\frac{\rho}{0.65}\right)^{1.41}$	2050	$+5280\,(\rho - 0.45)$
$\frac{E_T}{\nu_{TL}} = \frac{E_L}{\nu_{LT}} = -S_{TL}^{-1} = -S_{LT}^{-1}$	31,200	$\times\left(\frac{\rho}{0.65}\right)^{1.09}$	30,800	$+101,000\,(\rho - 0.45)$
G_{LR}	1260	$\times\left(\frac{\rho}{0.65}\right)^{1.14}$	861	$+2080\rho - 0.45)$
G_{RT}	366	$\times\left(\frac{\rho}{0.65}\right)^{1.74}$	83.6	$+228\,(\rho - 0.45)$
G_{TL}	971	$\times\left(\frac{\rho}{0.65}\right)^{1.26}$	745	$+989\,(\rho - 0.45)$

[1] Carefully selected wood used specifically for soundboards in stringed instruments.

The variability of the MC is given by sorption isotherm curves of tonewood. Between 25 and 75 % of relative humidity at 21°C, the MC varies from 8 and 13 %. As wood absorbs water, its density and dimensions change, as well as the components of the compliance matrix, according to the empirical relations proposed by Guitard [9]:

$$\begin{aligned} E_L^{MC} &= E_L^{12} \times [1 - 0.015 \times (MC - 12)] \\ E_R^{MC} &= E_R^{12} \times [1 - 0.03 \times (MC - 12)] \\ E_T^{MC} &= E_L^{12} \times [1 - 0.03 \times (MC - 12)] \\ G_{LR}^{MC} &= G_{LR}^{12} \times [1 - 0.03 \times (MC - 12)] \\ G_{RT}^{MC} &= G_{RT}^{12} \times [1 - 0.03 \times (MC - 12)] \\ G_{TL}^{MC} &= G_{TL}^{12} \times [1 - 0.03 \times (MC - 12)] \\ \rho^{MC} &= \rho^{12}[1 - 0.01\,(MC - 12)] \end{aligned} \tag{14.3}$$

As this study focuses on the material properties and not on the geometric variations of the structure, the effects of MC on the geometrical properties of wood are not taken into account.

14.3 Numerical Implementation and Application

The instrument under study is an unmounted violin, without strings, bridge, chinrest, tailpiece, tuning pegs, soundpost that are generally left to the discretion of violin makers and musicians and can be easily changed. This study focuses on the modal behavior of the fixed components of the instrument. While the neglected parts undoubtedly affect on the vibratory behavior, playability and aesthetic of the violin, they must accommodate always be adapted to the instrument on which they are installed. From an organological point of view, an instrument is defined mainly by its fixed components. Studying unmounted violins singles out the variety of ways to build violins in terms of wood selection, dimensions, craftsmanship, and assembly. The varnish and neck reversing are not taken into account in this study. The computer-aided design (CAD) of the model has been built using Solidworks 2013 software and exported to the pre and post processing software MSC Patran 2013 as a parasolid file. The model contains nine different parts, corresponding to the soundboard, the bass bar (top left of Fig. 14.2), the back (bottom right), the neck, the fingerboard (top right), the sides, the ribs, the corners and the heels (bottom left).

Fig. 14.2 CAD parts of the violin

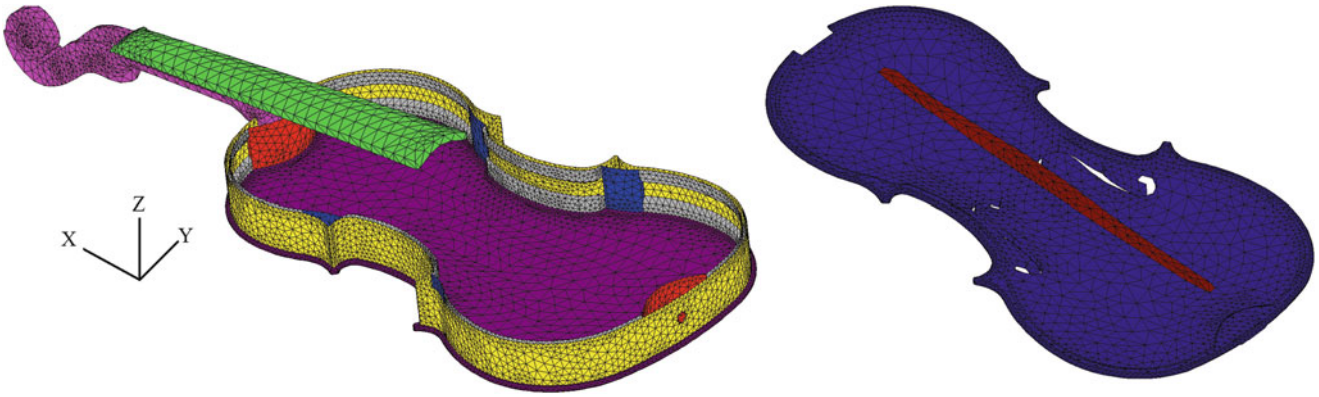

Fig. 14.3 Properties set of meshed violin

The finite element mesh is generated with quadratic tetrahedral elements to avoid overestimating the stiffness. The mesh is created at the same time for all of the parts in order to create coincident nodes at the different interfaces, shared by elements on both sides of the interfaces. The interfaces are defined as rigid connections between parts. In real violins, the different components are glued with hide glue implying that the interface stiffnesses are overestimated in the model. The resulting mesh is shown on Fig. 14.3 where the distinct material properties are displayed with different colors. The effects of the evolving orientation of the sides has not been implemented in the model but preliminary studies suggest that the stiffness parameters of the sides do not contribute significantly to the modal behavior of the instrument.

The orthotropic material properties for each component have been defined using the laws described above. A modal analysis has been calculated from 1 Hz to avoid rigid body modes to 3500 Hz and solved using MSC-Nastran. A Morris sensitivity analysis [12] has been used to drive the parameters screening with 10 trajectories and a total of 91 physical parameters corresponding to 10 parameters per component, 9 components, as well as the moisture content parameter that is applied the same way on all the parts. The number of calculations is given by N = number of trajectories*(number of parameters +1) which in our case leads to 920 computations, each run taking nearly 5 min for solving and post treatment. At each calculation, the reference modal basis has been compared with the modal basis with parameter modifications using a modal autocorrelation criterion (MAC) given by [13]:

$$(MAC)_{i,j} = \frac{\left| {}^{T}\{y_i^1\} \cdot \{y_j^2\} \right|^2}{\{y_i^1\}^2 \cdot \{y_j^2\}^2} \tag{14.4}$$

The MAC indicator is used to correlate two modal bases and yields a value between 0 (no correlation of eigenvectors) to 1 (complete correlation of eigenvectors e.g. same shape of modes). A mode matching algorithm is implement so that even if frequencies switch occurs when parameters vary, the MAC values remain physically meaningful. A set of features are extracted at each calculation, including eigenfrequencies, eigenvectors, modal density (number of modes per third octave bands) and modal overlap factor (overlap of modes per third octave bands) at given averaged damping ratio (0.6 %).

14.4 Results

Out a total of 91 parameters, the Morris analysis provides information on both the linear effects and coupling effects of parameters for the different features under study. The linear effects on the eigenfrequencies of all the parameters are ranked in Fig. 14.4.

The results indicate a preponderant effect of the moisture content, which influences all other material parameters simultaneously. This is no surprising since it induces variations from 88 to 103 % in the elastic parameters E_R, E_T, G_{LR}, G_{RT}, G_{TL} and from 94 to 101.5 % variations in the elastic parameter E_L. The effects of density variations are also significant due to the fact that they imply variations of mass in the structure but also due to the implied changes in the elastic parameters according to relationships presented in Table 14.1.

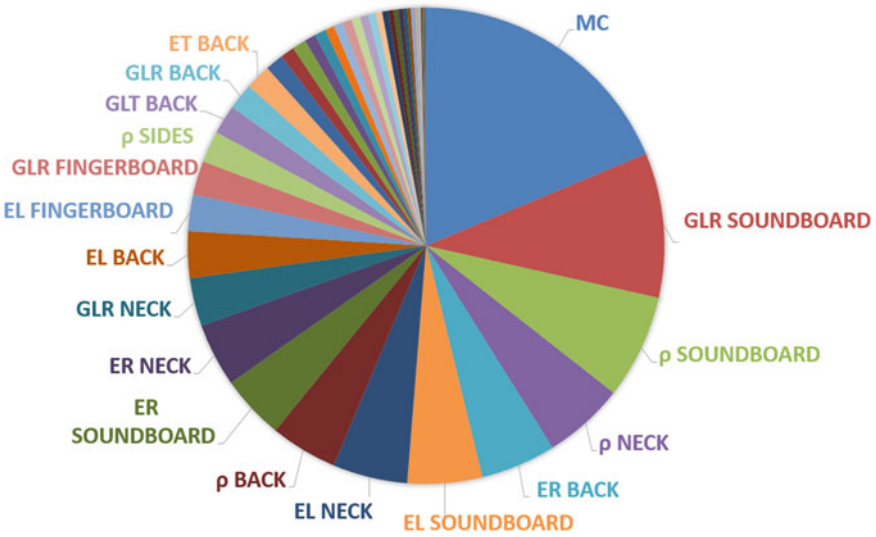

Fig. 14.4 Ranking of the parameters by their effects on the eigenfrequencies

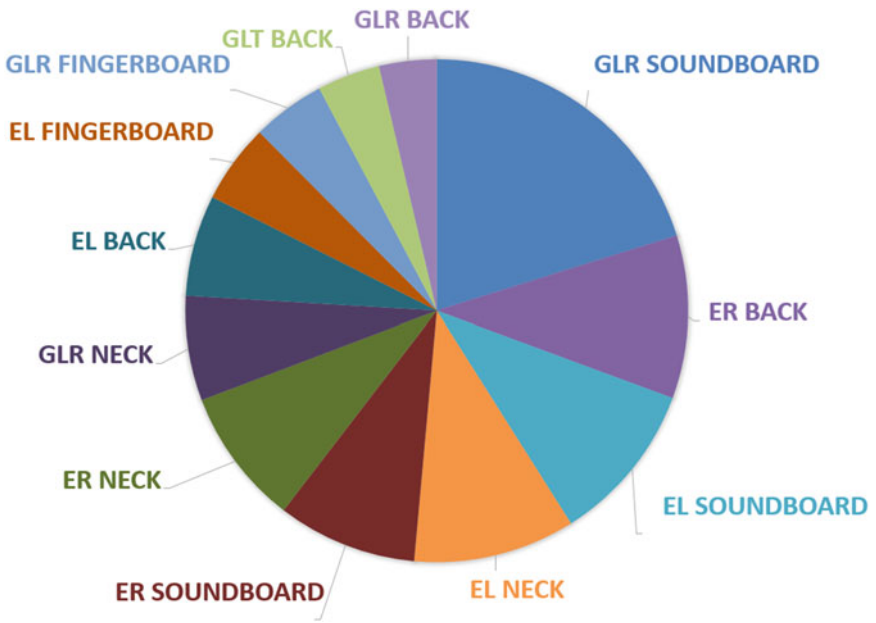

Fig. 14.5 Ranking of the elastic parameters by their effects on the eigenfrequencies

It is also worthwhile to screen material parameter variations at constant density and constant moisture content, reflecting the modeling and making of instruments with woods of known mass density and working under a stable relative humidity. These results are given on Fig. 14.5.

The shear modulus of the soundboard in the LR direction dominates when studying the eigenfrequencies of the violin. Indeed, instruments makers check the stiffness of soundboards by applying a torque to it, in other words, by testing the shear modulus in the LR directions at a given geometry. At low frequencies, the neck and fingerboard modes are mainly present, but less interesting acoustically than the soundboard modes, which is considered as the most important part of the violin for the sound emission.

14.5 Conclusion

A parametric model of a generic violin has been constructed using both CAD and FEM software as well as in-house post processing software to drive the effects screening analysis. This study has been performed to rank the material properties having a significant impact on the vibroacoustic behavior via the modal behavior of the instrument. Out of an initial set of 91 physical parameters a subset of only 20 are responsible for 90 % of the variations in the modal behavior of which moisture content proves to be preponderant.

The objective of this study is to highlight the most important factors that must to be taken into account when studying the modal response of stringed instruments. The next step will be to include geometry changes in the effects screening analysis as well as the material parameters included in this study in order to rank their contributions to the different features of interest, including eigenfrequencies, eigenvectors, modal overlap factor, and observed tendencies such as the bridge hill effect. This last effect will require the modeling of the full instrument including the bridge, strings and their tensions, tuning pegs, soundpost and tailpiece. The model developed for this study might also be used to compute the stress field inside the violin when the strings apply their tension on the bridge or when the violin is submitted to relative humidity variations, with the aim of investigating the sustainability of historical instruments.

References

1. Schwab, H.L.: Finite element analysis of a guitar soundboard. Catgut. Acoustical Soc. Newsl. **24**, 13–15 (1974)
2. Knott, G.A.: A Modal analysis of the violin using MSC/NASTRAN and PATRAN, Mechanics PhD thesis (1987)
3. Bretos, J., Santamaria, C., Alonso Moral, J.: Finite element analysis and experimental measurements of natural eigenmodes and random responses of wooden bars used in musical instruments. Appl. Acoust. **56**(3), 141–156 (1999)
4. Pyrkosz, M., Van Karsen, C.: Coupled vibro-acoustic model of the titian stradivari violin. In: International Modal Analysis Conference, Orlando FL, 3–6 February 2014
5. Davis, E.B.: On the effective material properties of violin plates. In: Stockholm Music Acoustics Conference, pp. 9–15 (2013)
6. Woodhouse, J.: On the 'bridge Hill' of the violin. Acta Acustica United Acustica **91**(1): 155–165 (2005)
7. Jansson, E.V.: Violin frequency response – bridge mobility and bridge feet distance. Appl. Acoustics **65**(12), 1197–1205 (2012). doi:10.1016/j.apacoust.2004.04.007
8. Moutee, M., Fortin, Y., Fafard, M.: "Modélisation du comportement mécanique du bois au cours du séchage" 2006. Adaptation of : Cloutier, A., "Anatomie et structure du bois. Notes de cours, chapitre 1" (2005)
9. Guitard, D.: Mecanique du materiau bois et composites. Collection Nabla, Toulouse (Cepadue-Editions) (1987)
10. Le Conte, S., Vaiedelich, S., François, M.: A wood viscoelasticity measurement technique and applications to musical instruments: first results. J. Violin Soc. Am. VSA Papers **21**, 1 (1997)
11. Goli, G., Fioravanti, M., Busoni, S., Carlson, B., Mazzanti, P.: Measurement and Modelling of Mass and Dimensional Variations of Historic Violins Subjected to Thermo-Hygrometric Variations: The Case Study of the Guarneri 'del Gesù' Violin (1743) Known as the 'Cannone'. J. Cult. Herit. **13**(3), S154–S160 (2012). doi:10.1016/j.culher.2012.04.007
12. Morris, M.D.: Factorial sampling plans for preliminary computational experiments. Technometrics **33**, 161–174 (1991)
13. Allemang, R.J., Brown, D.L.: A correlation coefficient for modal vector analysis. In: Proceedings of the International Modal Analysis Conference, pp. 110–116 (1982)

Chapter 15
Innovation Dilemmas, Design Optimization, and Info-Gaps

Yakov Ben-Haim

Abstract Engineering designers seek innovative solutions to operational problems. The power of technological innovation is tremendous, and we invest great effort in training and promoting innovative design practice. However, one of the challenges in time-constrained design is that innovative ideas are usually less well understood than standard state of the art methods. This implies that innovative design solutions may contain hidden vulnerabilities that are absent from state of the art methods. While the innovative design may indeed be surprisingly better than the state of the art, it may also fail in surprising ways. We begin with a brief discussion of the non-probabilistic nature of ignorance. We then introduce the idea of an innovation dilemma and its resolution by info-gap robust-satisficing. We consider an example from the analysis of stress concentration around holes with uncertain shape.

Keywords Innovation dilemma • Info-gap • Robustness • Engineering design • Stress concentration

15.1 What Is Info-Gap Theory?

Info-gap is a decision theory for prioritizing options and making choices under severe uncertainty [1, 2]. The options might be operational (design a system, choose a budget, decide to launch or not, etc.) or more abstract (choose a model structure, make a forecast, design a project flow chart, etc.). One uses data, scientific theories, empirical relations, knowledge and contextual understanding, all of which I'll refer to as one's *models*. Many models quantify uncertainty with probability distributions. If the models are correct (or judged to be reliable) then one can exploit them exhaustively to reliably achieve optimal outcomes, and one doesn't need info-gap. If the models will be much better next year when new knowledge has become available (but you must decide now), or if processes are changing in poorly known ways, or if important factors will be determined beyond your knowledge or control, then one faces severe uncertainties and info-gap theory might help.

15.2 Info-Gaps, Knightian Uncertainty, Ignorance, and Probability

Knight [9] distinguished between 'risk' (for which probability distributions are known) and 'true uncertainty' (for which probability distributions are not known). Knightian ('true') uncertainty reflects ignorance of underlying processes, functional relationships, strategies or intentions of relevant actors, future events, inventions, discoveries, surprises and so on. Info-gap models of uncertainty provide a non-probabilistic quantification of Knightian uncertainty. An info-gap is the disparity between what you *do know* and what you *need to know* in order to make a reliable or responsible decision. An info-gap is not ignorance *per se,* but rather those aspects of one's Knightian uncertainty that bear on a pending decision and the quality of its outcome.

An info-gap model of uncertainty is particularly suitable for representing uncertainty in the shape of a function. For instance, one might have an estimate of the stress-strain curve, or of a probability density function, but the shape of the function (e.g. the shape of the elastic-plastic transition or the tails of the pdf) may be highly uncertain. Info-gap models are also widely used to represent uncertainty in parameters or vectors or sometimes even in sets of such entities.

Y. Ben-Haim (✉)
Faculty of Mechanical Engineering, Yitzhak Moda'i Chair in Technology and Economics,
Technion—Israel Institute of Technology, Haifa, Israel
e-mail: yakov@technion.ac.il

S. Atamturktur et al. (eds.), *Model Validation and Uncertainty Quantification, Volume 3*, Conference Proceedings
of the Society for Experimental Mechanics Series, DOI 10.1007/978-3-319-29754-5_15

Info-gap theory is for the epistemically impoverished. If your models (including probability models) are basically correct, then you don't need info-gap theory. Otherwise, maybe info-gap can help protect against adverse uncertainty or exploit favorable uncertainty.

15.3 Optimize or Satisfice?

There is a moral imperative to do one's best: to optimize the outcome of one's decisions. That usually means to use one's best models to achieve the best possible outcomes. While optimization may have prohibitive psychological costs [10], or one may simply not need the best possible mouse trap, the aspiration for excellence is usually to be commended.

Outcome-optimization is the process of using one's models to choose the decision whose outcome will be best. This works fine when the models are pretty good, because exhaustively exploiting good models will reliably lead to good outcomes.

However, when one faces major info-gaps, then one's models hide major flaws, and exhaustively exploiting the models can be unrealistic, unreliable, and can lead to major shortfalls and poor decisions [3]. Under severe uncertainty it is better to ask: what outcomes are critical and must be achieved? This is the idea of *satisficing,* introduced by Herbert Simon [12].

While engineering designers may use the language of optimization (the lightest, the strongest, the fastest, ...), in practice, engineers have been satisficing for ages: satisfying a design specification (light enough, strong enough, fast enough, ...). Furthermore, in competitive situations, one only needs to design a product that is better (lighter, stronger, faster, ...) than the competition's product. Beating the competition means satisficing a goal. Engineering progress is piecemeal, one improvement at a time, sometimes converging on an unspecified optimum, but more often diverging innovatively over the unbounded space of design possibilities.

15.4 Robustness: Trade Off and Zeroing

It commonly happens that several or many alternative designs all satisfy the design requirements. A single option must be chosen, which may be done by optimizing some exogenous variable (such as cost). However, when dealing with major info-gaps, it is better to prioritize the putatively adequate options according to their robustness against Knightian uncertainty.

Consider a design option that satisfies the performance requirements according to one's models. One then asks: how wrong can those models be, and this design will *still* satisfy the requirements? Equivalently: how robust against (or tolerant to) uncertainty is this design? A design that is more robust against uncertainty is preferred over a design that is less robust. This prioritization of the design options is called *robust-satisficing*: one prioritizes according to the robustness for satisficing the performance requirements.

Each design is characterized by a robustness curve as shown schematically in Fig. 15.1. The horizontal axis represents the performance requirement, where a large value is better than a small value (e.g. long life or high stiffness is better than short or low values). The vertical axis is the robustness: the degree of immunity against ignorance, surprise, or uncertainty. The robustness curve displays two universal characteristics: trade off and zeroing.

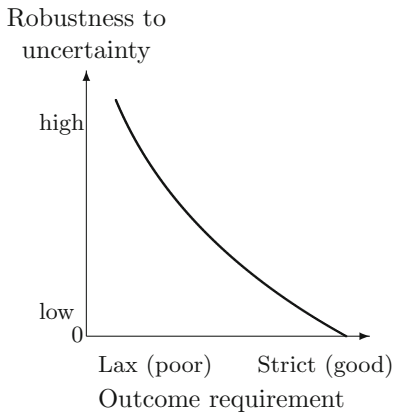

Fig. 15.1 Robustness vs requirement

The negative slope represents the *trade off between robustness and performance*: strict performance requirements, demanding very good outcome, are less robust against uncertainty than lax requirements. This trade off quantifies the intuition of any healthy pessimist: higher aspirations (more demanding requirements) are more vulnerable to surprise than lower aspirations.

The second property illustrated in Fig. 15.1 is *zeroing*: The robustness precisely equals zero when the outcome requirement equals the outcome that is predicted by the models. Models reflect our best understanding of the system and its environment. Nonetheless, the zeroing property means that model predictions are not a good basis for design decisions, because those predictions have no robustness against errors in the models. Recall that we're discussing situations with large info-gaps. If your models are correct (no info-gaps), then you don't need robustness.

The zeroing property asserts that the predicted outcome is not a reliable characterization of the design. The trade off property quantifies how much the performance requirement must be reduced in order to gain robustness against uncertainty. The slope of the robustness curve reflects the cost of robustness: what decrement in performance "buys" a specified increment in robustness. Outcome-quality can be "sold" in exchange for robustness, and the slope quantifies the cost of this exchange.

Info-gap robustness is non-probabilistic: it does not employ probability distributions and it does not explicitly provide insight about the likelihood of satisfying the design requirements. However, in many situations it is nonetheless true that a more robust design does indeed have greater probability of satisfying the requirements than a less robust design. When this is true we say that robustness is a "proxy" for probability. One can then maximize the likelihood of satisfying the requirements without knowing the probability distributions at all: one maximizes the info-gap robustness [5]. One will not know the value of this maximum probability of success because the probability distributions are unknown. However, one will nonetheless have found the design with greatest probability of success.

15.5 Preference Reversals and Innovation Dilemmas

Figure 15.2 shows schematic robustness curves for two designs. Design 1 is predicted, by the models, to have a better outcome than design 2: the horizontal intercept for design 1 is to the right of (better than) the horizontal intercept for design 2. However, from the zeroing property we know that this is not a good basis for preferring design 1 over design 2: these predictions have zero robustness against info-gap s. Furthermore, in this particular case the robustness curves cross one another, reflecting different costs of robustness for the two designs.

Suppose that the outcome requirement is somewhere between the predicted outcome for design 1 (horizontal intercept in Fig. 15.2) and the outcome at which the robustness curves cross one another ($r_\times$). Design 1 is more robust than design 2 for this outcome requirement. The robust satisficing designer will therefore prefer design 1 over design 2. Note that the outcome-optimizer, ignoring severe uncertainty, would also prefer design 1, but for a different reason: design 1 is predicted to be better than design 2. Outcome-optimization is a good basis for prioritization only if the models are reliable and we are not in a situation of severe uncertainty.

Now suppose that the outcome requirement is less than $r_\times$. Design 2 is more robust than design 1 for this requirement, and the robust satisficer will prefer design 2. The outcome-optimizer still prefers design 1, so these design strategies now prioritize the options differently.

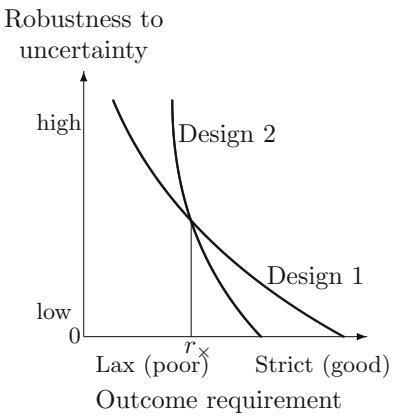

Fig. 15.2 Preference reversal between two designs

The crossing robustness curves in Fig. 15.2 reflect the possibility of a *preference reversal*: design 1 is preferred for larger outcome requirements, while design 2 is preferred for less demanding requirements.

Preference reversals are particularly common when facing an *innovation dilemma* [4, 7]. Consider the choice between a new, innovative and highly promising design, and a more standard state-of-the-art design. The innovation is less familiar and more uncertain because it is new. Prioritizing these two design options is an innovation dilemma: should one choose the putatively better but more uncertain innovation, or the less uncertain standard option?

In Fig. 15.2, design 1 is the innovative option and design 2 is the state of the art. Design 1 is putatively better (horizontal intercept further right), but more uncertain (lower slope; higher cost of robustness). The dilemma is expressed by the intersection of the robustness curves, and resolved as a preference reversal. One chooses the option that is more robust for the specified performance requirements.

15.6 Robust-Satisficing and Max-Min

Wald [13] studied statistical decisions when prior probability distributions are uncertain but bounded within a set of possible distributions. Based on identifying the most pernicious distribution, Wald proposed the idea of min-max: minimize the maximum possible loss. Wald's contribution was seminal by dealing non-probabilistically with uncertainty in probability distributions. (Note that max-min and min-max differ only in whether one is concerned with gain or loss respectively.)

Decisions based on info-gap robust-satisficing sometimes agree with Wald's max-min and sometimes do not, as explained with Fig. 15.3 and elsewhere [6].

In order to compare max-min with info-gap robustness in Fig. 15.3 one must understand that the vertical axis—robustness to uncertainty—can be thought of as a level of uncertainty (the greatest tolerable level). The method of max-min presumes knowledge of the level of uncertainty (which underlies identification of the worst case) and this known level of uncertainty is marked on the vertical axis. Design 2 is the max-min choice between the two designs in Fig. 15.3 at the specified known level of uncertainty. This is because outcome r_1 is the worst that can occur with design 2 and it is better than r_0 (the worst with design 1 at this known level of uncertainty).

Robust-satisficing agrees with the max-min choice if the outcome requirement is for the value r_1 (or other values less than the curve intersection, $r_\times$ in Fig. 15.2). They agree on the design, but for different reasons. Max-min ameliorates the worst case at known uncertainty. Robust-satisficing maximizes immunity against unbounded uncertainty while satisfying a design specification. Their reasons differ because their information differs. Min-max uses knowledge of the worst case. Robust-satisficing does not use a worst case (the info-gap model is unbounded so a worst case is unknown) but does use knowledge of an outcome requirement.

Now suppose that the robust-satisficer's outcome requirement is r_2 in Fig. 15.3. In this case the robust-satisficing choice is for design 1, even if the designer agrees that uncertainty could be (or is) as large as what the max-min analyst knows it to be. The max-min choice is still for design 2, while the robust-satisficer disagrees.

Max-min and info-gap robust-satisficing share much in common, especially the non-probabilistic representation of uncertainty. However, they may or may not agree prescriptively, as we have just explained.

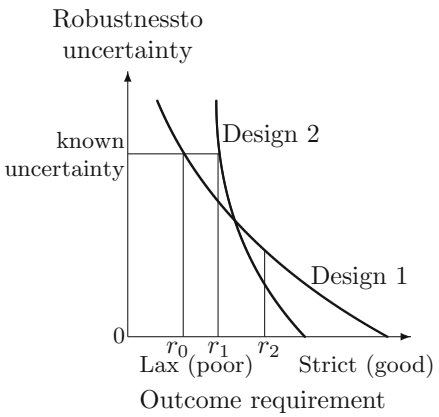

Fig. 15.3 Preference reversal between two designs

15.7 Innovation Dilemma in Design Against Stress Concentration

In this section we present a brief example of designing the pre-treatment of a drilled hole in an infinite plate, loaded at infinity with uniform radial stress, to deal with stress concentration on the boundary of the hole. This example is based on Sha'eir [11, Chap. 9].

15.7.1 Formulation

The hole is designed to be precisely circular with radius R. The actual radius, at azimuthal angle θ with respect to a reference direction, is $r(\theta)$. The fractional radius-deviation-function is defined as:

$$g(\theta) = \frac{r(\theta) - R}{R} \tag{15.1}$$

This is expanded in a truncated Fourier series as:

$$g(\theta) = \sum_{m=1}^{M} (A_m \cos m\theta + B_m \sin m\theta) \tag{15.2}$$

The Fourier coefficients are represented as a vector: $c^T = (A_1, \ldots, A_M, B_1, \ldots, B_M)$. The stress concentration factor at angle θ on the boundary of the hole, $\kappa(c, \theta)$, is a function of the shape of the hole [8] as expressed by the Fourier coefficients c.

The shape of the hole may deviate from the circular design specification due to uncertain manufacturing. Hence c is uncertain. We use an ellipsoid-bound info-gap model [1] to represent this uncertain shape:

$$\mathcal{U}(h) = \left\{c : \ (c - \tilde{c})^T W (c - \tilde{c}) \le h^2\right\}, \quad h \ge 0 \tag{15.3}$$

$\tilde{c}$ is the designer's best estimate of the Fourier coefficients. W is a real, symmetric, positive definite matrix representing the relative variability of the uncertain Fourier coefficients. Both $\tilde{c}$ and W are known. $\tilde{c}$ determines the centerpoint of the ellipsoid, and W determines its shape. The size of the ellipsoid is determined by h whose value is not known. Thus the info-gap model is not a single set of coefficients, but rather an unbounded family of nested sets. h represents the unknown horizon of uncertainty in the Fourier coefficients.

All info-gap models, of which Eq. (15.3) is a special case, have two properties. *Nesting* is the property that the uncertainty sets, $\mathcal{U}(h)$, become more inclusive as h increases. The nesting property endows h with its meaning as an horizon of uncertainty. *Contraction* is the property that $\mathcal{U}(0)$ is a singleton set: there is no uncertain variability of the Fourier coefficients when the horizon of uncertainty is zero.

The performance requirement, that the designer must satisfy, is that the stress concentration at the boundary of the hole not exceed a specified critical value, κ_c:

$$\max_{0 \le \theta \le 2\pi} \kappa(\theta, c) \le \kappa_c \tag{15.4}$$

However, the Fourier coefficients c are not known, so this equation, by itself, is not a operationally implemental basis for design. Nonetheless, the concept of robustness against uncertainty in the shape provides a solution.

We begin by requiring that the putative design—a hole with estimated Fourier coefficients $\tilde{c}$—satisfies the performance requirement in Eq. (15.4). The *robustness question* is: how large a deviation of the Fourier coefficients, c, from their estimated values $\tilde{c}$, can be tolerated without violating the performance requirement? Referring to the info-gap model in Eq. (15.3), the robustness question can be stated as: what is the maximum horizon of uncertainty, h, up to which all Fourier coefficients c in $\mathcal{U}(h)$, satisfy the performance requirement? The answer to this question is the robustness function, whose formal definition is:

$$\hat{h}(\kappa_c) = \max \left\{h : \ \left(\max_{c \in \mathcal{U}(h)} \max_{0 \le \theta \le 2\pi} \kappa(\theta, c)\right) \le \kappa_c\right\} \tag{15.5}$$

Reading this equation from left to right: the robustness (against shape uncertainty), $\hat{h}$, of performance requirement κ_c is the maximum horizon of uncertainty, h, up to which all shape realizations c in the set $\mathcal{U}(h)$ result in maximal stress concentration around the boundary that does not exceed κ_c.

15.7.2 Numerical Example

We now present a numerical example based on Sha'eir [11, Chap. 9]. The designer can choose between two alternatives: either *do* or *do not* polish the hole after drilling. The unpolished hole (design 1) has a putatively circular shape, but with the possibility of shape imperfections at high spatial frequency (entailing large stress concentration) due to manufacturing blemishes. The polished hole (design 2) is free of high-frequency shape imperfections, but the putative shape deviates from the nominal circular form due to small eccentricity of the polishing process.

We use the info-gap model of Eq. (15.3) where the shape matrix, W, is diagonal: $W = \pi\,\mathrm{diag}(s_1^{-2}, \ldots, s_M^{-2}, s_1^{-2}, \ldots, s_M^{-2})$. The two designs are specified as follows:

$$\text{Design 1:}\quad \tilde{c}^T = 0, \quad M = 100, \quad s_m = \frac{3}{2}(m+2),\ m = 1, \ldots, M \tag{15.6}$$

$$\text{Design 2:}\quad \tilde{c}^T \neq 0, \quad M = 20, \quad s_m = m,\ m = 1, \ldots, M \tag{15.7}$$

The elements of $\tilde{c}$ for design 2 are all zero except: $A_2 = 0.01$, $A_3 = 0.005$, $B_2 = -0.005$ and $B_5 = -0.055$. Thus design 1 is putatively better than design 2 ($\tilde{c} = 0$ is better than $\tilde{c} \neq 0$). However, design 1 is more uncertain than design 2 (large M and s_m entails greater uncertainty than small M and s_m). We have here an innovation dilemma, as we now explain.

The innovation dilemma is embodied in the robustness curves of the two designs, shown in Fig. 15.4. Design 1 (red) has a putative stress concentration factor (SCF) of 2.0, as seen from the horizontal intercept of its robustness curve. Design 2 (blue) has a putative SCF of 2.9, as seen from its horizontal intercept. Thus design 1 is putatively better than design 2.

We note, however, that the zeroing property asserts that the robustness for the designs to obtain these putative SCF's is zero, as seen from the value of the robustness at the horizontal intercepts.

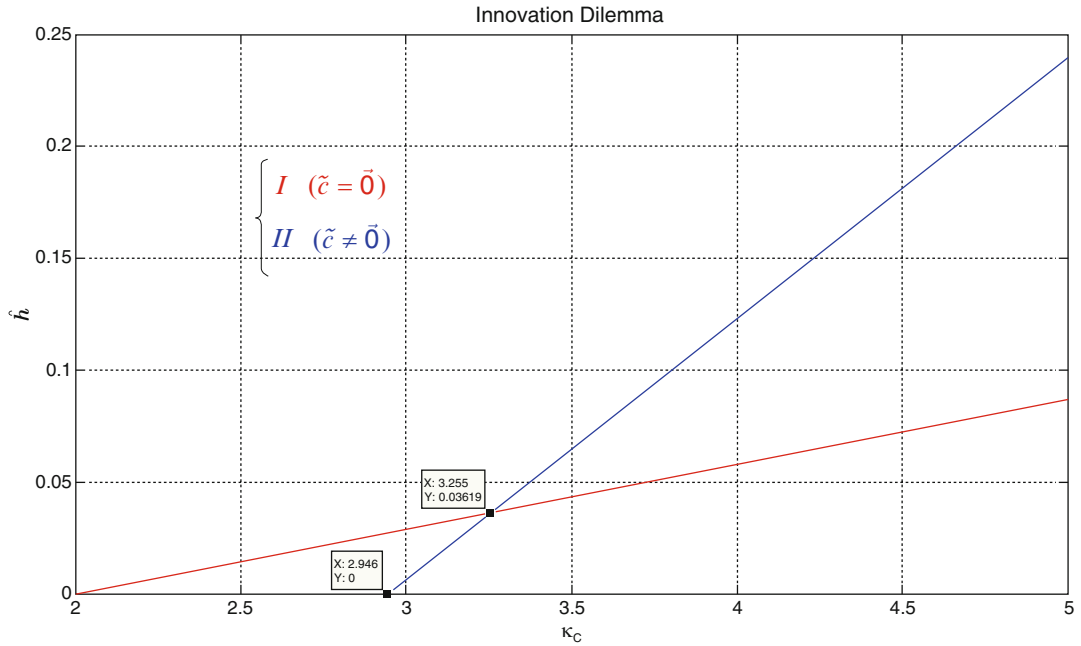

Fig. 15.4 Robustness, $\hat{h}(\kappa_c)$ vs. critical stress concentration, κ_c

Furthermore, the robustness trade offs are different for the two designs. The slope of the design-1 robustness curve is less than the slope for design 2. This implies that the cost of robustness is greater for design 1: the performance must be relaxed more with design 1 than with design 2 in order to achieve the same increase in robustness.

The innovation dilemma is that design 1 is putatively better but more uncertain than design 2. This is manifested in Fig. 15.4 by the intersection of the two robustness curves. The curve for design 1 is putatively better (horizontal intercept further to the left) but design 1 is more uncertain (lower slope); hence the curves intersect.

The resolution of the innovation dilemma is also represented by the intersecting robustness curves. The curves intersect at a critical SCF of 3.3. Design 1 is more robust, and hence preferred, if the designer requires an SCF less than 3.3, while design 2 is more robust, and hence preferred, if $\kappa_c > 3.3$ is acceptable.

References

1. Ben-Haim, Y.: Info-Gap Decision Theory: Decisions Under Severe Uncertainty, 2nd edn. Academic, London (2006)
2. Ben-Haim, Y.: Info-Gap Economics: An Operational Introduction. Palgrave-Macmillan, London (2010)
3. Ben-Haim, Y.: Doing our best: optimization and the management of risk. Risk Anal. **32**(8), 1326–1332 (2012)
4. Ben-Haim, Y.: Why risk analysis is difficult, and some thoughts on how to proceed. Risk Anal. **32**(10), 1638–1646 (2012)
5. Ben-Haim, Y.: Robust satisficing and the probability of survival. Int. J. Syst. Sci. **45**, 3–19 (2014)
6. Ben-Haim, Y., Dacso, C.C., Carrasco, J., Rajan, N.: Heterogeneous uncertainties in cholesterol management. Int. J. Approx. Reason. **50**, 1046–1065 (2009)
7. Ben-Haim, Y., Osteen, C.D., Moffitt, L.J.: Policy dilemma of innovation: an info-gap approach. Ecol. Econ. **85**, 130–138 (2013)
8. Givoli, D., Isaac, E.: Stress concentration at a nearly circular hole with uncertain irregularities. ASME J. Appl. Mech. **59**, S65–S71 (1992)
9. Knight, F.H.: Risk, Uncertainty and Profit. Houghton Mifflin, Boston (1921). Re-issued by University of Chicago Press, Chicago (1971)
10. Schwartz, B.: Paradox of Choice: Why More Is Less. Harper Perennial, New York (2004)
11. Sha'eir, O.: Analysis of stress concentration around a hole with uncertain shape, based on info-gap theory (in Hebrew). MSc thesis, Technion—Israel Institute of Technology (2014)
12. Simon, H.: Rational choice and the structure of the environment. Psychol. Rev. **63**(2), 129–138 (1956)
13. Wald, A.: Statistical decision functions which minimize the maximum risk. Ann. Math. **46**(2), 265–280 (1945)

Chapter 16
Approach to Evaluate and to Compare Basic Structural Design Concepts of Landing Gears in Early Stage of Development Under Uncertainty

Roland Platz, Benedict Götz, and Tobias Melz

Abstract Structural design concepts for load bearing mechanical systems vary due to individual usage requirements. Particularly strut-configurations for landing gears in airplanes push the envelope according to tight requirements in shock absorption, normal, lateral and torsional load capacity, rolling stability, storage dimensions, low drag, low weight, and maintenance as well as reliability, safety and availability. Since the first controlled and powered flight of the Wright-Brothers in 1903, design evolution generated different structural design concepts. Today's structures may have, seemingly, reached mature conformity with distinct load path architectures that have been prevailed.

In the proposed contribution, the authors evaluate and compare distinctive performance requirements like stroke ability and ride quality, elastic force retention, structure strength, and weight of mechanisms resulting from significant structural design concepts for main and nose landing gears. Loads in landing gears have always been distributed in struts with high and low amounts of strut members such as rods, beams, torque links, and joints as well as different types of absorbers. This paper's goal is to clarify pros and cons of the four different concepts with respect to their vulnerability due to uncertainty. Here, uncertainty mainly occurs due to variations in elastic force retention and their effect on the performance requirements. For that, simple mathematical models are derived to evaluate and compare the most significant characteristics of the four concepts in the earliest stage of development in order to make early decisions for or against a concept before time and cost consuming detailed development work including manufacturing and test takes over.

Keywords Landing gear • Design concepts • Early stage of development • Decision making • Uncertainty

16.1 Introduction

From the beginning of the twentieth century, airplane landing gears experience major enhancements with the invention of the telescopic oleo-pneumatic shock absorber for non retractable landing gears [1]. Since then, different designs for non-retractable and retractable landing gears constantly improve the shock absorbing potential as well as enhancing strength and light-weight design for high quality and the fulfillment of allowances in aerospace industry [7, 10]. Today, simple non retractable leaf-spring steel or composite designs for small airplanes and retractable oleo struts with and without trailing links for main and nose landing gear for small and large aircraft lead to a great variety of design concepts. It is always the landing gear's goal to absorb kinetic energy from landing, to guarantee steering, stability and adequate ride quality on the ground, high reliability, low cost, overall aircraft integration, airfield compatibility, compact design for storage, low weight etc. [3–5].

Until today, optimal damping properties of the oleo strut and optimal structural reliability and fatigue life as well as new ways of conceptional design are aspired and documented in several contributions from an academic point of view, e.g. [11, 12] and [9]. However, only a few contributions discuss the pros and cons of principal landing gear concepts and give useful recommendations for the engineer who he has to decide between the concepts and oppose their requirements and benefits. For that, the engineer has to make early choices in geometry, kinematics and dynamics, e. g. whether the landing gear should have a trailing link or not. If a trailing link is in favor, further decisions have to be made concerning

R. Platz (✉)
Fraunhofer Institute for Structural Durability and System Reliability LBF, Bartningstraße 47, 64289 Darmstadt, Germany
e-mail: roland.platz@lbf.fraunhofer.de

B. Götz • T. Melz
Technische Universität Darmstadt, System Reliability and Machine Acoustics SzM, Magdalenenstraße 4, 64289 Darmstadt, Germany

S. Atamturktur et al. (eds.), *Model Validation and Uncertainty Quantification, Volume 3*, Conference Proceedings of the Society for Experimental Mechanics Series, DOI 10.1007/978-3-319-29754-5_16

the position and stroke capability of the oleo strut. Yet, the position and stroke ability of the oleo strut affects the strength of the surrounding and supporting struts. For example, ride quality on uneven ground may be one of many criteria. The trailing link landing gear offers good ride quality since the kinematics allow larger deflection of the overall mechanism [6]. However, the cost is higher weight.

In this paper, the authors show an approach to discuss the pros and cons of four major landing gear design concepts:

a) telescopic design with fixed elastic strut and hinged upper/lower struts as torque links, see Fig. 16.2.
b) trailing link with fixed elastic strut and hinged upper/lower struts
c) trailing link with hinged elastic strut, fixed upper strut, hinged lower strut, and high leverage
d) trailing link with hinged elastic strut, fixed upper strut, hinged lower strut, and small leverage.

The concepts' structural performances are evaluated and compared with each other with respect to:

i) stroke ability and ride quality
ii) elastic force retention
iii) structure strength
iv) weight.

As seen in the concepts above, the potential for energy absorption during landing is neglected. The damping capability of an oleo strut depends particularly on individual fluid system design approaches that, however, is not is not the scope of this paper. In the author's humbled opinion, once the decision has been made to follow a certain structural landing gear concept, it is sufficient for this contribution's approach to take in to account an elastic strut based on spring forces for elastic force retention. Of course, the detailed design of combined elastic-damping strut for static and kinetic loading, for example an oleo strut, must be conducted according to the general design guidelines such as in [8]. In this contribution, the authors assume that properties from the detailed design do not alter the structural conceptional general performance. Principal differences between the four concepts' characteristics stay the same. However, the authors evaluate and compare the uncertainty within the design concepts due to possible deviations in building up the elastic force that may affect the performance requirements mentioned above.

In order to compare the four major landing gear design concepts a) to d), simplified mathematical models are introduced to ensure comparability as far as possible—knowing that usually detailed design approaches according to the guidelines in [2] and [8] differ and are unique for every airplane. Yet, it is the goal of this paper to find a way for early evaluation of uncertainty in different design concepts, *before* the designer gets lost in time consuming design details, loosing sight of overall performance requirement and, maybe, ignoring more adequate conceptional alternatives. So the mathematical models are kept simple, but not too simple. They all include a wheel, supporting struts and an elastic strut for elastic force retention, but arranged differently in common approaches that are included in the four major design concepts a) to d). Wheel stiffness, though, is neglected in this study.

16.2 Simplified Mathematical Models of General Concepts for Main and Nose Landing Gear

Figure 16.1 shows real examples of the general four concepts a) to d) introduced in Sect. 16.1 for main and nose landing gear. Their differences are based on different mounting conditions of the landing gear elements such as elastic strut and the supporting upper and lower struts or, respectively, torque links in a). These conditions lead to different landing gear mechanisms with their characteristic kinematics and resulting dynamics.

The concepts are simplified as schematic diagrams in Fig. 16.2 with the basic landing gear elements: elastic strut cylinder 1, elastic strut piston rod 2, upper supporting strut 3, lower supporting strut 4 or, respectively, upper torque link strut 3 and lower torque link strut 4 in a), and wheel 5. The elastic strut's piston rod is directly connected with the wheel 5 in concept a) or to the lower supporting strut 4 in b) to d). For comparative reasons, the four concepts have the same absolute installation length l_a, same vertical static and maximum stroke ability $z_{a,\,max}$ and $z_{a,\,stat}$ of the wheel, and same vertical static absolute load $F_a = F_{a,\,stat}$ that represents the airplane's weight. In addition, the distance $x_{c,\,us}$ between the elastic and upper struts support, the height h_{hinge} of the upper strut's hinge of upper strut for b) to d), and the distance d_{hinge} between the piston rod low end and the hinge of upper/lower strut are given for this study.

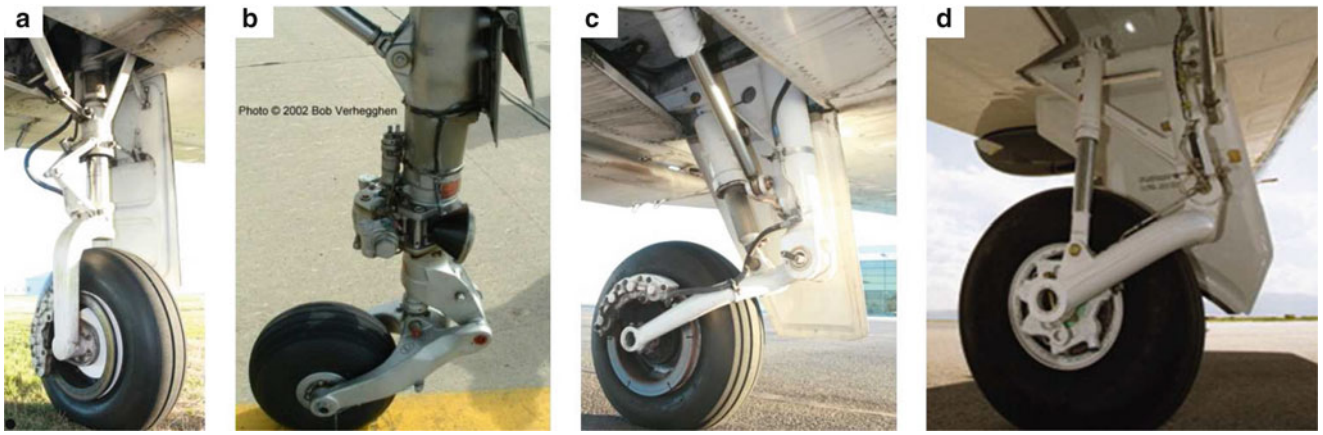

Fig. 16.1 Examples of general concepts for main and nose landing gear, (**a**) telescopic with fixed elastic strut and hinged upper/lower struts as torque links (from WIKIPEDIA), (**b**) trailing link with fixed elastic strut and hinged upper/lower struts, (from BOB VERHEGGHEN), (**c**) trailing link with hinged elastic strut, fixed upper strut, hinged lower strut, and high leverage (from WIKIPEDIA), (**d**) trailing link with hinged elastic strut, fixed upper strut, hinged lower strut, and small leverage (from PILATUS BUSINESS AIRCRAFT)

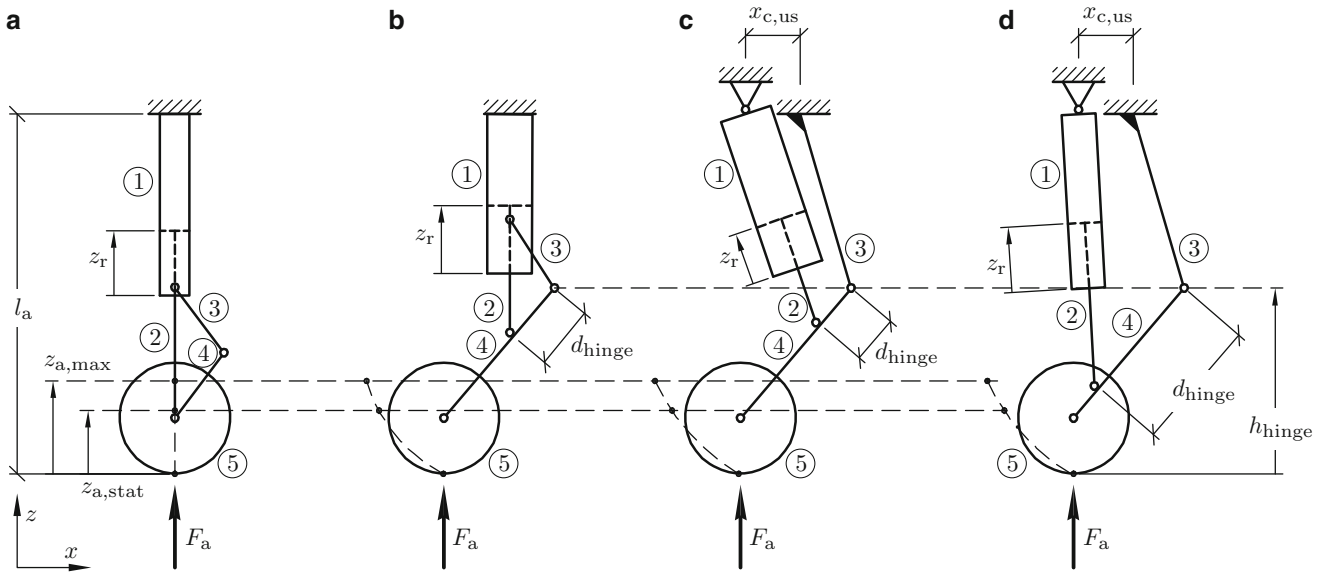

Fig. 16.2 Simplified general concepts for main and nose landing gear with: (**a**) telescopic with fixed elastic strut (cylinder 1 and piston rod 2), hinged upper/lower struts 3/4 as torque links and wheel 5, (**b**) trailing link with fixed elastic strut (cylinder 1 and piston rod 2), hinged upper/lower struts 3/4 and wheel 5, (**c**) trailing link with hinged elastic strut (cylinder 1 and piston rod 2), fixed upper strut 3, hinged lower strut 4 with high leverage, and wheel 5, (**d**) trailing link with hinged elastic strut (cylinder 1 and piston rod 2), fixed upper strut 3, hinged lower strut 4 with small leverage, and wheel 5

16.2.1 Prior Assumptions for Materials, Dynamics and Geometry to Achieve Comparability Between the Concepts

As mentioned earlier in Sect. 16.1, the four concepts' performance requirements: (i) stroke ability and ride quality, (ii) elastic force retention, (iii) structure strength, and (iv) weight are compared with each other. For that, a comparable basis is needed that allows the adequate comparison. Achieving comparability is only possible if simplifications for the mathematical model are defined that do not oversimplify and, therefore, falsify the landing gear conceptual characteristics. The prior assumptions to achieve comparability between the concepts a) to d) in are based on these equalities in materials, dynamics and geometry as seen in Fig. 16.2.:

- equal material in all considered elements of high strength low alloy steel D6AC 4335V, referring to basic design guidelines in [8]
- equal static absolute axial or, respectively, vertical load $F_{\mathrm{a,\,stat}}$, referring to basic design guidelines in [2]
- equal total absolute installation length l_{a} of the unloaded system, as the distance between bottom wheel and elastic strut mount
- equal cross-sections of upper and lower struts
- equal height h_{hinge} of upper struts' hinges from bottom of the wheel in concepts b) to d)
- equal distance $x_{\mathrm{c,\,us}}$ between mounting cylinder and upper strut in concepts c) and d)
- defined distances d_{hinge} between piston rod low end and hinge upper/lower strut
- equal maximum absolute axial or, respectively, vertical stroke ability $z_{\mathrm{a,\,max}}$ of the mechanisms
- equal static absolute axial or, respectively, vertical stroke $z_{\mathrm{a,\,stat}}$ due to static airplane weight of the mechanisms
- equal maximal static elastic strut pressure, referring to basic design guidelines in [8]
- equal relative wall thicknesses for the elastic struts in all concepts, assumed from basic design guidelines in [8]
- equal absolute wall thickness of upper and lower struts in concepts b) to d) as well as torque link in concept a), with the loading far below yield strength is assured
- equal size of the wheels, however, the wheel elasticity is neglected
- lateral and torsional loads acting on the landing gear are neglected.

16.2.2 Calculating Resulting Dynamic and Geometric Properties for Comparing the Concepts

With the assumptions in Sect. 16.2.1, the material, dynamic and geometric properties for the simplified concepts a) to d) are summarized in Table 16.1. The prior assumptions to ensure comparability are listed in the first half Table 16.1, calculated properties are listed in the second half due to the prior assumptions, including the resulting weight of the overall mechanisms. Note that not all properties Table 16.1 are shown in Fig. 16.2 due to limited display area like wheel radius r. The assumed and calculated properties represent a kind of baseline characteristics of the concepts. Of course, for implementation in a real airplane, further detailed design work will and must follow according to the guidelines such as in [2] and [8] to meet the manufacturer's and the regulating authorities' requirements.

The dynamic and geometric properties of the simplified mathematical model in Fig. 16.2, such as stiffness k and and cross sectional radii $r_{\mathrm{c,\,i}}$ and $r_{\mathrm{c,\,o}}$ of the elastic struts that are listed in the second half of Table 16.1, are calculated from the assumed properties that are summarized in the table's first half. The elastic strut's stiffness becomes

$$k = \frac{F_{\mathrm{r}}}{z_{\mathrm{r}}} \tag{16.1}$$

for each concept a) to d) due to relative elastic strut loads F_{r} and strokes z_{r}, with the identity to absolute loads and strokes $F_{\mathrm{r}} = F_{\mathrm{a}}$ and $z_{\mathrm{r}} = z_{\mathrm{a}}$ in a). The relation in (16.1) has been derived by adapting the relative load and stroke relation to the overall requirement of equal static absolute vertical load $F_{\mathrm{a}} = F_{\mathrm{a,\,stat}}$ and equal static absolute vertical stroke $z_{\mathrm{a,\,stat}}$ that are assumed for all four concepts and listed in Table 16.1. Thereby, the first performance characteristics such as stroke ability and ride quality (i) as well as elastic force retention (ii) can be evaluated and compared, Sect. 16.3.1, Fig. 16.3. The relative loads F_{r} and strokes z_{r} are the results from the kinematics according to the geometry shown in Fig. 16.2. The rather complex kinematic derivation has been done numerically with finite element calculation and is not shown here.

Now, the geometry of the elastic strut can be calculated, since it differs in all concepts if the same relative stroke z_{r} is assumed. The cylinder's inside radius $r_{\mathrm{c,\,i}}$ is equal to the piston's radius r_{p}, with

$$r_{\mathrm{c,\,i}} = r_{\mathrm{p}} = \sqrt{\frac{F_{\mathrm{r,\,stat}}}{p\,\pi}} \tag{16.2}$$

using the pressure p in Table 16.1, suggested in [8] for piston diameter design on the basis of the maximum static strut pressure. This results in the cylinder's outside radius

$$r_{\mathrm{c,\,o}} = \delta\, r_{\mathrm{c,\,i}} \tag{16.3}$$

Table 16.1 Dynamic, geometric and material properties as well as resulting weight for the simplified concepts a) to d) according to Figs. 16.1 and 16.2 to ensure comparability, density steel: $\rho = 7.850\,\mathrm{kg/m^3}$, material for all elements: D6AC 4335V, mass of wheel: neglected, n. s. = not specified

Prior assumptions to achieve comparability						
Property	Variable	Unit	a)	b)	c)	d)
Load, static absolute	$F_{\mathrm{a,\,stat}}$	kN	30.0	30.0	30.0	30.0
Length, total System, unloaded, absolute	l_{a}	m	0.850	0.850	0.850	0.850
Length of elastic strut incl. cylinder & piston rod, unloaded	l_{es}	m	0.700	0.520	0.568	0.660
Length, upper strut	l_{us}	m	0.188	0.188	0.417	0.417
Length, lower strut	l_{ls}	m	0.188	0.394	0.394	0.394
Height hinge of upper strut b) to d)	h_{hinge}	m	n. s.	0.450	0.450	0.450
Distance between mounting of cylinder and upper strut	$x_{\mathrm{c,\,us}}$	m	–	–	0.125	0.125
Distance piston rod low end to hinge upper/lower strut	d_{hinge}	m	n. s.	0.158	0.118	0.315
Stroke, vertical maximum absolute wheel	$z_{\mathrm{a,\,max}}$	m	0.250	0.250	0.250	0.250
Stroke, vertical static absolute wheel	$z_{\mathrm{a,\,stat}}$	m	0.170	0.170	0.170	0.170
Pressure, inside cylinder at static load	p	$10^6\,\mathrm{N/m^2}$	10.3	10.3	10.3	10.3
Ratio between outside and inside radius in elastic struts	δ	–	1.167	1.167	1.167	1.167
Radius, upper strut inside	$r_{\mathrm{us,\,i}}$	m	0.040	0.040	0.040	0.040
Radius, upper strut outside	$r_{\mathrm{us,\,o}}$	m	0.050	0.050	0.050	0.050
Radius, lower strut inside	$r_{\mathrm{ls,\,i}}$	m	0.040	0.040	0.040	0.040
Radius, lower strut outside	$r_{\mathrm{ls,\,o}}$	m	0.050	0.050	0.050	0.050
Radius, wheel	r_{w}	m	0.150	0.150	0.150	0.150
Calculated properties due to prior assumptions						
Property	Variable	Unit	a)	b)	c)	d)
Stiffness, elastic strut	k	kN/m	120.0	660.0	1260.0	241.2
Load, maximum absolute	$F_{\mathrm{a,\,max}}$	kN	44.118	40.410	37.328	42.000
Load, maximum relative elastic strut	$F_{\mathrm{r,\,max}}$	kN	44.118	85.085	119.289	52.095
Load, static relative elastic strut	$F_{\mathrm{r,\,stat}}$	kN	30.000	59.097	85.791	36.297
Stroke, maximum relative elastic strut	$z_{\mathrm{r,\,max}}$	m	0.250	0.129	0.095	0.216
Stroke, static relative elastic strut	$z_{\mathrm{r,\,stat}}$	m	0.170	0.090	0.068	0.150
Length, cylinder elastic strut	l_{c}	m	0.417	0.363	0.377	0.400
Radius, cylinder elastic strut—inside	$r_{\mathrm{c,\,i}}$	m	0.030	0.043	0.052	0.034
Radius, cylinder elastic strut—outside	$r_{\mathrm{c,\,o}}$	m	0.035	0.050	0.060	0.039
Length, piston rod	l_{p}	m	0.283	0.157	0.191	0.260
Radius, piston rod, full cross-section	r_{p}	m	0.030	0.043	0.052	0.034
Stress, cylinder, circumferential at maximum absolute stroke	$\sigma_{\varphi,\mathrm{max}}$	$10^6\,\mathrm{N/m^2}$	106.3	104.1	100.5	103.7
Stress, cylinder, circumferential at static absolute stroke	$\sigma_{\varphi,\mathrm{stat}}$	$10^6\,\mathrm{N/m^2}$	72.3	72.3	72.3	72.3
Mass, elastic strut (cylinder and piston rod)	m_{es}	kg	13.68	23.44	39.73	16.22
Mass, upper strut	m_{us}	kg	3.07	3.07	6.82	6.82
Mass, lower strut	m_{ls}	kg	3.07	6.45	6.45	6.45
Mass, wheel	–	–	–	–	–	–
Mass, total System	m_{total}	kg	19.82	32.96	53.00	29.49

by simply multiplying $r_{\mathrm{c,\,i}}$ with the ratio δ from Table 16.1, estimated from similar examples in [8] and in compliance with ratios allowed to calculate the circumferential stress σ_φ in (16.8) with BARLOW'S formula, taken from textbooks. The length of the elastic strut is defined, on the one hand, by its needed piston rod's length

$$l_{\mathrm{p}} = z_{\mathrm{r,\,max}} + 2.75 \cdot 2\,r_{\mathrm{p}} + l_{\mathrm{add}} \tag{16.4}$$

with minimum supporting length of $2.75 \cdot 2\,r_{\mathrm{p}}$ that reaches inside the cylinder according to [5], and an added term

$$l_{\mathrm{add}} = l_{\mathrm{es}} - (l_{\mathrm{c}} + z_{\mathrm{r,\,max}}), \tag{16.5}$$

with the total length l_{es} of elastic strut incl. cylinder and piston rod when unloaded, cylinder length l_c and maximum relative cylinder stroke $z_{r,\max}$, so that the elastic strut is connected to the wheel or lower struts. That leads, on the other hand, to the cylinder's length

$$l_c = z_{r,\max} + 2.75 \cdot 2\, r_p. \tag{16.6}$$

Next and for evaluating and comparing the loading condition (iii) in the landing gear's elements, the stresses in each element are of interest for the concepts a) to d). The piston rod's normal stress becomes

$$\sigma_{n,p} = \frac{F_r}{\pi\, r_p^2} \tag{16.7}$$

with the relative load F_r and radius r_p. The cylinder's circumference stress results in

$$\sigma_\varphi = p\, \frac{r_{c,o}}{r_{c,o} - r_{c,i}}. \tag{16.8}$$

Normal and bending stresses occur in the upper and lower struts. For evaluation and comparison reasons, the VON-MISES stress

$$\sigma_v = \sqrt{\frac{1}{2}\left[(\sigma_I - \sigma_{II})^2 + (\sigma_{II} - \sigma_{III})^2 + (\sigma_{III} - \sigma_I)^2\right]} \tag{16.9}$$

is taken into account with principal stresses σ_{I-III} that are calculated in this contribution via finite element calculations according to the assumed properties given in Table 16.1.

Eventually, the overall mechanism's weight (iv) is another feasible measure to compare concept a) to d). The masses are

$$m_x,\ l_x,\ r_{xo}^2,\ r_{xl}^2, \tag{16.10}$$

taking into account the density ρ for all elements according to Table 16.1 and the volume m_x, l_x, r_{xo}^2, r_{xl}^2 for each elastic strut cylinder (index $x = c$) and piston rod (p) as well as for upper (u) and lower (l) struts with their inside and outside radii.

16.3 Comparison of Structural Performances

In this section, the authors evaluate and compare the distinctive performance requirements (i) stroke ability and ride quality, (ii) elastic force retention, (iii) structure strength, and (iv) weight of mechanisms resulting from significant structural design concepts a) to d).

16.3.1 Comparison with Disregarded Uncertainty

Figure 16.3 shows the progress of load vs. stroke relations F_a and F_r vs. z_a and z_r for the absolute vertical wheel stroke z_a and the relative elastic strut stroke z_r for concepts a) to d), Fig. 16.2. The relations are normalized to the static absolute load $F_a = F_{a,stat}$ and vertical static absolute stroke $z_{a,stat}$. Uncertainty is not taken into account, the relations are derived from deterministic calculation.

In case of the Fig. 16.3 absolute load-stroke relation F_a vs. z_a of the overall mechanism, the relation in concept c) is most nonlinear due to the high leverage effect. Concept c) ensures smoothest ride quality of all, concept a) leads to rather bumpy rides. In case the absolute stroke exceeds the absolute static stroke by the factor of 1.47 due to higher loading than the static load, the maximum allowable stroke is reached. Concept a) allows highest absolute loading than concept c) with lowest absolute loading capability.

In case of the relative load-stroke relation F_r vs. z_a and z_a for the relative elastic strut, the relations are all linear, Fig. 16.3. The elastic strut of concept c) experiences the highest loading of all due to the leverage effect. Consequently, its relative stroke z_r ability is the lowest.

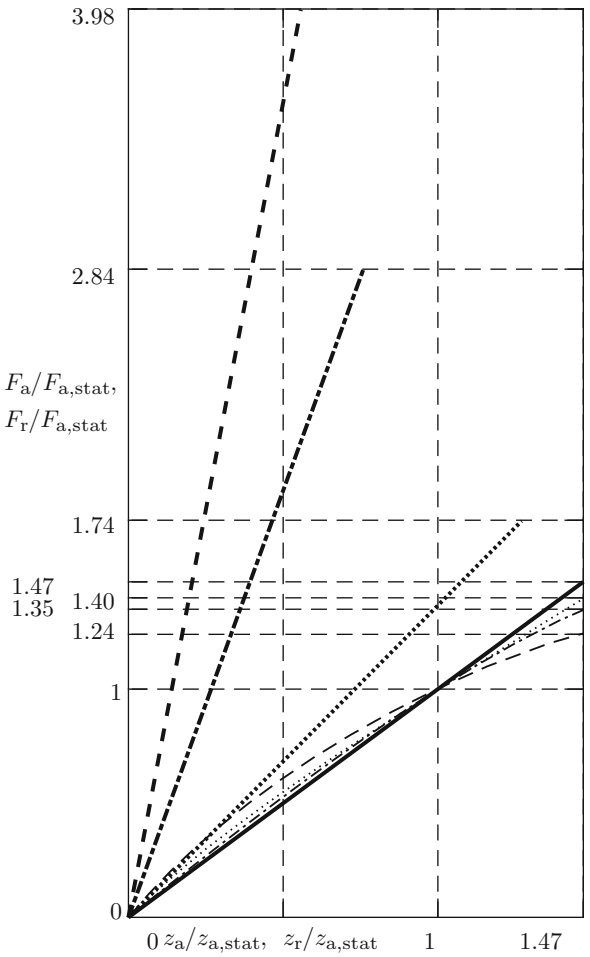

Fig. 16.3 Progress of load vs. stroke relations $F_a/F_{a,\,stat}$ and $F_r/F_{a,\,stat}$ vs. $z_a/z_{a,\,stat}$ and $z_r/z_{a,\,stat}$ for the absolute vertical wheel stroke z_a and the relative elastic strut stroke z_r, normalized to the static absolute load $F_{a,\,stat}$ and to the vertical static absolute stroke $z_{a,\,stat}$
absolute: concept
a) —, b) - - -, c) - - -, d) ····
relative: concept
a) ▬, b) ▬ ▪ ▬ ▪, c) ▬ ▪ ▪ ▬, d) ····

Figure 16.4 shows the progress of the piston's normal stress σ_n according to (16.7) vs. the relative stroke z_r for each concept a) to d), normalized to the corresponding maximum stresses $\sigma_{n,\,max}$ and to the static absolute stroke $z_{a,\,stat}$, Fig. 16.4a. Also in Fig. 16.4a, end points are marked with a cross. Only single values of the cylinder's circumferential stress σ_φ according to (16.8) vs. the static and maximum relative stroke $z_{r,\,stat}$ and $z_{r,\,max}$, normalized to the corresponding maximum stress $\sigma_{\varphi,max}$ and to the static maximum absolute stroke $z_{r,\,stat}$ are seen as circles.

The progress of the VON-MISES stress σ_v in the upper and lower struts according to (16.9) vs. the absolute vertical wheel stroke z_a, normalized to the corresponding maximum stress $\sigma_{v,\,max}$ and to the static absolute stroke $z_{a,\,stat}$ is shown in Fig. 16.4b. The maximum normal and circumferential stresses $\sigma_{n,\,max}$ and $\sigma_{\varphi,max}$ of piston and cylinder according to Fig. 16.4a are highest for concept a), they are lowest for concept c). So the elastic strut for telescopic design a) experiences highest loading, however the relative rise of loading with increasing relative stroke z_r is less then the trailing link design c) with its high leverage effect.

The progresses of the VON-MISES stress σ_v in the upper and lower struts in Fig. 16.4b are highest for concept c) and lowest in concept d). For concept a), no VON-MISES stresses exist, which is normal for torque links if torsional loads are neglected as assumed in Sect. 16.2.1 in this study.

16.3.2 Comparison with Uncertainty

In this section, the authors discuss briefly the results in the prior section if uncertainty is taken into account, such as the variation of the elastic strut stiffness k. The variability of k influences the resulting loading and stroke ability of the landing gear design concepts a) to d), leading to different stresses. In case of an assumed positive deviation of +15 % of the stiffness k from the nominal value, the stresses and loads also increase in concept a) by +15 %, in b) +14.4 %, in c) by +13.8 % and

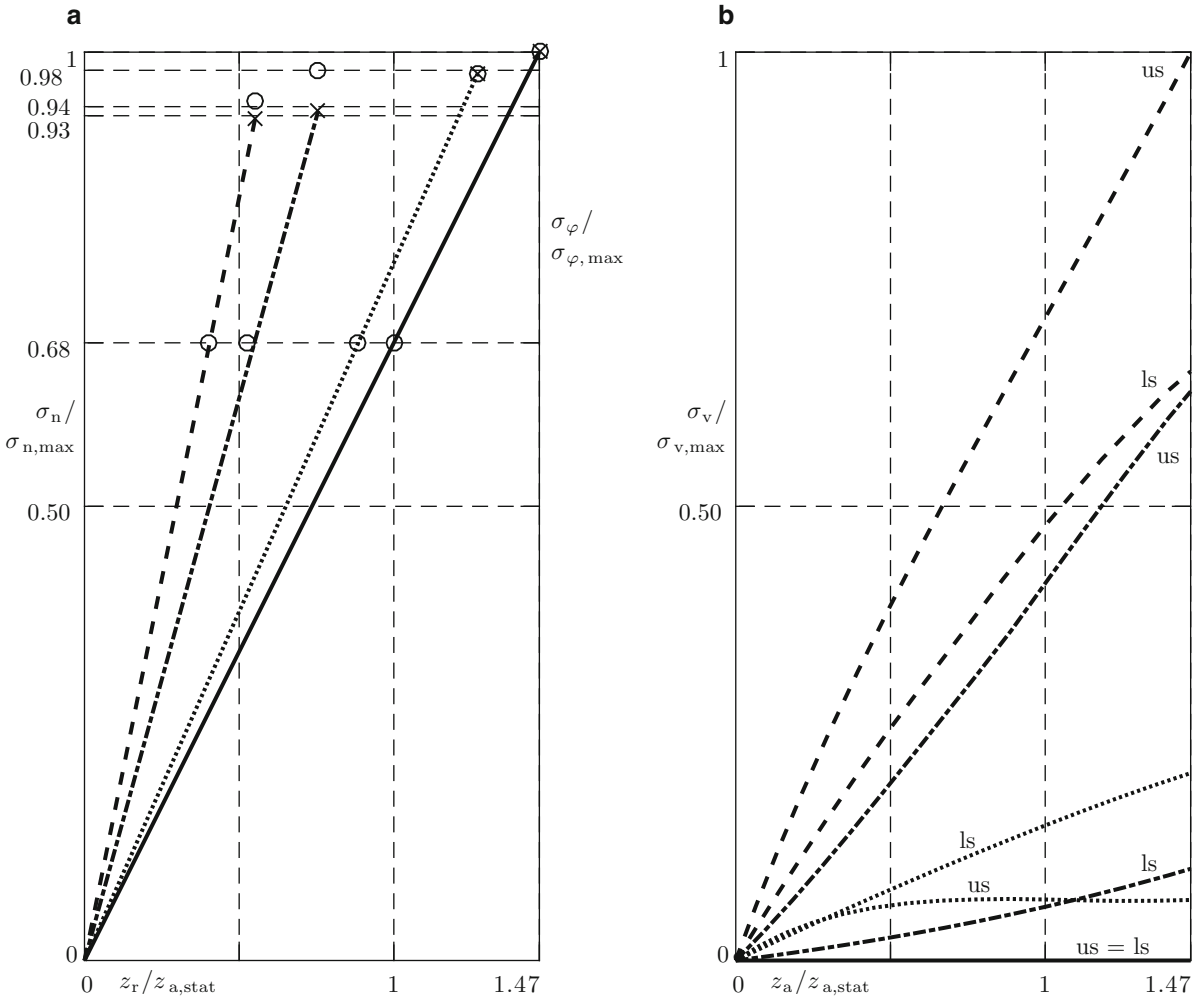

Fig. 16.4 (**a**) Progress of the piston's normal stress σ_n vs. the relative stroke z_r, normalized to the corresponding maximum stresses $\sigma_{n,max}$ and to the static absolute stroke $z_{a,stat}$. End points are marked with a cross. Single values of the cylinder's circumferential stress σ_φ vs. the static and maximum relative stroke $z_{r,stat}$ and $z_{r,max}$, normalized to the corresponding maximum stress $\sigma_{\varphi,max}$ and to the static maximum absolute stroke $z_{r,stat}$ as circles; (**b**) Progress of the VON-MISES stress σ_v in the upper struts (us) and lower struts (ls) vs. the absolute vertical wheel stroke z_a, normalized to the corresponding maximum stress $\sigma_{v,max}$ and to the static absolute stroke $z_{a,stat}$; concept a) ▬, b) ▪ ▪ ▪, c) ▬ ▬, d) ▪ ▪ ▪ ▪

in d) by +15 %. In case of a negative deviation of −15 % from the nominal value k, the stresses and loads decrease in a) by −15 %, in b) by −15.4 %, in c) by −15.7 % and in d) by −15 %.

16.4 Conclusion

It is shown that decisions to chose a structural concept for landing gears in early design phases highly depend on the individual performance requirements such as stroke ability and ride quality, elastic force retention, structure strength and weight. However, this work helps and gives an idea of how to evaluate and compare different concepts in the earliest stage of development. The decision can be made only by weighting individual performance requirements the designer wishes to follow before detailed design work starts. Yet, the authors believe that more detailed design work will not change the principal differences between the four basic concepts in this study in terms of stroke ability, elastic force retention, structure strength, and weight. Once the principal concept has been chosen by the designer, time consuming detailed design work begins, followed by even more time-consuming manufacturing preparations and processes including tests until ready to market products are available. Therefore, choosing the adequate concept in the earliest stage of development is the most critical part, since it determines the directions of all following development phases with the high costs in the continuing product life. There is, usually, no return to start all over again with an alternative, maybe more adequate concept without

more costs. Today's high amount of call backs, especially in the automotive industry with similar decisions in early stages of development might give an idea of high costs. In future work, the authors will go deeper into the uncertainty quantification to get a more profound view on how uncertainties effect the decisions in landing gear design that have to be made in the early design phase.

Acknowledgements The authors like to thank the German Research Foundation DFG for funding this research within the SFB 805.

References

1. Barfield, N.A.: Fifty years of landing gear development: a survey of the pioneering contribution to aircraft undercarriage development made by Vickers and B.A.C. at Weybridge. Aircr. Eng. Aerosp. Technol. **40**(1), 17–22 (1968)
2. Bruhn, E.F.: Analysis and Design of Flight Vehicle Structures. Jacobs, Indianapolis (1973)
3. Chai, S.T., Mason, W.H.: Landing gear integration in aircraft conceptual design. Report MAD 96-09-01, Multidisciplinary Analysis and Design Center for Advanced Vehicles. Virginia Polytechnic Institute and State University, Blacksburg, 24061-0203 (1997)
4. Conway, H.G.: Landing Gear Design. Chapman and Hall, London (1958)
5. Currey, N.S.: Aircraft Landing Gear Design: Principles and Practices. AIAA Education Series. American Institute of Aeronautics and Astronautics, Washington (1988)
6. Gudmundsson, S.: General Aviation Aircraft Design. Elsevier, Amsterdam (2014)
7. Hoare, R.G.: Aircraft landing gear: an account of recent developments in undercarriage design an the materials used. Aircr. Eng. Aerosp. Technol. **40**(1), 6–8 (1968)
8. Niu, M.C.Y.: Airframe Structural Design. Conmilit Press Ltd., Burbank (1988)
9. Pragadheswaran, S.: Conceptual design and linear static analysis of nose landing gear. In: International Conference on Robotics, Automation, Control and Embedded Systems – RACE 2015, 18–20 February 2015. Hindustan University, Chennai (2015)
10. Veaux, J.: New design procedures applied to landing gear development. J. Aircr. **25**(10), 904–910 (2014)
11. Wang, H., Xue, C.J., Jiang, W.T.: Fuzzy fatigue reliability analysis for a landing gear structure. In: 2010 Third International Joint Conference on Computational Science and Optimization (CSO), vol. 1, pp. 112–115 (2010). doi:10.1109/CSO.2010.130
12. Xue, C.J., Dai, J.H., Wei, T., Lui, B.: Structural optimization of a nose landing gear considering its fatigue life. J. Aircr. **49**(1), 225–236

Chapter 17
Robust Sensor and Exciter Design for Linear Structures

Fabien Maugan, Scott Cogan, Emmanuel Foltête, and Aurélien Hot

Abstract A wide variety of model-based modal test design methodologies have been developed over the past two decades using a non-validated baseline model of the structure of interest. Due to the presence of lack of knowledge, this process can lead to less than optimal distributions of sensors and exciters due to the discrepancy between the model and the prototype behaviors. More recent strategies take into account statistical variability in model parameters but the results depend strongly on the hypothesized distributions.

This paper provides a decision making tool using a robust satisficing approach that provides a better understanding of the trade-off between the performance of the test design and its robustness to model form errors and associated imprecisions. The latter will be represented as an info-gap model and the proposed methodology seeks a sensor and exciter distribution that will satisfy a given design performance while tolerating a specified degree of modeling error. The evolution of this performance for increasing horizons of uncertainty is an important information for the test planner in choosing the total number of sensors. The methodology will be illustrated on an academic but practically useful example under severe uncertainty.

Keywords Sensor placement • Robustness • Info-gap • Uncertainty • Lack of knowledge

17.1 Introduction

The growing size and complexity of spacecraft structures requiring qualification testing can benefit from model-based test design to insure the identification with the best possible information about the current dynamics of the structure. The constraints of qualification tests generally imply a relatively small number of sensors and limited test times while requiring adequate observability and distinguishability of the mode shapes of interest.

Over the past three decades, a wide variety of deterministic model-based strategies have been developed to define an optimal configuration of sensors and actuators. In most cases, an optimal design provides the best observability and distinguishability of the identified eigenmodes, including methodologies based on the Guyan reduction [9, 10], the effective independence criteria [7], the constraint energy of the structure [6], the QR decomposition of the modal matrix [13] or the Orthogonal Maximum Sequence (OMS) [3].

Improvements in computation power of computers has lead to sensor placement algorithms using stochastic approaches to account for model and measurement uncertainties, such as [1] based on residuals, [11] using the entropy, or [12]. Meanwhile, these methodologies target aleatory uncertainty and are not necessarily well adapted to lack of knowledge resulting from model form errors and unknown levels of parameter imprecision. This limitation is particularly important given that model-based test design is generally based on non-validated models.

In the space industry, structural finite element models (FEM) are generally composed of subsystems models provided by subcontractors. All of these models have different degrees of accuracy in modeling the true hardware behavior and this situation often leads to significant errors in the predicted mode shapes due to poorly estimated stiffness, mass and damping properties. The impact of these errors on the modal properties of the structure are discussed in [8] and various solutions

F. Maugan (✉) • S. Cogan • E. Foltête
Applied Mechanics Department, FEMTO-ST Institute, 24 chemin de l'Epitaphe, 25000 Besançon, France
e-mail: fabien.maugan@femto-st.fr

A. Hot
Spatial Center of Toulouse,18 avenue Edouard Belin, 31401 Toulouse Cedex 9, France

S. Atamturktur et al. (eds.), *Model Validation and Uncertainty Quantification, Volume 3*, Conference Proceedings of the Society for Experimental Mechanics Series, DOI 10.1007/978-3-319-29754-5_17

have been proposed to propagate uncertainties through the finite element model in order to determine the corresponding uncertainties in the modal properties [2, 4]. A first attempt to account for lack of knowledge for sensor placement in vibration test design can be found in [15].

This paper addresses the question of how best to plan a modal test under epistemic uncertainty. A methodology is proposed based on a robust satisficing approach allowing the trade off between test performance and model uncertainty to be investigated explicitly. It extends the approach proposed in [15] to the design of exciter configurations and to the testing of locally nonlinear structures.

17.2 Robust Design of Vibration Tests

17.2.1 Sensor Design

It is widely recognized that random uncertainties in a system and its environment must be taken into account in the design process [14] and an overview of robust design strategies in structural dynamics can be found in [17]. However, uncertainty can arise in many forms and modeling errors are not necessarily random in nature. For example, errors in model form or unknown levels of parameter imprecision often require non-probabilistic approaches to be accounted for correctly. Moreover, the concept of robust design is not restricted exclusively to structural design, it also proves useful in the development of algorithms in general. Next, we will seek to define a new strategy in order to maximize the robustness of a model-based sensor placement design for vibration tests to errors in the finite element model.

A sensor distribution must be able to identify and distinguish the significant modes of the structure within the frequency band of interest. The system model linking the unknown inputs of the ith system $\mathbf{m_i}$ can be defined as Eq. (17.1). $\mathbf{m_i}$ can contain material properties, thicknesses for instance, to the unknown output, which here is the modal basis Φ_i.

$$M(\mathbf{m}_i) = \Phi_i \tag{17.1}$$

In order to account for model uncertainties, the approach adopted here consists in sampling the uncertain model design space to assemble a set of modal bases Φ such as $\Phi = [\Phi_1, \cdots, \Phi_N]$ consistent with the defined uncertainty. Within the framework of the info-gap theory, this sampling must be done following an uncertain model $\mathscr{U}\left(\alpha, \mathbf{m}^{(0)}\right)$ where $\mathbf{m}$ is the vector of uncertain parameters, $\mathbf{m}^{(0)}$ is the nominal parameter values, and α the horizon of uncertainty. This model should represent the physics of the parameter uncertainty and, in the simplest case, define an interval in the uncertain design space where the unknown parameters are allowed to vary. In this study, an envelope-bound model is used **[4]**:

$$\mathscr{U}\left(\alpha, \mathbf{m}^{(0)}\right) = \left\{\mathbf{m} : \left|\mathbf{m}_i - \mathbf{m}_i^{(0)}\right| < \alpha w_i \mathbf{m}_i^{(0)},\ i = 1, \ldots, p\right\} \tag{17.2}$$

The advantage of a sampling approach is that there are no assumptions concerning the number or type of modes in the frequency band. A Singular Value Decomposition (SVD) [5] of the Φ matrix is performed, such that $U\Sigma V^T = \Phi$, in order to reduce the modal uncertainty space. The results are three matrices:

- U : orthogonal matrix containing the left singular vectors that are the singular directions, also called proper orthogonal modes (POM)
- Σ : pseudo-diagonal matrix containing the singular values, also called proper orthogonal values (POV) and linked to the POM energy
- V : orthogonal matrix containing the right singular vectors, temporal modulation of POMs

An examination of the singular values of this decomposition allows a reduced but representative subspace to be constructed. Under low levels of uncertainty, the resulting subspace will be the baseline natural eigenmodes. As uncertainty increases, the representative subspace will naturally increase in size as new modal behaviors are added. The dimension of this subspace conditions the minimum number of sensor locations in order to observe all the linear independent behaviors.

The reduced problem can be written as:

$$\left(U_r^T * K * U_r - \omega_\upsilon^2 U_r^T * M * U_r\right) * c_\upsilon = 0 \tag{17.3}$$

Where U_r is composed of the selected singular vectors of U.

This new system yields a reduced modal basis $\tilde{\Phi}$ which contains all of the realizable displacement fields for a given horizon of uncertainty. In order now to design the more robust sensor distribution the methodology must find the locations that maximize the identification and the distinguishability of the modes.

This reduced uncertain modal space can provide the input for any deterministic sensor placement algorithm. In this study, the approaches proposed by Kammer [7] and Schedlinski [13] will be implemented.

The question is now how to assess the robustness to lack of knowledge in the finite element model of the sensor distribution. A useful figure of merit is based on the distinguishability of the eigenmodes corresponding to a given eigen basis realization. Qualitatively, a set of eigenmodes is considered to be distinguishable when no single eigenvector can be expressed as a linear combination of the remaining eigenvectors in the basis. In [15] the distinguishability of an eigenbasis is quantified based on the condition number of the sensor matrix Φ_s corresponding to the modal matrix reduced to the sensor degrees of freedom. Indeed, distinguishability improves with decreasing condition number. The performance requirement can be then define as the maximum condition number of Φ_s over the sampled modal basis, at a given horizon of uncertainty, must be below a critical value κ_c.

$$\max\left(\text{cond}(\Phi_s)\right) \leq \kappa_c \tag{17.4}$$

The robustness function can then be evaluated for a range of horizons of uncertainty providing a useful decision making tool for comparing different candidate sensor placement designs.

$$\tilde{\alpha}_{MMIF} = \max\left\{\alpha\,,\ \max_{\mathbf{m}\in U(\alpha,\mathbf{m}^0)}\left(\text{cond}\left(\Phi_s\right)\right) \leq \kappa_{c_{cond}}\right\} \tag{17.5}$$

In this paper, the MAC indicator will also be used as a performance criterion of the sensor optimization strategy described in [13].

17.2.2 Excitation Design

In order to propose a complete robust test design, it is also necessary to address the robust excitation design. This proves to be a more challenging problem than sensor design due to the cost constraint of performing multiple tests under different loading configurations. This topic has already be treated in [13] in a deterministic way using the QR decomposition of the transposed exciter force matrix $M\Phi$ which is reduced to the sensor degrees of freedom in order to obtain exciter locations that coincide with the selected sensor degrees of freedom. The exciter design problem can be cast in a robust framework by analogy with the sensor placement approach describe above. The only difference is that the decomposition is not directly applied to the $\tilde{\Phi}$ matrix, but to its reduction to the sensor degrees of freedom (17.6).

$$QR = \left[M\tilde{\Phi}_s\right]^T E \tag{17.6}$$

The performance of an excitation design can be evaluated by calculating the Multivariate Mode Indicator Function (MMIF) [16]. This indicator is calculated for each eigenmode and takes on values from 0 and 1. The smaller the MMIF value, the better the associated mode is excited.

In the application presented in this paper, and for a fixed horizon of uncertainty, the maximum MMIF index computed over all the eigenfrequencies is kept as a performance criterion. The resulting robustness function is expressed in Eq. (17.7), with the exciters positions $\mathbf{x}_{exc}$, and the eigenfrequency vector $\mathbf{f}$ of the considered modal basis.

$$\tilde{\alpha}_{MMIF} = \max\left\{\alpha\,,\ \max_{\mathbf{m}\in U(\alpha,\mathbf{m}^0)}\left(\max\left(\text{MMIF}\left(\Phi_s,\,\mathbf{x}_{exc},\,\mathbf{f}\right)\right)\right) \leq \kappa_{c_{MMIF}}\right\} \tag{17.7}$$

17.3 Numerical Application

17.3.1 Sensor Design

The proposed methodology is illustrated on an aluminum frame, with a point mass at the center of each section, which represents a generic structure where an equipment will be attached at an unknown location. The position of the bottom right mass is thus considered to be uncertain. In other words, the point mass can be attached to another node location in the bottom right beam and this induces a direct and local modification of the structural modes 7, 9, 10 and 12 (see Fig. 17.1) where the maximum amplitudes have a natural tendency to follow the position of the mass. In addition, lack of knowledge are also applied on the value of the point mass and on the global Young's modulus of the structure.

In the figures presented in this paper, a horizon of uncertainty horizon of 10 refers to 100 % of uncertainty in the mass position (i.e. all the possible locations are taken into account) and a maximum uncertainty of 10 % in mass and Young's modulus. The corresponding uncertainty model is based on an envelope-bound model expressed in Eq. (17.8) with α between 0 and 10. The unknown vector $\mathbf{m}$ regroups the position of the point mass along the y axis with the mass and the Young's modulus of the structure.

$$m \in U\left(\alpha, \mathbf{m}^0\right) = \left\{\mathbf{m} : \ \mathbf{m}^0\left(1-\alpha\right) \leq \mathbf{m} \leq \mathbf{m}^0\left(1+\alpha\right)\right\} \tag{17.8}$$

Figure 17.2b shows the robustness curves calculated with the Kammer sensor design method using the nominal modal basis of the structure reduced to the modes under 250 Hz and allowing 9, 10, 11 and finally 12 sensors to be placed. These sensor placements are defined in a deterministic way, that is to say, only knowing the nominal modal basis of the structure. The robustness for each horizon of uncertainty is computed using the global uncertain sampling basis where each modal basis is limited to the eigenmodes under 200 Hz. As the number of modes in the modal basis grows larger or equal to the allowed number of sensors, each new sensor contributes to improve the distinguishability of the modal behavior and thus the condition number of the sensor matrix. Coupling this data with the Fig. 17.2b showing the place taken by the 10th to 12th sensors, it is noticeable that only the 12th sensor is well positioned allowing useful data from the part of the structure where the mass can move.

The same behavior can be observed using a QR sensor design method. Both algorithms will be used in the next section of the paper.

Comparing two robustness curves resulting from two different sensor designs can be a delicate task due to the sensitivity of the performance criterion to the number of sensors and the number of modes. The following parameters were used to insure that the robustness results can be compared between the different approaches:

- All of the test designs contain nine sensors.
- The deterministic designs use the same set of eigenmodes as Fig. 17.2b retaining all modes up to 250 Hz.
- The robust designs include the eigenmodes up to 200 Hz for all realizations and are constructed here for a horizon of uncertainty equal to 3.
- The performance criteria for the robust designs are calculated in the same way as for Fig. 17.2b retaining the modes under 200 Hz.

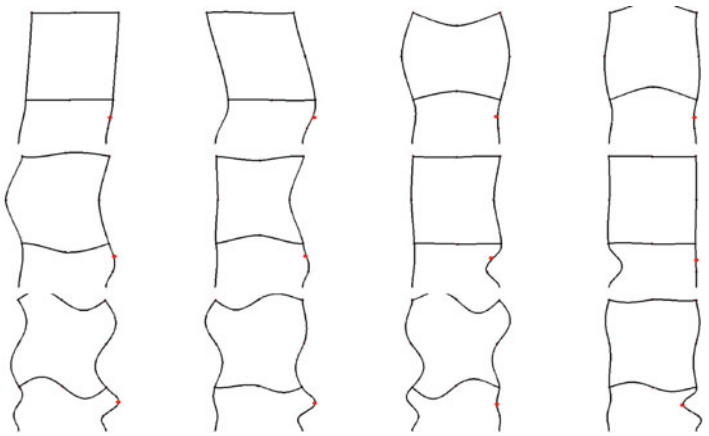

Fig. 17.1 Modal deformed shapes

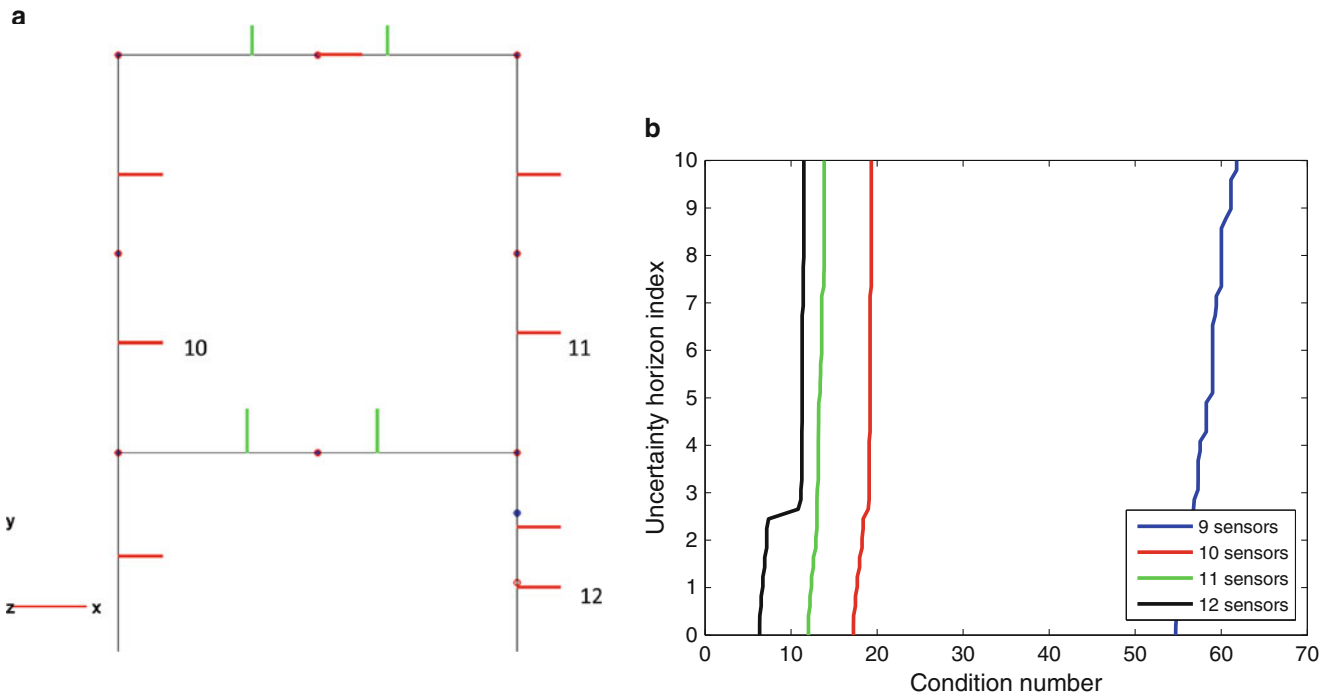

Fig. 17.2 Sensors positions (**a**) and robustness curves for different sensor numbers with a determinist Kammer approach (**b**)

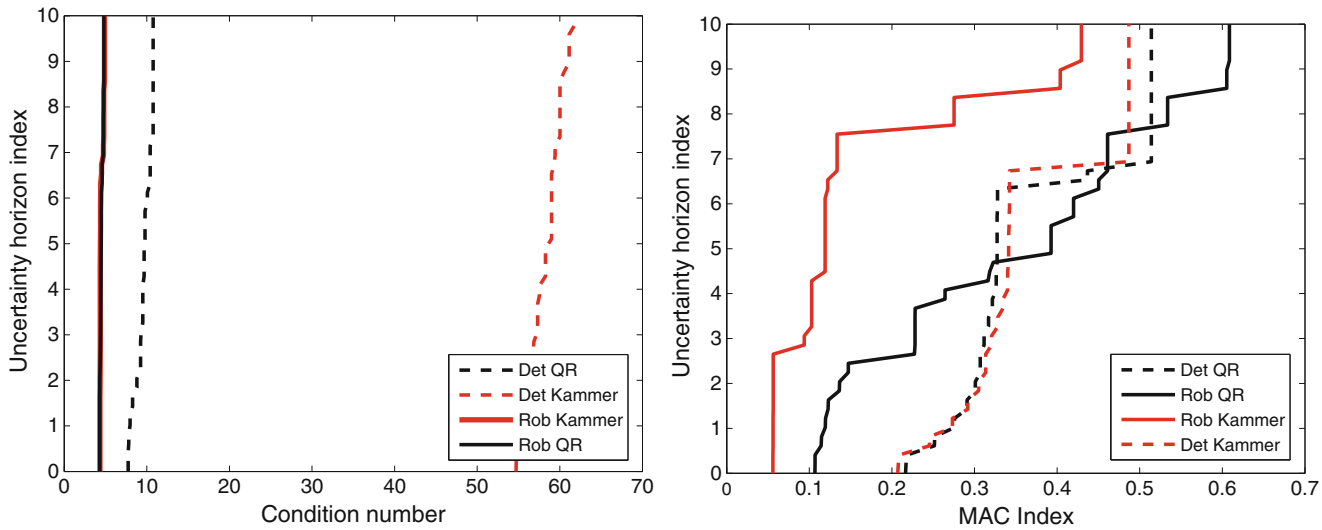

Fig. 17.3 Comparison of robustness curves for robust and determinist approaches

The robustness curves allow the results of the two sensor placement algorithms—Kammer and QR—to be compared. Focusing on the deterministic results (dotted lines), the behavior is seen to be very similar for the MAC indicator in Fig. 17.3b while significant differences are noted for the condition number indicator in Fig. 17.3a. This difference is explained by the fact that the QR algorithm explicitly minimizes the condition number of the observation matrix by maximizing its linear independence.

The results of the robust approach (solid lines) are very different from the deterministic approach. Considering the condition number indicator, a significant improvement of the results is visible for both sensor placement algorithms at all horizons of uncertainty. This improvement is due the introduction of information reflecting how the modal bases can change under structural uncertainty, in particular for modes 7 and 9 which are sensitive to the position of the point mass. Figure 17.3b confirms that the two robust algorithms lead to different sensor distributions and that the Kammer approach proves more effective in this application.

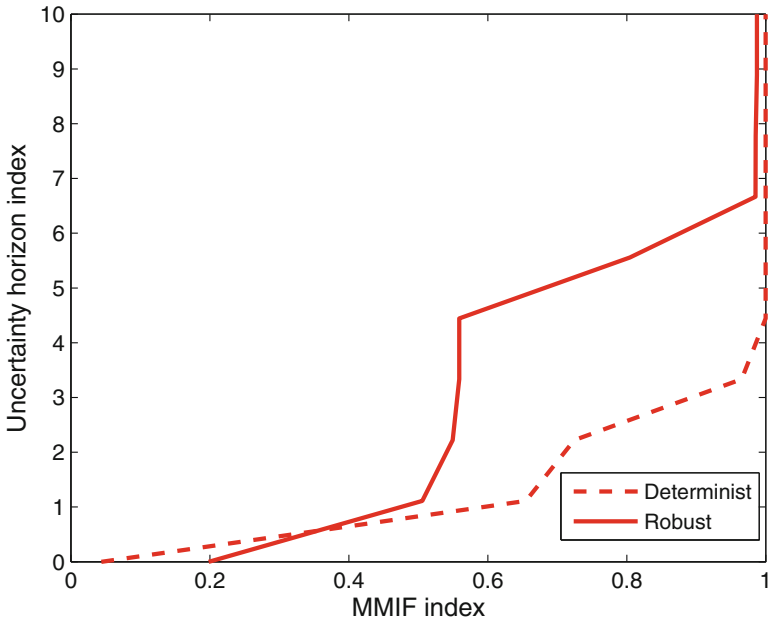

Fig. 17.4 Robustness curves for exciter design from using the Kammer robust and determinist approaches

17.3.2 Excitation Design

The sensor distributions obtained from the Kammer deterministic and robust approaches are now used to select exciter positions using the methodology presented in Sect. 17.2. Figure 17.4 shows the robustness curves for the placement of a single exciter.

This results can be divided into three regimes, each one leading to a different preference between the two designs. As a reminder, the smaller the MMIF index, the better is the excitation:

- Beyond a horizon of uncertainty of 0.75 the exciter position obtained by the deterministic approach is very efficient in exciting all the modes of the structure but its efficiency decreases rapidly as the horizon of uncertainty increases.
- From the crossing point between the two curves, between a horizon of uncertainty of 0.75 and 6.5, the curve obtained from the robust approach gives smaller MMIF value than the deterministic approach. This is the range of uncertainty where the robust approach yields a better design to excite the target modes.
- Above a horizon of uncertainty of 6.5, the two curves yield a MMIF close to 1. This means that at least one target mode is poorly excited and neither strategy provides an acceptable design. A new exciter configuration must be added to complete the missing information.

This application highlights the advantage of a robust approach exciter design under severe structural uncertainty where an optimal design without consideration of uncertainty may provide unreliable results.

17.4 Conclusion

A previously developed robust methodology for sensor design in vibration tests has been extended to exciter design. Lack of knowledge is represented in the framework of the info-gap decision theory. The proposed approach generates an augmented basis of eigenmodes consistent with the horizon of uncertainty under study and this basis provides the input for applying a variety of deterministic test design approaches. In this study, the QR decomposition and Kammer sensor selection methods has been illustrated on an academic example. The detrimental effect of uncertainty on optimal design approaches demonstrates the importance of formulating robust strategies for vibration test design, particularly for exciter design where the number of excitation points is generally small. Future work will aim at applying this global methodology to an industrial model in the presence of nonlinear joints.

Acknowledgements The authors want to thanks the CNES of Toulouse and Région Franche-Comté for their financial support.

References

1. Abdelghani, M., Friswell, M.I.: Sensor validation for structural systems with multiplicative sensor faults. Mech. Syst. Signal Process. **21**, 270–279 (2007)
2. Balmes, E.: Uncertainty propagation in experimental modal analysis. In: International Modal Analysis Conference (2004)
3. Balmes, E.: Orthogonal maximum sequence sensor placements algorithms for modal tests, expansion and visibility. In: International Modal Analysis Conference, Orlando (2005)
4. Ben-Haim, Y.: Info-Gap, Decision theory, Decisions Under Severe Uncertainty, 2nd edn. Academic, New York (2006)
5. Golub, G., Kahan, W.: Calculating the singular values and pseudo-inverse of a matrix. J. Soc. Ind. Appl. Math. Ser. B Numer. Anal. **2**(2), 205–224 (1965)
6. Hemez, F., Farhat, C.: An energy based optimum sensor placement criterion and its application to structural damage detection. In: International Modal Analysis Conference, pp. 1568–1575 (1994)
7. Kammer, D.C.: Sensor placement for non-orbitmodal identification and correlation of large space strucutres. J. Guid. Control Dyn. **14**(2), 251–259 (1991)
8. Kammer, D.C.: Effect of model error on sensor placement for on-orbit modal identification of large space structures. J. Guid. Control Dyn. **15**(2), 334–341 (1992)
9. Kammer, D.C., Falnigan, C.C., Dreyer, W.: A super-element approach to test-analysis model development. In: Proceedings of the Fourth International Modal Analysis Conference, pp. 663–673 (1986)
10. Lallement, G., Ramanitrajan, A., Cogan, S.: Optimal sensor deployment: application to model updating. J. Vib. Control **4**, 29–46 (1998)
11. Papapdimitriou, C., Beck, J.L., Au, S.K.: Entropy-based optimal sensor location for structural model updating. J. Vib. Control **6**, 781–800 (2000)
12. Qstro-Triguero, R., Murugan, S., Gallego, R., Friswell, M.I.: Robustnessofoptimalsensorplacementunder parametric uncertainty. Mech. Syst. Signal Process. **41**, 268–287 (2013)
13. Schedlinski, C., Link, M.: An approach to optimal pick-up and exciter placement. In: Proceedings-SPIE the International Society for Optical Engineering, SPIE International Society for Optical, pp. 376–382 (1996)
14. Schueller, G.I.: On the treatment of uncertainties in structural mechanics and analysis. Comput. Struct. **2007**, 235–243 (2007)
15. Vinot, P., Cogan, S., Cipolla, V.: A robust model-based test planning procedure. J. Guid. Control Dyn. **288**, 571–585 (2005)
16. Williams, R., Crowley, J., Vold, H.: The multivariate mode indicator function in modal analysis. In: International Modal Analysis Conference, pp. 66–70 (1985)
17. Zang, C., Friswell, M.I., Mottershead, J.E.: A review of robust design and its application in dynamics. Comput. Struct. **83**, 315–326 (2005)

Chapter 18
Robust Model Calibration Using Determinist and Stochastic Performance Metrics

P. Lépine, S. Cogan, E. Foltête, and M.-O. Parent

Abstract The aeronautics industry has benefited from the use of numerical models to supplement or replace the costly design-build-test paradigm. These models are often calibrated using experimental data to obtain optimal fidelity-to-data but compensating effects between calibration parameters can complicate the model selection process due to the non-uniqueness of the solution. One way to reduce this ambiguity is to include a robustness requirement to the selection criteria. In this study, the info-gap decision theory is used to represent the lack of knowledge resulting from compensating effects and a robustness analysis is performed to investigate the impact of uncertainty on both deterministic and stochastic fidelity metrics. The proposed methodology is illustrated on an academic example representing the dynamic response of a composite turbine blade.

Keywords Uncertainty • Model calibration • Info-gap approach • Performance metric • Robust solution

18.1 Introduction

Ceramic matrix composite (CMC) turbine blades have been developed by HERAKLES [1]. They consist of ceramic fibers embedded in a ceramic matrix. These textile composites show high resistance to extremely high temperature (1000 °C), low density and a good fracture toughness compared to conventional metallic alloys. Finite element models (FEM) applied to the design of composite parts are under investigation in order to obtain the predictive simulations.

Model calibration is commonly used to improve the correlation between FEM and measured data. Typically, fidelity-to-data is optimized in such approaches even though compensating effects between model parameters may lead to subspaces of fidelity-equivalent solutions [2]. These effects tend to hide missing physics in the model form and create ambiguity in the model selection process. A model is considered as predictive if it remains in a subdomain limited by a satisfying boundary at the required performance level. A satisfying boundary is a family of plausible models displaying the same comparable measure of fidelity [3]. A recent paper has proposed to complete a deterministic fidelity error metric with a robustness criteria quantifying the impact of compensating effects on the fidelity-to-data [3]. This paper will extend that approach to illustrate that it remains relevant for stochastic error metrics as well. Info-gap decision theory is used to provide a formal framework for investigating the impact of unknown compensating effects on both deterministic and stochastic fidelity metrics. A simplified model of a turbine blade is studied to illustrate the proposed methodology using simulated test results.

P. Lépine (✉)
Institut FEMTO-ST, Université de Bourgogne-Franche-Comté, 24 rue de l'épitaphe, 25000 Besançon, France

SNECMA-SAFRAN, Rond-point René Ravaud, Réau, 77550 Moissy-Cramayel, France
e-mail: paul.lepine@femto-st.fr

S. Cogan • E. Foltête
Institut FEMTO-ST, Université de Bourgogne-Franche-Comté, 24 rue de l'épitaphe, 25000 Besançon, France

M.-O. Parent
SNECMA-SAFRAN, Rond-point René Ravaud, Réau, 77550 Moissy-Cramayel, France

S. Atamturktur et al. (eds.), *Model Validation and Uncertainty Quantification, Volume 3*, Conference Proceedings of the Society for Experimental Mechanics Series, DOI 10.1007/978-3-319-29754-5_18

18.1.1 Fidelity-to-Data Metrics for Model Calibration

The fidelity of simulated outcomes to experimentally identified outcomes can be quantified with both deterministic and stochastic metrics. For example, a common deterministic metric is the normed Euclidean distance D_E:

$$D_E = \sum_{i=1}^{n} \frac{\sqrt{(v_{a_i} - v_{m_i})^2}}{v_{m_i}} \tag{18.1}$$

where v_m is a vector containing the experimentally identified outcomes (n outputs) and v_a the homologous vector containing the analytical outcomes.

When population data is available for simulations and/or experiments, stochastic metrics can be implemented. In this case, the model now provides uncertain outputs and can be calibrated using stochastic approaches such as covariance adjustment [4] or Gibbs sampling [5] and Metropolis-Hasting algorithm [6]. In this paper, the Bhattacharyya distance D_B will be used to quantify the fidelity-to-data for multivariate features [7] but other metrics could be used as well. The Bhattacharyya metric takes into account the differences between both the means and the covariances between the simulated and experimental distributions:

$$D_B = \frac{1}{8}(\bar{v}_a - \bar{v}_m)^T \Sigma^{-1} (\bar{v}_a - \bar{v}_m) + \frac{1}{2} \ln \left(\frac{\det(\Sigma)}{\sqrt{\det \Sigma_a \det \Sigma_m}} \right) \tag{18.2}$$

where $\bar{v}_m$ is the vector containing the mean values of the measured outcomes and $\bar{v}_a$ the mean values of the simulated outcomes. The pooled matrix $\Sigma = \frac{\Sigma_a + \Sigma_m}{2}$ combines the covariance matrices of the simulated and experimental outcomes.

18.1.2 Info-Gap Theory

Info-gap decision theory, developed by Ben-Haim [8], has been used to study a wide range of problems in various disciplines including climate models [9] and medical research [10]. The purpose of info-gap is to provide tools for decision-makers in order to assess risks and opportunities of model-based decisions under a severe lack of information. The reader is referred to [8] for more detailed information.

In the info-gap approach, a horizon of uncertainty α quantifies the difference between what is known and what needs to be known to make an informed decision. When considering fidelity-to-data R, the worst case fidelity $\hat{R}$, for a given horizon of uncertainty α_i, is evaluated by solving the following optimization problem [3]:

$$\hat{R}(\alpha) = \max_{\theta \in U(\alpha, \tilde{\theta})} R(\theta) \tag{18.3}$$

where $\tilde{\theta}$ is the vector of calibrated best-estimate parameters of the simulation. The robustness function expresses the greatest level of uncertainty at which performance remains acceptable.

$$\hat{\alpha} = \max\{\alpha : \hat{R}(\alpha) \geq R_c\} \tag{18.4}$$

where $\hat{\alpha}$ is the maximum horizon for which the performance function $R \leq R_c$ is satisfied.

The notional diagram in Fig. 18.1 illustrates how the robustness curve is obtained. Let u_1 and u_2 be the calibration parameters. The point $\alpha_A = 0$ corresponds to the nominal model with no uncertainty and $R(u_{1A}, u_{2A})$ the corresponding performance. As the horizon of uncertainty increases to α_B, the worst case performance over the uncertain domain is given by $R(u_{1B}, u_{2B})$, and so on. In practice, the robustness curve is obtained by solving an optimization problem with an appropriate algorithm based on either local or global approaches. For example, in [11], the authors search the space using a factorial design.

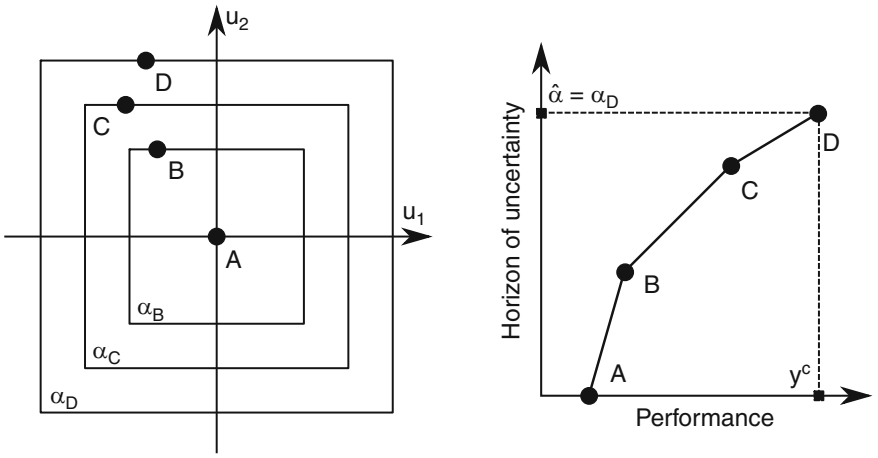

Fig. 18.1 Nested input sets (*left*) and the corresponding robustness curve (*right*)

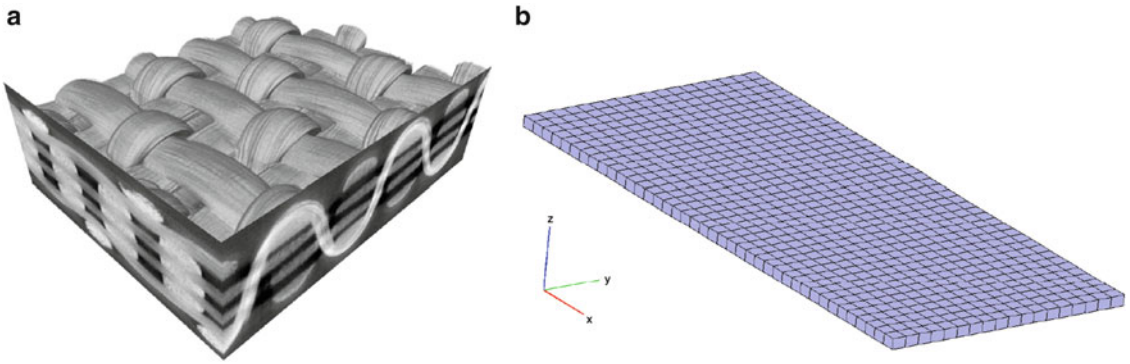

Fig. 18.2 3D tomography reconstruction (**a**) and the FEM plate studied (**b**) [15]

18.2 Numerical Application

Ceramic composite textiles are made of sets of tows Si-C sewn into a pattern as shown in Fig. 18.2. A ceramic matrix is filled into the fibres of the preform to enhance the mechanical properties. Composite textiles can be considered as periodic mesoscopic structures characterized by their smallest elementary pattern called the representative unit cell. A mesoscopic analysis allows the homogenized properties of the composite [12] to be computed. The mesoscopic structure of the studied material has been probed using an X-ray Micro Tomograph and its behavior through multi-instrumented experiments [13, 14].

These properties are then implemented in a numerical model to simulate the structural responses. It is not uncommon for the nominal test-analysis error to be unacceptably large. Given the uncertainties in the manufacturing process and experiments, stochastic calibration approaches are best adapted to improve model fidelity. Model form error (MFE)—due to poorly modeled boundary conditions, geometry, and material properties—is also a important source of discrepancy between simulated and experimental outcomes and remains a challenge in the calibration process.

The purpose of this section is to illustrate the impact of compensating effects and model form error on model selection with both optimal and robust strategies. A simple two parameters example is studied representing a free-free thin CMC plate with orthotropic properties. The calibration parameters are the Young's modulus E_1 and E_2 while the other parameters are assumed to be known. The experimental data are simulated based on the nominal model parameters. The fidelity error metric is formulated with respect to the eigenfrequencies of the structure.

The deterministic and stochastic calibration metrics for the first ten eigenfrequencies are calculated over the domain $[0.6 : 1.4]$, discretized into 21 levels, corresponding to the correction coefficients for the parameters E_1 and E_2. The center point $E_1 = E_2 = 1$ thus defines the nominal design used to simulated the tests. In order to reduce calculation costs for the population based fidelity metric, a neural network surrogate model is constructed from a preliminary full factorial design. The Bhattacharyya metric is then evaluated at each design point based on 10^5 Monte-Carlo samples.

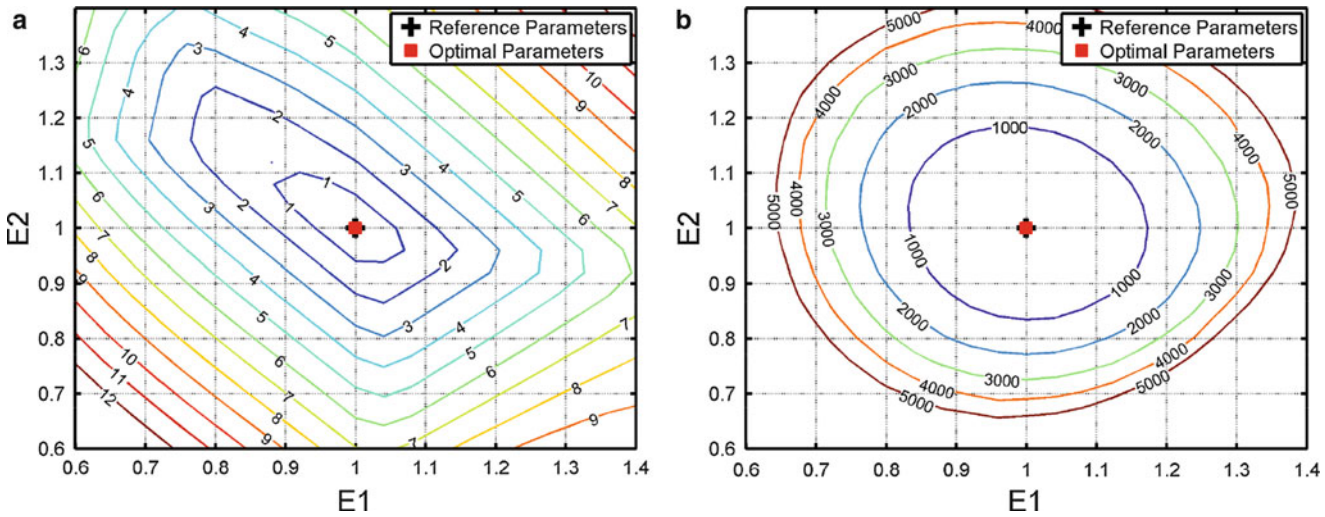

Fig. 18.3 Isocontour performance without model form error. (**a**) Euclidean metric. (**b**) Bhattacharyya metric

Table 18.1 Random parameter values for case 1

Parameters value	Output means value			Output standard deviation			Output covariance		
(E_1, E_2)	$\bar{\mu}_1$	$\bar{\mu}_2$	$\bar{\mu}_3$	$\sigma(\mu_1)$	$\sigma(\mu_2)$	$\sigma(\mu_3)$	$\text{cov}(\mu_1, \mu_2)$	$\text{cov}(\mu_2, \mu_3)$	$\text{cov}(\mu_1, \mu_3)$
(1,1)	1.00	1.13	2.52	1.00	0.03	1.13	0.18	0.20	1.12
(0.7,0.7)	0.84	1.12	2.23	1.58	0.00	5.43	−0.06	−0.12	2.92
(0.7,1.3)	0.84	1.12	2.27	1.53	0.00	5.42	−0.07	−0.12	2.88
(1.3,1.3)	1.11	1.17	2.60	0.53	0.20	0.03	0.33	0.07	0.12
(1.3,0.7)	1.11	1.17	2.58	0.52	0.21	0.03	0.33	0.06	0.10

18.2.1 Test Case Without Model Form Error

In this first case, we assume that the numerical eigenfrequencies are obtained with a perfect model, that is to say, without any model form error. The fidelity metrics are plotted in the space of the two parameters (Fig. 18.3). The contours indicate fidelity-equivalent solutions and define the satisfying boundaries. The square marker designates the globally minimum error and represents the optimal solution. As expected, this marker totally coincides with the design point used to generate the experimental data for distance metrics.

In Fig. 18.3a, there is a large area where the error remains below 5 %, illustrating that calibrated solutions can be very different for equivalent levels of fidelity. These compensating effects are inevitable even in the absence of bias in the model prediction. In Fig. 18.3b, the isocontours create nested contours centered on [1, 1]. The reference outputs at $E_1 = E_2 = 1$ and some numerical results are presented in Table 18.1.

18.2.2 Test Case with Model with Form Error

In this case we assume that the model contains a model form error and is unable to perfectly simulate the observed physics. In this academic example, the shear modulus G_{12} is overestimated about 20 %. The experimental eigenfrequencies remain the same as before. Figure 18.4 displays the new satisfying boundary maps.

The shape of the isocontours for the euclidean metric is similar to the previous case (Fig. 18.3a) with a noticeable shift toward the upper left of the domain. Thus the optimal parameters are no longer located in (1, 1) with 2.9 % error but (0.72, 1.12) with 1.5 %. The Bhattacharyya metric displays more complex isocontour lines and a shifted optimal solution as well. The implication of this shift is that any calibration algorithm based uniquely on optimizing the fidelity will invariably converge to the wrong solution. Although there is clearly no simple solution to this problem, it is possible in some cases to attenuate the impact of compensating effects on model fidelity.

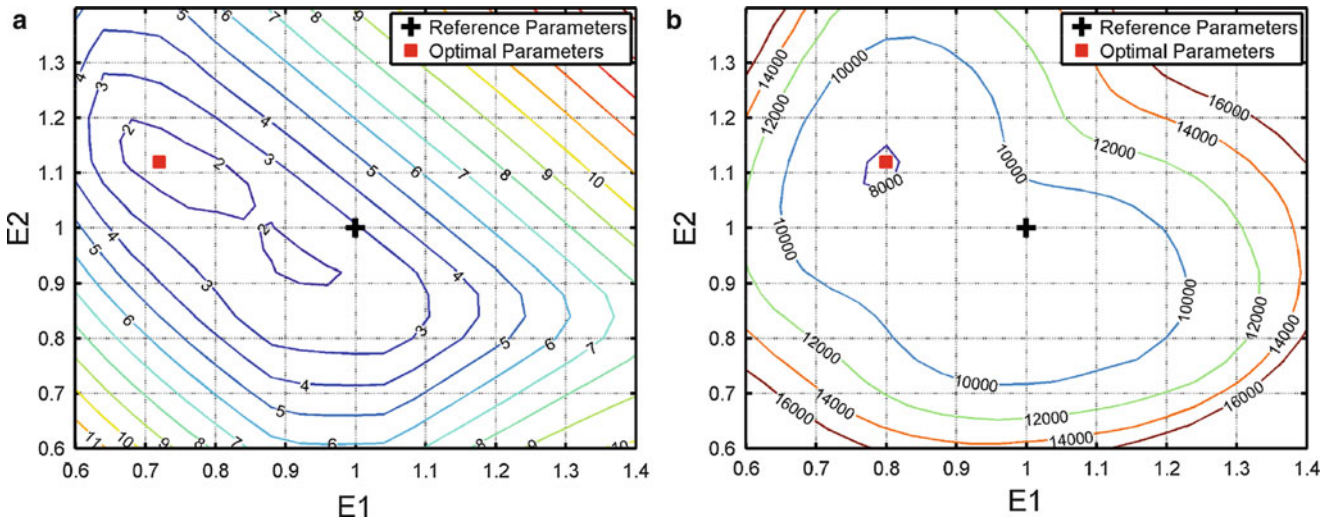

Fig. 18.4 Isocontour performance with model form error. (**a**) Euclidean metric. (**b**) Bhattacharyya metric

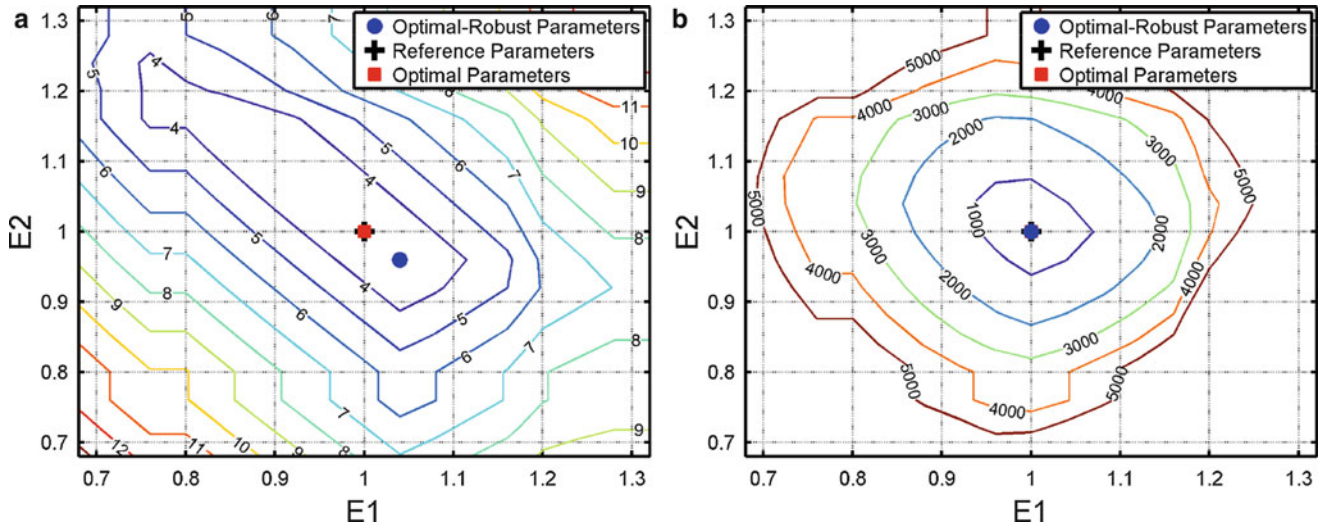

Fig. 18.5 Robust isocontour performances of the optimal model. (**a**) Euclidean metric. (**b**) Bhattacharyya metric

18.2.3 Robustness to Compensating Effects

Given the inevitable presence of compensating effects between calibration parameters—with and without model form error—the approach proposed in [3] has been adopted here with the objective of demonstrating that it remains relevant for both deterministic and stochastic fidelity metrics. In this context, the info-gap uncertainty represents the lack of knowledge in the parameter space due to compensating effects and the goal is to find the most robust sets of parameters E_1, E_2 insuring an acceptable level of fidelity.

With respect to the previous test case without model form error, the corresponding robust fidelity metric is shown in Fig. 18.5 for a horizon of uncertainty $\alpha = 10\,\%$. These contours are obtain by evaluating, for each design point (E_1^i, E_2^i), the worst-case fidelity within the uncertain subdomain, a square of sides 0.1×0.1, centered about the point. The contours have not changed significantly in shape but the overall errors have of course increased. The round marker indicates the best robust calibrated solution which is different from the optimal solution from before. These contours clearly depend on the horizon of uncertainty and increasing α will necessarily lead to larger fidelity errors and even different robust solutions.

The robust fidelity isocontours for the second test case containing model form error are shown in (Fig. 18.6), with markers for the reference solution (cross-shaped), the optimal solution (square), and the robust-optimal solution (round). Table 18.2

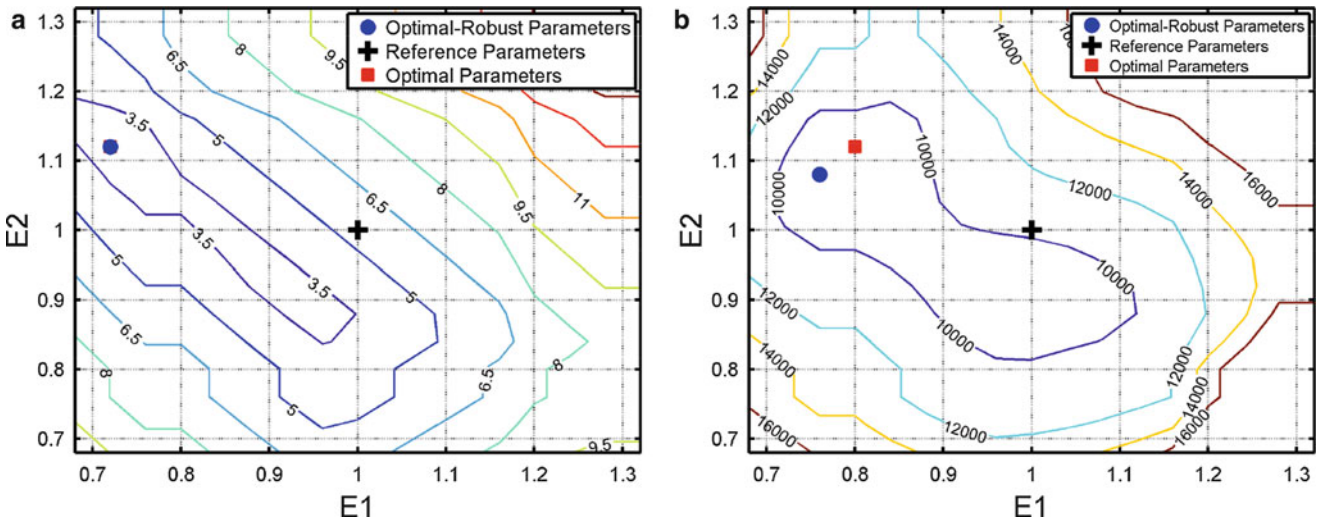

Fig. 18.6 Robust isocontour performances of the model with form error. (**a**) Euclidean metric. (**b**) Bhattacharyya metric

Table 18.2 Optimal-robust parameters comparison

	Nominal		Stochastic	
	Coordinates	Robust error (%)	Coordinates	Robust error
Reference	(1.00,1.00)	5.45	(1.00,1.00)	1.02×10^4
Optimal	(0.72,1.12)	2.81	(0.80,1.12)	9.13×10^3
Optimal-robust	(0.72,1.12)	2.81	(0.76,1.08)	8.76×10^3

provides a summary of these solutions. In this example, these solutions are clearly different and although it is generally impossible to know the true solution, it is possible to improve the robustness of the solution to compensating effects for both deterministic and stochastic fidelity metrics.

18.3 Conclusion

Model calibration based uniquely on fidelity-to-data metrics fall prey to compensating effects between model parameters due to the presence of model form errors and subspaces of fidelity-equivalent solutions. This paper extends earlier work that includes a robustness criteria in the model selection process and illustrates the relevance of such an approach for both deterministic and stochastic metrics. An academic test case representing a composite turbine blade is studied in a notional way with simulated test data. Two calibration metrics have been investigated, in particular a deterministic Euclidean error and a statistical Bhattacharyya error, and both are seen possess both fidelity optimal and robust optimal solutions which are distinct from one another.

References

1. SNECMA and HERAKLES: Aube de Turbomachine en Matériau Composite et Procédé pour sa Fabrication - Brevet. WO 2011/080443 A1 (2011)
2. Berman, A.: Multiple acceptable solutions in structural model improvement. AIAA J. **33**(5), 924–927 (1995)
3. Atamturktur, S., Liu, Z., Cogan, S., Juang, H.: Calibration of imprecise and inaccurate numerical models considering fidelity and robustness: a multi-objective optimization-based approach. Struct. Multidiscip. Optim. **51**, 659–671 (2014)
4. Govers, Y., Link, M.: Stochastic model updating - Covariance matrix adjustment from uncertain experimental modal data. Mech. Syst. Signal Process. **24**(3), 696–706 (2010)
5. Smith, A.F.M., Roberts, G.O.: Bayesian computation via the Gibbs sampler and related Markov chain Monte Carlo methods. J. R. Stat. Soc. **55**(1), 3–23 (1993)
6. Chib, S., Greenberg, E.: Understanding the Metropolis-Hastings algorithm. Am. Stat. **49**(4), 327–335 (1995)
7. Aherne, F.J., Thacker, N.A., Rockett, P.I.: The Bhattacharyya metric as an absolute similarity measure for frequency coded data. Kybernetika **34**(4), 363–368 (1998)

8. Ben-Haim, Y.: Info-Gap Decision Theory: Decisions Under Severe Uncertainty. Academic, New York (2006). [ISBN: 978-0-12-373552-2]
9. Hall, J.W., Lempert, R.J., Keller, K., Hackbarth, A., Mijere, C., McInerney, D.J.: Robust climate policies under uncertainty: a comparison of robust decision making and info-gap methods. Risk Anal. **32**(10), 1657–1672 (2012)
10. Ben-Haim, Y., Zacksenhouse, M., Keren, C., Dacso, C.C.: Do we know how to set decision thresholds for diabetes? Med. Hypotheses **73**(2), 189–193 (2009)
11. Kuczkowiak, A.: Modèle hybride incertain pour le calcul de réponse en fonctionnement d'un alternateur. PhD thesis, Université de Franche-Comté (2014)
12. Naouar, N., Vidal-Sallé, E., Schneider, J., Maire, E., Boisse, P.: Meso-scale FE analyses of textile composite reinforcement deformation based on X-ray computed tomography. Compos. Struct. **116**, 165–176 (2014)
13. Couégnat, G.: Approche multiéchelle du comportement mécanique de matériaux composites à renfort tissé. PhD thesis, Université Sciences et Technologies-Bordeaux I (2008)
14. Dupin, C.: Etude du comportement mécanique des matériaux composites à matrice céramique de faible épaisseur. PhD thesis, Bordeaux 1 (2013)
15. Naouar, N., Vidal-Salle, E., Schneider, J., Maire, E., Boisse, P.: 3d composite reinforcement meso F.E. analyses based on X-ray computed tomography. Compos. Struct. **132**, 1094–1104 (2015)

Chapter 19
Designing a Mechanical Latch for Robust Performance

François Hemez and Kendra Van Buren

Abstract Advances in computational sciences in the past three decades, such as those embodied by the finite element method, have made it possible to perform design and analysis using numerical simulations. While they offer undeniable benefits for rapid prototyping and can shorten the design-test-optimize cycle, numerical simulations also introduce assumptions and various sources of uncertainty. Examples are modeling assumptions proposed to represent a nonlinear material behavior, energy dissipation mechanisms and environmental conditions, in addition to numerical effects such as truncation error, mesh adaptation and artificial dissipation. Given these sources of uncertainty, what is the best way to support a design decision using simulations? We propose that an effective simulation-based design hinges on the ability to establish the robustness of its performance to assumptions and sources of uncertainty. Robustness means that exploring the uncertainty space that characterizes the simulation should not violate the performance requirement. The theory of information-gap ("info-gap") for decision-making under severe uncertainty is applied to assess the robustness of two competing designs. The application is the dynamic stress performance of a mechanical latch for a consumer electronics product. The results are that the variant design only yields 10 % improvement in robustness to uncertainty while requiring 44 % more material for manufacturing. The analysis provides a rigorous rationale to decide that the variant design is not viable. (*Approved for unlimited*, *public release*, *LA-UR-21296*, *unclassified*.)

Keywords Robust design • Mechanical latch • Finite element analysis • Uncertainty quantification

19.1 Introduction

This publication addresses a challenge posed by supporting decisions with numerical simulations. Advances in computational sciences in the past three decades, such as those embodied by the finite element method, have made it possible to perform design and analysis using simulation models [1]. This trend has been further accelerated in recent years by the development of software capabilities, parallel processing, data interrogation, and graphics.

While they offer undeniable benefits for rapid prototyping and can shorten the design-test-optimize cycle, numerical simulations also introduce assumptions and their own sources of uncertainty. Examples are modeling assumptions proposed to represent a nonlinear material behavior, energy dissipation mechanisms and environmental conditions, in addition to numerical effects such as truncation error, mesh adaptation, and artificial dissipation. Given these sources of uncertainty, what is the best way to support a design decision using numerical simulations?

Our contention is that an effective simulation-based design hinges on the ability to establish the robustness of model predictions to assumptions and sources of uncertainty. Robustness means that exploring the uncertainty space that characterizes the simulation should not violate the requirement of performance defined by the analyst. For some designs the requirement will be violated while exploring a smaller uncertainty space than for other designs. Given two designs of the same cost, preference should always be given to the more robust design, that is, the solution that tolerates more uncertainty without endangering performance.

Even though it is not discussed here, pursuing a robust design can also complement or replace strategies that optimize the margin between the requirement and performance delivered by the design. A commonly encountered approach to do so is

F. Hemez (✉)
Los Alamos National Laboratory, XTD-IDA, Mail Stop T087, Los Alamos, NM 87545, USA
e-mail: hemez@lanl.gov

K. Van Buren
Los Alamos National Laboratory, XCP-8, Mail Stop F644, Los Alamos, NM 87545, USA
e-mail: klvan@lanl.gov

S. Atamturktur et al. (eds.), *Model Validation and Uncertainty Quantification, Volume 3*, Conference Proceedings of the Society for Experimental Mechanics Series, DOI 10.1007/978-3-319-29754-5_19

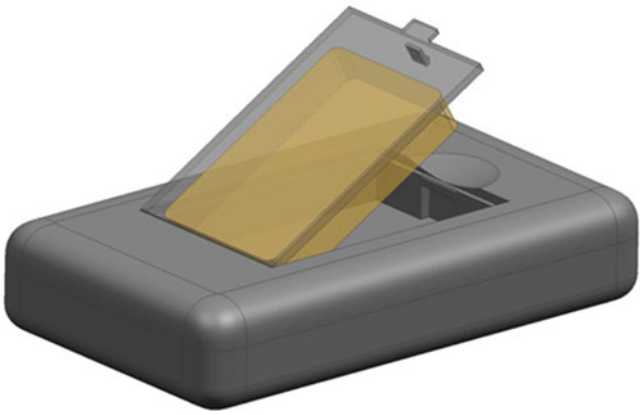

Fig. 19.1 Conceptual illustration of compartment for a consumer electronics product

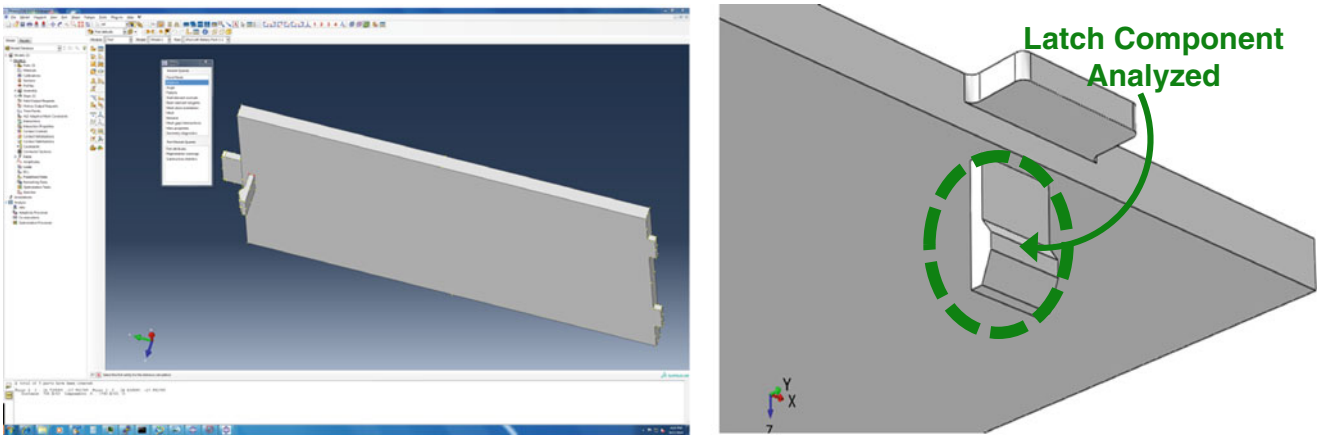

Fig. 19.2 Geometry of the door (*left*) and detail of the latch analyzed (*right*)

to apply a Factor of Safety (FOS). It can be shown that, by seeking the design solution with the worst possible performance that still meets the requirement, an analysis of robustness implicitly defines a FOS. For this reason, no FOS is considered in the application discussed below.

Many formulations have been developed to establish robustness, including Monte Carlo-based approaches, optimization methods, and fast probability integration. The theory of information-gap ("info-gap") for decision-making under severe uncertainty is used, here, to formulate the problem and assess the robustness of a design [2]. Info-gap offers the advantage of requiring minimum assumptions, which is convenient in early phases of the design cycle, while efficiently communicating the results of an analysis through the concept of robustness function.

Instead of offering a theoretical discussion, this publication is articulated around the steps followed to search for a robust design. The application is the mechanical latch of a compartment door for a consumer electronics product, as shown conceptually in Fig. 19.1. The objective is to design the latch to ensure a robust opening/closing performance of the compartment.

Figure 19.2 shows the geometry of the compartment door in the left image and its latch component in the image on the right. The first step is to define the problem, which entails simplifications of the geometry, loading scenario, and decision criterion. Expert judgment suggests that the analysis be focused on stresses generated in the latch part when opening and closing the door. For simplicity the rest of the compartment is ignored, the contact condition is idealized, and severe transient loads, such as those produced when dropping the product on the floor, are not considered. Non-elastic deformation, plasticity, damage, and failure mechanics are ignored.

The latch is fabricated using a generic polycarbonate material whose assumed material properties for linear elasticity are listed in Table 19.1. A loading scenario also needs to be defined. It is assumed that the latch's "head" locks in place to close the compartment door securely after deflecting by a distance comprised within:

Table 19.1 Generic material properties for polycarbonate material

Variable	Description	Nominal value
E	Modulus of elasticity	2.00 GPa
G	Shear modulus	0.73 GPa
ν	Poisson's ratio	0.37
ρ	Mass density	1200 kg/m^3
σ_{Yield}	Yield stress	55 MPa

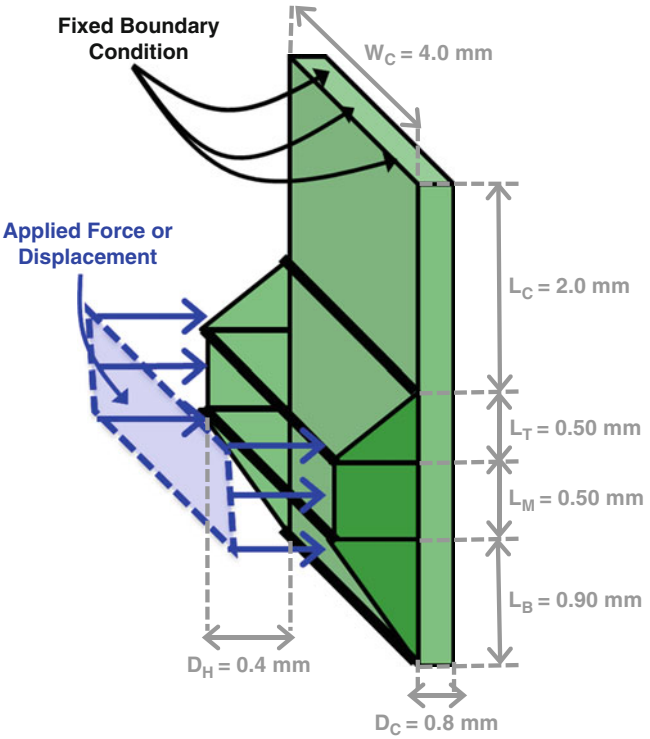

Fig. 19.3 Simplification of the latch geometry (nominal design shown)

$$0.20 \text{ mm} \leq u_{Contact} \leq 0.80 \text{ mm} \tag{19.1}$$

As further explained below, the simulation model imposes a displacement $U_{Contact}$ to the contact surface, which generates the deflection of the latch as the compartment door opens or closes. It produces a dynamic mating force that is assumed to be the main load applied to the latch.

Finally, a performance requirement needs to be defined for simulation-based decision-making. Multiple criteria are often considered in structural design, sometimes conflicting with each other. One wishes, for example, to reduce the weight of a component while increasing its stiffness. To keep this proof-of-concept as simple as possible, a single requirement is defined. The design is said to be requirement-compliant if the maximum value of dynamic stress of the latch does not exceed the yield stress of the material. This requirement is written mathematically as:

$$\sigma_{Max} \leq \sigma_{Yield} \tag{19.2}$$

Figure 19.3 concludes this brief description of the problem by showing the geometry adopted for numerical simulation. This geometry is for the nominal design. Many features are ignored, such as round corners meant to avoid stress concentrations, however, the overall dimensions, material properties, and loading scenarios are preserved in this simplified scenario.

In this publication, the methodology proposed to search for a design robust to uncertainties is emphasized rather than searching for the design that minimizes the stress induced in the material. The manuscript is organized as follows. Section 19.2 defines the simulation flow used in the study. The sources of uncertainty in the simulation and methodology for robustness analysis are given in Sect. 19.3. The comparison between two candidate designs is discussed in Sect. 19.4. Section 19.5 offers conclusions and directions for future work.

19.2 Definition of the Finite Element Simulation Flow

A numerical simulation is developed to study the performance of the latch design. The geometry shown in Fig. 19.3 for the nominal design is parameterized such that it can be easily modified and discretized using the Finite Element (FE) method. The tool used for this study is a stand-alone MATLAB®-based FE code written by the first author to support various teaching and training activities. This software implements basic capabilities for linear static and dynamic analyses. The geometry is discretized with eight-node (linear interpolation) "brick" elements [3] and responses are obtained using the Newmark time-integration algorithm [4].

Figure 19.4 illustrates the simulation flow. A FE mesh is generated for a specified latch geometry and mesh seed. A displacement profile is applied to integrate the equation-of-motion and obtain the deformation as a function of time. For simplicity, the moments are approximated using the analytical expression shown in the fourth box of Fig. 19.4, where the displacements and forces, U(x) and F(x), are predicted by the FE model. The final step is to calculate the peak stress, as shown in the fifth box of Fig. 19.4. This approach combines the FE simulation of latch deflections to the approximation of moments and stresses inspired from Timoshenko beam theory. The benefit of easy implementation that it offers needs to be contrasted with the fact that it relies on a theory that might not be fully justifiable for the problem. It is nevertheless pursued since our goal is to illustrate robust-design, rather than attempt to find a "real" design.

The simulation flow of Fig. 19.4 is implemented to assess the robustness to uncertainty of the nominal design. The mesh seed for the FE model is selected based on results obtained from the mesh refinement study discussed in [5]. Figure 19.5 illustrates the FE mesh chosen for analysis, which features a seed of $\Delta x = 200\ \mu m$ and a unit aspect ratio ($\Delta x \approx \Delta y \approx \Delta z$) as much as possible.

The rationale for selecting the mesh size is to find a trade-off between truncation error and time-to-solution. Running the calculation with a mesh size of 200 μm takes 3.8 min when the FE code is executed on the dual-core processor of a laptop computer, and yields an upper bound of truncation error of 4.75 MPa for the prediction of peak stress. This level of truncation is deemed acceptable to support decision-making since it represents a numerical uncertainty of only ≈10 % relative to the yield stress criterion, $\sigma_{Yield} = 55$ MPa (from Table 19.1).

19.3 Definition of the Robust-Design Methodology

This section discusses the robust-design methodology. The first step is to parameterize the latch geometry to render it easy to modify; this parameterization defines the design space. The second step is to define the sources of uncertainty that the design should be robust to. This uncertainty represents the fact that real-world conditions may differ from what is assumed in the simulation model by unknown amounts. The third and final step is to formulate the robust-design methodology and apply it to the nominal design of Fig. 19.3.

The first step is to select the design variables exercised in the study. Of all candidates shown in Fig. 19.3 (W_C, L_C, L_T, L_M, L_B, D_C, and D_H), two design variables are selected based on the results of a sensitivity analysis [5]. They are the length of the latch, $L_{Column} = L_C + L_T + L_M + L_B$, and its width, $W_{Column} = W_C$, whose nominal values are $L_{Column} = W_{Column} = 4.0$ mm. The methodology for sensitivity analysis follows the approach presented in [6, 7] for the verification and validation of a FE model of wind turbine blade.

The next step is to define the sources of uncertainty that the design must be robust to. This uncertainty accounts for the fact that real-world conditions might differ from what is assumed in the simulation model. To make matter worse, the magnitude of these differences, or by how much the model could be wrong, is unknown. Table 19.2 defines the main sources of uncertainty considered in this study. It can be observed that the first four variables (E; G; ν; ρ) represent variability of polycarbonate plastics estimated from surveying the material properties published by various manufacturers. The fifth variable, $U_{Contact}$, represents the unknown displacement to which the latch mechanism might be subjected when opening or closing the compartment door. The sixth variable, F_{OS}, is purely numerical in nature; it accounts for the fact that the actual loading might differ from how the contact displacement is specified in the simulation. Variable F_{OS} is a scaling factor that changes the dynamic overshoot resulting from the application of a short-duration transient load.

At this point of the analysis, a two-dimensional design space $p = (L_{Column}; W_{Column})$ is defined, together with the sources of uncertainty listed in Table 19.2 and the performance requirement (19.2). We now seek to assess the robustness of the nominal design, that is, the extent to which its performance is immune to the uncertainty considered in the analysis. The peak stress of the nominal design is predicted to be $\sigma_{Max} = 28 \pm 4.75$ MPa with the 0.2-mm mesh, which clears the requirement of not exceeding a yield stress of 55 MPa. The question is whether the design remains compliant as the uncertainty variables start to deviate from their nominal values.

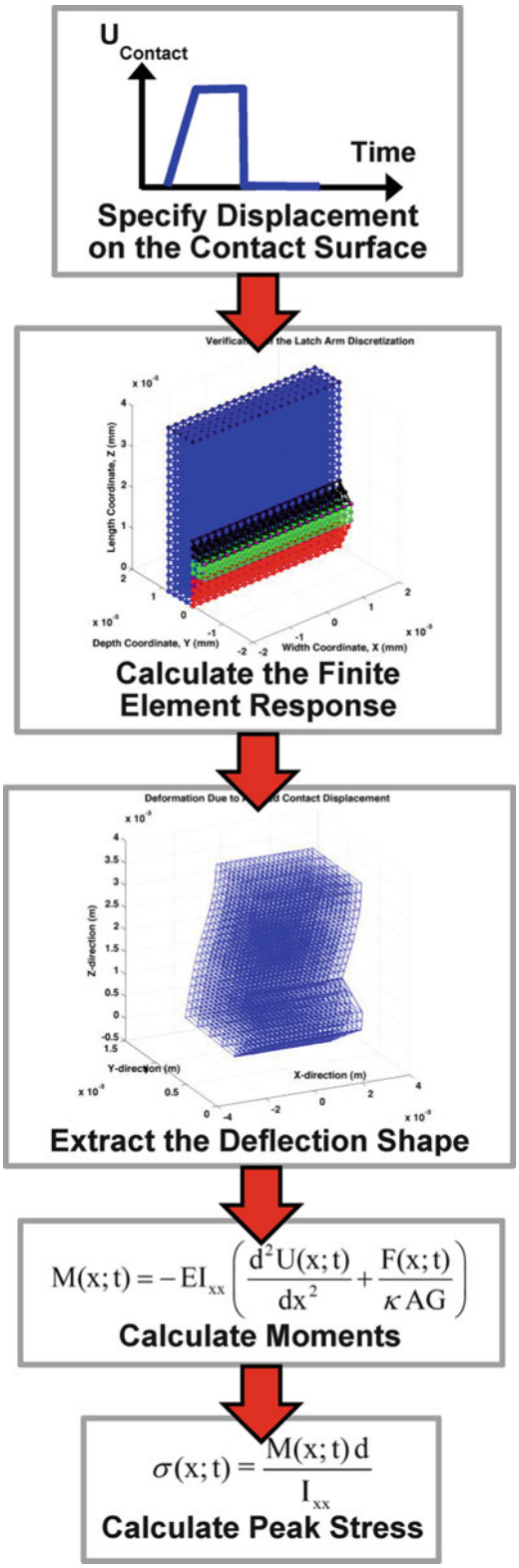

Fig. 19.4 Flowchart of the simulation strategy used in the study

Answering the question of robustness basically amounts to assessing how the performance of the design, such as the peak stress σ_{Max}, changes as increasingly more uncertainty is explored within the simulation. Uncertainty, here, is simply modeled as a six-dimensional hyper-cube:

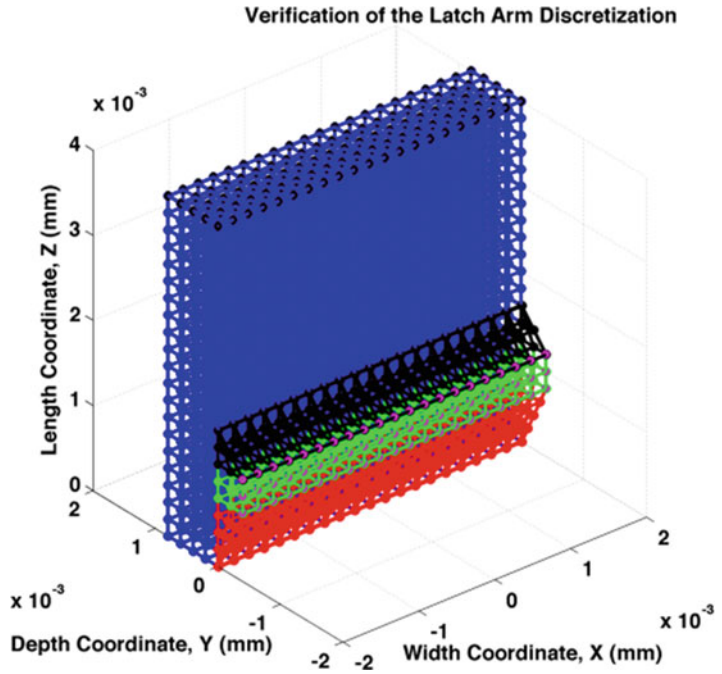

Fig. 19.5 Computational mesh of the latch at $\Delta x = 0.20$ mm (nominal design)

Table 19.2 Definition of the sources of uncertainty in the simulation model

Variable	Description	Nominal	Range
E	Modulus of elasticity	2.00 GPa	2.00–3.00 GPa
G	Shear modulus	0.73 GPa	0.71–1.11 GPa
ν	Poisson's ratio	0.37	0.35–0.40
ρ	Mass density	1200 kg/m^3	1200–1250 kg/m^3
$U_{Contact}$	Applied contact displacement	0.40 mm	0.20–0.80 mm
F_{OS}	Dynamic load overshoot factor	1.00	0.50–1.50

$$U(\theta_0;\alpha) = \{\theta \ \text{ such that } \alpha \cdot W_L \le \theta - \theta_0 \le \alpha \cdot W_U\} \tag{19.3}$$

where the symbol θ denotes one of the variables listed in Table 19.2, that is, $\theta = E, G, \nu, \rho, U_{Contact}$, or F_{OS}; θ_0 is the nominal value of the variable; and $(W_L; W_U)$ are weights used for convenience. In this model of uncertainty, the parameter α plays the role of a horizon-of-uncertainty, that is, the maximum amount by which a variable θ used in a FE run can deviate from its nominal value θ_0. The weights $(W_L; W_U)$ are defined judiciously to render α unit-less and such that the ranges of Table 19.2 are recovered when $\alpha = 1$. For example, $\alpha = 0.2$ defines a 20 % level of uncertainty where the shear modulus varies within $0.2 \times (0.71–0.73) \le G - 0.73 \le 0.2 \times (1.11 - 0.73)$ MPa.

Despite its apparent simplicity, the uncertainty model, $U(\theta_0;\alpha)$, recognizes that decision-making is usually confronted to a double challenge. The first challenge is that, for a fixed horizon-of-uncertainty, the variables θ are unknown and can assume any values within the intervals shown in Eq. (19.3). It expresses the fact that real-world conditions, which are represented by θ, can deviate from assumptions made in the FE calculation, which are represented by θ_0. A second challenge is that the horizon-of-uncertainty itself is unknown. It expresses the fact that the decision-maker might not be aware of the extent to which real-world conditions differ from what is assumed in the simulation model. The info-gap model of uncertainty of Eq. (19.3) measures the gap between what is assumed, which is θ_0, and what needs to be known, which is θ [2].

Decision-making is based on the concept of a robustness function illustrated in Fig. 19.6. It is a mapping of the worst-case performance (σ_{Max}) as a function of horizon-of-uncertainty (α). The shape of the robustness function indicates the extent to which the worst-case performance deteriorates as increasingly more uncertainty is considered in the analysis. A robust decision is one that tolerates as much uncertainty as possible without entering the "failure" domain.

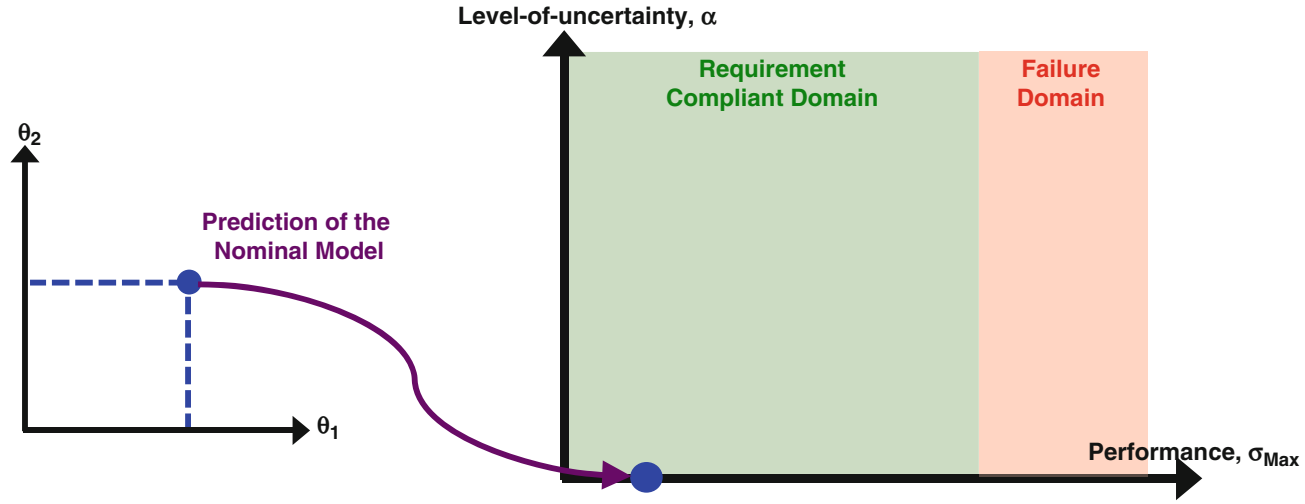

(6-a) Prediction of the nominal model used to initialize the robustness function.

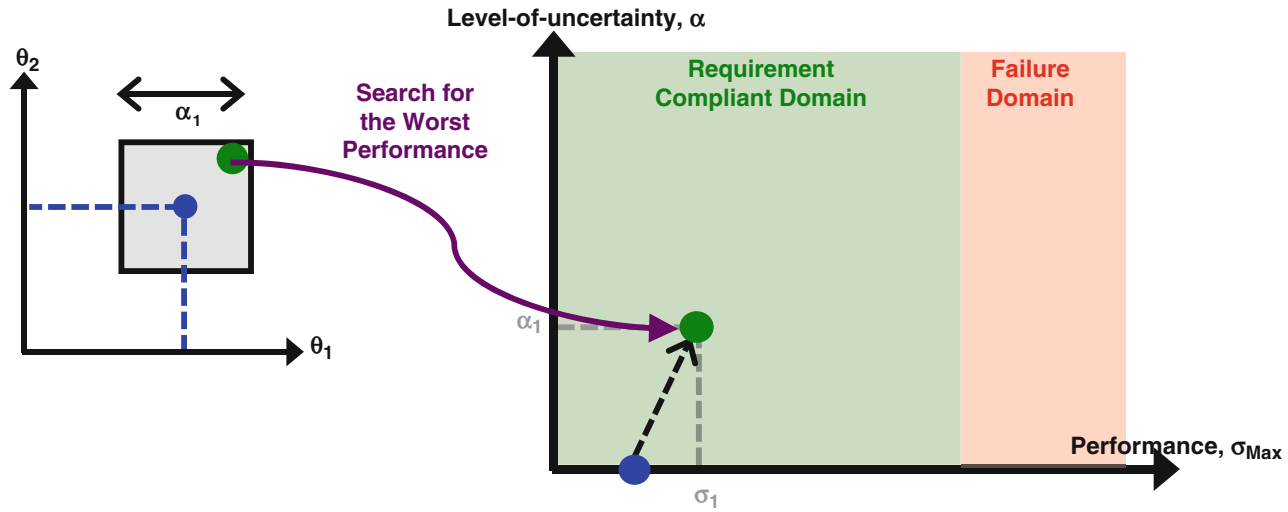

(6-b) Mapping of the worst performance found within the uncertainty space $U(\theta_0;\alpha_1)$.

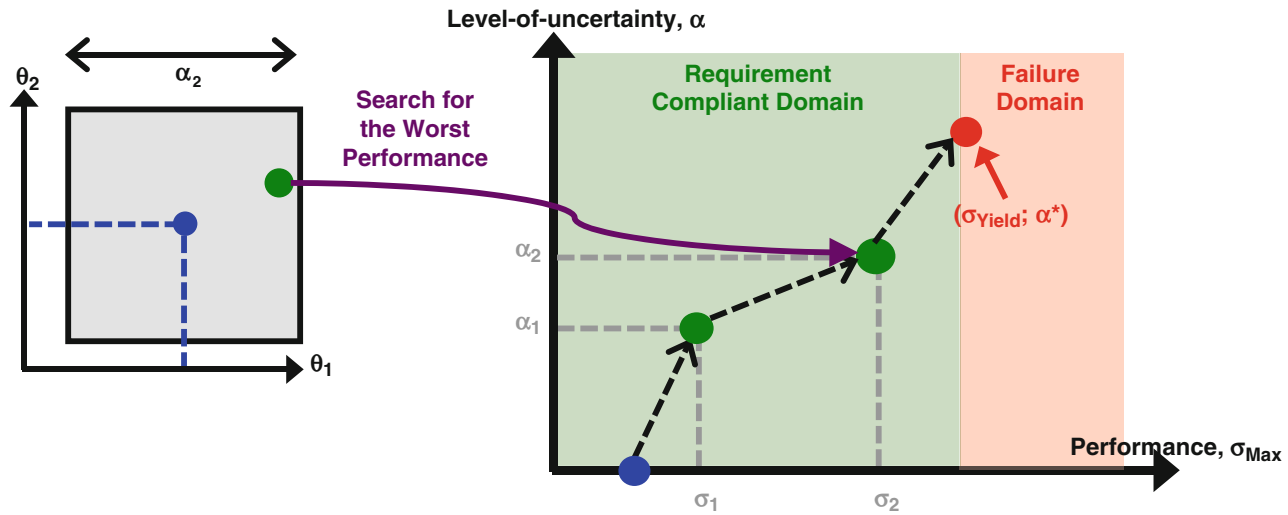

(6-c) Mapping of the worst performance found within the uncertainty space $U(\theta_0;\alpha_2)$.

Fig. 19.6 Conceptual illustration of how the robustness function is constructed. (**a**) Prediction of the nominal model used to initialize the robustness function. (**b**) Mapping of the worst performance found within the uncertainty space $U(\theta_0; \alpha_1)$. (**c**) Mapping of the worst performance found within the uncertainty space $U(\theta_0; \alpha_2)$

A brief explanation of the robustness function is provided next. Obviously the peak stress values obtained from FE simulations, where variables θ vary within the uncertainty space $U(\theta_0;\alpha)$, are "bracketed" by the following lower and upper bounds:

$$\min_{U(\theta_0;\alpha)} \sigma_{Max} \leq \sigma_{Max} \leq \max_{U(\theta_0;\alpha)} \sigma_{Max} \tag{19.4}$$

A necessary and sufficient condition to guarantee requirement-compliance, irrespective of the values taken by variables θ, is that the upper bound verifies the performance requirement (19.2):

$$\max_{U(\theta_0;\alpha)} \sigma_{Max} \leq \sigma_{Yield} \tag{19.5}$$

The idea, therefore, is to search for the worst-case peak stress within the uncertainty space, $U(\theta_0; \alpha)$. This is an optimization problem whose resolution provides one point of the robustness function, such as the point $(\sigma_1; \alpha_1)$ of Fig. 19.6. The horizon-of-uncertainty is then increased from α_1 to α_2, which means that the optimization search is performed in a larger-size uncertainty space. The procedure is repeated until the performance requirement is no longer guaranteed, which is identified as the point $(\sigma_{Yield}; \alpha^*)$. By definition, α^* is the robustness of the design, that is, the maximum level of uncertainty that can be tolerated while guaranteeing the requirement.

Figure 19.6 illustrates the successive steps implemented to map the robustness function. For simplicity, only two variables $(\theta_1; \theta_2)$ are used to represent the uncertainty space on the left side of the figure. The starting point at $\alpha = 0$, shown in Fig. 19.6a, simply represents the prediction of the nominal model where all variables are set to their nominal values, $\theta = \theta_0$. In Fig. 19.6b, the worst-case performance, shown as a green dot, is found using numerical optimization. The corresponding point $(\sigma_1; \alpha_1)$ is mapped to the two-dimensional performance-uncertainty domain. The procedure is then repeated within the larger uncertainty space of Fig. 19.6c.

The robustness and opportuneness functions of the nominal design are shown in Fig. 19.7. The robustness function (red line) represents the upper-bound performance of Eq. (19.4) while the opportuneness function (green line) corresponds to the

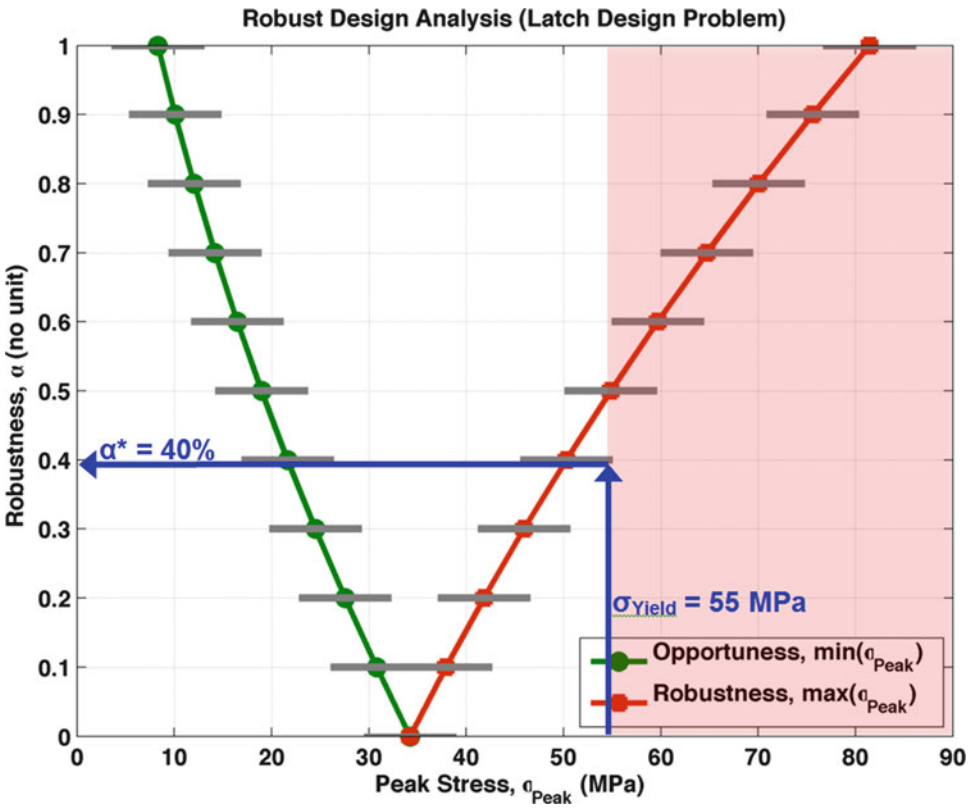

Fig. 19.7 Robustness (*red*) and opportuneness (*green*) functions of the nominal design

lower bound. An interval between the green and red lines indicates the range of peak stresses obtained by performing FE simulations within an uncertainty space $U(\theta_0;\alpha)$ of size α. The horizontal grey segments added to the figure represent the truncation error (± 4.75 MPa) assessed through mesh refinement [5].

The overall conclusion is that the nominal design fails the performance requirement (19.2) when one of the variables $\theta = (E; G; \nu; \rho; U_{Contact}; F_{OS})$ deviates from its nominal value by more than 40 %, approximately. Choices offered to the decision-maker are clear. If real-world conditions cannot possibly deviate from those assumed in the FE simulation by more than 40 %, then, the design is guaranteed to be requirement-compliant. Otherwise, an alternative design, that offers a higher level of robustness, can be pursued. This second path is illustrated in Sect. 19.4.

19.4 Comparison of Two Candidate Designs

To conclude our demonstration of how a robust-design methodology can help to find better solutions, this section discusses how to compare two competing designs. The comparison is between two geometries that differ by the choice of their design variables L_{Column} and W_{Column}. The procedure is to compare robustness functions and determine which one offers the best trade-off between robustness and performance. In this work, the design iterations are not fully automated; potential geometries are chosen by trial-and-error and iterations are carried out "by hand." The next step, not addressed here, would be to automate the entire procedure.

Figure 19.8 compares the two geometries. The left side is the nominal design analyzed earlier. The right side is the variant geometry where the dimensions L_{Column} and W_{Column} are increased by 20 % relative to those of the nominal case, that is, $L_{Column} = W_{Column} = 4.0$ mm for the nominal geometry and $L_{Column} = W_{Column} = 4.8$ mm for the variant (same thickness). The volume of the variant design, therefore, increases by 44 %, approximately. It is another factor that influences the decision because selecting the variant design means a higher manufacturing cost. Both FE meshes have the same spatial resolution, $\Delta x = 0.2$ mm, with a unit aspect ratio ($\Delta x \approx \Delta y \approx \Delta z$).

The methodology proposed to assess which one is a "better" design is simple. The robustness functions are compared to find the largest value of α^*, which is the most robust design. It is emphasized that "better" does not refer, here, to a design that would yield more performance. By definition of the robustness functions, the designs compared all meet the same performance requirement; only comparing their performances, therefore, is a moot point. The rationale, instead, is to find the design that offers more "insurance," which is α^*, against unknown real-world conditions embodied in the uncertainty model, $U(\theta_0;\alpha)$.

Figure 19.9 compares robustness functions of the two candidate geometries. The nominal design is shown with a red line and the variant is shown in magenta. Horizontal grey lines indicate the truncation error resulting from mesh discretization,

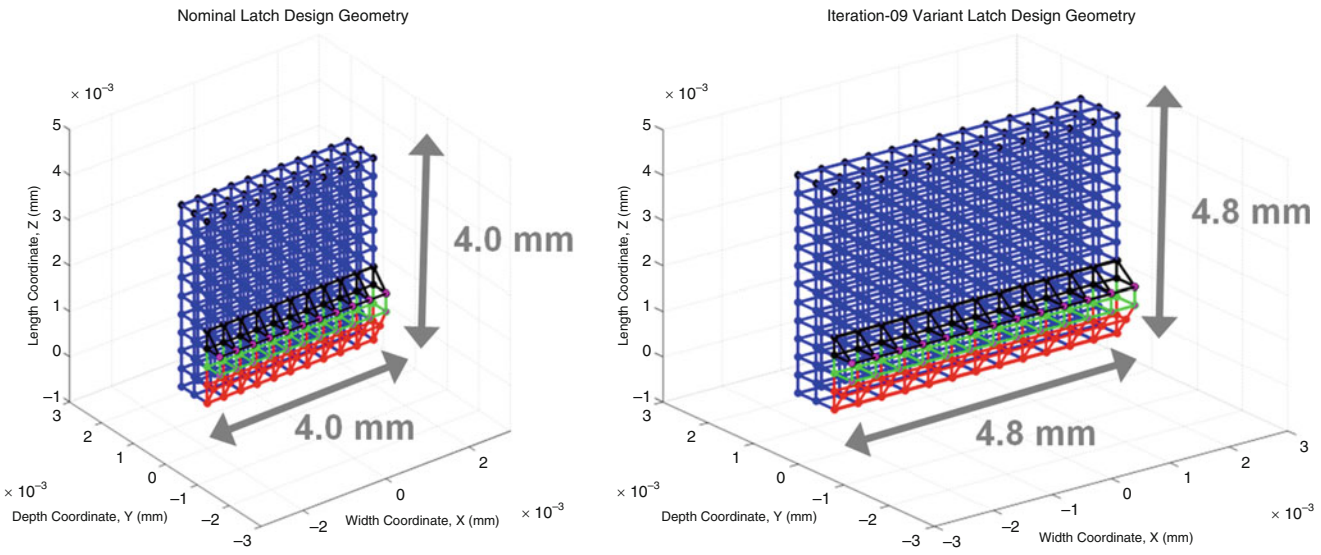

Fig. 19.8 Meshes of the nominal design (*left*) and 20 %-larger variant design (*right*)

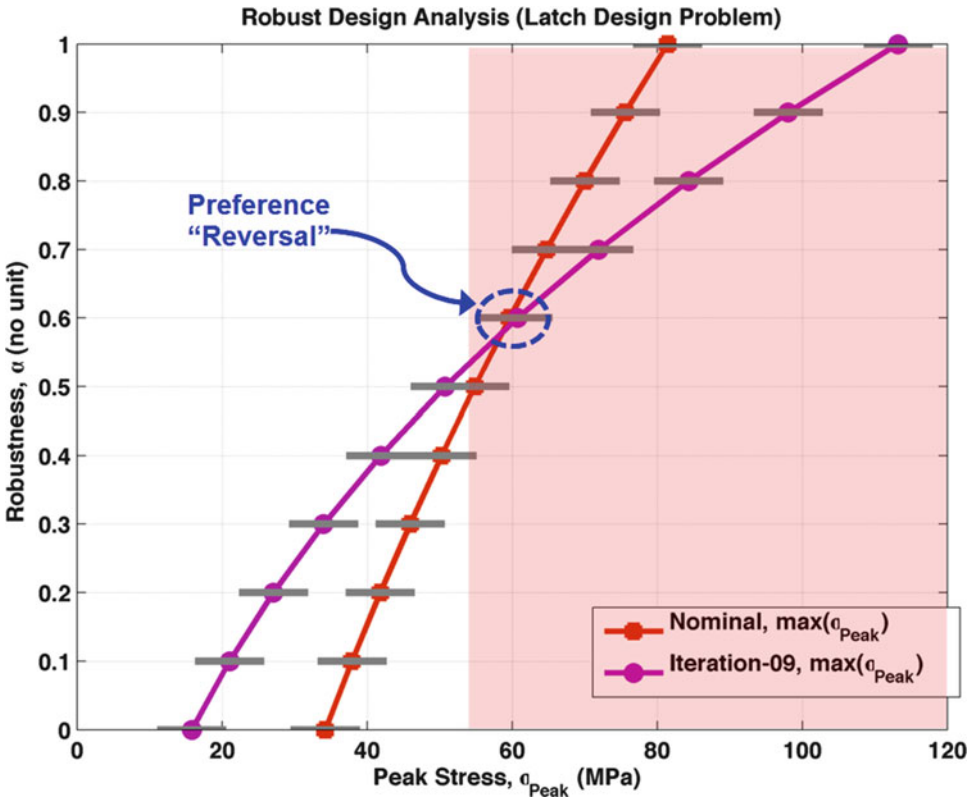

Fig. 19.9 Robustness functions of the nominal (*red*) and variant (*magenta*) designs

as plotted in Fig. 19.7. The trends discussed below ("*which design offers more performance or more robustness*?") are meaningful precisely because these bounds of truncation error are sufficiently small.

When accounting for truncation error, it is observed that the robustness of the variant design is $\alpha^* = 50\,\%$, approximately. It means that real-world conditions can deviate from those assumed in the simulation by up to 50 % without endangering the requirement that the peak stress remains below 55 MPa. Robustness of the nominal design, in comparison, is only $\alpha^* = 40\,\%$ before the robustness function crosses over in the failure domain.

Based on the robustness criterion alone, selecting the 20 %-larger variant design is un-doubtfully a better decision since it can tolerate more uncertainty while remaining requirement-compliant. Recalling, however, that its manufacturing cost is higher due to the $\approx$44 % increase in material, it is unlikely that the modest 10 % improvement in robustness offered by the variant design would justify this choice. Resources needed for the higher manufacturing cost might be better spent on small-scale experimental testing to reduce the material variability and dynamic load uncertainty of Table 19.2. Better constraining this uncertainty would translate into a lesser need for robustness, which might be enough to convince the decision-maker that the level of $\alpha = 40\,\%$ offered by the nominal design is sufficient to robustly meet the performance requirement.

19.5 Conclusion

This work discusses simulation-based robust-design. We argue that an effective design hinges on the ability to establish the robustness of its performance to assumptions and sources of uncertainty present in the simulation. Robustness means that exploring the uncertainty space that characterizes the problem should not degrade the performance to a point where the design requirement is no longer met. The theory of information-gap for decision-making under severe uncertainty is used to formulate the concept of robustness. The procedure for robust-design is applied to the analysis of a mechanical latch for a consumer electronics product.

The robustness of the nominal design is studied to assess the extent to which performance (peak stress) is immune to sources of uncertainty in the problem. This uncertainty expresses that real-world conditions might differ from what is

assumed in the simulation; it also represents modeling assumptions that could be incorrect. The analysis indicates that the nominal design can tolerate up to 40 % uncertainty, approximately, without jeopardizing the performance requirement defined as a peak stress not to exceed.

The last part of this work suggests how to compare two candidate designs. The "better" choice is not necessarily the design that offers the best nominal performance. It is, instead, the design that tolerates more uncertainty about what real-world conditions might actually be, given that the performance requirement is met. For this application, the performance of the alternate design is initially better, as indicated by a lower peak stress, than what the nominal design achieves. The alternate design can tolerate up to 50 % uncertainty, approximately. Its volume, however, is $\approx$44 % larger than the volume of the nominal design. It is unlikely that the modest improvement in robustness of the alternate design justifies a potentially higher manufacturing cost. The analysis of robustness helps the decision-maker answer the question of whether an initial improvement in performance, or the ability to withstand more lack-of-knowledge about real-world conditions, warrants the cost associated with the design change.

References

1. Oden, J.T., Belytschko, T., Fish, J., Hughes, T.J.R., Johnson, C., Keyes, D., Laub, A., Petzold, L., Srolovitz, D., Yip, S.: Revolutionizing engineering science through simulation. National Science Foundation Blue Ribbon Panel on Simulation-Based Engineering (2006)
2. Ben-Haim, Y.: Info-Gap Decision Theory: Decisions Under Severe Uncertainty, 2nd edn. Academic, Oxford (2006)
3. Zienkiewicz, O.C., Taylor, R.L.: The Finite Element Method, Vol. 1: The Basis. Butterworth-Heinemann, London (2000)
4. Newmark, N.M.: A method of computation for structural dynamics. ASCE J. Eng. Mech. **85**, 67–94 (1959)
5. Hemez, F.M., Van Buren, K.L.: Simulation-based robust design of a mechanical latch. Technical Report LA-UR-15-21296, Los Alamos National Laboratory, Los Alamos, New Mexico (2015)
6. Mollineaux, M.G., Van Buren, K.L., Hemez, F.M., Atamturktur, S.: Simulating the dynamics of wind turbine blades: Part I, model development and verification. Wind Energy **16**, 694–710 (2013)
7. Van Buren, K.L., Mollineaux, M.G., Hemez, F.M., Atamturktur, S.: Simulating the dynamics of wind turbine blades: Part II, model validation and uncertainty quantification. Wind Energy **16**, 741–758 (2013)

Chapter 20
From Model Calibration and Validation to Reliable Extrapolations

Gabriel Terejanu

Abstract The purpose of this paper is to propose and explore a validation and predictive assessment process that supports extrapolative predictions for models with known sources of error. In general, the ultimate purpose of most computational models is to make predictions, which are not experimentally observable. As a result assessing the validity of extrapolative predictions is more challenging than situations encountered in classical validation, where model outputs for observed quantities are compared to observations. In this paper a comprehensive approach is proposed to justify extrapolative predictions for models with known sources of error. The connection between model calibration, validation and prediction is made through the introduction of alternative uncertainty models used to model the localized errors. In addition a prediction assessment tool is introduced to characterize the reliability of model predictions in the absence of data. The proposed methodology is applied to an illustrative extrapolation problem involving a misspecified nonlinear oscillator.

Keywords Prediction validation • Model error • Discrepancy model • Structural uncertainty • Bayesian inference

20.1 Introduction

Recently, the author and collaborators [6] have developed a new prediction validation approach that addresses the necessary conditions that entitle us to make extrapolative predictions for engineering applications using physics-based models. This new prediction validation framework goes beyond the classical validation approach which is based on simply comparing the output of the model with experimental data [1, 2, 4, 5, 7–9]. The key observation used to derive the prediction validation methodology is that the models used to predict the behavior of physical systems are often based on theories that are known to be highly reliable (e.g. conservation laws), but these are usually augmented with one or more embedded models that are less reliable. Based on this observation a new model discrepancy approach is proposed that extends the Kennedy and O'Hagan [3] framework.

The goal of prediction validation is to ensure that the computed uncertainties are credible given available information. This framework can be summarized by the following six-step procedure: (1) Model requirements—models are based on highly reliable theories that contain empirical embedded models that are less reliable; (2) Uncertainty representation—identify all the important sources of uncertainty and build appropriate uncertainty models by exploiting the structure of the models as previously defined; (3) Model calibration—infer the model parameters and further constrain the uncertainty models; (4) Model validation—ensure that the model and all probabilistic statements and inferences are consistent with the observed process; (5) Prediction assessment—in this step the model is challenged with respect to quantities of interest to be predicted, and it is mainly build around sensitivity analysis methods to ensure consistency with the scientific knowledge of the phenomenon being simulated; (6) Prediction calculation—if the model obeys the above requirements and passes all the stated challenges, it can be declared "conditionally valid" and it can be used for extrapolative predictions.

One of the challenges with prediction validation methodology is that it relies heavily on knowledge of the characteristics of the embedded models and their accompanying inadequacy models and their effect on prediction of quantities of interests. This relates to the fifth step in the prediction validation, namely prediction assessment. The goal of this paper is to explore a parallel between communication channels and mathematical models to recommend a sensitivity analysis tool that can be used during the prediction assessment step. A numerical example is provided to showcase the prediction validation methodology on a misspecified nonlinear oscillator, and emphasize the importance of the proposed prediction assessment tool.

G. Terejanu (✉)
Department of Computer Science and Engineering, University of South Carolina, 315 Main St., Columbia, SC 29208, USA
e-mail: terejanu@cec.sc.edu

S. Atamturktur et al. (eds.), *Model Validation and Uncertainty Quantification, Volume 3*, Conference Proceedings of the Society for Experimental Mechanics Series, DOI 10.1007/978-3-319-29754-5_20

20.2 Prediction Validation

Many models used in engineering practice are known to be deficient, in that model predictions do not accurately represent experimental observations. The key innovation behind prediction validation is an extension to Kennedy and O'Hagan [3] framework. Prediction validation provides a general formulation based on internal discrepancy models to deal with modeling errors by exploiting the structure of composite models.

In their seminal paper, Kennedy and O'Hagan [3] define the model discrepancy/inadequacy as "the difference between the true value of the real world process and the code output at the true values of the inputs". In this approach the uncertainty model is posed in terms of the observables. Specifically one would write

$$\mathcal{R}(u, \tau_m; \xi) = 0, \tag{20.1}$$

$$y = \mathcal{Y}(u, \tau_m; \xi) + \delta_y, \tag{20.2}$$

$$q = \mathcal{Q}(u, \tau_m; \xi) + \delta_q, \tag{20.3}$$

where $\mathcal{R}$ is some differential operator representing a reliable conservation statement, u is the solution or state variable, τ_m is a less reliable embedded model, and ξ is a set of scenario variables needed to precisely define the case being considered. The models underlying operators $\mathcal{Y}$ and $\mathcal{Q}$ are presumed to be as reliable as the models embodied by $\mathcal{R}$. The observable model (20.2) is the main outlet for model calibration and validation exercises. In contrast, the quantity of interest (QoI) map (20.3) is required for prediction.

The structural inadequacy due to the unreliable embedded model τ_m induces a discrepancy in the observable. In the Kennedy and O'Hagan [3] framework this uncertainty is modeled using δ_y, which is independent of the code output $\mathcal{Y}(u, \tau_m; \xi)$. Similarly, δ_q is used to model the discrepancy in the quantity of interest. Note that there is no explicit relationship between δ_y and δ_q because the generating error in τ_m is not recognized. Thus, while one is free to pose such models, only δ_y can be calibrated and tested against data. That is, it is impossible to validate δ_q, and thus, it should not be used for prediction.

It is critical to recognize and take advantage of the structure of the composite model to introduce model uncertainty representations in the less reliable embedded models. Given such a composite model with uncertainty representations, prediction validation must inform and challenge this complete model. In the prediction validation process, a mathematical relationship between the observables and the QoIs is constructed by formulating uncertainty models to represent errors at their sources. Such models are able to provide uncertain predictions for both the observables and the QoIs. Thus, observational data can be used to inform these uncertainty models, and that information can be transferred to the QoI. To accomplish this, we replace the embedded physical model with a model that represents not only the physics of the original model but also the uncertainty introduced by the structural inadequacy of that model, denoted here with ϵ_m. The combination of the physical and uncertainty models forms a new model, which takes the following form:

$$\mathcal{R}(u, \tau_m + \epsilon_m; \xi) = 0, \tag{20.4}$$

$$y = \mathcal{Y}(u, \tau_m + \epsilon_m; \xi), \tag{20.5}$$

$$q = \mathcal{Q}(u, \tau_m + \epsilon_m; \xi). \tag{20.6}$$

Since ϵ_m automatically appears in the calculation of both y and q, structural uncertainty can be propagated to both the observables and the QoIs. After identifying the source of the error, the next step in predictive validation is to stochastically model ϵ_m. The development of the stochastic model is driven by the physical knowledge about the structure of error.

Given such a model, the parameters of the models are determined from observations during the model calibration phase. The validation step checks the consistency between predictions of the observables and actual measurements. If the inadequacy model ϵ_m faithfully represents the discrepancies between the model for the observables $\mathcal{Y}$ and the observations, we then use it in the model for the QoIs $\mathcal{Q}$ to predict how the observed discrepancies impact uncertainty in the QoI. The details behind the model calibration and how to check the consistency of model predictions with observations in model validation step are presented in [6].

Models and uncertainty models that plausibly account for all the data are an important necessary condition for making credible predictions of unobserved QoIs, but they are not sufficient. One of the questions that needs to be answered is whether the uncertainties are sufficiently small such that the predictions are still driven by physics. A parallel can be constructed between the computational model and a communication channel. By analogy, the variation of the QoI as a function of the scenario is considered a physics-based signal. All uncertainties present in the model are regarded as noise that distorts

the physics-based signal, namely the dependence between the scenario (input) and the QoI (output). Since we can only trust extrapolative predictions because of the physics and not because of statistical models, one objective in the predictive assessment stage is to determine whether model predictions are dominated by the uncertainties in the model. Information-theoretic measures such as mutual information can be used to assess the influence of the uncertainty on the predictive capability of our model. If it is found to be zero or close to zero, this implies that there is no dependence between input and output, then the model is rejected on the basis that the predictions are not driven by physics, and thus they are dominated by statistical models. Otherwise it is declared adequate for prediction. One such scenario is presented in the numerical simulation presented in the next section.

20.3 Case Study: Misspecified Oscillator

In the followings, the proposed approach is applied on an extrapolation problem using a misspecified nonlinear oscillator. The measurement data for both model calibration and validation is generated from a quintic oscillator, which is considered here the true model ("the reality"). The misspecified/inadequate model, which gives an approximation of the true model, is given by a cubic oscillator. The extrapolation problem requires the cubic oscillator to predict the stationary pdf of the displacement at a scenario other than the observed ones. The utility of the prior knowledge is illustrated by designing stochastic models at state equation level. Furthermore, the proposed processes to build confidence in the predictive capability of our models are used to both train the models and reject the models that do not pass the validation and the prediction assessment stage.

20.3.1 Problem Setting

The true model that generates "the reality" is a quintic oscillator, described in Eq. (20.7) using its state space representation.

$$\begin{cases} \frac{dx_1(t)}{dt} = x_2(t) \\ \frac{dx_2(t)}{dt} = -x_2(t) + \xi x_1(t) - 0.1x_1(t)^3 - x_1(t)^5 \end{cases} \tag{20.7}$$

The inadequate model used to make prediction is given by a cubic oscillator, Eq. (20.8).

$$\begin{cases} \frac{dx_1(t)}{dt} = x_2(t) \\ \frac{dx_2(t)}{dt} = -x_2(t) + \xi x_1(t) - 0.1x_1(t)^3 \end{cases} \tag{20.8}$$

Note that the only difference between the two dynamical systems is due to the nonlinear spring. The simulation scenario is given by the adjustable linear stiffness coefficient, ξ. The scenarios for calibration are given by $\xi_d^{cal} \in \{0.1, 0.2, 0.3\}$, $\xi_d^{val} = 0.6$ is used as the validation scenario, and we require to make predictions at $\xi_q = 1.8$.

The observation model and the QoI model is given in Eqs. (20.9) and (20.10). Both models are given by the stationary displacement, the only difference between them is the simulation scenario. The QoI model requires a scenario of interest which is well outside the range of the calibration and validation scenarios.

$$d = x(t = \infty, \xi_d) \quad , \quad \xi_d^{cal} \in \{0.1, 0.2, 0.3\} \, , \, \xi_d^{val} = 0.6 \tag{20.9}$$

$$q = x(t = \infty, \xi_q) \quad , \quad \xi_q = 1.8 \tag{20.10}$$

There are no physical parameters that need to be calibrated for the inadequate model. The only parameters that need calibration are introduced by various discrepancy models presented in the following section. The data is noise-free and generated by the quintic oscillator using the following initial condition, which is also assumed to be perfectly known to the inadequate model.

$$x_1(t = 0) = 0 \quad , \quad x_2(t = 0) = -7 \tag{20.11}$$

Both nonlinear oscillators have an unstable equilibrium at the origin and two stable equilibrium points. The quintic oscillator has also a pair of purely imaginary eigenvalues. For both, by varying the linear stiffness coefficient we vary the

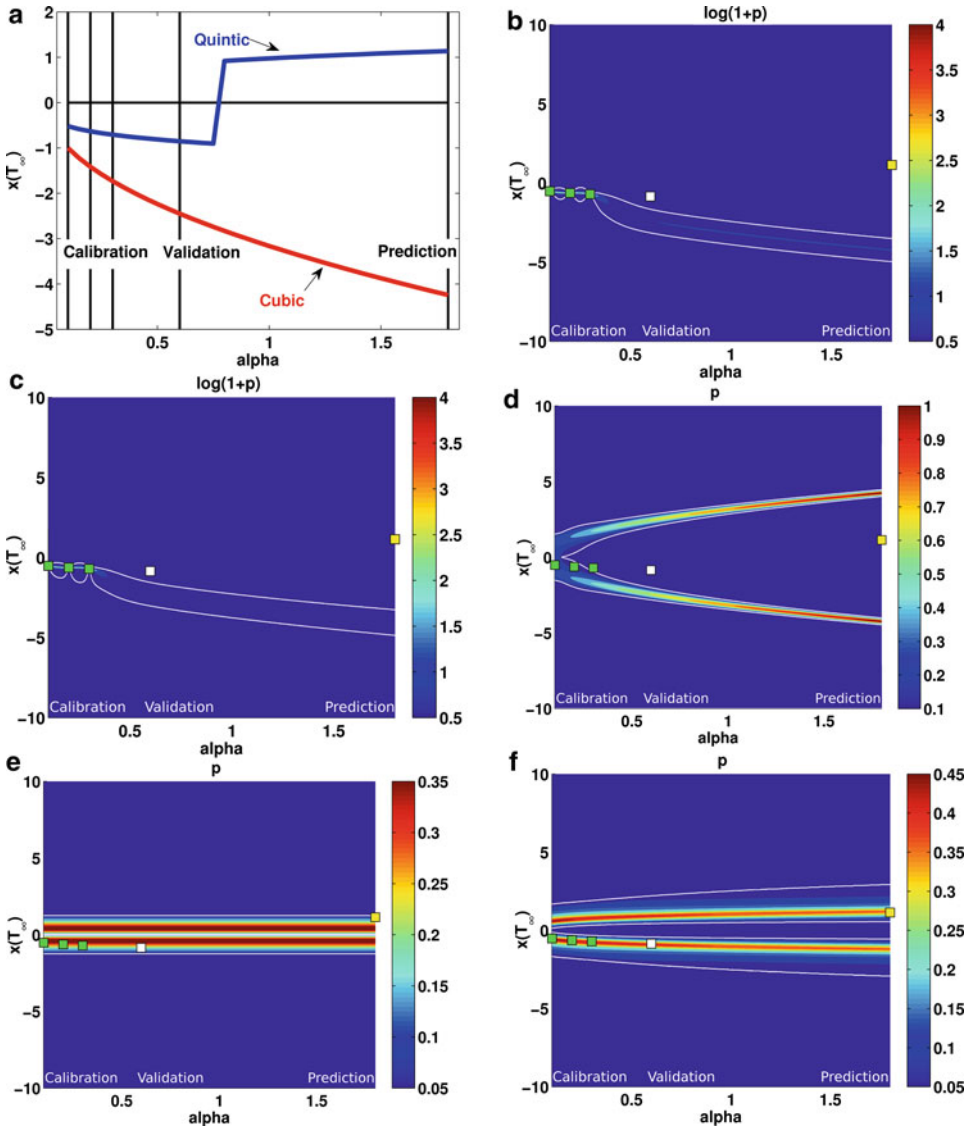

Fig. 20.1 Numerical results (**a**) Problem setting; (**b**) Prediction for Model 1; (**c**) Prediction for Model 2; (**d**) Prediction for Model 3; (**e**) Prediction for Model 4; (**f**) Prediction for Model 5

distance between the two stable equilibrium points. In addition, for the quintic oscillator the change in the linear stiffness coefficient will yield a change in the basin of attraction of the equilibrium points. The testbed is designed such that the change in the basin of attraction for the quintic oscillator is not captured by the cubic oscillator, see Fig. 20.1a.

20.3.2 Stochastic Models

Two approaches are used to add a model discrepancy to the inadequate model. The first one is to add the model discrepancy at the observable level. This is equivalent with ignoring the fact that the errors are located in the physics-based model, not in the observation model, which is the case in general. Two stochastic models based on Gaussian processes are designed in this particular case. The second approach exploits this prior knowledge and the model discrepancy is introduced at the state equation level. This is accomplished by driven the cubic oscillator with a white noise process. Three models are designed in this case by incorporating additional information.

20.3.2.1 Model Discrepancy at the Observable Level

The first two stochastic models for the model discrepancy are located at the observation level as given in Eq. (20.12). The cubic oscillator in Eq. (20.8) is kept unchanged for these particular cases.

$$y = x_1(t = \infty, \xi) + \delta_y(\xi) \tag{20.12}$$

$$q = x_1(t = \infty, \xi_q) \tag{20.13}$$

Two stochastic models based on Gaussian processes are designed to explain the discrepancy of the inadequate model with the true model. The first model, Eq. (20.14) assumes a zero-mean Gaussian process parameterized by the standard deviation, σ, and the characteristic length, l, which are both open for calibration.

$$\text{Model 1}: \quad \delta_y(\xi) \sim GP(0, k_{SE}(\xi, \xi'; \sigma, l)) \tag{20.14}$$

The second model, Eq. (20.15) assumes a Gaussian process with a mean linear in the scenario. Thus, in addition to the parameters that describe the square exponential kernel covariance, $k_{SE}(\cdot)$, we also open for calibration the parameters a and b that describe the mean of the process.

$$\text{Model 2}: \quad \delta_y(\xi) \sim GP(a + b\xi, k_{SE}(\xi, \xi'; \sigma, l)) \tag{20.15}$$

Even in this case, where both the observable and the QoI are given by the stationary position, the propagation of model discrepancy to the QoI is not trivial. This is due to the scenario of interest which is outside the range of the calibration and validation range. So just tacking the inferred Gaussian process to the prediction scenario is already subject to invalidation even from the onset, because the extrapolation is not given by physics.

To calibrate the above two models one needs to define the prior pdf for their parameters and specify the likelihood function. The prior pdf for the parameters is presented in Table 20.1, where $\mathcal{N}(\cdot, \cdot)$ is a Gaussian pdf with mean and standard deviation as the first and second argument, respectively. The variant $\mathcal{N}^+(\cdot, \cdot)$ is just the folded Gaussian pdf. In addition, the likelihood function is solely defined by the model discrepancy which in our case is a Gaussian process. This tractable and greatly simplifies its evaluation during the calibration using MCMC.

20.3.2.2 Model Discrepancy at the State Equation Level

The last three models exploit the knowledge that the source of error is located in the physics-based model and introduce the model discrepancy at the state equation level. In this particular case we make use of white noise processes to design the stochastic models for the discrepancy. One of the advantage for choosing this uncertainty representation is that it yields tractable likelihood functions. However, white noise is not a prerequisite for designing these stochastic models. Depending on the type of prior knowledge about the structure of the error one could introduce for example stochastic models based on colored noise that obeys the prior information.

The models generated are as follows: Eq. (20.16)—additive white noise, Eq. (20.20)—multiplicative white noise, and Eq. (20.21)—additive and multiplicative white noise. Because we are dealing with stochastic differential equations, the equations are presented in the Ito form.

$$\text{Model 3}: \quad \begin{cases} dx_1(t) = x_2(t)dt \\ dx_2(t) = (-x_2(t) + \xi x_1(t) - 0.1x_1(t)^3)dt + \sigma dw(t) \end{cases} \tag{20.16}$$

$$y = x_1(t = \infty, \xi) \tag{20.17}$$

$$q = x_1(t = \infty, \xi_q) \tag{20.18}$$

Table 20.1 Prior pdfs for parameters of Gaussian processes

Model	σ	l	a	b
Model 1	$\mathcal{N}^+(0.01, 0.1)$	$\mathcal{N}^+(0.0, 0.1)$	–	–
Model 2	$\mathcal{N}^+(0.01, 0.1)$	$\mathcal{N}^+(0.0, 0.1)$	$\mathcal{N}(0.0, 0.1)$	$\mathcal{N}(0.0, 0.1)$

Note that in contrast with the previous two stochastic models, here the observation model is not directly polluted by an additive model discrepancy. The effect of model discrepancy is indirect, through the state, and affects both the observation model and the QoI model, which is conceptually valid and consistent with our prior knowledge about the source of the error. Thus, any inference on model discrepancy during calibration can be propagated to the QoI.

Compared with the Gaussian process models, in general for these type of models the likelihood function is intractable and its evaluation requires a forward propagation of uncertainty. Thus, one needs to solve the Fokker-Planck-Kolmogorov equation to obtain the stationary pdf $p(y|\sigma,\xi)$. However, for this type of systems the solution of the stationary pdf can be found analytically. The likelihood function for Model 3 is given by Eq. (20.19).

$$\text{Model 3 (stationary pdf)}: \quad p(y|\sigma,\xi) \propto exp\left[-\frac{2}{\sigma^2}\left(-\frac{\xi}{2}y^2 + \frac{0.1}{4}y^4 \right) \right] \tag{20.19}$$

The last two models, Models 4 and 5, can be seen as making use of additional information beyond the source of the error. Namely, for these two models we assume that we know that the error is dependent on the state of the system.

$$\text{Model 4}: \quad \begin{cases} dx_1(t) = x_2(t)dt \\ dx_2(t) = (-x_2(t) + \xi x_1(t) - 0.1x_1(t)^3)dt + \sigma x_1(t)dw(t) \end{cases} \tag{20.20}$$

$$\text{Model 5}: \quad \begin{cases} dx_1(t) = x_2(t)dt \\ dx_2(t) = (-x_2(t) + \xi x_1(t) - 0.1x_1(t)^3)dt + \sigma_1 dw_1(t) + \sigma_2 x_1(t)dw_2(t) \end{cases} \tag{20.21}$$

The stationary pdfs for Models 4 and 5 are given in Eqs. (20.22) and (20.23), respectively.

$$\text{Model 4 (stationary pdf)}: \quad p(y|\sigma,\xi) = \frac{1}{20\sigma^2} exp\left(-\frac{y^2}{20\sigma^2} \right) |y| \tag{20.22}$$

$$\text{Model 5 (stationary pdf)}: \quad p(y|\sigma_1,\sigma_2,\xi) \propto \sqrt{\frac{\pi}{2}} exp\left(\frac{0.5\xi y^2 - 0.025y^4}{\sigma_1^2 + \sigma_2^2 y^2} \right) \times \sqrt{\sigma_1^2 + \sigma_2^2 y^2} \tag{20.23}$$

The prior pdf for the parameters of these last three models are given in Table 20.2.

20.3.2.3 Numerical Results

The calibration results and the confidence building analysis for Model 1 is summarized in Fig. 20.1b. This depicts the posterior predictive pdf for the QoI as a function of the scenario ξ. Included in the figure is also the 95 % high probability density (HPD) interval for the QoI and the true value of the QoI as given by the quintic oscillator. Note that the true value of the QoI at the prediction scenario is not used in the analysis and it is shown just to judge the final outcome of the methodology.

While the calibration of Model 1 perfectly captures the three data points in the calibration set, the model fails to pass the consistency check in the validation stage. Namely the validation data falls outside the predicted 95 % HPD interval. Thus, our model along with all the probabilistic statements and inference results is inconsistent with validation data and it is labeled invalid for extrapolative prediction purposes. This example clearly depicts why the addition of model discrepancy at the observation level is conceptually invalid. The predictive uncertainty is dictated by the Gaussian process which looses physical meaning as we predict beyond the calibration scenario range. The same discussion also holds for Model 2. The effect of the bias in this case is marginal.

Table 20.2 Prior pdfs for the white noise processes

Model	σ	σ_1	σ_2
Model 3	$\mathcal{N}^+(0.01, 0.1)$	–	–
Model 4	$\mathcal{N}^+(0.01, 0.1)$	–	–
Model 5	–	$\mathcal{N}^+(0.01, 0.1)$	$\mathcal{N}^+(0.01, 0.1)$

Starting with Model 3, the model discrepancy is introduced at the source of the error in the physical model. While conceptually this agrees with our prior knowledge, in general there is no guarantee that the proposed model discrepancy will capture the missing physics. The diagnostic checks proposed in the methodology can help eliminate the models which are inconsistent with the data and the prediction requirements.

In Fig. 20.1d we can see that the additive white noise used in Model 3 is not able to capture the validation data. Furthermore the predictive uncertainty fails to cover also one of the calibration data points, which again is a consistency failure. Even though the uncertainty in this model is propagated through the physical model which we trust, the form of the model discrepancy is an inappropriate model for the missing physics. This is detected by the consistency check and the model is labeled invalid at the model validation stage.

Model 4, which uses a multiplicative white noise, passes the validation stage. All the calibration and the validation data points fall inside the predictive 95 % HPD interval. Note however that the predictive uncertainty, Fig. 20.1e remains unchanged as the scenario is varied. This is an indication that the probabilistic predictions are no longer physics driven. This is due to model discrepancy that disrupts/decouples the physics based communication between the scenario (input) and the QoI (output), which. As such the model is labeled invalid at the prediction assessment stage.

In Model 5, the model discrepancy is modeled using a combination of additive and multiplicative white noise. In this case the model is capable to pass both the diagnostic checks in the validation and prediction assessment stage, see Fig. 20.1f. The probabilistic predictions are consistent with both calibration and validation data and the model does not losses it prediction capability due to model discrepancy. We, thus, can label the model conditionally valid for extrapolative prediction purposes. It is only conditionally valid because the validity depends on all probabilistic statements, data, inference results, QoI, and diagnostic checks. Additional data or prediction of a different QoI will require a reassessment of its validity.

Only after the model has been labeled conditionally valid, its predictions can be provided to the decision maker to determine their utility. Note that in the case of Model 5, the decision maker may reach the conclusion that the predictive uncertainty for the QoI at the scenario of interest is too large and provides very low or no utility in the decision making process. However, the prediction is considered reliable as no evidence has been found to dismiss the quantified uncertainties.

20.4 Conclusion

A new tool based on statistical dependence has been explored for assessing the predictability of models used in the prediction validation framework. Prediction assessment is challenging as no data is available at the prediction scenario, otherwise the prediction will not be required. This framework is applied to a misspecified oscillator where one of the models presented passes the model validation step however fails to pass the newly introduced prediction assessment test. It is shown that certain statistical structural uncertainty models can dominate model predictions, which in turns diminishes significantly the effect of the physics-based model components. As a result, these predictions cannot be trusted. This is also one of the main challenges in implementing the prediction validation methodology, namely it is found to be difficult in general to construct uncertainty models that are constrained by physics based knowledge.

References

1. Babuška, I., Nobile, F., Tempone, R.: A systematic approach to model validation based on Bayesian updates and prediction related rejection criteria. Comput. Methods Appl. Mech. Eng. **197**, 2517–2539 (2008)
2. Balci, O.: Verification validation and accreditation of simulation models. In: Proceedings of the 29th Winter Simulation Conference, WSC '97, pp. 135–141. IEEE Computer Society, Washington, DC (1997)
3. Kennedy, M.C., O'Hagan, A.: Bayesian calibration of computer models. J. R. Stat. Soc. Ser. B (Stat Methodol.) **63**(3), 425–464 (2001)
4. Oberkampf, W., Roy, C.: Verification and Validation in Scientific Computing. Cambridge University Press, Cambridge (2010)
5. Oberkampf, W.L., Trucano, T.G.: Verification and validation benchmarks. Technical Report SAND2007-0853, Sandia National Laboratories (2007). Unlimited Release
6. Oliver, T.A., Terejanu, G., Simmons, C.S., Moser, R.D.: Validating predictions of unobserved quantities. Comput. Methods Appl. Mech. Eng. **283**, 1310–1335 (2015)
7. Roache, P.J.: Perspective: validation - what does it mean? ASME J. Fluid Eng. **131**(3), 1–3 (2008)
8. Roache, P.J.: Fundamentals of Verification and Validation. Hermosa Publishers, Albuquerque (2009)
9. Sargent, R.G.: Verification and validation of simulation models. In: Proceedings of the 30th Winter Simulation Conference, WSC '98, Los Alamitos, CA, pp. 121–130. IEEE Computer Society Press, New York (1998)

Chapter 21
Application of PCA-SVD Validation Metric to Develop Calibrated and Validated Structural Dynamic Models

Hasan G. Pasha, Randall J. Allemang, and Manish Agarkar

Abstract Calibrated/validated models that can predict the dynamic response of a structure accurately need to be developed to avoid expensive testing. The quantification of *margin* and *uncertainty* using validation metric(s) provides the basis for calibrating/validating a model with respect to characterizing system response. The principle component analysis—singular value decomposition (PCA-SVD) validation metric uses SVD to quantify the margin and uncertainty. This method involves decomposing the spatial information into its singular values and vectors at each temporal point. The set of largest singular values of one data-set can be plotted against the other, which ideally should result in a straight line with unit slope and zero variance. The PCA-SVD validation metric is relatively easy to implement. It gives a clear indication of both the margin and the uncertainty by utilizing the dominant singular values. It also gives a clear indication of *spatial correlation* by utilizing the singular vectors associated with the dominant singular values. In this paper, an application of the PCA-SVD validation metric to develop calibrated/validated models of a rectangular steel plate structure is presented.

Keywords Quantification of margin and uncertainty • Principle component analysis • Singular value decomposition • Verification • Calibration • Validation

Notation

Symbol	Description	
$[\cdot]^H$	Hermitian (conjugate transpose) of matrix $[\cdot]$	
r	Mode number	
AC	Assurance Criteria	
D	Flexural rigidity	$psi \cdot in^3$
E	Young's modulus	psi
EU	Engineering Units	
$H_{pq}(\omega)$	FRF measured at p while applying an excitation at q	
$[H(\omega)]$	FRF matrix $\left(\frac{X}{F}\right)$	
MAC	Modal Assurance Criteria	
N_f	Number of frequency lines	
N_L	Number of elements in the long dimension	
N_S	Number of elements in the short dimension	
PCA	Principal Component Analysis	
QMU	Quantification of Margin and Uncertainty	
SVD	Singular Value Decomposition	
α	Mass matrix multiplier for damping	
β	Stiffness matrix multiplier for damping	

H.G. Pasha (✉) • R.J. Allemang
University of Cincinnati—Structural Dynamics Research Lab (UC-SDRL), Cincinnati, OH, USA
e-mail: pashahg@mail.uc.edu

M. Agarkar
Alcon Laboratories, Lake Forest, CA, USA

S. Atamturktur et al. (eds.), *Model Validation and Uncertainty Quantification, Volume 3*, Conference Proceedings of the Society for Experimental Mechanics Series, DOI 10.1007/978-3-319-29754-5_21

Symbol	Description	
ν	Poisson's ratio	
ρ	Mass density	lb_m/in^3
ω	Natural frequency	rad s^{-1}
ζ	Damping ratio	

21.1 Introduction

To characterize the dynamics of a structure accurately and to minimize uncertainties, it is important to perform structural testing in various configurations. However, performing such rigorous testing of structures can be a resource intensive process. In addition, simulating certain loading and/or support conditions may not be possible/feasible in the lab. This situation has made it necessary to develop analytical/mathematical models that can predict the response of system in real time without performing actual tests. Such models need to undergo verification, calibration and validation with actual test data before they can be relied upon to extrapolate results for future studies. In this context, *verification* and *validation* (V&V) are defined as below:

(1) *Verification* refers to process of determining that a model implementation accurately represents the developer's conceptual description of the model and the solution to the model [1]. Frequently, the verification portion of the process answers the question *"Are the model equations correctly implemented?"*
(2) *Validation* refers to the process of determining the degree to which a model is an accurate representation of the real world system from the perspective of the intended uses of the model [1]. Frequently, the validation process answers the question *"Are the correct model equations implemented?"*

Margin refers to the difference between the design requirement and the mean of the expected or measured result, and *uncertainty* refers to the variation about the mean of the expected or measured result. The quantification of margin and uncertainty (QMU) using calibration/validation metric(s) provides the basis for calibrating/validating a model with respect to characterizing system response (Fig. 21.1).

Developing calibrated and validated models that can predict the dynamic response of a structure accurately can be a key to address this issue. Calibration experiments are designed *to develop* correct model order, *to verify* the parameters in the models and *to assist* in the quantification of uncertainty associated with the probable environment(s), model(s) and also with the physical experiment(s). While, validation experiments are designed *to compare* results between the analytical model predictions and the measured data.

The principle component analysis—singular value decomposition (PCA-SVD) validation metric uses SVD to try to quantify the margin and uncertainty between two datasets. This method involves decomposing the spatial information in to its singular values and singular vectors at each temporal point. The set of largest singular values of one dataset can be plotted against the other, which ideally should result in a straight line with unit slope and with no variance about it. The PCA-SVD validation metric is relatively easy to implement. It gives a clear indication of both the margin and the uncertainty, utilizing the dominant singular values, as shown in Fig. 21.2. It also gives a clear indication of spatial correlation, utilizing the singular vectors associated with the dominant singular values.

In this paper, an application of the PCA-SVD calibration/validation metric to develop calibrated/validated models of a rectangular steel plate structure is presented. The validation criteria were achieved using the calibrated model and thus proved that the model could reliably predict the dynamic response of the structure.

The sensors (accelerometers and impact hammer load cells) need to be calibrated before data is acquired. Sensors generally tend to have variability in the sensitivity in the order of 2–5 %, which when not accounted for could skew the measurement magnitudes. When a calibration/validation metric involving modal frequencies alone is used, uncertainty due to measurement magnitudes is not accounted. In such cases, utilizing the PCA-SVD based metric would be ideal as it captures the variation in the level, in addition to variation in the modal frequencies and spatial correlation of vectors.

21.2 PCA-SVD Based Validation Metric

The singular value decomposition (SVD) as a principal component analysis (PCA) method to estimate the validation metric involves decomposing the datasets into their singular value sets and then comparing the biggest contributors. For example, the primary singular values and their corresponding vectors can be compared against each other to determine the degree of correlation between the two.

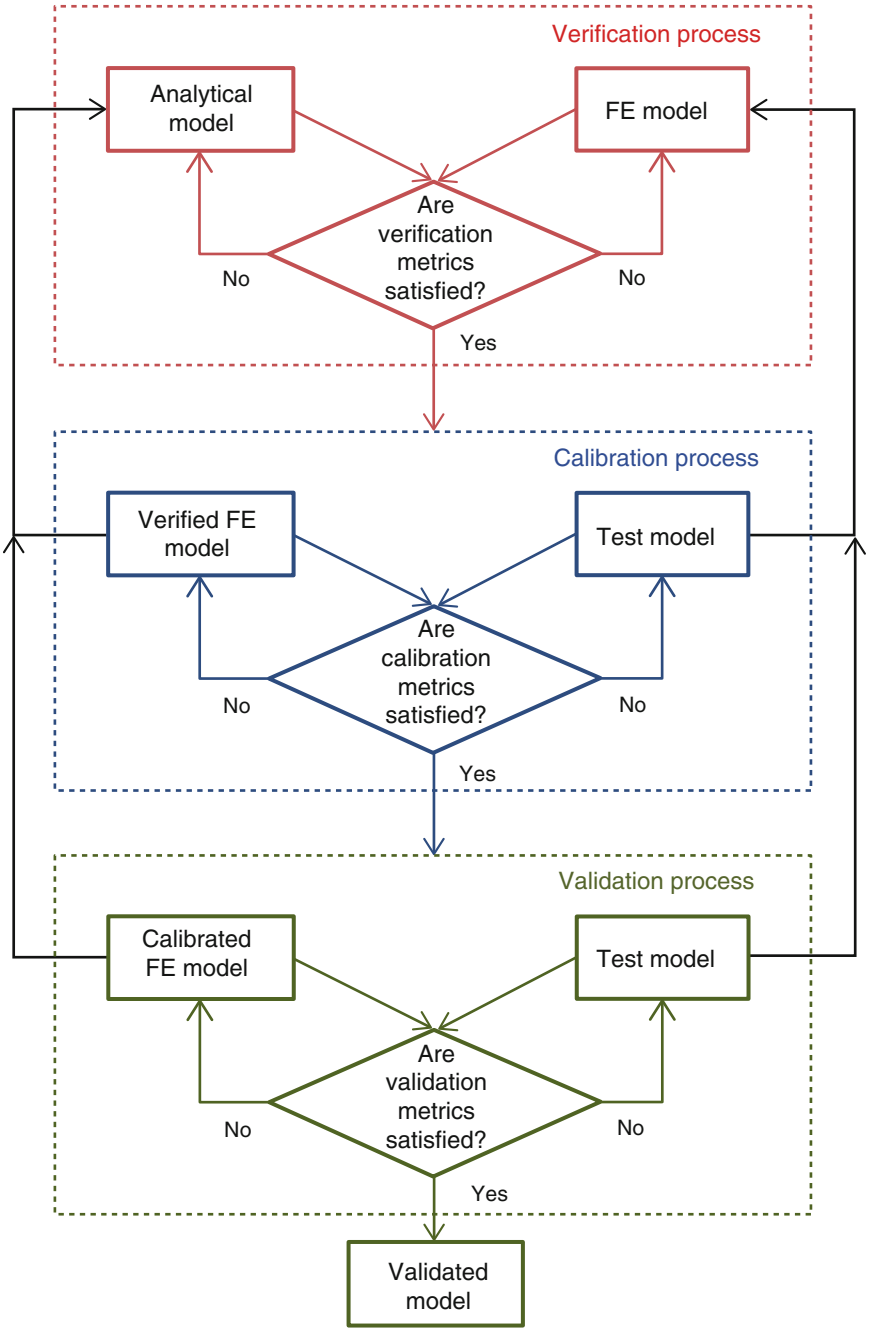

Fig. 21.1 Verification, calibration and validation processes [2]

21.2.1 Theory

$$[B]_{N_L x N_S} = [U]_{N_L x N_S} \lceil S \rfloor_{N_S x N_S} [V]^H_{N_S x N_S} \tag{21.1}$$

In the above equation, the matrix [B] represents the data matrix that will be evaluated. In general, this matrix will be complex-valued and rectangular of size $N_L x N_S$ (size of the long and short dimension of the data). The [U] matrix is the left singular vectors and the [V] matrix is the right singular vectors and both are complex-valued and unitary. The superscript H represents the hermitian (conjugate transpose) of the matrix. The $\lceil S \rfloor$ matrix is the singular value matrix which is diagonal, square and real-valued. As the [U] and [V] matrices are unitary, the magnitude characteristics of the data matrix [B] are

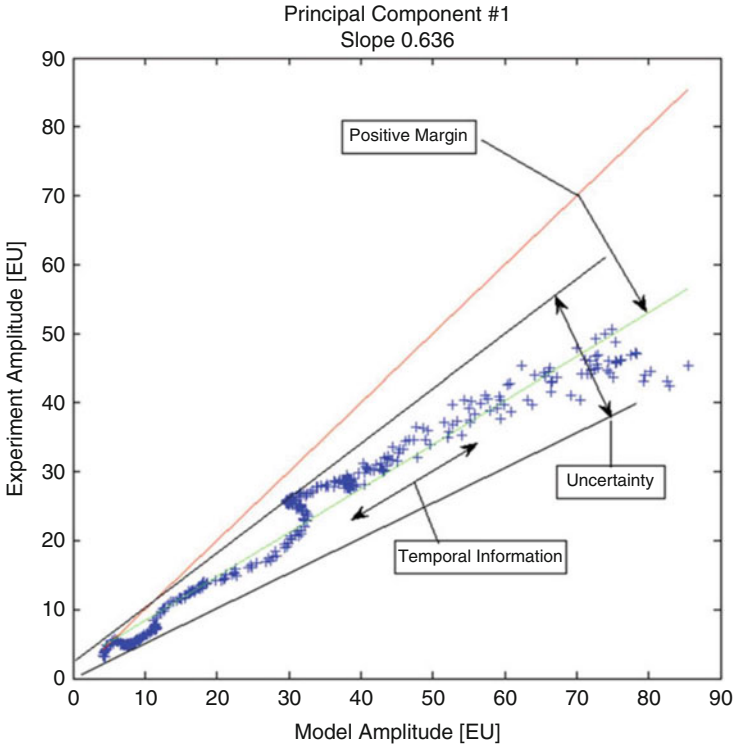

Fig. 21.2 PCA-SVD validation metric—relation to QMU [7]

captured in the singular values and with proper scaling they have the same engineering units (EU) as the data matrix [B] [3–6].

An assurance criteria (AC) computation, analogous to the Modal Assurance Criteria (MAC) computation for the modal vectors, between the primary singular vectors at each temporal point results in a curve that depicts the similarity in the spatial distribution of the information present in the two datasets. Using the longer of the two sets of singular vectors ($[U]_{N_L x N_S}$ in this case) for calculating the AC helps to capture the differences between the two datasets better. The correlation of nearly 1.0 indicates that the singular vectors are spanning the same 3-D space as a function of frequency [4, 7, 8].

21.3 Application Example

A FE model of a rectangular plate structure was developed to determine its dynamic characteristics (modal frequencies and mode shapes). A step by step approach was adopted to verify, calibrate and validate the results generated by the model in different test configurations.

21.3.1 Verification

Verification is the process of comparing different analytical models to be certain that the analysis results are correct [1, 9]. In this case, a FE model is compared to the analytical, closed form results for a rectangular plate. A value of 2 % or less for the relative difference in the modal frequencies was chosen as the *verification criteria* or *verification metric*. An analytical rectangular plate model, with aspect ratio of 1.5 was developed, such that the first mode is a torsion mode roughly at 40 Hz and the second mode is a bending mode roughly at 44 Hz. Closed form expressions were used to develop an analytical model [10].

The natural frequency of the plate is defined as $f_{ij} = \frac{\lambda_{ij}^2}{2\pi l^2}\sqrt{\frac{Eh^3}{12\gamma(1-\nu^2)}}$, where i is the number of half-waves in mode shape along horizontal axis, j is the number of half-waves in mode shape along vertical axis, λ_{ij} is a dimensionless frequency

parameter (which is a function of the applied boundary condition, aspect ratio and in some cases Poisson's ratio), l is the length of the plate, E is the Young's modulus, h is the thickness of the plate, γ is the mass per unit area and ν is the Poisson's ratio. Flexural rigidity of plate is defined as $D = \frac{Eh^3}{12(1-\nu^2)}$.

A comparable rectangular plate FE model was developed using the dimensions and material properties chosen for the analytical, closed form model of the plate. Analytical modal analysis was performed on the plate FE model. The modal frequencies and mode shapes for the first six deformation modes were retrieved and compared with the analytical model prediction.

The modes were in the expected sequence and the relative difference in modal frequencies was less than 2 %. This verified the FE model (Table 21.1).

21.3.2 Calibration

Calibration of a model involves comparing the analytical results to equivalent experimental results. Calibration in this case involves correlating the modal parameters obtained from an analytical modal analysis of the rectangular plate FE model and impact testing of the fabricated rectangular plate structure (Fig. 21.3). The details of the various activities performed in the calibration process are explained in the subsequent sections.

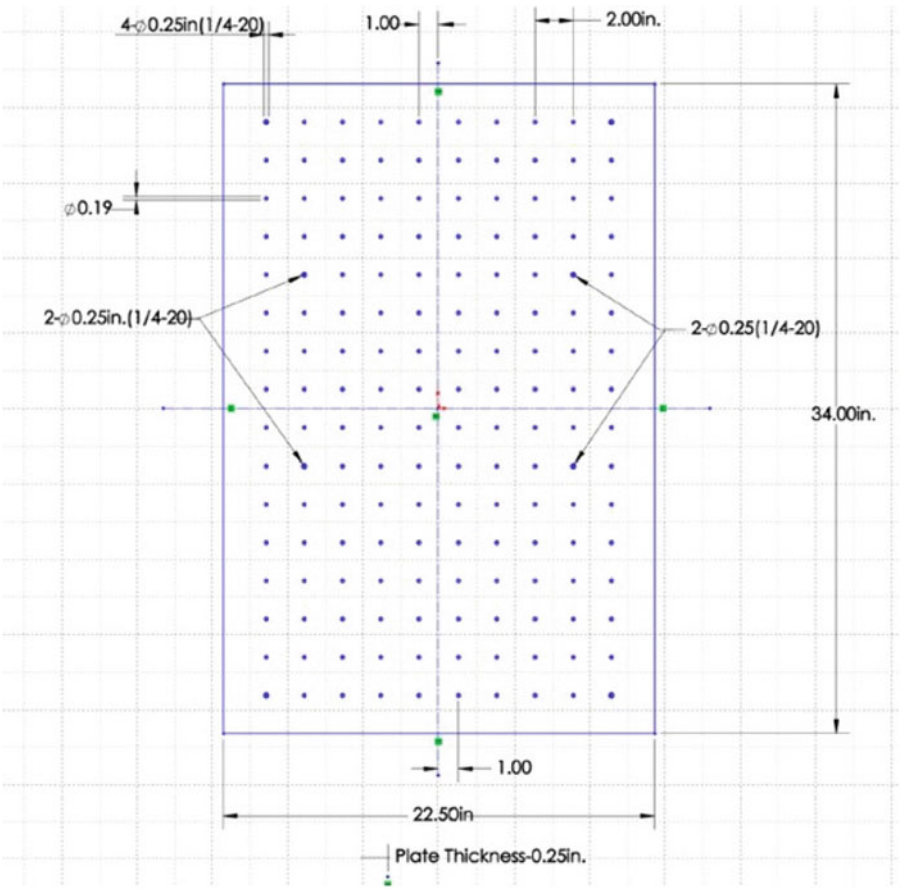

Fig. 21.3 Rectangular plate dimensions

21.3.2.1 Modal Correlation

The sequence of the modes was established to be in the same order for both cases by viewing the mode shape animations. However, the relative difference between the modal frequencies obtained from FE modal analysis and impact testing was greater than 2 %. It was identified that there were various sources of uncertainty. On the modeling side, the sources of uncertainty were geometric and material properties of the steel plate. In addition, the soft supports had not been modeled and damping was not prescribed in the model. On the testing side, the support system, location of supports, sensor calibration, impact hammer tip and signal processing parameters were considered to be the sources of uncertainty. The relative difference in modal frequencies was desired to be less than 2 % and was set as the *calibration criteria* or *calibration metric*.

21.3.2.2 Model Updating

(1) *Geometric parameters*: It was established that the plate thickness, originally intended to be 0.25 in, was not constant. The plate was weighed (52.5 $\mathrm{lb_m}$) and the thickness of the plate model was adjusted (0.243 in) to match the measured weight of the plate.
(2) *Material model*: The relative difference for the third mode (second torsion mode) was reasonably high compared to other modes. A parametric study was performed in which the effect of varying the Young's modulus, mass density and Poisson's ratio on the modal frequencies was studied. For the calibrated model, the material properties were established as: Young's modulus $\mathrm{E} = 2.05 \times 10^{11}$ Pa (2.9734×10^7 psi), mass density $\rho = 7850$ $\mathrm{kg/m^3}$ (0.2836 $\mathrm{lb/in^3}$) and Poisson's ratio $\nu = .29$.
(3) *Modeling the support system*: Four racquet balls were used to support the plate during impact testing. These racquet balls act as springs and their stiffness value was estimated to be approximately 40 $\mathrm{lb_f/in}$. At locations corresponding to the supports, linear springs were added in the FE model. This reduced the relative difference for the modal frequencies further.
(4) *Prescribing damping*: The rectangular steel plate is lightly damped structure. However, as a force-exponential window was used while acquiring the impact data, high damping values are estimated. Modal damping factors estimated from the measured data were used to calculate the mass and stiffness proportionality constants (α and β respectively) for prescribing Rayleigh damping in the FE model [11, 12]. From the estimated modal damping (listed in Table 21.2), the mass and stiffness proportionality constants—α and β respectively, were calculated to be 2.2081 and 0 respectively using a least squares solution to the following equation.

$$\frac{\alpha}{2\omega_r} + \frac{\beta\omega_r}{2} = \zeta_r \tag{21.2}$$

21.3.2.3 Testing Related Changes

(1) *Support system*: Free-free boundary conditions are relatively easier to achieve compared to other boundary conditions such as a fixed boundary condition. Support systems add stiffness and can also interact with the test structure. Certain precautions need to be followed while selecting support systems [13].

Table 21.1 Preliminary verification of the FE model—modal frequency comparison

Mode #	Description	Modal frequency (Hz)		Rel. diff. (%)
		Analytical	FE	
1	First torsion	41.55	41.34	0.51
2	First X bending	44.59	43.95	1.46
3	Second torsion	96.3	95.12	1.24
4	First Y bending	103.8	102.99	0.79
5	Second X bending	121	119.16	1.54
6	Anti-symmetric X bending	139.3	137.39	1.39

Table 21.2 Modal damping estimated from the measured data

Mode # (r)	Modal frequency		Damping factor ζ_r
	f_r (Hz)	ω_r (rad/s)	
1	42.16	264.90	0.0036
2	44.16	277.47	0.0044
3	95.58	600.55	0.0016
4	104.6	657.22	0.0014
5	119.06	748.08	0.0019
6	137.98	866.95	0.0011
7	176.38	1108.23	0.001
8	203.72	1280.01	0.0003
9	244.98	1539.25	0.0003

Initially, shock chords were used to support the structure. However, it was observed that the shock chord supports dynamically interacted with the third deformation mode (second torsion mode) and acted as a vibration absorber. As a result, a support system with four racquet balls that provided air suspension was chosen. The racquet ball support system reasonably isolated the test structure.

(2) *Sensor calibration*: The sensors (accelerometers and impact hammer load cells) need to be calibrated before data is acquired. Sensors generally tend to have variability in the sensitivity in the order of 2–5 %, which when not accounted for could skew the measurement magnitudes (but would have no effect on the calibration metric involving modal frequencies).

(3) *Impact hammer tip*: The impact hammer tip should be selected such that the modes in the required frequency range are adequately excited without exciting higher frequency modes. When the focus is to acquire data in lower frequency range, using a harder tip would possibly cause overloads on the data acquisition channels associated with sensors near the impact location. An appropriate hammer tip was selected.

(4) *Signal processing parameters*: The rectangular plate is a very lightly damped structure. It was noted that after every impact, it took over 16 s for the response to die out. After selecting the frequency bandwidth, the frequency resolution should be chosen such that the response at all the reference locations is completely observed in the captured time segment. If this condition is not met, it would result in leakage errors. If desired, the force-exponential windows can be applied to condition the signal to avoid leakage and measurement noise. The number of ensembles acquired per average also affects the ability to obtain good quality data and minimize measurement noise. In this test, data was acquired in the 0–100 Hz and 0–250 Hz frequency ranges. The frequency resolution (ΔF) was chosen for each case such that each ensemble was observed for 16 s. The force-exponential window was chosen, with a cutoff value of 10 % for the force window and an end value for exponential window as 20 %.

21.3.3 Validation

Validation is the process of determining the correctness of a model in its description of the reference system under a set of test conditions [1, 9]. For validating the calibrated rectangular plate FE model and thereby establishing the robustness of the model, it was decided to perform modal correlation of the updated FE model with the experimental results obtained from the modified test setup. The results of modal correlation are presented in Table 21.3. The relative difference for modal frequencies was less than 2 %.

FRFs were synthesized from the FE model at locations corresponding to the reference and response points. It is not required to choose the same input and output locations where measured data was acquired while synthesizing FRFs from FE models. In fact, the SVD-PCA validation metric enables comparison of global properties without spatial dependence. However, choosing the locations in the FE model that correspond to the test data helped in comparing the measured FRFs with the corresponding synthesized FRFs, which served as a further calibration metric that involves damping and sensor calibration issues.

A plot comparing the measured FRF with the synthesized FRF for a driving-point and cross-point are shown in Figs. 21.4 and 21.5 respectively. It is apparent from the comparison that the peaks of both the measured and the synthesized FRF are damped. In reality the modes do not have the amount of damping that is evident in the FRF comparison plot as the rectangular plate is a lightly damped structure. The damped peaks in the measured FRF are a result of the artificial damping introduced by the force-exponential window that was used to eliminate leakage while performing the impact testing [14]. As Rayleigh

Table 21.3 Correlation of modal frequencies (updated FE models)

Mode	Modal frequency (Hz)			Rel. diff. (%)	
	Experimental	FE model I	FE model II	FE model I	FE model II
First torsion	42.16	41.33	41.34	2	1.98
First X bending	44.16	43.71	43.65	1.02	1.16
Second torsion	95.58	95.04	95.12	0.57	0.48
First Y bending	104.6	103.1	102.99	1.45	1.56
Second X bending	119.06	118.19	118.16	0.74	0.76
Anti-sym. X bending	137.98	137.38	137.39	0.44	0.43
Third torsion	176.38	175.52	175.81	0.49	0.32
X and Y bending	203.72	202.86	203.25	0.42	0.23
Third X bending	244.98	243.65	244.1	0.54	0.36

$h = 6.17$ mm (.243"), $\mathsf{E} = 2.05 \times 10^{11}$ Pa (2.9734×10^7 psi)
FE model I: $\rho = 7810$ kg/m^3 (0.2821 lb/in^3), $m = 23.8$ kg (52.44 lb)
FE model II: $\rho = 7850$ kg/m^3 (0.2836 lb/in^3), $m = 23.9$ kg (52.69 lb)

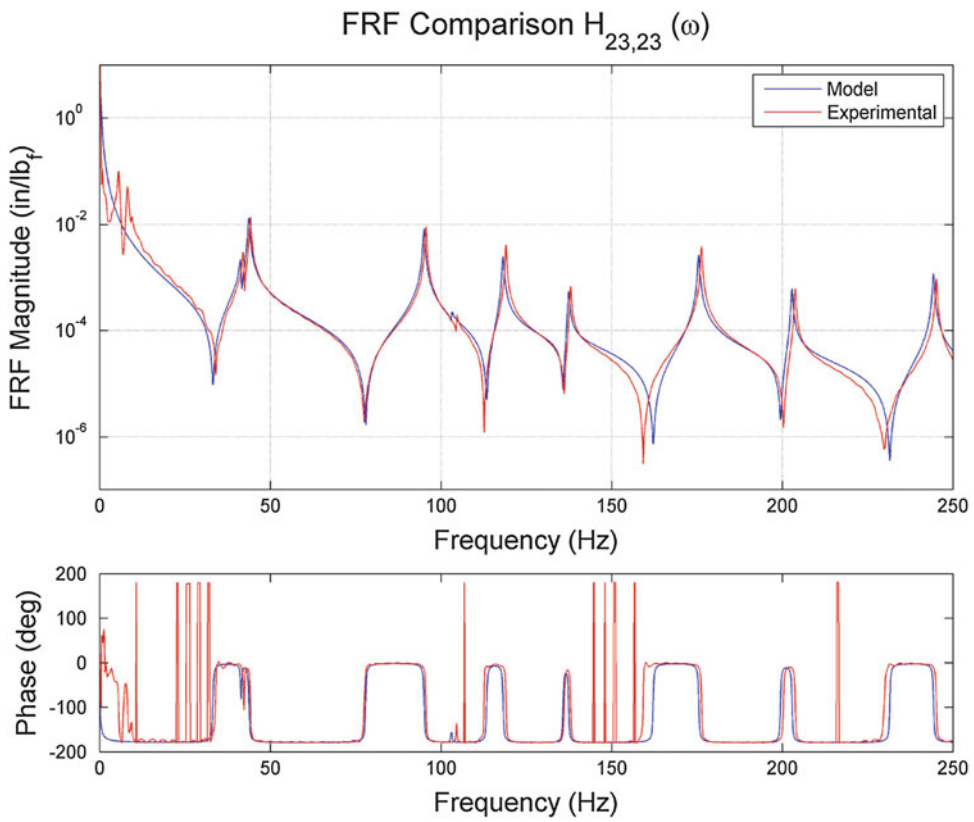

Fig. 21.4 Comparison of a driving-point FRF

damping (commensurate with the modal damping estimated from measured data) was defined in the analytical model, the peaks of the synthesized FRFs are also damped in the same order as the measured FRFs.

Figure 21.6 compares the principal components of the measured and the analytical data when damping was not prescribed in the analytical model. As expected, the principal components corresponding to the analytical data have sharp peaks. The anti-resonances observed in the plot are attributed to the limited spatial resolution (four output and four input locations) in the datasets compared initially. On increasing the spatial resolution, saddles would be noticed. For example, in Fig. 21.7, FRF data from 160 output and 4 input locations was used and damping was prescribed in the analytical model. The response at resonances in the analytical model is comparable with that in the measured data. Also, saddles are observed instead of anti-resonances as the spatial resolution was increased.

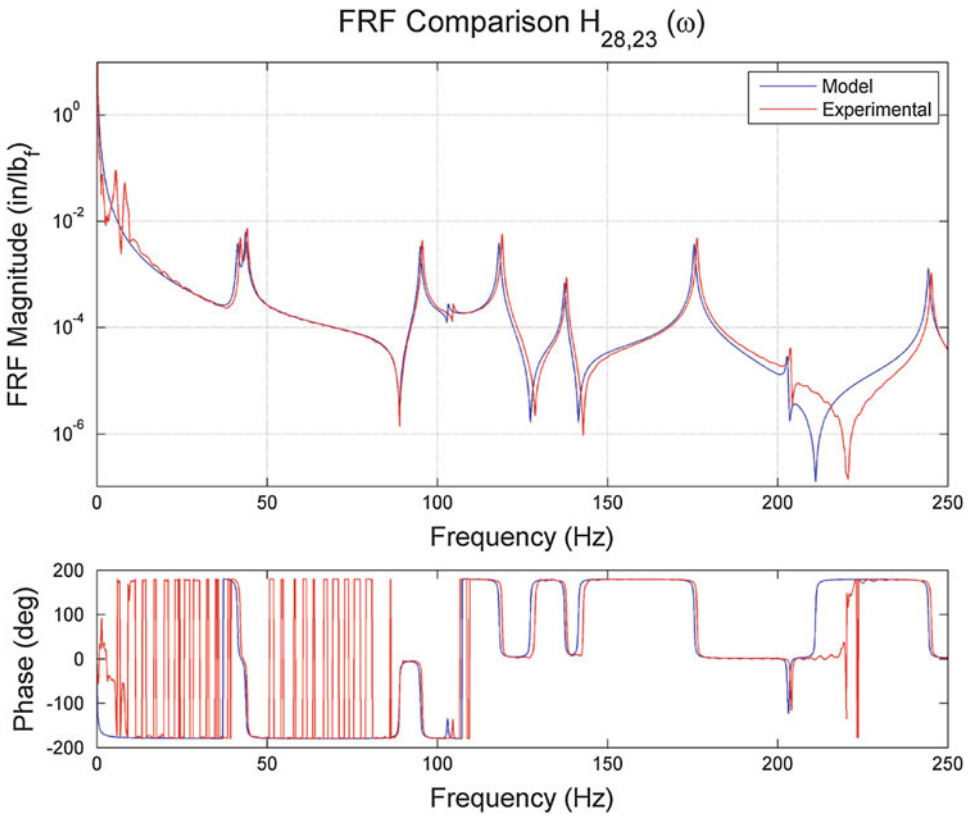

Fig. 21.5 Comparison of a cross-point FRF

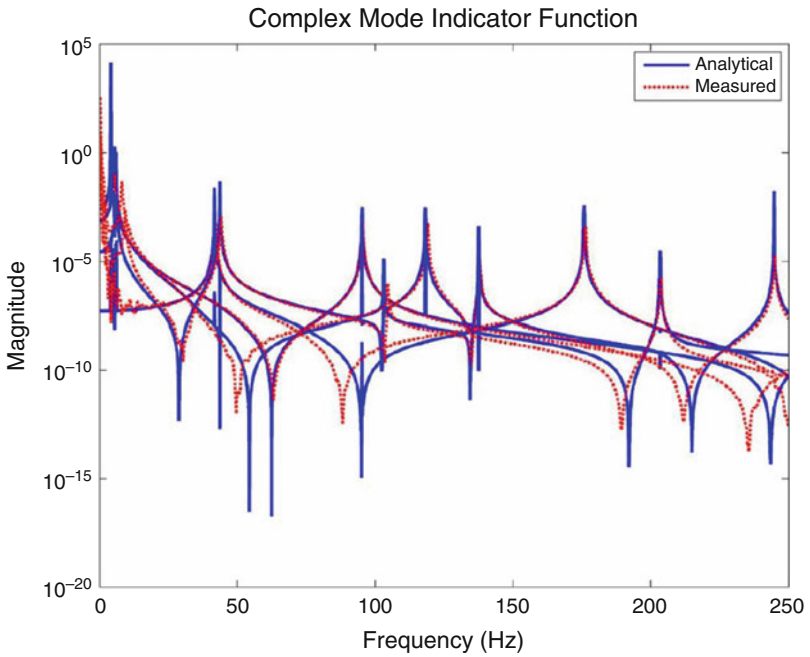

Fig. 21.6 Comparison of the principal components, limited spatial resolution and no damping in the analytical model

The principle response comparison for the first principal component corresponding to the case where damping was not prescribed in the analytical model is shown in Fig. 21.8. It is evident that there are outliers as highlighted in the figure. This extreme deviation is due to the fact that the peaks corresponding to resonances in the analytical model are sharp compared

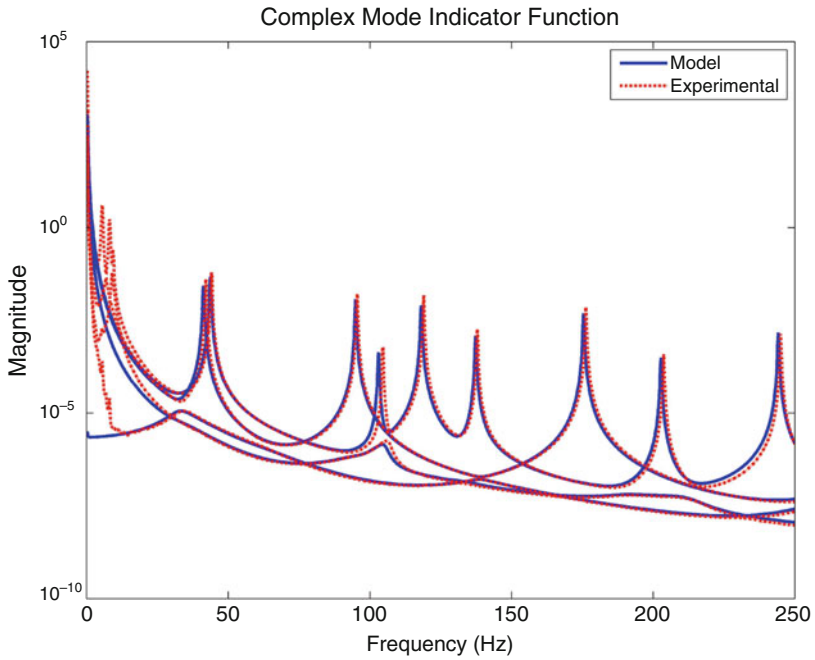

Fig. 21.7 Comparison of the principal components, damping prescribed in the analytical model, 160 output and 4 input locations

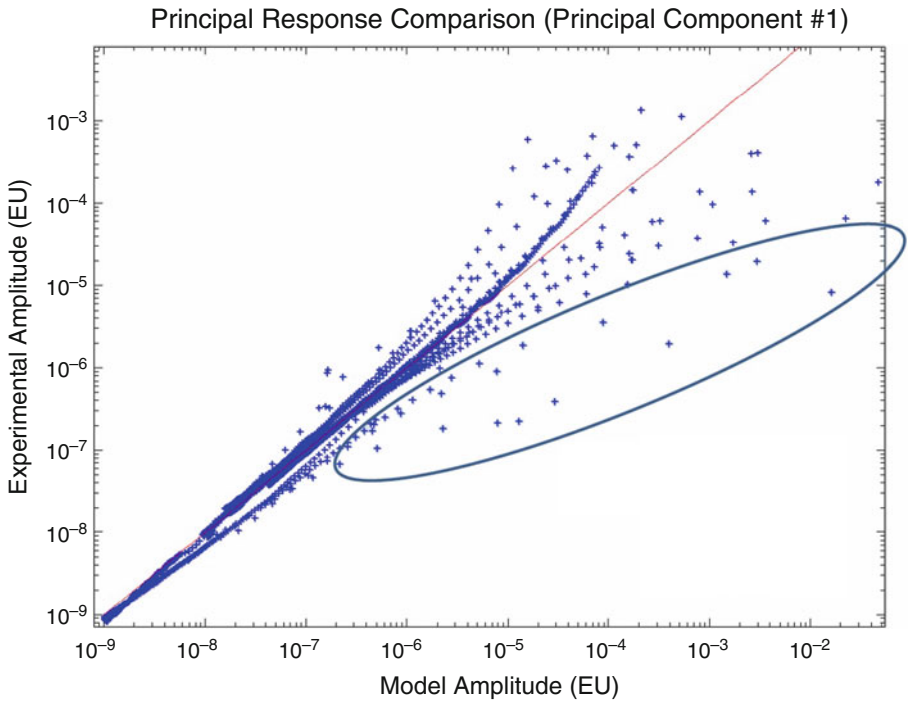

Fig. 21.8 Comparison of the principal components, no damping in the analytical model

to the measured data, in which damping was introduced due to using a force-exponential window. This demonstrates that the SVD-PCA metric is sensitive to difference in magnitudes. After damping was introduced in the analytical model, the spread was reduced. This is evident from the principle response comparison for the first principal components as shown in Fig. 21.9b. It is apparent that when the magnitude of one of the datasets is consistently higher, it affects the margin and when there is a frequency shift between the measured response and analytical response, the variance results in higher uncertainty.

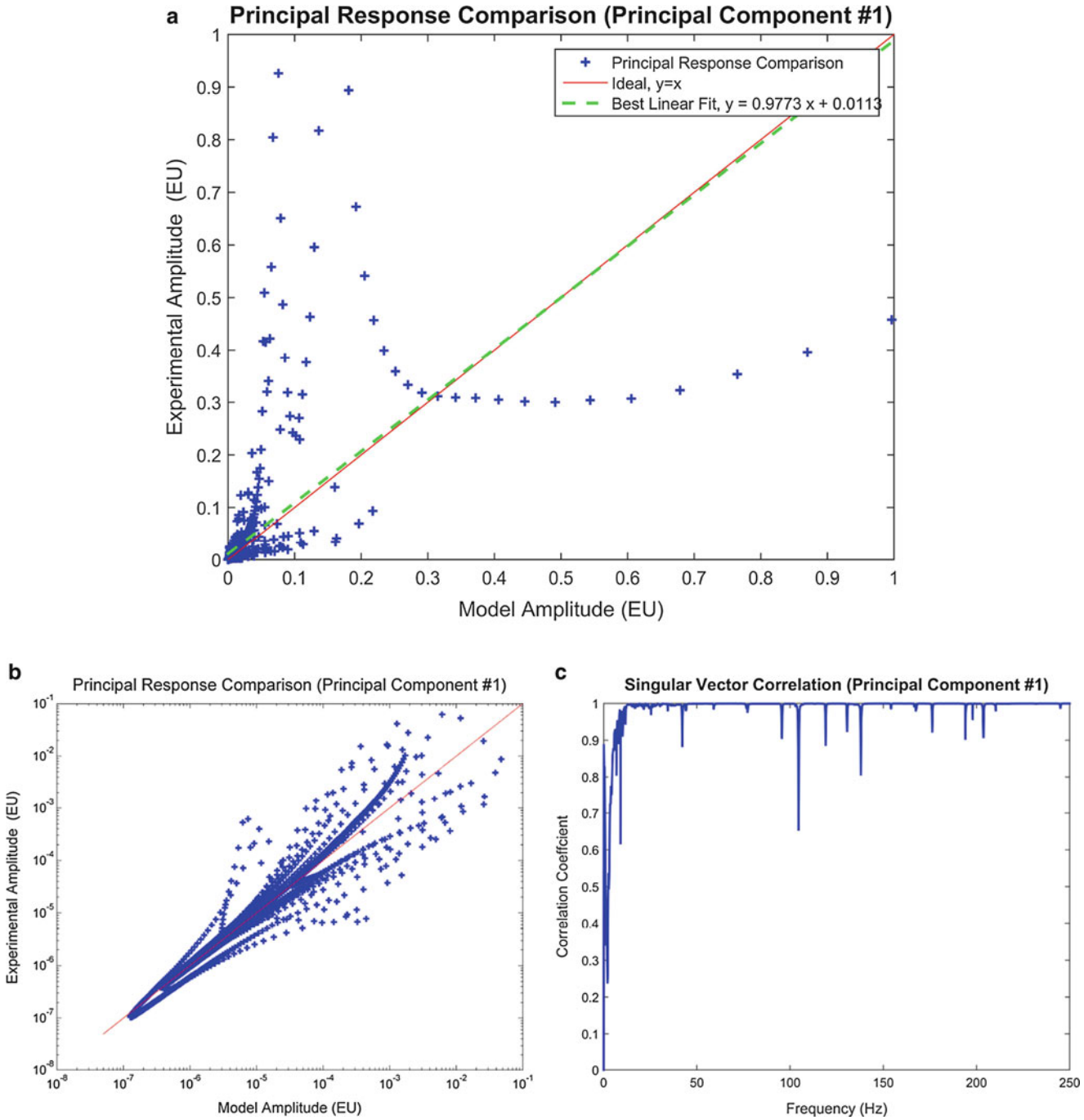

Fig. 21.9 Principal component #1. (**a**) Principal response comparison (linear-linear plot). (**b**) Principal response comparison (log-log plot). (**c**) Assurance criteria

The principal response comparison and the assurance criteria for the primary principal component are shown in Fig. 21.9. It is evident from Fig. 21.9a that the margin is 0.0227, the slope of the best linear fit is 0.9773, which is very close to the ideal case. The corresponding singular vectors are well correlated. The principal response comparison and the assurance criteria for Principal Components #2 and #3 are shown in Figs. 21.10 and 21.11 respectively.

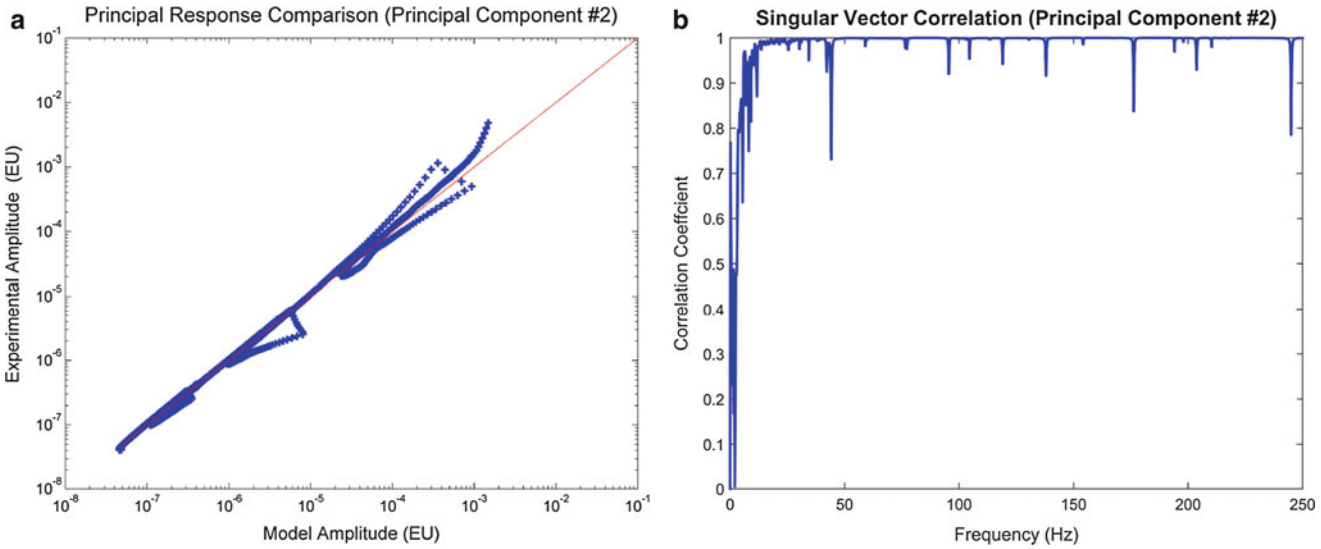

Fig. 21.10 Principal component #2. (**a**) Principal response comparison. (**b**) Assurance criteria

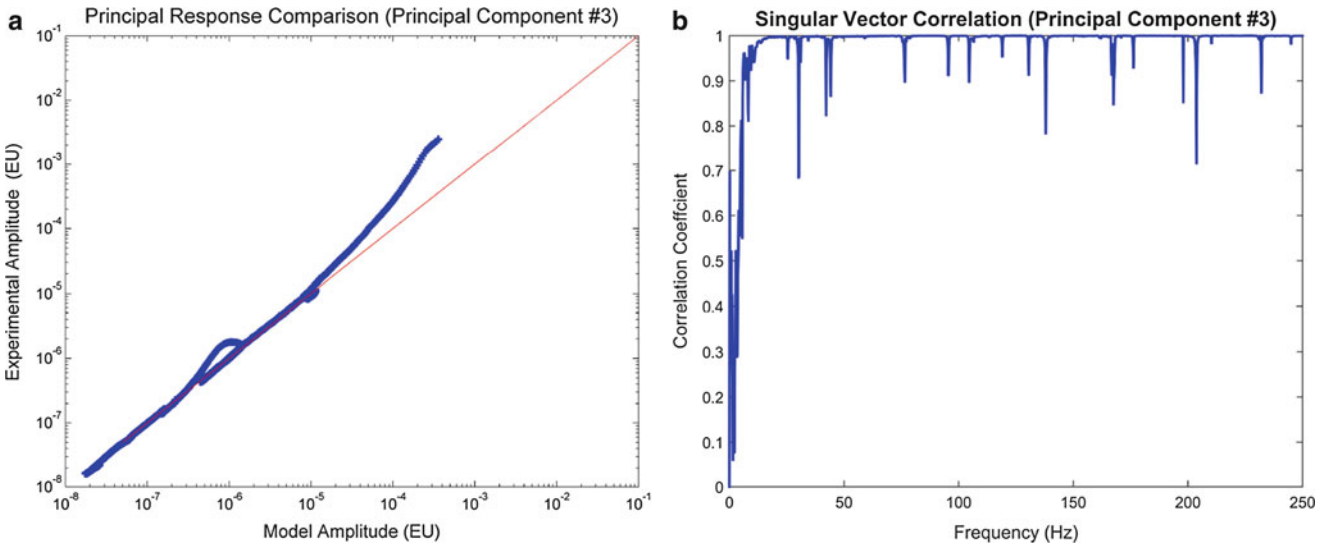

Fig. 21.11 Principal component #3. (**a**) Principal response comparison. (**b**) Correlation coefficient

21.4 Conclusions and Summary

Calibrated/validated FE models of structures assist in predicting system response with increased confidence in the model predictions. Calibration/validation metrics that quantify both the frequency shifts and magnitude difference in datasets being compared are desirable. The principle component analysis—singular value decomposition (PCA-SVD) validation metric uses SVD to quantify the margin and uncertainty. It is relatively easy to implement and gives a clear indication of both the margin and the uncertainty by utilizing the dominant singular values. Spatial correlation of the singular vectors associated with the dominant singular values can be ascertained using the Assurance Criteria. The PCA-SVD validation metric captures the global characteristics of the structure, which offers flexibility in terms of the choice of spatial distribution of measurement points.

The PCA-SVD validation metric was used to develop validated FE models for the rectangular steel plate structure. A systematic procedure was followed to update the FE model and to modify the test setup. This insured that the relative error in the modal frequencies was reduced. The PCA-SVD metric was sensitive to the high response at resonances in the frequency calibrated analytical model as damping was not defined initially. The damping calibration resulted in less margin (0.0227) and good correlation of the singular vectors.

Acknowledgements The authors would like to acknowledge the contributions and support from Murali Kolluri of Altair Engineering.

References

1. AIAA: Guide for the verification and validation of computational fluid dynamics simulations. American Institute of Aeronautics and Astronautics (AIAA-G-077-1998) (1998)
2. Pasha, H., Kohli, K., Allemang, R., Brown, D., Phillips, A.: Structural dynamics model calibration and validation of a rectangular steel plate structure. In: Proceedings of the International Modal Analysis Conference (IMAC) XXXIII – A Conference and Exposition on Structural Dynamics, Feb 2015
3. Allemang, R., Spottswood, M., Eason, T.: A principal component analysis (PCA) decomposition based validation metric for use with full field measurement situations. In: Proceedings of the International Modal Analysis Conference (IMAC) XXXII – A Conference and Exposition on Structural Dynamics, Feb 2014
4. Allemang, R.: Validation metrics and quantification of margin and uncertainty (QMU) in the extreme environments of the hypersonic vehicle program. Final Report- US Air Force Summer Faculty Fellowship Program (2012)
5. Allemang, R.: Validation metrics and quantification of margin and uncertainty (QMU) in the extreme environments of the hypersonic vehicle program. Final Report- US Air Force Summer Faculty Fellowship Program (2013)
6. Allemang, R., Phillips, A., Allemang, M.: Application of principal component analysis methods to experimental structural dynamics. In: Proceedings of the International Modal Analysis Conference (IMAC) XXVIII – A Conference and Exposition on Structural Dynamics (2010)
7. Allemang, R., Spottswood, M., Eason, T.: A principal component analysis (PCA) decomposition based validation metric for use with full field measurement situations. In: Proceedings of the International Modal Analysis Conference (IMAC) XXVII – A Conference and Exposition on Structural Dynamics, Feb 2014
8. Kolluri, M.M.: Developing a validation metric using image classification techniques. Master's thesis, University of Cincinnati (2014)
9. ASME: Guide for Verification and Validation in Computational Solid Mechanics. American Society of Mechanical Engineers (ASME V&V 10) (2006)
10. Blevins, R.: Formulas for Natural Frequency and Mode Shape. Butterworth-Heinemann, Boston (1979)
11. ANSYS Mechanical Linear and Nonlinear Dynamics, Lecture 3: Damping. Ansys Release 14.5, pp. 1–24 (2013)
12. Pasha, H., Allemang, R., Phillips, A.: Techniques for synthesizing FRFs from analytical models. In: Proceedings of the International Modal Analysis Conference (IMAC) XXXII – A Conference and Exposition on Structural Dynamics, pp. 73–79, Feb 2014
13. Pasha, H., Allemang, R., Brown, D., Phillips, A., Kohli, K.: Support systems for developing system models. In: Proceedings of the International Modal Analysis Conference (IMAC) XXXII – A Conference and Exposition on Structural Dynamics, pp. 183–193, Feb 2014
14. Fladung, W., Rost, R.: Cause and effect of applying the exponential window to an impact force signal. In: Proceedings of the International Modal Analysis Conference (IMAC) XIV – A Conference and Exposition on Structural Dynamics (1996)

Chapter 22
An Enhanced Metropolis-Hastings Algorithm Based on Gaussian Processes

Asif Chowdhury and Gabriel Terejanu

Abstract Markov Chain Monte Carlo (MCMC) has become the main computational workhorse in scientific computing for solving statistical inverse problems. It is difficult however to use MCMC algorithms when the likelihood function is computational expensive to evaluate. The status quo tackles this problem by emulating the computationally models upfront based on a number of forward simulations, and then the emulator is used in the MCMC simulation instead of the actual model. However, this strategy has an obvious drawback: how should one choose the initial number of forward simulations to capture the complexity of the model response? This is the main driver question that this paper tries to answer. Here, a novel Metropolis-Hastings algorithm is proposed to sample from posterior distributions corresponding to computationally expensive simulations. The main innovation is emulating the likelihood function using Gaussian processes. The proposed emulator is constructed on the fly as the MCMC simulation evolves and adapted based on the uncertainty in the acceptance rate. The algorithm is tested on a number of benchmark problems where it is shown that it significantly reduces the number of forward simulations.

Keywords Gaussian process • Markov chain Monte Carlo • Metropolis-Hastings algorithm • Likelihood function

22.1 Introduction

Markov Chain Monte Carlo (MCMC) is a class of algorithms to sample from a probability distribution by using Markov chain. One broad subclass of this is random walk MCMC algorithms which include Metropolis-Hastings (MH) algorithm, Gibbs sampling etc. Algorithms such as Metropolis-Hastings require evaluation of likelihood function for each of the proposed points. This evaluation is very time consuming in many cases involving complex physics-based models and hence can make the overall process of finding the samples quite slow.

There are many areas in statistics and statistical physics where some flavor of MCMC algorithm are used. In many of these cases, the evaluation of likelihood function is costly in terms of time. Since the quality of the sample improves with the number of steps, it is undesirable to reduce the number of steps in order to minimize the calls to the likelihood function. We need some other approach to address this issue. Any proposed approach needs to run faster and at the same time make sure that the quality of the sample is not diminished.

In this paper we propose a method that reduces the number of calls by approximating the likelihood function using a Gaussian process (GP). Since the GP approximation provides also uncertainty associated with its prediction, this uncertainty has been used within the MH algorithm to decide whether the proposed sample should evaluate the actual likelihood function of its GP approximation. This results in a reduction in the number of likelihood function evaluations.

22.2 Background

Markov Chain Monte Carlo (MCMC) algorithms are extensively used in many fields of science and engineering [1]. These methods use Markov chain to sample from a probability distribution. A particularly popular algorithm under this class is the Metropolis-Hastings algorithm. In a survey, this algorithm was placed among the top ten algorithms in the twentieth century that had great impact on scientific and engineering development [1].

A. Chowdhury • G. Terejanu (✉)
Department of Computer Science and Engineering, University of South Carolina, 315 Main St., Columbia, SC 29208, USA
e-mail: terejanu@cec.sc.edu

S. Atamturktur et al. (eds.), *Model Validation and Uncertainty Quantification, Volume 3*, Conference Proceedings of the Society for Experimental Mechanics Series, DOI 10.1007/978-3-319-29754-5_22

In this paper we propose a faster way to run random walk MCMC methods. Here, we have used the plain vanilla Metropolis-Hastings algorithm, the pseudocode of which is given below [2]:

Algorithm 1 Plain Metropolis-Hastings algorithm

1: **procedure** METROPOLIS–HASTINGS
2: Initialize $x^{(0)}$
3: **for** $i = 0$ to N - 1 **do**
4: Sample $u \sim U_{[0,1]}$
5: Sample $x^* \sim q(x^*|x^{(i)})$
6: **if** $u < A(x^{(i)}, x^*) = min\left\{1, \frac{p(x^*)q(x^{(i)}|x^*)}{p(x^{(i)})q(x^*|x^{(i)})}\right\}$ **then**
7: $x^{(i+1)} = x^*$
8: **else**
9: $x^{(i+1)} = x^{(i)}$
10: **end if**
11: **end for**
12: **end procedure**

Here the target distribution $p(x^*)$ has to be evaluated N times. This evaluation can be computationally expensive, especially when it involves running complex physics-based models. Each iteration means one evaluation of the target distribution for the new proposed point. It involves calculation of likelihood of each of the data items in each iteration to decide whether to accept or reject that proposed point. For large data sets this means a significant amount of calculations for each of the proposed points. In order to make the algorithm faster there needs to be a mechanism to address this issue. The goal of this paper is to propose an enhancement on the plain algorithm to tackle this bottleneck.

There is work to make MCMC faster when working with big data by using parallelization through multithreading [3]. This approach takes advantage of multiprocessing machines to perform iterations in parallel. There is also work on using distributed MCMC algorithm to achieve better performance [4]. To make the algorithm itself faster, irrespective of which type of system it is run on, there have been some work to cut the computational cost of the accept/reject step by using smaller fraction of data [5]. For each new proposed point, instead of using the whole data set to decide whether to accept or reject the point, this approach proposes a way to use a subset of the data with high confidence. This decreases the cost of each call to the target distribution.

We approach the problem from a different angle. Since the core problem is the large number of times the target distribution (and hence the likelihood function) needs to be evaluated, our approach involves making the required number of target distribution evaluation much smaller. Instead of evaluating the target distribution at each iteration we can apply machine learning techniques like Gaussian processes (GP) to approximate the target distribution and evaluate the distribution only when the GP is uncertain about the new proposed point.

22.3 Methodology

As we can see on line 6 of the plain MH algorithm, there are at least N calls to the target distribution. That involves calculation of the likelihood function which is expensive for large data sets. Our approach is to approximate the target distribution by Gaussian process (GP) so that the total number of evaluations of the likelihood function decreases. GP regression is a function approximation process that not only predicts the function but also gives a measure of the uncertainty associated with the prediction [6]. For each of the desired prediction points we get the mean prediction and also the measure of how certain the algorithm is about its mean prediction. As more data points are added to the training set, the GP model becomes more certain about the structure of the function. It is more certain in the area where more training points reside and less certain where there are few training points. GP can use any kernel for the similarity measure provided that the kernel satisfies some condition [6]. Here we have used the well known squared exponential (SE) kernel. In our problem we want to approximate the posterior target distribution. So for each proposed point we need the mean prediction. In addition, we get the uncertainty about the prediction. Based on this uncertainty we can decide whether to use the mean prediction as the approximation of the actual distribution or to evaluate the actual target distribution for the proposed point.

Due to positivity of probability density functions (pdf), in this paper the GP is used to approximate the log of the target pdf instead of using it directly to the original pdf. Let us consider one iteration of the algorithm. x is the last sampled point and x^* is the new proposed point that the proposal distribution has given; D is the data. So, $p(D|x)$ is the likelihood of the last sampled point; $p(D|x^*)$ is the likelihood of the proposed point; $p(x)$ is the prior probability of the last sampled point; $p(x^*)$ is

the prior probability of the proposed point. Furthermore, $p(x|D)$ and $p(x^*|D)$ are the posterior probabilities of the last point x and proposed point x^*, respectively. The acceptance probability, a can be written as:

$$a = \frac{p(D|x^*)p(x^*)}{p(D|x)p(x)} = \frac{p(x^*|D)}{p(x|D)} \tag{22.1}$$

$$\ln a = \ln p(x^*|D) - \ln p(x|D) \tag{22.2}$$

We build our GP on the log of the target pdf. So each of the values $\ln p(x^*|D)$ and $\ln p(x|D)$ are Gaussian distributed. This means if we take the log of the acceptance probability, it is the subtraction of two Gaussian which makes it Gaussian, too. Thus we have: $\ln a \sim \mathcal{N}(\mu, \sigma^2)$. This makes the probability of the acceptance rate a log-normal distribution: $a \sim \ln \mathcal{N}(\mu, \sigma^2)$.

In our algorithm as new points are evaluated for the target posterior distribution they are added to the training set of the GP. Each time a new point x^* is proposed from the proposal distribution, we measure how certain our GP is about the acceptance probability there. The measurement is done by computing $\sqrt{Var[a]}/E[a]$ and see if it is larger than some threshold value. At the moment we use some fixed value as the threshold. But it can be made adaptive which poses a scope for further improvement and refinement of the algorithm. Based on the value of the computation being larger than the threshold or not, we decide whether to read the $p(x^*)$ from the GP or to evaluate the target distribution.

To calculate $\sqrt{Var[a]}/E[a]$ for the log-normal distribution, we use the standard mean and variance formula for log-normal, which are $e^{\mu+\sigma^2/2}$ and $(e^{\sigma^2}-1)e^{2\mu+\sigma^2}$, respectively. This gives us $\sqrt{e^{\sigma^2}-1}$ as our desired ratio. So we need to calculate the value of σ^2. For current point x and new proposed point x^* the GP prediction gives us the covariance matrix containing $\sigma^2_{xx}, \sigma^2_{x^*x^*}, \sigma^2_{xx^*}$ where σ^2_{xx} is the mean-squared error at point x, $\sigma^2_{x^*x^*}$ is the mean-squared error at point x^* and $\sigma^2_{xx^*}$ is the covariance between x and x^*. Since $\ln a$ was a subtraction of two Gaussian, the value of σ^2 for the log-normal will be $\sigma^2_{xx} + \sigma^2_{x^*x^*} - 2\sigma^2_{xx^*}$.

The enhanced algorithm is presented below. Here we have denoted the posterior probability of x and x^* as $p(x)$ instead of $p(x|D)$ and $p(x^*)$ instead of $p(x^*|D)$ respectively to make the code less cluttered. On line 7 the call to $GP(predict(x, x^*))$ returns the mean vector μ and covariance matrix Σ. Covariance matrix is a symmetric matrix with $\sigma_{xx^*} = \sigma_{x^*x}$ and the mean vector μ contains μ_x and μ_{x^*} which denotes the mean predictions for x and x^*, respectively:

$$\mu = \begin{bmatrix} \mu_x \\ \mu_{x^*} \end{bmatrix} \qquad \text{and} \qquad \Sigma = \begin{bmatrix} \sigma_{xx} & \sigma_{xx^*} \\ \sigma_{x^*x} & \sigma_{x^*x^*} \end{bmatrix}$$

Algorithm 2 Metropolis-Hastings algorithm enhanced with Gaussian Process

```
1:  procedure MHGP
2:      Initialize x^(0)
3:      Initialize GP with (x^(0), p(x^(0)))
4:      for i = 0 to N - 1 do
5:          Sample u ~ U_[0,1]
6:          Sample x* ~ q(x*|x^(i))
7:          μ, Σ = GP(predict(x*, x^(i)))
8:          if sqrt(e^(σ²_xx + σ²_x*x* − 2σ²_xx*) − 1) > threshold then
9:              if p(x) was obtained by evaluating target distribution then
10:                 calculate p(x*) from target distribution and add the data to the training set for GP
11:             else
12:                 p(x) came from GP, now calculate p(x) from target distribution;
                    if after that the ratio is still greater than the threshold then calculate p(x*) from target distribution
13:             end if
14:         else
15:             get p(x*) from GP's prediction
16:         end if
17:         if u < A(x^(i), x*) = min{1, p(x*)q(x^(i)|x*) / p(x^(i))q(x*|x^(i))} then
18:             x^(i+1) = x*
19:         else
20:             x^(i+1) = x^(i)
21:         end if
22:     end for
23: end procedure
```

22.4 Experimental Results

To compare the outcome between plain Metropolis-Hastings and our proposed MHGP algorithm, we have used two experimental models. First of these is inference of modulus of elasticity (E) in Euler beam model [7]. In this model, the deflection of the beam, w, is given by:

$$w(x) = \frac{Px^2(3l - x)}{6EI}$$

where x is where point load P is applied, l is the length of the beam, I is the second moment of inertia of the beam's cross section, and E is the modulus of elasticity. For our experiment we calculate w for P applied at $x = l$ point. Taking natural logarithm on the above equation, assuming P, l, x, I to be constants, and adding noise ϵ, we get an equation for the data point with the following form:

$$d = a - \theta + \epsilon$$

where $d = \ln w$, a represents the constant part, and $\theta = \ln E$. We generate data point for some value of E. The goal is to infer the value of E from the data point using prior and likelihood. We set some Gaussian prior $p(\theta) \sim \mathcal{N}(\mu_{prior}, \sigma_{prior})$. Likelihood is $p(d|\theta) \sim \mathcal{N}(a - \theta, \sigma_\epsilon)$. For this case we can find an analytical solution for the posterior which is given by $p(\theta|d) \sim \mathcal{N}(\mu_{posterior}, \sigma_{posterior})$ where

$$\sigma_{posterior} = \left(\frac{1}{\sigma^2_{prior}} + \frac{1}{\sigma^2_\epsilon} \right)^{-1} \quad \text{and}$$

$$\mu_{posterior} = \mu_{prior} \frac{\sigma^2_\epsilon}{\sigma^2_{prior} + \sigma^2_\epsilon} + (a - d) \frac{\sigma^2_{prior}}{\sigma^2_{prior} + \sigma^2_\epsilon}$$

Next we compare the analytical solution with the sampling distribution from both the algorithms (Fig. 22.1) which shows that the proposed algorithm reaches similar result with much fewer evaluation of the target distribution.

The model for the second experiment is Lorenz system [8]. Starting with an initial condition and parameters the system reaches some new location after some specified amount of time. The model consists of three ordinary differential equations:

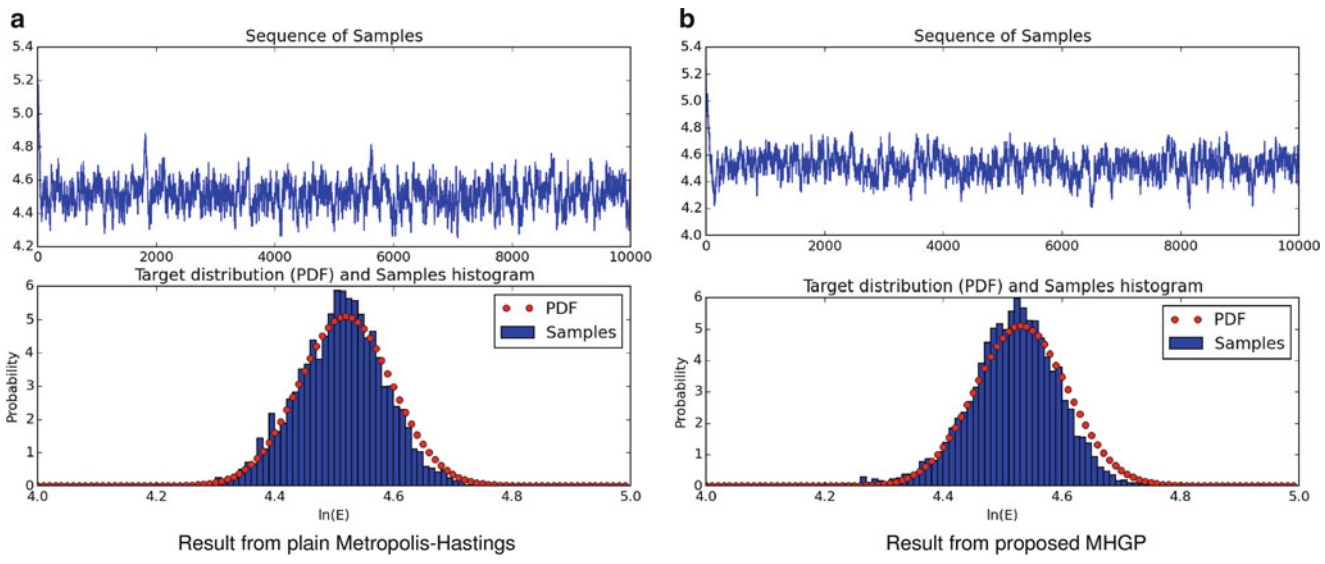

Fig. 22.1 Side by side view of results for inference of modulus of elasticity (E) in Euler beam model for plain Metropolis-Hastings and the proposed MHGP. The proposed model gives similar result to the original one but with fewer calls to the target distribution. Plain MH had 10,000 calls whereas MHGP had less than 200 calls to reach the same result. (**a**) Result from plain Metropolis-Hastings. (**b**) Result from proposed MHGP

$$\frac{dx}{dt} = s(y - x) \quad , \quad \frac{dy}{dt} = x(p - z) - y \quad , \quad \frac{dz}{dt} = xy - bz$$

where x, y, and z together are the system state, t is the time, and s, p, and b are the system parameters. Our goal is to infer the initial location based on the data for the final location using prior and likelihood. We can model the system like this:

$$\begin{bmatrix} x_f \\ y_f \\ z_f \end{bmatrix} = L^t \left(\begin{bmatrix} x_i \\ y_i \\ z_i \end{bmatrix} \right) + \begin{bmatrix} \epsilon_x \\ \epsilon_y \\ \epsilon_z \end{bmatrix}$$

where L^t stands for the Lorenz system running for time t; x_i, y_i, z_i make up the initial coordinate; x_f, y_f, z_f make up the final coordinate after the system is run for time t. The ϵ_x, ϵ_y, and ϵ_z are the measurement errors, which are normally distributed with zero mean and 0.01 variance. We specify some prior which contains our prior knowledge of the initial location, if any. The likelihood measures the likelihood of the value of the final location given the starting location. We sample from the posterior distribution which we get from the prior and the likelihood. We do this for both the plain MH algorithm and our proposed enhanced MHGP algorithm. The results from both the algorithms showed similarity but with fewer number of calls to the target distribution in the enhanced algorithm (Fig. 22.2). The figure has nine plots. The diagonal plots show the comparison of the samples between plain MH and the MHGP along each of the axes using histograms. The non-diagonal plots contain scatter plots showing the pairwise correlation among the samples for each of the axes. Plots in the upper triangle are from the MHGP, plots from the lower triangle (each of which has its symmetric counterpart in the upper triangle) are from the plain MH.

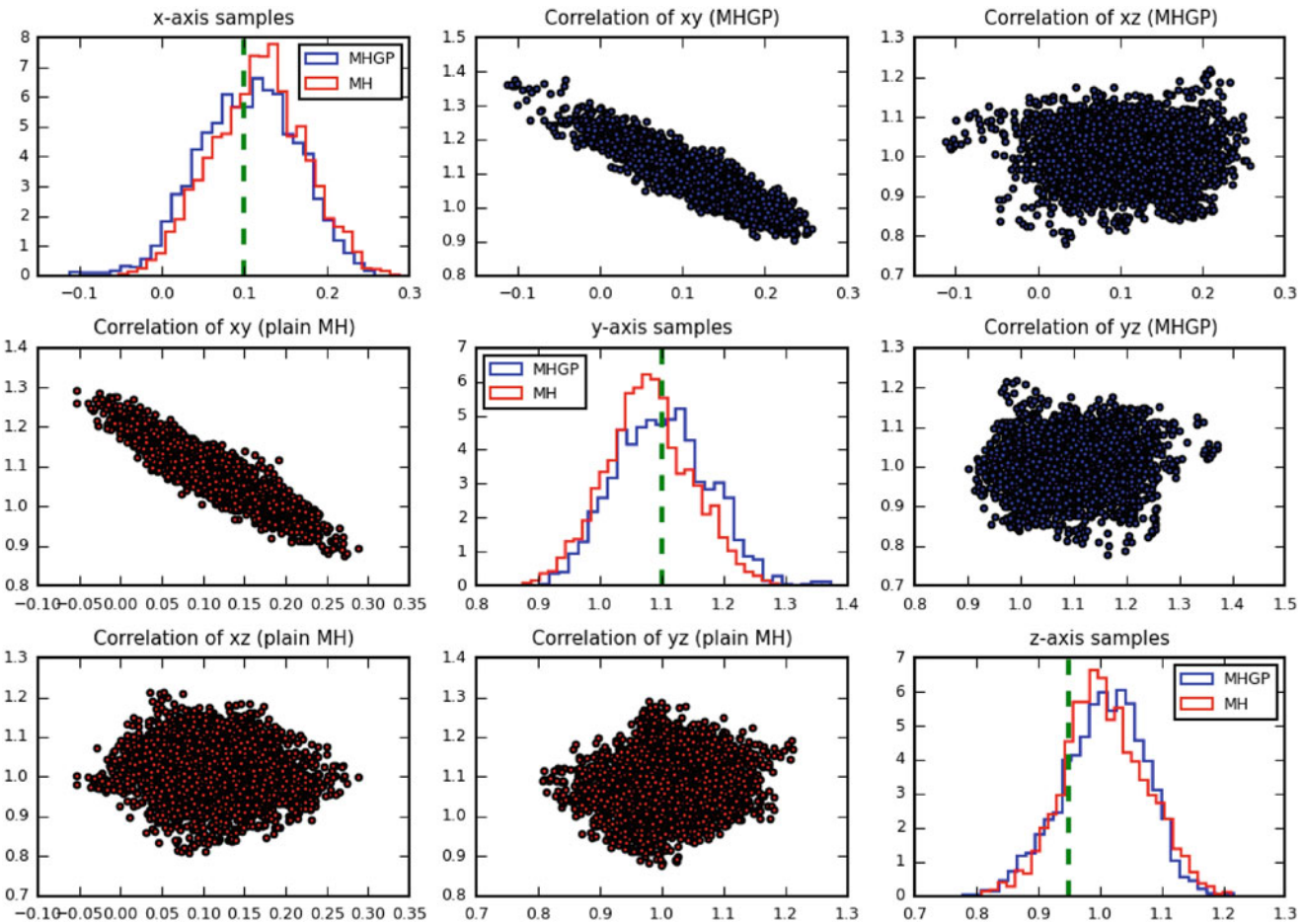

Fig. 22.2 Stacked view of results from plain Metropolis-Hastings and the proposed MHGP. The *green dotted lines* show the actual values. The proposed model gives similar result to the original one but with fewer calls to the target distribution. Plain MH had 10,000 calls whereas MHGP had less than 2000 calls to reach the same result

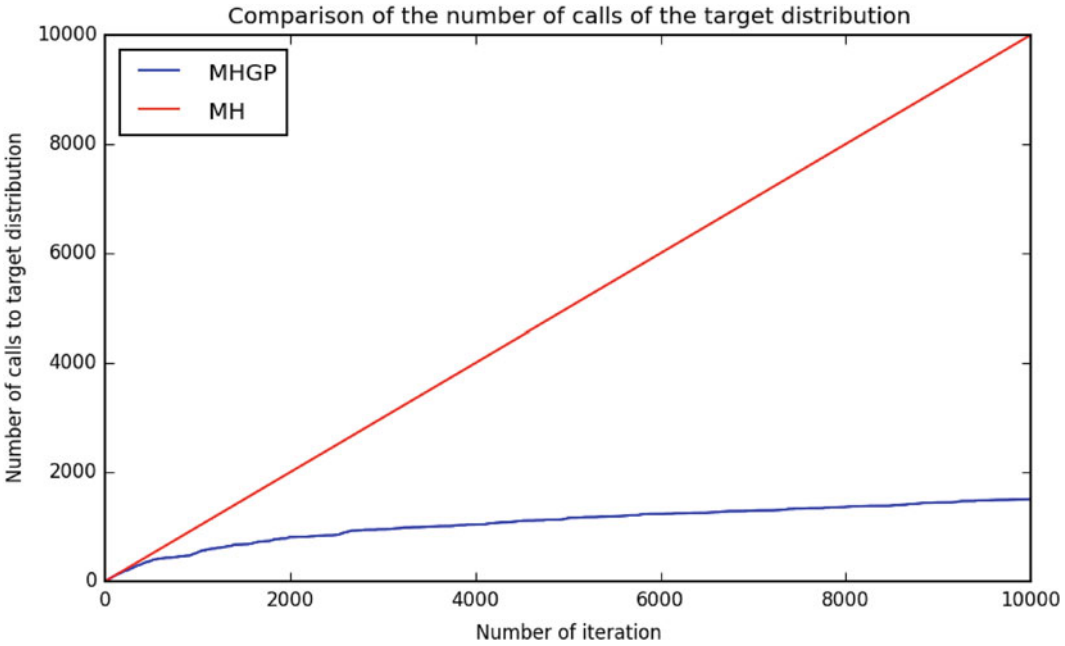

Fig. 22.3 Plot of the number of calls to the target distribution that plain MH and the proposed MHGP make. MHGP needs far less calls than the plain MH. Also, the growth of the number of calls diminishes as more iterations are run for the MHGP

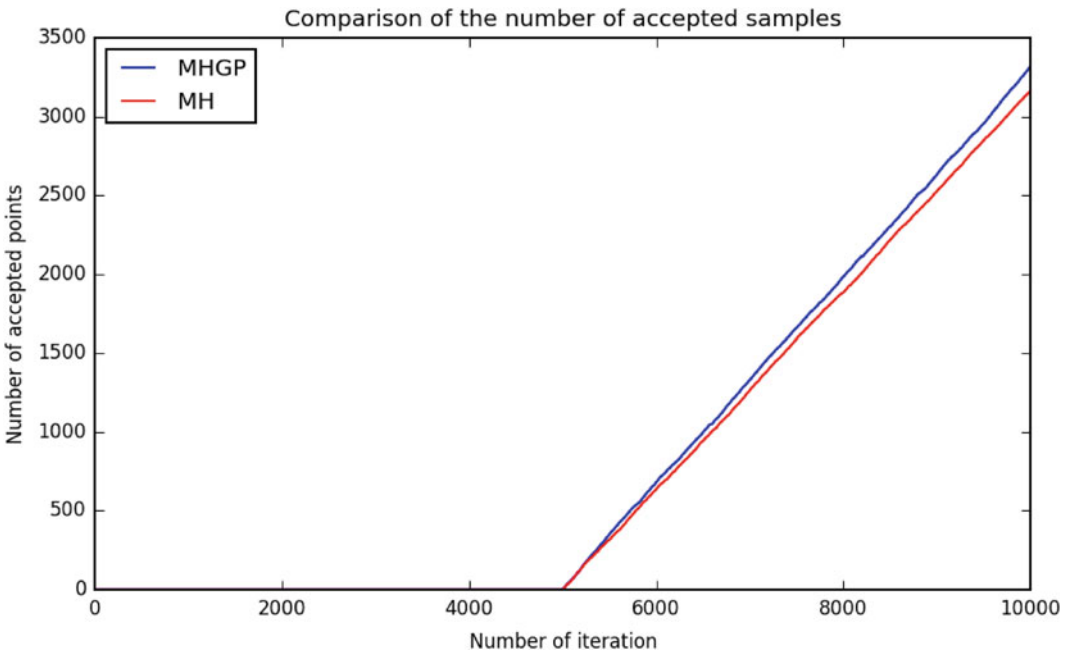

Fig. 22.4 Plot of the number of points that plain MH and the proposed MHGP accepts. The results show that they achieve similar results. The first half of the iterations were considered to be burn-in periods for both the algorithms and hence was discarded

The comparison between the number of calls to the target distribution that both the algorithms perform shows the advantage of the proposed algorithm over the plain Metropolis-Hastings algorithm (Fig. 22.3). In case of plain MH, the number of calls increase linearly with the number of iterations. But in case of the MHGP, the slope of the curve goes down with the increase of the iteration number. This is the result of the fact that the GP approximates the target distribution better and better as it gains more and more training points along the feature space, resulting more certain predictions for new proposed points and hence fewer calls to the target distribution as the iteration number grows. At the beginning, its

predictions are highly uncertain, so there are more calls to the target distribution and these are used to fit the GP. After a while, the GP begins to get more certain of its predictions which causes the number of calls to the target distribution to gradually decrease.

Both algorithms achieve similar results. This can also be demonstrated by comparing the number of points accepted by them as the number of iteration grows (Fig. 22.4). While running both the algorithm, the first half was considered the burn-in period. The second half shows very similar growth of accepted points which shows both of these converge to the relevant portion of the feature space in similar time, with MHGP requiring far less calls to the expensive target distribution.

22.5 Conclusion

A faster Metropolis-Hastings algorithm has been introduced by reducing the number of calls to costly likelihood function with the use of Gaussian process. An adaptive algorithm has been proposed to achieve this. Two benchmark problems, the Euler beam problem and the Lorenz system, have been used to show the improvement of the Gaussian process enhanced Metropolis-Hastings over the plain Metropolis-Hastings algorithm. We have also showed that the proposed method can be generalized to other MCMC methods. Since these methods are used in many areas in computational science, and many of them require computationally expensive simulations, the proposed faster method is likely to have a broader impact on numerous areas.

References

1. Andrieu, C., Freitas, N.D., Doucet, A., Jordan, M.I.: An introduction to mcmc for machine learning. Mach. Learn. **50**, 5–43 (2003)
2. Freitas, N.D.: Importance sampling and mcmc. Available: http://www.cs.ubc.ca/~nando/540-2013/lectures/l14.pdf (2013) [Online]
3. Byrd, J.M.R., Jarvis, S.A., Bhalerao, A.H.: Reducing the run-time of mcmc programs by multithreading on smp architectures. In: IEEE International Symposium on Parallel and Distributed Processing, IPDPS 2008, pp. 1–8 (2008)
4. Ahn, S., Shahbaba, B., Welling, M.: Distributed stochastic gradient mcmc. In: Proceedings of the 31st International Conference on Machine Learning (ICML-14). JMLR Workshop and Conference Proceedings, pp. 1044–1052 (2014). Available: http://jmlr.org/proceedings/papers/v32/ahn14.pdf [Online]
5. Korattikara, A., Chen, Y., Welling, M.: Austerity in mcmc land: cutting the metropolis-hastings budget. Available: http://arxiv.org/abs/1304.5299v4 (2013) [Online]
6. Rasmussen, C.E.: Gaussian processes for machine learning. In: *Gaussian Processes for Machine Learning*. MIT Press, Cambridge (2006)
7. Han, S.M., Benaroya, H., Wei, T.: Dynamics of transversely vibrating beams using four engineering theories. J. Sound Vib. **225**, 935–988 (1999)
8. Lorenz, E.N.: Deterministic nonperiodic flow. J. Atmos. Sci. **20**, 130–141 (1963)

Chapter 23
The Challenge of Dynamic Similarity Assessment

Adam C. Moya, Julie M. Harvie, and Mike J. Starr

Abstract Throughout the development cycle of structural components or assemblies that require new and unproven manufacturing techniques, the issue of unit to unit variability inevitably arises. The challenge of defining dynamic similarity between units is a problem that is often overlooked or forgotten, but can be very important depending on the functional criteria of the final product. This work aims to provide some guidance on the approach to such a problem, utilizing different methodologies from the modal and vibration testing community. Expanding on previous efforts, a non-intrusive dynamic characterization test is defined to assess similarity on an assembly that is currently being developed. As the assembly is qualified through various test units, the same data sets are taken to build a database of "similarity" data. The work presented here will describe the challenges observed with defining similarity metrics on a multi-body structure with a limited quantity of test units. Also, two statistical characterizations of dynamic FRFs are presented from which one may choose criterion based on some judgment to establish whether units are in or out of family. The methods may be used when the "intended purpose" or "functional criteria" are unknown.

Keywords Modal testing • Correlation • Frequency response functions • Similarity

Nomenclature

$G_T(\omega)$	Complex average of all FRF's in data set
i	Degree of freedom
n	Total number of DOF's
T	Individual test run
$H_i(\omega)$	FRF for individual DOF
N	Total number of variability tests
L	Individual test unit
$P_L(\omega)$	Complex average of all FRF's for individual test unit L
$\overline{X}(\omega)$	Mean of all average FRF's, $P_L(\omega)$
N_t	Total number if test units available
α	Bounding scale factor
$\overline{\sigma}(\omega)$	Average standard deviation from all test units
ECSAC	Experimental Cross Signature Scale Factor
ECSF	Experimental Cross Signature Assurance Criterion
ECSC	Experimental Cross Signature Correlation value
^{H}	Hermitian transpose

Sandia National Laboratories is a multi-program laboratory managed and operated by Sandia Corporation, a wholly owned subsidiary of Lockheed Martin Corporation, for the U.S. Department of Energy's National Nuclear Security Administration under contract DE-AC04-94AL85000.

A.C. Moya (✉)
Experimental Mechanics, NDE, and Model Validation Department, Sandia National Laboratories, P.O. Box 5800 – MS 0557, Albuquerque, NM 87185, USA
e-mail: acmoya@sandia.gov

J.M. Harvie • M.J. Starr
Program and Test Integration Department, Sandia National Laboratories, P.O. Box 5800 – MS 0557, Albuquerque, NM 87185, USA
e-mail: jharvie@sandia.gov; mjstarr@sandia.gov

S. Atamturktur et al. (eds.), *Model Validation and Uncertainty Quantification, Volume 3*, Conference Proceedings of the Society for Experimental Mechanics Series, DOI 10.1007/978-3-319-29754-5_23

23.1 Introduction

At Sandia National Laboratories, many of the structures tested are complex multi-bodies with many assembled joints. There exists a need to define a quick testing process that could identify assembly errors while minimizing the downtime required on the unit. Similarity testing at Sandia has traditionally been performed on a vibration table where the unit is exposed to a low level random input in all three principal directions; however this is very timely and costly due to the various facilities involved and the hardware required. This testing is also less than ideal as the force inputs are unknown and visual comparison of transfer functions and resonant frequencies are highly subjective. There is also a large variability of the dynamic response introduced by the vibration table. Due to these reasons, Sandia chose modal testing as the test method for developing a unit-to-unit similarity metric. Unfortunately, the physical geometry of the assemblies tested often allows for only limited sets of internal instrumentation, which would make mode shape correlation difficult and time consuming. In comparison, a single FRF taken at a strategic external location gives an indicator of the test article's similarity to a previously tested unit. As a result, the engineer can perform a simple modal test with limited instrumentation to obtain useful FRFs for correlation efforts. While the testing described above can be relatively easy, the difficulty in this process is quantifying similarity. This paper is intended to point out difficulties in defining such similarity metrics by comparing two similarity metrics.

Because structural dynamic correlation is commonly done using mode shapes, there has been significantly less research done on frequency response function correlation techniques. Allemang [1] provided a thorough overview of various correlation techniques, although most of the paper's focus is on the various mode shape correlation metrics. Pascual et al. [2] used both the Frequency Domain Assurance Criterion (FDAC) and Frequency Response Scale Factor (FRSF) in order to perform model updating. Heylen et al. [3] investigated multiple case studies using the Frequency Response Assurance Criterion (FRAC), although the majority of the paper focused on modal correlation metrics. Fotsch et al. [4] also examined the FDAC and FRAC while introducing a new tool called Modal FRF Assurance Criterion (MFAC), which used the combination of mode shapes, and FRFs to assess the correlation. Finally Dascotte et al. [5] employed the Cross Signature Assurance Criterion (CSAC) and Cross Signature Scale Factor (CSF) in order to study sensitivity based model updating. Moya and Marinone [6] started this similarity discussion by comparing multiple metrics used for finite element correlation on experimental data. This paper is intended to expand upon that work using a more realistic set of hardware, and discuss difficulties in assigning similarity acceptance metrics when searching for "in-family" responses.

23.2 Theory and Test Case

Two different approaches to similarity assessment are presented in this paper. The first method borrows tools often used in environment specification development for qualification purposes. This method essentially defines bounds based on the mean and standard deviation of spectral measurements of the tested units. The second method applies the Cross Signature Assurance Criterion (CSAC) and the Cross Signature Scale Factor (CSF) to experimental FRF's to gain a quantitative measurement on the FRF's variability. Before defining the equations used in these two methods, the test setup and procedure must first be described.

To assess the similarity metrics listed above, a total of seven assemblies consisting of multiple components connected with bolted and welded joints were used as test articles. These assemblies were designed to be identical and have been manufactured at various times over a span of 2 years, however the manufacturing process used on these assemblies has changed. This provides a perfect data set to examine the importance of defining unit to unit variability or "similarity" and demonstrates the difficulty in defining such metrics with the absence of large quantities of test articles. These assemblies were all individually attached to the same vibration fixture via four ¼-28 steel alloy bolts around the perimeter of the base. The vibration fixtures were square titanium plates with special features cut to adapt to the test article. A diagram of this test assembly and test setup is shown in Fig. 23.1. The experimental setup was designed to be non-intrusive and fast. This test setup consists of the test article/vibration fixture assembly resting on three blocks of foam to best represent a free-free boundary condition. The vibration fixture was instrumented with three PCB 356A03 triaxial accelerometers with a sensitivity of 10 mv/G and a PCB 288D01 impedance head attached to a 50 lb MB modal shaker. The modal shaker was oriented to input a 45° skewed burst random force input in all three perpendicular axes between 20 and 1000 Hz. This test setup was replicated for all assemblies.

This similarity test setup was replicated many times per assembly to gain a better picture of the test variability. To examine this variability, the test was repeated with different stinger lengths, at different force levels, and after unbolting and re-torqueing the assembly to the fixture. This combination of data sets was collected for each unit tested and used to define a test/non-linearity uncertainty.

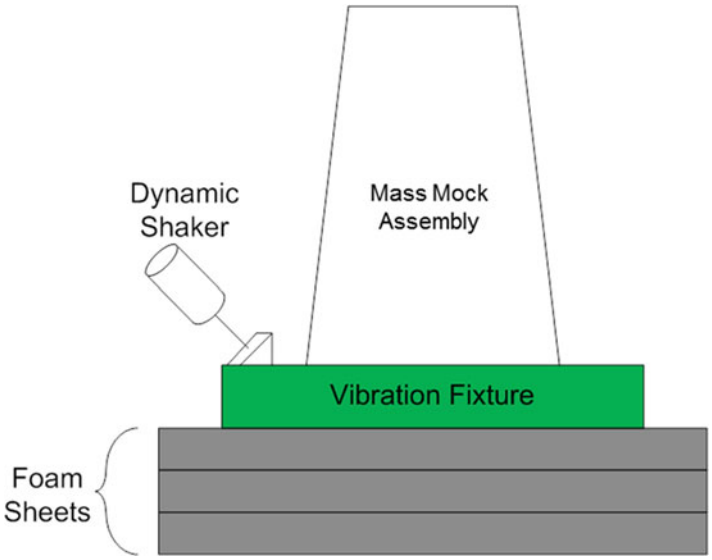

Fig. 23.1 Experimental test setup

Before any metrics can be defined, the individual FRF's are averaged across all degrees of freedom for each test. This gives us one compiled FRF per run to compare non-linearity and test variability. This is performed using Eq. (23.1). This average can then be quantitatively compared to the other averages for each unit to gain a measurement of test uncertainty as presented in Sect. 23.3.

$$G_T(\omega) = \frac{\sum_i^n (H_i(\omega))}{n} \tag{23.1}$$

Now that the test variability is quantified, an overall description of each unit's dynamic properties is required to define metrics. To do this, the compiled FRF's from Eq. (23.1), $G_T(\omega)$ can themselves be averaged for each test unit as shown in Eq. (23.2). This average FRF is now going to be the representative FRF for this assembly of which we will judge for similarity.

$$P_L(\omega) = \frac{\sum_T^N \left(G_T^N(\omega)\right)}{N} \tag{23.2}$$

The first metric assumes a normal distribution and attempts to measure the percentage of frequency lines that lie outside of defined bounds. To define the bounds, a single FRF average is calculated from of the entire sample as shown in Eq. (23.3). The bounds are calculated as shown in Eq. (23.4) where α is a scaling factor used to relax any acceptance criteria and $\overline{\sigma}(\omega)$ is the average standard deviation from all test units. The similarity metric is then found to be the percentage of frequency lines that lie outside of this bounding area, and is calculated for each unit.

$$\overline{X}(\omega) = \frac{\sum_L^{Nt} \left(P_L^{Nt}(\omega)\right)}{Nt} \tag{23.3}$$

$$Bounds(\omega) = \overline{X}(\omega) \pm \alpha\overline{\sigma}(\omega) \tag{23.4}$$

The second similarity metric presented borrows two calculations often performed in finite element model correlations. The Cross Signature Assurance Criterion (CSAC) is a form of the Modal Assurance Criterion (MAC) that has been adapted for the frequency domain. Typically this criterion compares an experimental and analytical set of FRF's at each DOF and frequency lines and is sensitive to mass and stiffness variations. For the purpose of similarity assignment, this equation has been adapted to simply compare two experimental FRF's instead of an experimental/analytical comparison. The Experimental Cross Signature Assurance Criterion (ECSAC) is defined below in Eq. (23.5).

$$ECSAC\left(j,\omega\right)=\frac{\left|\left(P_j^1\left(\omega\right)\right)^H\left(P_j^2\left(\omega\right)\right)\right|^2}{\left(\left(P_j^1\left(\omega\right)\right)^H\left(P_j^1\left(\omega\right)\right)\right)\left(\left(P_j^2\left(\omega\right)\right)^H\left(P_j^2\left(\omega\right)\right)\right)} \tag{23.5}$$

In addition to the ECSAC, the Cross Signature Scale Factor (CSF) has been similarly modified to work with experimental data. The Experimental Cross Signature Scale Factor (ECSF) shown in Eq. (23.6) compares differences in amplitude and is more sensitive to changes in damping. Both the ECSAC and ECSF compare two FRF's with a resulting value between zero (no correlation) and one (perfectly correlated FRF). In order to use these calculations as a single similarity metric, the Experimental Cross Signature Correlation value (ECSC) shown in Eq. (23.6) takes the average of the ECSAC and ECSF. This value gives us a single number with which to make comparisons between two units. To evaluate an assembly for its response to a family, then the ECSF and ECSAC can be calculated against $\overline{X}\left(\omega\right)$ instead of another individual assembly FRF.

$$ECSF\left(j,\omega\right)=\frac{2\left|\left(P_j^1\left(\omega\right)\right)^H\left(P_j^2\left(\omega\right)\right)\right|}{\left(\left(P_j^1\left(\omega\right)\right)^H\left(P_j^1\left(\omega\right)\right)\right)+\left(\left(P_j^2\left(\omega\right)\right)^H\left(P_j^2\left(\omega\right)\right)\right)} \tag{23.6}$$

$$ECSC=\frac{ECSAC^i+ECSF^i}{2} \tag{23.7}$$

23.3 Evaluation of Metrics

One of the most difficult aspects of similarity assignment is defining a satisfactory correlation metric that is appropriately strict. The two main challenges that influence the criteria are the test hardware geometry and its intended use. Geometrically simple, monolithic structures typically have little unit-to-unit variability and therefore the similarity metrics can be more easily defined. However, for complex assemblies with numerous bolted and welded joints, the dynamic response can vary significantly from one unit to the next. Thus similarity for these structures becomes much more difficult to delineate.

The intended use of the hardware can also effect the similarity metric. It may be that for the correct operation of a particular assembly that only one mode is deemed important. Thus the metric may focus on the consistency of that one mode for each unit. On the other hand, a different assembly may have many modes that are critical for proper functionality and therefore require the similarity metric to apply to a relatively larger bandwidth. For the metrics utilized in this work, the acceptance criteria was defined arbitrarily as 80 % correlation from 0 to 1000 Hz.

23.3.1 Bounding Method

The bounding method assumes a normal distribution for the compiled FRF's which expects 99.73 % of the population to lie within ± 3 times the standard deviation from the mean. This definition is the foundation for this method, however the bounds had to be relaxed rather significantly or no two units would ever be considered similar. To examine the variability of these assemblies, the mean of the entire sample was taken at each frequency line. The standard deviation was also taken at each frequency line between all data sets, ($G_T(\omega)$), and then averaged. Using this mean FRF and mean standard deviation, one can calculate the bounds shown in Eq. (23.4). Figure 23.2 below shows this bounding area along with all the compiled FRF's found in Eq. (23.2).

To further examine the bounding criteria, the scaling factor, α, in Eq. (23.4) was adjusted to loosen the acceptance bounds between $\pm 1\sigma$ and $\pm 9\sigma$. The percentage of frequency lines that lie outside of these bounds were then calculated and compared in a convergence plot shown in Fig. 23.3. By loosening this criteria, we can see a trend which obviously points to a certain outlier FRF. It appears that assembly 3 is not similar to the rest of the group, but the similarity is not so clear when comparing the other assemblies as two other assemblies do not satisfy the 80 % acceptance criteria at $\pm 3\sigma$ mentioned earlier. This result would eliminate these assemblies as similar, but it must be noted that the acceptance criteria is completely arbitrary.

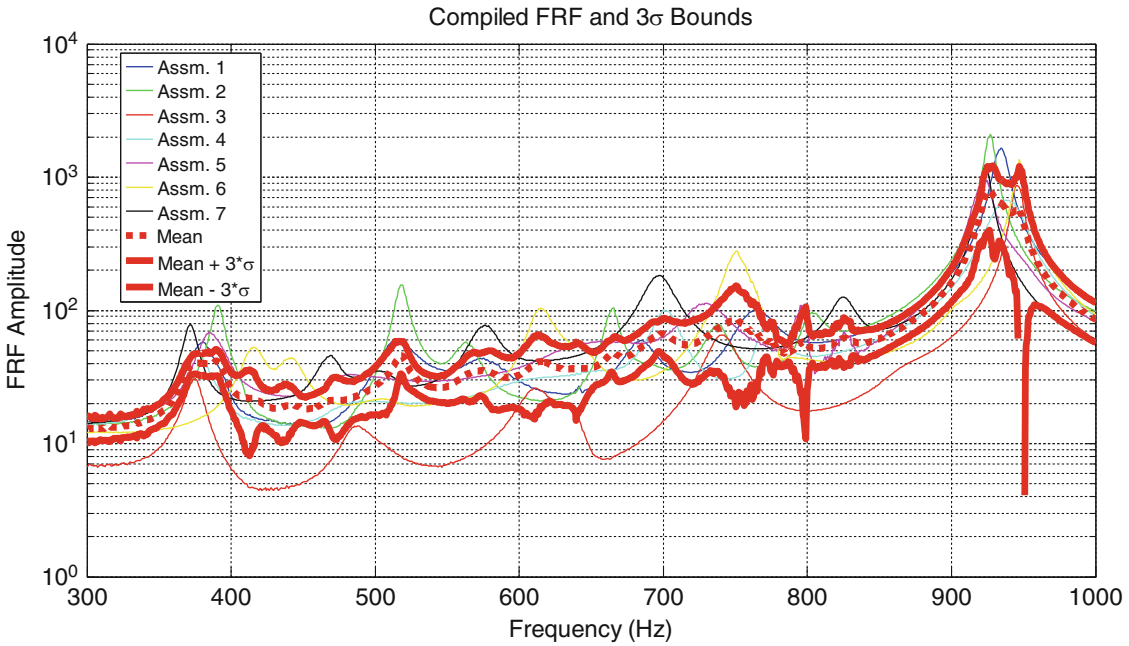

Fig. 23.2 Compiled FRF's for each unit compared to $\pm 3\sigma$ bounds (*bold red*)

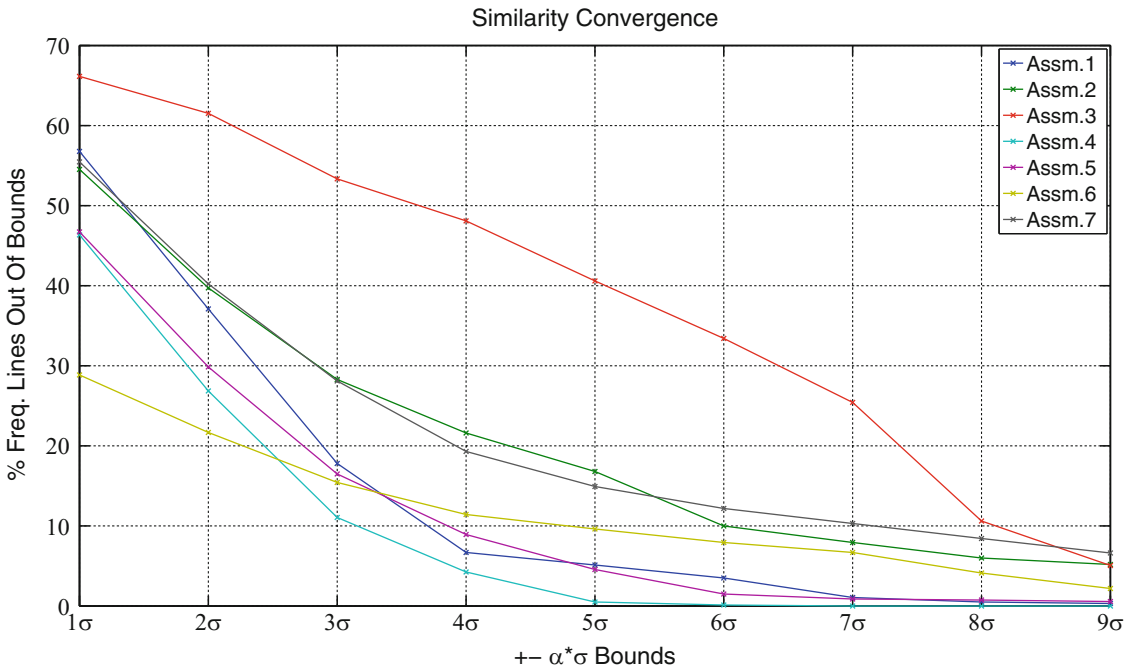

Fig. 23.3 Percentage of frequency lines outside of bounds for various bounding criteria

23.3.2 FRF Correlation Method

The second metric compared here is the ECSC metric from Eq. (23.7). This metric gives a single value ranging from zero to one where one is an exact correlation. Our acceptance criteria for the ECSC will therefore be a value of 0.8 which is consistent with the 80 % rule. To first examine the unit-to unit variability, the ECSC value was computed for each combination of assembly FRF's, $G_T(\omega)$. These calculations are presented in Fig. 23.4 as a matrix plot. This plot displays the ECSC value both numerically and on a color scale for convenient comparison. For example, each assembly compared with itself has a

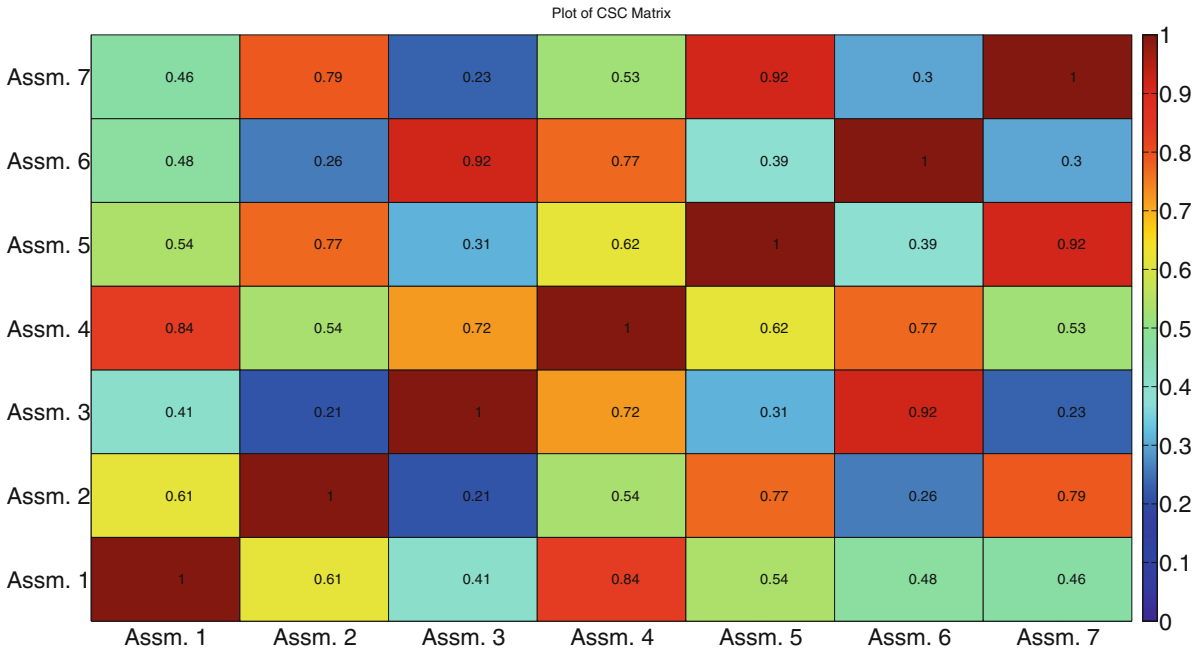

Fig. 23.4 Experimental cross signature criterion matrix plot comparing all units to each other

Table 23.1 Experimental cross signature values for each unit compared to mean FRF

Assembly #	ECSC (mean)
1	0.85
2	0.83
3	0.65
4	0.94
5	0.89
6	0.72
7	0.84

perfect ECSC value of one, but comparing assembly one to assembly two has an ECSC value of 0.61 which is a very poor correlation. This methodology shows another method for comparing units, and can be useful for finding similar units but the issue of a correct acceptance criteria still remains. It is also difficult to conclude from this plot which units belong to the same family.

In an effort to calculate each unit's ECSC value to a single representative "family" FRF, the ECSC calculation is repeated comparing each unit to the mean FRF calculated in Eq. (23.3). This value gives an indication to which unit lies outside the family and is more useful than the full ECSC plot. Table 23.1 lists this computed value and results in assemblies #3 and #6 failing the acceptance criteria. To gain a visual representation of these two failed units, the same FRF plot used in the bounding methodology is shown again in Fig. 23.5 but with the failed FRF's plotted in bold. Prior to calculating these two metrics, it was very difficult to determine which FRFs were similar, but taking upon second glance, we can easily see the difference between these two assemblies and the rest of the population.

23.4 Conclusion

In conclusion, two separate methodologies were presented for the use in identifying dynamic similarity between seven supposedly identical assemblies. Both metrics identified assembly #3 as an outlier with the ECSC metric also identifying assembly #6 as an outlier. The ECSC metric also identified assembly #3 and assembly # 6 as similar to each other, but not the rest of the population. While these metrics are interesting and can be helpful in detecting outliers, they also represent the complications that can arise when determining dynamic similarity.

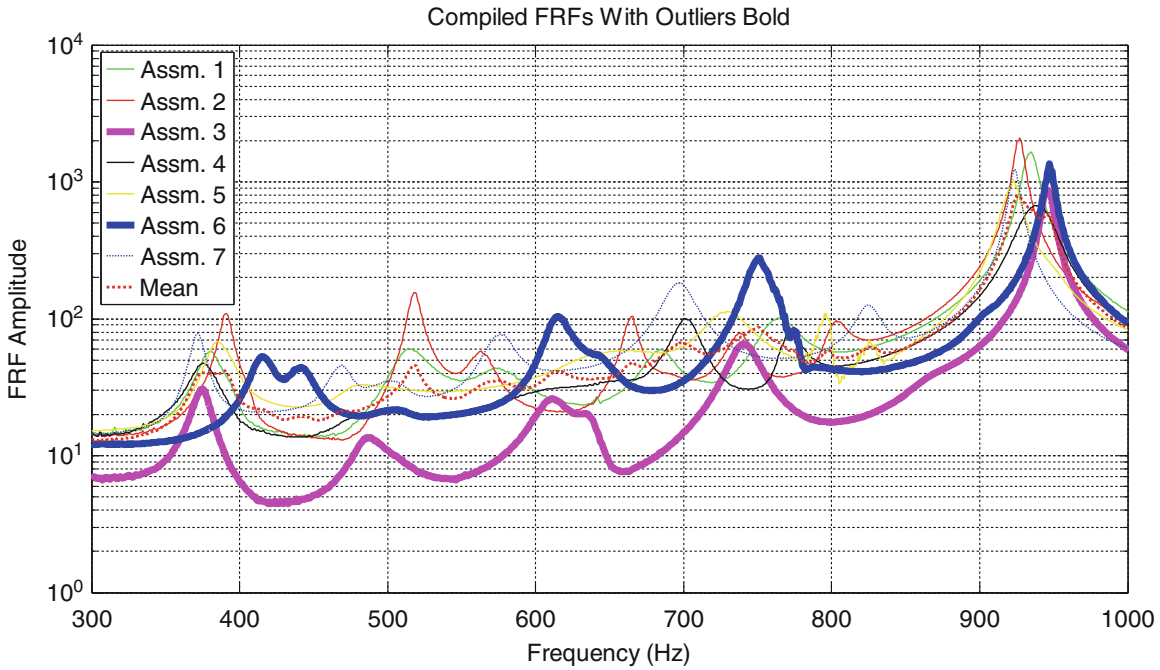

Fig. 23.5 Compiled FRF plot with bounds and outlier assemblies #3 and #6 (*bold blue and magenta*)

23.5 Future Work

The main complication in dynamic similarity assignment is the definition of a acceptance criteria. If the acceptance criteria is such that the response at a certain location does not reach a certain threshold for qualification reason, then a bounding method using only upper bounds may be the best metric. If this were the case, assembly #3 would have been found acceptable. Furthermore, the engineer may only be concerned with shifts in frequency and damping for control reasons. In this scenario, the ECSC criteria appears to be more applicable. Currently, there does not exist enough assemblies to have statistical confidence in these metrics, but they are presented to demonstrate the complications in dynamic similarity assignment.

The metrics presented here are continuously evolving as more data is acquired, and thus the acceptance criteria will mature over time. It is expected that the acceptance criteria or bounds will converge as more samples are acquired, and will vary based on the complexity of the part or assembly. The similarity test presented will continue to be performed on newer assemblies as the qualification of the product continues. As this data is acquired, it will be fed into a database for such similarity metrics to be defined and/or refined. Such data may also be used in model correlation efforts which can lead to an unlimited sample size.

References

1. Allemang, R.J.: The modal assurance criterion—twenty years of use and abuse. Sound Vib. Mag., August, 14–20 (2003)
2. Pascual, R., Golinval, J., Razeto, M.: A frequency domain correlation technique for model correlation and updating. In: Proceedings of the 15th International Modal Analysis Conference, pp. 587–592 (1997)
3. Heylen, W., Avitabile, P.: Correlation considerations—part 5 (degree of freedom correlation techniques). In: Proceedings of the 16th International Modal Analysis Conference, pp. 207–214 (1998)
4. Fotsch, D., Ewins, D.J.: Applications of MAC in the frequency domain. In: Proceedings of the 18th International Modal Analysis Conference, pp. 1225–1231 (2000)
5. Dascotte, E., Strobbe, J.: Updating finite element models using FRF correlation functions. In: Proceedings of the 17th International Modal Analysis Conference (1999)
6. Moya, A., Marinone, T.: Comparison of FRF correlation techniques. In: Proceedings of the 33rd International Modal Analysis Conference (2014)

Chapter 24
Model Based Robust Balancing Approach for Rotating Machines

Arinan Dourado Guerra Silva, Aldemir Ap Cavalini Jr., and Valder Steffen Jr.

Abstract Unbalance is one of the most common problems found in rotating machines in the context of industrial plants. This phenomenon can generate high vibration amplitudes that can lead to the fatigue of rotor elements. Various approaches have been proposed in order to solve the rotor balancing problem, as the so-called influence coefficients technique. This paper presents an alternative balancing methodology for rotating machines, aiming at overcoming the limitations faced by the frequently used methods. This alternative technique first identifies the model of the machine, and then the unbalance is determined by solving a typical inverse problem through an optimization method by taking into account the inherent uncertainties that affect the balancing performance. The robust balancing methodology is based on a multi-objective fuzzy optimization procedure, in which the uncertainties are treated as fuzzy variables. The robust optimum is determined by using an objective function which minimizes a predefined robustness metric. Finally, the numerical investigation is applied to a rotor composed by a horizontal flexible shaft, two rigid discs, and two ball bearings. The results indicate the effectiveness of the proposed technique.

Keywords Rotordynamics • Balancing • Fuzzy logic • Robust optimization • Decision making under uncertainties

24.1 Introduction

Balancing is a systematic procedure for adjusting the radial mass distribution of a rotor approximating its barycenter to the geometric centerline in order to reduce vibration and lateral forces applied to the bearings and surrounding structures [1]. Innumerous solutions have been proposed aiming at minimizing damage effects of unbalance. The most widely known balancing techniques are the following: modal balancing, four-run without phase, combined techniques, and the popular influence coefficients method [2–4].

Although widely used, the rotor balancing technique using influence coefficients (IC) presents some adverse points that encourage the search for alternative balancing approaches. As many of the balancing approaches, IC considers a linear relation between the unbalance excitation and the resulting vibration. However, if the structure presents nonlinearities the results obtained, regarding the correction weights and their corresponding angular positions, are not satisfactory. Additionally, IC method requires trial weights (known masses that are positioned at specific locations along the rotor) in order to determine the unbalance response sensitivity for constant rotation speed.

Aiming at overcoming the limitations faced by the IC technique, a model based balancing methodology was developed as shown in [5]. This methodology does not require a linear relationship between unbalance and vibration responses; besides, trial weights are not necessary. However, a reliable model of the rotating machine is required. Thus, from a reliable mathematical model, the proposed method shows up to be well adapted for industrial applications in which the non-producing time dispensed to reduce the synchronous vibration of the rotor to acceptable levels should be as small as possible. The unbalance is identified by solving a typical inverse problem by using a pseudo-random optimization method, such as the Genetic Algorithms, Simulated Annealing, Particle Swarm Optimization, Ant Colony, Differential Evolution, etc. This class of algorithms mimic specific natural phenomena and is attracting the attention of an increasing number of authors due to their capability of working successfully in complex optimization problems and also due to their robustness and ability to avoid local minima.

A.D.G. Silva • A.A. Cavalini Jr. • V. Steffen Jr. (✉)
LMEst—Laboratory of Mechanics and Structures, INCT (EIE)—National Institute of Science and Technology, Federal University of Uberlândia, School of Mechanical Engineering, Av. João Naves de Ávila, 2121, Uberlândia, MG 38408-196, Brazil
e-mail: arinandourado@doutorado.ufu.br; vsteffen@mecanica.ufu.br

S. Atamturktur et al. (eds.), *Model Validation and Uncertainty Quantification, Volume 3*, Conference Proceedings of the Society for Experimental Mechanics Series, DOI 10.1007/978-3-319-29754-5_24

In this context, this paper presents the numerical results obtained in the balancing of a horizontal rotating machine taking into account the inherent uncertainties that can affect the balancing performance. Besides, it is expected that the robust balancing keeps the vibration amplitudes under acceptable values (defined by proper balancing standards) for longer operation periods. The proposed methodology is based on a multi-objective fuzzy optimization procedure in which the uncertainties are treated as fuzzy variables. The robust optimum is determined introducing an additional objective function to the original optimization problem (i.e., the balancing problem). The additional function is used aiming at minimizing a predefined robustness metric.

It is worth mentioning that any optimum design of a mechanical system must be robust due to the unavoidable uncertainties that affect its dynamic behavior. Regarding the optimization issues, robustness can be understood as a solution that is frequently not the best for a particular dynamic problem, but is the best solution for the case in which the system is exposed to some fluctuation. G. Taguchi [6] was the pioneer regarding the application of robust optimization methodology: noise factors were introduced in the cost functions (written as mean square deviations) which have to be maximized. Commonly, the robust optimization approaches are based on the statistical moments [7–9] and the definition of a robustness objective function. Large combinatorial multi-objective problems are generated, imposing serious disadvantage regarding the computational costs. The fuzzy logic [10] is an intuitive approach, which associates the so-called fuzzy sets with the possibility theory [11]. A simple mathematical logic is formulated for uncertainty analysis, based on pessimistic and optimistic values of the considered objective function (i.e., fuzzy sets). Therefore, the fuzzy logic seems to be appropriate for robust optimization since it requires fewer evaluations of the cost functions, which reduce the computational cost associated with the process.

24.2 Rotor Model

The rotor model is obtained by considering the rotating system as a combination of several sub-systems, such as, shaft, discs, couplings, and bearings. The basic equation for the finite element model of the rotor is found in [12]. Equation (24.1) shows the matrix differential equation that describes the dynamic behavior of flexible rotors supported by ball bearings.

$$[M]\left\{\ddot{U}\right\} + [D + \Omega D_G]\left\{\dot{U}\right\} + \left[K + \dot{\Omega} K_{st}\right]\{U\} = \{W\} + \{F_u\} + \{F_s\} \tag{24.1}$$

where M is the mass matrix, D is the damping matrix, D_G is the gyroscopic matrix, K is the stiffness matrix, and K_{st} is the stiffness matrix resulting from the transient motion. All these matrices are related to the rotating parts of the system, such as couplings, discs, and shaft. U is the generalized displacement vector and Ω is the shaft rotation speed. W stands for the weight of the rotating parts, F_u represents the unbalance forces, and F_s is the vector of the shaft supporting forces produced by the bearings.

The shaft is modeled as a set of Timoshenko's beam elements with two nodes and four degrees of freedom per node, namely two displacements and two rotations. Due to the size of the matrices involved in the equation of motion, the pseudo-modal method is used to reduce the dimension of the finite element model (FE model). Through this procedure a reduced equation of motion is obtained as illustrated by Eq. (24.2).

$$\left[\widetilde{M}\right]\left\{\ddot{Q}\right\} + \left[\widetilde{D} + \Omega\widetilde{D}_G\right]\left\{\dot{Q}\right\} + \left[\widetilde{K} + \dot{\Omega}\widetilde{K}_{st}\right]\{Q\} = \left\{\widetilde{F}_u\right\} + \left\{\widetilde{F}_s\right\} + \left\{\widetilde{W}\right\} \tag{24.2}$$

where ϕ is the modal matrix containing the n first vibration modes of the non-gyroscopic and non-damped system, Q are the modal coordinates, $\widetilde{M} = \phi^T M\phi$, $\widetilde{D} = \phi^T D\phi$, $\widetilde{D}_G = \phi^T D_G\phi$, $\widetilde{K} = \phi^T K\phi$, $\widetilde{K}_{st} = \phi^T K_{st}\phi$, $\widetilde{F}_u = \phi^T F_u$, $\widetilde{F}_s = \phi^T F_s$, and $\widetilde{W} = \phi^T W$.

24.3 Balancing Methodology

Figure 24.1 shows a flowchart to illustrate the balancing methodology as proposed by [5]. The model based balancing method begins by inserting a set of randomly generated masses and phase angles in each balancing plane of the representative FE model. In this case, the simulated time-domain responses are obtained for each generated unbalance forces. The vibration responses are determined at the same positions along the shaft in which the responses were acquired from the rotor for an unknown unbalance condition (original configuration). The vibration responses are used to compute the objective function F presented in Eq. (24.3). If the best result of this function corresponds to a minimum, the unbalance affecting the rotor

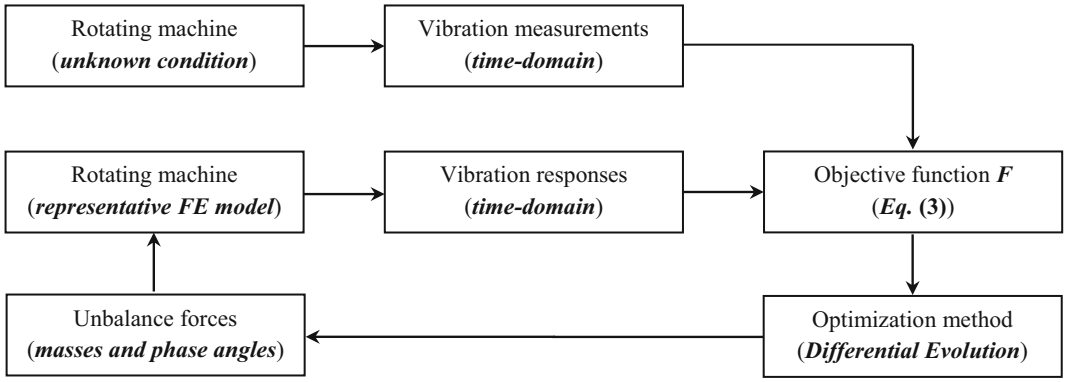

Fig. 24.1 Balancing scheme

is identified. This means that the found correction masses with their respective angular positions is capable of reproducing the unbalance response of the rotor in the original configuration. If the function does not find a value close to zero, the optimization method will propose new unbalance configurations and the process will continue iteratively until the target is found. In order to obtain the balancing conditions of the rotor, it is necessary to add 180° to the previously found phase angles, keeping however the same masses obtained, which are now the correction masses.

$$F = \sum_{i=1}^{n} \frac{\left\| U_i^{FEmodel}(x) - U_i^{Original} \right\|}{\left\| U_i^{Original} \right\|} \tag{24.3}$$

where n is the number of sensors used in the procedure, $U_i^{FEmodel}(x)$ is the vibration response obtained by using the FE model, x is the vector containing the proposed correction masses and associated phase angles by the optimization method, and $U_i^{Original}$ is the vibration response measured on the rotor in the original configuration.

The uncertainties considered in the applications presented in this contribution are introduced directly on the parameters of the FE model. The proposed robust balancing methodology is characterized by uncertainties affecting, for example, the stiffness and damping of the bearings (i.e., due to fixation problems and wear), the dimensions of the discs and shaft (i.e., due to the fabrication process). Therefore, a superior balancing performance is expected as the correction masses and associated phase angles determined by the robust methodology are used for unbalance correction. Possible variations on the geometric and physic properties of the rotating machine can be considered during the balancing process, which explains the expected performance of the procedure.

24.4 Fuzzy Robust Optimization

Fuzzy logic is the term used to the intuitive formulation proposed by Lofti A. Zadeh [10] that generalizes the membership notion of an element in a mathematical set, creating a graded notion represented by the membership function. In a classical sense, a math set is the collection of elements that belongs to a given definition. Any element can either belong or not to the mentioned set. Regarding the fuzzy approach, the Boolean notion of the membership function is replaced by a graded one. Thus, an element can belong, not belong or partially belong to the so-called fuzzy set.

Based on the possibility theory [11], a fuzzy set can be understood as the union of the pessimistic and optimistic values of an uncertain parameter with each level of possibility (i.e., levels of the membership function) been possible realizations of the uncertain parameter. It is important to point out that the membership function is a possibility distribution, not a probability distribution as considered when the stochastic theory is applied. Possibility is the measure of whether an event can happen, while probability is a measure of whether an event will happen. Therefore, the possibility distribution of a given parameter u quantifies the possible values that this parameter can assume. Differently, a probability distribution quantifies the chances that the parameter u has to assume a certain value x.

In the fuzzy set theory, the uncertainties are described as fuzzy inputs and the mathematical model is represented as a fuzzy function that maps those inputs. The so-called α-level optimization [13] is a method used for mapping fuzzy

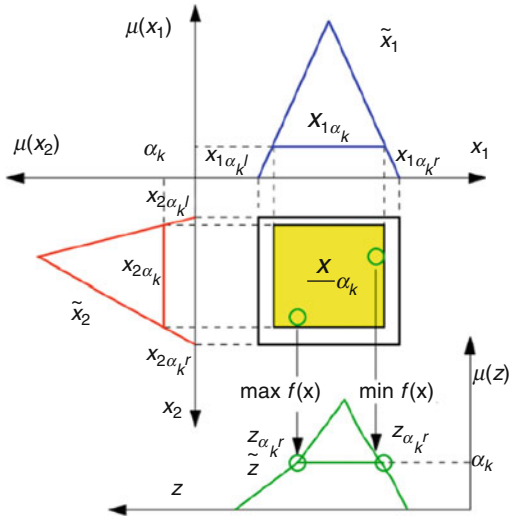

Fig. 24.2 The α-level optimization method

inputs, in which, the fuzzy inputs are discretized by means of α-cuts creating a *crisp* subspace that is the search space of a optimization problem. The optimization process is carried out in order to find the minimum and maximum values of the model output for each α-level (i.e., lower and upper limits of the correspondent α-level, respectively; see Fig. 24.2). The associated minimization and maximization process can be performed through direct optimization procedures, such as the SQP (Sequential Quadratic Programing) [14], reducing the computational effort associated with the uncertainty analysis.

At the end of the fuzzy uncertainty analysis of a system, the set of values of the uncertain information that maximizes the model response (the optimistic values) and the set of values that minimizes the model response (the pessimistic values) are known. Therefore, two uncertain scenarios can be considered: (1) a scenario in which the uncertain values assumes its pessimistic values; (2) a scenario where the uncertain values are at its optimistic values. Thus, it is expected that a robust approach will represent a better solution when both scenarios are taken into account. Considering the proposed robust balancing methodology, the pessimistic and the optimistic scenarios are defined, respectively, as follows:

$$Pe\left(x,\underline{p}\right) = \sum_{i=1}^{n}\left(\frac{\left\|U_i^{FEmodel}\left(x,\underline{p}\right) - U_i^{Balanced}\left(x^*,p_n\right)\right\|}{\left\|U_i^{Balanced}\left(x^*,p_n\right)\right\|}\right) \tag{24.4}$$

$$Op\left(x,\overline{p}\right) = \sum_{i=1}^{n}\left(\frac{\left\|U_i^{FEmodel}\left(x,\overline{p}\right) - U_i^{Balanced}\left(x^*,p_n\right)\right\|}{\left\|U_i^{Balanced}\left(x^*,p_n\right)\right\|}\right) \tag{24.5}$$

where *Pe* and *Op* are the objective functions associated with the pessimistic and optimistic evaluations, respectively. The lower and upper limits of the uncertain information are represented by $\overline{p}$ and $\underline{p}$, respectively. $U_i^{FEmodel}\left(x,\underline{p}\right)$ stands for the vibration response determined from the FE model considering the lower limit values of the uncertain parameters. Consequently, $U_i^{FEmodel}\left(x,\overline{p}\right)$ stands for the vibration response determined from the FE model considering the upper limit values of the uncertain parameters. In this case, $U_i^{Balanced}(x^*,p_n)$ represents the vibration response of the rotor determined after the application of a previous deterministic balancing procedure on the rotating machine (following the scheme presented in Fig. 24.1 and using Eq. (24.3) as the objective function). Thus, x^* is the vector containing the deterministic correction masses and phase angles and p_n is the nominal values of the considered uncertain parameters (for example, the stiffness and damping values of the bearings).

Therefore, a robustness metric can be defined based on Eqs. (24.4) and (24.5) dealing with the two sets of uncertain scenarios. The robustness metric is illustrated by Eq. (24.6). In this case, the minimization of the Eq. (24.6) (i.e., the optimistic evaluation) leads to a robust balance solution for the considered rotor in the original configuration.

$$ro = Pe\left(x,\underline{p}\right) + Op\left(x,\overline{p}\right) \tag{24.6}$$

The robustness evaluation procedure presented was formulated as a single optimization problem. However, the formulation can be easily extended to the multi-objective optimization context in which the objectives are related to Eqs. (24.3) and (24.6).

24.5 Model Updating

Figure 24.3a shows the rotor test rig used as a reference for the numerical analysis performed in this work. The rotor system is mathematically represented by a model with 33 finite elements (FE model; Fig. 24.3b). It is composed of a flexible steel shaft with 860 mm length and 17 mm of diameter ($E = 205$ GPa, $\rho = 7850$ kg/m^3, $\upsilon = 0.29$), two rigid discs D_1 (node #13; 2637 kg; according to the FE model) and D_2 (node #23; 2649 kg), both of steel and with 150 mm of diameter and 20 mm of thickness ($\rho = 7850$ kg/m^3), and two roller bearings (B_1 and B_2, located at the nodes #4 and #31, respectively). Displacement sensors are orthogonally mounted on the nodes #8 (S_{8X} and S_{8Z}) and #28 (S_{28X} and S_{28Z}) to collect the shaft vibration. The system is driven by an electric DC motor.

A model updating procedure was used in order to obtain the representative FE model. In this sense, a heuristic optimization technique (Differential Evolution [15]) was used to determine the unknown parameters of the model, namely the stiffness and damping coefficients of the bearings, the proportional damping added to D (coefficients γ and β; $D_p = \gamma M + \beta K$), and the angular stiffness k_{ROT} due to the coupling between the electric motor and the shaft (added around the orthogonal directions X and Z of the node #1). The frequency domain analysis (i.e., comparison between simulated and experimental frequency response functions, FRFs) was performed 10 times, considering 100 individuals in the initial population of the optimizer. The objective function adopted was the one given by Eq. (24.3). However, in this case only the regions close to the peaks associated with the natural frequencies were taken into account to compute the frequency responses.

The experimental FRFs were measured on a test rig (see Fig. 24.3) for the rotor at rest by applying impact forces along the X and Z directions of the discs, separately. The response signals were measured by the two proximity probes positioned along the same directions of the impact forces, resulting 8 FRF. The measurements were performed by the analyzer *Agilent*® (model 35670A) in a range of 0–200 Hz and steps of 0.25 Hz.

Table 24.1 summarizes the parameters determined in the end of the minimization process associated with the minimal value of the objective function. Figure 24.4 compares simulated and experimental Bode diagrams, considering the parameters shown in Table 24.1. Note that the FRF generated from the FE model is satisfactorily close to the one obtained experimentally from the test rig.

Figure 24.5 compares the experimental orbit obtained at the measure plane S_8 (acquisition time of 4 s in steps of 0.002 s, approximately) with the one determined by the updated FE model. The operational rotation speed of the rotor Ω was fixed to 1200 rev/min and an unbalance of 487.5 g mm/0° applied to the disc D_1. Note that the responses are close, as for the FRF previously shown, thus validating the updating procedure performed. Due to the size of the matrices involved in the equation

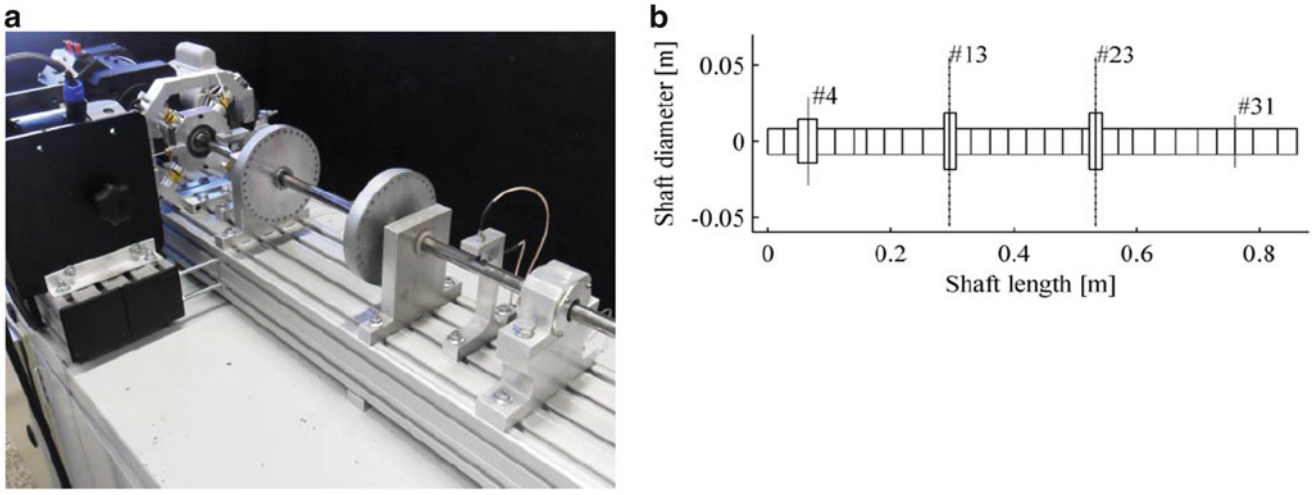

Fig. 24.3 Rotor used in the analysis of this work. (**a**) Test rig; (**b**) FE model

Table 24.1 Parameters determined through the model updating procedure

Parameters	Value
k_X/B_1	8.551×10^5
k_Z/B_1	1.198×10^6
d_X/B_1	7.452
d_Z/B_1	33.679
k_X/B_2	5.202×10^7
k_Z/B_2	7.023×10^8
d_X/B_2	25.587
d_Z/B_2	91.033
γ	2.730
β	4.85×10^{-6}
k_{ROT}	770.442

k stiffness (N/m), d damping (Ns/m)

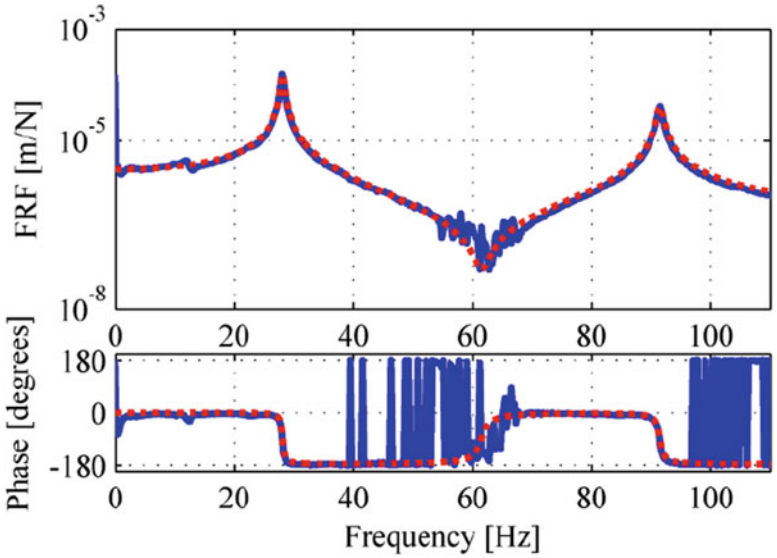

Fig. 24.4 Simulated (*red colored dashed line*) and experimental (*blue colored solid line*) FRF, and associated phases, obtained from impact forces on D_1 (X Direction and S_{8X})

Fig. 24.5 Simulated (*red colored dashed line*) and experimental (*blue colored solid line*) orbits for the rotor under operation

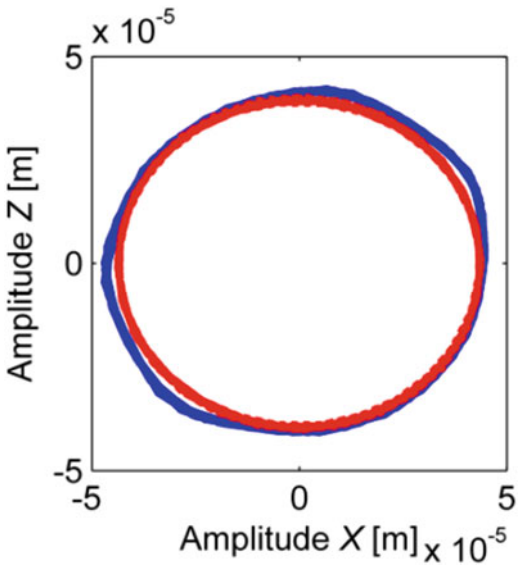

of motion, the pseudo-modal method is used to reduce the dimension of the FE model and the solution is obtained as shown in [12]. In this work, the first twelve vibration modes of the rotor were used to generate the displacement responses.

24.6 Robust Balancing Application

As previously mentioned, the proposed robust balancing methodology is characterized by uncertainties affecting, for example, the stiffness and damping parameters of the bearings and the dimensions of the discs and shaft. Therefore, it is expected that a good balancing performance is obtained when the correction masses and associated phase angles determined by using the robust methodology are used. In this context, the performance of the proposed methodology was evaluated in this paper by considering the stiffness along the horizontal and vertical directions of the bearing B_2 (k_X/B_2 and k_Z/B_2, respectively; see Fig. 24.3 and Table 24.1) as uncertain information. Table 24.2 shows the uncertainty scenario considered in the present contribution. The stiffness variation was introduced in order to simulate an abrupt screw loss at the fixation support of the bearing.

Three different optimization methodologies devoted to robust balancing were tested in this application, namely the deterministic approach (cost function given by Eq. (24.3)), robustness evaluation (cost function related exclusively to Eq. (24.6)), and a multi-objective optimization associated with both pessimistic and optimistic cost functions (Eqs. (24.4) and (24.5), respectively). Table 24.3 presents the correction masses and phase angles obtained by using the proposed optimization procedure for the rotor operating at 1200 rev/min. In this case, unbalance masses were randomly distributed along the rotor ($0 \leq$ unbalance—g mm ≤ 300; $-\pi \leq$ phase angle—rad $\leq \pi$). Thus, unbalance forces were introduced randomly at each node of the FE model (see Fig. 24.3). It is worth mentioning that applying the considered unbalance forces on the deterministic FE model (i.e., using the parameters shown in Table 24.1), the maximum amplitude of the vibration responses (0 to peak amplitude) obtained by the displacement sensors S_{8X}, S_{8Z}, S_{28X}, and S_{28Z}, were 43.6 μm, 38.9 μm, 31.5 μm, and 29.8 μm, respectively.

Figure 24.6 shows the orbits determined at the measurement planes S_8 and S_{28} from the FE model, considering the optimistic uncertain information, which is the upper limit of the uncertain interval (see Table 24.2). Note that the optimistic information is identical to the deterministic case ($k_X/B_2 = 5.202 \times 10^7$ N/m and $k_Z/B_2 = 7.023 \times 10^8$ N/m). The orbits were obtained by using the correction masses and phase angles presented in Table 24.3. As expected, the deterministic solution provided the best balancing performance, presenting maximum vibration amplitudes of 1 μm. Differently, the robust design leads to the worst result with vibration amplitudes around 40 μm. The multi-objective design showed an intermediary result, with vibration amplitudes reaching 6 μm. The orbits obtained from the FE model considering the pessimistic uncertain information (lower limit of the uncertain interval; see Table 24.2) are presented in Fig. 24.7.

Considering the pessimistic analysis, Fig. 24.7, it shows that the performance of the robust multi-objective balancing processes (see Fig. 24.7a, b, respectively) seems to be better than the one obtained from the deterministic process. Remember that the pessimistic information is associated with the lower limit of the uncertain interval (simulating an abrupt screw loss at the fixation support of the bearing). In this case, the stiffness of the bearing B_2 along the horizontal and vertical directions were considered as $k_X/B_2 = 5.202 \times 10^3$ N/m and $k_Z/B_2 = 7.023 \times 10^3$ N/m (see Table 24.2). Consequently, it can be observed that the robust multi-objective solutions present the expected superior balancing performance as compared with

Table 24.2 Uncertainty scenario

Stiffness	Experimental parameters	Uncertainty intervals
k_X/B_2 (N/m)	5.202×10^7	$5.202 \times 10^3 \leq k_X \leq 5.202 \times 10^7$
k_Z/B_2 (N/m)	7.023×10^8	$7.023 \times 10^3 \leq k_Z \leq 7.023 \times 10^8$

[a]The Experimental Parameters are also presented in Table 24.1

Table 24.3 Optimization results

Parameters	Deterministic	Robust	Multi-objective
unbalance/D_1	669.66 g mm	55.97 g mm	861.13 *g* mm
phase/D_1	−90.82°	−29.17°	−78.75°
unbalance/D_2	333 g mm	0 g mm	462.32 *g* mm
phase/D_2	50.22°	0°	89.73°

[a]The Multiobjetive solution was found through the compromise programing approach [14]

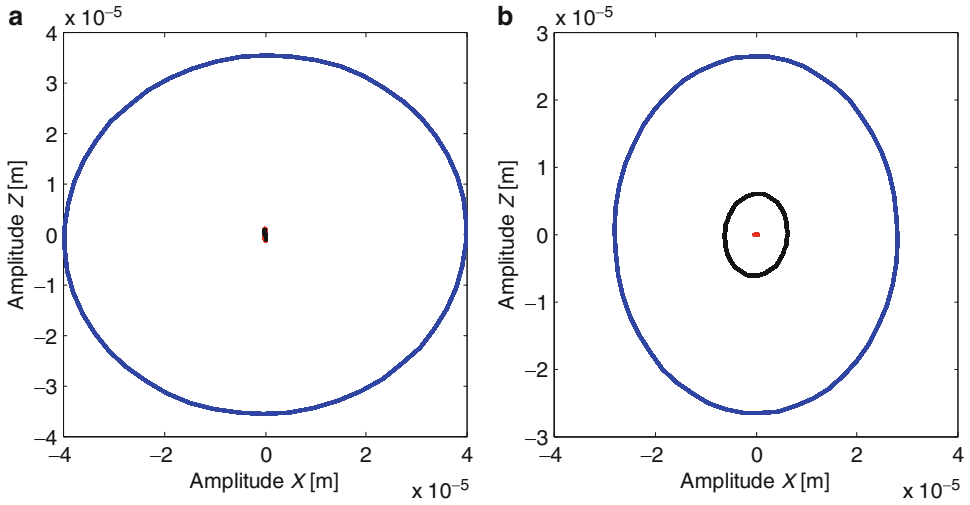

Fig. 24.6 Deterministic (*red colored solid line*), robust (*blue colored solid line*) and multi-objective (*black colored solid line*) vibration responses considering the optimistic uncertain information. (**a**) Measurement plane S_8, (**b**) Measurement plane S_{28}

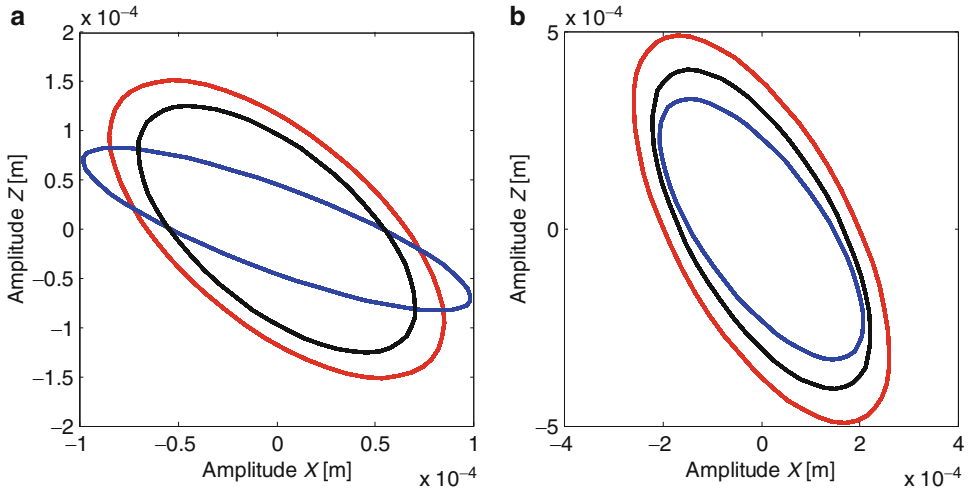

Fig. 24.7 Deterministic (*red colored solid line*), robust (*blue colored solid line*) and multi-objective (*black colored solid line*) vibration responses considering the pessimistic uncertain information. (**a**) Measurement plane S_8, (**b**) Measurement plane S_{28}

the deterministic approach. Evaluating both pessimistic and optimistic information, it can be observed that the deterministic design presents a fluctuation of approximately 500 times in amplitude (the difference between the maximum displacement associated with pessimistic and optimistic cases). The multi-objective design presented a fluctuation of nearly 66 times between the mentioned displacements, while the robust design showed a fluctuation of about 6.5 times among the maximum amplitudes obtained. Figure 24.8 illustrate this feature.

24.7 Final Remarks

In this work, three different model based balancing approaches were evaluated namely the deterministic, robust, and multi-objective process. The deterministic methodology was previously applied and the correction masses and phase angles obtained from this approach were compared with two different methods based on uncertainty analysis (fuzzy logic). In this case, the multi-objective optimization problem was evaluated using a compromise optimization strategy.

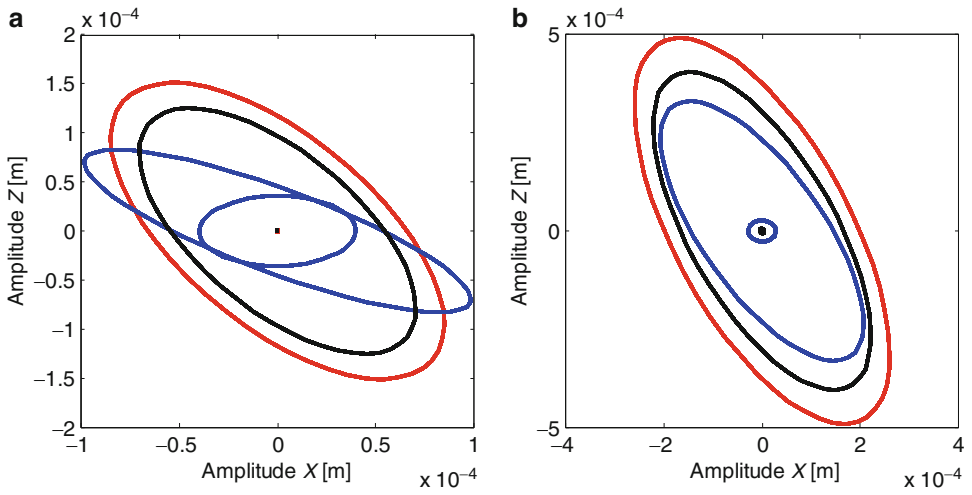

Fig. 24.8 Deterministic (*red colored solid line*), robust (*blue colored solid line*) and multi-objective (*black colored solid line*) vibration responses considering the optimistic and pessimistic uncertain information. (**a**) Measurement plane S_8, (**b**) Measurement plane S_{28}

The uncertainties considered in the applications conveyed were introduced directly on the stiffness coefficients of the bearing. The proposed robust balancing methodology was characterized by uncertainties affecting the stiffness fixation support of the bearing.

The numerical applications showed that the proposed methodologies are able to find robust solutions, regardless the amplitude of the uncertain information fluctuation. Therefore, the results are very encouraging in the sense that robust balancing through fuzzy robust optimization is feasible using experimental data.

The vibration amplitudes shown in Fig. 24.7 clearly represent poor balancing performances with the vibration amplitudes of the balanced system varying from 300 to 500 μm. As mentioned, the unbalanced rotating machine presented displacement amplitudes of 43.6 μm, 38.9 μm, 31.5 μm, and 29.8 μm (sensors S_{8X}, S_{8Z}, S_{28X}, and S_{28Z}, respectively). However, this paper was dedicated to prove the robust balancing concept. Therefore, an experimental investigation should be performed in order to ascertain the results obtained in the numerical application. However, due to the risks associated to the abrupt variation of the bearing stiffness a different uncertain scenario should be evaluated.

Acknowledgments The authors gratefully acknowledge the Brazilian Research Agencies FAPEMIG, CNPq, and CAPES for the financial support provided to this research effort through the National Institute of Science and Technology of Smart Structures in Engineering (INCT-EIE).

References

1. Eisenmann, R.C., Eisenmann Jr., R.C.: Machinery Malfunction Diagnosis and Correction. Prentice Hall, New Jersey (1998)
2. Steffen Jr., V., Lacerda, H.B.: On the balancing of flexible rotors. Int. J. Anal. Exp. Modal Anal. **11**, 96–105 (1996)
3. Wowk, V.: Machinery Vibration: Balancing, 1st edn. McGraw-Hill, New York (1998)
4. Bently, D.E., Hatch, C.T.: Fundamentals of Rotating Machinery Diagnostics, 1st edn. Bently Pressurized Bearing Company, Minden (2002)
5. Saldarriaga, M.V., Steffen Jr., V., Der Hagopian, J., Mahfoud, J.: On the balancing of flexible rotating machines by using an inverse problem approach. J. Vib. Control. **17**(7), 1021–1033 (2011)
6. Taguchi, G.: Quality Engineering Through Design Optimization. Kraus International Publications, New York (1984)
7. Paenke, I., Branke, J., Jin, Y.: Efficient search for robust solutions by means of evolutionary algorithms and fitness approximation. IEEE Trans. Evol. Comput. **10**, 405–420 (2006)
8. Beyer, H.G., Sendhoff, B.: Robust optimization—a comprehensive survey. Comput. Methods Appl. Mech. Eng **196**, 3190–3218 (2007)
9. Soroudi, A., Amraee, T.: Decision making under uncertainty in energy systems: state of the art. Renew. Sustain. Energy Rev. **28**, 376–384 (2013)
10. Zadeh, L.A.: Fuzzy sets. Inf. Control. **8**, 338–353 (1965)
11. Zadeh, L.A.: Fuzzy sets as basis for a theory of possibility. Fuzzy Set. Syst. **1**, 3–28 (1968)
12. Lalanne, M., Ferraris, G.: Rotordynamics Prediction in Engineering, 2nd edn. Wiley, New York (1998)
13. Möller, B., Graf, W., Beer, M.: Fuzzy structural analysis using α-level optimization. Comput. Mech. **26**, 547–565 (2000)
14. Vanderplaats, G.N.: Numerical Optimization Techniques for Engineering Design. Vanderplaats Research and Development, Colorado Springs (1999)
15. Storn, R., Price, K.: Differential evolution: a simple and efficient adaptive scheme for global optimization over continuous spaces. Int. Comput. Sci. Inst. **12**, 1–16 (1995)

Chapter 25
Statistical Modeling of Wavelet-Transform-Based Features in Structural Health Monitoring

Aral Sarrafi and Zhu Mao

Abstract In this paper, a probabilistic model is established in quantifying the uncertainty of wavelet-transform-based features in structural health monitoring (SHM), thus the decision-making in regard to damage occurrence will be conducted under a quantified confidence. Wavelet transform has been adopted in processing online-acquired data for decades, and the adaptability of wavelet transform in handling time and scale resolutions make it a powerful tool to interpret the time-variant data series. For the complexity of real SHM problems, uncertainty from both the operational/environmental variability and the inaccuracy of data acquisition hardware degrades the SHM performance. This paper aims to derive a probabilistic uncertainty quantification model to describe the distribution of wavelet-transform-based features, to facilitate more reliable SHM decision-makings, and uncertainty-induced false-positive (Type-I error) and true damage detection rate will be traded-off in a confidence-quantified sense. The distribution derived in this paper is validated via Monte Carlo simulation.

Keywords Structural health monitoring • Uncertainty quantification • Statistical modeling • Signal processing • Wavelet transform

25.1 Introduction

Structural health monitoring (SHM) has been widely applied to the fields of aerospace, mechanical and civil infrastructures, since two to three decades ago [1]. In the early years, structural health monitoring was conducted primarily as sensing data and analyzing in simple ways. Natural frequency based method was very popular because of the intuitive physical meanings [2]. Modal analysis was soon adopted, and damages were detected via estimating mode shapes or their curvatures [3, 4]. In the 1990s, Wavelet theories were being developed by mathematicians, such as Haar, Levy, and Littlewood. Right after that, wavelet transform was employed by Liew and Wang [5], Hsu [6] and Lu [7] about 2000 for the purpose of damage detection, when the structure is subject to vibrational input. Wavelet transforms are defined based on the idea that any time series can be decomposed as a suite of local basis functions, named wavelets. Any particular SHM feature extracted from the monitored signal can be analyzed based on the scale and translation of those aforementioned basis functions. In nowadays, wavelet transform is known as one of the most powerful tools for signal and image processing, especially in the area of system identification, structural damage detection, and diagnosis.

Inherent to the data acquisition, signals in realistic applications are inevitably contaminated with measurement noise, as well as other sorts of variabilities and uncertainties. As a result, the SHM features extracted from the contaminated data, such as power spectrum and frequency response function, are noisy as well [8, 9]. Uncertainty could contaminate the extracted SHM features dramatically if the data quality is poor, and thereby cause ambiguity in interpreting the features. Usually the uncertainty will arouse false alarms to the damage detection, i.e. non-damage-induced feature deviation from the undamaged baseline. Therefore quantification of uncertainty in SHM feature, wavelet transform features in this paper specifically, should be taken into serious consideration.

Uncertainty analysis, with respect to the statistical models and outlier data is necessary to improve the outcome of wavelet transform analysis, facilitate to interpret the features and make SHM decisions as well. In this paper, closes-form models are developed to quantify the uncertainty in wavelet transform features, and probability density function (PDF) of wavelet transforms with Haar and Mexican hat bases are given analytically. The rest of this paper starts withintroduction of wavelet

A. Sarrafi • Z. Mao (✉)
Structural Dynamics and Acoustic Systems Laboratory, Department of Mechanical Engineering, University of Massachusetts Lowell, One University Avenue, Lowell, MA 01854, USA
e-mail: zhu_mao@uml.edu

S. Atamturktur et al. (eds.), *Model Validation and Uncertainty Quantification, Volume 3*, Conference Proceedings of the Society for Experimental Mechanics Series, DOI 10.1007/978-3-319-29754-5_25

transform theory, and derivation of the analytical PDFs of wavelet coefficients as random variables. Then the closed-form PDFs are validated by means of Monte Carlo simulation, and the characterized distributions are compared to the observed histograms.

25.2 Background

Continuous wavelet transform decompose a function in continuous-time domain into wavelets, and reconstructs a time-frequency representation of the original function that offers both good time and frequency resolution. The continuous wavelet transform of signal $x(t)$ at scale $a > 0$ and translation value b is expressed by the following integral:

$$C_{a,b} = \frac{1}{\sqrt{a}} \int_{-\infty}^{+\infty} x(t) \overline{\psi} \left(\frac{t-b}{a} \right) dt, \tag{25.1}$$

in which $\overline{\psi}$ is the mother wavelet function, and, $C_{a,b}$ is wavelet transform coefficient. In most of engineering applications, the signals are sampled into discrete-time domain, therefore the integral in Eq. (25.1) should be converted to the summation below:

$$C_{a,b} = \frac{1}{\sqrt{a}} \sum_{k=-\infty}^{k=+\infty} x\left(kT_s\right) \overline{\psi} \left(\frac{kT_s - b}{a} \right) T_s. \tag{25.2}$$

Since the time step T_s is a constant value, and not going to effect the overall time series analysis, T_s could be eliminated as shown in Eq. (25.3):

$$C_{a,b} = \frac{1}{\sqrt{a}} \sum_{k=-\infty}^{k=+\infty} x\left[k\right] \overline{\psi} \left[\frac{k-b}{a} \right]. \tag{25.3}$$

Signal $x[k]$ in Eq. (25.3) is composed of two parts including a deterministic part and a sequence of random variables which represent the measurement noise or uncertainties:

$$x\left[k\right] = D\left[k\right] + N\left[k\right],$$

where D stands for the signal and N stands for the noise term.

By substituting the two-term representation for x in Eq. (25.3), it may be updated as:

$$C_{a,b} = \frac{1}{\sqrt{a}} \sum_{k=-\infty}^{k=+\infty} D\left[k\right] \overline{\psi} \left[\frac{k-b}{a} \right] + \frac{1}{\sqrt{a}} \sum_{k=-\infty}^{k=+\infty} N\left[k\right] \overline{\psi} \left[\frac{k-b}{a} \right]. \tag{25.4}$$

In Eq. (25.4), the non-deterministic term, which is $\frac{1}{\sqrt{a}} \sum_{k=-\infty}^{k=+\infty} N\left[k\right] \overline{\psi} \left[\frac{k-b}{a} \right]$, is apparently a weighted sum of the noise series N. In most of the realistic monitoring activities, the noise N itself is a complicated series. In this paper, we assume it is a smooth and stationary process. If the length of series N is sufficiently long, the weighted sum $\frac{1}{\sqrt{a}} \sum_{k=-\infty}^{k=+\infty} N\left[k\right] \overline{\psi} \left[\frac{k-b}{a} \right]$ will be asymptotically a Gaussian distributed random variable as per the central limit theorem. Moreover, the uncertainty in N will be most likely quasi-normal, and this will make the weighted sum better be characterized as Gaussian variable. Therefore, the non-deterministic term guarantees the wavelet coefficient $C_{a,b}$ in Eq. (25.4) is a Gaussian variable as well:

$$C_{a,b} \sim \mathcal{N}\left(m_{a,b}, \sigma_{a,b}\right).$$

By finding analytical solutions for $m_{a,b}$ and $\sigma_{a,b}$, the closed-form PDF of $C_{a,b}$ is available given the approximation that the noise/uncertainty in the acquired data is quasi-normal.

For $m_{a,b}$ the solution is derived as follows by means of calculating expectations:

$$m_{a,b} = E\{C_{a,b}\} = E\left\{\frac{1}{\sqrt{a}}\sum_{k=-\infty}^{k=+\infty} D[k]\overline{\psi}\left[\frac{k-b}{a}\right] + \frac{1}{\sqrt{a}}\sum_{k=-\infty}^{k=+\infty} N[k]\overline{\psi}\left[\frac{k-b}{a}\right]\right\}, \tag{25.5}$$

$$m_{a,b} = E\left\{\frac{1}{\sqrt{a}}\sum_{k=-\infty}^{k=+\infty} D[k]\overline{\psi}\left[\frac{k-b}{a}\right]\right\} + E\left\{\frac{1}{\sqrt{a}}\sum_{k=-\infty}^{k=+\infty} N[k]\overline{\psi}\left[\frac{k-b}{a}\right]\right\}. \tag{25.6}$$

Since the noise is fully random and would be zero-mean in most practical cases, and the signal term D is deterministic:

$$m_{a,b} = \frac{1}{\sqrt{a}}\sum_{k=-\infty}^{k=+\infty} D[k]\overline{\psi}\left[\frac{k-b}{a}\right] + \underbrace{E\left\{\frac{1}{\sqrt{a}}\sum_{k=-\infty}^{k=+\infty} N[k]\overline{\psi}\left[\frac{k-b}{a}\right]\right\}}_{0}, \tag{25.7}$$

$$m_{a,b} = \frac{1}{\sqrt{a}}\sum_{k=-\infty}^{k=+\infty} D[k]\overline{\psi}\left[\frac{k-b}{a}\right]. \tag{25.8}$$

Solving for $\sigma_{a,b}$ is more complicated, and it depends on the specific mother wavelets and noise characteristics such as covariance. In this section, two mother wavelets, namely Haar and Mexican hat, are considered, and noise is assumed to be from an uncorrelated stationary random process. With this approximation, the covariance matrix is diagonal and time independent. Consider the definition of variance $\sigma_{a,b}^2$:

$$\sigma_{a,b}^2 = E\left\{[C_{a,b} - m_{a,b}]^2\right\}, \tag{25.9}$$

$$\sigma_{a,b}^2 = E\left\{\left[\left(\frac{1}{\sqrt{a}}\sum_{k=-\infty}^{k=+\infty} D[k]\overline{\psi}\left[\frac{k-b}{a}\right] + \frac{1}{\sqrt{a}}\sum_{k=-\infty}^{k=+\infty} N[k]\overline{\psi}\left[\frac{k-b}{a}\right]\right) - \frac{1}{\sqrt{a}}\sum_{k=-\infty}^{k=+\infty} D[k]\overline{\psi}\left[\frac{k-b}{a}\right]\right]^2\right\}, \tag{25.10}$$

$$\sigma_{a,b}^2 = E\left\{\left[\frac{1}{\sqrt{a}}\sum_{k=-\infty}^{k=+\infty} N[k]\overline{\psi}\left[\frac{k-b}{a}\right]\right]^2\right\} = Var\left\{\frac{1}{\sqrt{a}}\sum_{k=-\infty}^{k=+\infty} N[k]\overline{\psi}\left[\frac{k-b}{a}\right]\right\}. \tag{25.11}$$

To calculate the argument in Eq. (25.11), Theorem 1 below is applied:

Theorem 1. *If X_i are random variables, then variance for weighted sum of these variables is*:

$$Var\left(\sum_{i=1}^{N} a_i X_i\right) = \sum_{i,j=1}^{N} a_i a_j Cov\left(X_i, X_j\right). \tag{25.12}$$

The equation above can be written as bellow:

$$Var\left(\sum_{i=1}^{N} a_i X_i\right) = \sum_{i=1}^{N} a_i^2 Var\left(X_i\right) + \sum_{i\neq j}^{N} a_i a_j Cov\left(X_i, X_j\right). \tag{25.13}$$

If noise X_i is assumed to be uncorrelated, thus the covariance matrix is diagonal. As a result:

$$Cov\left(X_i, X_j\right) = 0 \;\; \forall\, (i \neq j), \tag{25.14}$$

$$Var\left(\sum_{i=1}^{N} a_i X_i\right) = \sum_{i=1}^{N} a_i^2 Var\left(X_i\right). \tag{25.15}$$

In this work, the extraneous noise is considered as from a stationary process, so the components on the diagonal of covariance matrix are all the same:

$$Var\,(X_i) = \sigma^2, \tag{25.16}$$

therefore:

$$Var\left(\sum_{i=1}^{N} a_i X_i\right) = \sigma^2 \sum_{i=1}^{N} a_i^2. \tag{25.17}$$

25.2.1 Case Study

In the previous section, the formulation of the statistical modeling of wavelet transform coefficients are introduced, and by this means, the closed-form PDFs will characterize the distribution of wavelet features as random variables. In this section, two particular case studies are included with PDFs explicitly derived. Wavelet bases which are adopted for case study are Haar, and Mexican Hat wavelets.

Case 1. Haar Wavelet

Haar wavelet function is defined in the equation:

$$\psi(t) = \frac{1}{\sqrt{a}} \begin{cases} 1 & 0 \le x < \frac{1}{2} \\ -1 & \frac{1}{2} \le x < 1 \\ 0 & otherwise \end{cases} \Rightarrow \psi\left(\frac{k-b}{a}\right) = \frac{1}{\sqrt{a}} \begin{cases} 1 & b \le k < \frac{1}{2}a + b \\ -1 & \frac{1}{2}a + b \le x < a + b \\ 0 & otherwise \end{cases},$$

and

$$\psi^2\left(\frac{k-b}{a}\right) = \begin{cases} \frac{1}{a} & b \le k < a + b \\ 0 & otherwise \end{cases} \tag{25.18}$$

By substituting into Eq. (25.17):

$${\sigma^2}_{a,b} = \begin{cases} \sigma^2 & a + b < N \\ \frac{N - b + 1}{a}\sigma^2 & a + b \ge N \end{cases}. \tag{25.19}$$

Equation (25.19) shows the analytical form wavelet coefficient variance, using Haar wavelet as mother wavelet. As abovementioned, the distribution of wavelet coefficients is asymptotically Gaussian, and the mean and variance are characterized analytically by Eqs. (25.8) and (25.19).

Case 2. Mexican hat wavelet

Mexican hat wavelet function is described by the following equation:

$$\psi(t) = \frac{1}{\sqrt{2\pi}}\left(1 - \frac{t^2}{\sigma^2}\right)\exp\left(-\frac{t^2}{2\sigma^2}\right), \tag{25.20}$$

and the discretized version of Mexican wavelet is:

$$\psi\left(\frac{kT_s - b}{a}\right) = \frac{1}{\sqrt{2\pi}\sigma^3}\left(1 - \frac{(kT_s - b)^2}{a^2\sigma^2}\right)\exp\left(-\frac{(kT_s - b)^2}{2a^2\sigma^2}\right). \tag{25.21}$$

By substituting into Eq. (25.17):

$$Var\left(C_{a,b}\right) = \sum_{k=0}^{N} \left\{ \frac{1}{\sqrt{2\pi}\sigma^3} \left(1 - \frac{(kT_s - b)^2}{a^2\sigma^2}\right) \exp\left(-\frac{(kT_s - b)^2}{2a^2\sigma^2}\right) \right\}^2 Var\left(X_i\right), \tag{25.22}$$

$$Var\left(C_{a,b}\right) = \sigma^2 \sum_{k=0}^{N} \left\{ \frac{1}{\sqrt{2\pi}\sigma^3} \left(1 - \frac{(kT_s - b)^2}{a^2\sigma^2}\right) \exp\left(-\frac{(kT_s - b)^2}{2a^2\sigma^2}\right) \right\}^2. \tag{25.23}$$

For the sake of brevity, the coefficient is defined as:

$$\beta_{a,b} = \sum_{k=0}^{N} \left\{ \frac{1}{\sqrt{2\pi}\sigma^3} \left(1 - \frac{(kT_s - b)^2}{a^2\sigma^2}\right) \exp\left(-\frac{(kT_s - b)^2}{2a^2\sigma^2}\right) \right\}^2, \tag{25.24}$$

therefore:

$$Var\left(C_{a,b}\right) = \beta_{a,b}\sigma^2. \tag{25.25}$$

Likewise Haar wavelet mother function variance for Mexican hat wavelet has been derived.

25.3 Model Validation via Monte Carlo Simulation

In previous section, closed-form PDFs are introduced to characterize the distribution of wavelet coefficients. Validation of these solutions is presented using a Monte Carlo simulation.

Case 1. Haar Wavelet is widely used to determine spikes and other type of steep discontinuities in signals, therefore a signal consisting of two spikes contaminated by Gaussian white noise is adopted for validating the case with Haar wavelet transform, as illustrated in Fig. 25.1.

Noise contamination in the data measurement will definitely degrades the quality of feature estimations, and Fig. 25.2 shows the wavelet coefficients of pure signal and contaminated signal. Obviously, the time of arrival for the discontinuities at 25, 50 and 100 are blurred in the contaminated plot on the right.

As above mentioned, the wavelet coefficients are Gaussian distributed. Figure 25.3 shows the PDF curve given by the derived statistical model, for a specific set of shift and scale parameters, decomposed by Haar wavelet.

Figure 25.3 shows a nice consistency between the predicted distribution and observed histogram, and the mean and variance values match with analytical solutions. For the order statistics, especially standard deviation, Fig. 25.4 shows the sigma-values from both Monte Carlo simulation and the analytical value given by Eq. (25.19). There is slight fluctuation comparing the two plots, but it can be definitely eliminated by increasing the number of iterations in the Monte Carlo validation.

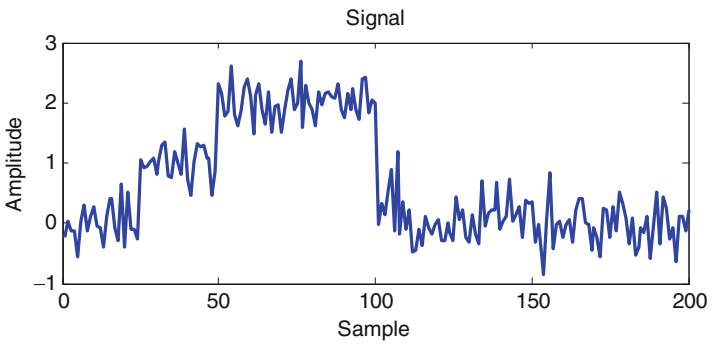

Fig. 25.1 Signal for case study—Haar wavelet transform

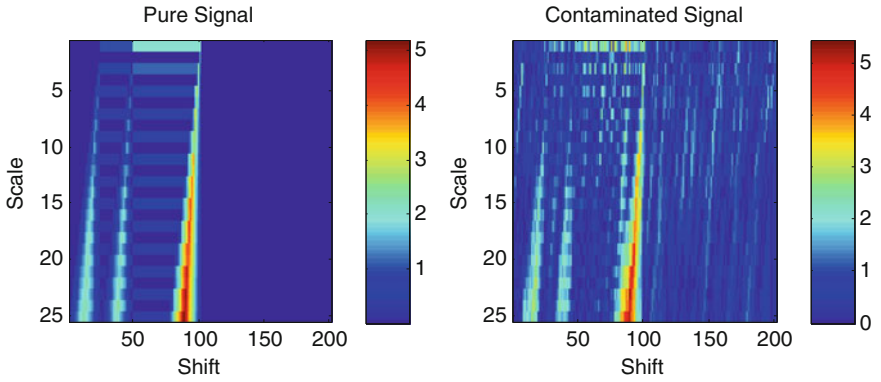

Fig. 25.2 Wavelet coefficients for pure and contaminated signal

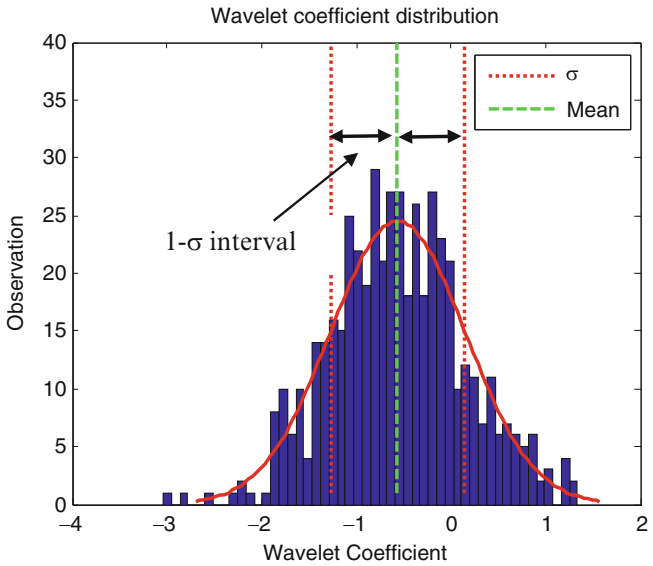

Fig. 25.3 Distribution of wavelet coefficient with arbitrary scale and time delay

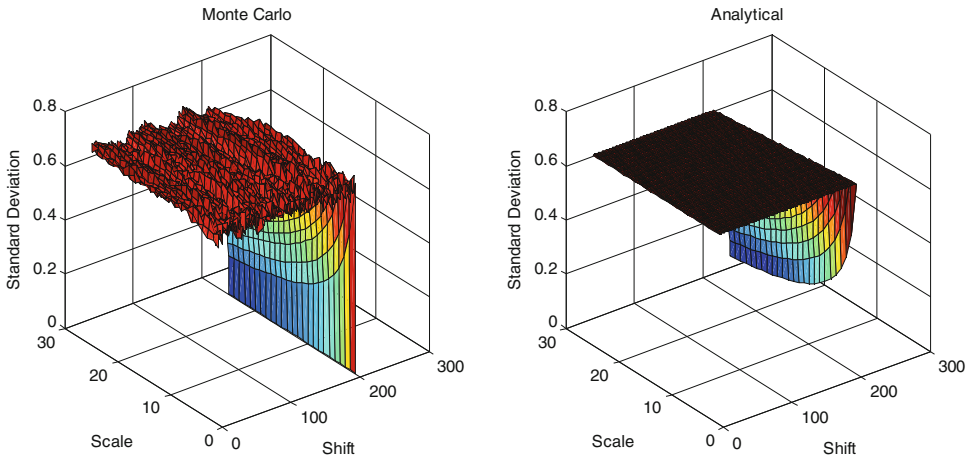

Fig. 25.4 Standard deviation of wavelet coefficients

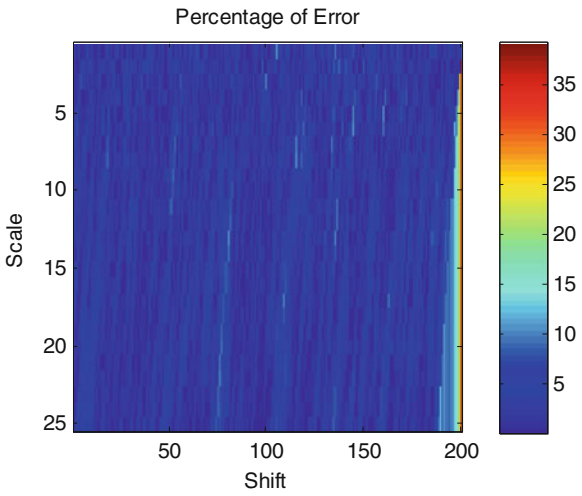

Fig. 25.5 Percentage of error in analytical solution compared to Monte Carlo approach

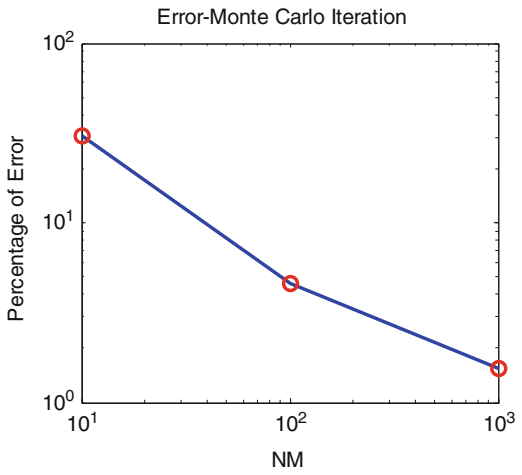

Fig. 25.6 Effect of number of iterations in Monte Carlo method on prediction error

Figure 25.5 represent percentage of error for analytical solution and results gained by Monte Carlo approach in most of points error is below 5 % except for wavelet coefficients related to last samples of signal. High error percentages at the end of signal occurs because signal vanishes suddenly, and discontinuity causes these errors. Monte Carlo approach is an iterative method and accuracy of this method is very sensitive to the number of iterations. Therefore, error can be reduced by increasing number of iterations. Figure 25.6 below shows how increasing the Monte Carlo iterations can reduce the amount of error. NM stands for the number of iterations in Monte Carlo simulation. Constrained by the computational limitation, yet not losing validity, the maximum value for NM is set to be 1000.

Case 2. Mexican hat wavelet or Ricker wavelet is another type of widely-used category, especially for seismic data analysis. In this case study, a pure sine wave is adopted, contaminated by uncorrelated Gaussian white noise, and Monte Carlo validation is conducted (Fig. 25.7).

Similar to case 1, effect of contamination is illustrated in Fig. 25.8.

The distribution for a specific set of wavelet parameters with Mexican hat bases is plotted in Fig. 25.9, and in Fig. 25.10, the standard deviation prediction and measurement are plotted, as a function of the shift and scale parameters.

For better comparison between analytical solution and Monte Carlo validation, relative error is calculated and presented in Fig. 25.11.

In Fig. 25.11, it is clear that the relative error is below 2 % for most scale and shift values, and the maximum percentage of error is no higher than 5 %. Similar to case 1, error can be reduced by increasing number of iterations for Monte Carlo simulations, as is shown in Fig. 25.12 as the NM increases.

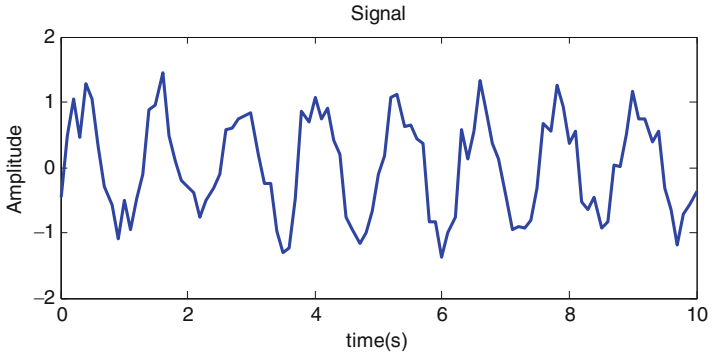

Fig. 25.7 Signal for Mexican Hat Monte Carlo approach

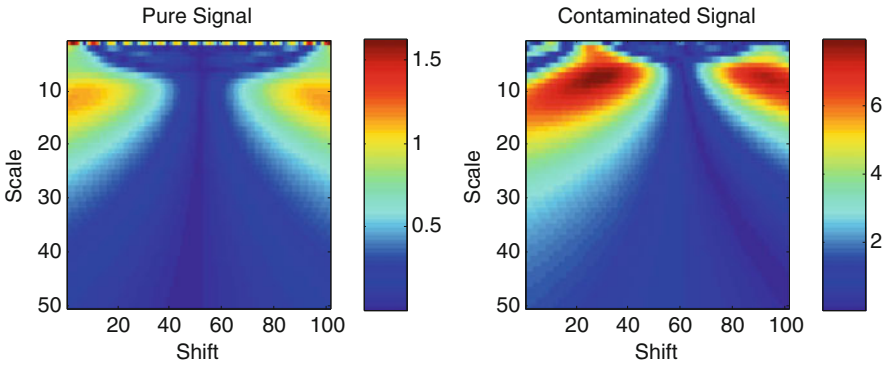

Fig. 25.8 Wavelet coefficients for pure and contaminated signal

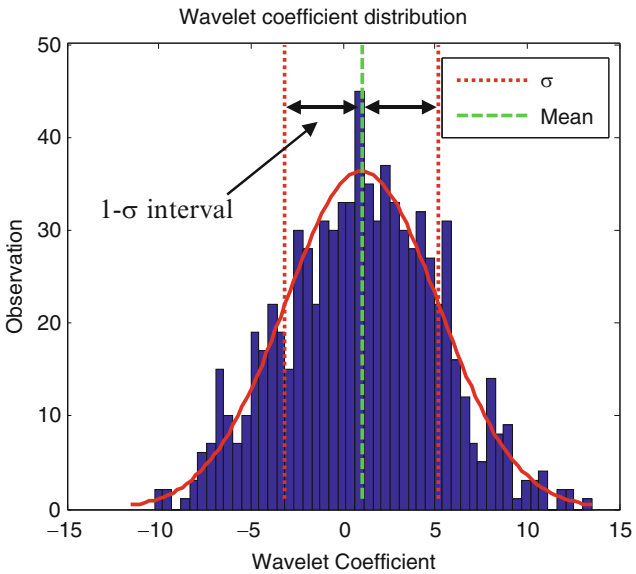

Fig. 25.9 Distribution of wavelet coefficient with arbitrary scale and time delay

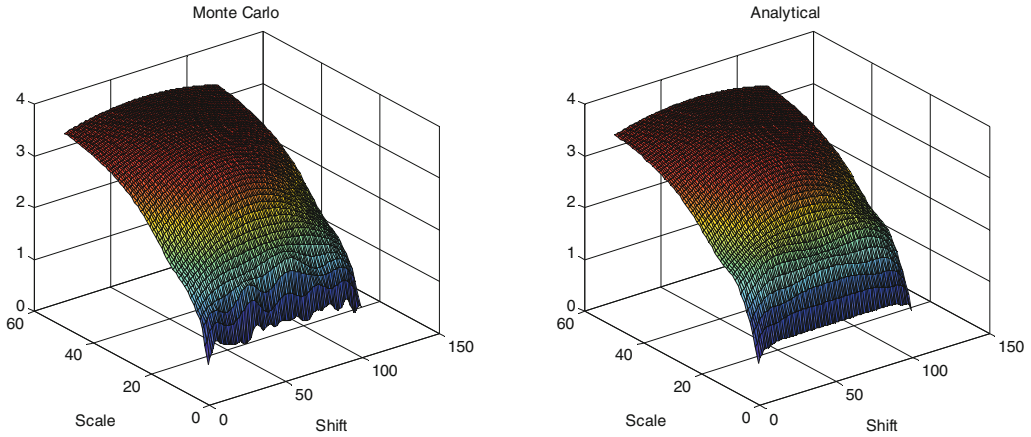

Fig. 25.10 Analytical and Monte Carlo standard deviation

Fig. 25.11 Percentage of error in analytical solution compared to Monte Carlo approach

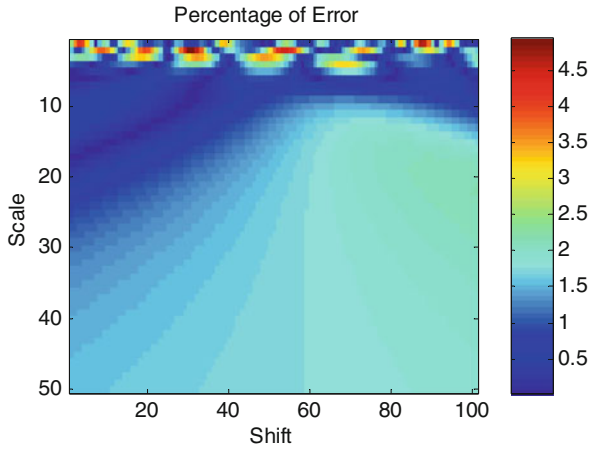

Fig. 25.12 Effect of number of iterations in Monte Carlo method on prediction error

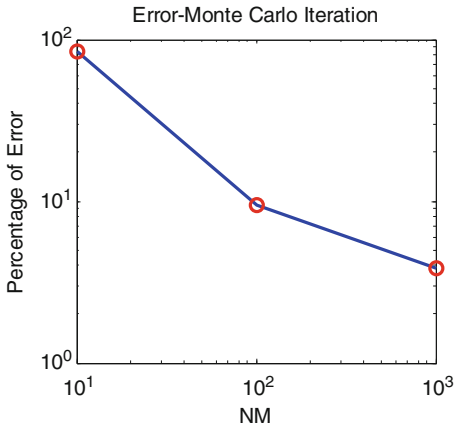

25.4 Conclusion

In this paper, the effect of noise on wavelet transform and wavelet coefficients is investigated. The distribution of wavelet coefficient is proved to be Gaussian, and this will hold even when the signal is not ideally normally distributed. Analytical forms of PDF are derived for different mother wavelets, and characterize the uncertainty of contaminated wavelet transform estimations. One thing which need to be emphasized is, the order statistics, i.e. mean and variance, of the wavelet estimation do not rely on a huge number of samplings, but are derived from the order statistics of time series itself. For every pair of shift and scale parameters in wavelet transform, there is a PDF, which is validated via Monte Carlo simulation. The validation

results show very promising and consistent performance, comparing the test histograms and the predicted distributions. These established probabilistic models quantify the uncertainty in wavelet based SHM features, and will help to enhance the decision-making in the SHM applications.

References

1. Farrar, C.R., Doebling, S.W.: Damage detection II: field applications to large structures. In: Silva, J.M.M., Maia, N.M.M. (eds.) Modal Analysis and Testing, Nato Science Series. Kluwer, Dordrecht (1999)
2. Salawu, O.S.: Detection of structural damage through changes in frequency: a review. Eng. Struct. **19**(9), 718–723 (1997)
3. Ewins, D.J.: Modal Testing: Theory and Practice. Research Studies Press Ltd., Hertfordshire (1984)
4. Maia, N.M.M., Silva, J.M.M. (eds.): Theoretical and Experimental Modal Analysis. Research Studies Press Ltd., Somerset (1997)
5. Liew, K.M., Wang, Q.: Application of wavelet theory for crack identification in structures. J. Eng. Mech. **124**(2), 152–157 (1998)
6. Hou, Z., Noori, M., Amand, R.S.: Wavelet based approach for structural damage detection. J. Eng. Mech. **126**(7), 677–683 (2000)
7. Lu, C., Hsu, Y.: Vibration analysis of an inhomogeneous string for damage detection by wavelet transform. Int. J. Mech. Sci. **44**, 745–754 (2002)
8. Mao, Z., Todd, M.: A model for quantifying uncertainty in the estimation of noise-contaminated measurements of transmissibility. Mech. Syst. Signal Process. **28**, 470–481 (2012)
9. Mao, Z., Todd, M.: Statistical modeling of frequency response function estimation for uncertainty quantification. Mech. Syst. Signal Process. **38**(2), 333–345 (2013)
10. Papolis: Probability, Random Variables and Stochastic Processes, 4th edn.

Chapter 26
A Bayesian Framework for Optimal Experimental Design in Structural Dynamics

Costas Argyris and Costas Papadimitriou

Abstract A Bayesian framework for optimal experimental design in structural dynamics is presented. The optimal design is based on an expected utility function that measures the value of the information arising from alternative experimental designs and takes into account the uncertainties in model parameters and model prediction error. The evaluation of the expected utility function requires a large number of structural model simulations. Asymptotic techniques are used to simplify the expected utility functions under small model prediction error uncertainties, providing insight into the optimal design and drastically reducing the computation effort involved in the evaluation of the multi-dimensional integrals that arise. The framework is demonstrated using the design of sensors for modal identification and is applied to the design of a small number of reference sensors for experiments involving multiple sensor configuration setups accomplished with reference and moving sensors. In contrast to previous formulations, the Bayesian optimal experimental design overcomes the problem of the ill-conditioned Fisher information matrix for small number of reference sensors by exploiting the information in the prior distribution.

Keywords Bayesian inference • Information entropy • Relative entropy • Kullback–Leibler divergence • Structural dynamics

26.1 Introduction

Bayesian optimal experimental design formulations for model parameter estimation have been developed that are based on utility functions that measure the value of the information contained in the data. The optimal design is then obtained by maximizing the expected utility function over the model and prediction error uncertainties with respect to the design variables. A rational choice of the utility function is the information gain or relative entropy or the Kullback–Leibler divergence between the posterior and the prior distribution of model parameters. The estimation of expected information gain involves a nested sampling procedure [1]. The optimization of the utility function involves a moderate to large number of expected utility function evaluations. Thus, the computational effort becomes excessive even for relatively small models. Surrogate techniques have been introduced to reduce the computational effort [1].

In this work, we use asymptotic expansions and small prediction error uncertainties to simplify the formulation and the number of system analyses. For linear models the expected utility function depends on the information entropy of the posterior distribution of the model parameters which can be formulated as a function of the determinant of the sum of the Fisher information matrix and the Hessian of the prior. For nonlinear models and small prediction error uncertainties it is shown that the expected utility function can also be formulated as the robust information entropy which is a weighted integral of the information entropy of the posterior distribution of the model parameters evaluated at control points in the support of the prior PDF of the model parameters, weighted by the prior distribution of these parameters. This result has been independently derived in [2–4] based on information entropy concepts. The results show that the experimental design is based on a scalar measure of the sensitivities of the output quantities of interest predicted by the model at the corresponding measured locations with respect to the model parameters.

The theoretical developments and the effectiveness of the proposed algorithms are applicable to optimal sensor placement problems encountered in structural dynamics, including the optimal sensor placement for finite element model updating, damage detection, as well as model predictions of output quantities. In addition, the proposed optimal experimental design framework can also be applied for optimizing the excitation characteristics, such as frequency content and amplitude, of linear and nonlinear structures in order to enhance the value of information to be obtained from the experimental designs for

C. Argyris • C. Papadimitriou (✉)
Department of Mechanical Engineering, University of Thessaly, Volos, Greece
e-mail: costasp@uth.gr

S. Atamturktur et al. (eds.), *Model Validation and Uncertainty Quantification, Volume 3*, Conference Proceedings of the Society for Experimental Mechanics Series, DOI 10.1007/978-3-319-29754-5_26

model parameter estimation and predictions. In this work, in light of the new results, the optimal sensor placement problem for estimating the modes in structural dynamics application is revisited. It is demonstrated that the information entropy and thus the optimal sensor placement depends on the sum of the Fisher information matrix and the Hessian of the prior, instead of only the Fisher information entropy proposed in previous formulations [4, 5]. As a result, it is demonstrated that the optimal sensor placement problem can be carried out also for number of sensors less than the number of modes with the aid of the information contained in the prior PDF of the model parameters. The optimal sensor placement design is demonstrated by designing the optimal sensor location of a small number of reference sensors in multiple sensor placement setups using reference and moving (roving) sensors.

26.2 Bayesian Parameter Estimation

The Bayesian framework for the estimation of the parameters of a structural dynamics model based on experimental data is first outlined and the results are used in the optimal experimental design formulation. Consider a model of a structure and let $\underline{\theta} \in R^{N_\theta}$ be the vector of model parameters to be estimated using a set of measured data $\underline{y} \equiv \underline{y}(\underline{\delta}) \in R^N$ of output quantities that depend on design variables $\underline{\delta}$. Let $\underline{g}(\underline{\theta};\underline{\delta}) \in R^N$ be the vector of the values of the same output quantities predicted by a structural model for specific values of the parameter set $\underline{\theta}$. The design variables can be related to the location of sensors placed in a structure or to the characteristics of the excitation. For design variables related to sensor locations, the location vector $\underline{\delta}$ contains the coordinates of the sensors with respect to a coordinate system. For design variables related to excitation characteristics, the vector $\underline{\delta}$ contain the values of the parameters of the excitation and the location of the excitation in the structure.

The following prediction error equation is introduced

$$\underline{y} = \underline{g}(\underline{\theta};\underline{\delta}) + \underline{e} \tag{26.1}$$

where $\underline{e}$ is the additive prediction error term due to model and measurement error. The prediction error is modeled as a Gaussian vector, whose mean value is equal to zero and its covariance is equal to $\Sigma(\underline{\sigma}) \in R^{N\times N}$, where $\underline{\sigma}$ contains the parameters that define the correlation structure of $\Sigma(\underline{\sigma})$. Applying the Bayesian theorem, the posterior probability density function (PDF) of the model parameters $\underline{\theta}$, given the measured data or outcome $\underline{y}$, is given by

$$p\left(\underline{\theta}\middle|\underline{y},\underline{\sigma},\underline{\delta}\right) = c\frac{1}{(2\pi)^{N/2}[\det\Sigma(\underline{\sigma})]^{1/2}}\exp\left[-\frac{1}{2}J\left(\underline{\theta};\underline{y},\underline{\sigma},\underline{\delta}\right)\right]\pi(\underline{\theta}) \tag{26.2}$$

where

$$J\left(\underline{\theta};\underline{y},\underline{\sigma},\underline{\delta}\right) = \left[\underline{y}-\underline{g}(\underline{\theta};\underline{\delta})\right]^T\Sigma^{-1}(\underline{\sigma})\left[\underline{y}-\underline{g}(\underline{\theta};\underline{\delta})\right] \tag{26.3}$$

expresses the deviation between the measured and model predicted quantities. The PDF $\pi(\underline{\theta})$ is the prior distribution for $\underline{\theta}$, and c is a normalization constant guaranteeing that the posterior PDF $p\left(\underline{\theta}\middle|\underline{y},\underline{\sigma},\underline{\delta}\right)$ integrates to one.

For sufficiently large number of data, the posterior PDF can be asymptotically approximated by a Gaussian PDF $N\left(\underline{\theta};\underline{\widehat{\theta}},Q^{-1}\right)$ centered at the most probable value $\underline{\widehat{\theta}} \equiv \underline{\widehat{\theta}}\left(\underline{y};\underline{\sigma},\underline{\delta}\right)$ that is obtained by minimizing the function $J\left(\underline{\theta};\underline{y},\underline{\sigma},\underline{\delta}\right)$, i.e.

$$\underline{\widehat{\theta}}\left(\underline{y};\underline{\sigma},\underline{\delta}\right) = \arg\min_{\underline{\theta}}\left[J\left(\underline{\theta};\underline{y},\underline{\sigma},\underline{\delta}\right) - \ln\pi(\underline{\theta})\right] \tag{26.4}$$

and covariance matrix $C = C\left(\underline{\widehat{\theta}};\underline{y},\underline{\sigma},\underline{\delta}\right)$ equal to the inverse of the Hessian of $-\ln p\left(\underline{\theta}\middle|\underline{y},\underline{\sigma},\underline{\delta}\right)$, given by

$$C^{-1}\left(\underline{\theta};\underline{y},\underline{\sigma},\underline{\delta}\right) = \underline{\nabla}_\theta\underline{\nabla}_\theta^T\left[-\ln p\left(\underline{\theta}\middle|\underline{y},\underline{\sigma},\underline{\delta}\right)\right] = Q\left(\underline{\theta};\underline{y},\underline{\sigma},\underline{\delta}\right) + Q_\pi(\underline{\theta}) \tag{26.5}$$

And evaluated at the most probable value $\underline{\widehat{\theta}}\left(\underline{y};\underline{\sigma},\underline{\delta}\right)$, where

$$Q\left(\underline{y},\underline{\sigma},\underline{\delta}\right)=\frac{1}{2}\underline{\nabla}_{\theta}\underline{\nabla}_{\theta}^{T}J\left(\underline{\theta};\underline{y},\underline{\sigma},\underline{\delta}\right) \tag{26.6}$$

is the Hessian of $J\left(\underline{\theta};\underline{y},\underline{\sigma},\underline{\delta}\right)$ and $Q_{\pi}\left(\underline{\theta}\right)=\underline{\nabla}_{\theta}\underline{\nabla}_{\theta}^{T}\left[-\ln\pi\left(\underline{\theta}\right)\right]$ is the Hessian of the prior PDF. Both the most probable value and the covariance or Hessian depend on the data $\underline{y}$, the values of the prediction error parameter set $\underline{\sigma}$ and the design variables $\underline{\delta}$.

26.3 Optimal Experimental Design

The objective of an experiment is to maximize the information contain in the data for estimating the parameters of the model. Lindley [6] has introduces the expected utility function $U\left(\underline{\delta}\right)$ to reflect the usefulness of the experiment in estimating the model parameters. The expected utility function has the form

$$U\left(\underline{\delta}\right)=\int_{\Upsilon}\int_{\Theta}u\left(\underline{\delta};\underline{\theta},\underline{y}\right)\,p\left(\underline{\theta},\underline{y}\middle|\underline{\delta}\right)\,d\underline{\theta}\,d\underline{y} \tag{26.7}$$

where $u\left(\underline{\delta};\underline{\theta},\underline{y}\right)$ is the utility function given a particular value of the model parameter set $\underline{\theta}$ and the outcome $\underline{y}$ from the experiment, $p\left(\underline{\theta},\underline{y}\middle|\underline{\delta}\right)=p\left(\underline{\theta}\middle|\underline{y},\underline{\delta}\right)\,p\left(\underline{y}\middle|\underline{\delta}\right)$, $p\left(\underline{\theta}\middle|\underline{y},\underline{\delta}\right)$ is the posterior uncertainty in the model parameters given the outcome $\underline{y}$ and $p\left(\underline{y}\middle|\underline{\delta}\right)$ is the uncertainty in the data. The utility function is chosen to be related to the information gained by the experiment. Based on information theory, it is chosen to be the relative entropy or the Kullback–Leibler divergence between the prior and posterior probability distribution given an outcome $\underline{y}$ obtained from an experimental design $\underline{\delta}$. The expected utility function is an average of the utility function over all possible values of the model parameters as they are inferred from the data, and all the possible outcomes of the experiment. Using the relative entropy in place of the utility function in Eq. (26.7), the expected utility function takes the form

$$\begin{aligned}U\left(\underline{\delta}\right)&=\int_{\Upsilon}\int_{\Theta}p\left(\underline{\theta}\middle|\underline{y},\underline{\delta}\right)\,\ln\frac{p\left(\underline{\theta}\middle|\underline{y},\underline{\delta}\right)}{\pi\left(\underline{\theta}\right)}\,d\underline{\theta}\,p\left(\underline{y}\middle|\underline{\delta}\right)\,d\underline{y}\\&=\int_{\Upsilon}\int_{\Theta}p\left(\underline{\theta}\middle|\underline{y},\underline{\delta}\right)\,\ln\,p\left(\underline{\theta}\middle|\underline{y},\underline{\delta}\right)\,d\underline{\theta}\,p\left(\underline{y}\middle|\underline{\delta}\right)\,d\underline{y}-\int_{\Theta}\int_{\Upsilon}p\left(\underline{\theta}\middle|\underline{y},\underline{\delta}\right)\,p\left(\underline{y}\middle|\underline{\delta}\right)\,d\underline{y}\,\ln\,\pi\left(\underline{\theta}\right)\,d\underline{\theta}\end{aligned} \tag{26.8}$$

where, for prior PDF that it is independent of the design variables, the second term is independent of the design variables and does not affect the optimal values of the design variables. Introducing the information entropy of the posterior PDF of the model parameters

$$H\left(\underline{y},\underline{\delta}\right)=-\int_{\Theta}p\left(\underline{\theta}\middle|\underline{y},\underline{\delta}\right)\,\ln\,p\left(\underline{\theta}\middle|\underline{y},\underline{\delta}\right)\,d\underline{\theta} \tag{26.9}$$

for a given outcome of the experiment $\underline{y}$ obtained from design $\underline{\delta}$, substituting Eq. (26.9) into Eq. (26.8) and noting that the second integral is a constant, say a, the expected utility function takes the form

$$U\left(\underline{\delta}\right)+a=-\int_{\Upsilon}H\left(\underline{y},\underline{\delta}\right)\,p\left(\underline{y}\middle|\underline{\delta}\right)\,d\underline{y}=-\int_{\Theta}\int_{\Upsilon}H\left(\underline{y},\underline{\delta}\right)\,p\left(\underline{y}\middle|\underline{\theta},\underline{\delta}\right)\,d\underline{y}\,p\left(\underline{\theta}\middle|\underline{\delta}\right)\,d\underline{\theta}=-\int_{\Theta}\overline{H}\left(\underline{\theta},\underline{\delta}\right)\,\pi\left(\underline{\theta}\right)\,d\underline{\theta} \tag{26.10}$$

where $\overline{H}\left(\underline{\theta},\underline{\delta}\right)$ is a function of the parameters $\underline{\theta}$ given by

$$\overline{H}\left(\underline{\theta},\underline{\delta}\right)=\int_{\Upsilon}H\left(\underline{y},\underline{\delta}\right)\,p\left(\underline{y}\middle|\underline{\theta},\underline{\delta}\right)\,d\underline{y} \tag{26.11}$$

which is the average information entropy over all outcomes, conditions on the value $\underline{\theta}$ of the model parameters.

The optimal experimental design is formulated as finding the optimal values $\underline{\delta}_{\max}$ of the design variables $\underline{\delta}$ the maximize the utility function $U(\underline{\delta})$, i.e.

$$\underline{\delta}_{opt} = \arg\max_{\underline{\delta}} U(\underline{\delta}) \tag{26.12}$$

Optimal experimental design problems involving the design the position of sensors often results in multiple local and local solutions. Also the gradient of the objective function with respect to the design variables in most cases of practical interest cannot be evaluated analytically. To avoid premature convergence to a local optimum and the evaluation of sensitivities of the utility function with respect to the design variables, stochastic optimization algorithms can be used to find the optimum. Herein the CMA-ES algorithm [7] is used for solving the optimization problem, requiring only evaluation of the objective function at different values of the design variables.

Using sampling techniques to approximate the integrals involved in the expected utility function, a nested sampling scheme has been developed [1] which can result in excessive computational effort for each evaluation of the expected utility function since a very large number of model runs are required. To reduce the computational effort a number of surrogate techniques have been proposed [1]. Herein, we provide asymptotic estimates of the utility function that reduce the computational burden and provide insight into the optimal design.

26.4 Optimal Experimental Design Based on Asymptotic Approximation

Note that from Eq. (26.1) the PDF $p\left(\underline{y}\middle|\underline{\theta},\underline{\delta}\right)$ is Gaussian with respect to $\underline{y}$ with mean $\underline{g}(\underline{\theta},\underline{\delta})$, the predictions from the model given the value of the parameter $\underline{\theta}$ and covariance Σ. Using Laplace asymptotic approximation [8], the integral in Eq. (26.11) can be asymptotically approximated, for small prediction error variance, by

$$\overline{H}(\underline{\theta},\underline{\delta}) = H\left(\underline{g}(\underline{\theta},\underline{\delta}),\underline{\delta}\right) \tag{26.13}$$

Substituting in Eq. (26.10), the expected utility function is given by

$$U(\underline{\delta}) + a = -\int_{\Theta} H\left(\underline{g}(\underline{\theta},\underline{\delta}),\underline{\delta}\right)\ \pi(\underline{\theta})\ d\underline{\theta} \tag{26.14}$$

which is an integral of the information entropy of the posterior PDF of the model parameters corresponding to the outcome $\underline{y} = \underline{g}(\underline{\theta};\underline{\delta})$ conditioned on the values of the model parameters over the support of the prior PDF, weighted by the prior distribution of the model parameters. The integral (26.9) represents the robust information entropy over all possible values of the model parameters quantified by the prior PDF.

Using Monte Carlo simulations or sparse grid techniques [9, 10], the integral (26.14) can be evaluated in the form

$$U(\underline{\delta}) + a \approx -\sum_{j=1}^{n} w_j \overline{H}\left(\underline{\theta}^{(j)},\underline{\delta}\right) \sim -\sum_{j=1}^{n} w_j H\left(\underline{g}\left(\underline{\theta}^{(j)},\underline{\delta}\right),\underline{\delta}\right) \tag{26.15}$$

where $\underline{\theta}^{(j)}, j = 1,\ldots,n$, are either the samples drawn from the prior $\pi(\underline{\theta})$ or the sparse grid points in the parameters space, and w_j are weights equal to $w_j = 1/n$ for the Monte Carlo technique or, for sparse grid techniques, their values depend on the sparse grid order and the prior distribution selected [9].

Using the Bayesian asymptotic approximation for the posterior PDF, valid for large number of data, the information entropy for the outcome $\underline{y} = \underline{g}\left(\underline{\theta}^{(j)};\underline{\delta}\right) \equiv \underline{g}_j(\underline{\delta})$ is given by

$$H\left(\underline{g}\left(\underline{\theta}^{(j)},\underline{\delta}\right),\underline{\delta}\right) \equiv H\left(\underline{g}_j(\underline{\delta}),\underline{\delta}\right) = \frac{1}{2}N_\theta \ln(2\pi) - \frac{1}{2}\ln\det\left[\widehat{Q}_j(\underline{\sigma},\underline{\delta}) + Q_\pi\left(\widehat{\underline{\theta}}_j\right)\right] \tag{26.16}$$

where $\widehat{Q}_j(\underline{\sigma},\underline{\delta}) \equiv Q\left(\widehat{\underline{\theta}}_j;\underline{g}\left(\widehat{\underline{\theta}}_j,\underline{\delta}\right),\underline{\sigma},\underline{\delta}\right)$ and $\widehat{\underline{\theta}}_j = \widehat{\underline{\theta}}\left(\underline{g}\left(\underline{\theta}^{(j)},\underline{\delta}\right);\underline{\sigma},\underline{\delta}\right)$.

In the special case of a linear model with respect to the model parameters, i.e. $\underline{g}\left(\underline{\theta};\underline{\delta}\right) \equiv \underline{a}_0 + A\underline{\theta}$, and Gaussian prior $\pi\left(\underline{\theta}\right) = N\left(\underline{\theta};\underline{\mu},S\right)$ with mean $\underline{\mu}$ and covariance S, the information entropy in Eq. (26.16) is independent of $\widehat{\underline{\theta}}_j$ and is given by

$$H\left(\underline{g}\left(\underline{\theta}^{(j)},\underline{\delta}\right),\underline{\delta}\right) \equiv H\left(\underline{g}_j\left(\underline{\delta}\right),\underline{\delta}\right) = \frac{1}{2}N_\theta \ln\left(2\pi\right) - \frac{1}{2}\ln\det\left[A\Sigma^{-1}A + S^{-1}\right] \tag{26.17}$$

For the general case, for each point $\underline{\theta}^{(j)}$ in the parameter space, one can use a first-order approximation of the model prediction $\underline{g}\left(\underline{\theta},\underline{\delta}\right)$ in the neighborhood of each point $\underline{\theta}^{(j)}$ in Eq. (26.15) to obtain for Gaussian prior that

$$\widehat{\underline{\theta}}_j = \underline{\theta}^{(j)} + \left(A_j^T\Sigma A_j + S^{-1}\right)^{-1}S^{-1}\left(\underline{\mu} - \underline{\theta}^{(j)}\right) \tag{26.18}$$

and

$$H\left(\underline{g}\left(\underline{\theta}^{(j)},\underline{\delta}\right),\underline{\delta}\right) \equiv H\left(\underline{g}_j\left(\underline{\delta}\right),\underline{\delta}\right) = \frac{1}{2}N_\theta \ln\left(2\pi\right) - \frac{1}{2}\ln\det\left[A_j^T\Sigma^{-1}A_j + S^{-1}\right] \tag{26.19}$$

where $A_j = \underline{\nabla}_\theta\underline{g}\left(\underline{\theta},\underline{\delta}\right)\Big|_{\underline{\theta}=\widehat{\underline{\theta}}_j}$. In this case the information entropy evaluated at a point $\underline{\theta}^{(j)}$ depends on the sensitivity of the output quantity of interest with respect to the model parameters, evaluated at the neighbor point $\widehat{\underline{\theta}}_j$. The analysis holds if $\widehat{\underline{\theta}}_j$ is close to $\underline{\theta}^{(j)}$ so that the first order approximation of $\underline{g}\left(\underline{\theta},\underline{\delta}\right)$ about $\underline{\theta}^{(j)}$ applies. To study the conditions under which the first order approximation can be used and the results Eqs. (26.18) and (26.19) are valid, let $\Sigma = \varepsilon^2\Sigma_0$ and $S = s^2S_0$, denoting that Σ and S are of order of ε^2 and s^2, respectively. Substituting in Eq. (26.18) one derives that

$$\widehat{\underline{\theta}}_j = \underline{\theta}^{(j)} + \frac{\varepsilon^2}{s^2}\left[S_0A_j^T\Sigma_0^{-1}A_j + \frac{\varepsilon^2}{s^2}\right]^{-1}\left(\underline{\mu} - \underline{\theta}^{(j)}\right)$$

The ratio ε^2/s^2 is a measure of how close the optimum $\widehat{\underline{\theta}}_j$ is to the point $\underline{\theta}^{(j)}$ and can be used as a direct measure of the validity of the first-order approximation of $\underline{g}\left(\underline{\theta},\underline{\delta}\right)$ about $\underline{\theta}^{(j)}$. For $\varepsilon^2/s^2 << 1$ the following approximation holds $\widehat{\underline{\theta}}_j \approx \underline{\theta}^{(j)}$. This approximation is true for small prediction error variance in relation to the variance of the prior distribution. Thus, the information entropy evaluated at a point $\underline{\theta}^{(j)}$ depends on the sensitivity of the output QoI with respect to the model parameters, evaluated at $\underline{\theta}^{(j)}$, the sparse grid point or the sample points in an MC estimate. It should be noted that the estimate (26.15) with $H\left(\underline{g}\left(\underline{\theta}^{(j)},\underline{\delta}\right),\underline{\delta}\right)$ given by Eq. (26.19) and $A_j \approx \underline{\nabla}_\theta\underline{g}\left(\underline{\theta},\underline{\delta}\right)\Big|_{\underline{\theta}=\underline{\theta}^{(j)}}$ is equivalent to the asymptotic estimate given in [3, 11] based on the change of information entropy between the prior and posterior distribution, yielding the robust information entropy measure using the prior uncertainties.

26.5 Implementation is Structural Dynamics

The optimal experimental design methodology is implemented in structural dynamics for estimating the optimal sensor locations for modal identification. Specifically, the problem of estimating the modal coordinate vector $\underline{\xi} \in R^m$ $(m \leq N_d)$ encountered in modal identification is re-visited. Using modal analysis, the response vector $\underline{u} \equiv \underline{g}\left(\underline{\theta}\right) \in R^N$ is given with respect to the parameter set $\underline{\theta}$ in the form $\underline{u} = \Phi\underline{\theta}$, where $\Phi \in R^{N\times m}$ is the mode shape matrix for m contributing modes. The objective is to design the sensor configuration that provides the most information in order to estimate the modal coordinate vector $\underline{\xi}$ which constitute the parameter set $\underline{\theta} \equiv \underline{\xi}$. Noting that $\underline{\nabla}_\theta\underline{g}\left(\underline{\theta}\right) = \Phi$ and substituting into Eq. (26.19), the expected utility function takes the form

$$U\left(\underline{\delta}\right) = \frac{1}{2}\ln\det\left[\widehat{Q}\left(\underline{\sigma},\underline{\delta}\right) + S^{-1}\right] - a - \frac{1}{2}N_\theta \ln\left(2\pi\right) \tag{26.20}$$

where

$$\widehat{Q}\left(\underline{\sigma},\underline{\delta}\right) = \left\{L_{\underline{\delta}}\Phi\right\}^T\left\{L_{\underline{\delta}}\Sigma\left(\underline{\sigma}\right)L_{\underline{\delta}}^T\right\}^{-1}\left\{L_{\underline{\delta}}\Phi\right\} \tag{26.21}$$

which is independent of the model parameters. In addition, the optimal sensor locations are independent of the excitation used. The information matrix $\widehat{Q}(\underline{\sigma}, \underline{\delta})$ in Eq. (26.21) has exactly the same form as the one proposed in [4] for designing the optimal sensor location. So, with the same assumed prediction error correlation matrix Σ, the optimal sensor location from the proposed methodology and the effective independence are based on exactly the same information matrix Q given in Eq. (26.20).

Based on the form of Eq. (26.20), a non-singular FIM matrix $\widehat{Q}(\underline{\sigma}, \underline{\delta})$ is obtained if the number of sensors N is at least equal to the number of contributing modes m ($N_\theta = m$). For $N < m$, the matrix $Q(L, \Sigma)$ in Eq. (26.20) is singular and for uniform prior PDF the determinant of the FIM will be zero for any sensor configuration. Thus, for $N_0 < m$ the optimal sensor location problem cannot be performed for uniform prior PDF. This means that the information content in the measured data and the prior is not sufficient to estimate all the parameters simultaneously. The problem is critical for the FSSP algorithm where one starts with no sensors placed on the structure and sequentially adds one sensor at a time on the structure. Previous formulations on the subject based only on the Fisher information matrix [4, 5] failed to address this problem. Moreover, forward sequential sensor placement algorithms could not be used due to the singular $\widehat{Q}(\underline{\sigma}, \underline{\delta})$. The Bayesian optimal experimental design formulation yields a nonsingular matrix, provided that the prior is non-uniform distribution. The non-uniform prior yields a Hessian that is added to the Fisher information matrix $\widehat{Q}(\underline{\sigma}, \underline{\delta})$ and makes the combined matrix $\widehat{Q}(\underline{\sigma}, \underline{\delta}) + S^{-1}$ non-singular. Assuming without loss of generality, an isotropic covariance matrix $S = (1/\rho) I$, the utility function is given by

$$U(\underline{\delta}) = \frac{1}{2} \sum_{k=1}^{N_\theta} \log(\lambda_k + \rho) \tag{26.22}$$

where λ_k, $k = 1, \ldots, N_\theta$, are the eigenvalues of the Fisher information matrix. Note that when one takes the limit when $\rho \to 0$, the optimal experimental design of equivalent to the one proposed in Papadimitriou and Lombaert [4] where the non-zero eigenvalues were considered in the sum in Eq. (26.22), which was equivalent of maximizing the product of the non-zero eigenvalues in the FIM, instead of maximizing the product of all eigenvalues. This procedure allows to systematically place the sensors optimally in the structure even for the unidentifiable case that arises for a small number of sensors. This procedure also considerably improves the FSSP estimates for $N \geq m$.

26.6 Applications

To demonstrate the use of the optimal sensor placement for modal identification in the case of singular Fisher information matrix, consider the case of selecting the reference sensors in a multiple sensor configuration set up experiment conducted with limited number of sensors in order to obtain the modal frequencies and assemble the modeshapes from multiple setups. It is important in this case that the reference sensor contain the maximum possible information for all modes that are planned to be identified. Wrong locations of the reference sensor may degrade the modal information for one or more modes, degrading the accuracy of the corresponding assembled modeshapes since such accuracy is based on the information contained in the reference sensors. The number of reference sensors is in most cases smaller than the number of modes to be identified. The methodology presented is convenient to optimize the location of sensors in a structure.

The effectiveness is illustrated by designing the optimal location of the reference sensors for the Metsovo bridge. A description of the bridge and the finite element model is given in [12]. The sensors are located along the pedestrian walkway in the two sides of the bridge deck. The problem is formulated separately for the vertical and the transverse modes. One reference sensor is located optimally in the sidewalk so that the measurement contain the maximum possible information for the lowest seven vertical modes of the bridge. The optimal location of a second reference sensor is designed so that the lowest eight transverse modes are identified. The number of design variables for each optimization problem is one, while the number of optimization problems solved are two. In both cases the Fisher information matrix $\widehat{Q}(\underline{\sigma}, \underline{\delta})$ in Eq. (26.21) and a number of eigenvalues λ_k in Eq. (26.22) are zero. To successfully proceed with the design, a non-uniform prior distribution has to be used so that the information from the prior makes the matrix $\widehat{Q}(\underline{\sigma}, \underline{\delta}) + S^{-1}$ in Eq. (26.21) non-singular. Herein the optimal design is based on a isotropic Gaussian prior with value ρ in Eq. (26.22) selected to be much smaller than the lowest non-zero eigenvalue λ_k. The optimization is performed using CMA-ES [7] over a continuous curve along the two sidewalks of the bridge deck. The results for the optimal sensor placement of the reference sensors are shown in Fig. 26.1, for the lowest seven vertical and eight transverse modes. It is seen that the vertical reference sensor is optimally located at a distance 255 m from the left end of the deck, while the transverse sensor is optimally located at a distance of 263 m from the left end.

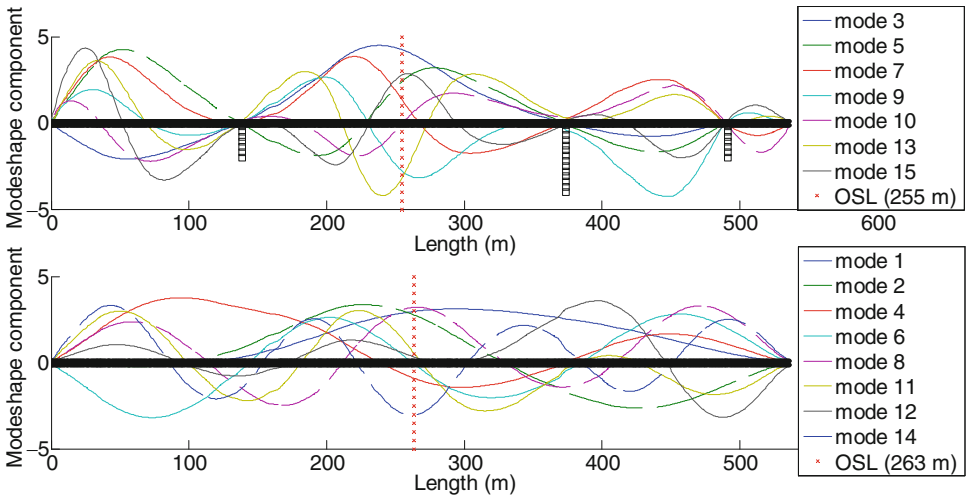

Fig. 26.1 Optimal location of the reference sensors in multiple sensor configuration setups for identifying the lowest seven vertical modes (*top*) and the lowest eight transverse modes (*bottom*) of the bridge. The corresponding modes of the bridge are also shown, drawn along the sidewalk curve using the finite element model

26.7 Conclusion

Asymptotic approximations, valid for sufficiently large number of data and small prediction error, are introduced to simplify the expected information gain used for optimal experimental design. The utility is based on relative entropy between posterior and prior PDF in Bayesian inference. The asymptotic estimate of the expected utility function depends on the sensitivity of the output quantity of interest predicted by the model to the model parameter, evaluated at control points in the support of the prior PDF. These control points are the sparse points in a sparse grid technique or the sample points in a MC technique used to estimate the robust information entropy, an integral of the information entropy over the support of the prior PDF of the model parameters. The asymptotic estimate based on the expected information gain is equivalent to the one obtained using the concept of robust information entropy [2, 11] for optimal experimental design. Application of the proposed Bayesian optimal experimental design to the optimal sensor placement for modal identification results in optimal design even for small number of sensors in relation to the number of contributing modes, avoiding the problem of singular Fisher information matrix encountered in previous approaches. The non-singularity arises from the information contained in the prior which is taken into account in a Bayesian experimental design approach. The method was successfully used to design the reference sensors for use in multiple configuration setups with reference and roving sensors in order to accurately assemble the modeshapes of a R/C bridge.

Acknowledgement This research has been implemented under the "ARISTEIA" Action of the "Operational Programme Education and Lifelong Learning" and was co-funded by the European Social Fund (ESF) and Greek National Resources.

References

1. Huan, X., Marzouk, Y.M.: Simulation-based optimal Bayesian experimental design for nonlinear systems. J. Comput. Phys. **232**(1), 288–317 (2013)
2. Papadimitriou, C., Beck, J.L., Au, S.K.: Entropy-based optimal sensor location for structural model updating. J. Vib. Control. **6**(5), 781–800 (2000)
3. Papadimitriou, C.: Optimal sensor placement methodology for parametric identification of structural systems. J. Sound Vib. **278**(4), 923–947 (2004)
4. Papadimitriou, C., Lombaert, G.: The effect of prediction error correlation on optimal sensor placement in structural dynamics. Mech. Syst. Signal Process. **28**, 105–127 (2012)
5. Kammer, D.C.: Sensor placements for on orbit modal identification and correlation of large space structures. J. Guid. Control. Dyn. **14**, 251–259 (1991)
6. Lindley, D.V.: On a measure of the information provided by an experiment. Ann. Math. Stat. **27**, 986–1005 (1956)
7. Hansen, N., Muller, S.D., Koumoutsakos, P.: Reducing the time complexity of the derandomized evolution strategy with covariance matrix adaptation (CMA-ES). Evol. Comput. **11**(1), 1–18 (2003)

8. Bleistein, N., Handelsman, R.: Asymptotic Expansions for Integrals. Dover, New York (1986)
9. Gerstner, T., Griebel, M.: Numerical integration using sparse grids. Numer. Algorithms **18**, 209–232 (1998)
10. Bungartz, H.J., Griebel, M.: Sparse grids. Acta Numer. **13**, 147–269 (2004)
11. Papadimitriou, D.I., Papadimitriou, C.: Optimal sensor placement for the estimation of turbulence model parameters in CFD. Int. J. Uncertain. Quantif. **5**, 1 (2015)
12. Papadimitriou, C., Papadioti, D.C.: Component mode synthesis techniques for finite element model updating. Comput. Struct. **126**, 15–28 (2013)

Chapter 27
Towards the Diagnosis and Simulation of Discrepancies in Dynamical Models

P.L. Green

Abstract Models are frequently used to make predictions in regions where experimental testing is difficult. This often involves extrapolating to regions far from where the model was validated. In this paper an example is shown where, despite using a Bayesian analysis to quantify parameter estimation uncertainties, such an extrapolation performs poorly. It is then demonstrated that, in the presence of measurement noise, treating a system's parameters as being time-variant (even if this is not believed to be true) can reveal fundamental flaws in a model. Finally, existing methods which can be used to quantify *model error*—the inevitable discrepancies that arise because of approximations made during model development—are extended towards dynamical systems.

Keywords Verification and validation • Particle filter • Gaussian process • Nonlinear dynamics • System identification

27.1 Introduction

Engineers frequently use computational models to make predictions in regions where testing is difficult/expensive and, as such, often use models in regions where they have not been validated using measurement data. This lack of data in the model's 'domain of applicability' prevents the use of validation methods such as [1, 2] and makes it very difficult to establish the confidence that can be placed in simulated predictions.

To illustrate this issue, the calibration of a SDOF dynamical system will be considered. The system of interest is a Duffing oscillator:

$$\ddot{y} + c^*\dot{y} + k^*y + k_3^*y^3 = u(t). \tag{27.1}$$

To create training data, the response of the system to a random forcing vector, u, was simulated. The resulting displacement time history was then corrupted with Gaussian 'measurement noise'. To introduce model error into the problem, the current example considers the case where the system is, incorrectly, believed to be linear (such that $k_3^* = 0$). The vector of parameters to be estimated is therefore $\boldsymbol{\theta} = (c^*, k^*)^T$. While a host of different identification methods could be used to tackle this problem, a Bayesian approach is used here. This is simply to illustrate how taking account of parameter uncertainties does not necessarily allow one to accurately quantify the trust that can be placed in simulated predictions.

Bayes' theorem allows the posterior parameter distribution to be written as $p(\boldsymbol{\theta}|\boldsymbol{D}) \propto p(\boldsymbol{D}|\boldsymbol{\theta})p(\boldsymbol{\theta})$ where $\boldsymbol{D} = \{D_1, \ldots, D_N\}$ is the set of training data. In this case the prior is chosen to be Gaussain and the likelihood is chosen according to the principle of Maximum Entropy [3] which asserts that, if the first two moments of the likelihood are known, the distribution which assumes the least amount of additional information is

$$p(\boldsymbol{D}|\boldsymbol{\theta}) = \mathcal{N}(z; \boldsymbol{y}(\boldsymbol{\theta}), \beta \boldsymbol{I}) \tag{27.2}$$

where $\boldsymbol{z} = (z_1, \ldots, z_N)^T$ is the vector of displacement measurements, $\boldsymbol{y}(\boldsymbol{\theta}) = (y_1(\boldsymbol{\theta}), \ldots, y_N(\boldsymbol{\theta}))^T$ is the vector of displacements predicted by the linear model and β is a precision parameter which needs to be identified. The moments of the prior and the true parameter values are given in Table 27.1

P.L. Green (✉)
School of Engineering, Centre for Engineering Sustainability, Institute for Risk and Uncertainty, University of Liverpool, Liverpool L69 3GQ, UK
e-mail: p.l.green@liverpool.ac.uk

S. Atamturktur et al. (eds.), *Model Validation and Uncertainty Quantification, Volume 3*, Conference Proceedings of the Society for Experimental Mechanics Series, DOI 10.1007/978-3-319-29754-5_27

Table 27.1 True parameter values and moments of prior distribution (SI units)

Parameter	True value
k	10
c	0.1
k_3	100
β	1×10^5

Parameter	Prior mean	Prior variance
k	10	5
c	0.1	0.05
β	1×10^5	4×10^5

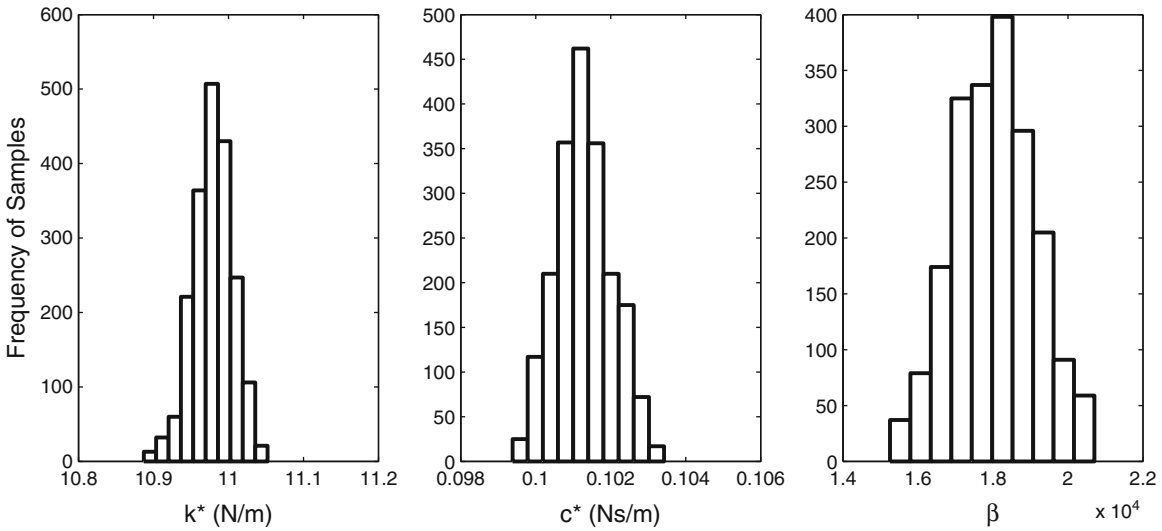

Fig. 27.1 MCMC samples

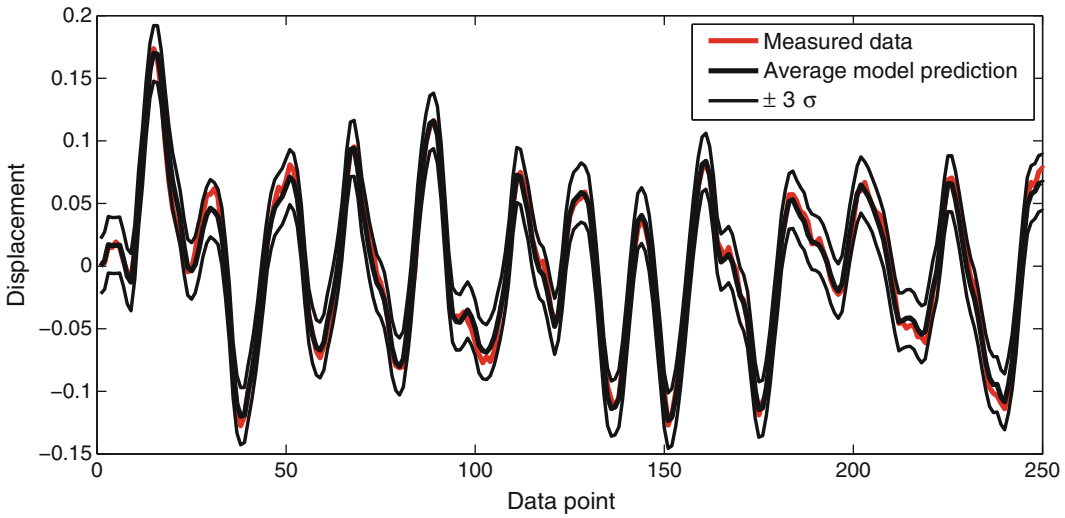

Fig. 27.2 Predictions within the model's validation domain (where the confidence bounds represent the uncertainties associated with parameter estimation)

1000 samples were generated from the posterior parameter distribution using a Markov chain Monte Carlo (MCMC) algorithm [4]—the resulting samples are shown in Fig. 27.1.

Using these samples as part of a Monte Carlo simulation, it is possible to propagate these parameter uncertainties into simulated predictions. The response of the system to a new excitation (of a similar amplitude to the excitation that was used to create the training data) was then simulated. Figure 27.2 shows the ability of the model to predict the response of the

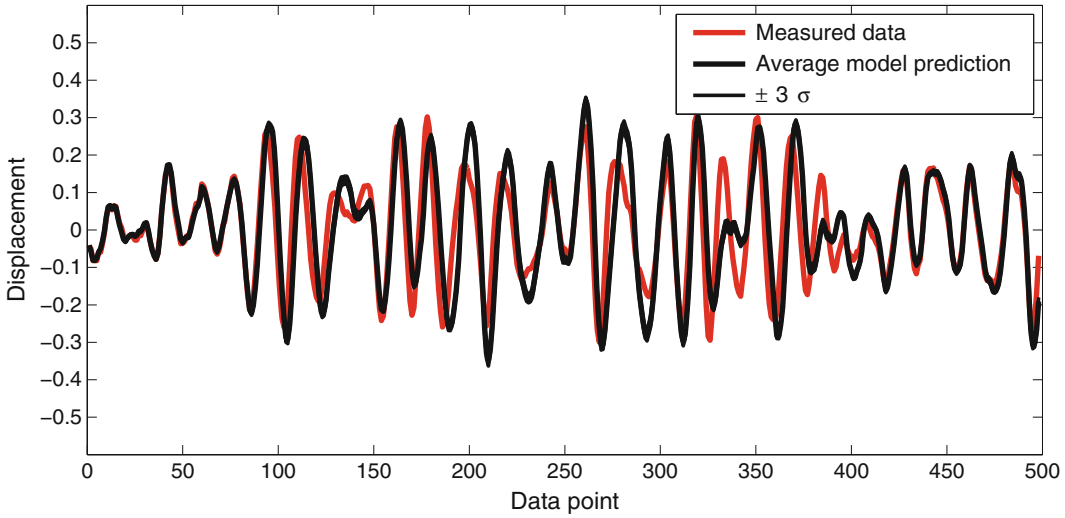

Fig. 27.3 Predictions outside of the model's validation domain (where the confidence bounds represent the uncertainties associated with parameter estimation)

system to this new input—despite the use of an incomplete model, the predictions are good. However, if the model is used to predict the response of the system to a higher amplitude excitation, the predictions are poor and the confidence bounds arising from the propagation of parameter uncertainties fail to accurately measure the confidence that can be placed in the predictions (Fig. 27.3).

To overcome the limitations demonstrated by this example, one must tackle two issues:

1. Diagnosis. If the model performs well in the validation domain, it is difficult to identify and resolve the issues which may affect its performance when extrapolation is undertaken.
2. Model discrepancy. Even if the model is believed to be incomplete, it is not always obvious how it is to be improved.

The current paper proposes two methods which can help to address these issues. As with the previous example, it focuses on the situation where one's system of interest is believed to be dynamical.

27.2 Background

The methodologies proposed here involves the application of Bayesian tracking algorithms (particle filters) and nonparametric regression techniques (Gaussian processes). A very brief introduction to these methodologies is given here—more information on particle filters can be found in the excellent tutorial [5] while the books [6, 7] give accessible introductions to Gaussian Processes.

27.2.1 Particle Filters

Here the vector $\boldsymbol{s}_n$ is used to represent the state of a dynamical system at the nth discrete time interval. Particle filters are applicable in situations where one is able to define a 'prediction equation',

$$\boldsymbol{s}_n = f_n(\boldsymbol{s}_{n-1}, \boldsymbol{u}_n, \boldsymbol{v}_{n-1}), \tag{27.3}$$

and a measurement equation,

$$\boldsymbol{z}_n = h_n(\boldsymbol{s}_n, \boldsymbol{r}_n) \tag{27.4}$$

where, as before, $\boldsymbol{z}$ and $\boldsymbol{u}$ are used to represent measurements and system inputs respectively while $\boldsymbol{v}$ and $\boldsymbol{r}$ are 'noise terms':

$$\boldsymbol{v}_n \sim \mathcal{N}(\boldsymbol{0}, \boldsymbol{V}_n), \qquad \boldsymbol{r}_n \sim \mathcal{N}(\boldsymbol{0}, \boldsymbol{R}_n). \tag{27.5}$$

Defining $\boldsymbol{s}_{1:n} \equiv (\boldsymbol{s}_1 \dots \boldsymbol{s}_n)^T$ and $\boldsymbol{z}_{1:n} \equiv (\boldsymbol{z}_1 \dots \boldsymbol{z}_n)^T$ then, in short, particle filters use recursive importance sampling to analyse quantities related to the distribution $p(\boldsymbol{s}_{1:n}|\boldsymbol{z}_{2:n})$ 'online', as new measurements are obtained.

The key aspect to note here is that, by including a system's parameters in the state vector, it is possible to track how one's parameter estimates vary with time. This was exploited, within the context of structural dynamics, in [8]. In the current example this involves defining the state of the model, at time n, as

$$\boldsymbol{s}_n = \begin{pmatrix} y_n \\ \dot{y}_n \\ \boldsymbol{\theta}_n \end{pmatrix} \tag{27.6}$$

(noting that the system's parameters are now a function of time). The prediction equation, in this case, was defined as the solution of

$$\frac{d}{dt}\begin{pmatrix} y_n \\ \dot{y}_n \\ \boldsymbol{\theta}_n \end{pmatrix} = \begin{pmatrix} \dot{y}_n \\ (m^*)^{-1}(u_n - k_n^* y_n - c_n^* \dot{y}_n) \\ \boldsymbol{0} \end{pmatrix} \tag{27.7}$$

(approximated using numerical integration techniques). As displacements are being measured, the measurement equation is simply

$$\boldsymbol{z}_n = \begin{pmatrix} 1 & 0 & 0 & 0 \end{pmatrix} \boldsymbol{s}_n + \epsilon \qquad \epsilon \sim \mathcal{N}(0, \beta^{-1}) \tag{27.8}$$

where ϵ represents measurement noise.

27.2.2 Gaussian Processes

Defining $\{\boldsymbol{x}_1, \dots, \boldsymbol{x}_N\}$ as a set of system inputs then, in the current paper, Gaussian processes are essentially used to fit to $\boldsymbol{t} = (t_1(\boldsymbol{x}_1) \dots t_N(\boldsymbol{x}_N))^T$, a vector of training data. This involves first defining a prior probability distribution,

$$p(\boldsymbol{t}) = \mathcal{N}(\boldsymbol{0}, \boldsymbol{K}), \qquad K_{ij} = k(\boldsymbol{x}_i, \boldsymbol{x}_j) \tag{27.9}$$

where $k(\cdot, \cdot)$, the 'kernel function', is user-defined. By defining the kernel function appropriately, one can induce correlation between $t_i(\boldsymbol{x}_i)$ and $t_j(\boldsymbol{x}_j)$ which is depended on the 'closeness' of $\boldsymbol{x}_i$ and $\boldsymbol{x}_j$. This is convenient as it allows one to impose a prior belief in the *smoothness* of the interpolant. For example, in the current case the kernel function is defined as

$$k(\boldsymbol{x}_i, \boldsymbol{x}_j) = \exp\left(-\frac{\alpha}{2}(\boldsymbol{x}_i - \boldsymbol{x}_j)^T(\boldsymbol{x}_i - \boldsymbol{x}_j)\right) \tag{27.10}$$

where α is a hyperparameter—selecting a small value of α will induce large correlations between 'neighboring' values of $\boldsymbol{x}$ and, as a result, induce smoothness in the interplant. Using t^* to represent a new data point which has been generated in response to a new input, $\boldsymbol{x}^*$, the kernel function can then be used to construct the joint distribution

$$p(\boldsymbol{t}, t^*) = \mathcal{N}\left(\boldsymbol{0}, \begin{bmatrix} \boldsymbol{K} & \boldsymbol{a} \\ \boldsymbol{a} & c \end{bmatrix}\right) \tag{27.11}$$

where

$$a_n = k(\boldsymbol{x}_n, \boldsymbol{x}^*), \quad c = k(\boldsymbol{x}^*, \boldsymbol{x}^*). \tag{27.12}$$

As this is a multivariate Gaussian, it is then possible to show that

$$p(t^*|\boldsymbol{t}) = \mathcal{N}(m, \sigma^2), \tag{27.13}$$

where

$$m = \boldsymbol{a}^T \boldsymbol{K}^{-1} \boldsymbol{t}, \qquad \sigma^2 = c - \boldsymbol{a}^T \boldsymbol{K}^{-1} \boldsymbol{a}, \tag{27.14}$$

thus allowing one to form a probabilistic estimate of t^*.

27.3 Diagnosis

One of the issues with the identification procedure described in Sect. 27.1 is that, essentially, it has 'masked' the fundamental flaws present in the model. To overcome this, it is suggested here that it may be beneficial to treat the system's parameters as being *time variant*—even if this is not believed to be the case. This is based on the hypothesis that, if the model is sufficiently accurate, one's parameter estimates will quickly converge and appear to be time invariant (relatively speaking). However, if the model is incomplete then, to closely fit the training data, one's parameter estimates may vary significantly with time.

The variation in the expected values of k^* and c^*, as a function of time, are shown in red in Fig. 27.4. It can be seen that, for the model to closely match the training data, significant changes in the linear stiffness are required. The black lines in Fig. 27.4 illustrate how one's parameter estimates vary in a situation where one's model is a perfect representation of reality (using training data generated from a linear system). It is clear that, relatively speaking, these variations in one's parameter estimates are small. Furthermore, as it is the stiffness term which experienced the largest variation, these results also seem to indicate exactly which *parts* of the model may require refinement. While these results certainly are not conclusive they do, at least, demonstrate a scenario where treating one's parameters as being time invariant—even if this is believed to be unphysical—can reveal useful information about the flaws in one's model.

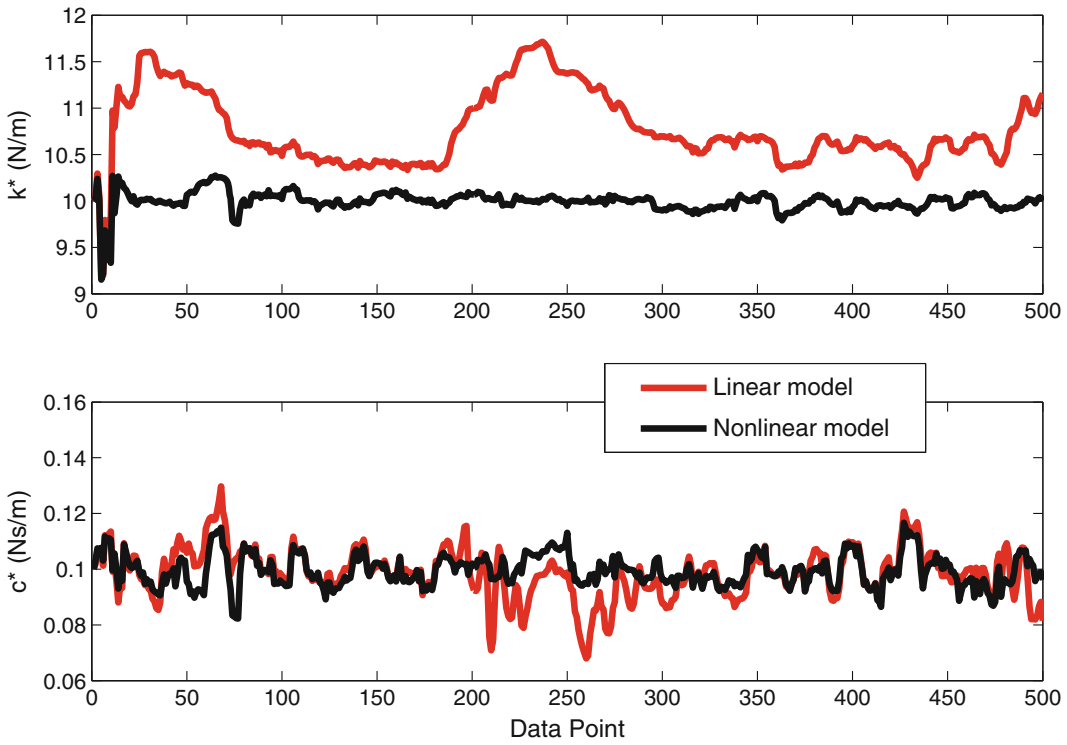

Fig. 27.4 The variation in parameter estimates for the case where model error is present (*red*) and model error is absent (*black*)

27.4 Model Discrepancy

Having identified that a model is flawed, it still may not be obvious how the model can be improved. A general approach that can be used to address this issue was proposed in the seminal paper [9]. This involves writing the relationship between one's measurements and the outputs of one's model as

$$z_i = y_i(\boldsymbol{\theta}) + \eta_i + \epsilon_i \tag{27.15}$$

where ϵ is measurement noise and, crucially, η is used to represent *model error*—the inevitable discrepancy between model output and measurement data. One then uses a Gaussian process to infer the relationship between the inputs to the system and the model error—thus quantifying what is often a huge source of uncertainty.[1] While this idea has been applied to various engineering applications (see [10] for example), the author does not believe that it has not been extended towards *dynamical systems*.

In this paper it has been found that, if one's system is dynamical, then a Gaussian process which is designed to predict model error has to be *autoregressive*—the current prediction of model error has to be dependent on previous predictions of model error (as well as the current input to the system). In the current case it was found that, to predict the current model error (η_n), one must define the inputs to the GP as

$$\boldsymbol{x}_n = \begin{pmatrix} \eta_{n-2} \\ \eta_{n-1} \\ u_n \end{pmatrix} \tag{27.16}$$

(this leads to the formulation of a 'GP NARX model'—see [11] for more information). Figure 27.5 shows how, for the example described in this paper, utilising a GP NARX model to emulate model error can significantly improve the accuracy

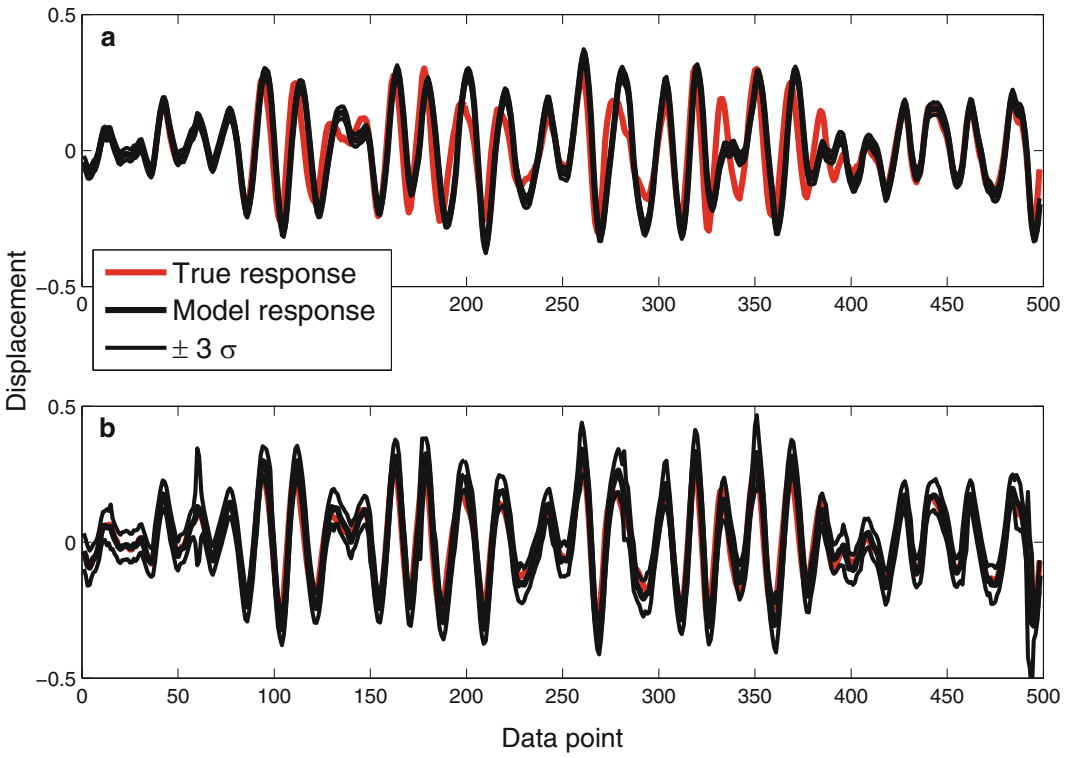

Fig. 27.5 Simulated predictions outside of the model's validation domain where (**a**), model error is ignored and (**b**), model error is considered

[1] The methodology described in [9] is actually more detailed than this, and also takes account of the scenario where one's model is emulated using a Gaussian process. This is not considered in the current paper.

of the model predictions as well as the resulting confidence bounds, when making high amplitude predictions which are far from the validation domain. It is important to note, however, that these results were obtained using one-at-a-time predictions. For future work the author aims to establish the applicability of full-model-predictions (where the output of the GP NARX model is conditional on its own, previous estimates of model error).

27.5 Conclusions

This paper describes two methods which, it is believed, can be used to help establish and increase the confidence that can be placed in simulations of dynamical systems which are conducted outside of a model's validation domain. Firstly, it was shown how treating a system's parameters as being time invariant during the calibration process can, in some situations, be used to identify which parts of a model may require improvement. It is hoped that, in the future, this will allow one to isolate and focus on the specific parts of very large models which need redevelopment. Secondly, the framework proposed in [9] was extended towards dynamical systems. This involved using a GP NARX model to emulate model error—the inevitable discrepancy between measurements and model outputs. While the initial results are promising, the author has thus far only used to approach to make one-at-a-time predictions of model error. The extension to full-model-predictions is being investigated currently.

References

1. Hemez, F., Atamturktur, S., Unal, C.: Defining predictive maturity for validated numerical simulations. Comput. Struct. **88**(7), 497–505 (2010)
2. Atamturktur, S., Hemez, F., Williams, B., Tome, C., Unal, C.: A forecasting metric for predictive modeling. Comput. Struct. **89**(23), 2377–2387 (2011)
3. Jaynes, E.T.: Probability Theory: The Logic of Science. Cambridge University Press, Cambridge (2003)
4. Ching, J., Chen, Y.C.: Transitional Markov chain Monte Carlo method for Bayesian model updating, model class selection, and model averaging. J. Eng. Mech. **133**(7), 816–832 (2007)
5. Arulampalam, M.S., Maskell, S., Gordon, N., Clapp, T.: A tutorial on particle filters for online nonlinear/non-Gaussian Bayesian tracking. IEEE Trans. Signal Process. **50**(2), 174–188 (2002)
6. Bishop, C.M.: Pattern Recognition and Machine Learning. Springer, New York (2006)
7. MacKay, D.J.C.: Information Theory, Inference and Learning Algorithms. Cambridge University Press, Cambridge (2003)
8. Ching, J., Beck, J.L., Porter, K.A.: Bayesian state and parameter estimation of uncertain dynamical systems. Probab. Eng. Mech. **21**(1), 81–96 (2006)
9. Kennedy, M.C., O'Hagan, A.: Bayesian calibration of computer models. J. R. Stat. Soc. Ser. B Stat. Methodol. **63**(3), 425–464 (2001)
10. Higdon, D., Gattiker, J., Williams, B., Rightley, M.: Computer model calibration using high-dimensional output. J. Am. Stat. Assoc. **103**(482), 570–583 (2008)
11. Worden, K., Manson, G., Cross, E.J.: On Gaussian process NARX models and their higher-order frequency response functions. In: *Solving Computationally Expensive Engineering Problems*, pp. 315–335. Springer, Cham (2014)

Chapter 28
Effects of Prediction Error Bias on Model Calibration and Response Prediction of a 10-Story Building

Iman Behmanesh, Seyedsina Yousefianmoghadam, Amin Nozari, Babak Moaveni, and Andreas Stavridis

Abstract This paper investigates the application of Hierarchical Bayesian model updating to be used for probabilistic model calibration and response prediction of civil structures. In this updating framework the misfit between the identified modal parameters and the corresponding parameters of the finite element (FE) model is considered as a Gaussian distribution with unknown parameters. For response prediction, both the structural parameters of the FE model and the parameters of the misfit error functions are considered. The focus of this paper is to (1) evaluate the performance of the proposed framework in predicting the structural modal parameters at a state that the FE model is not calibrated (extrapolation from the model), and (2) study the effects of prediction error bias on the accuracy of the predicted values. The test structure considered here is a ten-story concrete building located in Utica, NY. The modal parameters of the building at its reference state were identified from ambient vibration data using the NExT-ERA system identification method. The identified modal parameters are used to calibrate parameters of the initial FE model as well as the misfit error functions. Before demolishing the building, six of its exterior walls were removed and ambient vibration measurements were also collected from the structure after wall removal. These data are not used to calibrate the model; they are only used to validate the predicted results. The model updating framework of this paper is applied to estimate the modal parameters of the building after removal of the six walls. Good agreement is observed between the model-predicted modal parameters and those identified from vibration tests.

Keywords Hierarchical Bayesian modeling • Uncertainty quantification • Modeling errors • Prediction bias • Response prediction

28.1 Introduction

In current structural engineering practice, the response of structure to future loadings is usually predicted using finite element (FE) models. Examples include prediction of structural response to dynamic excitations such as wind or seismic loads. It is also common in practice to validate linear FE models by comparing their modal parameters with the ones identified from vibration data [1, 2], however, response predictions are still obtained based on the FE models only. The FE models of civil structures are often associated with many sources of uncertainties and modeling errors. Calibration/updating of the FE models using static/dynamic data can reduce some of these uncertainties [3]. In common model updating/calibration techniques, model parameters are adjusted so that the model-predicted time histories, modal parameters, or frequency response functions best match the corresponding quantities obtained from the test data. In some cases, the updated FE models cannot even predict the data that were used to calibrate the model without bias [4–6]. This problem is not limited to the deterministic model updating frameworks; the accuracy of probabilistic frameworks, such as [7–9], has been discussed by a number of researchers. In [10], the effects of weighting factors (or prediction error variances) on the model updating results in the presence of modeling errors were studied, while reference [11] reported modeling errors to be the major source of incorrect damage identification results of their case study. In [12, 13], the authors proposed model falsification instead of model

I. Behmanesh (✉)
Building Structures, WSP|Parsons Brinckerhoff, New York, NY, USA
e-mail: Iman.Behmanesh@wspgroup.com

S. Yousefianmoghadam • A. Stavridis
Department of Civil and Environmental Engineering, University at Buffalo, Buffalo, NY, USA

A. Nozari • B. Moaveni
Department of Civil and Environmental Engineering, Tufts University, Medford, MA, USA

S. Atamturktur et al. (eds.), *Model Validation and Uncertainty Quantification, Volume 3*, Conference Proceedings of the Society for Experimental Mechanics Series, DOI 10.1007/978-3-319-29754-5_28

identification to overcome the challenges in accounting for modeling errors. A major argument in the last two references is that the estimated structural parameters from Bayesian updating techniques are biased from their true values in the presence of modeling errors.

In a recent study by the authors, the Hierarchical Bayesian model updating technique [14] was introduced. This technique can provide a measure of modeling error statistics in addition to estimating the structural parameters and their variabilities. The objective of this updating process is not limited to the identification of structural parameters and their estimation uncertainties. In the presence of modeling errors, the correct values of structural parameters, assuming they exist, may not be identified correctly in an identification process. They may also be regarded as falsified values in a model falsification process since there is a biased set of parameter values that provides a better fit to the data. In the proposed framework, a probabilistic distribution with unknown mean and covariance matrix is considered for the error function between the data and the model predictions. The parameters of the probabilistic distribution and the structural FE model (usually stiffness or mass parameters) are updated based on the measured structural dynamic responses. Hence, both types of updated parameters (structural and error function) will finally be used for response prediction. By accounting for model uncertainties, a better fit between the model-calculated and the identified modal parameters is obtained, and therefore, more accurate response predictions to future loadings are expected.

The focus of this study is the application of Hierarchical Bayesian model updating to predict the structural response after a known change to the structure. This known change can be caused by observable damage, where a quick decision regarding the operational status of the structure, especially after a major catastrophic event, has to be taken [15]. The known change can also be an enhancement to an existing structure. For retrofit applications [16], practicing engineers might be interested to have more accurate estimations of the structural modal parameters to predict the seismic load demands after retrofit as well as accurate vibration response predictions due to the wind loads [17, 18].

In the following section, the theoretical background of the structural identification and response prediction frameworks are presented. Then, the application to a 10-story concrete building is presented. The initial FE model of the building is first calibrated using modal parameters identified from ambient vibration data. Then the calibrated model is used to predict the modal parameters of the building after six of its concrete walls are removed, representing the known change to the existing structure. To validate the proposed updating framework, the model predicted results are compared with the identified modal parameters obtained from vibration testing of the building after removing the six concrete walls.

28.2 Theory

In structural dynamics [19], the following second order differential equation predicts the motion in terms of the acceleration $\ddot{\mathbf{u}}(\mathbf{t})$, velocity $\dot{\mathbf{u}}(\mathbf{t})$, and the displacement $\mathbf{u}(\mathbf{t})$ of a linear structural system with mass $\mathbf{M}$, damping $\mathbf{C}$, and stiffness $\mathbf{K}$ under a time-dependent load $\mathbf{F}(\mathbf{t})$:

$$\mathbf{M}\ddot{\mathbf{u}}(\mathbf{t}) + \mathbf{C}\dot{\mathbf{u}}(\mathbf{t}) + \mathbf{K}\mathbf{u}(\mathbf{t}) = \mathbf{F}(\mathbf{t}) \tag{28.1}$$

Equation (28.1) suggests that the accuracy of response estimation depends on the accurate forecast of the input excitation $\mathbf{F}(\mathbf{t})$ and the accuracy of the model ($\mathbf{M}$, $\mathbf{C}$, and $\mathbf{K}$). For civil structures, the input excitation $\mathbf{F}(\mathbf{t})$ is mostly caused by seismic or wind loads, and their uncertainties are well-documented in the literature and in design codes [20, 21]. The effects of modeling errors on the accuracy of the prediction responses has been the subject of a number of studies as well [22–25]. However, most of these studies limit the model uncertainties to the inherent variability of the structural parameters, such as Young's modulus, Shear modulus, damping ratios, or material yield strength. Haukaas and Gardoni [26] and Gardoni et al. [24] discuss that the consideration of the uncertainty related to the values of structural parameter is not sufficient for model uncertainty propagation. They highlighted the need for a probabilistic model which can propagate all sources of modeling uncertainties into model-calculated responses. Few examples of modeling error uncertainties that cannot be represented via the variability of the structural parameters include discretization in FE models of continuous structural systems, linear assumption of stiffness properties (can be represented by parameter variability only if nonlinearities are perfectly known) or classical damping assumption in many civil structure applications.

For classically damped systems, Eq. (28.1) can be simplified into N_{nz} equations:

$$\ddot{q}_m(\mathbf{t}) + 2\xi_m\omega_n\dot{q}_m(\mathbf{t}) + \omega_m^2 q_m(\mathbf{t}) = \frac{\boldsymbol{\Phi}_m^T\mathbf{F}(\mathbf{t})}{\boldsymbol{\Phi}_m^T\mathbf{M}\boldsymbol{\Phi}_m} \qquad m = 1 : N_{nz} \tag{28.2}$$

where m is the mode index and N_{nz} is the total number of modes (number of non-zero mass degrees of freedoms), $\omega_m = 2\pi f_m$ is the circular frequency (f_m is natural frequency), ξ_m is modal damping ratio, and $\mathbf{\Phi}_m$ is the mode shape of mode m. In this case, the structural response can be calculated by adding the modal responses:

$$\ddot{\mathbf{u}}(\mathbf{t}) = \sum_{m=1}^{N_{nz}} \mathbf{\Phi}_m \ddot{q}_m(\mathbf{t}), \qquad \dot{\mathbf{u}}(\mathbf{t}) = \sum_{m=1}^{N_{nz}} \mathbf{\Phi}_m \dot{q}_m(\mathbf{t}), \qquad \mathbf{u}(\mathbf{t}) = \sum_{m=1}^{N_{nz}} \mathbf{\Phi}_m q_m(\mathbf{t}) \tag{28.3}$$

If vibration measurements are available, the identified modal parameters, $\tilde{\boldsymbol{\omega}}$, $\tilde{\boldsymbol{\xi}}$, and $\tilde{\mathbf{\Phi}}$ can be directly used in Eqs. (28.2) and (28.3) for response predictions, which will result in accurate predictions for a known excitation force [19]. However, in reality, only the first few modes are accurately identifiable and the identified mode shapes are usually incomplete. Therefore, FE model updating techniques [3] can be used to first calibrate the initial FE model with the available measured/identified data, and then predict the structural responses based on both the identified modal parameters from vibration tests and model-calculated modal parameters of the modes that are not identified from vibration testing. For civil structures the most important response for design and evaluation is the displacement, whose prediction accuracy depends mostly on the first few modes. Therefore, the identification of the first few modes is sufficient in most applications to civil structures. There are few exceptions that the participation of higher modes can become important such as the assessment of the human comfort under wind excitations [27]. The focus of this paper is to predict the structural responses after a known change, while the vibration data is available before the change is applied. In this paper, the state of the structure before the change is referred to as "reference state" and the structure after the change is referred to as "future state".

28.2.1 Model Updating at Reference State

As mentioned in the previous section, the response prediction process starts with the calibration of the initial FE model and estimation of model error uncertainties using the measured data at the reference state. The structural updating parameters (usually stiffness or mass parameters) are shown by $\boldsymbol{\theta}$ and assumed to be distributed as Gaussian with mean $\boldsymbol{\mu}_{\boldsymbol{\theta}}$ and covariance matrix $\boldsymbol{\Sigma}_{\boldsymbol{\theta}}$ to account for structural stiffness/mass variability due to changing environmental/ambient conditions. For simplicity, no correlations are assumed between the structural updating parameters, i.e., $\theta_p \sim N\left(\mu_{\theta_p}, \sigma^2_{\theta_p}\right)$ where the sub-index p refers to the pth structural updating parameter. To account for modeling errors, the misfit between the identified and model-calculated modal parameters is defined by the following error functions for mode m:

$$\frac{\omega_m^2(\boldsymbol{\theta}_t) - \tilde{\omega}_{tm}^2}{\bar{\tilde{\omega}}_m^2} = e_{\omega_{tm}} \qquad m = 1 : N_m \tag{28.4}$$

$$\cos(\varphi_{tm}) \frac{\mathbf{\Gamma}\mathbf{\Phi}_m(\boldsymbol{\theta}_t)}{\|\mathbf{\Gamma}\mathbf{\Phi}_m(\boldsymbol{\theta}_t)\|} - \frac{\tilde{\mathbf{\Phi}}_{tm}}{\left\|\tilde{\mathbf{\Phi}}_{tm}\right\|} = \mathbf{e}_{\mathbf{\Phi}_{tm}} \tag{28.5}$$

In Eqs. (28.4) and (28.5) the sub-index t refers to the data set t, and therefore $\omega_m(\boldsymbol{\theta}_t)$ and $\mathbf{\Phi}_m(\boldsymbol{\theta}_t)$ are the model-calculated circular frequency and model shape of mode m given $\boldsymbol{\theta}_t$, where $\boldsymbol{\theta}_t$ is the value of structural parameters during the collection of data set t. The quantities $\tilde{\omega}_{tm}$ and $\tilde{\mathbf{\Phi}}_{tm}$ are the identified circular frequency and mode shape of mode m from data set t, and $\bar{\tilde{\omega}}_m$ is the average of identified circular frequencies. N_m is the total number of available identified modes, the matrix $\mathbf{\Gamma}$ picks the measured mode shape components, and finally φ_{tm} is the angle between identified and model-calculated mode shapes:

$$\cos(\varphi_{tm}) = \frac{\tilde{\mathbf{\Phi}}_{tm}^T \cdot (\mathbf{\Gamma}\mathbf{\Phi}_m(\boldsymbol{\theta}_t))}{\|\mathbf{\Gamma}\mathbf{\Phi}_m(\boldsymbol{\theta}_t)\| \left\|\tilde{\mathbf{\Phi}}_{tm}\right\|} \tag{28.6}$$

As described in [28], the error functions (28.4) and (28.5) provide a bridge between the actual structural responses and the responses predicted by the FE model. The mode shape error function of Eq. (28.5) is the same as the function originally used in [14], written in a different format. The eigenvalue error function of Eq. (28.4) however, is slightly different from [14]. The eigenvalue error function of this study is easier to implement in response prediction applications.

The error functions are modeled as Gaussian distributions [28–30]:

$$\mathbf{e}_t = \begin{bmatrix} \mathbf{e}_{\omega_t} \\ \mathbf{e}_{\mathbf{\Phi}_t} \end{bmatrix} \sim N\left(\boldsymbol{\mu}_{\mathbf{e}}, \boldsymbol{\Sigma}_{\mathbf{e}}\right) \tag{28.7}$$

The number of independent updating parameters in $\boldsymbol{\mu}_{\mathbf{e}}$ and $\boldsymbol{\Sigma}_{\mathbf{e}}$ can be defined by the analyst. Without introducing any constrains, $\boldsymbol{\mu}_{\mathbf{e}}$ should be considered as a full vector and $\boldsymbol{\Sigma}_{\mathbf{e}}$ as a full matrix with all their components considered as updating parameters. However, this approach increases the computational cost and complicates the response prediction process.

If the correlations between the error functions are not considered, the error functions can be written as:

$$e_{\omega_{tm}} \sim N\left(\mu_{\omega_m},\ \sigma^2_{\omega_m}\right) \tag{28.8}$$

$$\mathbf{e}_{\mathbf{\Phi}_{tm}} \sim N\left(\boldsymbol{\mu}_{\mathbf{\Phi}_m},\ diag\left(\sigma^2_{\phi_{m1}}, \ldots,\ \sigma^2_{\phi_{ms}}, \ldots\right)\right) \qquad s = 1 : N_s \tag{28.9}$$

where $\sigma^2_{\phi_{ms}}$ is the variance of sth mode shape component error of mth mode. N_s is the total number of identified mode shape components which is essentially equal to the number of sensors. In the following two subsections, the updating process is presented when the error means are considered in the updating process, followed by the case where the error functions are considered as zero mean.

28.2.1.1 Updating with Non-zero Mean Error Functions

The posterior joint probability distribution of all the updating model parameters can be written as:

$$p\left(\mathbf{\Theta},\ \boldsymbol{\mu}_{\boldsymbol{\theta}}, \boldsymbol{\Sigma}_{\boldsymbol{\theta}}, \boldsymbol{\mu}_{\mathbf{e}}, \boldsymbol{\Sigma}_{\mathbf{e}} \middle| \tilde{\boldsymbol{\omega}}^2, \tilde{\mathbf{\Phi}}\right) \propto \prod_{t=1}^{N_t} \prod_{m=1}^{N_m} p\left(\tilde{\omega}^2_{tm}, \tilde{\mathbf{\Phi}}_{tm} \middle| \boldsymbol{\theta}_t, \boldsymbol{\mu}_{\mathbf{e}}, \boldsymbol{\Sigma}_{\mathbf{e}}\right) p\left(\boldsymbol{\theta}_t \middle| \boldsymbol{\mu}_{\boldsymbol{\theta}}, \boldsymbol{\Sigma}_{\boldsymbol{\theta}}\right) p\left(\boldsymbol{\mu}_{\boldsymbol{\theta}}\right) p\left(\boldsymbol{\Sigma}_{\boldsymbol{\theta}}\right) p\left(\boldsymbol{\mu}_{\mathbf{e}}\right) p\left(\boldsymbol{\Sigma}_{\mathbf{e}}\right) \tag{28.10}$$

where $\Theta = \{\boldsymbol{\theta}_1, \ldots,\ \boldsymbol{\theta}_t, \ldots,\ \boldsymbol{\theta}_{N_t}\}$, and N_t is the total number of available data sets. Note that the two covariance matrixes $\boldsymbol{\Sigma}_{\boldsymbol{\theta}}$ and $\boldsymbol{\Sigma}_{\mathbf{e}}$ do not have any non-diagonal terms, $\boldsymbol{\Sigma}_{\boldsymbol{\theta}}$ includes N_p variance terms of $\sigma^2_{\theta_p}$, and $\boldsymbol{\Sigma}_{\mathbf{e}}$ includes N_m variance terms of eigenvalue errors $\sigma^2_{\omega_m}$ and $N_s \times N_m$ mode shape error variances $\sigma^2_{\phi_{ms}}$. In Eq. (28.10), $p\left(\tilde{\omega}^2_{tm}, \tilde{\mathbf{\Phi}}_{tm} \middle| \boldsymbol{\theta}_t, \boldsymbol{\mu}_{\mathbf{e}}, \boldsymbol{\Sigma}_{\mathbf{e}}\right)$ is the likelihood function, assessing the probability of how plausible model parameters $\boldsymbol{\theta}_t$, $\boldsymbol{\mu}_{\mathbf{e}}$ and $\boldsymbol{\Sigma}_{\mathbf{e}}$ represent the data $\tilde{\omega}^2_{tm}$ and $\tilde{\mathbf{\Phi}}_{tm}$. As already mentioned, the prior $p\left(\boldsymbol{\theta}_t \middle| \boldsymbol{\mu}_{\boldsymbol{\theta}}, \boldsymbol{\Sigma}_{\boldsymbol{\theta}}\right)$ is considered to be a Gaussian distribution $N\left(\boldsymbol{\theta}_t \middle| \boldsymbol{\mu}_{\boldsymbol{\theta}}, \boldsymbol{\Sigma}_{\boldsymbol{\theta}}\right)$. Uninformative priors are assumed for $\boldsymbol{\mu}_{\boldsymbol{\theta}}$ and $\boldsymbol{\mu}_{\mathbf{e}}$, i.e., $p\left(\boldsymbol{\mu}_{\boldsymbol{\theta}}\right) p\left(\boldsymbol{\mu}_{\mathbf{e}}\right) \propto 1$, and an Inverse-Gamma distribution is considered for the variance terms, $p\left(\sigma^2_{\theta_p}\right) = Inverse\ Gamma\left(\alpha, 1/\beta\right)$, $p\left(\sigma^2_{\omega_m}\right) = Inverse\ Gamma\left(\alpha_e, 1/\beta_e\right)$ and $p\left(\sigma^2_{\Phi_{ms}}\right) = Inverse\ Gamma\left(\alpha_e, 1/\beta_e\right)$ [29].

It can be shown that the Maximum A Priori (MAP) estimates of the updating parameters can be written as:

$$\widehat{\boldsymbol{\theta}}_t = Arg \min_{\boldsymbol{\theta}_t} \left(\left(\mathbf{e}_t - \widehat{\boldsymbol{\mu}}_{\mathbf{e}}\right)^T \widehat{\boldsymbol{\Sigma}}_{\mathbf{e}}^{-1} \left(\mathbf{e}_t - \widehat{\boldsymbol{\mu}}_{\mathbf{e}}\right) + \left(\boldsymbol{\theta}_t - \widehat{\boldsymbol{\mu}}_{\boldsymbol{\theta}}\right)^T \widehat{\boldsymbol{\Sigma}}_{\boldsymbol{\theta}}^{-1} \left(\boldsymbol{\theta}_t - \widehat{\boldsymbol{\mu}}_{\boldsymbol{\theta}}\right) \right) \tag{28.11}$$

$$\widehat{\boldsymbol{\mu}}_{\boldsymbol{\theta}} = \frac{1}{N_t} \sum_{t=1}^{N_t} \widehat{\boldsymbol{\theta}}_t \tag{28.12}$$

$$\widehat{\sigma}^2_{\theta_p} = \frac{\frac{2}{\beta} + \sum_{t=1}^{N_t} \left(\widehat{\theta}_{tp} - \widehat{\mu}_{\theta_p}\right)^2}{N_t - 2 + 2\alpha} \qquad p = 1 : N_p \tag{28.13}$$

$$\widehat{\boldsymbol{\mu}}_{\mathbf{e}} = \frac{1}{N_t} \sum_{t=1}^{N_t} \widehat{\mathbf{e}}_t \tag{28.14}$$

$$\widehat{\sigma}^2_{\omega_m} = \frac{\frac{2}{\beta_e} + \sum_{t=1}^{N_t} \left(\widehat{e}_{\omega_{tm}} - \widehat{\mu}_{\omega_m}\right)^2}{N_t - 2 + 2\alpha_e} \qquad m = 1 : N_m$$

$$\widehat{\sigma}^2_{\phi_{ms}} = \frac{\frac{2}{\beta_e} + \sum_{t=1}^{N_t} \left(\widehat{e}_{\phi_{tms}} - \widehat{\mu}_{\phi_{ms}}\right)^2}{N_t - 2 + 2\alpha_e} \qquad m = 1 : N_m \quad s = 1 : N_s \tag{28.15}$$

The final solution for the parameters in Eqs. (28.11)–(28.15) is achieved through multiple iterations. More information can be found in [14].

28.2.1.2 Updating with Zero Mean Error Functions

In a similar manner, if the mean of the error functions is set to zero, the analytical expressions become:

$$\widehat{\boldsymbol{\theta}}_t = Arg \min_{\boldsymbol{\theta}_t} \left(\mathbf{e}_t^T \, \widehat{\boldsymbol{\Sigma}}_{\mathbf{e}}^{-1} \, \mathbf{e}_t + (\boldsymbol{\theta}_t - \widehat{\boldsymbol{\mu}}_{\boldsymbol{\theta}})^T \widehat{\boldsymbol{\Sigma}}_{\boldsymbol{\theta}}^{-1} \, (\boldsymbol{\theta}_t - \widehat{\boldsymbol{\mu}}_{\boldsymbol{\theta}}) \right) \tag{28.16}$$

$$\widehat{\boldsymbol{\mu}}_{\boldsymbol{\theta}} = \frac{1}{N_t} \sum_{t=1}^{N_t} \widehat{\boldsymbol{\theta}}_t \tag{28.17}$$

$$\widehat{\sigma}^2_{\theta_p} = \frac{\frac{2}{\beta} + \sum_{t=1}^{N_t} \left(\widehat{\theta}_{tp} - \widehat{\mu}_{\theta_p}\right)^2}{N_t - 2 + 2\alpha} \qquad p = 1 : N_p \tag{28.18}$$

$$\widehat{\sigma}^2_{\omega_m} = \frac{\frac{2}{\beta_e} + \sum_{t=1}^{N_t} \widehat{e}^2_{\omega_{tm}}}{N_t - 2 + 2\alpha_e} \qquad m = 1 : N_m$$

$$\widehat{\sigma}^2_{\phi_{ms}} = \frac{\frac{2}{\beta_e} + \sum_{t=1}^{N_t} \widehat{e}^2_{\phi_{tms}}}{N_t - 2 + 2\alpha_e} \qquad m = 1 : N_m \quad s = 1 : N_s \tag{28.19}$$

Similar to the previous section, the final MAP values can be estimated through an iterative procedure. By comparing Eqs. (28.15) and (28.19), it can be inferred that excluding the error means results in higher error variances $\sigma^2_{\omega_m}$ and $\sigma^2_{\phi_{ms}}$. Hence, by setting the error mean values to zero, the error variance terms will increase to compensate for the bias. Therefore it is expected that more conservative variance estimates are obtained if $\boldsymbol{\mu}_{\mathbf{e}} = 0$. Due to the complexity of modeling errors, there is no guarantee that the FE model, calibrated based on the data at the reference state, would have the same bias $\boldsymbol{\mu}_{\mathbf{e}}$ at the future state. If $\boldsymbol{\mu}_{\mathbf{e}}$ is considered as an updating parameter, the improvement of prediction accuracies at the future state depends on the difference of the bias at the current and future states.

28.2.2 Prediction at Future State

The updated FE model of the previous section is used here for predicting the modal parameters at the future state. As it can be inferred from Eq. (28.2), for a given excitation load, accurate predictions can be obtained if the modal parameters are predicted accurately at the future state. From model updating process of previous section, we have the updated structural parameters $\theta_p \sim N\left(\widehat{\mu}_{\theta_p}, \widehat{\sigma}^2_{\theta_p}\right)$ for $p = 1{:}N_p$. Moreover, the model updating process gives a measure of modeling errors; represented by the error functions of Eqs. (28.4) and (28.5), and modeled by a multivariate Gaussian distribution $\mathbf{e} \sim N\left(\widehat{\boldsymbol{\mu}}_{\mathbf{e}}, \widehat{\boldsymbol{\Sigma}}_{\mathbf{e}}\right)$. Therefore, based on the model updating procedure of Sect. 28.3.1, the mth eigenvalue of the structure at the future state FS can be estimated as:

$$\left(\tilde{\omega}_m^{FS}\right)^2 = \omega_m^2 \left(\boldsymbol{\theta} \middle| \boldsymbol{\rho}, \, \widehat{\boldsymbol{\mu}}_{\boldsymbol{\theta}}, \, \widehat{\boldsymbol{\Sigma}}_{\boldsymbol{\theta}}\right) - \overline{\tilde{\omega}}_m^2 \times \left(e_{\omega_m} \middle| \widehat{\mu}_{\omega_m}, \, \widehat{\sigma}^2_{\omega_m}\right) \qquad m = 1 : N_m \tag{28.20}$$

where the known changes in structural mass and/or stiffness properties in the state *FS* is shown by $\boldsymbol{\rho}$. In Eq. (28.20), $\boldsymbol{\theta}\left|\boldsymbol{\rho},\ \widehat{\boldsymbol{\mu}}_{\boldsymbol{\theta}},\ \widehat{\boldsymbol{\Sigma}}_{\boldsymbol{\theta}}\right.$ represents Monte Carlo simulations of $\boldsymbol{\theta}$ from $N\left(\widehat{\boldsymbol{\mu}}_{\boldsymbol{\theta}},\ \widehat{\boldsymbol{\Sigma}}_{\boldsymbol{\theta}}\right)$ after changes $\boldsymbol{\rho}$ are applied to the updated FE model. Also $e_{\omega_m}\left|\widehat{\mu}_{\omega_m},\ \widehat{\sigma}^2_{\omega_m}\right.$ represents Monte Carlo simulations of e_{ω_m} from $N\left(\widehat{\mu}_{\omega_m},\ \widehat{\sigma}^2_{\omega_m}\right)$. Note that if a mode is not identified from the vibration data and/or is not included in the updating process of Sect. 28.3.1, no posterior values for μ_{ω_m} and $\sigma^2_{\omega_m}$ would be available. Therefore, the μ_{ω_m} and $\sigma^2_{\omega_m}$ of unidentified eigenvalues rely on the prior information and engineering judgement.

Similarly, the *m*th mode shape of the structure at the observed DOFs of the state *FS* can be estimated as:

$$\tilde{\boldsymbol{\Phi}}_m^{FS} = \cos\left(\varphi_m\right)\frac{\boldsymbol{\Gamma}\boldsymbol{\Phi}_m\left(\boldsymbol{\theta}\left|\boldsymbol{\rho},\ \widehat{\boldsymbol{\mu}}_{\boldsymbol{\theta}},\ \widehat{\boldsymbol{\Sigma}}_{\boldsymbol{\theta}}\right.\right)}{\left\|\boldsymbol{\Gamma}\boldsymbol{\Phi}_m\left(\boldsymbol{\theta}\left|\boldsymbol{\rho},\ \widehat{\boldsymbol{\mu}}_{\boldsymbol{\theta}},\ \widehat{\boldsymbol{\Sigma}}_{\boldsymbol{\theta}}\right.\right)\right\|} - \left(\mathbf{e}_{\boldsymbol{\Phi}_m}\left|\boldsymbol{\mu}_{\boldsymbol{\Phi}_m},\ diag\left(\sigma^2_{\phi_{m1}},\ldots,\ \sigma^2_{\phi_{ms}},\ldots\right)\right.\right) \tag{28.21}$$

The model error parameters of the mode shape components at unmeasured DOFs or the unidentified mode shapes should be estimated based on engineering judgement and prior information.

As already mentioned, the correlations can potentially be included in the updating process. However, including the correlations between the error functions adds $N_m\left(N_s+1\right)\left(N_m\left(N_s+1\right)-1\right)/2$ updating parameters, which increases both the computational cost and the estimation uncertainties of the updating parameters.

28.3 Application to a 10 Story Concrete Building

28.3.1 Ten-Story Concrete Building and Instrumentation

The structure, shown in Fig. 28.1 was a 10-story, eight-bay by four-bay concrete building with a slab-column structural system and reinforced concrete infill walls in the exterior bays. The building, constructed in 1914, was located in Utica, NY and was used as a warehouse before it was slated to be demolished to allow the construction of a new highway bridge. The plan view dimensions of the building were 24.4 m by 48.8 m (80 ft. by 160 ft.) while the story height was 259 cm (8′6″). Figure 28.2 presents the building plan view of a typical story. As shown in the figure, the bays had the same length in both directions of the building. The concrete columns in the building were circular in the interior, and rectangular along

Fig. 28.1 Building view from south west corner

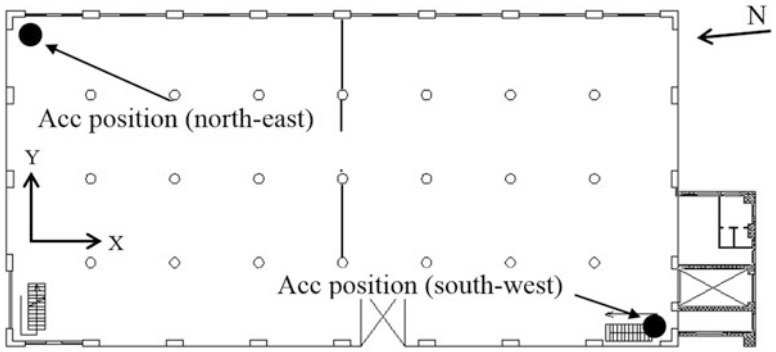

Fig. 28.2 Plan view of second story showing removed walls and acceleration position in each story

Table 28.1 The identified and model-calculated natural frequencies at structural reference state

	Model 1		Mode 2		Mode 3	
	Mean	Standard deviation	Mean	Standard deviation	Mean	Standard deviation
Identified natural frequencies	2.2325	0.0092	3.3318	0.0128	4.6704	0.0370
MAC between identified and initial FE model mode shapes	0.9806	0.0040	0.9835	0.0053	0.9735	0.0043
Natural frequencies of initial FE model	2.2635		3.5000		4.7807	

the perimeter, except for the corner columns which had L-shape sections. Due to the lack of beams, all columns had corbels at their connections to the slab above. Flat slabs, having a thickness of 22.9 cm (9 in.), with drop panel at the location of columns were used in the structure. The RC walls in the perimeter bays of the building had a thickness of 20.3 cm (8 in.). Some of the walls initially had window openings. The majority of these openings were later infilled with concrete masonry units, while in some of the walls, portion of the window had been filled with clay masonry assemblies. More information can be found in [31].

The acceleration along the vertical and the two horizontal directions at two locations of every slab except the roof were recorded with force-balance accelerometers. The accelerometers were installed near the North-West (NW) and South-East (SE) corners as indicated in Fig. 28.2. This configuration was selected in order to monitor both the translational and torsional motions. Overall, 302 sets of 5-min ambient vibration data are available, 50 of which are used in this paper. NExT-ERA technique [32] is used to extract the modal parameters from ambient vibration data. Table 28.1 presents the statistics of the identified natural frequencies, and Fig. 28.3 shows the average of the identified mode shapes of the first three modes.

28.3.2 Future Structural State

The considered change to the existing building shown in Fig. 28.1 is the removal of six concrete walls, shown in Fig. 28.4. Overall 22 sets of 5-min ambient vibration data are collected from the building at this state, however, they are be used to update the structural models. The identified modal parameters of the building at this state are only used to validate the response prediction methodology of this paper. The statistics of the identified natural frequencies at this state are reported in Table 28.2.

28.3.3 Initial FE Model

An initial FE model of the structure is created using SAP2000 [33], and FEDEASLAB [34, 35]. This model includes 2914 nodes, 2555 frame elements and 2593 shell elements. The slab floors are modeled as beams [36] to simplify the FE model. The natural frequencies of the initial model are reported in Table 28.1. Note that no statistics are provided for the natural frequencies as they are obtained from a deterministic FE model. The statistics of the MAC values over the 50 sets of the identified mode shapes and the mode shapes of the initial model are also reported in Table 28.1. As it can be seen, the

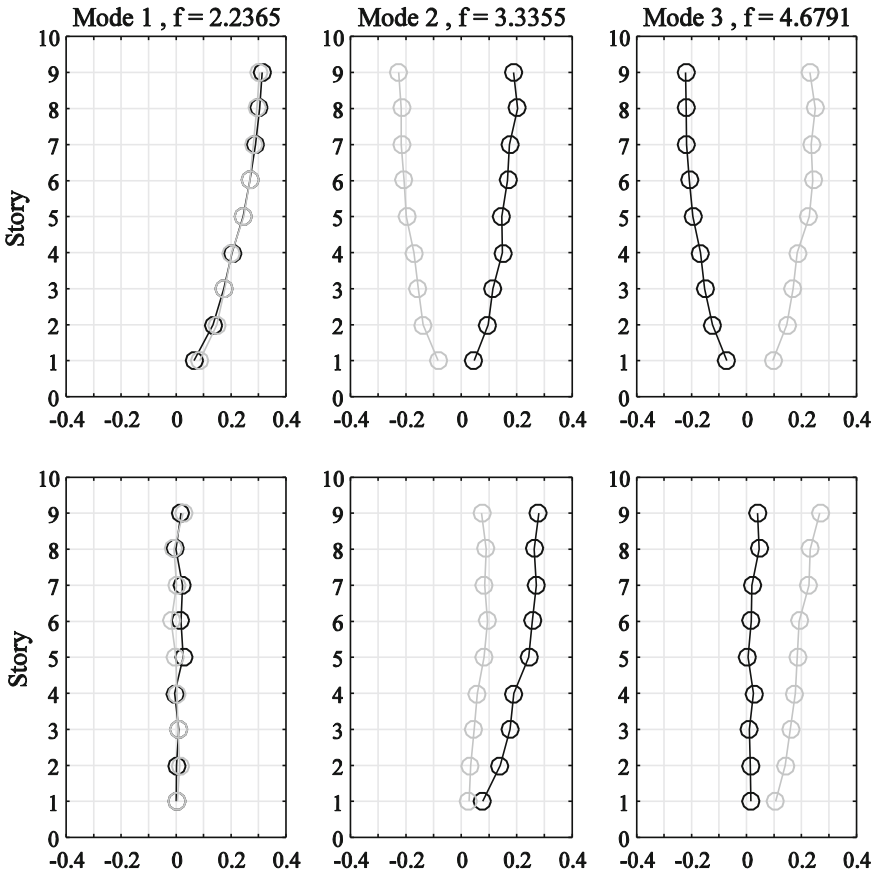

Fig. 28.3 Average of the identified mode shapes of the first three modes; *black SW corner*, *gray NE corner*; *top three* subplots Y components, *bottom three* subplots X components

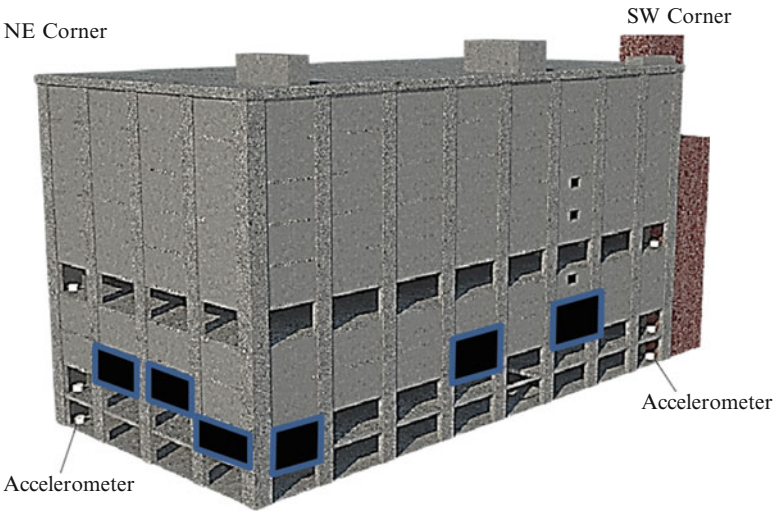

Fig. 28.4 Building in the future state; the removed walls are shown by *black*

frequencies calculated using the initial model are in relatively good agreement with their identified counterparts but still discrepancies can be observed. Table 28.2 reports the modal parameters of the building after the removal of the six walls shown in Fig. 28.4.

Two structural updating parameters are defined in this application ($N_p = 2$): the effective Young's modulus of all the exterior walls and the effective Young's modulus of the slab beams. The term "effective" for the exterior walls refers to

Table 28.2 The identified and model-calculated natural frequencies at structural future state

	Model 1		Mode 2		Mode 3	
	Mean	Standard deviation	Mean	Standard deviation	Mean	Standard deviation
Identified natural frequencies	2.1039	0.0044	3.0992	0.0107	4.6551	0.0335
MAC between identified and initial FE model mode shapes	0.9898	0.0016	0.9852	0.0075	0.9792	0.0017
Natural frequencies of initial FE model	2.0980		3.1828		4.7058	

Table 28.3 Updating results for the three model updating cases

	E of exterior walls		E of slab beams		Eigenvalue error means			Eigenvalue error standard deviations		
Parameters	$\widehat{\mu}_{\theta_1}$	$\widehat{\sigma}_{\theta_1}$	$\widehat{\mu}_{\theta_2}$	$\widehat{\sigma}_{\theta_2}$	$\widehat{\mu}_{\omega_1}$	$\widehat{\mu}_{\omega_2}$	$\widehat{\mu}_{\omega_3}$	$\widehat{\sigma}_{\omega_1}$	$\widehat{\sigma}_{\omega_2}$	$\widehat{\sigma}_{\omega_3}$
Case I	0.7380	0.0224	1.6799	0.1287	N.C.[a]	N.C.	N.C.	0.0046	0.0221	0.1674
Case II	0.7651	0.0180	1.5508	0.0917	N.C.	N.C.	−0.1437	0.0046	0.0288	0.0107
Case III	0.8573	0.0158	1.2150	0.0910	N.C.	0.0546	−0.0694	0.0098	0.0075	0.0050

N.C. not considered

the fact that some parts of the exterior walls are made from clay or concrete masonry material. Differentiating the two was not feasible at the site and therefore, the walls are modeled with the constant material properties with an effective Young's modulus. The effective Young's modulus of the slab beams reflects the effect of both the Young's modulus of concrete material of the slab and the effective width of the slab beams. The width of the slab beams in the initial FE model is considered as 6.1 and 12.2 m for the exterior and interior beams respectively.

28.3.4 Model Updating

The initial FE model of the building is calibrated given 50 sets of identified modal parameters. Three different probability distribution models are considered for the error functions, and therefore three different updating cases are examined. The updating results of the three updating cases are presented in Table 28.3. In Case I, all the error functions are modeled as zero-mean Gaussian, which results in 111 (3 eigenvalue, 3×36 mode shape components) error variance updating parameters in addition to structural parameters. Case II includes the mean of the third mode eigenvalue as an updating parameter, yet all other error functions are modeled as zero-mean Gaussian. This case have 111 variance and one mean error updating parameters. In Case III, all the 111 error variances and the mean of eigenvalue error of mode 2 and 3 are considered as updating parameters.

The reduction of $\widehat{\sigma}_{\omega_3}$ value in case II (or III) compared to case I is due to including of the error mean μ_{ω_3} as an updating parameter in Case II/III. Similar trend can be observed for $\widehat{\sigma}_{\omega_2}$ values of Cases II and III, reduction in Case III is due to addition of μ_{ω_2} in the updating process. The most drastic changes to the structural updating hyper-parameters ($\boldsymbol{\mu}_{\boldsymbol{\theta}}$ and $\boldsymbol{\Sigma}_{\boldsymbol{\theta}}$) are observed in Case I, i.e., the change of the structural parameters is larger compared to their initial values when the error means are set to zero. Note that all cases including the initial FE model can be used for response prediction. The difference is in the uncertainty of model-calculated responses. Figure 28.5 shows the identified frequencies from the available 302 sets of data versus the frequencies generated from the three model updating cases through Eq. (28.20). Seven hundred Monte Carlo samples are generated. It can be seen that the identified frequencies fall in the high probability region of the predictions although only 50 data sets are used to calibrate the model parameters.

To highlight the effects of modeling error parameters, the frequencies are also generated using the updated FE model only and the results are shown in Fig. 28.6. In this figure only the first term of the right hand side of Eq. (28.20) is considered. It can be observed that variability of the FE model frequencies are similar to the variability of the identified frequencies from the ambient vibration tests. However, there is a considerable bias between the data and FE-model results; in the proposed model updating framework, this bias is modeled as a random variable by Eqs. (28.8) and (28.9).

The updated FE model in the three cases can predict the first mode frequencies better than the frequencies of mode 2 or 3. The third mode seems to be the most inaccurate mode. The uncertainties of the predicted frequencies of mode 3 in Case I is very high, meaning that Case I is not a suitable model. This effect is due to high misfit between the frequencies calculated by the FE model and the identified frequencies as shown in Fig. 28.6. This problem can be resolved either by including more structural parameters in the updating framework or by including the mean of the error function of this mode as an updating parameter. Usually the former is recommended, however in this paper the latter is considered. The uncertainties of the predicted frequencies for the third mode are in an acceptable range in Case II and Case III. The comparison of the

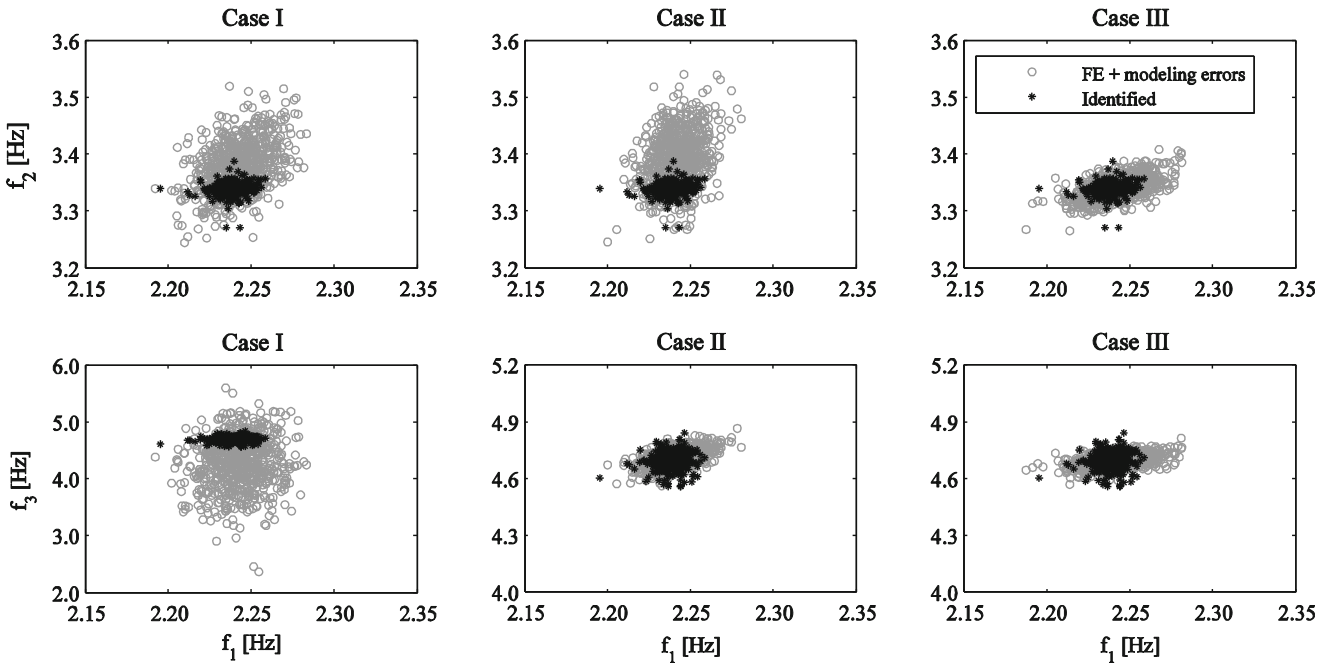

Fig. 28.5 Predicted versus identified frequencies considering variability of structural parameters and modeling errors at the reference state

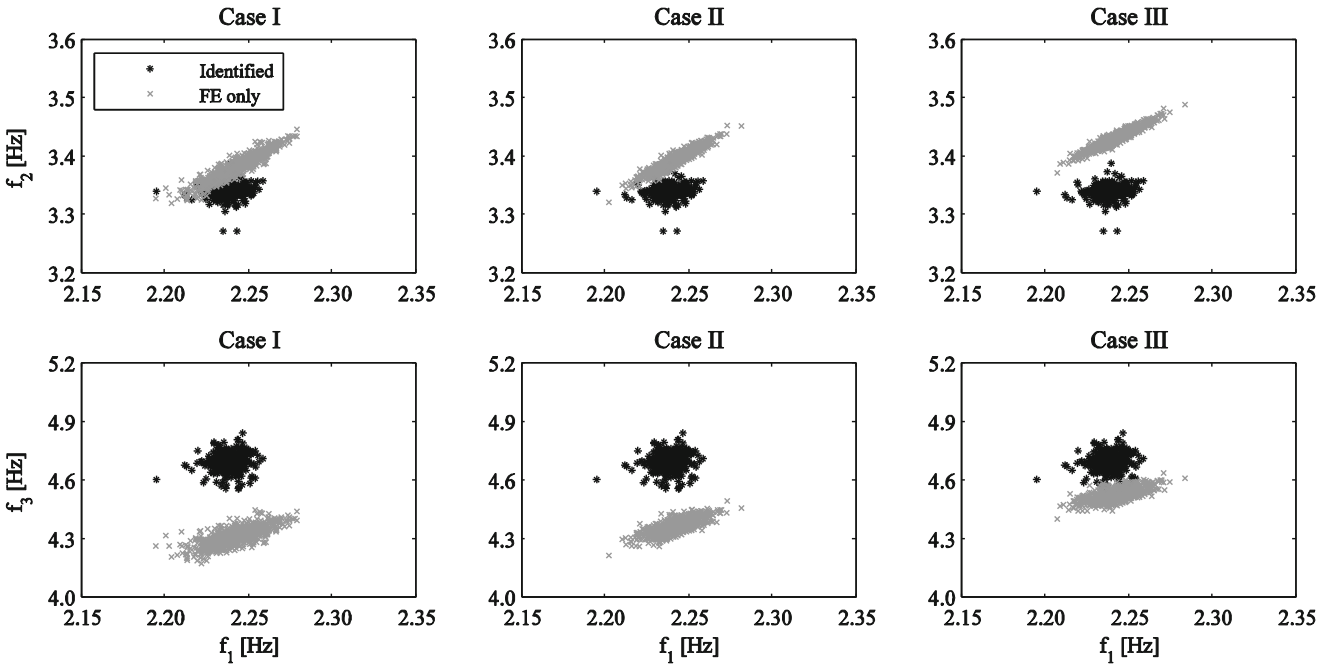

Fig. 28.6 Predicted versus identified frequencies considering the variability of structural parameters at the reference state

uncertainties of the predicted frequencies indicates that Case III leads to the best fit to the data. In the next section the ability to predict the modal parameters at a state that the model is not calibrated at is examined (model extrapolation).

28.3.5 Prediction at Future State

The three updated models are used to predict the modal parameters of the structure after the six exterior walls are removed. Figure 28.7 shows the model-calculated natural frequencies versus those identified from vibration testing. Figure 28.8

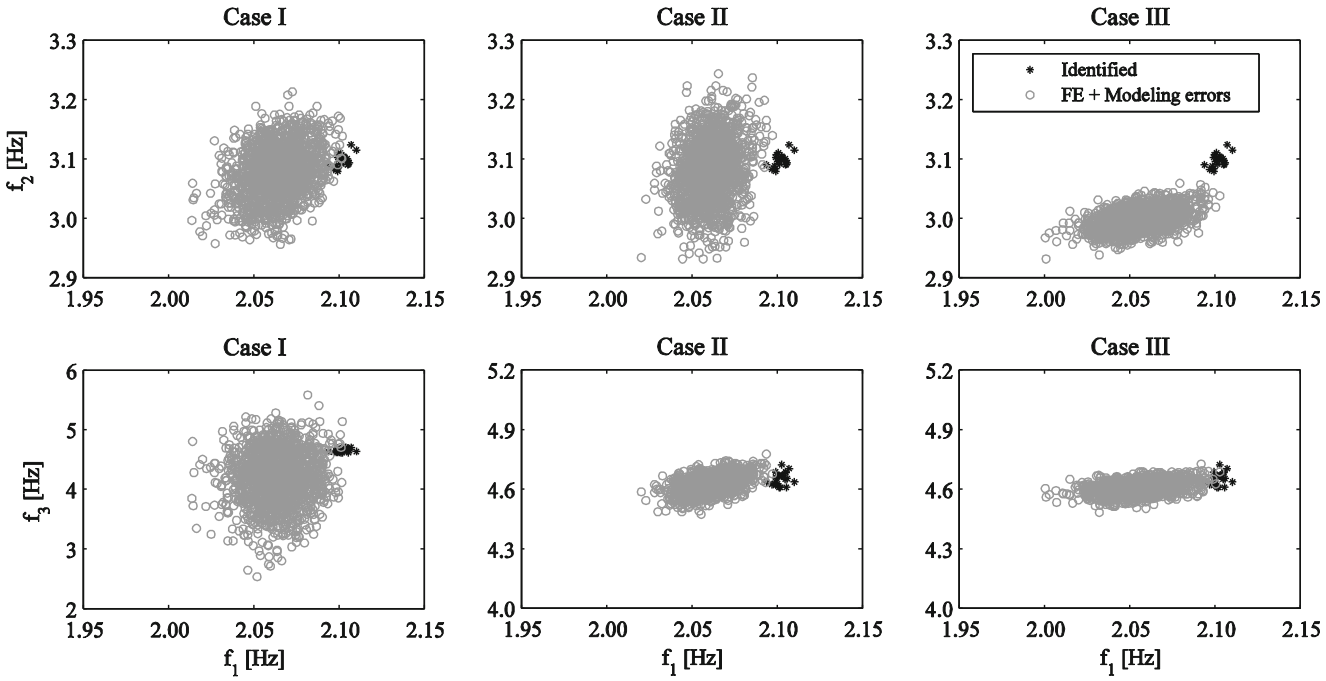

Fig. 28.7 Predicted versus identified frequencies considering variability of structural parameters and modeling errors at the future state

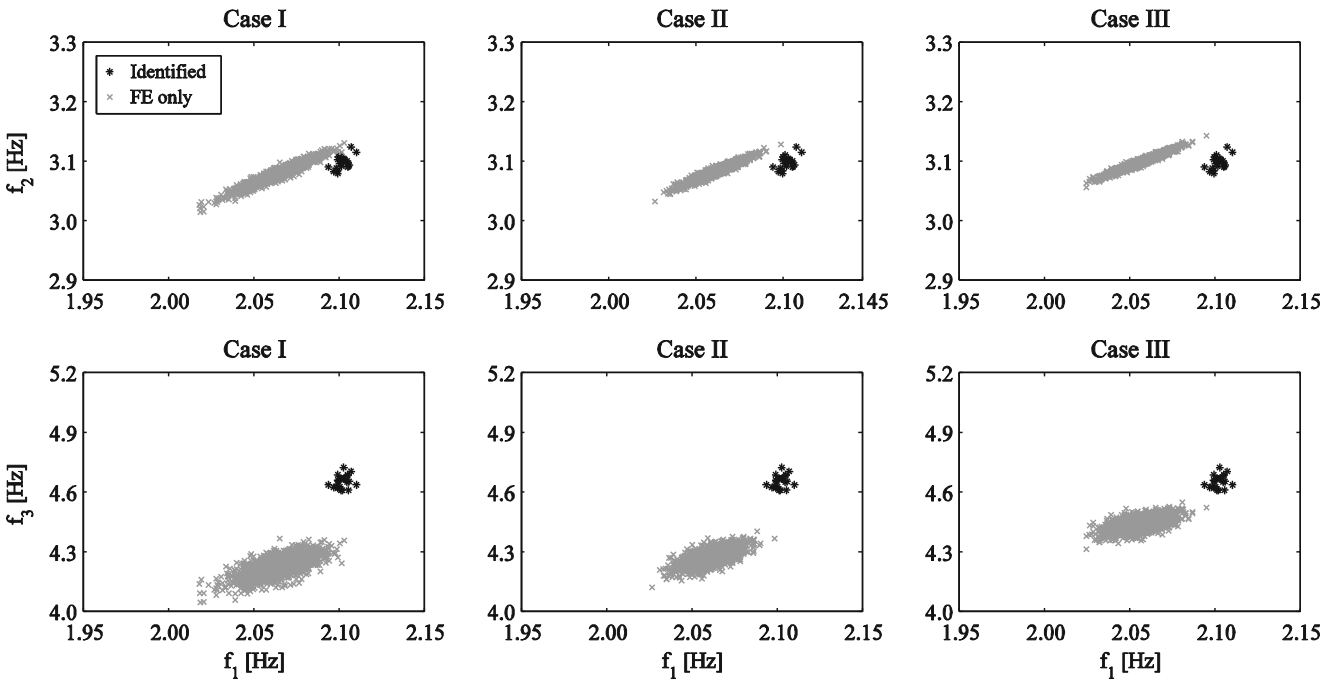

Fig. 28.8 Predicted versus identified frequencies considering variability of structural parameters and modeling errors at the future state

presents the results when only the variability of structural parameters is considered. The number of generated Monte Carlo samples is 1500. Similar to Fig. 28.5, the predicted frequencies of the third mode in Case I have inflated uncertainties to account for the bias which is not considered in the updating process. Cases II and III provide good estimates on the frequencies of both the first and third modes. However, it is not easy to judge which case provides a better estimation for the second mode. Although all the identified 22 sets of natural frequencies of mode 2 fall in the high probability region of Case II prediction, there is almost 0.05 Hz bias in the predictions of Case III. On the other hand the prediction uncertainties of Case II are higher than Case III. Hence, selecting one over the other is a subjective decision. This effect is due to the

difference of prediction bias at the two structural states. By comparing the first subplots of Figs. 28.6 and 28.8, it can be seen that the FE model overestimates the frequency of the second mode in the reference state, while the frequencies are slightly underestimated in the future state predictions. This observation indicates that including the error function means (bias) in the updating process may not always improve the predictions accuracies. In this case, the predictions accuracies depend on the difference between modeling errors in the reference and future states for each mode.

28.4 Summary and Conclusion

A new response prediction framework based on probabilistically calibrated FE models through Hierarchical Bayesian model updating is presented in this paper. The framework is applied to a ten-story concrete building using its identified modal parameters from ambient vibration measurements. It is demonstrated that the calibrated FE models alone may not lead to accurate predictions, and the uncertainties in the model parameters as well as the uncertainties due to the modeling errors should also be included in the predictions. The modeling errors are represented by Gaussian error functions, and defined as the difference between the FE model-calculated and the identified natural frequencies and mode shapes. Two updating formulations have been presented considering zero-mean (unbiased) and non-zero mean (biased) error functions. In the application of the proposed framework to the 10-story building, the structural parameters of the initial FE model are calibrated first and error functions from the measured data at the reference state of structure. Three different calibrated models are created based on three different error function definitions: (I) considering all the error mean values as zero and updating the error variances only, (II) including the error mean of the third eigenvalue in the updating process in addition to the variance terms of all the error functions, and (III) including the error mean of the second and the third mode in addition to all the variance terms. The calibrated models are then used to predict the modal parameters at a different structural state, referred to as "future state" in this paper. Six exterior walls are removed from the structure at the future state.

The results show that if the bias between the data and FE model at the reference state is significant, excluding the error mean values from the updating process will result in large uncertainties in the predicted frequencies. In this case, the inflated error variances compensate for the modeling error bias. When the error mean of the third mode is included in the updating process (Case II), the identified frequencies at the future state fall in the high probability region of the predictions, and reasonable posterior uncertainties are observed in the predicted results. Including the error mean of this mode significantly reduces the error variance of this error function. However, including the error means as updating parameter may not always improve the accuracy of the predictions. Due to complexity of the modeling errors, there is no guarantee that the structural FE models have identical error means at two different states. For the building considered in this study, the FE model overestimates the frequency of the second mode at the reference state, while slightly underestimates this frequency at the future state. Therefore, it is recommended to exclude the error function means in the updating process unless the estimated uncertainty of the model prediction results from zero-mean error functions is not within acceptable ranges.

Acknowledgment The study presented here is part of a project supported by the National Science Foundation (Grant No. 1430180). The collaboration of NEES@UCLA during the planning and execution stages of the experiments is sincerely acknowledged. The authors would also like to thank the New York State Department of transportation (NYSDOT) personnel and their director Andrew Roberts for allowing the execution of these tests and for their remarkable cooperation in every part of the experiment. The supports from Tufts Technology Services, and Mr. Fatih Yalniz Vice President at WSP|PB are highly appreciated. The opinions expressed in this paper are those of the authors and do not necessarily represent those of the sponsor or the collaborators.

References

1. Li, Q.S., Wu, J.R.: Correlation of dynamic characteristics of a super-tall building from full-scale measurements and numerical analysis with various finite element models. Earthq. Eng. Struct. Dyn. **33**, 1311–1336 (2004)
2. Rahimian, A., Hiller, K.: Rising high in Manhattan, Trump World Tower, the tallest residential building in the world. CTBUH J. Fall 10–13 (2004)
3. Friswell, M.I., Mottershead, J.E.: Finite Element Model Updating in Structural Dynamics. Kluwer, Boston/Dordrecht (1995)
4. Goller, B., Schueller, G.: Investigation of model uncertainties in Bayesian structural model updating. J. Sound Vib. **330**, 6122–6136 (2011)
5. Živanović, S., Pavic, A., Reynolds, P.: Finite element modelling and updating of a lively footbridge: the complete process. J. Sound Vib. **301**, 126–145 (2007)
6. Wu, J., Li, Q.: Finite element model updating for a high-rise structure based on ambient vibration measurements. Eng. Struct. **26**, 979–990 (2004)

7. Beck, J.L., Katafygiotis, L.S.: Updating models and their uncertainties. I: Bayesian statistical framework. J. Eng. Mech. ASCE **124**, 455–461 (1998)
8. Vanik, M.W., Beck, J.L., Au, S.K.: Bayesian probabilistic approach to structural health monitoring. J. Eng. Mech. ASCE **126**, 738–745 (2000)
9. Sohn, H., Law, K.H.: A Bayesian probabilistic approach for structure damage detection. Earthq. Eng. Struct. Dyn. **26**, 1259–1281 (1997)
10. Christodoulou, K., Ntotsios, E., Papadimitriou, C., Panetsos, P.: Structural model updating and prediction variability using Pareto optimal models. Comput. Methods Appl. Mech. Eng. **198**, 138–149 (2008)
11. Ching, J., Beck, J.L.: Bayesian analysis of the Phase II IASC-ASCE structural health monitoring experimental benchmark data. J. Eng. Mech. ASCE **130**, 1233–1244 (2004)
12. Goulet, J.A., Smith, I.F.C.: Structural identification with systematic errors and unknown uncertainty dependencies. Comput. Struct. **128**, 251–258 (2013)
13. Pasquier, R., Smith, I.F.: Robust system identification and model predictions in the presence of systematic uncertainty. Adv. Eng. Inform. **29**, 1096–1109 (2015)
14. Behmanesh, I., Moaveni, B., Lombaert, G., Papadimitriou, C.: Hierarchical Bayesian model updating for structural identification. Mech. Syst. Signal Process. **64–65**, 360–376 (2015)
15. Inman, D.J., Farrar, C.R., Lopes Jr., V., Steffen Jr., V.: Damage Prognosis. Wiley, Hoboken (2005)
16. Soyoz, S., Taciroglu, E., Orakcal, K., Nigbor, R., Skolnik, D., Lus, H., et al.: Ambient and forced vibration testing of a reinforced concrete building before and after its seismic retrofitting. J. Struct. Eng. **139**, 1741–1752 (2012)
17. Li, Q.S., Zhi, L.H., Yi, J., To, A., Xie, J.: Monitoring of typhoon effects on a super-tall building in Hong Kong. Struct. Control Health. Monit. **21**, 926–949 (2014)
18. Wu, J.R., Liu, P.F., Li, Q.S.: Effects of amplitude-dependent damping and time constant on wind-induced responses of super tall building. Comput. Struct. **85**, 1165–1176 (2007)
19. Chopra, A.K.: Dynamics of Structures. Prentice Hall, New Jersey (1995)
20. FEMA. HAZUS. Federal Emergency Management Agency (2015)
21. ASCE: Minimum Design Loads for Buildings and Other Structures (ASCE/SEI 7-10). American Society of Civil Engineers (2010)
22. Celik, O.C., Ellingwood, B.R.: Seismic fragilities for non-ductile reinforced concrete frames – role of aleatoric and epistemic uncertainties. Struct. Saf. **32**, 1–12 (2010)
23. Liel, A.B., Haselton, C.B., Deierlein, G.G., Baker, J.W.: Incorporating modeling uncertainties in the assessment of seismic collapse risk of buildings. Struct. Saf. **31**, 197–211 (2009)
24. Gardoni, P., Der Kiureghian, A., Mosalam, K.M.: Probabilistic capacity models and fragility estimates for reinforced concrete columns based on experimental observations. J. Eng. Mech. **128**, 1024–1038 (2002)
25. Kwon, O.-S., Elnashai, A.: The effect of material and ground motion uncertainty on the seismic vulnerability curves of RC structure. Eng. Struct. **28**, 289–303 (2006)
26. Haukaas, T., Gardoni, P.: Model uncertainty in finite-element analysis: Bayesian finite elements. J. Eng. Mech. **137**, 519–526 (2011)
27. Kwok, K.C.S., Hitchcock, P.A., Burton, M.D.: Perception of vibration and occupant comfort in wind-excited tall buildings. J. Wind Eng. Ind. Aerodyn. **97**, 368–380 (2009)
28. Beck, J.L.: Bayesian system identification based on probability logic. Struct. Control. Health Monit. **17**, 825–847 (2010)
29. Gelman, A.: Prior distributions for variance parameters in hierarchical models (comment on article by Browne and Draper). Bayesian Anal. **1**, 515–534 (2006)
30. Gilks, W.R., Richardson, S., Spiegelhalter, D.J.: Markov Chain Monte Carlo in Practice. Chapman & Hall, Boca Raton (1998)
31. Yousefianmoghadam, S., Behmanesh, I., Stavridis, A., Moaveni, B., Nozari, A.: Dynamic testing, system identification and modeling of a 10-Story RC Frame Building. Earthq. Eng. Struct. Dyn. (under review)
32. Juang, J.-N., Pappa, R.S.: An eigensystem realization algorithm for modal parameter identification and model reduction. J. Guid. Control. Dyn. **8**, 620–627 (1985)
33. CSI: Integrated Finite Element Analysis and Design of Structures Basic Analysis Reference Manual. Computers and Structures, Berkeley (2015)
34. Filippou, F.C., Constantinides, M.F.: Getting started guide and simulation examples. Technical Report NEESgrid-2004-22. Civil and Environmental Engineering Department, University of California at Berkeley, Berkeley (2004)
35. MathWorks: MATLAB User's Guide. MathWorks Inc., Natick (2014)
36. ACI-318: Building Code Requirements for Structural Concrete and Commentary. ACI Committee 318 (2011)

Chapter 29
Finite Element Model Updating Techniques of Complex Assemblies with Linear and Nonlinear Components

Alexandros Arailopoulos and Dimitrios Giagopoulos

Abstract In this work, finite element model updating techniques are presented for identifying the linear and nonlinear parts of dynamic systems using vibration measurements of their components. The measurements are taken to be either response time histories or frequency response functions of linear and nonlinear components of the system. The model updating techniques were coupled with robust and accurate finite element analysis software in order to produce computational effective results. The developed framework is applied to a geometrically complex and lightweight experimental bicycle frame with nonlinear suspension fork components. The identification of modal characteristics of the frame (linear part) is based on an experimental investigation of its dynamic response. The modal characteristics are then used to update the finite element model. The nonlinear suspension components are identified using the experimentally obtained response spectra for each of the components tested separately. Single and multi-objective structural identification methods with appropriate substructuring methods, are used for estimating the parameters (material properties, shell thickness properties and nonlinear properties) of the finite element model, based on minimizing the deviations between the experimental and analytical dynamic characteristics. Finally, the numerical result of the complete system assembly was compared to experimental results of the equivalent physical structure of the bike.

Keywords System identification • Nonlinear dynamics • Substructuring

29.1 Introduction

Current industrial design requirements lead frequently to the study, improvement, development and modification of some mechanical parts or even of an entire structure. For many of these parts, there is not available necessary information, such as drawings or material properties. In order to address this issue, it is necessary to apply a reverse engineering process. In this process, many issues are taken into account, related to the development of FE model, the experimental modal analysis procedure and the development of effective computational model updating techniques. The main objective of the present work is to demonstrate the advantages of applying appropriate numerical and experimental methodologies in order to identify, update and optimize the model parameters and develop a high fidelity finite element model of both linear and non-linear components, comprising the whole assembly of the examined structure.

The equations of motion of mechanical systems with complex geometry are first set up, applying classical finite element techniques. As the order of these models increases, the existing numerical and experimental methodologies for a systematic determination of their dynamic response become inefficient to apply. Therefore, there is a need for the development, improvement and application of new suitable methodologies for investigating dynamics of large-scale mechanical models in a systematic and efficient way. Moreover, in order to optimize the FE model of a structure, structural model updating methods [1], have been proposed in order to reconcile the numerical (FE) model, with experimental data. Structural model parameter estimation based on measured modal data (e.g. [2–8]) are often formulated as weighted least-squares estimation problems in which metrics, measuring the residuals between measured and model predicted modal characteristics, are build up into a single weighted residuals metric formed as a weighted average of the multiple individual metrics using weighting factors. Standard gradient-based optimization techniques are then used to find the optimal values of the structural parameters that minimize the single weighted residuals metric representing an overall measure of fit between measured and model predicted modal characteristics. Due to model error and measurement noise, the results of the optimization are affected by the values assumed for the weighting factors.

A. Arailopoulos • D. Giagopoulos (✉)
Department of Mechanical Engineering, University of Western Macedonia, Kozani, Greece
e-mail: dgiagopoulos@uowm.gr

S. Atamturktur et al. (eds.), *Model Validation and Uncertainty Quantification, Volume 3*, Conference Proceedings of the Society for Experimental Mechanics Series, DOI 10.1007/978-3-319-29754-5_29

In this work, the applicability and effectiveness of the updating methods, coupled with robust, accurate and efficient finite element analysis software are applied on linear and non-linear components of a whole structure using experimentally identified modal data. A lightweight and geometrically complex bicycle frame as well as the suspension-fork subassembly of a real bicycle are examined, comprising the linear and nonlinear subsystems of the whole bike assembly. Furthermore, the suspension-fork subassembly is consisted of two linear parts (upper and lower fork part) connected with two springs and two seals which impose strong nonlinearity in the system. Issues related to estimating unidentifiable solutions [9–12] arising in FE model updating formulations are also addressed. A systematic study is carried out to demonstrate the effect of model error, finite element model parameterization, number of measured modes and number of mode shape components on the optimal models and their variability. It is demonstrated that the updated finite element models obtained using measured modal data may vary considerably.

The organization of this paper is as follows. First in the first section, the theoretical formulation of finite element model updating based on modal characteristics and frequency response functions is briefly presented. In the second section, the experimental device is introduced. More specifically, first a quick presentation of the digitization of the bicycle components leading to the final parametric CAD model is shown with the corresponding detailed FE models. Next presented the experimental modal analysis procedure followed in order to identify the modal characteristics and the FRF's. Finally the parametric studies on updating the linear and nonlinear FE models of the bicycle components, with the predictions of frequency response functions and time histories, based on the optimal models, are presented in the fourth section. Conclusions are summarized in the fifth section.

29.2 Finite Element Model Updating Methods

29.2.1 Modal Residuals

Let $D = \left\{\widehat{\omega}_r,\ \widehat{\underline{\phi}}_r \ \in R^{N_o},\ \ r = 1, \cdots, m\right\}$ be the measured modal data from a structure, consisting of modal frequencies $\widehat{\omega}_r$ and mode shape components $\widehat{\underline{\phi}}_r$ at N_o measured DOFs, where m is the number of observed modes. Consider a parameterized class of linear structural models used to model the dynamic behavior of the structure and let $\underline{\theta} \in R^{N_\theta}$ be the set of free structural model parameters to be identified using the measured modal data. The objective in a modal-based structural identification methodology is to estimate the values of the parameter set $\underline{\theta}$ so that the modal data $\left\{\omega_r(\underline{\theta}),\ \underline{\phi}_r(\underline{\theta}) \in R^{N_0}, r = 1, \cdots, m\right\}$ predicted by the linear class of models at the corresponding N_0 measured DOFs best matches the experimentally obtained modal data in D. For this, let

$$\varepsilon_{\omega_r}(\underline{\theta}) = \frac{\omega_r^2(\underline{\theta}) - \widehat{\omega}_r^2}{\widehat{\omega}_r^2} \quad \text{and} \quad \varepsilon_{\underline{\phi}_r}(\underline{\theta}) = \frac{\left\|\beta_r(\underline{\theta})\,\underline{\phi}_r(\underline{\theta}) - \widehat{\underline{\phi}}_r\right\|}{\left\|\widehat{\underline{\phi}}_r\right\|} \tag{29.1}$$

be the measures of fit or residuals [13] between the measured modal data and the model predicted modal data for the r-th modal frequency and mode shape components, respectively, where $||\underline{z}||^2 = \underline{z}^T\underline{z}$ is the usual Euclidean norm, and $\beta_r(\underline{\theta}) = \widehat{\underline{\phi}}_r^T\underline{\phi}_r(\underline{\theta}) / \left\|\underline{\phi}_r(\underline{\theta})\right\|^2$ is a normalization constant that guaranties that the measured mode shape $\widehat{\underline{\phi}}_r$ at the measured DOFs is closest to the model mode shape $\beta_r(\underline{\theta})\,\underline{\phi}_r(\underline{\theta})$ predicted by the particular value of $\underline{\theta}$. To proceed with the model updating formulation, the measured modal properties are grouped into two groups. The first group contains the modal frequencies while the second group includes the mode shape components for all modes. For each group, a norm is introduced to measure the residuals of the difference between the measured values of the modal properties involved in the group and the corresponding modal values predicted from the model class for a particular value of the parameter set $\underline{\theta}$. For the first group, the measure of fit $J_1(\underline{\theta})$ is selected to represent the difference between the measured and the model predicted frequencies for all modes. For the second group, the measure of fit $J_2(\underline{\theta})$ is selected to represent the difference between the measured and the model predicted mode shape components for all modes. Specifically, the two measures of fit are given by

$$J_1(\underline{\theta}) = \sum_{r=1}^{m} \varepsilon_{\omega_r}^2(\underline{\theta}) \quad \text{and} \quad J_2(\underline{\theta}) = \sum_{r=1}^{m} \varepsilon_{\underline{\phi}_r}^2(\underline{\theta}) = \sum_{r=1}^{m} \left[1 - MAC_r^2(\underline{\theta})\right] \tag{29.2}$$

where $MAC_r(\underline{\theta}) = \underline{\phi}_r{}^T\widehat{\underline{\phi}}_r(\underline{\theta}) / \left\|\underline{\phi}_r\right\| \left\|\widehat{\underline{\phi}}_r\right\|$ is the Modal Assurance Criterion [14] between experimentally identified and estimated mode shapes for the rth mode. Alternative measures of fit can easily be used and found in literature [15–19].

29.2.2 Response Residuals

Derived from the MAC for any measured frequency point, ω_k a global correlation coefficient may be used [20, 21]:

$$x_s(\omega_k) = \frac{\left|\{H_X(\omega_k)\}^H \{H_A(\omega_k)\}\right|^2}{\left(\{H_X(\omega_k)\}^H \{H_X(\omega_k)\}\right)\left(\{H_A(\omega_k)\}^H \{H_A(\omega_k)\}\right)} \tag{29.3}$$

where $\{H_X(\omega_k)\}$ and $\{H_A(\omega_k)\}$ are the experimental (measured) and the analytical (predicted) response vectors at matching excitation—response locations. As the MAC value, $x_s(\omega_k)$ assumes a value between zero and unity and indicates perfect correlation with $x_s(\omega_k) = 1$. For $x_s(\omega_k) = 0$, no correlation exists. Similar to the MAC, $x_s(\omega_k)$ is unable to detect scaling errors and is only sensitive to discrepancies in the overall deflection shape of the structure. To emphasis this characteristic, $x_s(\omega_k)$ is accordingly called the shape correlation coefficient [21].

The lack of sensitivity to scaling of the shape correlation coefficient does not allow the identification of identical FRFs. This insufficiency becomes even more dramatic if just one measurement and its corresponding prediction are correlated. In this case, the column vectors reduce to scalars and $\{H_A(\omega_k)\} = k\{H_X(\omega_k)\}$ is always satisfied (constant k may be complex), therefore leading to $x_s = 1$ across the full frequency spectrum for uncorrelated FRFs.

As a result, a supplementary correlation coefficient $x_a(\omega_k)$ is proposed by targeting the discrepancies in amplitude. The amplitude correlation coefficient is defined as:

$$x_a(\omega_k) = \frac{2\left|\{H_X(\omega_k)\}^H \{H_A(\omega_k)\}\right|}{\left(\{H_X(\omega_k)\}^H \{H_X(\omega_k)\}\right) + \left(\{H_A(\omega_k)\}^H \{H_A(\omega_k)\}\right)} \tag{29.4}$$

where the response vectors are identical to those used for $x_s(\omega_k)$. As for the shape correlation coefficient, $x_a(\omega_k)$ is defined to lie between zero and unity. This time, however, the correlation measure is more stringent and only becomes unity if $\{H_A(\omega_k)\} = \{H_X(\omega_k)\}$. That is to say, all elements of the response vectors must be identical in both phase and amplitude even if only one measurement is considered. Similarly to modal residuals, two measures of fit are proposed using $x_s(\widehat{\omega}_r)$ and $x_a(\widehat{\omega}_r)$ which correspond to the identified resonant frequencies of the system:

$$J_3(\underline{\theta}) = \sum_{r=1}^{m}\left[1 - x_s(\widehat{\omega}_r, \underline{\theta})^2\right] \text{ and } J_4(\underline{\theta}) = \sum_{r=1}^{m}\left[1 - x_a(\widehat{\omega}_r, \underline{\theta})^2\right] \tag{29.5}$$

29.2.3 Weighting Residuals Method

Minimizing at global minimum the following single objective, traditionally solves the parameter estimation problem:

$$J(\underline{\theta}; \underline{w}) = w_1 J_1(\underline{\theta}) + w_2 J_2(\underline{\theta}) + w_3 J_3(\underline{\theta}) + w_4 J_4(\underline{\theta}) \tag{29.6}$$

formed by the four objectives $J_i(\underline{\theta})$, using the weighting factors $w_i \geq 0$, $i = 1, 2, 3, 4$, with $w_1 + w_2 + w_3 + w_4 = 1$. The objective function $J(\underline{\theta}; \underline{w})$ represents an overall measure of fit between the measured and the model predicted characteristics. The relative importance of the residual errors in the selection of the optimal model is reflected in the choice of the weights. The results of the identification depend on the weight values used. The optimal solutions for the parameter set $\underline{\theta}$ for given $\underline{w}$ are denoted by $\widehat{\underline{\theta}}(\underline{w})$ [9–12].

29.3 Experimental Application

The model updating methodologies are applied in order to update the FE model of a real bicycle. The bicycle consisted of the main frame, which presented in Fig. 29.1 and is made of aluminum and from the front suspension which also consisted of two main parts which are presented respectively in Figs. 29.3 and 29.4. The lower part of the fork, has the same material

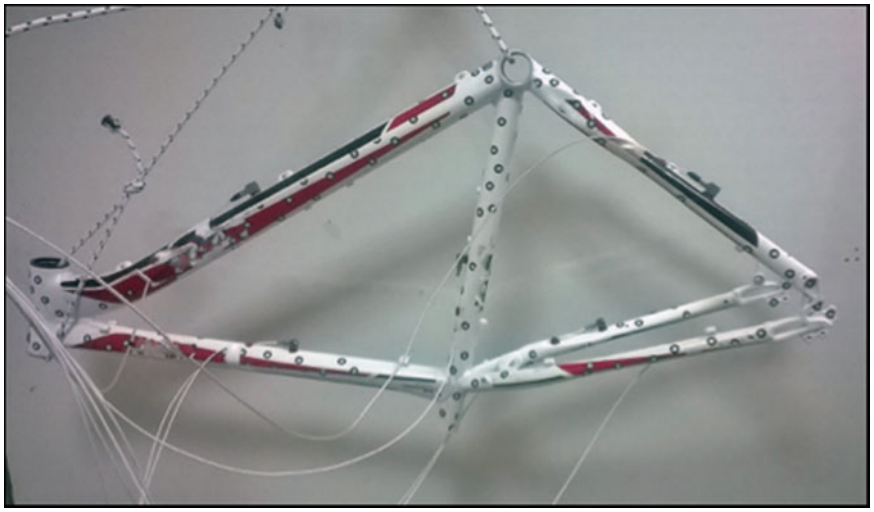

Fig. 29.1 Bicycle frame

properties with the bicycle frame, while the upper fork part, consisted of steel tubes which are connected with a solid aluminum part. The thicknesses of the cross sections of the main frame as long as the lower part of the fork can vary along their length.

29.3.1 Digitization and FE Models

First, using 3D Laser Scanner, DSR (Digital Shape Reconstruction) method was applied. Four basic steps are being followed in order to collect, process and design the final CAD model. First, the geometry of the bicycle was captured, exploiting the 3D scanner's functionalities, as well as its software tools in order to produce a primary stereo-lithography (STL) file. Next, compatible utilities were used to pre-process the initial raw model in order to create the final STL file of the digitized geometry, before designing the CAD surfaces [22–24]. Next, in order to produce the initial CAD model, a segmentation of the triangulated STL model and NURBS (Non-uniform Rational B-Splines) surface fitting, were applied. Finally, in order to achieve a full correspondence of the real frame to the CAD model, several details were re-designed and parts of the structure that were recognized as solid or fixed-thickness, were changed accordingly.

The geometry of the bicycle frame is discretized mainly by shell elements (triangular) and solid elements (tetrahedral). The total number of DOFs was 1,000,000. Similarly, the upper part of the fork was modeled with shell (triangular and quadrilateral) and solid (tetrahedral) elements resulting to 125,000 DOFs and the lower part of the fork was modeled only with solid (tetrahedral) elements resulting to 205,000 DOFs. The detailed FE models are presented in Figs. 29.2, 29.3 and 29.4. For the development and solution of the finite element models appropriate software was used [25, 26]. Indicative mode shapes of the main frame and of the fork parts predicted by the nominal FE models in a free-free state, are shown in Fig. 29.5.

29.3.2 Experimental Modal Analysis

After developing the nominal finite element models, an experimental modal analysis of the frame and fork parts, was performed to quantify its dynamic characteristics. The frame and fork parts were hung up using a crane and straps, to approximate free-free boundary conditions for the test. First, all the necessary elements of the FRF matrix required for determining the response of the substructures were determined by imposing impulsive loading [3–7]. The measured frequency range was 0–2048 Hz, which includes the analytical frequency range of interest for the frame, 0–600 Hz, as well as for the fork parts, 0–500 Hz. An initial investigation indicated 11 natural frequencies for the frame and 4 for the fork parts, in this frequency range. A schematic illustration of the experimental arrangement is presented in Fig. 29.6. In these figures, the locations and directions of acceleration measurements are presented, applying an impulsive load in all directions

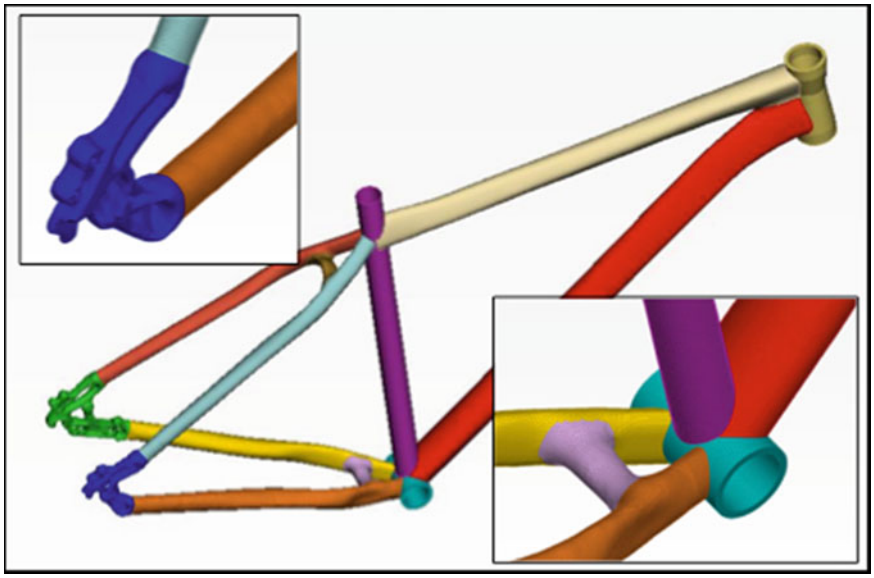

Fig. 29.2 Finite element model of the frame

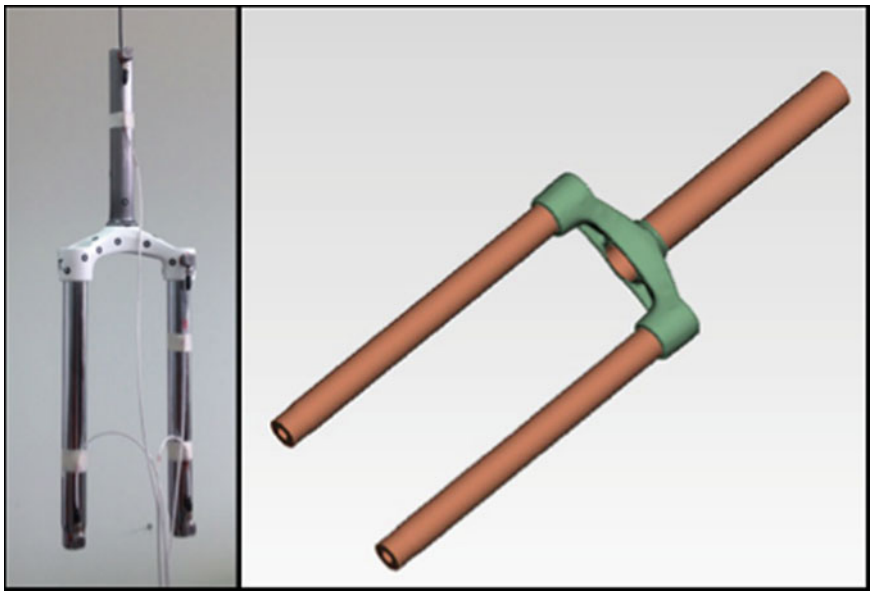

Fig. 29.3 *Upper* (part 1) of the suspension-fork

and at several locations. Indicatively, Fig. 29.7 shows the magnitude of one typical element of the FRF matrix of the frame, before (continuous line) and after (dashed line) application of the Welsh's smoothing method. Based on the measured FR functions, the natural frequencies and the damping ratios of the substructures were estimated applying the "Rational Fraction Polynomial Method" (RFPM). This method has certain attractive merits, especially for systems with high modal density, like the systems under consideration [1, 8, 12]. The identified mode shapes have also been recorded so that they can be used for updating the finite element models.

As an outcome of the above two procedures, in the Table summarized the modal analysis results for the main frame. More specifically, the first column of Table 29.1 presents the values of the lowest natural frequencies (ω_{rE}), while the corresponding damping ratios are included in the fourth column. In the same table, the second column presents the values of the natural frequencies obtained from the analysis of the nominal finite element model ($\omega_{r\,N_{FE}}$) and the third column compares these frequencies with the corresponding frequencies obtained by the experimental data. The errors determined between the nominal FE model and the experimental measurements are not insignificant, indicating that the FE model updating process is necessary. Similar results presented for the fork part 1 and 2 in the Table 29.2.

Fig. 29.4 *Lower* (part 2) of the suspension-fork

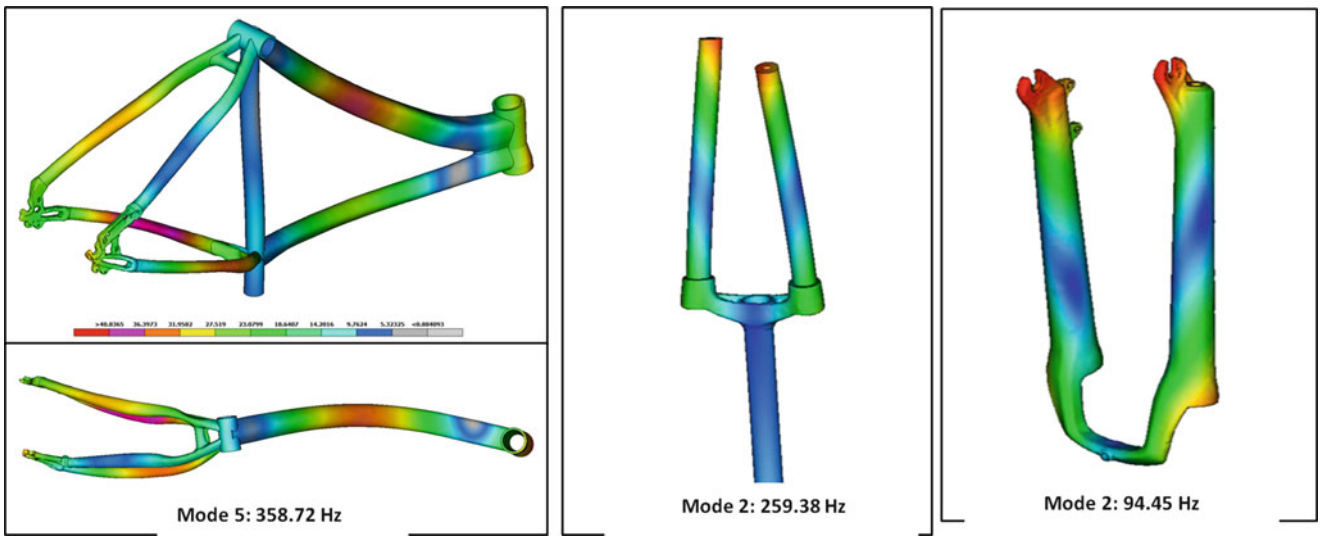

Fig. 29.5 Fifth and second eigenmodes of the main frame and fork parts 1 and 2 predicted by the nominal FEM

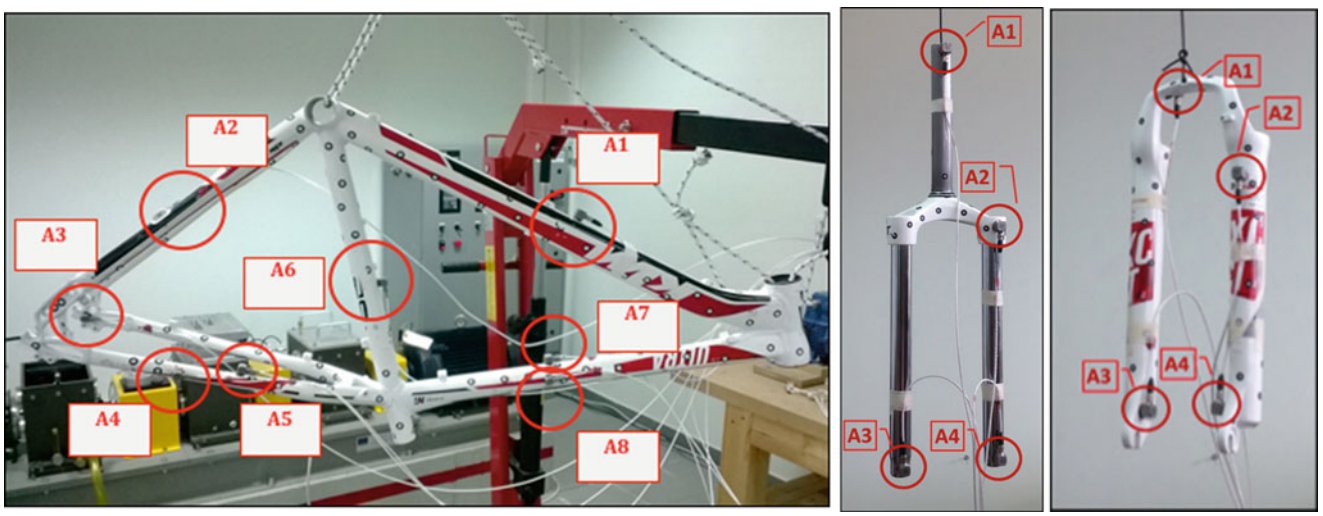

Fig. 29.6 Accelerometer locations on main frame and fork parts 1 and 2

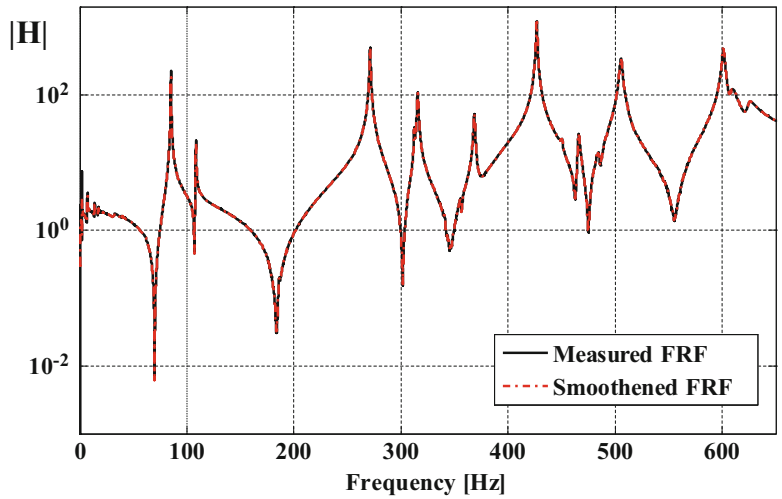

Fig. 29.7 Typical elements of the FRF matrix of the frame

Table 29.1 Modal frequencies and modal damping ratios of the frame

Mode	Identified modal frequency ω_{rE}[Hz]	Nominal FE predicted modal frequency $\omega_{rN_{FE}}$ [Hz]	Difference between identified and FE predicted modal frequencies $\frac{\omega_{rN_{FE}}-\omega_{rE}}{\omega_{rN_{FE}}}100\%$	Identified modal damping ratio $\zeta_{rE}(\%)$
1	84.88	96.46	12.01	0.21
2	108.29	118.72	8.78	0.19
3	270.69	319.15	15.19	0.12
4	311.96	357.30	12.69	0.08
5	315.15	358.72	12.15	0.13
6	368.01	414.69	11.26	0.13
7	425.73	491.11	13.31	0.12
8	450.25	494.05	8.87	0.16
9	465.19	530.79	12.36	0.16
10	484.45	545.44	11.18	0.35
11	504.86	575.88	12.33	0.23

Table 29.2 Modal frequencies and modal damping ratios of the two parts of the suspension-fork

Mode	Identified modal frequency ω_{rE}[Hz]	Nominal FE predicted modal frequency $\omega_{rN_{FE}}$ [Hz]	Difference between identified and FE predicted modal frequencies $\frac{\omega_{rN_{FE}}-\omega_{rE}}{\omega_{rN_{FE}}}100\%$	Identified modal damping ratio $\zeta_{rE}(\%)$
Fork part 1				
1	188.26	168.18	11.94	0.15
2	268.79	259.38	3.63	0.11
3	419.36	453.39	7.51	0.39
4	452.13	499.42	9.47	0.43
Fork part 2				
1	79.65	80.88	1.51	0.48
2	86.21	94.45	8.72	0.15
3	425.04	429.20	0.97	0.12
4	497.25	553.03	10.09	0.11

29.4 Finite Element Model Updating

29.4.1 Linear FE Model Parameterization

The parameterization of the finite element models is introduced in order to demonstrate the applicability of the proposed finite element model updating method. The parameterized models are consisted of 13, 2 and 4 parts, for the frame, fork part 1 and fork part 2, respectively, as shown in Fig. 29.8. The first four parts (P1, P2, P3 and P4) of the frame are modeled with solid elements, while the remaining nine parts (P5–P13) are modeled with shell elements. Fork part 1 is modeled with shell and solid elements for P1 and P2 respectively and fork part 2 is modeled solely with solid elements. The thickness of the shell elements, the Young's modulus and the density are used as design variables. Thus, the final numbers of the design parameters are thirty-five (35), five (5) and eight (8) variables for the frame, fork part 1 and part 2 respectively.

The FE models of the main frame and the fork parts are updated using the identified modal frequencies and mode shapes shown in Tables 29.1 and 29.2. The identified mode shapes include components at all sensor locations. Additionally, we define as design response the total weight of the model, in order to be taken into consideration during the optimization process.

29.4.2 Linear FE Model Updating Results

The results from the FE model updating method are shown in Tables 29.3 and 29.4 for the frame and fork parts respectively. A comparison between identified (ω_{rE}) and optimal FE predicted modal frequencies ($\omega_{r\,O_{FE}}$) is also presented.

The FRF predicted by the optimal FE model (black dashed line) for the frame are compared in Fig. 29.9 with the FRF computed directly from the measured data (red continuous line) at two indicative measurement locations in the frequency range [50–550 Hz]. The FRF of the initial nominal model (blue dashed dot line) is also shown in these figures to be inadequate to represent the measured FRF. Compared to the FRF of the initial nominal model, it is observed that the updated optimal model tend to considerably improve the fit between the model predicted and the experimentally obtained FRF close to the resonance peaks.

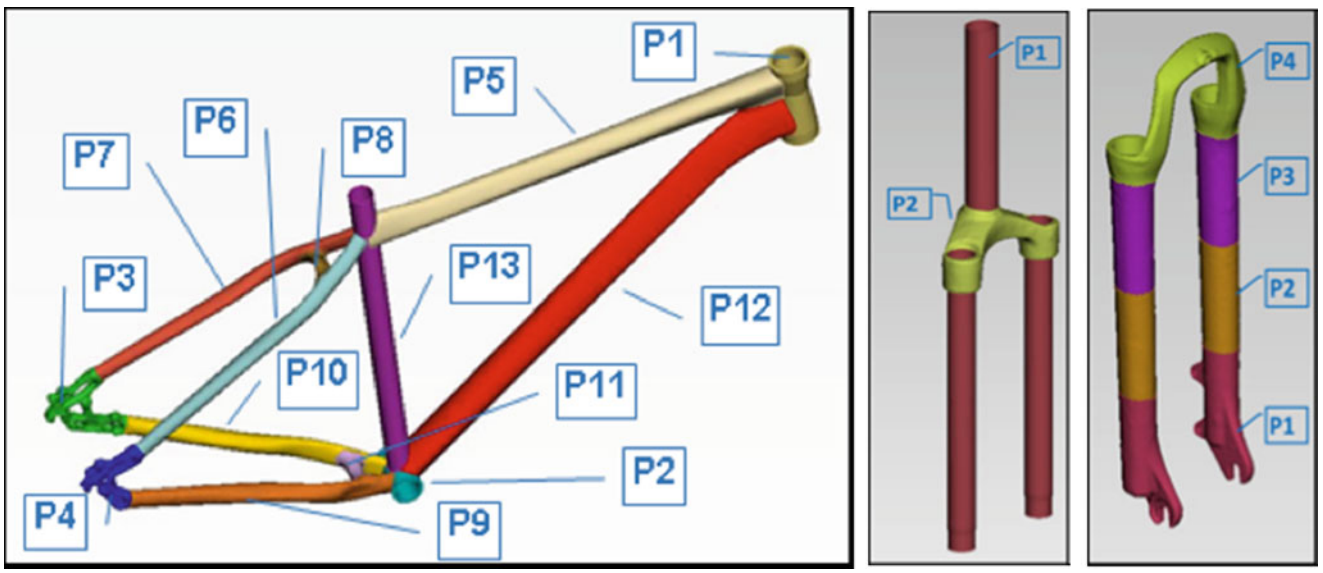

Fig. 29.8 Parts of the parameterized FE Models of the frame and suspension- fork parts

Table 29.3 Comparison between identified and optimal FE predicted modal frequencies for the main frame

Mode	Identified modal frequency ω_{rE}[Hz]	Optimal FE predicted modal frequency $\omega_{rO_{FE}}$ [Hz]	Difference between identified and FE predicted modal frequencies $\frac{\omega_{rO_{FE}}-\omega_{rE}}{\omega_{rO_{FE}}}100\%$
1	84.88	84.89	0.01
2	108.29	108.29	0.00
3	270.69	270.61	0.03
4	311.96	312.16	0.06
5	315.15	315.47	0.10
6	368.01	368.01	0.00
7	425.73	426.01	0.07
8	450.25	449.51	0.17
9	465.19	465.59	0.09
10	484.45	484.38	0.02
11	504.86	505.23	0.07

Table 29.4 Comparison between identified and optimal FE predicted modal frequencies for the fork parts 1 and 2

Mode	Identified modal frequency ω_{rE}[Hz]	Optimal FE predicted modal frequency $\omega_{rO_{FE}}$ [Hz]	Difference between identified and FE predicted modal frequencies $\frac{\omega_{rO_{FE}}-\omega_{rE}}{\omega_{rO_{FE}}}100\%$
Fork part 1			
1	188.26	188.53	0.14
2	268.79	267.86	0.35
3	419.36	420.83	0.35
4	452.13	452.10	0.01
Fork part 2			
1	79.65	79.65	0.00
2	86.21	86.21	0.00
3	425.04	425.04	0.00
4	497.25	497.25	0.00

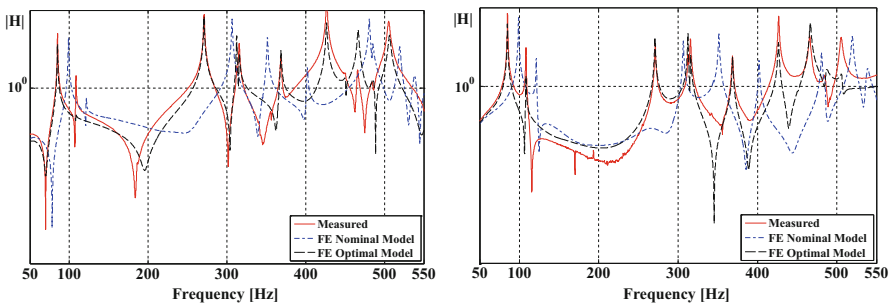

Fig. 29.9 Comparison between measured, nominal and optimal FRF in two typical elements of the FRF matrix

29.5 Analysis of Non-linear System

The FE model, of the nonlinear subassembly of the suspension-fork, was created connecting fork part 1 and 2 with two springs simulating the restoring force $f_r(x)$ and two non-linear bushing elements simulating the damping force $f_d(\dot{x})$. The final nonlinear suspension FE model with the corresponding lumped model presented in Fig. 29.10.

In order to identify the parameters of the subsystem, which exhibit strongly nonlinear characteristics, a series of experimental trials was performed. In the experimental device shown in Fig. 29.11 two electromagnetic devices are used, at the top and at the bottom of the suspension, imposing harmonic excitation with $\pi/2$ rad phase difference using 0.2 Hz frequency step for three different forcing levels.

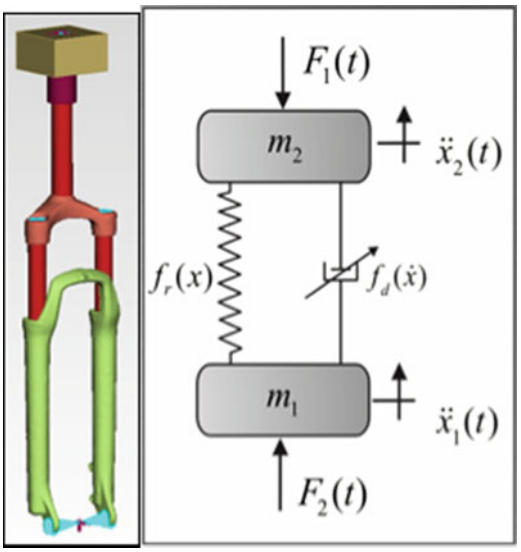

Fig. 29.10 FE model of the suspension-fork and theoretical lumped model

Fig. 29.11 Schematic illustration and experimental arrangement of suspension sub-assembly

The graphs of Fig. 29.12 depict the imposed forces $F_1(t)$ and $F_2(t)$ for the three different forcing levels at $\omega = 6Hz$ which is approximately the resonant frequency of the system. The graphs of Fig. 29.13 depict the acceleration transmissibility functions of measurement location 2, for the three different forcing levels.

A number of models of the restoring and damping forces, say f_r and f_d, respectively, were tried for modeling the action of the supports and compared with the experimental results. The classic linear dependence of the restoring force on the displacement and of the damping forces on the velocity of the support unit was first assumed. However, critical comparison with the experimental results using the Bayesian model selection framework demonstrated that the outcome was unacceptable in terms of accuracy. Eventually it was found that an acceptable form of the restoring forces is the one where they remain virtually in a linear relation with the extension of the spring, namely

$$f_r(x) = kx \tag{29.7}$$

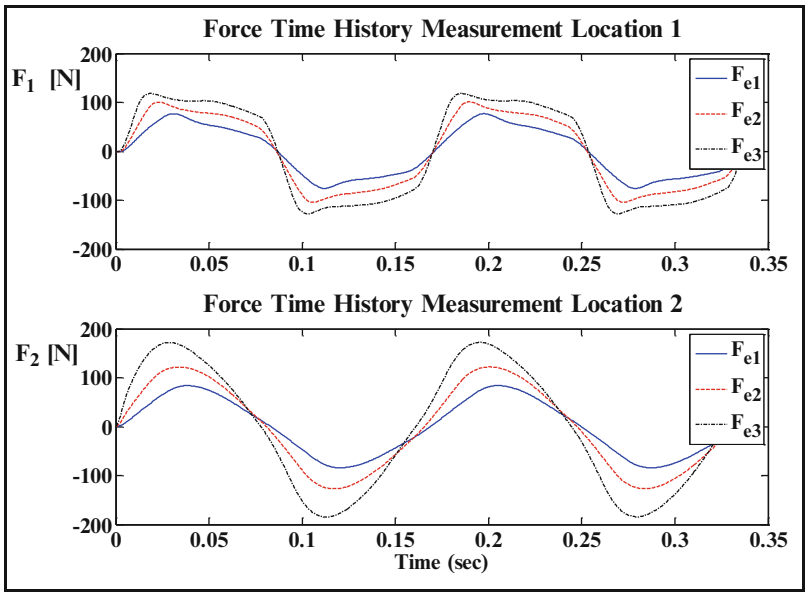

Fig. 29.12 Time-history of the external forces applied at a fundamental harmonic frequency $\omega = 6$ Hz

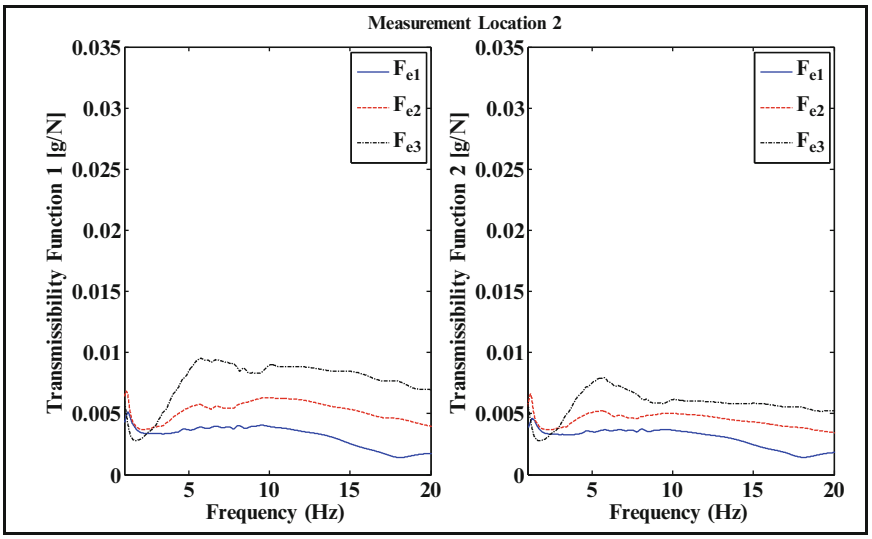

Fig. 29.13 Transmissibility functions of the support system for three different forcing levels

while the damping force was best approximated by the following formula

$$f_d\left(\dot{x}\right) = c_1\dot{x} + \frac{c_2\dot{x}}{c_3 + \left|\dot{x}\right|} \tag{29.8}$$

As usual, the linear term in the last expression is related to internal friction at the support, while the nonlinear part is related to the existence and activation of dry friction. More specifically, in the limit $c_3 \to 0$, the second term in the right hand side of Eq. (29.8) represents energy dissipation action corresponding to dry friction. On the other side, in the limit $c_3 \to \infty$ this term represents classical viscous action and can actually be absorbed in the first term.

The results for k, c_1, c_2 and c_3 are obtained based on the experimental response spectra values for the accelerations of the two suspension components, using the parameters of the updated linear parts (1 and 2) of the suspension

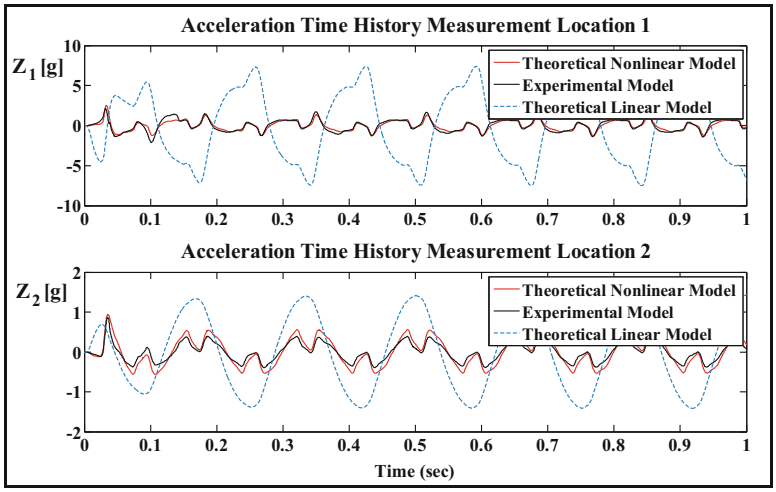

Fig. 29.14 Acceleration time histories at two measured locations for $\omega = 6$ Hz excitation frequency

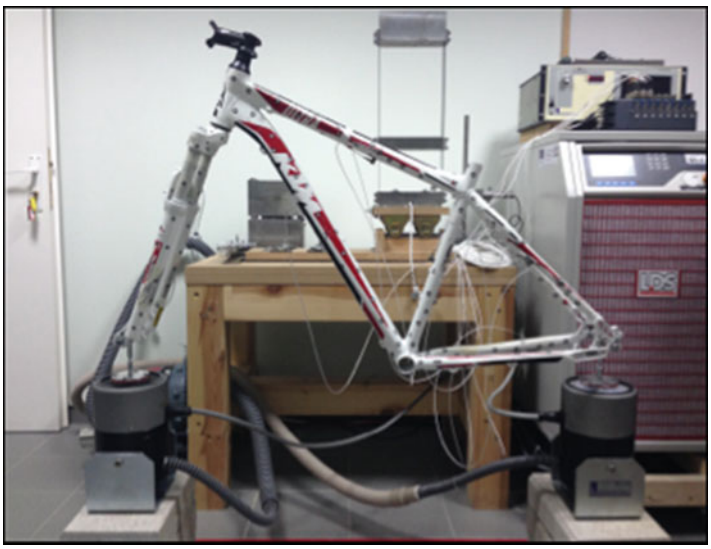

Fig. 29.15 Fixed-free arrangement on electrodynamic shakers

fork subassembly and the transmissibility functions of the support system for three different forcing levels. Let $S = \left\{\widehat{s}_r\left(\omega_r\right) \in R^{N_r},\ \ r = 1, \cdots, n\right\}$ be the measured transmissibility functions at N_r measured frequencies where n is the number of involved frequencies. Let $\underline{\theta} = \left(k_1, c_1, c_2, c_3 \in R^{N_\theta}\right)$ be a parameter space, corresponding to the linear and nonlinear coefficients of the restoring and damping forces respectively. Similarly to the linear model, the objective is to estimate the values of the parameter set $\underline{\theta}$ so that the analytical response spectra values, namely the transmissibility functions match the experimentally obtained functions estimated in S.

After estimating the stiffness and damping properties of the system, a comparison of the nonlinear response analysis at $\omega = 6Hz$ showed good matching of the theoretical nonlinear to the experimental model, as shown in the graphs of Fig. 29.14 depicted with the red and black line respectively for two measured locations. The blue line was derived using the equivalent theoretical linear model and is presented for comparison purposes.

As a second approach, imposing random base excitation with the use of two electrodynamic shakers and determining the response of the frame substructure the FRF matrix was restructured and modal parameters were re-examined. An illustration of the fixed-free arrangement of the bike on the shakers is presented in Fig. 29.15 while in Fig. 29.16 the finite element model of the whole bike assembly is shown.

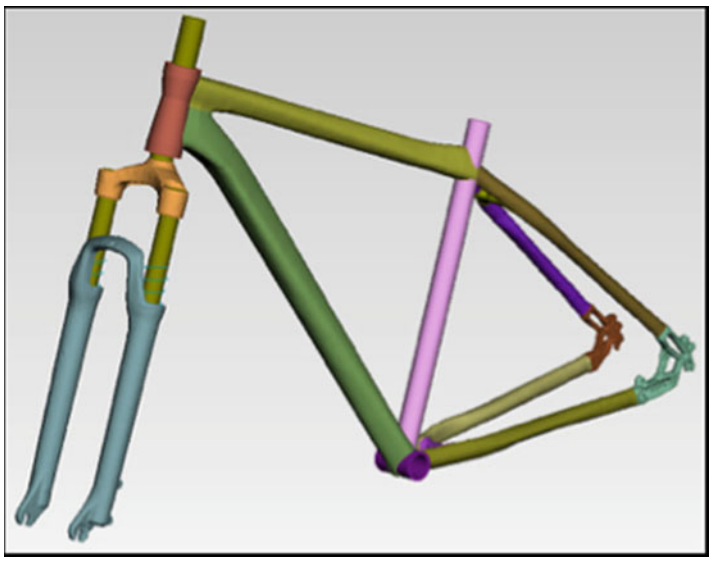

Fig. 29.16 FE model of the bike assembly

29.6 Summary

An integrated reverse engineering strategy was presented that takes into account the complete process, from the developing of CAD model and the experimental modal analysis procedures to computational effective model updating techniques. Numerical and experimental methodologies were applied in order to identify the model parameters and develop a high fidelity finite element model of the structure examined. The applicability and effectiveness of the methods applied, namely the model updating method, is explored by updating finite element model of a lightweight and geometrically complex bicycle assembly, using experimentally identified modal data. Direct comparison of the numerical and experimental data verified the reliability and accuracy of the methodology applied.

References

1. Mottershead, J.E., Friswell, M.I.: Model updating in structural dynamics: a survey. J. Sound Vib. **167**, 347–375 (1997)
2. Cuppens, K., Sas, P., Hermans, L.: Evaluation of FRF Based Substructuring and Modal Synthesis Technique Applied to Vehicle FE Data, ISMA 2000, pp. 1143–1150. K.U. Leuven, Leuven (2000)
3. Giagopoulos, D., Natsiavas, S.: Hybrid (numerical-experimental) modeling of complex structures with linear and nonlinear components. Nonlinear Dyn. **47**, 193–217 (2007)
4. Giagopoulos, D., Natsiavas, S.: Dynamic response and identification of critical points in the superstructure of a vehicle using a combination of numerical and experimental methods. Exp. Mech. **55**(3), 529–542 (2015)
5. Ewins, D.J.: Modal Testing: Theory and Practice. Research Studies Press, Somerset (1984)
6. Mohanty, P., Rixen, D.J.: Identifying mode shapes and modal frequencies by operational modal analysis in the presence of harmonic excitation. Exp. Mech. **45**, 213–220 (2005)
7. Spottswood, S.M., Allemang, R.J.: On the investigation of some parameter identification and experimental modal filtering issues for nonlinear reduced order models. Exp. Mech. **47**, 511–521 (2007)
8. Richardson, M.H., Formenti, D.L.: Global curve fitting of frequency response measurements using the rational fraction polynomial method. In: Proceedings of the Third IMAC Conference, Orlando (1985)
9. Papadimitriou, C., Ntotsios, E., Giagopoulos, D., Natsiavas, S.: Variability of updated finite element models and their predictions consistent with vibration measurements. Struct. Control. Health Monit. **19**, 630–654 (2012)
10. Giagopoulos, D., Papadioti, D.-Ch., Papadimitriou, C., Natsiavas, S.: Bayesian uncertainty quantification and propagation in nonlinear structural dynamics. In: Proceedings of the IMAC-XXXI 2013, Garden Grove (2013)
11. Christodoulou, K., Ntotsios, E., Papadimitriou, C., Panetsos, P.: Structural model updating and prediction variability using Pareto optimal models. Comput. Methods Appl. Mech. Eng. **198**(1), 138–149 (2008)
12. Ntotsios, E., Papadimitriou, C.: Multi-objective optimization algorithms for finite element model updating. In: International Conference on Noise and Vibration Engineering (ISMA2008). Katholieke Universiteit Leuven, Leuven, 15–17 September 2008
13. Mottershead, J., Link, M., Friswell, M.: The sensitivity method in finite element model updating: a tutorial. Mech. Syst. Signal Process. (2010). doi:10.1016/j.ymssp.2010.10.012

14. Allemang, R., Brown, D.: A correlation coefficient for modal vector analysis. In: Proceedings of the 1st International Modal Analysis Conference, Orlando (1982)
15. Fritzen, C.P., Jennewein, D., Kiefer, T.: Damage detection based on model updating methods. Mech. Syst. Signal Process. **12**(1), 163–186 (1998)
16. Moaveni, B., He, X., Conte, J.P., Restrepo, J.I.: Damage identification study of a seven-story full-scale building slice tested on the UCSD-NEES shake table. Struct. Saf. **32**(5), 347–356 (2010)
17. Moaveni, B., He, X., Conte, J.P., De Callafon, R.A.: Damage identification of a composite beam using finite element model updating. Comput. Aided Civ. Infrastruct. Eng. **23**(5), 339–359 (2008)
18. Weber, B., Paultre, P., Proulx, J.: Structural damage detection using nonlinear parameter identification with Tikhonov regularization. Struct. Control. Health Monit. **14**, 406–427 (2007)
19. Yuen, K.-V., Beck, J.L., Katafygiotis, L.S.: Efficient model updating and health monitoring methodology using incomplete modal data without mode matching. Struct. Control. Health Monit. **13**, 91–107 (2006)
20. Grafe, H.: Model updating of large structural dynamics models using measured response functions. Ph.D. thesis, Imperial College of Science, Department of Mechanical Engineering, Dynamics Section (1998)
21. Grafe, H.: Review of frequency response function updating methods. Technical Report No. 1.01, BRITE-URANUS BRE2-CT94-0946 (1995, May)
22. Rypl, D., Bittnar, Z.: Generation of computational surface meshes of STL models. Faculty of Civil Engineering, Department of Structural Mechanics, Czech Technical University, Prague (2005)
23. Bechét, E., Cuilliere, J.C.: Generation of a finite element MESH from stereolitography (STL) files. Computer-Aided Design, Paris (2002)
24. Bianconi, F.: Bridging the gap between CAD and CAE using STL files. Department of Industrial Engineering, University of Perugia, Perugia (2002)
25. DYNAMIS 3.1.1: Solver Reference Guide. DTECH, Thessaloniki (2013)
26. ANSA and META-Post, BETA CAE Systems S.A., Thessaloniki

Chapter 30
Metamodeling of Model Evidence

Ramin Madarshahian and Juan M. Caicedo

Abstract The Bayesian model evidence can be used for model selection in model updating problems. The evidence is calculated by computing the integral of the prior multiplied by the likelihood probability density functions (PDF). This integral is usually solved numerically using Monte Carlo integration techniques. A large number of samples of the likelihood and prior should be computed to implement such algorithms. This process might not be achievable when the model is computationally expensive. Researchers have proposed the use of metamodels to replace the computationally expensive model to solve this problem. In this paper we propose a different strategy. The evidence integrand is replaced by a metamodel, simplifying the model selection process because the scale parameter of the metamodel approximates the value of the integral and no Monte Carlo integration is needed. The proposed technique is explored using a set of numerical problems.

Keywords Model evidence • Metamodeling • Bayesian inference • MCMC • Computational cost

30.1 Introduction

Stochastic modeling is intensively used in empirical sciences [1, 2]. Data and the experience of researchers are used to make inference about models and their parameters [3–8]. For modeling of complex phenomena usually several models are suggested, and sometimes it is hard to select one model over the others based on the nature of the problem. Data based model selection is commonly applied to select the suitable model among all candidates. The Bayesian model evidence is a good indicator for model selection. However, calculating the Bayesian model evidence for a complex model is a time consuming and computationally expensive process. In this paper, a new method to reduce the computational cost associated with the Bayesian model selection is introduced. This will be achieved by using a surrogate model for the model evidence. Traditionally, surrogate models are used to approximate the response of computationally expensive models that represent a physical system (e.g. finite element models). In this research the surrogate model will be used to represent the model's evidence. In most scientific problems, when Bayesian inference is used, it is not easy or sometimes possible to obtain the evidence in a close form. In these scenarios one of the most common methods to sample the evidence is the Markov Chain Monte Carlo (MCMC) [9–11]. However, a large number of samples is needed to obtain an appropriate representation of the evidence. For each sample, the model should be run, but when the model is computationally expensive hundreds or even thousands of simulations might not be feasible. To overcome this problem, more powerful and faster computers can be used, or parallel computing techniques may be implemented. However, even this might not be enough for some particular problems. For example, the OpenSees model of the Humboldt Bay Middle Channel Bridge has over 100,000 degrees of freedom and it takes over 100 min per run with four cores [12]. Also, some authors have proposed modifications to the numerical methods to reduce the computational cost [13, 14]. Alternatively, it is possible to reduce the cost of computation by making faster models. Computationally expensive models can be "remodeled" with surrogate models (at the by sake of) sacrificing a small amount of precision [15]. The expensive model is defined as a function of the model's parameters. Usually, some points of the function are sampled and a surrogate model is fitted to them. Unfortunately, surrogate models are not easy to implement in some applications and the error by the surrogate model can be significant [16]. In another work by authors of this paper, it was suggested to use probability distribution function as the metamodel for approximating the posterior of a Bayesian inference [17]. This paper proposes the function that is being modeled is obtained from the model's evidence. This could lead to several advantages over traditional methods, which include:

R. Madarshahian (✉) • J.M. Caicedo
University of South Carolina, 300 Main St., Columbia, SC 29208, USA
e-mail: mdrshhn@email.sc.edu; caicedo@cec.sc.edu

S. Atamturktur et al. (eds.), *Model Validation and Uncertainty Quantification, Volume 3*, Conference Proceedings of the Society for Experimental Mechanics Series, DOI 10.1007/978-3-319-29754-5_30

- The metamodel is a probability distribution function that satisfies the Kolmogorov axioms. It is always positive and has an area of one under its curve. These properties provide more information, and could make the metamodeling process easier.
- The fact that the area under a probability distribution function has an area of one provides a powerful tool to directly calculate the evidence. This is explained in the methodology section of this paper.
- Using a surrogate model usually introduces some precision error to the problem. If the computationally expensive model is replaced by a surrogate model, errors are added before the Bayesian inference. However, a hypothesis is that using the surrogate model at the level of the Bayesian model may prevent error propagation.

30.2 Methodology

Bayes equation is expressed as:

$$p(\theta|DM) = \frac{p(\theta|M)p(D|\theta M)}{p(D|M)} \tag{30.1}$$

where $p(\theta|DM)$ is called posterior of the model M, which is the inference about the parameter(s) given taken data (D). The likelihood ($p(D|\theta M)$) describes the probability of the sampled data given a specific value of the parameters $\theta|M$. $p(\theta|M)$ or the prior describes the initial belief about θ [18]. The denominator describes the model's evidence, which can be used to select the most probable model for representation of a studied phenomena [19]:

Then the normalizing constant can be obtained as:

$$p(D|M) = \int p(D\theta|M)d\theta = \int p(D|\theta M)p(\theta|M)d\theta \tag{30.2}$$

So for a given set of models it can be written as:

$$p(M_j|D) = p(M_j)\frac{p(D|M_j)}{p(D)} \tag{30.3}$$

So in the case of comparing two models, Eq. (30.3) can be extended to:

$$\frac{p(M_j|D)}{p(M_k|D)} = \frac{p(M_j)}{p(M_k)}\frac{p(D|M_j)}{p(D|M_k)} \tag{30.4}$$

Solving the integral in Eq. (30.2) for a computationally expensive model is not possible in many cases.

Since the integral leads to the model's evidence, we call the integrand "evidence density function" (EDF) in this paper. This function is obtained by multiplication of several (PDFs). This paper suggests estimating this function by an appropriate PDF. Considering the characteristics of PDF, such as its nonnegative values in all of its domain makes it a good candidate for being a metamodel for EDF. The most helpful advantages of using PDF for metamodel comes from the Kolmogorov axioms, which say the area under a PDF is one. Therefore the scale factor for the metamodel would represent the area of EDF. In other words, by fitting the metamodel to the EDF, there is no need to calculate the integral in Eq. (30.2) anymore. Showing the metamodel by $g_m(\theta_m)$ and recalling Eq. (30.2):

$$p(D|M) = \int p(D|\theta M)p(\theta|M)d\theta = \int \theta_0 g_m(\theta_m)d\theta_m = \theta_0 \tag{30.5}$$

where θ_0 is the scale factor.

30.3 Example

30.3.1 Model Selection Example

To illustrate how the proposed methodology can reduce the computational cost, a simple regression problem is designed and solved using Python program. A few samples are collected from the function showed in Eq. (30.6), which is defined by a

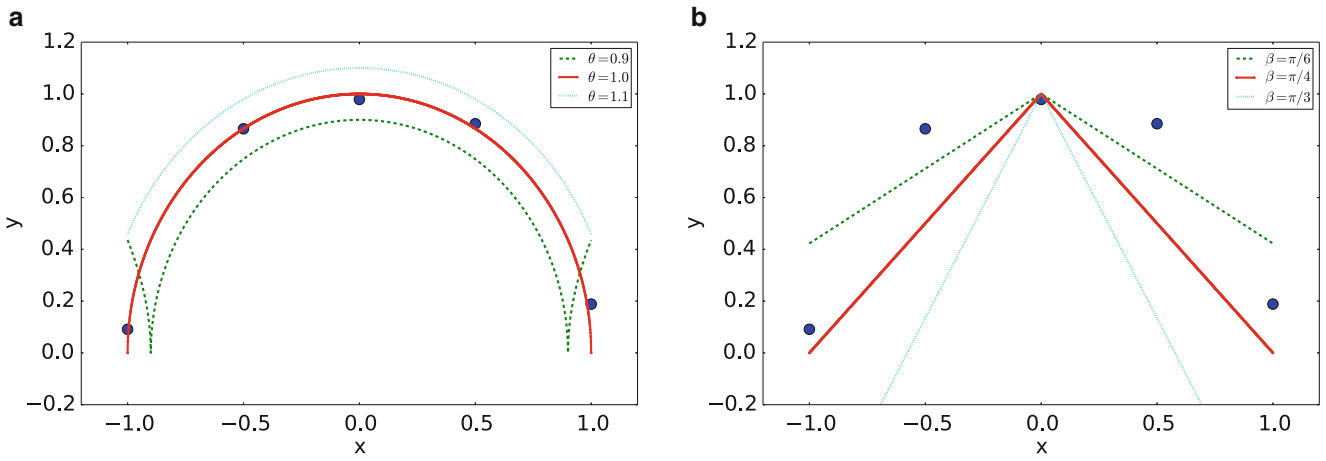

Fig. 30.1 Samples and the two proposed regression models for some different values of their parameter. (**a**) Half-circle model. (**b**) Chevron model

half-circle. This half-circle's radius is a random variable with a mean value of one and a standard deviation of 0.01 with a center of $(0, 0)$ in the plane of x and y. Data is collected in a constant sampling step of 0.5 along the x axis, from -1 to 1.

$$y = \sqrt{|N(1., 0.01) - x^2|} \tag{30.6}$$

To explain the obtained data, two models are used: A) Half-circle, B) Chevron:

$$M_{half-circle} : \sqrt{\theta - x^2}, M_{chevron} : 1 - tan(\beta)|x| \tag{30.7}$$

These models have only one parameter: θ for the half-circle model, and β for the chevron. The data and these two proposed models are shown in the Fig. 30.1. The models are shown based on three different values of their parameter.

30.3.2 Bayesian Model Evidence

The Bayesian model evidence, $P(D|M)$, is the probability of data given the model. In this section the model evidence of these two models are calculated with Monte Carlo integration. In this example the prior for the half-circle model's parameter is selected as a uniform distribution between zero and two. Zero is selected because the radius can never be a negative number, and two is selected as a very large number for radius. Uniform distribution is selected to show no more information is available for this parameter. In the second model, the slope of lines is shown by $tan(\beta)$. It is because for a line slope, uniform distribution is not an uninformative one, and it is in favor of steeper slopes. This can be shown by plotting several lines with constant change of the slope, e.g. one. To solve this issue the slope is shown by $\tan(\beta)$, then the prior for β can be chosen as a uniform distribution from $\frac{-\pi}{2}$ to $\frac{\pi}{2}$ [20]. Evidence for both models are calculated as follows:

$$\int_0^2 \left(\frac{1}{\sqrt{2\pi\sigma^2}}\right)^5 e^{\frac{-1}{2\sigma^2}\sum_1^5 (M_{half-circle}(\theta)-y_i)} \left(\frac{1}{2}\right)^5 d\theta \tag{30.8a}$$

$$\int_{\frac{-\pi}{2}}^{\frac{\pi}{2}} \left(\frac{1}{\sqrt{2\pi\sigma^2}}\right)^5 e^{\frac{-1}{2\sigma^2}\sum_1^5 (M_{chevron}(\beta)-y_i)} \left(\frac{1}{\pi}\right)^5 d\beta \tag{30.8b}$$

Figure 30.2 shows the EDF for both models.

The evidence is calculated by implementing Monte Carlo integration using *scikit-monaco 0.2.1* python package [21, 22]. To calculate the integral 5000 samples were used, and the area of the half-circle EDF and the chevron EDF are obtained respectively as 0.1259 ± 0.0030, and 0.0994 ± 0.0025. Error is defined as one standard deviation. Therefore Bayes factor is obtained as follows:

$$B = \frac{P(D|M_{half\ circle})}{P(D|M_{chevron})} = \frac{0.1259}{0.0994} = 1.266 \tag{30.9}$$

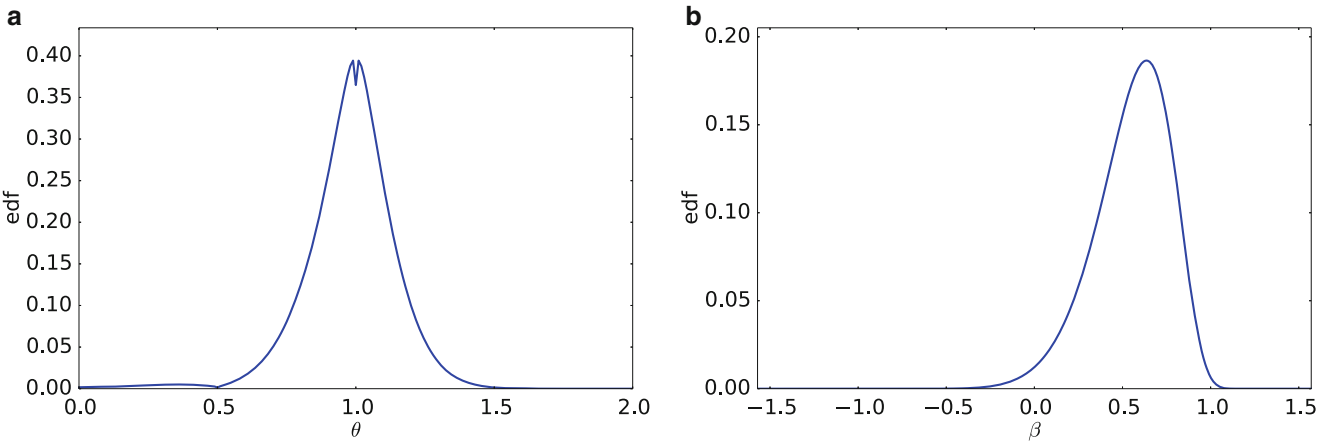

Fig. 30.2 EDF of the two proposed regression models with one parameter. (**a**) Half-circle. (**b**) Chevron

30.3.3 Applying the Proposed Method

In this part, a metamodel from the PDF type is selected to approximate the EDF. The main advantage of using a PDF as a metamodel comes from the probability axiom that the integral of PDF in its domain is equal to one [23]. When the metamodel is fitted to the EDF, the scale factor would be an approximation of area under the EDF curve, or the model evidence. PDF of normal distribution is used. Here as the metamodel candidate. The equation of the metamodel for the half-circle model is shown as:

$$G_1(\theta) = a_0 g_1(a_1, a_2) = a_0 \frac{1}{\sqrt{2\pi a_2^2}} e^{\frac{-1}{2a_2^2}(\theta - a_1)} \tag{30.10}$$

Here a_0 is scale factor and a_1 and a_2 are mean and standard deviation of the normal distribution respectively. The metamodel for the chevron is exactly the same as the mentioned equation, and its parameters are shown by b_0, b_1, and b_2 respectively. Some samples should be taken from EDF to use as the data needed for Bayesian inference about the metamodel's parameters. The goal is to take fewer numbers of samples, since in practice EDF is supposed to be a computationally expensive function to collect samples. Sampling would be done in several stages until the stopping criteria is satisfied. Here, because the scale factor is the most important parameter, the stopping criteria is defined as follows:

$$\frac{\text{scale factor at iteration}(i) - \text{scale factor at iteration } (i-1)}{\text{scale factor at iteration } (i)} < 0.02 \tag{30.11}$$

Sampling region is updated in each iteration. First, based on the prior information for the model's parameter, five samples are taken from the EDF the metamodel is fitted. Using these samples however, because the EDF peak is located in a small domain of initial prior and most of the samples are located in the tails, there is little chance that the metamodel fits well enough to the EDF. However, in most cases there are samples from both tails of the EDF, so it is expected that metamodel's high probability region overlaps with the region with higher values of the EDF. Taking advantage of this matter, new samples are taken from a uniform distribution which is the metamodel mean bounded by three standard deviation (obtained parameters of metamodel in first updating). The mean and standard deviation of the metamodel are updated in each updating step. Five new samples are added to the old samples and the metamodel is updated. Then stopping criteria is checked to see if another iteration is needed or not. Figure 30.3 shows this process for both models. Diamond markers show the first five samples from uniform prior of the original model's parameter. The second five samples, shown by red circles, are from a narrower region based on the obtained updated metamodel. This process should be continued until the stopping criteria are satisfied.

Parameters of the metamodel and their associated uncertainty can be obtained using a general probabilistic approach like the Markov chain Monte Carlo, or recursive Bayesian filters (e.g. Kalman and Particle filters) [24, 25]. Here, for the metamodel updating, MCMC with the Metropolis-Hastings algorithm is used. Priors of the metamodel's parameters are defined based on available information for original models. For the mean value the same prior as θ for half-circle model and

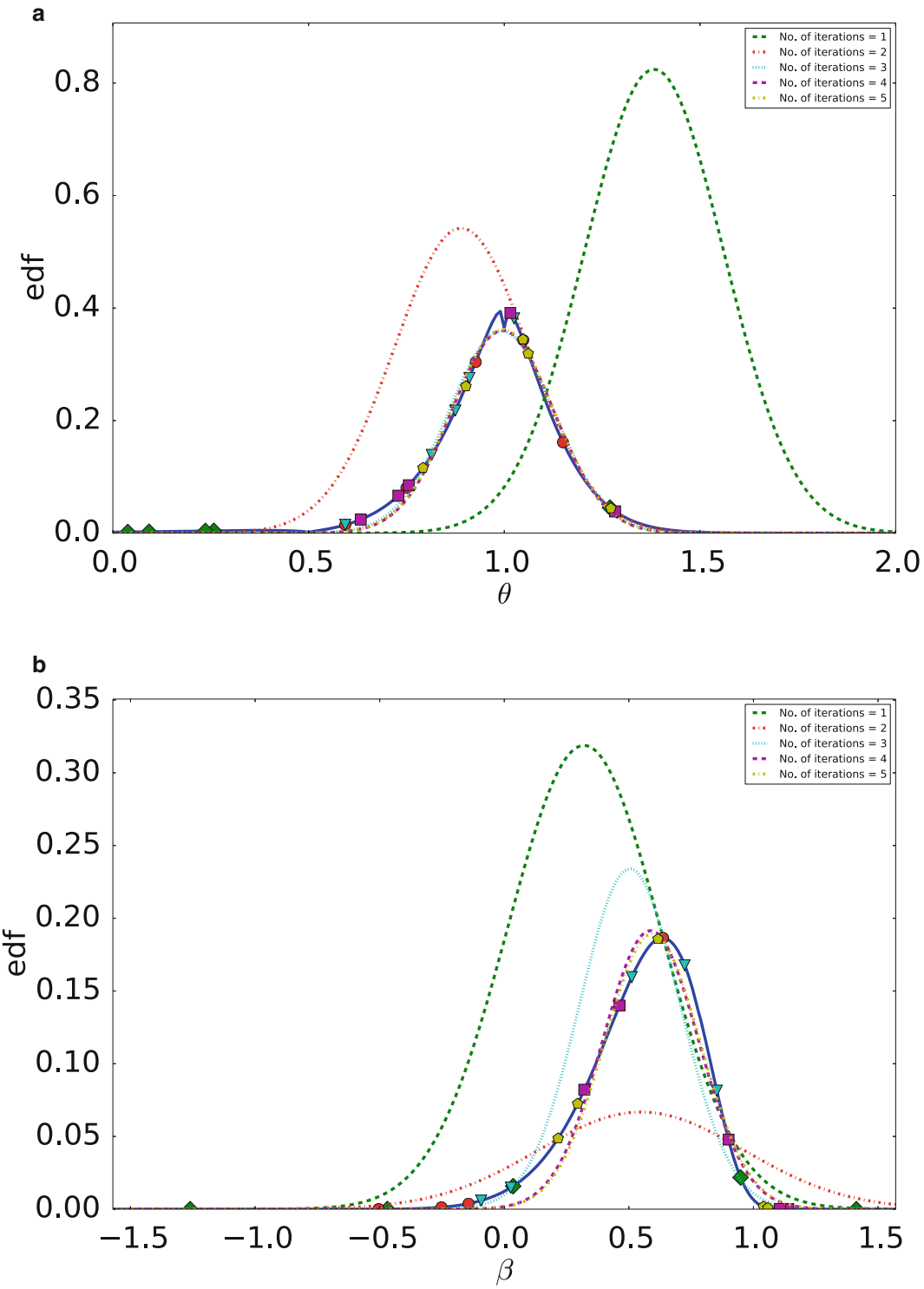

Fig. 30.3 Metamodel updating. (**a**) Half-circle. (**b**) Chevron

β for chevron model is reasonable. Also, the prior for standard deviation can be obtained from standard deviation of these priors. The standard deviation of a uniform distribution between a and b is:

$$\frac{1}{2\sqrt{3}}(b-a) \tag{30.12}$$

This results in a uniform distribution bounded by zero and $\frac{1}{\sqrt{3}}$ for half-circle model. For the chevron model, prior of metamodel standard deviation is a uniform distribution between zero and $\frac{\pi}{2\sqrt{3}}$ for the chevron model.

The prior of the scale factor is selected aa a uniform distribution limited by zero and one. Figure 30.4 shows the marginal histograms of the MCMC chain.

Results are summarized in Table 30.1.

Based on what is shown in Table 30.1, an estimator of Bayes factor is obtained by $\frac{0.118}{0.091} = 1.297$. From 95 % HPD interval it can be said that Bayes factor is bounded by $[\frac{0.115}{0.097} = 1.186, \frac{0.121}{0.085} = 1.423]$. The true value of Bayes factor was calculated as 1.266 which is in the interval obtained by the proposed method.

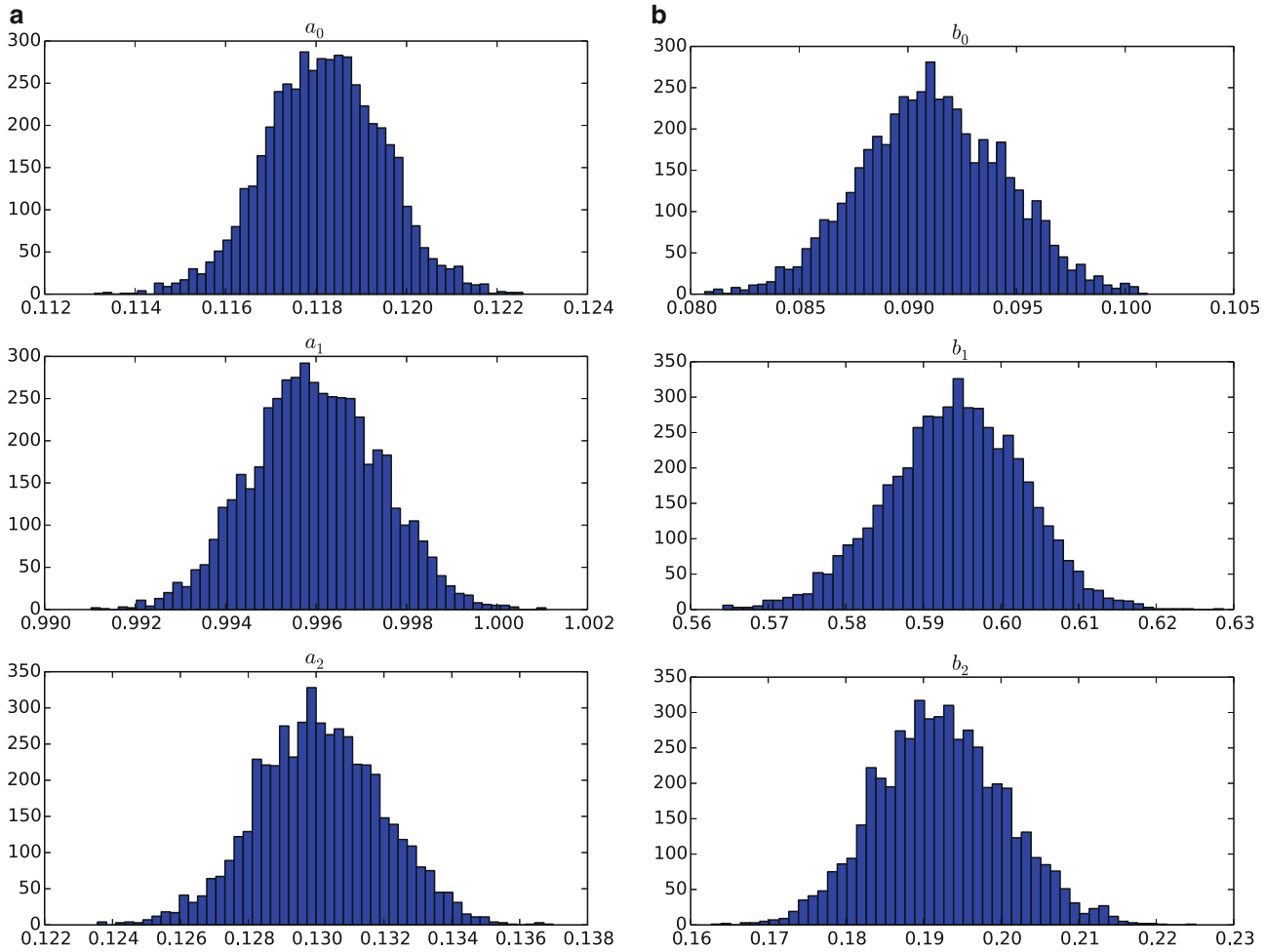

Fig. 30.4 Marginal histograms for the parameters of the metamodel. (**a**) Half-circle. (**b**) Chevron

Table 30.1 Summary of the metamodels' inferences

Metamodel's parameters for half-circle			Metamodel's parameters for chevron		
Parameter	Mean	95 % HPD interval	Parameter	Mean	95 % HPD interval
a_0	0.118	[0.115, 0.121]	b_0	0.091	[0.085, 0.097]
a_1	0.996	[0.993, 0.999]	b_1	0.594	[0.576, 0.610]
a_2	0.130	[0.127, 0.134]	b_2	0.192	[0.176, 0.208]

30.4 Concluding Remarks

In this paper probability distribution functions are introduced as candidates for approximating the Bayesian model's evidence. Since the area under a PDF is one, the scale factor parameter of the metamodel approximates the model's evidence, eliminating the need of numerically integrating the evidence.

The method is illustrated by a numerical example. Two models are suggested for artificially generated data. The Bayes factor was calculated by the traditional Monte Carlo integration with 5000 samples. Then a normal distribution was selected to approximate the integrand of the evidence function (EDF). A sampling strategy is discussed, and the stopping criteria was satisfied with less than 30 samples of the likelihood. The results show good consistency with the traditional method.

The method should be tested for more complex problems. A potential challenge with the proposed technique lies with large data sets. In these cases, the EDF has very small values and fitting a metamodel is not straightforward.

References

1. Caicedo, J.M., Zárate, B.A., Giurgiutiu, V., Yu, L., Ziehl, P.: Bayesian finite element model updating for crack growth. In: Structural Dynamics, vol. 3, pp. 861–866. Springer, New York (2011)
2. Zárate, B.A., Caicedo, J.M., Wieger, G., Marulanda, J.: Bayesian finite element model updating using static and dynamic data. In: Structural Dynamics, vol. 3, pp. 395–402. Springer, New York (2011)
3. Burnham, K.P., Anderson, D.R.: Model Selection and Multimodel Inference: A Practical Information-Theoretic Approach. Springer, New York (2002)
4. Yuen, K.-V., Beck, J.L., Katafygiotis, L.S.: Unified probabilistic approach for model updating and damage detection. J. Appl. Mech. **73**(4), 555–564 (2006)
5. Beck, J.L., Katafygiotis, L.S.: Updating models and their uncertainties, I: Bayesian statistical framework. J. Eng. Mech. **124**(4), 455–461 (1998)
6. Behmanesh, I., Moaveni, B.: Probabilistic identification of simulated damage on the dowling hall footbridge through Bayesian finite element model updating. Struct. Control Health Monit. **22**(3), 463–483 (2015)
7. Ortiz-Lasprilla, A.R., Caicedo, J.M.: Comparing closed loop control models and mass-spring-damper models for human structure interaction problems. In: Dynamics of Civil Structures, vol. 2, pp. 67–74. Springer, New York (2015)
8. Vakilzadeh, M.K., Yaghoubi, V., Johansson, A.T., Abrahamsson, T.: Manifold Metropolis adjusted Langevin algorithm for high-dimensional Bayesian FE model updating in structural dynamics. In: Cunha, A., Caetano, E., Ribeiro, P., Müller, G. (eds.) Proceedings of the 9th International Conference on Structural Dynamics, EURODYN 2014. Porto, 30 June-2 July (2014). https://web.fe.up.pt/~eurodyn2014/CD/papers/422_MS18_ABS_2065.pdf [ISBN 978-972-752-165-4]
9. Boulkaibet, I., Marwala, T., Mthembu, L., Friswell, M., Adhikari, S.: Sampling techniques in Bayesian finite element model updating. In: Topics in Model Validation and Uncertainty Quantification, vol. 4, pp. 75–83. Springer, New York (2012)
10. Boulkaibet, I., Mthembu, L., Marwala, T., Friswell, M., Adhikari, S.: Finite element model updating using the shadow hybrid monte carlo technique. In: Special Topics in Structural Dynamics, vol. 6, pp. 489–498. Springer, New York (2013)
11. Boulkaibet, I., Mthembu, L., Marwala, T., Friswell, M., Adhikari, S.: Finite element model updating using the shadow hybrid monte carlo technique. Mech. Syst. Signal Process. **52**, 115–132 (2015)
12. McKenna, F.: Opensees: a framework for earthquake engineering simulation. Comput. Sci. Eng. **13**(4), 58–66 (2011)
13. Melchers, R.: Importance sampling in structural systems. Struct. Saf. **6**(1), 3–10 (1989)
14. Cheung, S.H., Beck, J.L.: Bayesian model updating using hybrid monte carlo simulation with application to structural dynamic models with many uncertain parameters. J. Eng. Mech. **135**(4), 243–255 (2009)
15. Wan, H.-P., Mao, Z., Todd, M.D., Ren, W.-X.: Analytical uncertainty quantification for modal frequencies with structural parameter uncertainty using a gaussian process metamodel. Eng. Struct. **75**, 577–589 (2014)
16. Jones, D.R.: A taxonomy of global optimization methods based on response surfaces. J. Glob. Optim. **21**(4), 345–383 (2001)
17. Madarshahian, R., Caicedo, J.M.: Reducing mcmc computational cost with a two layered Bayesian approach. In: Model Validation and Uncertainty Quantification, vol. 3, pp. 291–297. Springer, Cham (2015)
18. James, F.: Statistical Methods in Experimental Physics, vol. 7. World Scientific, Singapore (2006)
19. Jaynes, E.T.: Probability Theory: The Logic of Science. Cambridge University Press, Cambridge (2003)
20. VanderPlas, J.: Frequentism and Bayesianism: a python-driven primer. arXiv preprint. arXiv:1411.5018 (2014)
21. Bugnion, P.: Scikit-monaco: a python toolkit for monte carlo integration. https://pypi.python.org/pypi/scikit-monaco (2013)
22. Robert, C., Casella, G.: Monte Carlo Statistical Methods. Springer, New York (2013)
23. Kolmogorov, A.: Foundations of the theory of probability. Second English edition: (trans: Morrison, N.). Chelsea Publishing Company, New York (1956). http://www.york.ac.uk/depts/maths/histstat/kolmogorov_foundations.pdf
24. Azam, S.E., Mariani, S.: Dual estimation of partially observed nonlinear structural systems: a particle filter approach. Mech. Res. Commun. **46**, 54–61 (2012)
25. Azam, S.E., Bagherinia, M., Mariani, S.: Stochastic system identification via particle and sigma-point kalman filtering. Sci. Iran. **19**(4), 982–991 (2012)

Chapter 31
Calibration, Validation and Uncertainty Quantification of Nominally Identical Car Subframes

Mladen Gibanica, Thomas J.S. Abrahamsson, and Magnus Olsson

Abstract In this paper a finite element model, with over half a million degrees-of-freedom, of a car front subframe has been calibrated and validated against experimental MIMO data of several nominally identical components. The spread between the individual components has been investigated and is reported. Sensor positioning was performed with an extended effective independence method, using system gramians to reject sensors with redundant information. The Fisher information matrix was used in the identification of the most significant model calibration parameters. Validation of the calibrated model was performed to evaluated the difference between the nominal and calibrated model, and bootstrapping used to investigate the validity of the calibrated parameters. The parameter identification, calibration, validation and bootstrapping have been performed using the open-source MATLAB tool FEMCali.

Keywords Model updating • Uncertainty quantification • Parameter identification • Bootstrapping • Femcali

31.1 Introduction

Finite element (FE) modelling is commonly used in many industries today, including the automotive industry, for research and development purposes. It allows for very quick and cost efficient design alterations of complicated models, compared to prototype models, which is crucial in advanced industries. However, there are drawbacks in terms of the confidence engineers can have in their FE models. To address this issue, verification is usually performed to verify that the FE solver is free from errors and the mesh is sufficiently fine such that the underlying mathematical model is properly solved. The FE model can then be compared to an experimental model, usually acquired through experimental modal analysis (EMA) [1], in a procedure denoted model validation. If the FE model does not predict the responses acquired from the experimental model, to within some given tolerances, it is possible to update the model. This step is called calibration, or model updating, which seeks to minimise some deviation metric between the two models [2].

It is well known that mass produced components exhibit some amount of spread in dynamic and static properties between individuals in a population. The spread can originate from multiple sources such as material spread and geometry spread, to name a few. In the automotive industry it is common to have thousands of nominally identical components, and even whole cars, that are supposed to be represented by one FE model. Validating and calibrating against one of these components will not necessarily produce a model that better captures the characteristics of another, nominally identical, component. Therefore, it is of interest to quantify the spread between the individuals and to calibrate and validate towards some sample set from the whole population.

In a recently initiated project at Volvo Car Corporation, the goal is to better understand the uncertainties in components and their propagation through other components. This paper presents the first part of the project where three nominally identical front subframes of a Volvo XC90 (2015) have been studied, shown in Fig. 31.1. The component properties are important since it provides support for the engine and connects the suspension link arms to the car body. This means that

M. Gibanica (✉)
Applied Mechanics, Chalmers University of Technology, Hörsalsvägen 7A, 41296 Göteborg, Sweden

Volvo Car Corporation, 40531 Göteborg, Sweden
e-mail: mladen.gibanica@chalmers.se

T.J.S. Abrahamsson
Applied Mechanics, Chalmers University of Technology, Hörsalsvägen 7A, 41296 Göteborg, Sweden

M. Olsson
Volvo Car Corporation, 40531 Göteborg, Sweden

S. Atamturktur et al. (eds.), *Model Validation and Uncertainty Quantification, Volume 3*, Conference Proceedings of the Society for Experimental Mechanics Series, DOI 10.1007/978-3-319-29754-5_31

Fig. 31.1 The front subframe is an important part from a vibration perspective as it connects the suspension link arms and engine to the car body. (**a**) Parts of an XC90; (**b**) Front subframe location in the car

vibrations are transferred through the component and further to the driver and passengers. It is also an important part from a safety perspective as a crash box is attached to it. Therefore it is of interest to investigate this component thoroughly.

In this paper the calibration was performed with the open-source tool FEMcali as described in reference [3]. The method works by creating a parametrised surrogate model of the FE model and it then seeks to minimise a deviation metric between the created surrogate and experimental model's frequency response functions (FRFs) using normalised damping in both models. Previous work using this method has been performed on various industrial components with good results [4–7]. Pretest planing has been performed with the expansion method of effective independence (EfI) [8] with an added gramian rejection step, described further in [9]. The three components were tested in a vibration-test with an improved frequency strategy [10] for subspace state-space system identification [11]. The FE model consists of a 556,758 degrees-of-freedom mesh and has been calibrated against all three components. Bootstrapping has been used in order to quantify the uncertainty in the chosen calibration parameters.

The paper is organised as follows. In Sect. 31.2 the theoretical part of the calibration procedure is presented briefly and in Sect. 31.3 the vibration testing is explained and the finite element model presented. In Sect. 31.4 the findings from calibration, validation and bootstrapping are shown. Section 31.5 concludes the paper.

31.2 Theory

A brief overview of the theory presented in [3], where the calibration and validation methods used in this paper are presented, is recited here.

31.2.1 Mechanical Systems Theory

The equations of motion for a mechanically vibrating system can be written as

$$\mathbf{M}\ddot{\mathbf{q}} + \mathbf{V}\dot{\mathbf{q}} + \mathbf{K}\mathbf{q} = \mathbf{f}(t) \tag{31.1}$$

where $\mathbf{M}$, $\mathbf{V}$ and $\mathbf{K} \in \mathbb{R}^{m\times m}$ represent the mass, damping and stiffness matrices, respectively. The general displacement vector is denoted by $\mathbf{q}$ and the external force vector by $\mathbf{f}(t)$. The dot notation is used for time differentiation. The full load vector can be mapped to the input vector $\mathbf{u} \in \mathbb{R}^{n_u}$ with the Boolean transformation matrix $\mathbf{U}$ as $\mathbf{f} = \mathbf{U}\mathbf{u}$. A parametrisation of the mass and stiffness matrices, $\mathbf{M}$ and $\mathbf{K}$, can be made where the physical parameters are placed in a vector $\mathbf{P} \in \mathbb{R}^{n_p}$. The parametrised mass and stiffness matrices can then be expressed as $\mathbf{M} = \mathbf{M}(\mathbf{P})$ and $\mathbf{K} = \mathbf{K}(\mathbf{P})$. Minimiser methods usually work better with scaled unknowns, and thus the parameter vector $\mathbf{P}$ can be related to a normalised parameter vector $\mathbf{p}$ and some fixed non-zero nominal parameter setting $\mathbf{P}_0$ so that $\mathbf{P} = \mathbf{P}_0(1 + \mathbf{p})$ holds [3].

The system on second order form in Eq. (31.1) can be transformed to first order form by forming the state vector $\mathbf{x} = [\mathbf{q}^T, \dot{\mathbf{q}}^T]^T$ and using the dummy equation $\mathbf{I}\dot{\mathbf{q}} - \mathbf{I}\dot{\mathbf{q}} = 0$ which gives

$$\begin{cases} \dot{\mathbf{x}} = \mathbf{A}\mathbf{x} + \mathbf{B}\mathbf{u} \\ \mathbf{y} = \mathbf{C}\mathbf{x} + \mathbf{D}\mathbf{u} \end{cases} \tag{31.2}$$

with $\mathbf{A} \in \mathbb{R}^{n \times n}$ representing the system matrix, $\mathbf{B} \in \mathbb{R}^{n \times n_u}$ representing the input matrix, $\mathbf{C} \in \mathbb{R}^{n_y \times n}$ representing the output matrix, $\mathbf{D} \in \mathbb{R}^{n_y \times n_u}$ representing the force throughput matrix and $\mathbf{y}$ representing the system outputs. The relationship between n and m is $n = 2m$. The system matrices can be shown to be

$$\mathbf{A} = \begin{bmatrix} \mathbf{0} & \mathbf{I} \\ -\mathbf{M}^{-1}\mathbf{K} & -\mathbf{M}^{-1}\mathbf{V} \end{bmatrix} \qquad \mathbf{B} = \begin{bmatrix} \mathbf{0} \\ \mathbf{M}^{-1}\mathbf{U} \end{bmatrix} \tag{31.3}$$

where $\mathbf{C}$ and $\mathbf{D}$ are formed appropriately so that linear combinations of the system states $\mathbf{x}$ and inputs $\mathbf{u}$ form the system outputs $\mathbf{y}$.

31.2.2 Calibration, Validation and Bootstrapping

A deviation metric that is smooth and does not discriminate against low structural responses is used in a gradient based minimiser during the calibration procedure. The deviation metric used, as a metric for both calibration and validation is

$$\delta = \frac{\boldsymbol{\epsilon}^T \boldsymbol{\epsilon}}{N} \qquad \text{with} \qquad \boldsymbol{\epsilon}(\mathbf{p}) = \log_{10}\text{vect}(\mathbf{H}^A(\mathbf{p})) - \log_{10}\text{vect}(\mathbf{H}^X) \tag{31.4}$$

where the transfer function matrix $\mathbf{H}^X$ stand for the experimental model representation and $\mathbf{H}^A(\mathbf{p})$ stand for the FE model representation, at parameter $\mathbf{p}$. Here N stands for the total number of data points in the FRF matrix, as explained below. The transfer function matrix can be formed from the system in Eq. (31.2), at frequency ω_i, as

$$\mathbf{H}(\omega_i) = \mathbf{C}(j\omega_i\mathbf{I} - \mathbf{A})^{-1}\mathbf{B} + \mathbf{D} \tag{31.5}$$

where j given by $j^2 = -1$ is the imaginary number and $\mathbf{I}$ the identity matrix of appropriate dimension. Here vect$(\cdot)$ stands for the vectorisation operation in which a matrix is transformed into a vector by stacking the columns of the matrix. Therefore the transfer function matrix $\mathbf{H} \in \mathbb{C}^{n_y \times n_u}$ at each frequency step with n_f frequency steps in total is transformed into an $n_y n_u n_f \times 1$ column vector.

The deviation metric must be evaluated at the same frequencies for the FE and experimental model. Therefore a system identification procedure is introduced in order to obtain a state-space system on the form shown in Eq. (31.2) where the identified system can be evaluated at any frequency. This step is also necessary for damping equalisation mentioned below, and in addition removes the noise found in the measured data. The calibration metric is comparing the FE model with the identified model and it is therefore crucial that the identified model is very well estimated. In this paper the N4SID, linear subspace state-space system identification, method is used [11].

In [3] the authors advise in selecting the frequencies based on the half-band width, $\Delta\omega_i$, of the eigenmodes. The half-band width for a damped structural resonance at a certain frequency ω_i can be expressed as $\Delta\omega_i = 2\xi_i\omega_i$ where ξ_i is the i:th relative modal damping. This is used in the calibration procedure, but in the EMA frequency lines were selected based on a more recent paper by Vakilzadeh et al. [10] in which the authors advise in another selection strategy for improving the estimated state-space system with the N4SID method [11].

The obtained data from an EMA is split into two sets, one for a classical leave out validation $\mathbf{H}_v^X$ and the other for calibration $\mathbf{H}_c^X$. While classical leave out validation is used to verify that the calibrated model is in fact improved on, by letting it make predictions on previously unseen data, bootstrapping is commonly used in many fields for quantifying the uncertainty in model parameters [12]. It works by resampling the calibration data set $\mathbf{q} = \text{vect}(\mathbf{H}_c^X) = \{\mathbf{q}_1 \dots \mathbf{q}_{n^X}\}$, with $n^X = n_y^X n_u^X n_f^X$ and superscript X representing the calibration data set, such that k random draws are taken where each draw is the same length as $\mathbf{q}$ and can contain overlapping data. Statistical properties can then be evaluated from these k models and used to quantify the uncertainty in the calibration parameters.

31.2.3 Damping Equalisation

Since damping is very hard to model and is crucial in FRF based model calibration it is often assigned as a simple representation in the FE model. Commonly the damping is measured in an experimental modal analysis experiment and the measured value is assigned to the FE model. The issue then is that damping usually varies between modes which make it very hard to map an experimental model's damping to a complex FE model with high mode density. Therefore, damping equalisation was proposed in [3]. The same level of damping is enforced for all modes in both the FE model and identified model from the experimental model, rendering mode pairing unnecessary.

The state-space system in Eq. (31.2) can be brought to diagonal form by a similarity transformation, here being the eigenvector matrix $\mathbf{X}$ of the eigenvalue problem $\mathbf{AX} = \mathbf{X\Lambda}$ where $\mathbf{\Lambda}$ is the diagonal eigenvalue matrix. With coordinate transformation $\mathbf{x} = \mathbf{Xz}$ the diagonal system becomes

$$\begin{cases} \dot{\mathbf{z}} = \mathbf{X}^{-1}\mathbf{AXz} + \mathbf{X}^{-1}\mathbf{Bu} \\ \mathbf{y} = \mathbf{CXz} + \mathbf{Du} \end{cases} \tag{31.6}$$

where $\mathbf{X}^{-1}\mathbf{AX} = \bar{\mathbf{A}} = \text{diag}(\lambda_i)$ and λ_i is the i:th complex valued system pole. For small damping the relative damping ξ_i is

$$\xi_i = -\frac{\mathbb{R}(\lambda_i)}{|\mathbb{C}(\lambda_i)|} \tag{31.7}$$

where $|\cdot|$ represent the absolute value and $\mathbb{R}(\cdot)$ and $\mathbb{C}(\cdot)$ represent the real and complex part of an imaginary number, respectively. In the damping equalisation step all modal damping are set to a fixed value $\xi_i = \xi_0 \forall i$. Thus a new system is obtained

$$\begin{cases} \dot{\mathbf{z}} = \tilde{\mathbf{A}}\mathbf{z} + \mathbf{X}^{-1}\mathbf{Bu} \\ \mathbf{y} = \mathbf{CXz} + \mathbf{Du} \end{cases} \tag{31.8}$$

with $\tilde{\mathbf{A}} = \text{diag}(\tilde{\lambda}_i)$ and

$$\tilde{\lambda}_i = \mathbb{C}(\lambda_i)(-\xi_0 + i) \quad \forall \mathbb{C}(\lambda_i) > 0, \quad \tilde{\lambda}_i = \mathbb{C}(\lambda_i)(\xi_0 + i) \quad \forall \mathbb{C}(\lambda_i) < 0. \tag{31.9}$$

The FE model's modal viscous damping can then be formed as [13]

$$\mathbf{V} = \mathbf{MX}\text{diag}(m_i^{-1})\text{diag}(2\xi_0 m_i \omega_i)\text{diag}(m_i^{-1})\mathbf{X}^T\mathbf{M} \tag{31.10}$$

where ω_i are the eigenfrequencies, m_i the modal masses and $\mathbf{X}$ the eigenvector matrix from the undamped eignevalue problem of the system in Eq. (31.1), $\mathbf{KX} = \mathbf{MX}\text{diag}(\omega_i^2)$.

31.2.4 Model Reduction

In industry, very large FE models are commonly used that may consist of more than millions degrees-of-freedom. It is therefore not feasible to perform model calibration on full scale models, but rather on reduced or surrogate models. The eigenvector matrix at the nominal parameter setting $\mathbf{T}$ is used as a reduction basis and is kept constant during the calibration procedure, which is formed from the undamped eigenvalue problem of the system in Eq. (31.1).

$$\mathbf{K}(\mathbf{p}_0)\mathbf{T} = \mathbf{M}(\mathbf{p}_0)\mathbf{T\Omega}, \quad \mathbf{\Omega} = \text{diag}(\omega_i^2) \quad \forall \omega = [\omega_{low}, \omega_{high}] \tag{31.11}$$

Here $[\omega_{low}, \omega_{high}]$ represent the frequency range of interest. It is now possible to form the reduced mass and stiffness matrices at any parameter setting $\mathbf{p}$

$$\bar{\mathbf{M}}(\mathbf{p}) = \mathbf{T}^T\mathbf{M}(\mathbf{p})\mathbf{T}, \quad \bar{\mathbf{K}}(\mathbf{p}) = \mathbf{T}^T\mathbf{K}(\mathbf{p})\mathbf{T} \tag{31.12}$$

with the reduced mass and stiffness matrices at the nominal parameter setting $\mathbf{p}_0$ being represented by $\bar{\mathbf{M}}_0$ and $\bar{\mathbf{K}}_0$. Gradients of the reduced mass and stiffness matrices are

$$\bar{\mathbf{M}}_j = \mathbf{T}^T \left(\frac{d\mathbf{M}}{dp_j}\Big|_{p=p_0} \right) \mathbf{T}, \quad \bar{\mathbf{K}}_j = \mathbf{T}^T \left(\frac{d\mathbf{K}}{dp_j}\Big|_{p=p_0} \right) \mathbf{T} \tag{31.13}$$

for the i:th calibration parameters. By taking the first order expansions of the Taylor series of the reduced mass $\bar{\mathbf{M}}$ and stiffness $\bar{\mathbf{K}}$ matrices about $\mathbf{p}_o$ it is possible to form a surrogate model that is linear in the parameters.

$$\tilde{\mathbf{M}}(\mathbf{p}) = \bar{\mathbf{M}}_0 + \sum_{j=1}^{n_p} \left(\mathrm{p} - \mathrm{p}_{\mathrm{j},0}\right) \bar{\mathbf{M}}_j, \quad \tilde{\mathbf{K}}(\mathbf{p}) = \bar{\mathbf{K}}_0 + \sum_{j=1}^{n_p} \left(\mathrm{p} - \mathrm{p}_{\mathrm{j},0}\right) \bar{\mathbf{K}}_j \tag{31.14}$$

The new state-space matrix quadruple $\{\tilde{\mathbf{A}}, \tilde{\mathbf{B}}, \tilde{\mathbf{C}}, \tilde{\mathbf{D}}\}$ can be formed with a state transformation $\mathbf{x} = \mathbf{T}\boldsymbol{\xi}$ and with a viscous damping matrix $\tilde{\mathbf{V}}$ formed as in Eq. (31.10).

$$\tilde{\mathbf{A}} = \begin{bmatrix} \mathbf{0} & \mathbf{I} \\ -\tilde{\mathbf{M}}^{-1}\tilde{\mathbf{K}} & -\tilde{\mathbf{M}}^{-1}\tilde{\mathbf{V}} \end{bmatrix} \qquad \tilde{\mathbf{B}} = \begin{bmatrix} \mathbf{0} \\ \tilde{\mathbf{M}}^{-1}\mathbf{T}^T\mathbf{U} \end{bmatrix} \qquad \tilde{\mathbf{C}} = \begin{bmatrix} \mathbf{T} & \mathbf{0} \\ \mathbf{0} & \mathbf{T} \end{bmatrix} \qquad \tilde{\mathbf{D}} = \mathbf{D} \tag{31.15}$$

Its frequency response functions can then be evaluated using Eq. (31.5).

31.3 Experimental and FE Model Preparation

In this section the experimental modal analysis is explained in detail followed by an explanation of the FE model and the calibration parameter selection.

31.3.1 Experimental Modal Analysis

The structure considered is a front subframe of a Volvo XC90 (2015). Three individual subframes were used in this paper, which focuses on the spread in dynamic properties of these. The subframes were also weighted. A steel frame support structure was mounted in which the components were hung, at the exhaust hangers, in long thin high-strength lines, see Fig. 31.2a, attached to steel springs on the supporting structure for a low bounce rigid body mode. Thus, the subframes were efficiently isolated from its surrounding and the rigid body modes were kept low, with eigenfrequencies below 5 Hz.

Sensor positions were selected by the modified set expansion EfI [8] algorithm with added gramian rejection for nodes containing similar information [9]. The candidate set consisted of 170 possible locations, or 510 degrees-of-freedom. The 10 triaxial accelerometers were placed first, with a rejection threshold of $T_s = 0.05$, see [9]. Two accelerometers were initially positioned at the exhaust hangers seen at the top middle in Fig. 31.2a. These positions were selected as a few local modes excited these parts and it was of interest to find their vibration pattern. Then 15 uniaxial accelerometers were positioned, with a rejection threshold of $T_s = 0.01$, from an initial set of the 10 triaxial accelerometers previously positioned. The last 12 uniaxial accelerometers were placed for visualisation purposes. In the end only 31 accelerometers, shown in Fig. 31.3, were used for calibration and validation. Two input locations were used, one seen in Fig. 31.2a and the other seen in Fig. 31.2b. The second input was added to capture an edge wise mode, mode 6 in Fig. 31.5g. The shaker used was a Modal Shop type K2007E01 with a plastic stinger. This shaker was compared to another shaker, Ling Dynamic Systems type V201, with a metallic stinger and the frequency response functions started to deviate over 700 Hz, well out of the region for this study. A Brüel&Kjær force sensor, of type 8203 with an IEPE converter 2647B, was used to measure the excitation force. Two small stinger attachment plates of 0.2 g each were glued at the two input positions. Direct transfer functions were obtained by placing accelerometers directly on the back side of the input position. This was considered best practice as the metal plates were flat and thin (approximately 2 mm). Three types of piezoelectric accelerometers were used, 10 triaxial PCB Piezotronic type 356A03 weighting 1 g each, 26 uniaxial PCB Piezotronic type PCB 352C22/NC weighting 0.5 g each and 1 uniaxial PCB Piezotronic type PCB 333B32 weighting 4 g. One triaxial accelerometer with its z component normal to the surface was used as direct accelerence at position 2 as seen in Fig. 31.3a. Accelerometer 31 was of type PCB 333B32 and used as the

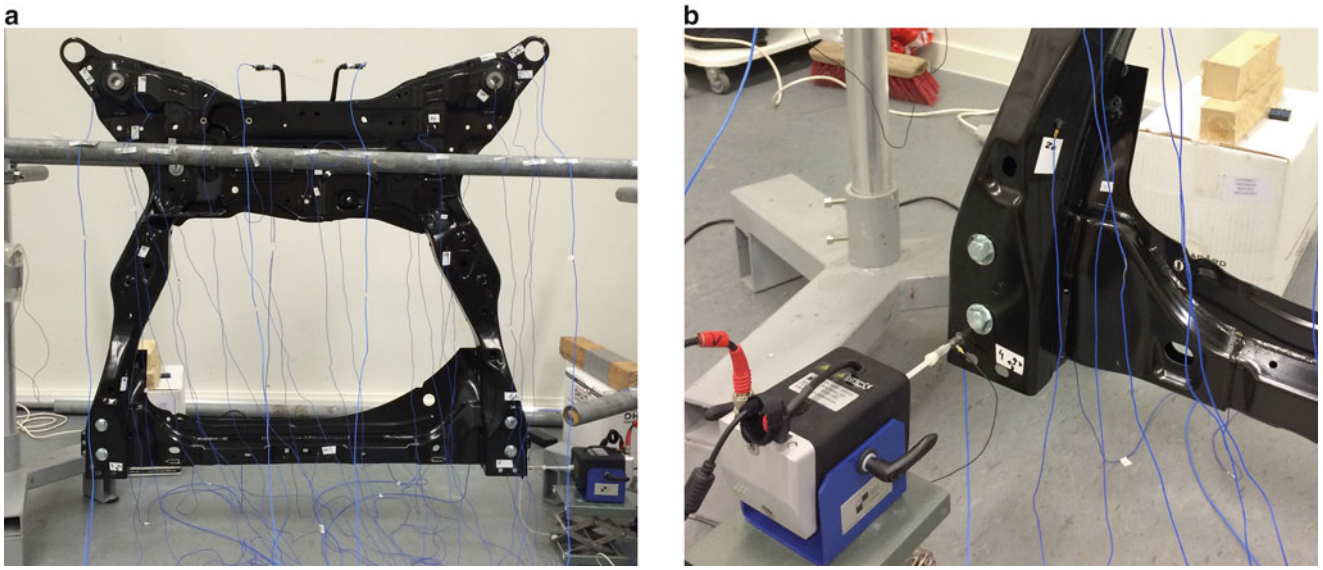

Fig. 31.2 Front subframe shown in (**a**) with input at location 31, and (**b**) with input at location 2z

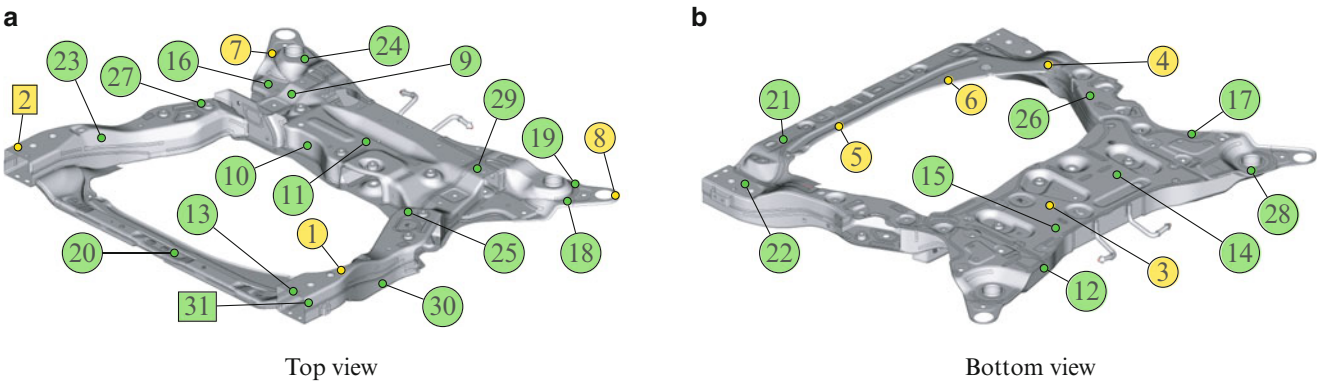

Fig. 31.3 Top view of subframe in (**a**) and bottom view in (**b**) with *colour* markings. *Yellow and green circles* represent a triaxial and uniaxial sensor, respectively. The *two square markings* represent the input positions. The excitations were normal to the surface

direct accelerence for the second input, see Fig. 31.3a. All accelerometers were attached with synthetic wax. It was difficult to orient the triaxial accelerometers with synthetic wax and keep the orientation during a vibration test, thus the x and y components must be considered more uncertain than the normal component.

Bolts were added to the structure, seen in Fig. 31.2b, due to contact between two metal parts that caused non-linear effects. Two small wedges were also placed between two metal sheets due to possible contact between the two areas, and because it was found that the modes exciting this area, modes 4–7 seen in Fig. 31.5e–h, greatly varied between the three components. To place accelerometers firmly on the exhaust hangers it was necessary to glue washers at the hangers. The same alterations were added to the FE model.

Multiple tests were performed for two types of excitation methods. For each input a periodic chirp, from 5 to 700 Hz, was performed at different amplitudes to rule out non-linearities. Then the calibration data was gathered from an adaptive multisine test where 10 frequencies were sent to the shaker simultaneously. The improved frequency selection [10] for system identification with N4SID [11] was used in a frequency range from 40 to 700 Hz with 8200 frequency lines for the multisine test.

A very good mathematical model must be identified from the measured data for good calibration results. Thus, the rigid body modes influence was substracted from the experimental data by using the FE model rigid body modes. Three systems were then identified for the three components with the same model order, 38, that gave modes ranging from 50 to 490 Hz. Rigid body modes and a few residual high frequency modes with very low damping were manually added to the obtained systems and a reestimation of the state-space model's **B** and **C** matrices was performed with the multisine data used in the identification procedure. Data from the chirp testing in the region from 10 to 50 Hz was used in the reestimation, too. This

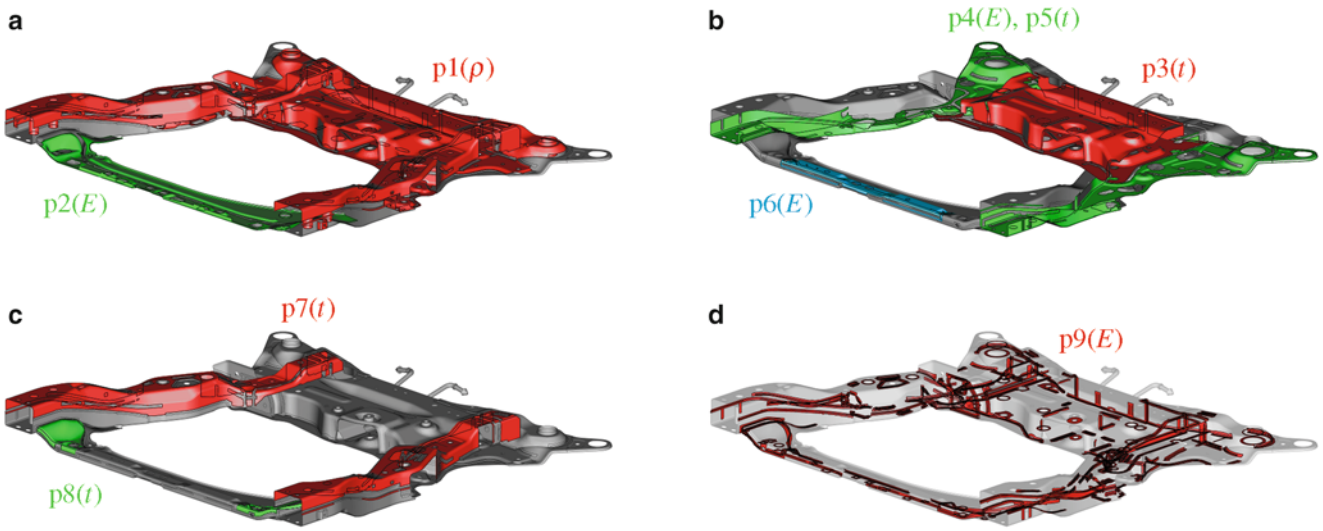

Fig. 31.4 The 9 different parameters and their physical meaning, where ρ represent density, E stiffness and t thickness. (**a**) Parameters p1(ρ) and p2(E); (**b**) Parameters p3(t), p4(E), p5(t) and p6(E); (**c**) Parameters p7(t) and p8(t); (**d**) Parameter p9(E)

resulted in a very good model that corresponded well to test data, even after damping equalisation. The equalisation was only performed on the modes in the frequency range of interest, doing so on the manually added rendered a very poor estimate. Some channels gave poorer fit than others, and those were chosen as validation data, as the validation procedure uses raw data and no identified model is needed. Thus the validation channels selected from the 31 accelerometers or, 47 channels, for both inputs were $\{2, 5, 7, 9, 12, 13, 17, 18, 24, 27, 30, 32, 34, 36, 38, 40, 42, 43\}$. In Fig. 31.3, with x, y, and z components for the triaxial sensors, this represents the following accelerometers $\{1_y, 2_y, 3_x, 3_z, 4_z, 5_x, 6_y, 6_z, 8_z, 11, 14, 16, 18, 20, 22, 24, 26, 27\}$.

31.3.2 Finite Element Model

The finite element model was updated to the best available CAD data. It was also verified visually that the FE model corresponded well to the three components. The thickness of the red highlighted part in Fig. 31.4b was updated manually from direct measurement so that the FE model corresponded to the mean mass of the three component. The FE model consisted of 556,758 degrees-of-freedom with 96,550 shell elements, 11,017 solid elements, 6 CBAR elements, 23 groups of RBE2 elements and 22 groups of CONM2 elements. No verification of the mesh discretisation was performed as it was considered that the mesh quality was satisfactory.

The inverse Fisher information matrix (FIM) was used in an identifiability analysis to fix parameters that would render the calibration problem unidentifiable. Figure 31.4 indicates the different parameters, and their representation is shown in Table 31.1. Non highlighted parameters in Fig. 31.4 were fixed to their nominal value. In short, three parameter types were used, stiffness, density and thickness. A lower and upper bound to these three types was decided to be approximately 20 %, with some deviations.

Four modes were found to be local around the exhaust hanger hooks, which can be seen at the top in Fig. 31.2a. A sensitivity analysis was therefore performed to understand how sensitive they were to mass differences using a Rayleigh quotient analysis (RQ) [13].

$$RQ = \omega_n^2 = \frac{\boldsymbol{\phi}_n^T \mathbf{K} \boldsymbol{\phi}_n}{\boldsymbol{\phi}_n^T \mathbf{M} \boldsymbol{\phi}_n} = \frac{\omega_n^2}{1}, \quad \omega_n'^2 = \frac{\omega_n^2}{\boldsymbol{\phi}_n^T (\mathbf{M} + \Delta\mathbf{M}) \boldsymbol{\phi}_n} = \frac{\omega_n^2}{1 + \boldsymbol{\phi}_n^T \Delta\mathbf{M} \boldsymbol{\phi}_n} \tag{31.16}$$

Here $\boldsymbol{\phi}_n$ is the eigenvector associated with the nth eigenvalue ω_n^2. A small mass perturbation $\Delta\mathbf{M}$ resulted in the new, approximate, eigenvalue $\omega_n'^2$. It was found that adding 4 g on the tip of each hanger made the first two local exhaust modes, mode 8 and 9 in the flexible mode order as seen in Fig. 31.5i and j, switch place with flexible mode 7, seen in Fig. 31.5h. The calibration was performed without considering these modes. A similar behaviour was found for three higher modes, 11, 12 and 13, seen in Fig. 31.5l–n, respectively. One of these three higher modes was observable from test data and therefore used in the calibration.

Table 31.1 Nominal parameters, calibrated parameters denoted $FE_{c3\#}$, mean of bootstrapping parameters denoted FE^B_{μ} and their coefficient of variation (COV, %) denoted $FE^B_{COV\#}$ are shown

#	Parameter	Nominal	FE_{c1}	FE_{c2}	FE_{c3}	$FE^B_{\mu 1}$	$FE^B_{\mu 2}$	$FE^B_{\mu 3}$	FE^B_{COV1}	FE^B_{COV2}	FE^B_{COV3}
p1	ρ (kg/m^3)	7850.00	7299.31	7425.24	7411.31	7837.2	8531.21	7409.87	0.19	2.61	0.71
p2	E (GPa)	210.00	243.56	204.29	218.72	255.71	212.38	226.59	0.10	2.68	1.83
p3	t (mm)	2	1.82	1.79	1.79	1.88	1.98	1.73	0.07	2.23	3.33
p4	E (GPa)	210.00	234.44	234.94	226.99	231.07	254.25	214.83	0.36	2.22	2.06
p5	t (mm)	2	1.80	1.85	1.98	2.06	1.99	2.00	0.45	2.27	4.37
p6	E (GPa)	220.00	180.00	180.00	180.00	169.44	179.01	177.80	0.16	1.15	0.70
p7	t (mm)	2	1.88	1.84	1.86	2.25	2.34	1.83	0.41	5.54	3.97
p8	t (mm)	2	2.20	2.20	2.20	1.70	2.70	1.21	0.89	11.40	44.23
p9	E (GPa)	210.00	208.75	208.60	208.53	197.67	166.14	230.19	0.11	6.79	6.02

In this table E represent material stiffness, t denote thickness and ρ denote density

31.4 Results from Calibration, Validation and Bootstrapping

Three experimental datasets with 47 output channels and 2 input channels were used. The calibration set was formed with 29 output channels and 2 input channels and the validation set with 18 output channels and 2 input channels. Thus, approximately 38 % of the data was used for validation. The frequency region covered was from 55 to 430 Hz. The calibration was run with a damping equalisation of 0.2 %, 3 frequencies per half-band width, 100 Latin hypercube [14] samples, 20 start locations, including the nominal model, and maximum 100 iterations. While the calibration procedure uses data from the identified model, the calibration in the bootstrapping step is performed towards the raw data. Before the bootstrapping procedure the surrogate model is updated with respect to the improved parameter setting. In [12] it is proposed to run the bootstrapping $k = 100$ times. This was not feasible because of the large data sets used. Instead $k = 10$ was chosen. The surrogate model was created with model order 50 and 9 parameters. The nominal Young's modulus was 210 GPa and the density 7850 kg/m^3. The thickness of the various parts varied from 4 to 1.6 mm. In Table 31.1 the parameters used in the calibration are described. It can be seen that there are some differences in the parameters between the three calibrated components. Most notably, all of them reach the lower bound set on parameter p6 and the upper bound on parameter p8. The bootstrapping results varies between the three calibrated components, but this was expected because real experimental data is used here. More interesting is that the coefficient of variation was 44 % for the thickness parameter p8 for component 3. This parameter had the largest variation for all three components. In Fig. 31.4c it can be seen that this is a small part and it is connected to a region where many modes are locally active. It should be noted that the bootstrapping was run very few times and there was some deviation between the raw data and identified model which could partly explain the high spread in some of the parameters.

In Table 31.2 the eigenfrequencies for the three measured components are given, along with their mean μ and coefficient of variation COV in percent. Eigenfrequencies for the nominal FE model is also shown, followed by the eigenfrequencies for the three calibrations, one per component. The mean and coefficient of variation is also given for these three calibrations. Note that the 8th, 9th, 12th and 13th flexible modes from the FE model were omitted, as mentioned earlier. They were omitted by analysing their modeshapes and eigenfrequencies. It can be noted in Table 31.2 that the coefficient of variation between the three tested components is highest, 2.06 %, for mode 4 and lowest for mode 2 with a value of 0.15 %. It can also be noted that the modes that differ the most come in groups. This is most noticeable in modes 4–7. Mode 1, mode 13 and mode 15 also have a coefficient of variation larger than 1 %.

The deviation metric for calibration of component ID 1 is lowered by 21.60 % from 1.63 to 1.33 for raw measurement data. The validation metric decreases by 23.38 % from 1.76 to 1.35. For component ID 2 the calibration metric is reduced by 16.68 % from 1.59 to 1.28 and the validation metric is lowered by 17.59 % from 1.67 to 1.37. Lastly, for component ID 3 the calibration metric is reduced by 16.86 % from 1.56 to 1.31 and the validation metric is reduced by 16.28 % from 1.65 to 1.38. It is noticed that the calibration of component ID 1 was more successful than the two other, but also that the initial deviation was higher resulting in a similar calibration and deviation metric for the three components.

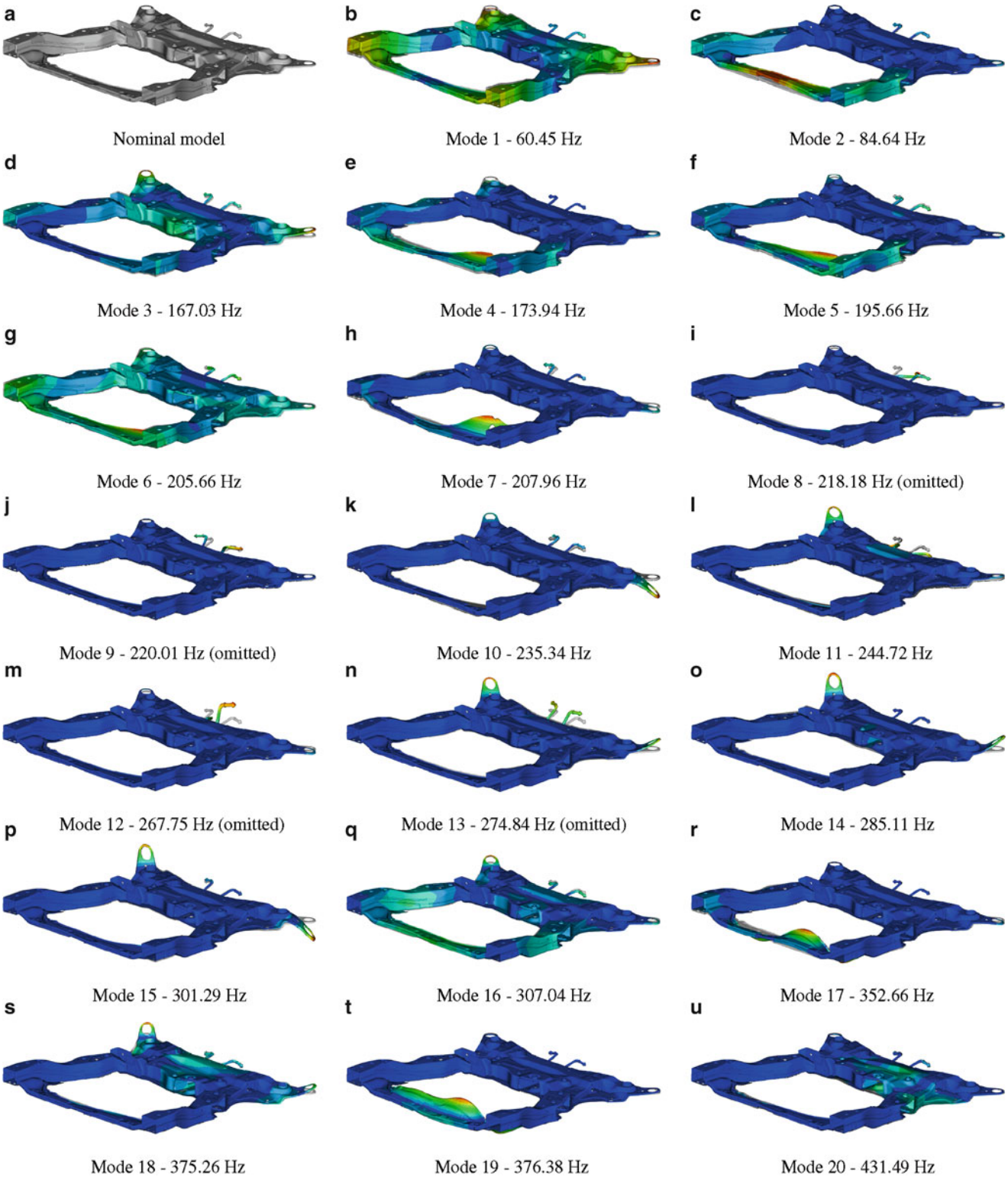

Fig. 31.5 The nominal model (**a**) along with the 20 first non-calibrated modes, from mode 1 (**b**) to mode 20 (**u**). *Blue* indicate small modal motion and *red* large motion

Table 31.2 Eigenfrequencies (Hz) for the 1st and up to the 15th flexible mode of the three components (ID #), the nominal FE model (FE_n) and the calibrated FE models ($F_{c\#}$) against the three components are shown

Mode	ID 1	ID 2	ID 3	ID_μ	ID_{COV}	FE_n	FE_{c1}	FE_{c2}	FE_{c3}	FE_μ	FE_{COV}
1	60.282	59.464	58.988	59.578	1.10	60.45	60.15	59.43	59.20	59.59	0.83
2	80.224	80.252	80.036	80.171	0.15	84.64	83.71	82.13	82.87	82.91	0.95
3	169.80	168.44	168.74	168.99	0.42	167.03	169.79	168.08	168.18	168.68	0.57
4	178.42	171.24	174.48	174.72	2.06	173.94	176.41	173.03	174.25	174.56	0.98
5	201.48	197.63	200.49	199.87	1.00	195.66	198.99	195.28	197.39	197.22	0.94
6	208.49	203.93	204.82	205.75	1.17	205.66	210.89	206.00	209.01	208.63	1.18
7	215.64	208.59	209.36	211.20	1.83	207.96	217.64	207.96	209.36	211.65	2.47
8	247.12	244.73	244.13	245.33	0.64	235.34	238.89	237.40	236.81	237.70	0.45
9	257.49	256.15	258.07	257.24	0.38	244.72	243.36	241.56	241.13	242.02	0.49
10	285.75	291.17	289.51	288.81	0.96	285.11	288.58	287.35	287.43	287.78	0.24
11	304.19	303.04	303.57	303.60	0.19	301.29	305.38	303.84	305.18	304.80	0.28
12	306.55	303.77	305.39	305.24	0.46	307.04	311.94	307.82	310.05	309.94	0.67
13	361.67	348.98	353.64	354.76	1.81	352.66	361.17	346.51	353.55	353.75	2.07
14	374.46	371.68	369.97	372.04	0.61	375.26	377.94	372.18	374.75	374.96	0.77
15	397.58	385.60	388.83	390.67	1.59	376.38	394.35	374.66	380.62	383.21	2.63

Also, the mean (μ, Hz) and the coefficient of variation (COV, %) are given for each mode. For the FE model only the calibrated models are considered in the statistics

The FRFs of two different input output combinations are shown in Fig. 31.6. It can be seen that the region between 310 and 350 Hz contains some spurious modes that were not identified and used in the calibration, but they were included in the bootstrapping. It can also bee seen that small improvements is gained from the calibration.

31.5 Conclusions

Three front subframe of a car have been calibrated, validated and uncertainties quantified with bootstrapping. The eigenfrequency variation between the three components and the three calibrated FE models has been investigated, followed by the variations in the calibration parameters. It was found that the calibrated components had a similar deviation metric, from initially different metric values. Parameter p8 was found to be uncertain and parameters p6 and p8 were bound in the calibration procedure. Both of the parameters were located on the area where many modes were locally excited and it was believed, before calibration, that this area caused the difference between the components. The structure exhibited many local modes that were hard to measure accurately. A better parametrisation of the FE model is necessary for a better calibration outcome. Thus, further investigation is necessary in finding the reason for the deviation between the components and the FE model.

Considerable time was spent on performing the tests. The structures exhibited very different modal characteristics in some frequency intervals, while they were very equal in others. It was concluded that the plate seen in the middle bottom part of Fig. 31.2a deviated in some way between the three components. It has also been concluded by investigating the FE model modeshapes in Fig. 31.5 that many modes activated the outer thin rounded parts of the structure. There was no direct way of introducing a physical parameter to control these parts as they were connected to another part, together forming one large part of the structure, seen in green in Fig. 31.4b. It is therefore believed that neither stiffness, density nor thickness are sufficient parameter types. Rather, a mapped thickness would probably yield better results. If no mapped thickness is available, a random thickness variation in the part of interest would be another way to overcome the problem. Further, the curvature would be another interesting parameter to try out.

The calibration, validation and bootstrapping has been performed using the open source MATLAB program FEMcali, downloadable from Mathwork's webpage at www.mathworks.com.

Acknowledgements Volvo Car Corporation is gratefully acknowledged for providing the funding for this paper.

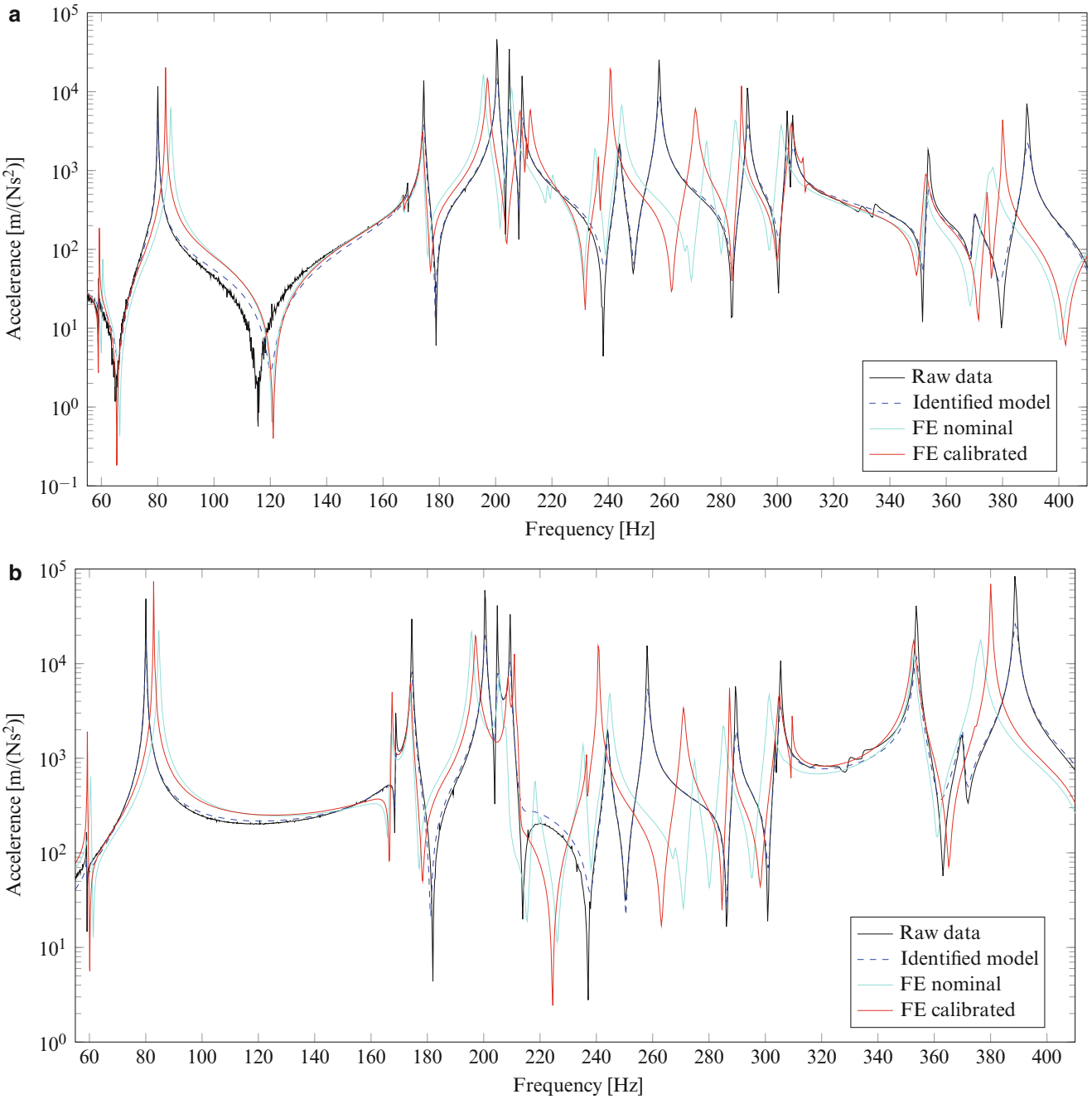

Fig. 31.6 Frequency response functions of component ID 3 with raw data (*black*), identified model (*dashed blue*), nominal FE model (*cyan*) and calibrated FE model (*red*). In (**a**) the input is at position 31 while the output is at position 1x and in (**b**) the input is at position 31 and output is at position 5z (normal to the surface)

References

1. Ewins, D.J.: Modal Testing: Theory, Practice and Application, 2nd edn., 576pp. Wiley-Blackwell, Baldock, Hertfordshire, Philadelphia, PA (2000)
2. Friswell, M.I., Mottershead, J.E.: Finite Element Model Updating in Structural Dynamics. Solid Mechanics and Its Applications, vol. 38. Springer Netherlands, Dordrecht (1995)
3. Abrahamsson, T.J.S., Kammer, D.C.: Finite element model calibration using frequency responses with damping equalization. Mech. Syst. Signal Process. **6263**, 218–234 (2015). doi:10.1016/j.ymssp.2015.02.022

4. Abrahamsson, T., et al.: Calibration and cross-validation of a car component using frequency response functions and a damping equalization technique. In: 26th International Conference on Noise and Vibration Engineering, ISMA 2014, Including the 5th International Conference on Uncertainty in Structural Dynamics, USD 2014, pp. 2625–2640 (2014)
5. Abrahamsson, T.J.S., et al.: Calibration and validation of a car subframe finite element model using frequency responses. In: Mains, M. (ed.) Topics in Modal Analysis. Conference Proceedings of the Society for Experimental Mechanics Series, vol. 10, pp. 9–22. Springer International Publishing, Cham (2015)
6. Larsson, K.-J., et al.: Calibration and cross-validation of a car component model using repeated testing. In: Atamturktur, H.S., et al. (eds.) Model Validation and Uncertainty Quantification. Conference Proceedings of the Society for Experimental Mechanics Series, vol. 3, pp. 339–350. Springer International Publishing, Cham (2015)
7. Granado, I.E.: Model calibration of a vehicle tailgate using frequency response functions. Chalmers Student Theses (2015). http://studentarbeten.chalmers.se. Accessed on 22 Oct 2015
8. Kammer, D.C.: Sensor set expansion for modal vibration testing. Mech. Syst. Signal Process. **19**(4), 700–713 (2005). doi:10.1016/j.ymssp.2004.06.003
9. Gibanica, M., Abrahamsson, T.J.S., Kammer, D.C.: Redundant information rejection in sensor localisation using system gramians. In: Proceedings of the 34th IMAC, Orlando, FL (2016)
10. Vakilzadeh, M.K,. et al.: Experiment design for improved frequency domain subspace system identification of continuous-time systems. In: Proceedings of the 17th IFAC Symposium on System Identification, Bejing (2015)
11. McKelvey, T., Akçay, H., Ljung, L.: Subspace-based identification of infinite-dimensional multivariable systems from frequency-response data. Automatica **32**(6), 885–902 (1996). doi:10.1016/0005-1098(96)00022-2
12. Hastie, T., Tibshirani, R., Friedman, J.: The Elements of Statistical Learning - Data Mining, Inference, and Prediction. Springer Series in Statistics. Springer, New York (2009)
13. Craig, R.R.J., Kurdila, A.J.: Fundamentals of Structural Dynamics, 2nd edn, 744pp. Wiley, Hoboken, NJ (2006)
14. McKay, M.D., Beckman, R.J., Conover, W.J. Comparison of three methods for selecting values of input variables in the analysis of output from a computer code. Technometrics **21**(2), 239–245 (1979). doi:10.1080/00401706.1979.10489755

Chapter 32
Modeling and Experimental Test Study of a Multilayer Piezoelectric Actuator

ZhongZhe Dong, Cassio T. Faria, Wim Desmet, and Martin Hromcik

Abstract In order to increase the performance of piezoelectric actuators/sensors, a common practice is to stack thin layers of active materials with electrodes in between such that higher electric fields are achieved inside the piezoelectric elements. Modeling this composite material requires either a detailed description of the layers components or the use of equivalent properties. The work presented in this paper achieved a comparative study between these two modeling approaches. The predictions are verified against experimental result. It shows that the both modeling approaches obtain similar results in modal analysis, and in each numerical model, a consistent natural frequency mismatch was found to compare with the experimental modal analysis. A Frequency Response Function (FRF) comparison between experimental measurement and equivalent properties modeling approach also carried out to check its dynamic prediction capability. A simple model updating has been carried out at the end; the updated numerical models exhibit a good consistency with experimental measurement.

Keywords Piezoelectric • Multilayer actuator • Equivalent properties • FEM models • Experimental modal analysis

32.1 Introduction

Smart materials have been widely investigated for applications in automotive, aerospace and other industry-related applications. In particular, piezoelectric materials are of interest due to their dual actuator/sensor characteristics that can be implemented in a large number of mechanical applications, for example vibration suppression, active control, damage detection etc. Various types of piezoelectric materials have been developed over the past few decades and many of them have been already introduced into industry application as actuators/sensors. In order to maximize the actuation capacity/sensitivity of piezoelectric actuators/sensors, thin layers of piezoceramic are stacked with electrodes in between such that higher electric fields are achieved inside the piezoelectric elements. And modeling this composite material requires either a detailed description of the components or the use of piezoelectric equivalent properties.

Many piezoelectric models using equivalent properties approach can be found from literature [1–8]. Therein, Hariri et al. [2, 3] created beam and plate models of non-collocated unimorph piezoelectric patches bonded to a thin structure. Wang [6] developed a FEM model that combines finite 2D single-layer elements with 3D type piezoelectric sublayer elements for the static and dynamic analysis of a piezoelectric bimorph. The piezoelectric sublayers were used for the electric field approximation in piezoelectric materials. Marinkovic et al. [8] gave the important aspects on the modeling piezoelectric active thin-walled structures, such as modeling of electric fields in piezoelectric patches. Erturk et al. [9] proposed the analytical solution to characterize the dynamic behavior of the beam-type piezoelectric bimorph structure on energy harvesting. A common feature in the above researches is focus on the single layer piezoelectric actuators/sensors with host structures, and

Z. Dong (✉)
Engineering Service Division, Siemens Industry Software NV, Interleuvenlaan 68, 3001, Leuven, Belgium

Department of Mechanical Engineering, Katholieke University Lueven, Celestijnenlaan 300, 3001 Heverlee, Leuven, Belgium

Faculty of Electrical Engineering, Czech Technical University in Prague, Karlovo namesti 13, 121 35 Prague 2, Czech Republic
e-mail: zhongzhe.dong@siemens.com

C.T. Faria
Engineering Service Division, Siemens Industry Software NV, Interleuvenlaan 68, 3001, Leuven, Belgium

W. Desmet
Department of Mechanical Engineering, Katholieke University Lueven, Celestijnenlaan 300, 3001 Heverlee, Leuven, Belgium

M. Hromcik
Faculty of Electrical Engineering, Czech Technical University in Prague, Karlovo namesti 13, 121 35 Prague 2, Czech Republic

S. Atamturktur et al. (eds.), *Model Validation and Uncertainty Quantification, Volume 3*, Conference Proceedings of the Society for Experimental Mechanics Series, DOI 10.1007/978-3-319-29754-5_32

the host structures are most likely dominant the dynamic behavior of the system. A research of piezoelectric multilayer beam bending actuator, which focused on experiment test and theoretical aspects, has been carried out in [10]. A tip deflection was studied in static case on different cantilever bi-layer actuator in [11]. The constitutive equations of the symmetrical triple layer piezoelectric bender has been carried out in [12]. And the electromechanical coupling correction and efficiency was carried out from [13, 14]. Few of the above work achieved a dynamic validation of multilayer piezoelectric actuators/sensors, which is important in many applications such as precise positioning and shape control etc.

Both detailed description modeling (detailed models) and equivalent properties modeling (simplified models) approaches can be used for piezoelectric multilayer actuators/sensors modeling. The simplified models, such as beam and plate models could be more suitable to model small thin multilayer actuators/sensors, but the performance of the simplified models is vague for such multilayer actuators/sensors modeling. Therefore, the simplified models need to be reviewed, and a comparative study between detailed models and simplified models need to be carried out. Furthermore, an accurate complete property of the actuator is necessary in numerical models, especially for detailed models. A general way in real applications is to use the piezoelectric material data sheet in the numerical models, which is to the effective properties of the multilayer actuators/sensors. This could cause a mismatch between numerical models and experimental measurement in multilayer actuators/sensors applications. This material properties mismatch uncertainty is another issue need to be addressed.

The work in this paper presents a comparative study between those two modeling approaches on a multilayer piezoelectric bending actuator and the predictions are verified against experimental result.

32.2 Piezoelectric Bending Actuator

The multilayer concept leads to a thickness reduction of the piezoceramic layers in the actuator. Assuming a certain voltage applied on one piezoceramic layer, a thinner piezoceramic layer can generate a lager electric filed, yielding a larger deformation on this layer. Therefore, the multilayer actuator can produce large actuation movement with relative low operating voltage.

The studied piezoelectric bending actuator (type PI PL140) in this paper is made of two piezoceramic layers with three electrodes (Fig. 32.1). The dimension of the actuator is 45 mm × 11 mm × 0.6 mm with 40 mm available free length. The polarization directions are the same on both piezoceramic layers. The electrodes 1 and 3 are respectively connected to the ground and the maximum voltage, and the third operating voltage is applied on the electrode 2 between the two piezoceramic layers. In this case, the actuator can be controlled over the full range (from zero to the maximum voltage) [15]. In a clamped-free boundary condition configuration, by applying different voltages on each piezoelectric layer, it can be made to expand or contract on each layer and resulting bending movement. Thus, the bending displacement is caused by the contraction d31-effect. The design concept of the bending actuator leads a transverse isotropic material property. It is made of PIC251 which has a similar piezoelectric property as PIC255 [16]. The material information (Table 32.1) can be found in [16, 17].

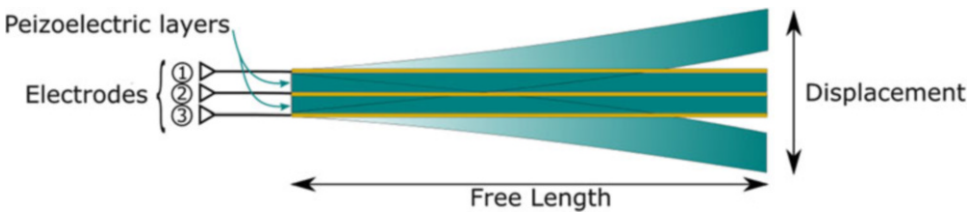

Fig. 32.1 Piezoelectric bending actuator configuration

Table 32.1 Mechanical and piezoelectric properties of the piezoceramic PIC251

Density (kg/m^3)	7800
Mechanical compliance ${s_{11}}^E$ (m^2/N)	15.9×10^{-12}
Mechanical compliance ${s_{33}}^E$ (m^2/N)	20.7×10^{-12}
Piezoelectric constant d_{31} (C/N)	160×10^{-12}
Relative permittivity ${\epsilon_{33}}^T$	3300

32.3 Numerical Models

The numerical models are usually based on the piezoelectric constitutive equations which describe the piezoelectric effect as a linear phenomenon, in which the mechanical and electrical variables are interdependent [18]:

$$\sigma = K_E \varepsilon - e\Phi \tag{32.1}$$

$$D = e^T \varepsilon - \epsilon_E \Phi \tag{32.2}$$

Where σ is stress, ε is strain, D is electric displacement, Φ is electric field, K_E is the stiffness matrix, e is the piezoelectric constants and ϵ_E is the dielectric matrix.

Different Finite Element Method (FEM) models have been carried out to predict the dynamic behavior of the piezoelectric actuator. Samcef Field® solid element model was used to achieve the detailed models due to its special multilayer piezoelectric modeling capability. Two separated layers of solid elements were defined to represent the two piezoelectric layers on the actuator (Fig. 32.2), and the two layers element are linked together by using nodes connection. The piezoelectric material properties must be assigned on each element layer to assign the piezoelectric element. In this case each node on the piezoelectric elements has six mechanical degrees of freedom (three translation and three rotation in Cartesian coordinates) and a seventh electric degree of freedom. The nodes on each up and bottom surface of the solid element layer were linked together by using the virtual master nodes (in cell form) to form the virtual electrodes. The boundary condition and loads were imposed on the mesh as a standard FEM model.

Comparing with the solid model, the plate model applies a simplification on the thickness of the actuator. And various two dimensional plane piezoelectric models can be found in literature [1, 3, 4, 19]. Basically the piezoelectric constitutive equations are simplified with two dimensional plane strain or plane stress assumptions. Different beam piezoelectric models exist in [2, 9, 19]. The beam model only consider the structural behavior on the primary bending direction. The formulation of the piezoelectric FEM model was adopted from [6] for both beam and plate models. This formulation combined the two dimensional single-layer representation model with a finite number of sublayer for the electric potential field.

The bending actuator was modeled as a single mechanical structure and a two electrical layers for both beam and plate models. Wherein, the Bernoulli beam theory was applied to the beam model and the plate model was based on Kirchhoff plate assumption. The stiffness induced by the piezoelectric effect was modeled respectively for each sublayer in both models. The equation of motion can be expressed as Eq. (32.3) for both simplified models.

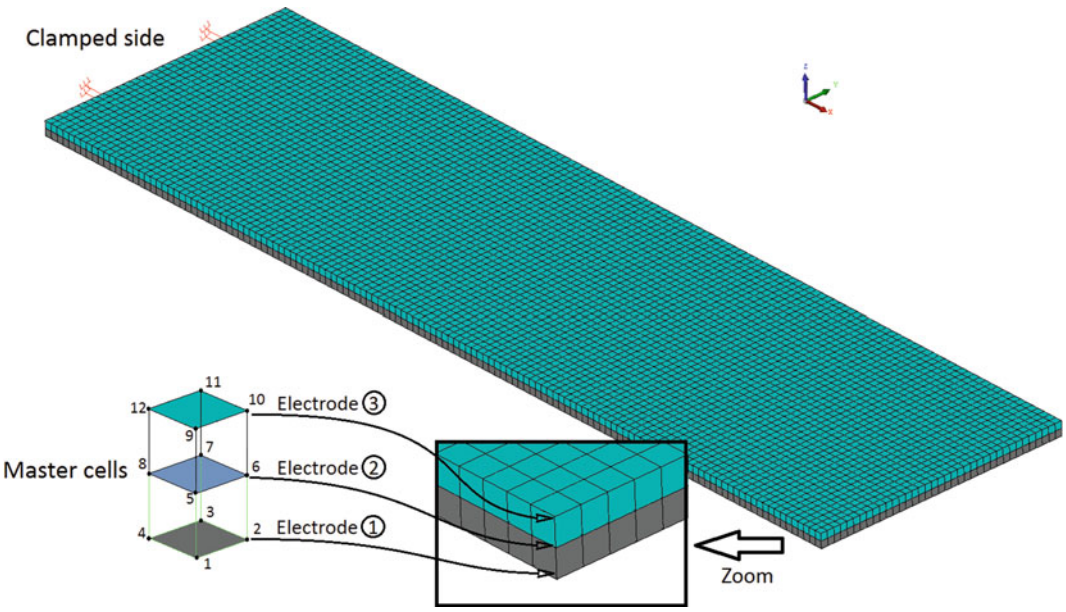

Fig. 32.2 Solid element model mesh

Table 32.2 Proportional damping coefficients

	α	β
Beam model	6.5976	8.8680e-07
Plate model	6.7808	8.6922e-07

$$M\ddot{w} + C\dot{w} + \left(K - \sum_{i=1}^{i=n} \Theta_{w\Phi}^{i} \left(\Theta_{\Phi\Phi}^{i}\right)^{-1} {\Theta_{w\Phi}^{i}}^{T}\right) \quad w = 0\ i = 1,\ 2,\ 3, \ldots,\ n \tag{32.3}$$

Where C, M, and K are respectively the damping matrix, mass matrix and stiffness matrix. $\Theta_{w\Phi}^{i}$ and $\Theta_{\Phi\Phi}^{i}$ are respectively the piezoelectric coupling matrix and the piezoelectric capacity matrix of ith piezoelectric layer.

Since the thickness of the electrodes is unknown, the presence of the electrodes is neglected in all models. Linear electric potential distribution is assumed through the thickness of each piezoelectric layer in all the numerical models. The size of the elements is $0.3 \times 0.3 \times 0.3$ mm in solid element model, and the total number of element is 9844. The size of the element is 1×1 mm in the plate element model, so there are 440 elements in total. Since the size of the element is 1 mm in the beam element model, there are only 40 elements (Table 32.2).

The proportional damping is introduced into the numerical models (Eq. (32.3)). The proportional damping coefficients are calculated by using the orthogonal transformation in Eq. (32.4). Table 32.3 shows the estimated proportional damping coefficients.

$$C = \alpha M + \beta K \tag{32.4}$$

$$c_i = \frac{1}{2\omega_i}\alpha + \frac{\omega_i}{2}\beta, \quad i = 1,\ 2,\ 3, \ldots \tag{32.5}$$

Where c_i and ω_i are respectively the critical damping ratio and natural frequencies of ith mode, α and β are the proportional coefficients.

To be consistent with the experiment measurement, the velocity over force FRFs are formulated for both mechanical and electric excitation cases (resp. Eqs. (32.6), (32.7)). Since the piezoelectric effect cannot totally transform the electric energy into mechanical energy, especially, the multilayer actuators have the coupling effect between layers, Therefore, a piezoelectric actuator maximum mechanic-electric energy transmission coefficient λ (expressed in Eq. (32.8)) [17] is introduced here, then the electromechanical coupling vectors can be directly used as the input localization vector.

$$\frac{v}{F} = \sum_{i=1}^{i=\infty} j\omega \frac{\phi_i^T \phi_i}{m_i\left(\omega_i^2 + 2j\xi_i\omega_i\omega - \omega^2\right)} L, \quad i = 1,\ 2,\ 3, \ldots \tag{32.6}$$

$$\frac{v}{V} = \sum_{i=1}^{i=\infty} j\omega \frac{\phi_i^T \phi_i}{m_i\left(\omega_i^2 + 2j\xi_i\omega_i\omega - \omega^2\right)} \Theta_{w\Phi}\lambda, \quad i = 1,\ 2,\ 3, \ldots \tag{32.7}$$

$$\lambda = \frac{32}{9k_{31}^2}\left(\sqrt{1 - k_{31}^2/4} - \sqrt{1 - 13k_{31}^2/16}\right)^2, \quad k_{31} = \sqrt{\frac{d_{31}^2}{\epsilon s_{11}}} \tag{32.8}$$

Where ϕ_i, ω_i, m_i and ξ_i are respectively the mode shape, natural frequencies, modal mass and damping ratio calculated from the proportional damping of ith mode. L is the input localization vector.

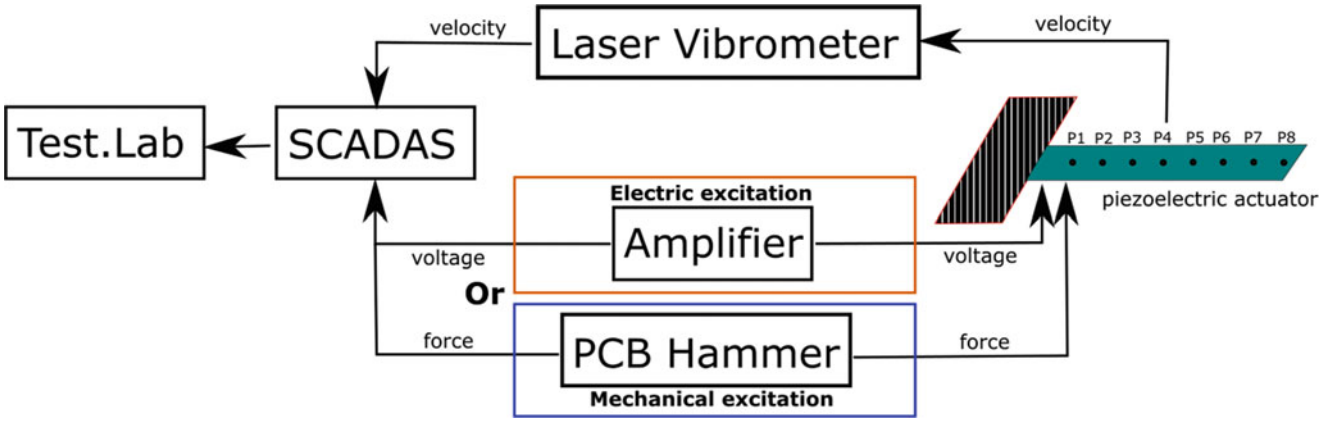

Fig. 32.3 Experimental setup

32.4 Experiment Modal Analysis

A bending actuator has been tested to understand its dynamic behavior. The impact test has been carried out using an impact hammer type PCB Piezotronics SN14893. The impact test advantage is that it avoids the shaker dynamic and base excitation complexity comparing with spectral test [9]. The Polytec model OFV3001S-LMS laser vibrometer was used to achieve the non-contact velocity measurement on the tested specimen, the SCADAS® model SC316 and Test.Lab® version 14A were used to collect the test data and carry out the experimental modal analysis. Figure 32.3 shows the experiment setup configuration.

The linearity and the reciprocity are very important to validity the FRF measurement. The linearity can be verified by running measurement with different levels input (force and voltage) and the FRFs should be close to each other to indicate that the system response is independent of the input level. The reciprocity test is performed by measuring the first FRF with input at point A and velocity measurement at the point B and then measure the second FRF by reversing the input and measurement locations. The two FRFs should be similar to signify that the system behavior is independent with the input location. The linearity are checked for both mechanical excitation case and electric excitation case. The measurement shows that the actuator linearly behaves in both cases. Then, the reciprocity check is achieved between p1 and p3. The measured FRFs proved that the reciprocity holds.

In the mechanical excitation case, the excitation is due to a hammer impact on the point p1 at clamped side (see Fig. 32.3), the velocity at different locations on the actuator is measured. In the electric excitation case, the excitation is subject to the input voltage from the amplifier to the actuator, and then the velocity is measured at different location. So the velocity over input (force and voltage) FRFs are respectively measured in mechanical and electric excitation cases. The experimental data has been used to complete the experimental modal analysis using Test.Lab®.

32.5 Result and Discussion

32.5.1 Modal Analysis Comparison

The numerical modal analysis has been achieved by using the PIC251 material properties in Table 32.1. The experimental modal analysis has been carried out by using PolyMax method in Test.Lab.

Table 32.3 First five modes natural frequencies comparison between different models

	1st mode (Hz)	2nd mode (Hz)	3rd mode (Hz)	4th mode (Hz)	5th mode (Hz)
Beam model	174	1082	–	3022	–
Plate model	179	1102	1475	3077	–
Solid model	180	1129	1656	3158	3175
Test.Lab modal analysis	164	1027	–	2867	–

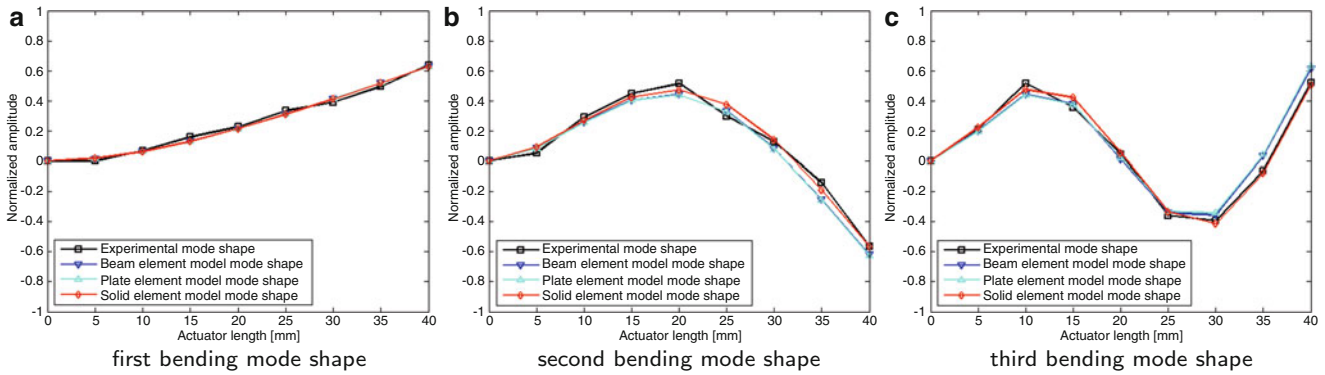

Fig. 32.4 First three normalized bending mode shapes comparison

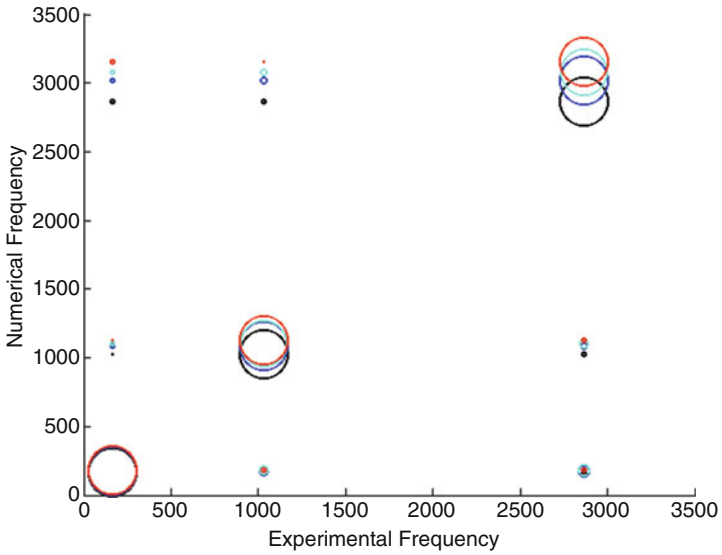

Fig. 32.5 MAC matrix between numerical models and experimental measurement

Table 32.4 Natural frequencies errors comparison between numerical models

	1st mode (%)	2nd mode (%)	3rd mode (%)	4th mode (%)	5th mode (%)
Beam model	6.1	5.3	–	5.4	–
Plate model	9.1	7.3	–	7.3	–
Solid model	9.8	9.9	–	10.0	–

The mode shapes in Fig. 32.4 are in agreement between numerical models and experimental measurement. Figure 32.5 shows the Modal Assurance Criterion (MAC) comparison between numerical models and experimental measurement: The black circles represent the auto-MAC of the experimental measurement, the blue circles show the MAC between beam model and experimental measurement, the cyan circles indicate the MAC between plate modal and experimental measurement and the red circles are the MAC between volume modal and experimental measurement. It clearly shows a good MAC correlation between numerical models and experimental modal analysis, but there exist a mismatch in frequency domain. Especially the solid element model shows the largest mismatch. Meanwhile, the first five modes natural frequencies in Table 32.2 show that the numerical models give similar results on bending modes, but the simplified models are less detailed comparing with solid model. Table 32.4 shows that, in each numerical model, there is a consistent natural frequency mismatch to compare with the experimental measurement. Therefore, the main reason is due to the mechanical properties of the bending actuator are overestimated. Since the solid model is more sensitive on the material property and the mesh quality than the beam element model and plate element model. So, it is reasonable that the solid element model shows the largest natural frequency mismatch in the comparison here.

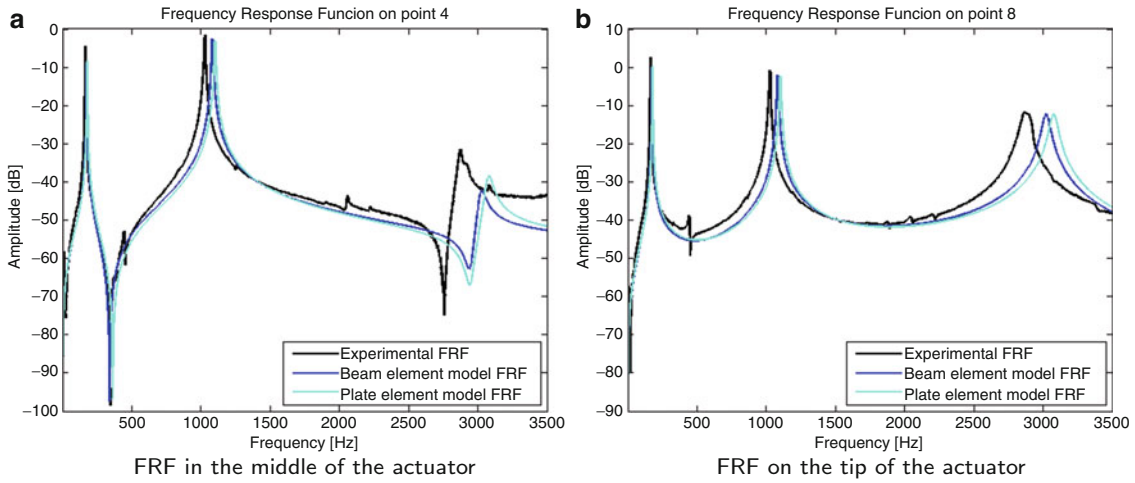

Fig. 32.6 Mechanical excitation velocity over force FRFs

32.5.2 FRFs Validation

The FRFs validation is carried out in this section. The solid element model was not considered in this section, because the simplified models need to be validated for real application. And there is not a easy way to obtain the FRFs in Samcef Field. The Modal FRF Assurance Criterion (MFAC) (Eq. (32.9)) is used here to check the correlation between numerical models and the experimental measurement [20]. It combines both space correlation and frequency domain comparison using the numerical mode shapes and the experimental FRFs.

$$MFAC = \frac{\left(\{\phi\}^T \{H\}\right)^2}{\left(\{\phi\}^T \{\phi\}\right)\left(\{H\}^T \{H\}\right)} \tag{32.9}$$

Where ϕ is the numerical mode shape and H is the experimental FRFs. the MFAC yields values between 0 and 1. and MFAC = 1 indicates a perfect correlation, while 0 indicates no correlation the MFAC value is indicated as the circle surface in the following figures. The MFAC values are indicated by the size of the circles in the figures.

Figure 32.6 shows the FRFs comparison between test and simplified numerical models on point 4 and point 8 in mechanical excitation case and Fig. 32.7 shows the FRFs comparison between test and simplified numerical models in electric excitation case. It shows a good agreement between the experimental measurement and numerical models in mechanical excitation case. In electric excitation case, the FRFs are comparatively similar between beam model and plate model. And the plate element model is slightly more accurate considering the FRFs amplitude.

In Fig. 32.8, the black circles represent the auto-MFAC of the experimental measurement, the blue circles indicate the MFAC between beam element model and experimental measurement, and the cyan circles show the MFAC between plate element modal and experimental measurement. The MFACs are consistent between experimental measurement and numerical models. It shows a good correlation between numerical models and experimental measurement in mechanic excitation case. Both auto-MFAC and MFACs exhibit the similar spatial aliasing in electric excitation case. That's due to the lack of measurement. Because only four points (p2, p4, p6 and p8) are measured in electric excitation case. The modes shapes cannot be well described by using only 4 points. In addition, the numerical mode shapes do not contains the damping information of the system. That also affects the correlation between auto-MFAC and MFACs in both cases.

32.5.3 Simple Model Updating

Since there is the mismatch between the numerical models and experimental measurement, a simple model updating was applied here to improve the numerical models quality based on experimental measurement. Considering the bending as an beam-type actuator, then, it is easy to identify the stiffness of the piezoelectric actuator by using the natural frequencies

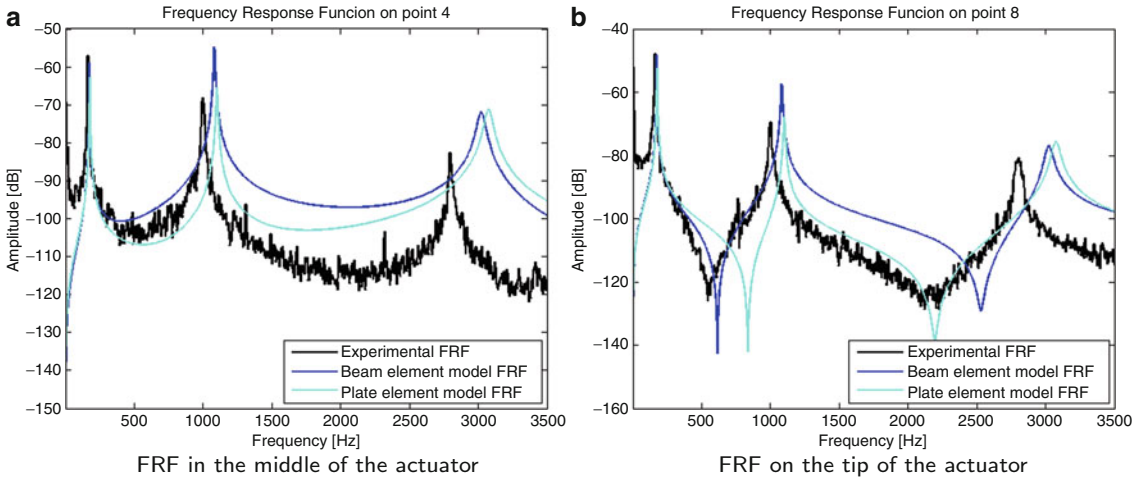

Fig. 32.7 Electric excitation velocity over voltage FRFs

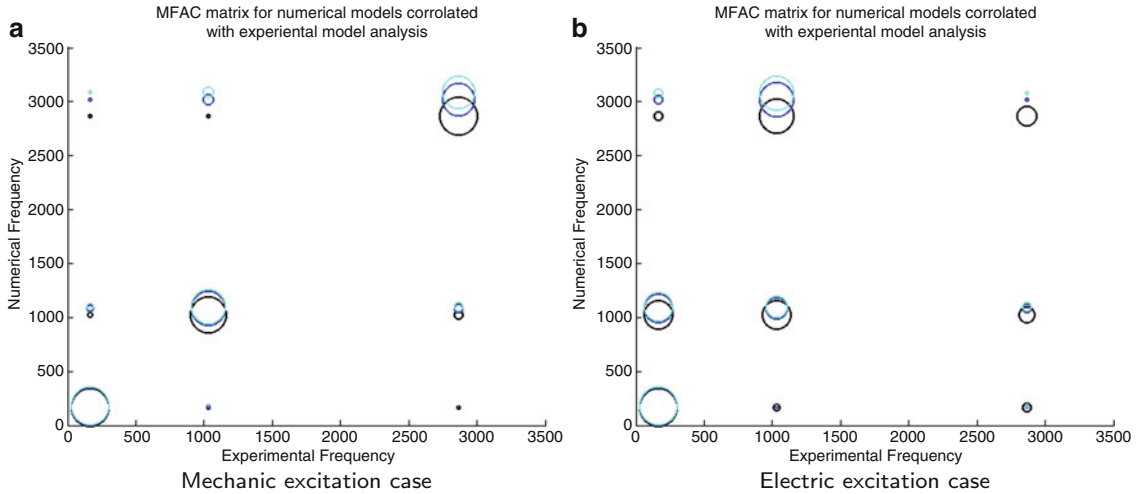

Fig. 32.8 MFAC between numerical models and experimental modal analysis

Table 32.5 First three bending modes natural frequencies comparison

	1st mode (Hz)	2nd mode (Hz)	3rd mode (Hz)
Beam model	167	1037	2899
Test.Lab modal analysis	164	1028	2867

formula, and the density of the piezoelectric can also be measured: the identified compliance $s_{11} = 19.059e\text{-}12$ and the measured density $\rho = 7070$ kg/m^3. So the material property that was defined in Table 32.1 is certainly overestimated to compare with the identified parameters. The experimental modal damping ratios are also applied into the numerical models here. The piezoelectric constants are the same as in Table 32.1. Table 32.5 shows the updated natural frequencies.

Figures 32.9, 32.10, and 32.11 exhibit that the updated beam model is highly consistent with experimental measurement. There is a significant improvement to compare with the numerical models which use the material data sheet of the piezoelectric actuator. The identified parameters are the effective properties of the actuator including the electrodes. So the possible cause of the mismatch in properties is the existence of the electrodes which is not taken into account by the presented modeling approaches. Those electrodes affect the actuator mechanical properties even they are very thin.

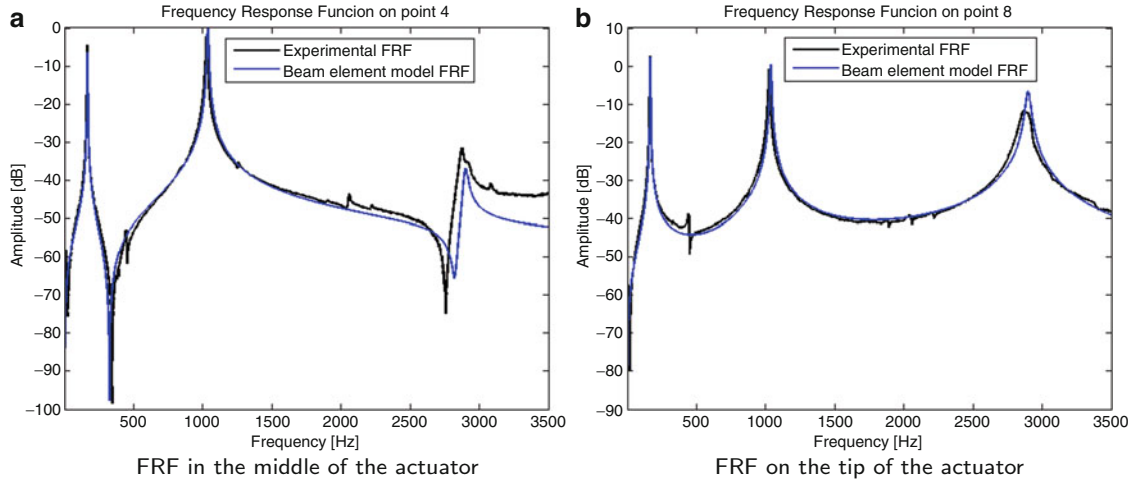

Fig. 32.9 Mechanical excitation velocity over force FRFs

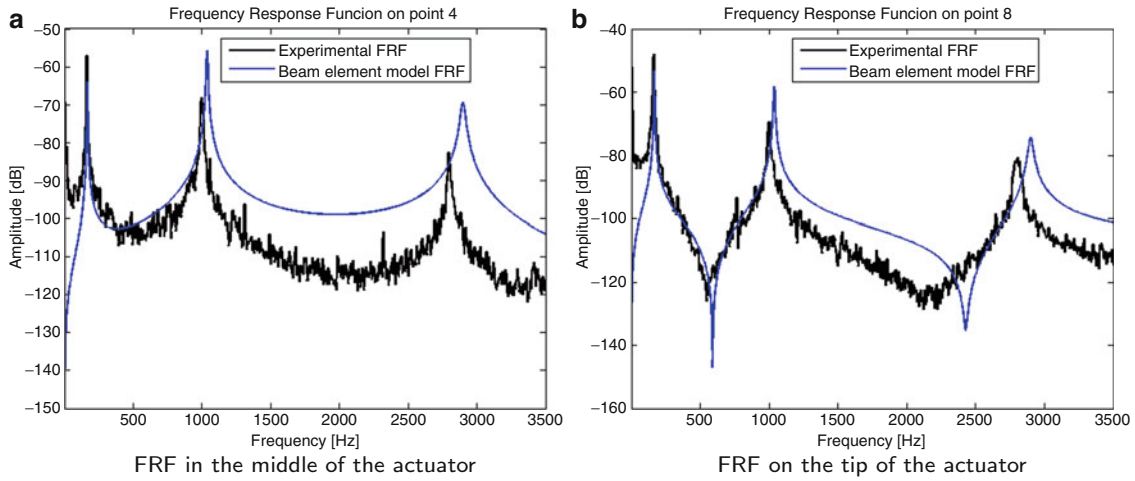

Fig. 32.10 Electric excitation velocity over voltage FRFs

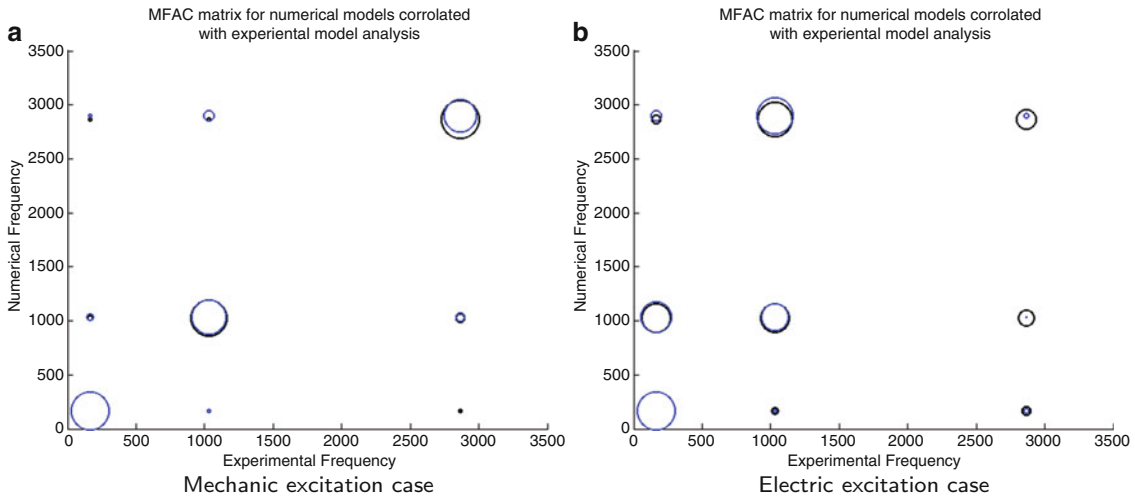

Fig. 32.11 MFAC between numerical models and experimental modal analysis

32.6 Conclusion

The dynamics of a piezoelectric multilayer bending actuator was tested to validate the numerical models. The simplified models are reviewed to model the multilayer actuator and compared with a Samcef solid model using the peizoelectric material data sheet. A consistent mismatch on natural frequencies was found in each model comparing with the experimental measurement. The FRFs validation has been achieved in both mechanical and electric extrication cases. The Modal FRF Assurance Criterion shows that the simplified models are consistent with the experimental measurement. Therefore, the equivalent properties modeling approach is suitable to model this type piezoelectric actuators. In the electric excitation case, a mechanic-electric energy transmission coefficient is introduced into the model to model dynamic the multilayer piezoelectric actuator to simplified the electric excitation modeling. A simple model updating exercise has been carried out at the end. The updated model exhibited a significant improvement. It indicated that the presence of the electrodes in multilayer actuator is not negligible for the material properties in the numerical models. So a modal updating or effective properties characterization of the multilayer piezoelectric actuator is preferable to guarantee the accuracy of the numerical models.

Acknowledgment The authors would like to thank the European Commission via the EU funded Marie Curie ITN for the financial support to project called Application of distributed control on smart structures(ARRAYCON), grant number 605087.

References

1. de Abreu, G.L.C.M., Ribeiro, J.F., Steffen Jr., V.: Finite element modeling of a plate with localized piezoelectric sensors and actuators. J. Braz. Soc. Mech. Sci. Eng. **XXVI**(2), 117–128 (2004)
2. Hariri, H., Bernard, Y., Razek, A.: Mod´elisation par ´el´ements finis d'un syst'eme asym´etrique de type poutre avec des patchs pi´ezo´electriques. E´lectrotechnique du Futur **14&15** (2011)
3. Hariri, H., Bernard, Y., Razek, A.: A two dimensions modeling of non-collocated piezoelectric patches bonded on thin structure. Curved Layer. Structures **2**, 15–27 (2014)
4. de Marqui Junoir, C., Erturk, A., Inman, D.J.: An electromechanical finite element model for piezoelectric energy harvester plates. J. Sound Vib. **327**, 9–25 (2009)
5. Piefort, V., Loix, N., Preumont, A.: Modeling of piezolaminated composite shells for vibration control. In: ESA Conference on Spacecraft Structures, Materials and Mechanical Testing, 4–6 November 1998. Brunschweig, Germany (1998)
6. Wang, S.Y.: A finite element model for the static and dynamic analysis of a piezoelectric bimorph. Int. J. Solids Struct. **41**, 4075–4096 (2004)
7. Chung, S.H., Fung, E.H.K.: A nonlinear finite element model of a piezoelectric tube actuator with hysteresis and creep. J Smart Mater. Struct. **19**, 045028 (2010)
8. Marinkovic, D., Koppe, H., Gabbert, U.: Aspects of modeling peizoelectric active thin-walled structures. J. Intell. Mater. Syst. Struct. **20**(15), 1835–1844 (2009)
9. Erturk, A., Inman, D.J.: Piezoelectric Energy Harvesting. Wiley, New York, ISBN: 978-0-470-68254-8 (2011)
10. Ballas, R.G.: Piezoelectric Multilayer Beam Bending Actuators: Static and Dynamic Behavior and Aspects of Sensor Integration. Springer-Verlag, Berlin (2007)
11. Brissaud, M., Ledren, S., Gonnard, P.: Modelling of a cantilever non-symmetric piezoelectric bimorph. J. Micromech. Microeng. **13**, 832–844 (2003)
12. Wang, Q.M., Cross, L.E.: Constitutive equations of symmetrical triple layer piezoelectric benders. IEEE Trans. Ultrason. Ferroelectr. Freq. Control **46**(6), 1343–1351 (1999)
13. Tadmor, E.B., Ksa, G.: Electromechanical coupling correction for piezoelectric layered beams. IEEE J. Microelectromech. Sys. **12**(6), 899–906 (2003)
14. Wang, Q.M., Du, X.H., Xu, B., Cross, L.E.: Electromechanical coupling and output efficiency of piezoelectric bending actuators. IEEE Trans. Ultrason. Ferroelectr. Freq. Control **46**(3), 638–646 (1999)
15. PI piezoelectric actuators: Piezoelectric Actuator, p-45, www.piceramic.com, Physik Instrumente (PI) GmbH & Co. KG
16. Vaccarone, R., Moller, F.: Cryogenic behavior of piezoelectric bimorph actuators. Adv. Cryog. Eng. (Mater.) **46**, 277–282 (2000)
17. Seitz, H., Heinzl, J.: Modelling of a microfluideic device with piezoelectric actuators. J. Micromech. Microeng. **14**, 1140–1147 (2004)
18. Leo, D.J.: Engineering Analysis of Smart Material System. Wiley, New York (2007)
19. Zhu, M., Leighton, G.: Dimensional reduction study of piezoelectric ceramics constitutive equations from 3-D to 2D and 1-D. IEEE Trans. Ultrason. Ferroelectr. Freq. Control **55**(11), 2377–2383 (2008)
20. Fotsch, D., Ewins, D.J.: Application of MAC in the frequency domain. 18th International Modal Analysis Conference San Antonio, United States, pp. 1225–1231 (2000)

Chapter 33
Study of Correlation Criteria for Spacecraft-Launch Vehicle Coupled Loads Analysis

J.F. Mercer, G.S. Aglietti, M. Remedia, and A.M. Kiley

Abstract In spacecraft structural verification, Coupled Loads Analyses (CLAs) use Finite Element Models (FEMs) of the spacecraft and launch vehicle to predict flight loads. It is therefore essential that the spacecraft FEMs to be used in these CLAs are first validated through comparison with test measured data. This study has been conducted in order to assess the metrics/criteria used to quantify the level of correlation between the analytical model and physical spacecraft test structure. To explore this, both baseline spacecraft FEM and altered versions (generated by introducing errors to the baseline) have been subjected to the same loading scenarios. Differences in response between the baseline and 'perturbed' models have been observed. Various correlation criteria, such as modal assurance criteria and cross-orthogonality checks, and a lesser-known comparison of base forces, have been applied to quantify the level of correlation between each altered model and its corresponding baseline FEM. The results indicate that the more popular modal vector correlation methods may not be the most effective at predicting the level of error in peak displacement responses, and that the base force criteria, known as BFAC, may be more sensitive to changes in these responses.

Keywords Validation • Correlation • Criteria • Metrics • Coupled loads analysis (CLA)

33.1 Introduction

From a structural perspective, launch is one of the most challenging phases in the mission of a spacecraft. The interaction of the spacecraft and the launch vehicle is an important aspect of this; however, it is not possible to practically test the two systems together. Thus, in order to simulate the launch experience it is necessary to rely on computations, and Coupled Loads Analyses (CLAs) are carried out which couple mathematical models, i.e., a Finite Element Model (FEM) of the spacecraft with a model of the launch vehicle, to predict loads during critical flight events.

If there is to be confidence in the results of the CLA, it is necessary to first validate the spacecraft FEM against appropriate test measured data to ensure that the mathematical model displays dynamic responses representative of the real hardware. During this validation process, the analytical and experimental results are compared and the FEM updated where necessary to improve its representation of the behaviour of the real structure. This correlation and model update process can take a considerable amount of time and effort, and in certain cases may result in minimal improvement in the model. Therefore, containing this process and ensuring meaningful targets and efficient processes is an important task with the potential to greatly aid in improving industrial practices. As such this study has been undertaken in an effort to assess the capability of metrics used to quantify the level of correlation between test structure and FEM.

The frequency difference between the test and FEM natural frequencies are typically used as an initial correlation comparison. This frequency comparison is easily performed without the need for extensive data processing, such as that required to extract mode shapes from test data. Some of the most commonly used modal correlation metrics are the Modal Assurance Criteria (MAC) [1] and Cross-Orthogonality Checks (XOC) [2]. With these methods, finite element normal mode shapes are compared to mode shapes estimated from frequency response functions (FRFs) derived from measured test data. When performing the MAC check, the vectors describing the mode shapes must be of equal vector order and the mass matrix dimensions must match this for the XOC. It is therefore necessary to either expand the experimental data to a DOF count matching the FEM or reduce the analytical results to a DOF count equal to that of the test acquisition count [3]. A potential

J.F. Mercer (✉) • G. Aglietti • M. Remedia
University of Surrey, Guildford, Surrey, UK
e-mail: j.mercer@surrey.ac.uk

A. Kiley
Airbus Defence and Space, Gunnels Wood Road, Stevenage, Hertfordshire, UK

S. Atamturktur et al. (eds.), *Model Validation and Uncertainty Quantification, Volume 3*, Conference Proceedings of the Society for Experimental Mechanics Series, DOI 10.1007/978-3-319-29754-5_33

problem with using the FEM to expand the test data is that any errors in the FEM, which is still to be validated, may corrupt the experimental data and therefore undermine the following correlation and update process. It is therefore generally considered that the modal reduction of the FEM to the test measured DOFs is the preferred approach [4]. The reduced FEM is commonly known as the Test Analysis Model (TAM), and there are many methods currently available for performing these reductions. There have already been several studies (e.g., [5, 6]) comparing the various methods including; static (or Guyan) reduction [7], improved reduction system (IRS) [8] and the System Equivalent Reduction Expansion Process (SEREP) [9].

A previous study by Sairajan and Aglietti found [10] that MAC and XOC often failed to predict whether the analytical model can successfully predict the frequency response within acceptable margins. From further Monte-Carol simulations, their continued investigations [11] found that there was not a good correlation between XOC value and the difference forced responses between a given two models. In response to this, a new correlation metric, focusing on the comparison of base forces, was presented by Sairajan and Aglietti [12], in an attempt to overcome this limitation of current popular correlation metrics. Initial studies indicated that the suggested Base Force Assurance Criteria (BFAC) values gave a good indication of the level of difference in peak displacement and acceleration responses for the considered three spacecraft structures; which ranged from a small-sat of only 75 kg to a large, scientific spacecraft. One of the proposed benefits of this BFAC metric is that the base forces can be analysed in the FEA and are generally measured during vibration testing, and so a direct comparison can be readily applied.

Here these criteria are applied to an even more complex spacecraft structure such that the capabilities of MAC, XOC and BFAC to predict peak responses can be assessed. As with the previous study [12], these investigations have been conducted by using nominal results from a baseline FEM as the 'true', in place of test results, and comparing these nominal results with those of modified FEMs, where 'errors' have been introduced to the baseline FEM. From these comparisons it is clear that the BFAC gives the clearest indication of the correlation in peak displacement between the baseline and 'perturbed' FEMs. The trends in peak acceleration are less pronounced and further investigations may be required to confirm whether BFAC is consistently more indicative than the more popular MAC and XOC.

33.2 Correlation Metrics

There are a wide variety of methods which may be used to perform these comparisons; some of the main methods are Modal Assurance Criteria and Cross-Orthogonality Checks, which are indicated as mandatory in the European Cooperation for Space Standardisation (ECSS) modal survey assessment document ECSS-E-ST-32-11C [13].

33.2.1 Modal Assurance Criteria

For MAC, the test mode shapes, ψ, and FEM eigenvectors, φ, are compared, resulting in a value between 0 and 1 which indicates how closely matched the vectors are, with a perfect match yielding a 1.

$$\mathrm{MAC} = \frac{\left(\psi^{\mathrm{T}}\phi\right)^2}{\left(\psi^{\mathrm{T}}\psi\right)\cdot\left(\phi^{\mathrm{T}}\phi\right)} \tag{33.1}$$

It is generally considered that target modes achieving a MAC of at least 0.9 indicates a good correlation and is the minimum required value for the fundamental bending modes of a spacecraft [13]. It is, however, also clear from ECSS-E-ST-32-11C [13] that the required degree of correlation is dependent on the perceived relative importance of the mode under consideration.

33.2.2 Cross-Orthogonality Checks

The XOC is also an ECSS [13] required check, and works similarly to MAC, but with the mass matrix employed to weight the relative importance of the DOFs being considered. This approach takes advantage of the orthogonal relationship between normal modes and the system mass matrix. An ideal result of perfectly matched mode shapes which are orthogonal to the mass matrix will yield a diagonal matrix, and for mass normalised modes this becomes an identity matrix. Again, in

ECSS-E-ST-32-11C [13] it is shown that off-diagonal values <0.1 and leading diagonal terms >0.9 are deemed to indicate a good correlation. The typical cross-orthogonality check is given by:

$$\mathrm{XOC} = \frac{\left(\psi^{\mathrm{T}} \mathrm{M}_{\mathrm{TAM}} \phi\right)}{\sqrt{\left(\psi^{\mathrm{T}} \mathrm{M}_{\mathrm{TAM}} \psi\right)} \sqrt{\left(\phi^{\mathrm{T}} \mathrm{M}_{\mathrm{TAM}} \phi\right)}} \tag{33.2}$$

The experimental and analytical mode shapes are again typically given by ψ and φ respectively, however this study uses a nominal FEM as a baseline for ψ rather than making comparison to experimental data. The introduction of the mass matrix has potential benefits to the effectiveness of the metric as the mass associated to the modal vectors is accounted for and as such there is a weighting of the DOFs depending on their relative influence, which is not accounted for by the MAC criteria. In this study the reduced mass matrix, referred to as the test analysis model (TAM), has been generated using the System Equivalent Reduction Expansion Process (SEREP) [9].

$$\mathrm{M}_{\mathrm{TAM}} = \left(\Psi^{\dagger}\right)^{\mathrm{T}} \Psi^{\dagger} \tag{33.3}$$

$\Psi^{\dagger}$ is the generalised inverse [14] of the modal matrix Ψ. Herein the modal matrix consists of the selected modes of interest partitioned to the ≈400 degrees of freedom (DOFs) corresponding to the test measurement point plan (MPP) of the spacecraft.

33.2.3 Base Force Assurance Criteria

In the previous study by Sairajan and Aglietti [12] the base force assurance criteria (BFAC) was introduced. Therein it was proposed that the base forces and moments may be an appropriate indicator of analytical model forced response characteristics.

In order to investigate this, the following BFAC metric was proposed:

$$\mathrm{BFAC}_{\mathrm{jk}} = \frac{\left(\mathrm{P}_{\mathrm{j}}^{\mathrm{T}} \mathrm{F}_{\mathrm{k}}\right)^{2}}{\left(\mathrm{P}_{\mathrm{j}}^{\mathrm{T}} \mathrm{P}_{\mathrm{j}}\right)\left(\mathrm{F}_{\mathrm{k}}^{\mathrm{T}} \mathrm{F}_{\mathrm{k}}\right)} \tag{33.4}$$

where P and F would typically represent the absolute values of force transmitted to the base in the direction of excitation during dynamic test and finite element analysis respectively. Both P and F vary with frequency, ω, and as such the vectors P_{j} and F_{k} each contain a set of values corresponding to each measured frequency within the entire frequency range of interest. The test measured frequencies for P can therefore be vector correlated to the corresponding FEM frequency responses in F before the BFAC is applied. The subscripts j and k vary from 1 to 6 and are representative of the degrees of freedom in which the base forces are moments are determined. As such, although BFAC equation is similar to MAC in that it yields values between 0 and 1 where all unity in the leading diagonal would indicate a perfect match, BFAC will always result in a 6×6 square matrix where the size of MAC matrices varies as it is dependent on the number of target modes under consideration. It should be noted that in spacecraft base-shake test campaigns the structure is typically subjected to excitation in all three translational directions independently and therefore the three BFAC matrices would be computed—one for each direction of base-shake—and either averaged or considered separately. Benefits of this base force comparison concept are that the base forces can be directly measured in the test and compared with the analytical results without the need for reduction of the FEM to test measured DOFs, as is required for the XOC [12].

33.3 Analytical Investigations

33.3.1 Example Application Spacecraft

The studies presented herein focus on the large, unique, scientific ESA/JAXA collaboration spacecraft BepiColombo. BepiColombo, which is intended for the exploration of Mercury, has a stacked configuration comprising of two planetary

orbiters and a propulsion module. The spacecraft has a mass of ≈6500 kg and the FEM consist of approximately 1,800,000 DOFs. Due to its size and stacked configuration, this is a more complex structure than any of those considered in the previous study by Sairajan and Aglietti [12] and as such presents the opportunity to determine whether the findings of that study are preserved in such a structure.

33.3.2 Base-Shake

Spacecraft such as BepiColombo will be subjected to the most extreme loading conditions during launch. In order to ensure that the structure is able to withstand the launch environment, vibration test are conducted to both test the structure and provide data for the correlation of the FEM to be used in CLAs. As large spacecraft, such as that considered herein, will ultimately be mounted vertically in the launch vehicle and constrained at the base, this is replicated in the test. An adaptor is used to attach the spacecraft to the electrodynamic shaker (via a force measurement device), allowing the excitations to be applied through the base of the structure in a similar manner to the transmission of loads during launch. A sinusoidal input excitation is applied to the structure, slowly sweeping through frequency range of interest (≈0–100 Hz). The sine sweep is performed on a single axis at a time, and is executed separately in the axial/horizontal X- and Y-directions, as well as along the longitudinal/vertical Z-direction.

The investigations presented herein are largely focused on the responses of the BepiColombo baseline FEM, and 'perturbed' versions generated for comparison, to a Y-direction base-shake type analysis (Fig. 33.1).

During base-shake sine-sweep vibration tests carried out on the structural thermal model (STM) of BepiColombo, data was collected using accelerometers capturing the response at approximately 400 DOFs. The corresponding ≈400 DOFs from the FEM will be considered in these investigations for the generation of mode shape vectors for MAC and XOC.

For the purposes of this investigation, the modes of interest (for applying MAC and XOC) have been selected on the basis of modal effective mass, modal kinetic energy and modal strain energy, as suggested by Chung and Sernaker [16] and as subsequently applied in the study by Sairajan and Aglietti [12].

Fig. 33.1 BepiColombo STM stack in readiness for base-shake test [15]

33.4 Analytical Results and Discussions

The BepiColombo spacecraft FEM is being used as a nominal baseline from which modified FEMs have been created for the purpose of comparing peak responses to a base-shake analysis and assessing the capability of different correlation criteria to predict the level of difference in response. In order to generate the 'perturbed'/'erroneous' models, changes have been made to the stiffnesses in joints and connections in the FEM. No change has been made to the overall mass or distribution of mass in the FEMs as this is typically a known quantity which is reasonably consistent between test and FEM. Stiffnesses are a more common source of poor correlation and as such errors relating to joint stiffnesses are among the most relevant in correlation criteria assessment.

The following equations have been used to assess the difference in natural frequency and modal effective mass between the nominal baseline and the results from models which had 'errors' introduced.

$$\text{Frequency Difference} = \left| \frac{f_{Nom} - f_{FEM}}{f_{Nom}} \right| 100 \tag{33.5}$$

$$\text{Modal Effective Mass Difference} = \left| \frac{Meff_{Nom} - Meff_{FEM}}{Meff_{Nom}} \right| 100 \tag{33.6}$$

The comparisons of frequency and modal effective mass for the Y direction fundamental bending mode are given in Table 33.1.

The MAC and XOC have been calculated for all of the selected target modes and then averaged to obtain a single MAC and XOC value for each 'perturbed' model. Likewise the BFAC comparing the baseline to each 'perturbed' model have been calculated. The results are summarised in Table 33.2.

The peak displacements and accelerations during the base-shake are examined at the selected locations as shown in Fig. 33.2. These are key locations selected from the original ≈400 DOF test measurement point plan based on the magnitude and independence of the responses.

The displacement and acceleration responses at the selected locations are plotted below in Figs. 33.3 and 33.4 respectively for Y-direction response to Y-direction base-shake sine-sweep analysis of the baseline FEM, wherein a constant modal damping (2 % of critical damping) has been applied.

The following equations show the calculations used to assess the level of 'error' in each modified FEM:

$$Error_{Displacement} = \left| \frac{d_{Nom} - d_{FEM}}{d_{Nom}} \right| 100 \tag{33.7}$$

$$Error_{Acceleration} = \left| \frac{a_{Nom} - a_{FEM}}{a_{Nom}} \right| 100 \tag{33.8}$$

Table 33.1 Perturbed models compared to baseline for Y direction fundamental bending mode

	Baseline	1	2	3	4	5	6	7	8
Frequency (Hz)	12.68	12.63	12.63	10.22	12.54	12.50	10.05	11.95	11.20
Frequency difference (%)	–	0.40	0.44	19.42	1.16	1.46	20.77	5.76	11.70
Modal effective mass (kg)	1673	1947	1756	1539	1700	1670	1522	1628	1577
Modal effective mass difference (%)	–	16.33	4.93	8.05	1.62	0.19	9.05	2.70	5.74

Table 33.2 Metric values for comparison of perturbed models compared to baseline

	Baseline	1	2	3	4	5	6	7	8
MAC	1	0.66	0.69	0.65	0.99	0.92	0.65	0.82	0.74
XOC	1	0.87	0.86	0.87	1.00	0.97	0.84	0.92	0.89
BFAC	1	0.59	0.51	0.16	0.98	0.96	0.42	0.71	0.54

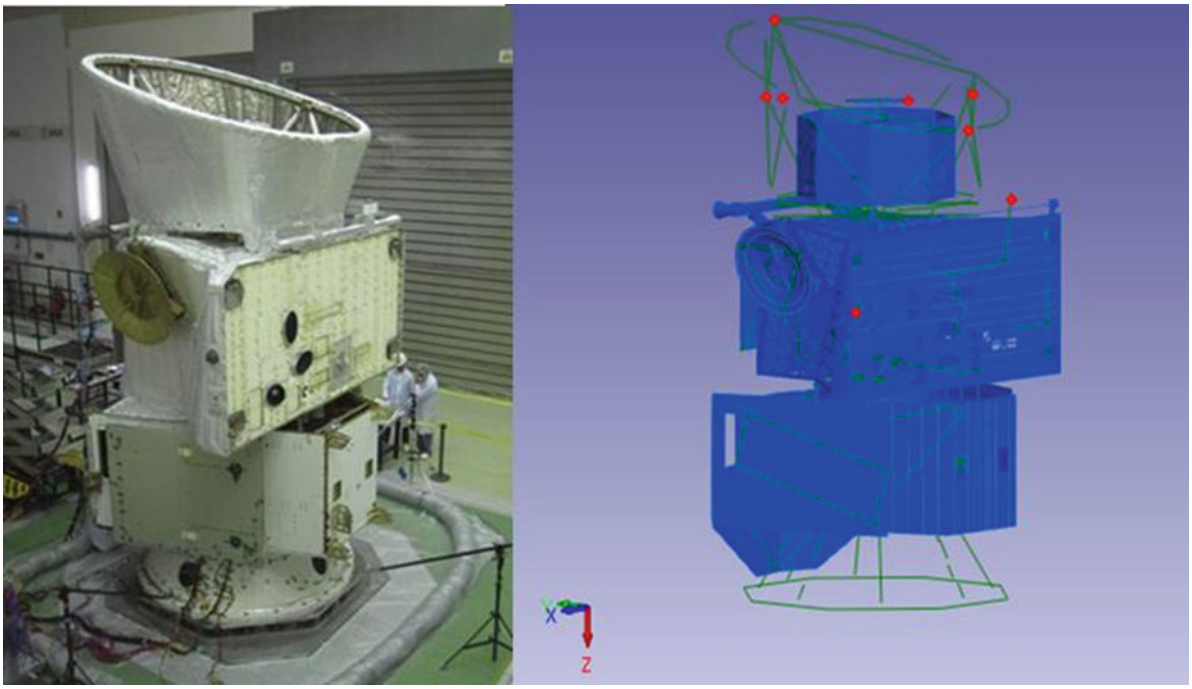

Fig. 33.2 BepiColombo FEM outline showing response locations

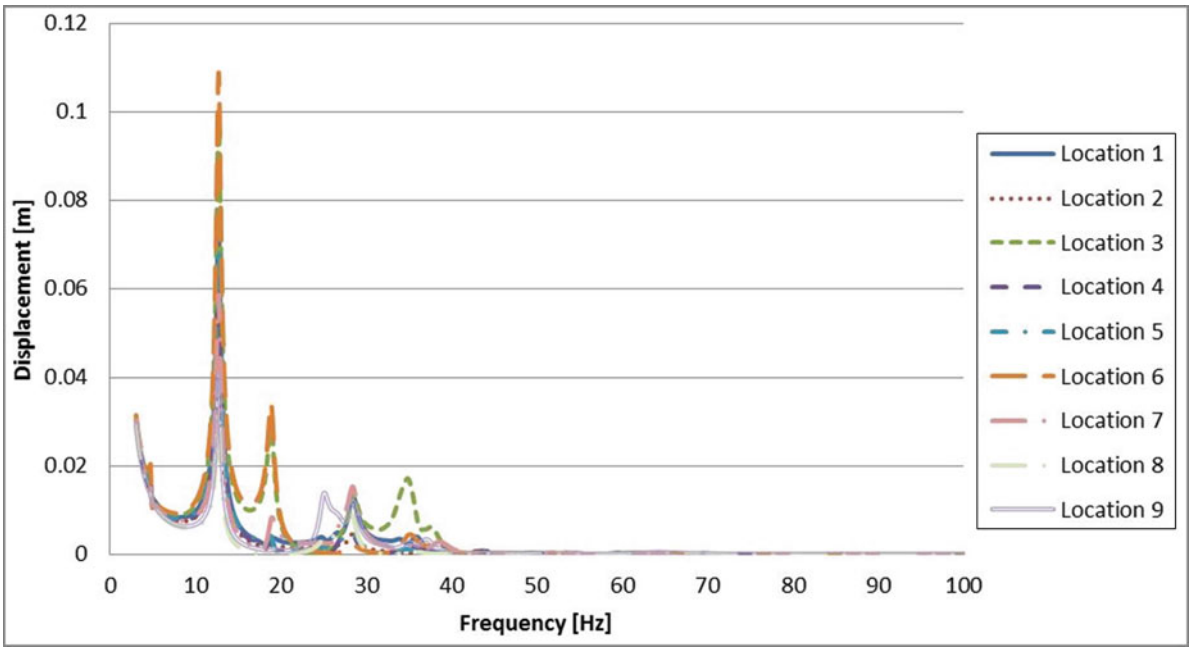

Fig. 33.3 Displacement responses varying with frequency at the selected locations on the baseline spacecraft FEM

These equations have been applied to calculate the percentage difference in peak displacement and acceleration, where the peak is considered as the maximum value across the entire 5–100 Hz frequency range analysed. The resulting values have been averaged across the selected response locations to obtain a displacement error and an acceleration error percentage value for each 'perturbed' FEM, as shown in Figs. 33.5 and 33.7.

In Fig. 33.5 in is clear that the displacement error between perturbed models follows a consistent trend for responses at all of the selected key locations. Figure 33.6 gives the average displacement error percentages against the values of MAC, XOC

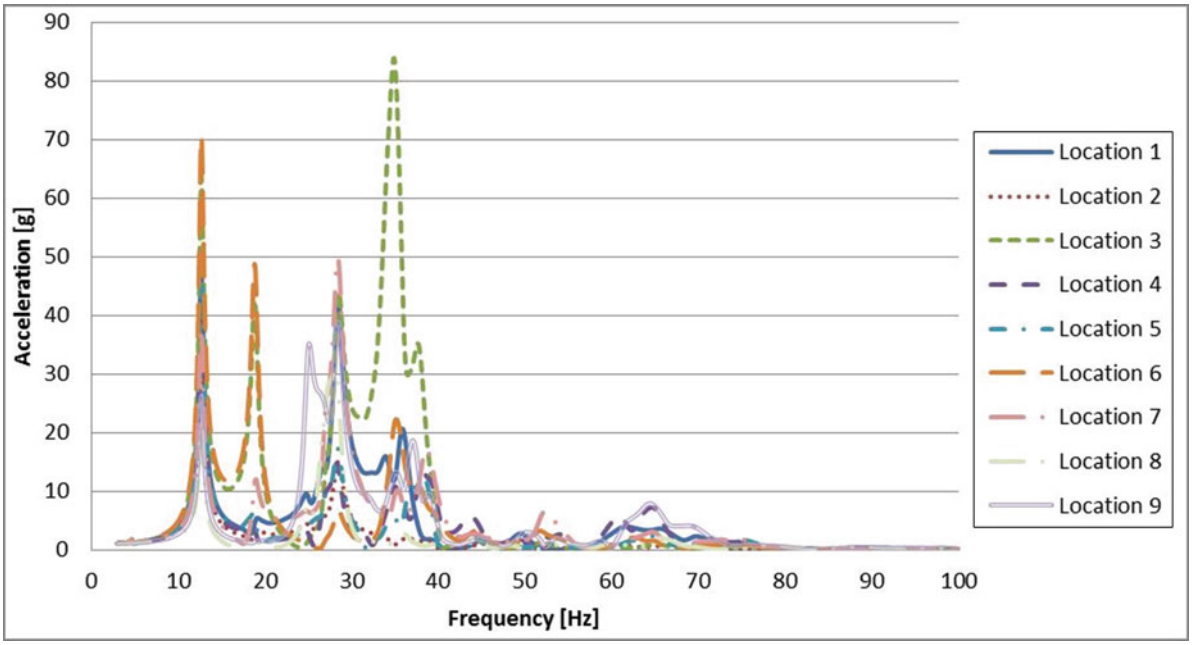

Fig. 33.4 Acceleration responses varying with frequency at the selected locations on the baseline spacecraft FEM

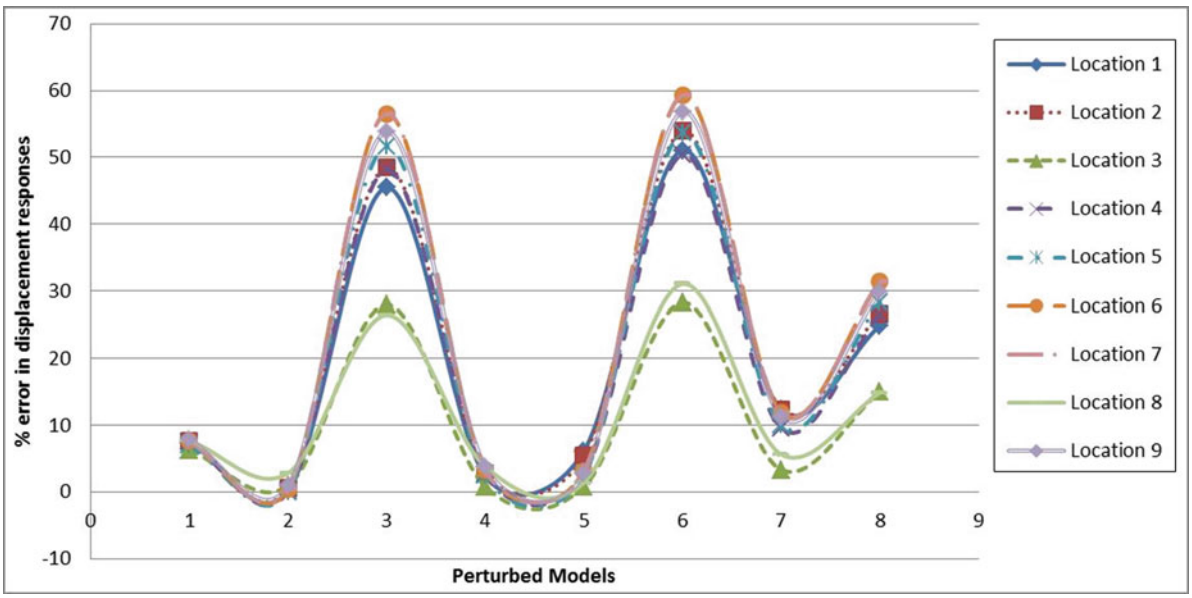

Fig. 33.5 Percentage error in peak displacement responses at the selected response locations on the spacecraft

and BFAC. It can be seen that the models with highest displacement error correspond to lower BFAC values, while the MAC and particularly the XOC appear to be less sensitive to the displacement error. For example, XOC ≈0.8–0.9 corresponds to models from negligible to over 45 % displacement error.

Conversely, Fig. 33.7 reveals that the level of error in peak acceleration responses varies widely between the different selected key response locations. Other than 'perturbed' model 4 giving consistently low error, there is no clear trend to the other perturbed models. As a consequence, the result of averaging the error across these response locations, given in Fig. 33.8, has little meaning as the result is extremely sensitive to the addition or omission of different response locations.

In the previous study [12] the results of analysing acceleration error were more consistent with those of the displacement. One possible explanation for the discrepancy in this study is the presence of significant peaks in acceleration response at different frequencies between the different response locations. To illustrate, Fig. 33.9 provides typical key acceleration

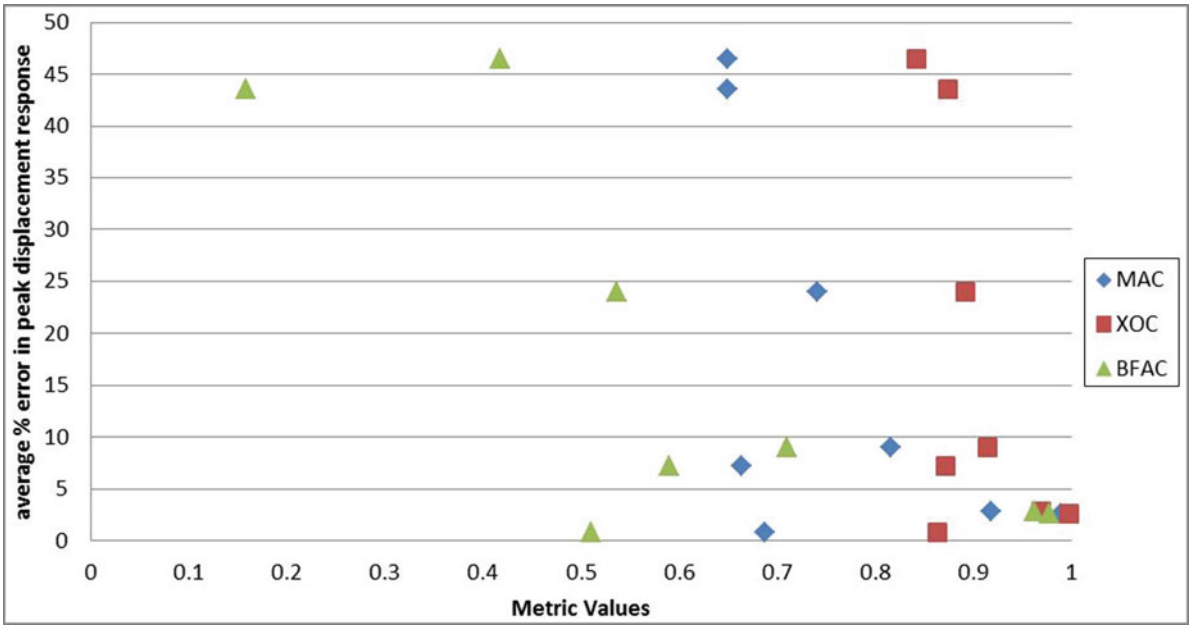

Fig. 33.6 Average percentage error in peak displacement plotted against metric values for MAC, XOC and BFAC

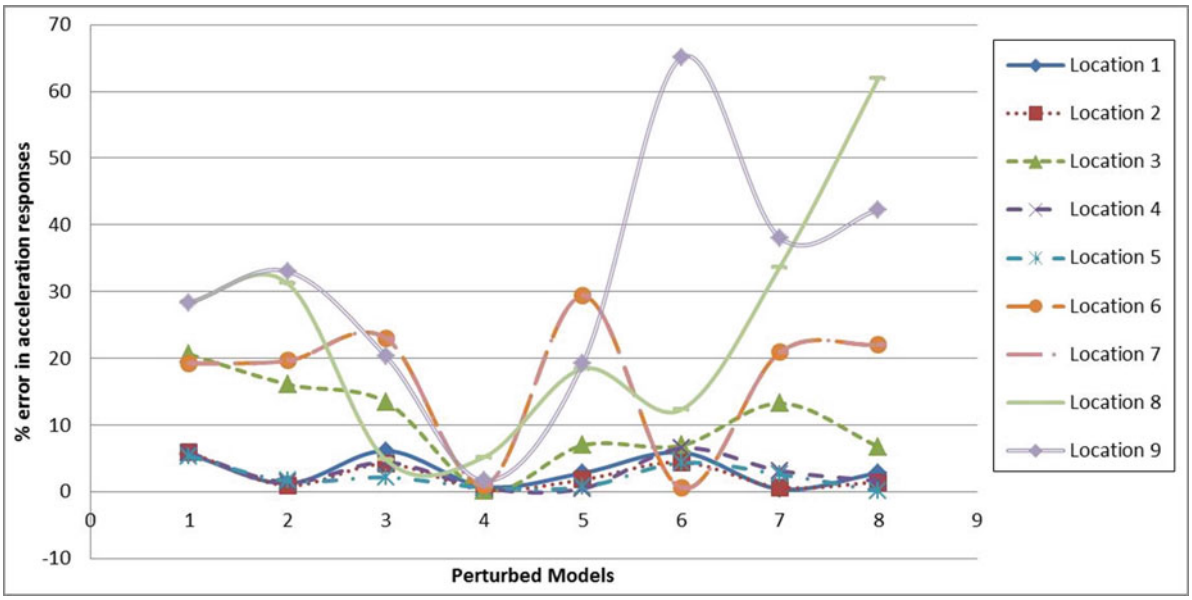

Fig. 33.7 Percentage error in peak/max. acceleration responses at the selected response locations on the spacecraft

responses to the largest of the three spacecraft structures analysed by Sairajan and Aglietti [12]. It can be noted that the spacecraft structure analysed by Sairajan and Aglietti [12] presents only two clear peaks in acceleration with the first consistently appearing as the more dominant at all of the considered response locations. Whereas in Fig. 33.4, for BepiColombo, there are multiple peaks in the responses and the absolute peak/maximum acceleration occurs at different frequencies between the different response locations, rather than at a single dominant frequency.

If, rather than extracting the maximum response in the entire frequency range, only the magnitude of acceleration at the first peak (around 12.6 Hz in the baseline FEM) is considered and tracked for the 'perturbed' models, the results are as shown in Figs. 33.10 and 33.11. There is again the more consistent trend in acceleration error level between responses in Fig. 33.10, much like Fig. 33.6 for the displacements. Figure 33.11 reveals that the BFAC is again more sensitive to the level of error than MAC or XOC. There is, however, some scatter in the BFAC and the smaller change in average error than for the displacements make the MAC and XOC appear slightly more representative for acceleration than for displacement.

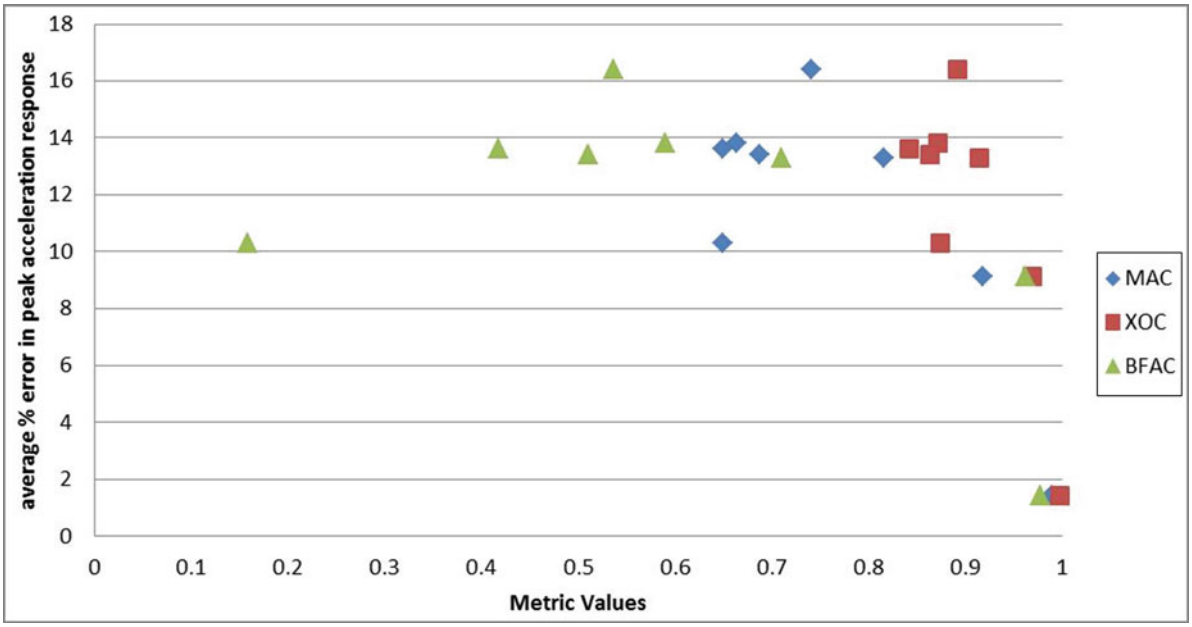

Fig. 33.8 Average percentage error in peak/max. acceleration plotted against metric values for MAC, XOC and BFAC

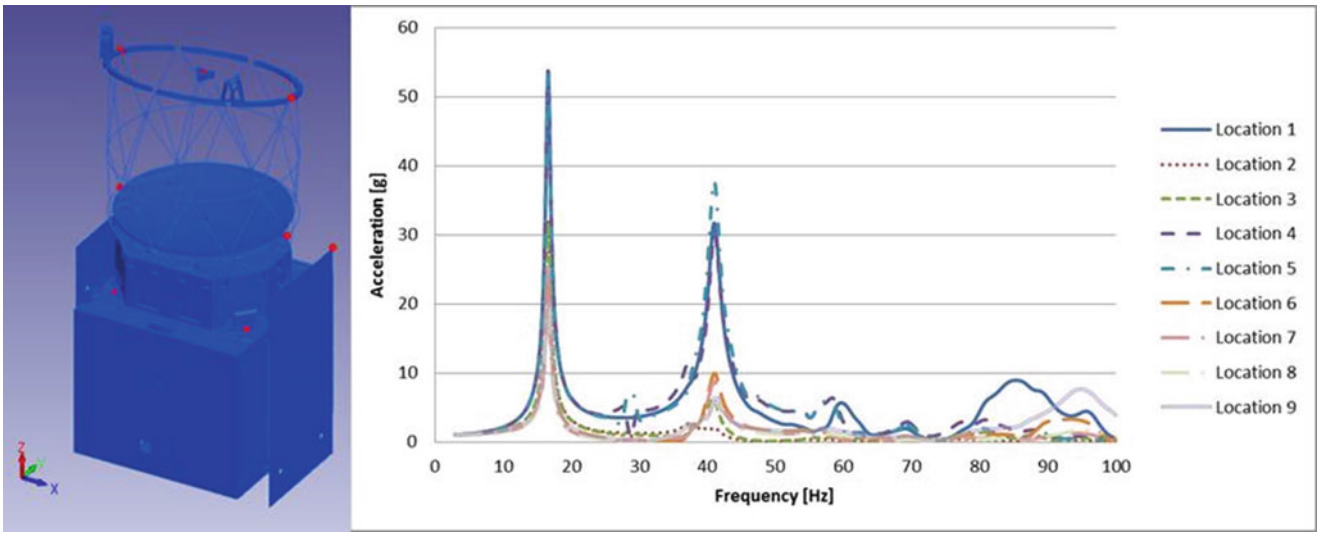

Fig. 33.9 Typical acceleration responses varying with frequency for another large scientific spacecraft

33.5 Conclusion

Different correlation criteria; MAC, XOC and BFAC, have been related to FEM internal (displacement and acceleration) responses in terms of each metric's sensitivity to inherent FEM error. In order to conduct this investigation, an initial baseline spacecraft model has been analysed under a base-shake sine-sweep. Comparisons have been made to the results of performing the same analyses with models created by introducing 'errors' to the baseline to form a set of 'perturbed' models as the basis for a comparison.

From the base-shake load case, this initial study has revealed that in general there is greater sensitivity between the BFAC value and the percentage error in peak displacement response compared with the other metrics. The MAC and XOC values appeared less sensitive to changes in peak displacement for the perturbed models considered. As such, the BFAC may be a useful criterion to apply, particularly in cases where there are structural concerns, as the peak displacements in the structure give an indication of the levels of deformation and therefore strain being experienced.

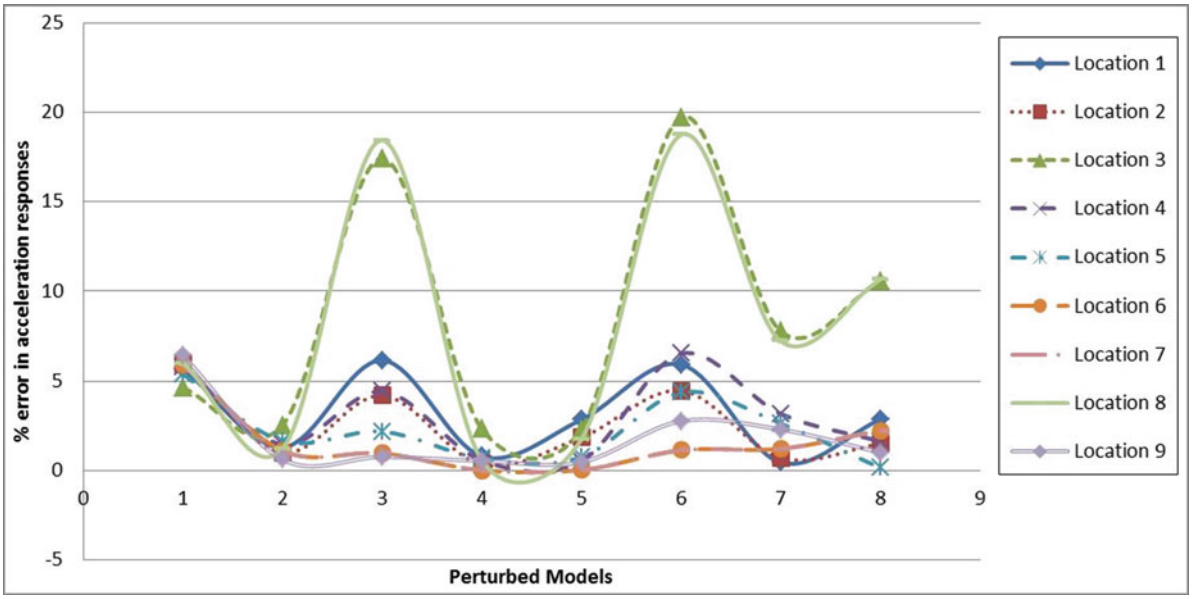

Fig. 33.10 Percentage error in first peak in acceleration responses at the selected response locations on the spacecraft

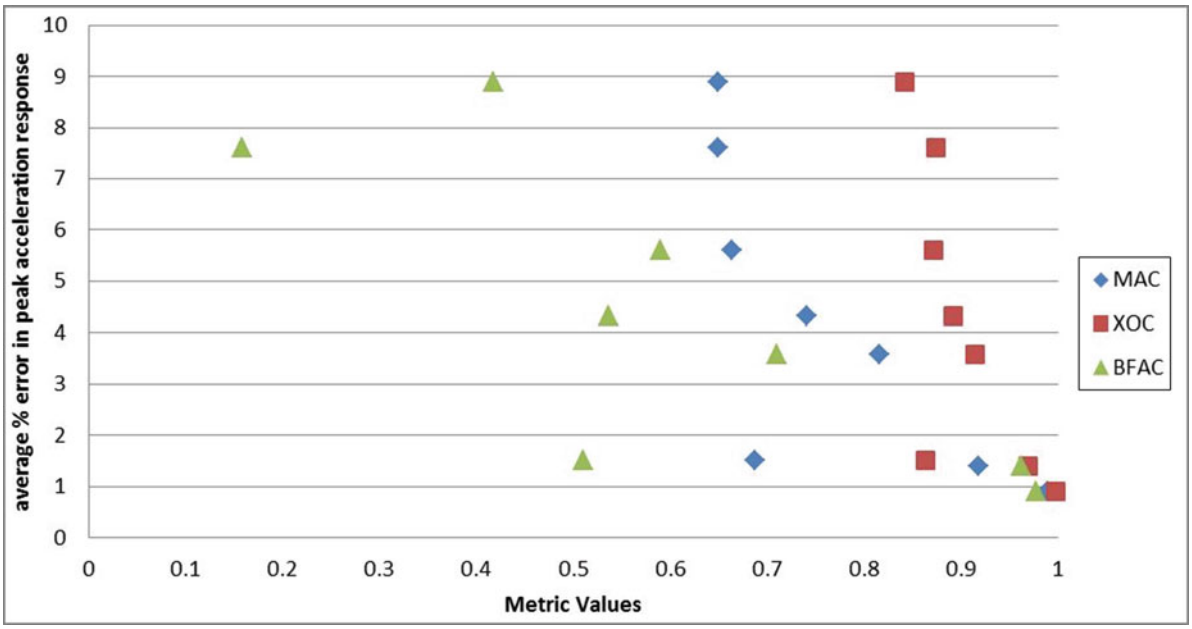

Fig. 33.11 Average percentage error in first peak in acceleration plotted against metric values for MAC, XOC and BFAC

Although a previous study found that the same trends were true for the peak acceleration responses, with BFAC giving a good indication of peak acceleration errors, this work has identified some limitations on those findings. It is expected that this is the result of the more complex behaviour of this spacecraft (with respect to those considered by the previous work), with multiple peaks in the acceleration response at different frequencies and more variation in acceleration response between different locations on the spacecraft than would be found in structures with simpler behaviour.

More in depth study is needed to establish whether these initial findings will hold true when more 'perturbed' models are considered. Ideally further 'perturbed' models would be included, perhaps with more significant changes in order to better view trends in MAC and XOC for the acceleration error. Additionally, this study has focused mainly on one spacecraft as a case study and therefore an investigation considering different baseline spacecraft is advisable before drawing final conclusions, particularly as the acceleration findings were slightly different to those of previous studies which analysed spacecraft with 'simpler' structural responses.

Future work may also extend these investigations into the relationship between correlation metrics and peak acceleration and displacement responses to actual CLA flight event load cases, as well as the base-shakes as considered herein. This is of interest as what is of concern ultimately is the ability of the FEM to represent the physical structure under coupled conditions.

References

1. Allemang R.J., Brown D.L.: A correlation coefficient for modal vector analysis. In: Proceedings of the 1st International Modal Analysis Conference, pp. 110–116. Orlando, FL (1982)
2. Wijker, J.J.: Mechanical Vibrations in Spacecraft Design. Springer, Berlin (2004)
3. Avitabile, P.: Model reduction and model expansion and their applications–part 1 theory. In: Proceedings of the Twenty-Third International Modal Analysis Conference, Orlando, FL (2005)
4. Kammer, D.C.: Test-analysis model development using an exact modal reduction. Int. J. Anal. Exp. Modal Anal. **2**, 174–9 (1987)
5. Bergman, E.J., Allen, M.S., Kammer, D.C., Mayes, R.L.: Probabilistic investigation of sensitivities of advanced test-analysis model correlation methods. J. Sound Vib. **329**, 2516–31 (2010)
6. Koutsovasilis, P., Beitelschmidt, M.: Comparison of model reduction techniques for large mechanical systems. Multibody Syst. Dyn. **20**, 111–28 (2008)
7. Guyan, J.R.: Reduction of mass and stiffness matrices. AIAA J. **3**, 380 (1964)
8. O'Callahan, J.C.: A procedure for an improved reduced system (IRS) model. In: Proceedings of the 7th International Modal Analysis Conference, pp. 17–21. Las Vegas, NV (1989)
9. O'Callahan, J. Avitabile, P., Riemer, R.: System equivalent reduction expansion process (SEREP). In Proceedings of the 7th International Modal Analysis Conference, pp. 29–37. Las Vegas, NV (1989)
10. Sairajan, K.K., Aglietti, G.S.: Validity of model correlation methods in FEM validation for forced vibration analysis. In: Proceedings of the 12th European Conference on Spacecraft Structures, Materials and Environmental Testing, Noordwijk (2012)
11. Sairajan, K.K., Aglietti, G.S.: Robustness of system equivalent reduction expansion process on spacecraft structure model validation. AIAA J. **50**, 2376–88 (2012)
12. Sairajan, K.K., Aglietti, G.S.: Study of correlation criteria for base excitation of spacecraft structures. J. Spacecraft Rockets **51**(1), 106–116 (2014). doi:10.2514/1.A32457
13. ESA-ESTEC: ECSS-E-ST-32-11 Modal Survey Assessment, p. 78. European Cooperation for Space Standardization, Noordwijk (2008)
14. Penrose, R.: A generalized inverse for matrices. Math. Proc. Camb. Philos. Soc. **51**, 406–13 (1955)
15. European Space Research and Technology Centre (ESTEC), the Netherlands. http://www.esa.int/spaceinimages/Images. Accessed 2 Feb 2015
16. Chung, Y.T., Sernaker, M.L.: Assessment target mode selection criteria payload modal survey. In: Proceedings of the 12th International Modal Analysis Conference, pp. 272–279. Honolulu, HI (1994)

Chapter 34
Full-Field Strain Prediction Applied to an Offshore Wind Turbine

Alexandros Iliopoulos, Wout Weijtjens, Danny Van Hemelrijck, and Christof Devriendt

Abstract Fatigue life is a design driver for the foundations of offshore wind turbines (OWT's). A full-scope structural health monitoring strategy for OWT's needs to consider the continuous monitoring of the consumption of fatigue life as an essential part. To do so, the actual stress distribution along the entire length of the structure and predominantly at the fatigue hotspots needs to be known. However installation of strain sensors at these hotspots is not always feasible since these hotspots are mainly situated beneath the water level (e.g., mudline). In practice this implies the installation of strain gauges on the monopile prior to pile driving and difficulty in maintaining these submerged sensors throughout the operational life of the turbine. Therefore, an effective and robust implemented technique using the more reliable accelerometers and very limited strain sensors at few easily accessible locations integrated within a new analytical structural dynamic approach is preferred. In this paper, a novel multi-band implementation of the well-known modal expansion approach, a.k.a. full-field strain prediction, is introduced. This technique utilizes the limited set of response data derived during a monitoring campaign and a calibrated Finite Element Model (FEM) to reconstruct the full field response of the structure. The obtained virtual responses are compared with measurements from an ongoing measurement campaign on an offshore wind turbine.

Keywords Modal expansion • Full-field strain prediction • Offshore wind turbines • Fatigue assessment • Structural health monitoring

34.1 Introduction

One of the key concerns for wind farm operators is the fatigue life consumption of OWT's. Decision making on wind farm inspections, repowering or lifetime extension can be assisted by the continuous monitoring of the accumulated fatigue damage and remaining useful life of the OWT. Moreover, feedback into design for optimization of future substructures through improved design codes can be given. To allow for continuous monitoring of fatigue progression, the actual stress distribution along the entire length of the structure and predominantly at the fatigue hotspots needs to be known. However, for OWT's on monopile foundations most of the fatigue hotspots are located beneath the water level (e.g., at the mudline). In practice this implies the installation of strain gauges on the monopile prior to pile driving and difficulty in maintaining these submerged sensors throughout the operational life of the turbine. Therefore, effective and robust implemented techniques for dynamic strain prediction are preferred.

On one side there are state-space techniques based on Kalman filtering methods [1–6]. All these applications though make assumptions on the input forces (known forces or broadband). Moreover, these approaches are potentially time consuming and computationally expensive due to the iterative algorithm.

On the other side there are techniques based on the concept of the modal expansion. These methods intelligently extrapolate measured data to generate virtual strain measurements. Non-contact methods like Digital Image Correlation and Dynamic Photogrammetry are known techniques used to measure sets of limited surface data that can be used in conjunction with an expansion algorithm for full field information [7–10]. However, all the aforementioned surveys correspond to laboratory scale applications and the excitation is exactly known or/and the responses can be measured in a sufficient large number of points.

A. Iliopoulos (✉) • D. Van Hemelrijck
Department of Mechanics of Materials and Constructions, Vrije Universiteit Brussel, Pleinlaan 2, 1050 Brussels, Belgium
e-mail: alexandros.iliopoulos@vub.ac.be

W. Weijtjens • C. Devriendt
Acoustic and Vibration Research Group, Vrije Universiteit Brussel, Pleinlaan 2, 1050 Brussels, Belgium

S. Atamturktur et al. (eds.), *Model Validation and Uncertainty Quantification, Volume 3*, Conference Proceedings of the Society for Experimental Mechanics Series, DOI 10.1007/978-3-319-29754-5_34

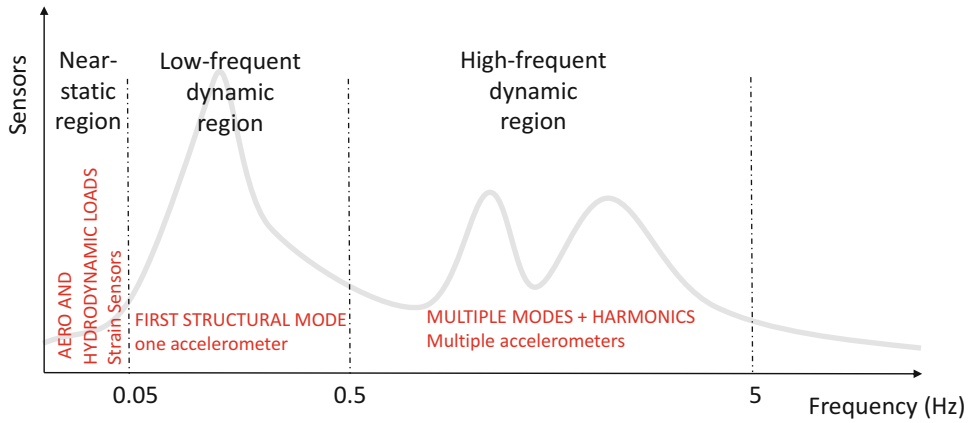

Fig. 34.1 Multi-band modal decomposition and expansion scheme

This paper deals with real scale offshore wind turbine instrumented with a limited number of sensors. A reduced-order model that exploits the limited information obtained by the acceleration sensor data in conjunction with a tuned finite element model (FEM) is utilized in order to reconstruct the full-field dynamic response of the structure [11]. The well-known modal decomposition and expansion technique is also used for this reconstruction. A comparative study between the aforementioned techniques for dynamic strain prediction is performed concluding that the techniques for this application are competitive and interchangeable providing very similar results [12].

Although accelerometers are functioning well for dynamic strain prediction, they pose a limitation for the near-static strain prediction since they are insensitive to low-frequency vibrations and thus to near-static strains. It is of utmost importance, though, to capture the low frequent oscillations since they contribute to fatigue cycles of large amplitude [13]. Therefore, the aforementioned limitation of the accelerometers should be surpassed. Towards this direction, strain data from easily accessible locations on the structure or SCADA data are used and implemented in a novel multi-band modal decomposition and expansion scheme. By that means, both the near-static a.k.a. quasi-static and the dynamic behavior of the estimated strain signals are captured. Figure 34.1 summarizes the overall concept of the multi-band modal decomposition and expansion approach with the main setting used in the analysis.

OWT's are complex structures subjected to various types of loadings mainly driven by wind and wave excitations. Additionally, complex interactions between the structure and its operating parts (e.g., tower-blade interaction) exist. These system changes imply strong variations of the dynamics of OWT's under the different environmental and operating conditions (EOC). To accommodate for them, a subdivision of the datasets into different operational cases as suggested in [13, 14] is performed. For each operating case (Fig. 34.2) the optimal sensor and mode settings are chosen in order to be adaptively incorporated to generate the optimal virtual strains considering system changes.

34.2 Theory

34.2.1 Modal Decomposition

Modal decomposition approach [15–17] allows to write the acceleration vector as a linear combination of the mode shape vectors:

$$\boldsymbol{a}(t) = \sum_{i=1}^{n} \boldsymbol{\Phi}_i q_{ia}(t) \tag{34.1}$$

where $\boldsymbol{a}(t) \in \mathbb{R}^{n_m \times 1}$ is a vector that contains the n_m measured accelerations, n is the total number of modes, $q_{ia}(t)$ is the acceleration modal coordinates for each time instance t and φ_i are the mode shape vectors. From expression (1) the modal coordinates $\boldsymbol{q}_{\boldsymbol{\alpha}}(t)$ that quantify the participation of each mode (Fig. 34.3) can be identified based on the known mode shapes (e.g., from FEM or OMA/EMA) and the measured accelerations split up in their constituting parts (in the direction of the nacelle, a.k.a. Fore–Aft (FA) and the perpendicular sideways direction, a.k.a. Side–Side (SS)). This process is called modal

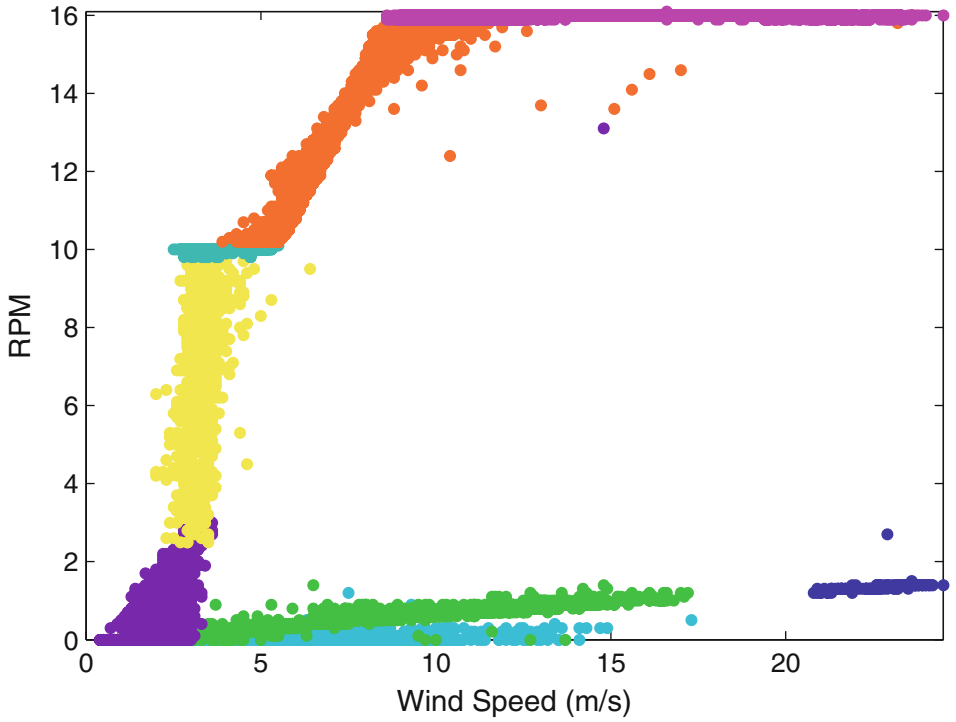

Fig. 34.2 RPM vs. Windspeed with colors indicating the different cases

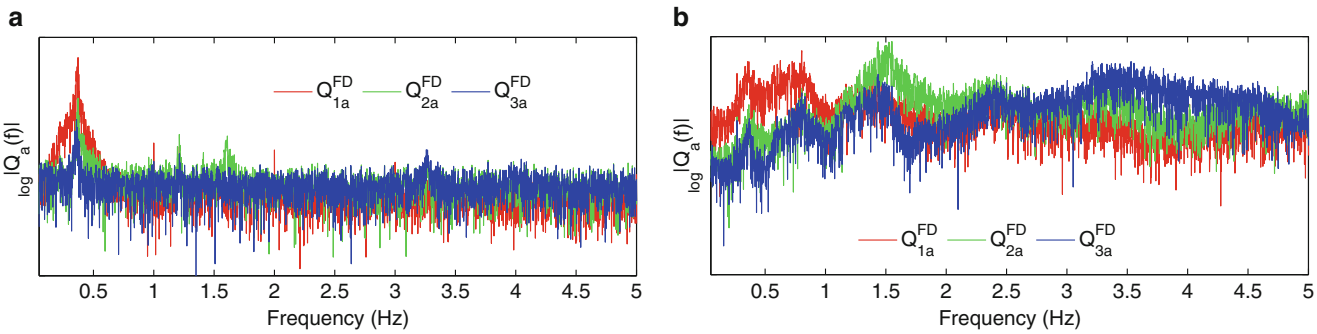

Fig. 34.3 Modal coordinates derived from modal decomposition of measured accelerations when the OWT is in *parked* (**a**) and in normal *rotating* conditions (**b**)

decomposition. Using these modal coordinates and known mode shapes, e.g., from FEM, Eq. (34.1) allows to predict the response at positions without sensors. This process is known as modal expansion or more general full-field strain prediction [7–9, 11, 18]. A schematic representation of the modal decomposition and expansion approach for the case of the OWT is presented in Fig. 34.4. This figure also illustrates the current sensor locations (left) and the mudline, which is a critical location for fatigue life. On the right the used FEM mode shapes are illustrated. Acceleration measurements are taken at four levels on nine locations using a total of ten accelerometers. Eight accelerometers capture the vibrations in the X–Y direction and the two additional accelerometers are utilised to identify torsional vibrations in the tower. The locations are chosen based on the convenience of sensor mounting, such as the vicinity of platforms. The accelerometers of the upper levels are used in order to predict the dynamic strains at the lower level situated at the interface between the tower (TW) and the transition piece (TP) of the OWT. Moreover two fiber brag strain sensors at the middle of the tower and four optical fiber brag sensors at the TW/TP interface have been installed. The technique is validated with the strain data from this lower level (TW/TP) using the strain gauges at the middle of the tower.

In most practical applications, a limited number of (dominant) modes can be sufficient for good response prediction through the so-called modal superposition process. Since the interest in this application lies within the lower frequency range

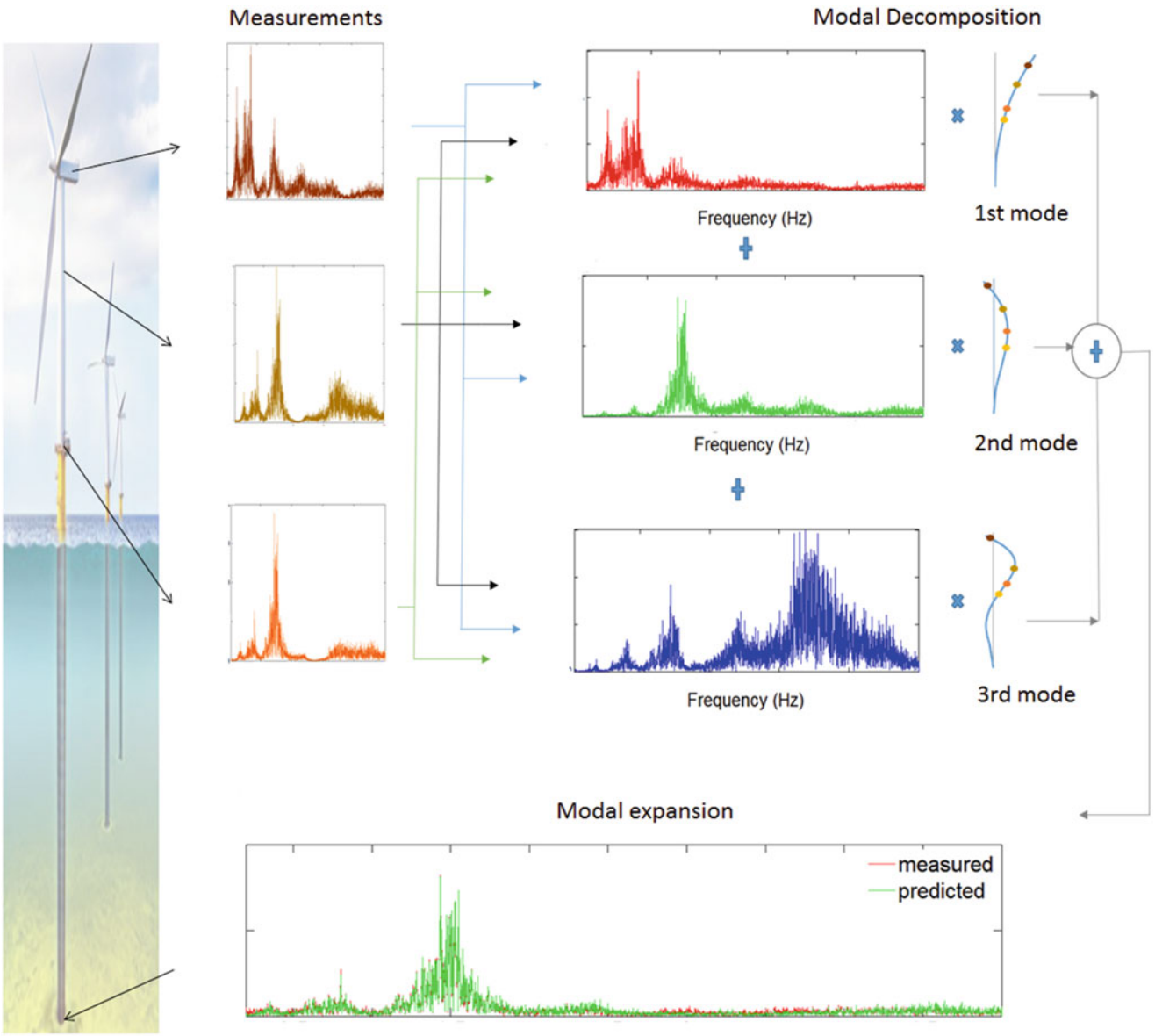

Fig. 34.4 Modal decomposition and expansion in a schematic representation for the case of OWT

(low-frequent accelerations imply large displacements and subsequently large strains and accelerated fatigue), the first two or three modes in the FA or SS direction are considered. Equation (34.1) can be split in its FA and SS components:

$$\boldsymbol{a}_{\boldsymbol{FA}}\,(\mathrm{t}) = \Phi_{FA}\boldsymbol{q}_{\boldsymbol{aFA}}(t) \tag{34.2}$$

$$\boldsymbol{a}_{\boldsymbol{SS}}\,(\mathrm{t}) = \Phi_{SS}\boldsymbol{q}_{\boldsymbol{a,SS}}(t) \tag{34.3}$$

Note that for an (axi)-symmetrical structure Φ_{FA} and Φ_{SS} are equal.

If we consider a set of n_{dof} finite element degrees of Freedom (DOF's) composed of a subset of n_m active DOF's corresponding to the measured locations of the real experimental model and n_p remaining DOF's corresponding to predicted locations, the displacement mode shape matrix of the related Finite Element Model (FEM) can be written as follows:

$$[\Phi]_{FEM} = \begin{bmatrix} [\Phi_m] \\ [\Phi_p] \end{bmatrix}_{FEM} \tag{34.4}$$

where subscript m corresponds to the measured DOF's and p to the predicted DOF's. $\Phi_m \in \mathbb{R}^{n_m \times n_\Phi}$, $\Phi_p \in \mathbb{R}^{n_p \times n_\Phi}$ are the displacement mode shapes of the n_Φ modes considered in the analysis at the active and remaining DOF's respectively. The total number of DOF's n_{dof} is equal to the sum of n_m measured DOF's and n_p predicted DOF's.

Only mode shapes derived from FEM allow to predict the output at locations without sensors. The numerical mode shapes can be compared with the experimentally determined mode shapes by using the Modal Assurance Criterion (MAC). By maximizing the MAC between experimental mode shapes and the numerical eigenvectors, the model is tuned to accurately represent the instrumented system. Hereafter, the subscript *FEM* when considering mode shapes will be omitted.

Assuming that the number of active modes, n_Φ, is less than or equal to the number of active/measured DOF's, n_m, Eq. (34.1) can be solved for the acceleration modal coordinates $\boldsymbol{q_{am}}$ by using the pseudo inverse as follows:

$$\boldsymbol{q_{am}}(t) = \left(\Phi_m^T \Phi_m\right)^{-1} \Phi_m^T \boldsymbol{a_m}(t) = {\Phi_m}^{\dagger} \boldsymbol{a_m}(t) \tag{34.5}$$

As seen in Fig. 34.3, in parked conditions of the OWT even one mode can be sufficient to fully describe its dynamic behavior as the spectrum is dominated by the first mode whereas in more complex cases (e.g., rotating) a linear combination of multiple modes should be taken. This motivates the use of different settings for different EOC.

34.2.2 Modal Expansion for Response Prediction

The estimated modal coordinates derived from Eq. (34.5) can be expanded to the predicted locations (n_p predicted DOF's) with the following expression:

$$\boldsymbol{a_p}(t) = \Phi_p \boldsymbol{q_{am}}(t) = \Phi_p \, {\Phi_m}^{\dagger} \boldsymbol{a_m}(t) \tag{34.6}$$

For the prediction of dynamic strains the same principle is applied. Firstly, a modal decomposition of the measured accelerations, $\boldsymbol{a_m}(t)$, results in the estimation of the acceleration modal coordinates, $\boldsymbol{q_{am}}(t)$, according to Eq. (34.5). Then, the displacement modal coordinates are estimated by a double integration of the acceleration modal coordinates. In this work, a double integration in the frequency domain was used. Finally, the relation between the displacement modal coordinate and the strain in any virtual location is established by using the corresponding numerically obtained strain mode shapes with the following formula:

$$\boldsymbol{\varepsilon_p}(t) = \Phi_{\varepsilon p} \boldsymbol{q_{dm}}(t) = \Phi_{\varepsilon p} \mathcal{L}^{-1} \left\{ \frac{1}{s^2} \mathcal{L} \left\{ \boldsymbol{q_{am}}(t) \right\} \right\} \tag{34.7}$$

where superscript p indicates predicted degrees of freedom (DOF's), $\Phi_{\varepsilon p}$ is the strain mode shape matrix and $\mathcal{L}^{-1}\{.\}$ and $\mathcal{L}\{.\}$ are the inverse and Laplace operators respectively.

The inevitable operation of double integration of accelerations implies a high risk of blowing up the low frequent noise of the measured accelerations resulting in large errors in the near-static components of the predicted strains (Fig. 34.5). The figure reveals that the strains below 0.15 Hz estimated from the modal expansion algorithm are predominantly due to measurement noise.

Near the static region of frequencies (very low frequencies situated well below the first Eigen frequency and below the site-specific wave peak frequency), the static deflection shape of the turbine is not accurately described by the lowest structural mode and therefore different strain components should be considered (Fig. 34.6). In order to obtain the numerical strain components due to static load a static analysis is performed with the aid of the tuned FEM. This analysis considers a representative load at the tower top derived from measured bending moments. The following formula is used for the prediction of the quasi-static strains:

$$\boldsymbol{\varepsilon_{p,QS}}(t) = \Phi_{\varepsilon,QS_p} \boldsymbol{q_{\varepsilon m}}(t) = \Phi_{\varepsilon,QS_p} \frac{\boldsymbol{\varepsilon_m}(t)}{\Phi_{\varepsilon,QS_m}} \tag{34.8}$$

where Φ_{ε,QS_p} and Φ_{ε,QS_m} are the strain mode shape components at the predicted DOF of interest, p, and the measured DOF respectively due to the applied static load and $\boldsymbol{\varepsilon_m}(t)$ is the strain time history at the corresponding measured DOF. It should be highlighted that according to Fig. 34.6, $\frac{\Phi_{\varepsilon,QS_p}}{\Phi_{\varepsilon,QS_m}} \neq \frac{\Phi_{\varepsilon,FA1/SS1_p}}{\Phi_{\varepsilon,FA1/SS1_m}}$ which motivates the use of the static strain mode shapes to predict low-frequent strain contributions in Eq. (34.8) instead of using the strain mode shape components of the first FA/SS mode.

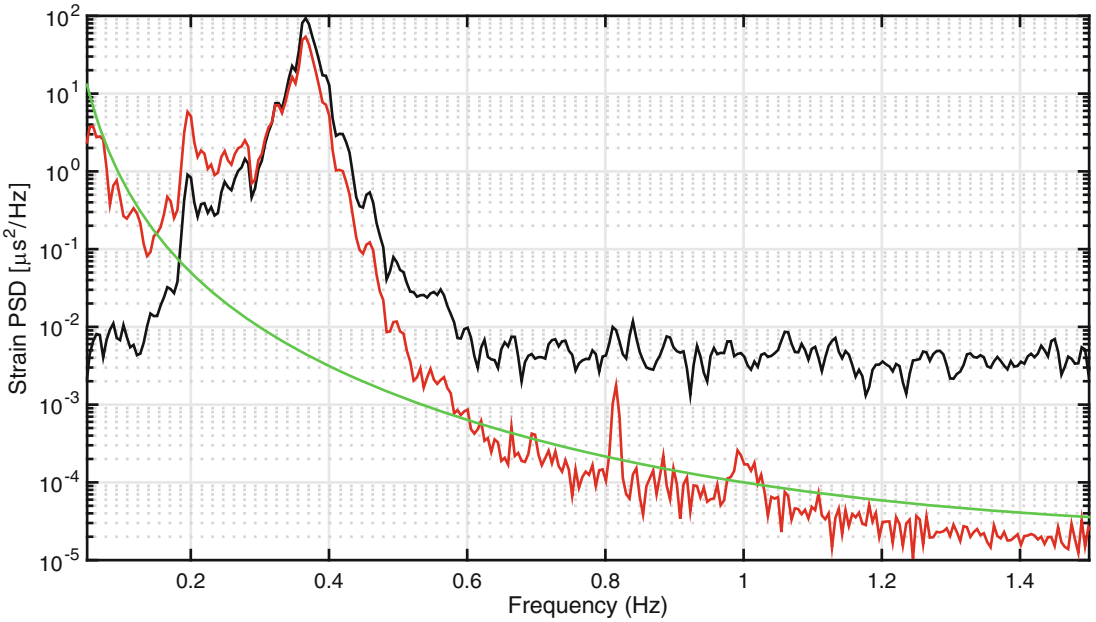

Fig. 34.5 Power spectral density (PSD) of the measured (*black*) and estimated (*red*) FA strain; the estimated strain is obtained from the modal expansion algorithm; the *green dashed line* shows a $1/\omega^4$ in order to illustrate the influence of noise on acceleration data

34.3 Multi Band Virtual Sensing

In order to predict the entire strain time history, the two distinctive strain contributions namely quasi-static and dynamic contributions are superimposed. The quasi-static contributions can mainly be attributed to gust induced low-frequent variations in the thrust loading or low-frequent wave loading whereas the dynamic contributions are linked to the turbine's dynamics and modal behavior. Accelerometers on their own cannot capture the very low frequency band below 0.05 Hz due to limitations related to measurement noise (Fig. 34.5). It should be highlighted that this lower frequency bound can be pushed further down by using accelerometers with better noise properties. However, ICP accelerometers will always have a lower frequency bound inhibiting their use for these quasi-static strains. MEMS accelerometers allow measurements down to 0 Hz, but in general have poorer noise properties. The necessary information at the very low-frequent band up to 0.05 Hz is obtained through modal decomposition and expansion of the measured strains according to Eq. (34.8).

The dynamic frequency band of interest ranging from 0.05 Hz up to 5 Hz is subdivided in two parts. The first part captures the lower frequency turbine dynamics including the first structural mode (0.05 Hz up to 0.5 Hz) and the second part (0.5 Hz up to 5 Hz) captures all the remaining dynamics and modal behavior of the structure. The reason for this subdivision is the benefit from the optimal use of the best performing sensors in each dynamic frequency band. For example, sensors near the top of the turbine are very valuable for assessing the first order motion, while sensors closer to the bottom are nearly insensitive to this first order motion and they are at the noise floor (e.g., as can been seen in Fig. 34.3a).

The aforementioned process summarized in Eq. (34.9) is hereafter called multi band virtual sensing and is validated over the entire range of EOC the turbine is subjected to.

$$\boldsymbol{\varepsilon}_{\boldsymbol{p}}(t) = \boldsymbol{\varepsilon}_{\boldsymbol{p},\boldsymbol{QS}}(t) \;+\; \boldsymbol{\varepsilon}_{\boldsymbol{p},\boldsymbol{D}}\,(t) = \boldsymbol{\varepsilon}_{\boldsymbol{p},\boldsymbol{QS}}\,(t) \;+\; \left(\boldsymbol{\varepsilon}_{\boldsymbol{p},\boldsymbol{D}1}\,(t) \;+\; \boldsymbol{\varepsilon}_{\boldsymbol{p},\boldsymbol{D}2}\,(t)\right) \tag{34.9}$$

where $\boldsymbol{\varepsilon}_{\boldsymbol{p},\boldsymbol{D}}\,(t) = \boldsymbol{\varepsilon}_{\boldsymbol{p},\boldsymbol{D}1}\,(t) + \boldsymbol{\varepsilon}_{\boldsymbol{p},\boldsymbol{D}2}\,(t)$ is the dual band dynamic response derived from the superposition of the low-frequent dynamic strain contribution $\boldsymbol{\varepsilon}_{\boldsymbol{p},\boldsymbol{D}1}\,(t)$ and the higher-frequent dynamic strain contribution $\boldsymbol{\varepsilon}_{\boldsymbol{p},\boldsymbol{D}2}\,(t)$.

34.4 Results of Long-Term Analysis

The obtained virtual responses from the novel multi band approach are compared with actual measurements from an ongoing measurement campaign on an offshore wind turbine [11, 14, 18]. Figure 34.7 shows the step-wise approach to achieve the optimal match between the measured and the predicted signals. It is noticeable that for every contribution as well as for

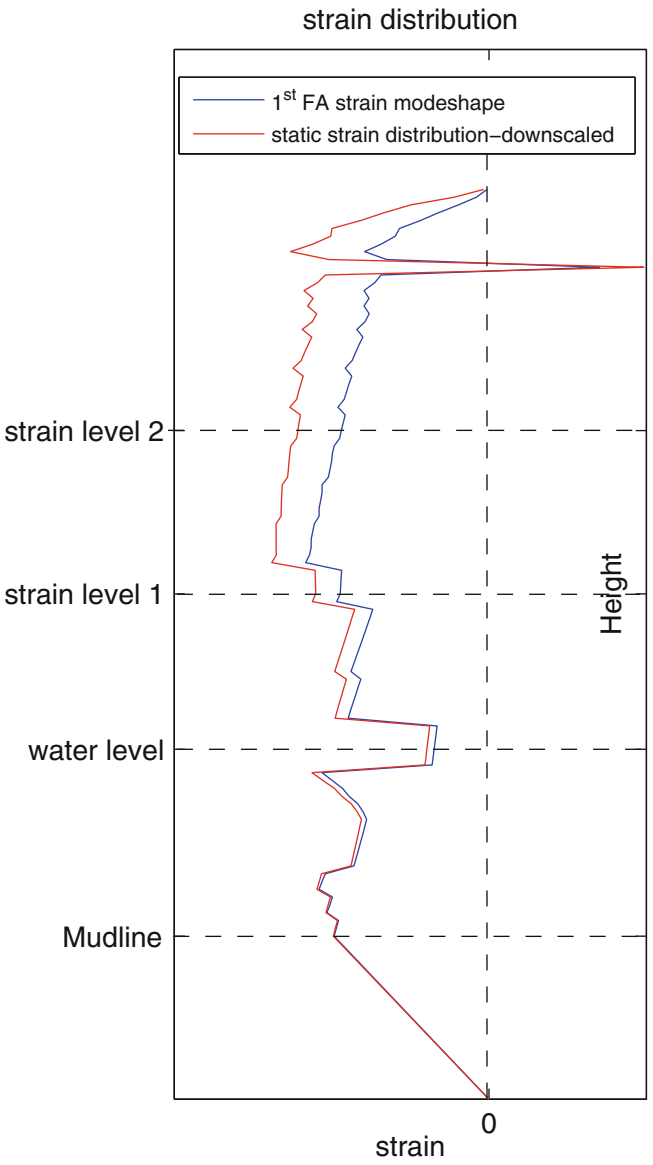

Fig. 34.6 First FA strain mode shape vs. static strain distribution

the entire strain history, there is a good agreement between the signals both in terms of amplitude and in terms of temporal evolution both in time domain and in the frequency domain.

The results of the comparison of measured and predicted strain signals over a period of 4 days are presented in Fig. 34.8. The quality indicators utilized for the comparison are the time response assurance criterion (TRAC) and the mean absolute error in the time domain (MAE) [7, 8, 11, 18].

It is worth stating that the proposed technique is capable of providing strain histories of high accuracy as indicated by the high TRAC values (one implies the best correlation between the signal and zero the worst) and the low mean absolute errors. Two timestamps indicated by arrow in Fig. 34.8 have the worst correlation which is attributed to alignment errors between the signals.

According to Fig. 34.8, the MAE occurring in the FA direction are larger than in SS direction, but this is expected due to the larger stresses that the OWT's are facing in the direction of the nacelle (FA). Although they seem poorer though in terms of MAE, the TRAC coefficient reveals a great prediction of the strain and perfect match of the measured with the predicted signals over the long term period examined.

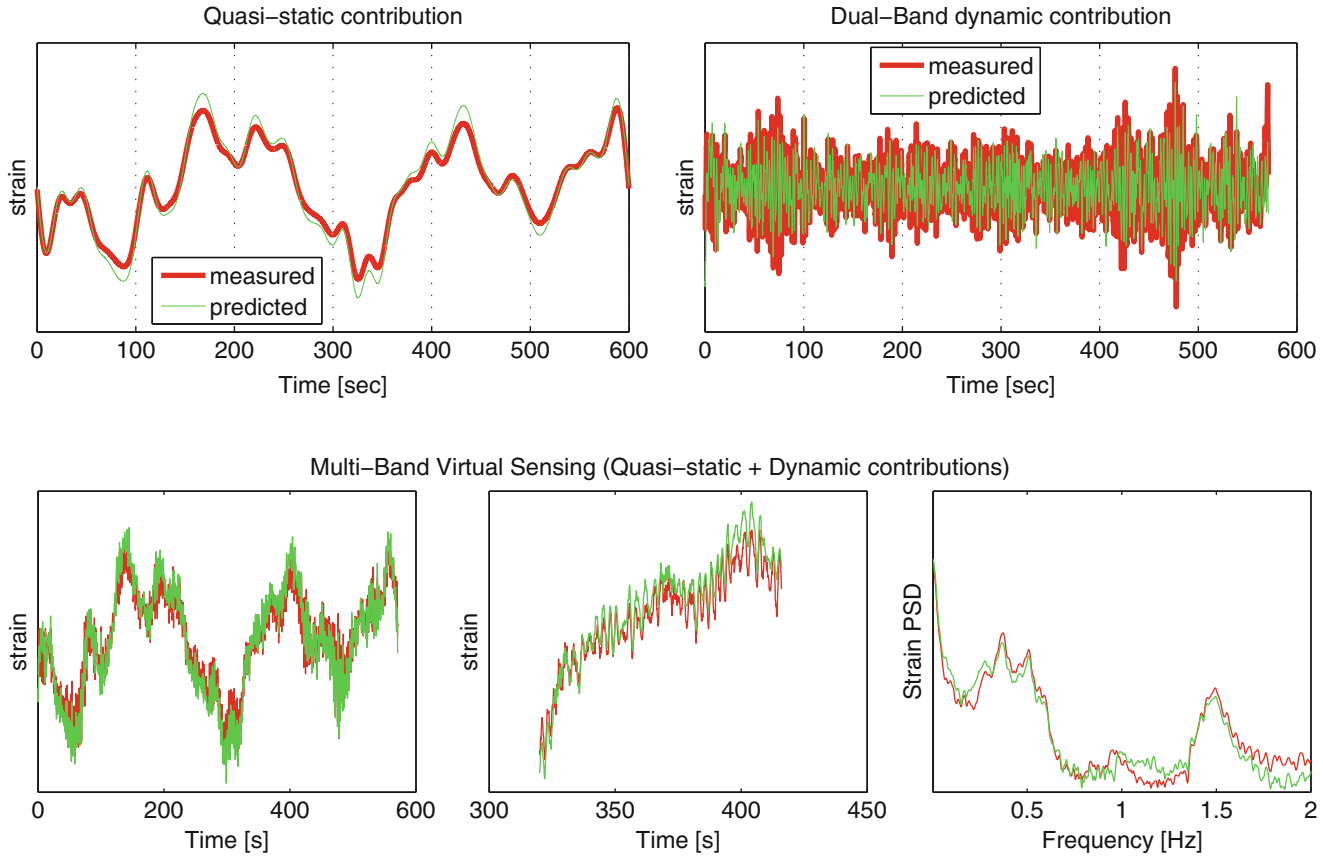

Fig. 34.7 Quasi-static strain prediction and dual band dynamic strain prediction (*top*) and superposition of the very low-frequent quasi-static component and the higher-frequent dynamic components resulting in the multi band virtual sensing (*bottom*)

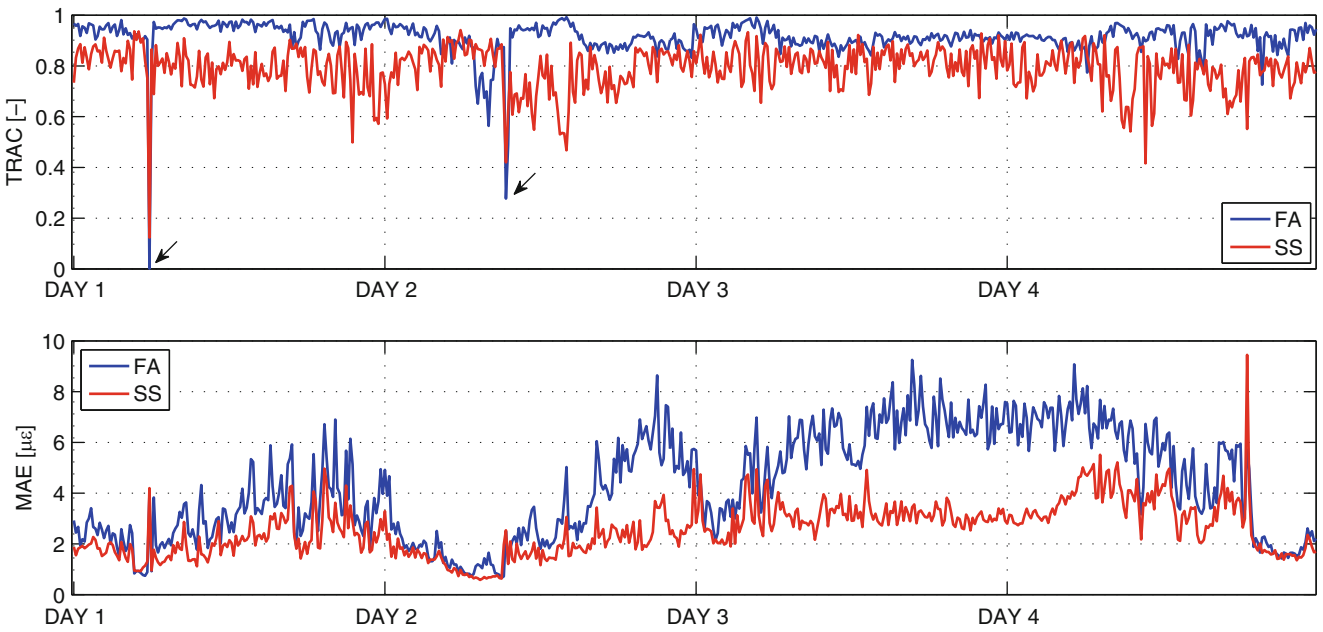

Fig. 34.8 Long term prediction of strains; comparison between the measured and the predicted signals using TRAC and MAE as quality indicators. The *arrows* indicate two timestamps with the worst correlation which is attributed to alignment errors between the signals

34.5 Conclusions

This paper presented a novel virtual sensing scheme based on a multi band modal decomposition and expansion of a few measured quantities (accelerations and strains) at accessible locations. The technique is capable of providing accurate predictions of quasi static and dynamic strain contributions as well as entire strain histories at fatigue hotspots of a monopile offshore wind turbine. It is validated over a long period of actual data while the wind turbine was subjected to different EOC. Therefore, this reliable, robust, easy to implement and inexpensive method constitutes a structural health, monitoring tool with the ability to interrogate an entire structure and accurately assess fatigue life consumption and remaining useful life at the true fatigue hot spots.

Acknowledgements This research has been performed in the framework of the Offshore Wind Infrastructure Project (http://www.owi-lab.be) and the O&O Parkwind project. The authors also acknowledge the financial support by the Agency for innovation by Science and Technology (IWT). The authors gratefully thank the people of Parkwind and Belwind and the colleagues in OWI-lab for their continuous support within this project.

References

1. Kalman, R.E., Bucy, R.S.: New results in linear filtering and prediction theory. J. Basic Eng. Trans. ASME D **83**(3), 95–108 (1961)
2. Papadimitriou, C., Fritzen, C.-P., Kraemer, P., Ntotsios, E.: Fatigue predictions in entire body of metallic structures from a limited number of vibration sensors using Kalman filtering. J. Struct. Control Health Monitor. **18**(5), 554–73 (2011)
3. Lourens, E., Papadimitriou, C., Gillijns, S., Reynders, E., De Roeck, G., Lombaert, G.: Joint-input-response estimation for structural systems based on reduced-order models and vibration data from a limited number of sensors. J. Mech. Syst. Signal Process. **29**, 310–27 (2012)
4. Lourens, E., Reynders, E., De Roeck, G., Degrande, G., Lombaert, G.: An augmented Kalman filter for force identification in structural dynamics. J. Mech. Syst. Signal Process. **27**, 446–60 (2012)
5. Maes, K., Smyth, A., De Roeck, G., Lombaert, G.: Joint input-state estimation in structural dynamics. J. Mech. Syst. Signal Process. **70–71**, 445–466 (2016)
6. Maes, K., De Roeck, G., Lombaert, G., Iliopoulos, A., Van Hemelrijck, D., Devriendt, C., Guillaume, P.: Continuous strain prediction for fatigue assessment of an offshore wind turbine using Kalman filtering techniques. In: Proceedings of the Environmental, Energy and Structural Monitoring Systems (EESMS), IEEE Workshop, pp. 44–49. Trento, 9–10 July 2015. doi:10.1109/EESMS.2015.7175850
7. Avitabile, P., Pingle, P.: Prediction of full field dynamic strain from limited sets of measured data. J. Shock Vib. **19**, 765–85 (2012)
8. Baqersad, J., Poozesh, P., Niezrecki, C., Avitabile, P.: Predicting full-field strain on a wind turbine for arbitrary excitation using displacements of optical targets measured with photogrammetry. In: Proceedings of the IMAC 33 Conference on Structural Dynamics, Orlando, FL (2015)
9. Helfrick, M.N., Niezrecki, C., Avitabile, P., Schmidt, T.: 3D digital image correlation methods for full-field vibration measurement. J. Mech. Syst. Signal Process. **25**, 917–27 (2011). doi:10.1016/j.ymssp.2010.08.013
10. Chipman, C., Avitabile, P.: Expansion of transient operating data. J. Mech. Syst. Signal Process. **31**, 1–12 (2012). doi:10.1016/j.ymssp.2012.04.013
11. Iliopoulos, A., Shirzadeh, R., Weijtjens, W., Guillaume, P., Van Hemelrijck, D., Devriendt, C.: A modal decomposition and expansion approach for prediction of dynamic responses on a monopile offshore wind turbine using a limited number of vibration sensors. J. Mech. Syst. Signal Process. **68**, 84–104 (2016). doi:10.1016/j.ymssp.2015.07.016
12. Maes, K., Iliopoulos, A., Weijtjens, W., Devriendt, C., Lombaert, G.: Dynamic strain estimation for fatigue assessment of an offshore monopile wind turbine using filtering and modal expansion algorithms. J. Mech. Syst. Signal Process. Available online 15 February 2016, ISSN 0888-3270, doi:http://dx.doi.org/10.1016/j.ymssp.2016.01.004
13. Weijtjens, W., Iliopoulos, A., Helsen, J., Devriendt, C.: Monitoring the consumed fatigue life of wind turbines on monopile foundations. In: Proceedings of the EWEA Offshore, Copenhagen (2015)
14. Weijtjens, W., Shirzadeh, R., De Sitter, G., Devriendt, C.: Classifying resonant frequencies and damping values of an offshore wind turbine on a monopile foundation. In: Proceedings of the EWEA, Barcelona (2014)
15. Heylen, W., Lammens, S., Sas, P.: Modal Analysis: Theory and Testing. Katholieke Universiteit Leuven, Leuven (1997)
16. Maia, N., Silva, J., He, J., Lieven, N., Lin, R-M., Skingle, G., To, W., Urgueira, A.: Theoretical and Experimental Modal Analysis. Research Studies Press Ltd, Somerset (1997)
17. Ewins, D.: Modal Testing 2, Theory, Practice and Application, 2nd edn. Research Studies Press Ltd, Baldock (2000)
18. Iliopoulos, A., Weijtjens, W., Van Hemelrijck, D., Devriendt, C.: Long-term prediction of dynamic responses on an offshore wind turbine using a virtual sensor approach. In: Proceedings of the 10th International Workshop on Structural Health Monitoring 2015: System Reliability for Verification and Implementation, pp. 2793–2800. Stanford, CA, 1–3 September 2015

Chapter 35
A State-Input Estimation Approach for Force Identification on an Automotive Suspension Component

E. Risaliti, B. Cornelis, T. Tamarozzi and W. Desmet

Abstract Input force evaluation is always a crucial step for the adequate design of any kind of mechanical system. Direct measurements of input forces typically involve devices that are expensive, intrusive or difficult to calibrate. This is also the case for Road Load Data Acquisition (RLDA) testing campaigns, where the loads due to the road excitations acting on a vehicle are acquired. During RLDA testing campaigns, expensive measurement wheels are commonly used. An appealing alternative procedure, which consists of the use of less expensive sensors in combination with a numerical model of the system, is investigated. In order to combine experimental and simulation data, a coupled state-input estimation approach is used in the proposed procedure. In this approach a finite element model of the system provides simulated data, while common accelerometers and strain gauges provide experimental data. A Kalman filter is then used in order to perform the estimation. This paper presents the derivation of the filter equations that are necessary for the envisioned approach. A numerical example is then performed where the system-under-investigation is an automotive suspension component.

Keywords Input estimation • Virtual Sensing • Automotive • Kalman filter • Multiple force estimation

35.1 Introduction

When designing any kind of mechanical system, it is essential to have a good knowledge of the external loads. In the automotive sector for instance, the forces acting on the wheel centers (Wheel Center Forces, WCFs) are needed for conducting both durability and handling analyses. In the case of durability analysis, Road Load Data Acquisition (RLDA) testing campaign are typically performed at the beginning of the design cycle of a new vehicle. During such testing campaigns the vehicle is instrumented with expensive measurement wheels or so-called Wheel Force Transducers (WFTs) in order to measure the WCFs. The vehicle is then driven on a proving ground for a given amount of laps with the intent of reproducing the forecast damage for the vehicle life-cycle. The previously mentioned measurement devices are normally extremely expensive, intrusive and time-consuming to install and calibrate. In order to alleviate some of these disadvantages, it would be helpful to develop a so-called virtual sensing strategy where information coming from more affordable and common sensors is combined with system behavioral information coming from available physical models. In such an approach the quantity-of-interest can be estimated without requiring a direct measurement device. Depending on the available resources and on the system-under-investigation, several combinations of models and sensors, acting on several levels of analysis (component, sub-system and system level analysis), can be exploited. This work investigates using the structural model of a component located next to the load which has to be identified. Strain and acceleration measurements are assumed to provide the experimental information.

This paper hence addresses the problem of identifying input loads for a structural system given measurements of the outputs. Mathematically speaking this is an inverse problem. Most of the time this problem is ill-posed in the sense that one of the uniqueness, existence or stability conditions of the solution is violated [1, 2]. Deterministic approaches for solving the problem exist both in the time and in the frequency domain. A review of time domain deterministic methods can be found in

E. Risaliti (✉) • T. Tamarozzi
Siemens Industry Software NV, Interleuvenlaan 68, 3001 Leuven, Belgium
Katholieke Universiteit Leuven, Division PMA, Celestijnenlaan 300B, 3001 Leuven, Belgium
e-mail: enrico.risaliti@siemens.com

B. Cornelis
Siemens Industry Software NV, Interleuvenlaan 68, 3001 Leuven, Belgium

W. Desmet
Katholieke Universiteit Leuven, Division PMA, Celestijnenlaan 300B, 3001 Leuven, Belgium

S. Atamturktur et al. (eds.), *Model Validation and Uncertainty Quantification, Volume 3*, Conference Proceedings of the Society for Experimental Mechanics Series, DOI 10.1007/978-3-319-29754-5_35

references [2, 3]. Regularization techniques [4], like Tikhonov regularization and truncated Singular Value Decomposition (SVD), are often adopted [2, 5] in order to circumvent the numerical ill-conditioning which typically occurs, since the problem is ill-posed. Frequency domain deterministic approaches involve the inversion of some Frequency Response Function (FRF) description of the system in order to perform the force identification [6]. Equivalent regularization techniques are normally also used in the frequency domain [7–9], since the just mentioned inversion process is again ill-conditioned. Pure stochastic techniques for force identification are based on finding statistical relations between the outputs and the inputs. Regression models are quite often used in this case in order to find these relations [10]. Other methods are based on artificial intelligence, e.g. Artificial Neural-Network (ANN) algorithms [11]. Both pure stochastic and artificial intelligence based methods require measurements of both the inputs and the outputs before the actual operational measurements can be conducted. This is required for finding the regression model in the former and for the learning process in the latter. In the case of deterministic methods a similar step is also needed for determining an experimental model that is later on used for the load identification. Although this step can be avoided if a numerical model of the system is available, the deterministic methods assume that the model is exact, which is never the case in practice. In this sense the use of state-estimation theory for the development of the virtual sensing strategy could be helpful, since it can account for the presence of uncertainties, both in the measurements and in the model.

State-estimators like Kalman filters [12] have been widely used, since they provide practical and efficient algorithms for estimating the states of a dynamic system. In the original formulation of the Kalman filter, the inputs of the system are known quantities that together with the knowledge of the outputs can lead to the estimation of the states. However, during the years several works have been published on coupled input and state estimation, where the goal is to estimate both the states and the unknown inputs. Ma et al. [13] implemented a scheme in which a Kalman filter is used for the estimation of the states while a recursive least-square estimator is used for the inputs evaluation. Gillijns and De Moor [14] proposed a recursive filter in which the estimation of the state and the input are interconnected. Hwang et al. [15] proposed a Kalman based approach in which the estimation of the input and the state are coupled by means of an additional pseudo-inversion.

Another approach introduces a model for the input, so that it is possible (after some manipulations on the equations) to include this latter in the state vector. This results in a so-called Augmented Kalman Filter (AKF), which first appeared in the work of Friedland [16] where a constant bias forcing term was estimated. The AKF was only recently adopted for force estimation in structural dynamics [17, 18]. In this paper, the AKF approach will be further investigated and applied to the case of multiple force estimation on an automotive suspension component. This will serve as a preliminary study of the applicability of the method to a complex industrial case.

The paper is organized as follows. In Sect. 35.2 the derivation of the AKF is presented starting from the equations of a linear Kalman filter in its original formulation. In Sect. 35.3 the virtual sensing strategy is explained more in detail, contextualizing the Kalman filter approach to the use of a structural model together with local measurements. Some theoretical considerations on observability for structural systems are reported in Sect. 35.4. These considerations are important for outlining minimal conditions for the proper design of the estimator. The numerical validation example with a more detailed description of the system-under-investigation is reported in Sect. 35.5. It will be shown that even though strain measurements are required in order to have an observable estimator, it is necessary to include acceleration measurements in order to obtain accurate results in particular estimation cases. Finally, the conclusions of the paper are presented in Sect. 35.6.

35.2 The Augmented Kalman Filter

In the original formulation of a linear Kalman filter a state-space model for the system is considered [12]:

$$\begin{cases} \dot{\mathbf{x}}(t) = \mathbf{A}\mathbf{x}(t) + \mathbf{B}\mathbf{u}(t) + \mathbf{w}(t) \\ \mathbf{y}(t) = \mathbf{C}\mathbf{x}(t) + \mathbf{D}\mathbf{u}(t) + \mathbf{v}(t) \end{cases} \tag{35.1}$$

This is a system of stochastic equations where $\mathbf{x} \in \mathbb{R}^{n_s}$ is the state vector, $\mathbf{y} \in \mathbb{R}^{n_o}$ is the output vector and $\mathbf{u} \in \mathbb{R}^{n_i}$ is the input vector with n_s, n_o and n_i representing number of states, outputs and inputs respectively; $\mathbf{A}$, $\mathbf{B}$, $\mathbf{C}$ and $\mathbf{D}$ are real matrices of appropriate dimensions. The first expression of Eq. (35.1) is referred to as the model equation, while the second expression is referred to as the measurement equation. Equation (35.1) has a stochastic nature due to the presence of $\mathbf{w}$ and $\mathbf{v}$, the so-called process and measurement noise respectively, which are introduced in order to take into account the presence of uncertainties in the model and in the measurements. These quantities are stochastic processes of adequate dimensions, with associated

covariance matrices $\mathbf{Q}$ and $\mathbf{R}$ for $\mathbf{w}$ and $\mathbf{v}$ respectively. In order to obtain the augmented system, a model for the unknown inputs needs to be introduced. In this work a so-called zeroth-order random walk model is adopted, which states [17–19]:

$$\dot{\mathbf{u}}(t) = \mathbf{0} + \mathbf{w}_u(t) \tag{35.2}$$

where $\mathbf{w}_u$ is a stochastic process with associated covariance matrix $\mathbf{Q}_u$, meaning that the rate of change of the input with respect to time can vary randomly. By plugging Eq. (35.2) into Eq. (35.1) and by rearranging the system one can obtain:

$$\begin{cases} \dot{\mathbf{x}}^*(t) &= \mathbf{A}^*\mathbf{x}^*(t) + \mathbf{w}^*(t) \\ \mathbf{y}(t) &= \mathbf{H}^*\mathbf{x}^*(t) + \mathbf{v}(t) \end{cases} \tag{35.3}$$

where the augmented state vector is defined as

$$\mathbf{x}^* = \begin{bmatrix} \mathbf{x} \\ \mathbf{u} \end{bmatrix}, \tag{35.4}$$

where the new system matrices are defined as

$$\mathbf{A}^* = \begin{bmatrix} \mathbf{A} & \mathbf{B} \\ \mathbf{0} & \mathbf{0} \end{bmatrix}, \quad \mathbf{H}^* = \begin{bmatrix} \mathbf{C} & \mathbf{D} \end{bmatrix}, \tag{35.5}$$

and where the new process noise and process covariance matrix are defined as

$$\mathbf{w}^* = \begin{bmatrix} \mathbf{w} \\ \mathbf{w}_u \end{bmatrix}, \quad \mathbf{Q}^* = \begin{bmatrix} \mathbf{Q} & \mathbf{0} \\ \mathbf{0} & \mathbf{Q}_u \end{bmatrix} \tag{35.6}$$

In this case it was assumed that all the inputs are unknown. In the case where some of the inputs are known, an analogous formulation can be obtained where also modified matrices $\mathbf{B}^*$ and $\mathbf{D}^*$ appear and where the state vector is augmented only with the unknown input components. Equation (35.3) represents again a stochastic state-space model suitable for the application of a Kalman filter in its original formulation, but now also the unknown forces will be estimated since they are included in the state vector. However, a discretized form of Eq. (35.3) is needed for the practical filter implementation. In this work an exponential integration scheme with zero-order hold for the input is chosen [20]. Only the first expression of Eq. (35.3) has to be discretized because of its time-evolutive form. Following the exponential integration scheme, the discretized time form of matrix $\mathbf{A}^*$ is given by

$$\mathbf{F}^* = \begin{bmatrix} e^{\mathbf{A}\Delta t} & \mathbf{A}^{-1}\left(e^{\mathbf{A}\Delta t} - \mathbf{I}\right)\mathbf{B} \\ \mathbf{0} & \mathbf{I} \end{bmatrix} \tag{35.7}$$

where Δt is the time step size and where the matrix partitioning is applied according to Eq. (35.4). The discrete-time augmented system is hence given by

$$\begin{cases} \mathbf{x}_k^* &= \mathbf{F}^*\mathbf{x}_{k-1}^* + \mathbf{w}_{k-1}^* \\ \mathbf{y}_k &= \mathbf{H}^*\mathbf{x}_k^* + \mathbf{v}_k \end{cases} \tag{35.8}$$

where subscript k refers to time sample k and where $\mathbf{w}_k^*$ is the discrete-time process noise vector with discrete-time covariance matrix $\mathbf{Q}_k^*$, i.e.

$$\mathbf{Q}_k^* = \int_0^{\Delta t} e^{\mathbf{A}t}\mathbf{Q}e^{\mathbf{A}^T t}\, d\tau \tag{35.9}$$

Some details about the computation of the integral in Eq. (35.9) can be found in [21].

For the system of Eq. (35.8) the discrete-time version of the Kalman filter can now be formulated. It provides a state vector estimate $\hat{\mathbf{x}}_k^*$ at time step k and consists of the following set of equations that are computed at each time step $k = 1, 2, \ldots$ [20]:

Time update

$$\hat{\mathbf{x}}_k^{*-} = \mathbf{F}^* \hat{\mathbf{x}}_{k-1}^{*+} \tag{35.10}$$

$$\mathbf{P}_k^- = \mathbf{F}^* \mathbf{P}_{k-1}^+ \mathbf{F}^{*T} + \mathbf{Q}_{k-1}^* \tag{35.11}$$

Measurement update

$$\mathbf{K}_k = \mathbf{P}_k^- \mathbf{H}^{*T} \left(\mathbf{H}^* \mathbf{P}_k^- \mathbf{H}^{*T} + \mathbf{R}_k \right)^{-1} \tag{35.12}$$

$$\hat{\mathbf{x}}_k^{*+} = \hat{\mathbf{x}}_k^{*-} + \mathbf{K}_k \left(\mathbf{y}_k - \mathbf{H}^* \hat{\mathbf{x}}_k^{*-} \right) \tag{35.13}$$

$$\mathbf{P}_k^+ = \left(\mathbf{I} - \mathbf{K}_k \mathbf{H}^* \right) \mathbf{P}_k^- \tag{35.14}$$

This is an unbiased linear state estimator designed to be optimal in the sense that it minimizes the trace of the error covariance matrix, defined as

$$\mathbf{P}_k = \mathbf{E} \left[\left(\mathbf{x}_k^* - \hat{\mathbf{x}}_k^* \right) \left(\mathbf{x}_k^* - \hat{\mathbf{x}}_k^* \right)^T \right] \tag{35.15}$$

During the time update in Eqs. (35.10)–(35.11) the so-called a priori state estimate $\hat{\mathbf{x}}_k^{*-}$ is computed, without taking into account the new measurement at time step k. The associated a priori error covariance matrix $\mathbf{P}_k^-$ is also computed. The latter is defined according to Eq. (35.15), with $\hat{\mathbf{x}}_k^{*-}$ in place of $\hat{\mathbf{x}}_k^*$. The so-called a posteriori $\hat{\mathbf{x}}_k^{*+}$ state estimate is then computed during the measurement update in Eqs. (35.12)–(35.14), where the new measurement is taken into account. The associated a posteriori error covariance matrix $\mathbf{P}_k^+$ is again defined as in Eq. (35.15) with $\hat{\mathbf{x}}_k^{*+}$ in place of $\hat{\mathbf{x}}_k^*$. In the derivation of the above filter equations it is assumed that the noise processes $\mathbf{w}_k^*$ and $\mathbf{v}_k$ are white, zero-mean and uncorrelated.

Since the augmented state vector $\mathbf{x}^*$ contains the unknown inputs, a coupled state-input estimation is effectively performed when Eqs. (35.10)–(35.14) are computed in each time step.

35.3 System Description

In this work the virtual sensing strategy is built by combining a Finite Element Model (FEM) [22] of a suspension component together with local measurements of accelerations and strains. These latter quantities can be measured by means of accelerometers and strain gauges respectively. More information about the specific system-under-investigation will be given in Sect. 35.5, while here the mathematical implementation of the virtual sensing strategy is presented.

The first step consists of building the state-space representation of the system, i.e. it is required[1] to find the matrices $\mathbf{A}$, $\mathbf{B}$, $\mathbf{C}$ and $\mathbf{D}$ defined in Eq. (35.1). In this work a so-called reduced FEM of a suspension component is considered. Model order reduction techniques [23] are hence used in order to reduce the size of the full FEM. This can considerably reduce the computational cost of the procedure, although computational cost is not a major bottleneck for the considered application. However, a likely practical scenario is that the available FEM is only validated for a few of its deformation modes (either normal or static modes). In this case the use of a reduced model, composed of few well-known deformation modes of the system, would represent a fair choice.

The FEM representation of a system is given by the following equations of motion

$$\mathbf{M}_z \ddot{\mathbf{z}}(t) + \mathbf{C}_z \dot{\mathbf{z}}(t) + \mathbf{K}_z \mathbf{z}(t) = \mathbf{B}_z \mathbf{u}(t) \tag{35.16}$$

where the vector $\mathbf{z} \in \mathbb{R}^{n_{dof}}$ contains the Degrees of Freedom (DOFs) of the system (with n_{dof} number of DOFs), the matrices $\mathbf{M}_z$, $\mathbf{C}_z$ and $\mathbf{K}_z$ are the mass, damping and stiffness matrices and the matrix $\mathbf{B}_z$ is an input shape matrix that distributes the inputs over the DOFs. The following reduction basis is used in this work

$$\boldsymbol{\Psi} = \left[\boldsymbol{\Psi}_{att} \; \boldsymbol{\Psi}_{nm} \right] \tag{35.17}$$

[1] Since the model is stochastic, in order to obtain its full description, also the process and measurement covariance matrices must be provided; details about this will be given in Sect. 35.5.

where matrix $\boldsymbol{\Psi}_{att} \in \mathbb{R}^{n_{dof} \times n_{att}}$ collects the so-called attachment modes and where matrix $\boldsymbol{\Psi}_{nm} \in \mathbb{R}^{n_{dof} \times n_{nm}}$ contains a reduced number of normal modes of the system. The attachment modes are essential for a good representation of the static behavior of the system for an input in a given location. They are defined as the static deformation of the system for a unit input force at a specific degree of freedom [24]. The reduction basis is used to approximate the DOFs vector of the system as

$$\mathbf{z} \simeq \boldsymbol{\Psi}\mathbf{q} \tag{35.18}$$

where vector $\mathbf{q} \in \mathbb{R}^{n_{red}}$ is the new vector of DOFs of the system, with $n_{red} = n_{att} + n_{nm}$ and normally $n_{red} \ll n_{dof}$. By plugging Eq. (35.18) into Eq. (35.16) and by projecting the latter onto the reduction basis $\boldsymbol{\Psi}$, it is possible to obtain the equations of motion of the reduced system, i.e.

$$\mathbf{M}_r\ddot{\mathbf{q}}(t) + \mathbf{C}_r\dot{\mathbf{q}}(t) + \mathbf{K}_r\mathbf{q}(t) = \mathbf{B}_r\mathbf{u}(t) \tag{35.19}$$

where $\mathbf{M}_r$, $\mathbf{C}_r$, $\mathbf{K}_r$ and $\mathbf{B}_r$ are the mass, damping, stiffness and input shape matrix of the reduced system. Starting from Eq. (35.19), it is then possible to obtain a state-space representation of the system considering the following state vector

$$\mathbf{x} = \begin{bmatrix} \mathbf{q} \\ \dot{\mathbf{q}} \end{bmatrix} \tag{35.20}$$

and with such a choice the matrices $\mathbf{A}$ and $\mathbf{B}$ related to the model equation are obtained as

$$\mathbf{A} = \begin{bmatrix} \mathbf{0} & \mathbf{I} \\ -\mathbf{M}_r^{-1}\mathbf{K}_r & -\mathbf{M}_r^{-1}\mathbf{C}_r \end{bmatrix}, \quad \mathbf{B} = \begin{bmatrix} \mathbf{0} \\ \mathbf{M}_r^{-1}\mathbf{B}_r \end{bmatrix} \tag{35.21}$$

while matrices $\mathbf{C}$ and $\mathbf{D}$ related to the measurement equation are obtained as

$$\mathbf{C} = \begin{bmatrix} \mathbf{C}_{acc} \\ \mathbf{C}_{strain} \end{bmatrix}, \quad \mathbf{D} = \begin{bmatrix} \mathbf{D}_{acc} \\ \mathbf{0} \end{bmatrix} \tag{35.22}$$

In these latter equations the blocks $\mathbf{C}_{acc}$ and $\mathbf{D}_{acc}$ are related to the acceleration measurements and are obtained by making direct use of the equations of motion, i.e.

$$\mathbf{C}_{acc} = -\mathbf{C}_{\ddot{z}}\boldsymbol{\Psi}\left[\mathbf{M}_r^{-1}\mathbf{K}_r \; \mathbf{M}_r^{-1}\mathbf{C}_r\right], \quad \mathbf{D}_{acc} = \left[\mathbf{M}_r^{-1}\mathbf{B}_r\right] \tag{35.23}$$

with $\mathbf{C}_{\ddot{z}}$ representing a boolean matrix which selects the appropriate outputs. The block $\mathbf{C}_{strain}$ in Eq. (35.22) is related to the strain measurements and in this work is obtained by means of the finite element formulation. Each of the rows of this matrix can be obtained by considering that the elongation ε_n along the direction identified by versor $\mathbf{n}$ is given by the following well-known solid mechanics relation:

$$\varepsilon_n = \mathbf{n}^T\boldsymbol{\varepsilon}\,\mathbf{n} \tag{35.24}$$

where $\boldsymbol{\varepsilon}$ represents the local Lagrangian strain tensor and where only small deformations are assumed to take place. If the strain tensor components in the global reference system are arranged in the column vector $\boldsymbol{\epsilon}$ as follows

$$\boldsymbol{\epsilon} = \left[\varepsilon_{11} \; \varepsilon_{22} \; \varepsilon_{33} \; \varepsilon_{12} \; \varepsilon_{23} \; \varepsilon_{31}\right]^T \tag{35.25}$$

and if moreover the direction cosines of $\mathbf{n}$ are arranged in the column vector $\mathbf{n}^*$ as follows

$$\mathbf{n}^* = \left[n_1^2 \; n_2^2 \; n_3^2 \; n_1n_2 \; n_2n_3 \; n_3n_1\right]^T \tag{35.26}$$

then the elongation ε_n can be computed as

$$\varepsilon_n = \mathbf{n}^{*T}\boldsymbol{\epsilon} \tag{35.27}$$

By virtue of the finite element formulation, it is possible to write the strain vector $\boldsymbol{\epsilon}$ in terms of the nodal displacements [22] as

$$\boldsymbol{\epsilon} = \mathbf{N}\mathbf{z} \tag{35.28}$$

where matrix $\mathbf{N}$ contains the derivatives of the elements shape functions, hence depending on the specific finite elements that constitute the model. By combining Eqs. (35.18), (35.20), (35.27) and (35.28) it is possible to relate the output strain to the state vector as

$$\varepsilon_n = \mathbf{n}^{*T}\mathbf{N}\boldsymbol{\Psi}\ \mathbf{q} = \begin{bmatrix}\mathbf{n}^{*T}\mathbf{N}\boldsymbol{\Psi} & \mathbf{0}\end{bmatrix}\begin{bmatrix}\mathbf{q}\\ \dot{\mathbf{q}}\end{bmatrix} = \begin{bmatrix}\mathbf{n}^{*T}\mathbf{N}\boldsymbol{\Psi} & \mathbf{0}\end{bmatrix}\mathbf{x} \tag{35.29}$$

where the matrix that multiplies the state vector represents one row of matrix $\mathbf{C}_{strain}$ for a specific measurement point.

Once the continuous state-space matrices $\mathbf{A}$, $\mathbf{B}$, $\mathbf{C}$ and $\mathbf{D}$ are available it is then possible, following the procedures of state augmentation and time-discretization explained in Sect. 35.2, to obtain system equations that are suitable for the application of the Kalman filter Eqs. (35.10)–(35.14).

35.4 Observability

A fundamental property that a system should possess is so-called observability. By definition, a discrete-time system like the one of Eq. (35.8) is said to be observable if for any initial state and for some final time step k, the initial state can be uniquely determined by knowledge of the outputs for all the time steps up to k [20]. Less formally stated the system is observable when the measurements provide enough information for estimating the state vector. Some theoretical considerations on observability for structural systems can be found in [18, 19] and are also reported in this section.

A test for observability is the Popov-Belevitch-Hautus (PBH) criterion [25]. It is applied in the continuous time and states that the system is observable if and only if

$$\operatorname{rank}\begin{bmatrix}\mathbf{A}^* - s\mathbf{I}\\ \mathbf{H}^*\end{bmatrix} = n_s, \quad \forall s \in \mathbb{C} \tag{35.30}$$

This should only be checked for the values of s equal to the eigenvalues of $\mathbf{A}^*$, as for the other values of s indeed the matrix $\mathbf{A}^* - s\mathbf{I}$ is full-rank by definition of the eigenvalue problem. Force estimation of mechanical systems normally presents problems for $s = 0$ (cf. [19]). Some considerations on this latter case can be made making use of the criterion in Eq. (35.30) with the expressions for $\mathbf{A}^*$ and $\mathbf{H}^*$ found in Sect. 35.3. These considerations are reported below:

- the number of DOFs of the reduced model represented by Eq. (35.19) should be equal or greater than the number of forces to be estimated, i.e. $n_{red} \geq n_F$. This means that when selecting the order of the reduced model, observability must be taken into account in addition to accuracy requirements.
- the number of independent position level measurements (e.g. position or strain measurements) should be equal or greater than the number of forces to be estimated, i.e. $n_{plmeas} \geq n_F$. If this is not satisfied there is not enough information to distinguish between the contribution of the different force components. Furthermore, velocity and acceleration measurements alone are not sufficient to detect constant force contributions, hence position or strain measurements have to be added.

These considerations provide minimal requirements that have to be satisfied when designing the estimator and will therefore be taken into account for the numerical validation in Sect. 35.5.

35.5 Numerical Validation

In this section, the estimation procedure outlined in Sects. 35.2 and 35.3 is applied to a numerical example. Virtual measurements are generated by means of a model of the system and are then used as input to the Kalman filter for the input forces estimation. The structure-under-consideration is a steering knuckle, which represents a key component in the McPherson sub-system (Fig. 35.1a), i.e. one of the most common automotive front suspension systems. The steering knuckle

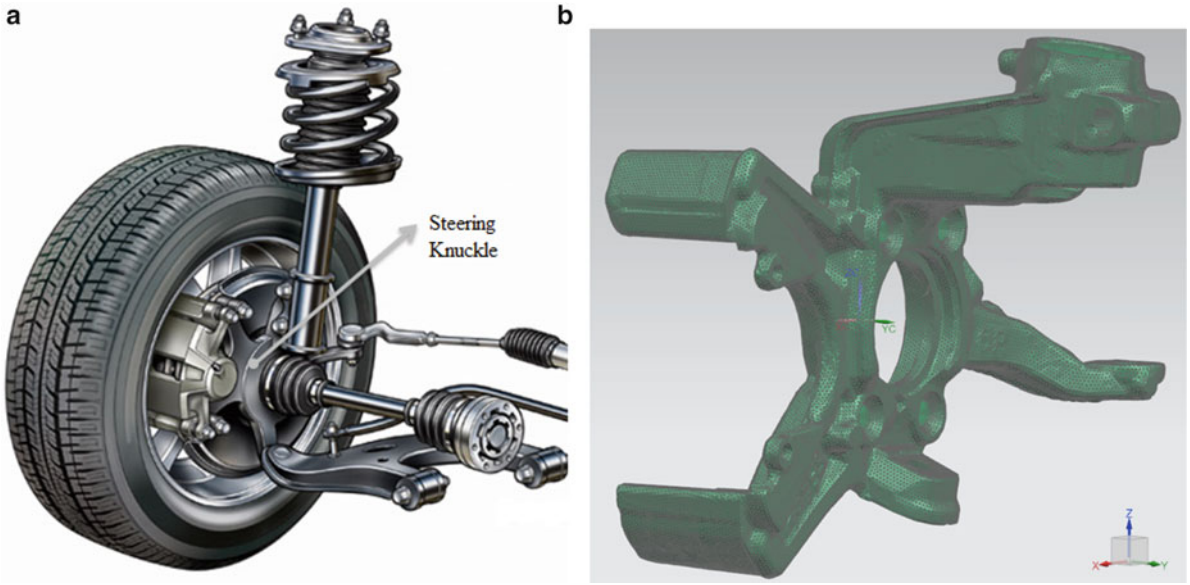

Fig. 35.1 System-under-investigation: steering knuckle component of McPherson suspension system; (**a**) McPherson suspension system; (**b**) Steering knuckle FEM

is crucial as it connects all the other parts of the suspension system together; it is also connected to the wheel and hence subjected to the WCFs. This work considers a simplified estimation exercise on the steering knuckle, whereby multiple perpendicular components of a force acting on the strut mount are estimated while the component is clamped in the four holes located in its central part.

Figure 35.1b shows the FEM of the steering knuckle. This model consists of 658,142 linear tetrahedral solid elements. Linear tetrahedral elements normally show poor spatial convergence properties, so that a relatively fine mesh is required. Figure 35.2a shows the constraints application. For each one of the four holes a rigid element is created which connects all the nodes of the inner surface of the hole to a central independent node. The four independent nodes (marked in blue) are then fixed. Figure 35.2b shows the location of the input forces that have to be estimated. Again a rigid element is used to connect all the nodes of the inner surface of the strut mount, corresponding to the location where the damper-spring subsystem is connected to the steering knuckle, to a central independent node. The input forces are assumed to be applied to this latter independent node (marked in red). Considering the boundary conditions application and the DOFs reduction due to the rigid elements, the total number of DOFs for the full FEM is 388,350. A reduced model is then computed starting from this full model. In the estimation cases herein described the same model is used both for the virtual measurements generation and for deriving the filter equations. Hence an exact knowledge of the model is assumed, while Gaussian noise with a signal-to-noise ratio equal to 15 dB is added on the simulated measurements. Sinusoidal input forces with a frequency of 5 Hz are applied to the system. Two different estimation cases are considered:

- In the first case two force components F_y and F_z acting on the input node are estimated. In this case the attachment modes corresponding to the two input components are used to compute the reduced model together with the first five normal modes, so that n_{red} is equal to seven.
- In the second case three force components F_x, F_y and F_z acting on the input node are estimated. In this case the reduced model is computed including again the first five normal modes, but now considering three attachment modes corresponding to the three input components, so that n_{red} is equal to eight.

In order to perform the estimation some filter parameters have to be tuned. These parameters correspond to the process and measurement covariance matrices $\mathbf{Q}^*$ and $\mathbf{R}$, which are assumed to be constant diagonal matrices in this work. The diagonal elements of matrix $\mathbf{R}$ are selected in accordance with the variance values of the noise added to the simulated measurements. This tuning is relatively straightforward also in the case of real measurements, since it is always possible to evaluate some statistics of the measurement noise. The covariance matrix $\mathbf{Q}^*$ consists of matrices $\mathbf{Q}$ and $\mathbf{Q}_u$, cf. Eq. (35.6). As in this work the same model is used both for generating the virtual measurements and for deriving the filter equations, there is no uncertainty on the model, so that the choice $\mathbf{Q} = \mathbf{0}$ can be made. The only uncertainties of the model equation are hence assumed to be related to the random walk model for the force, so that appropriate values for the diagonal elements

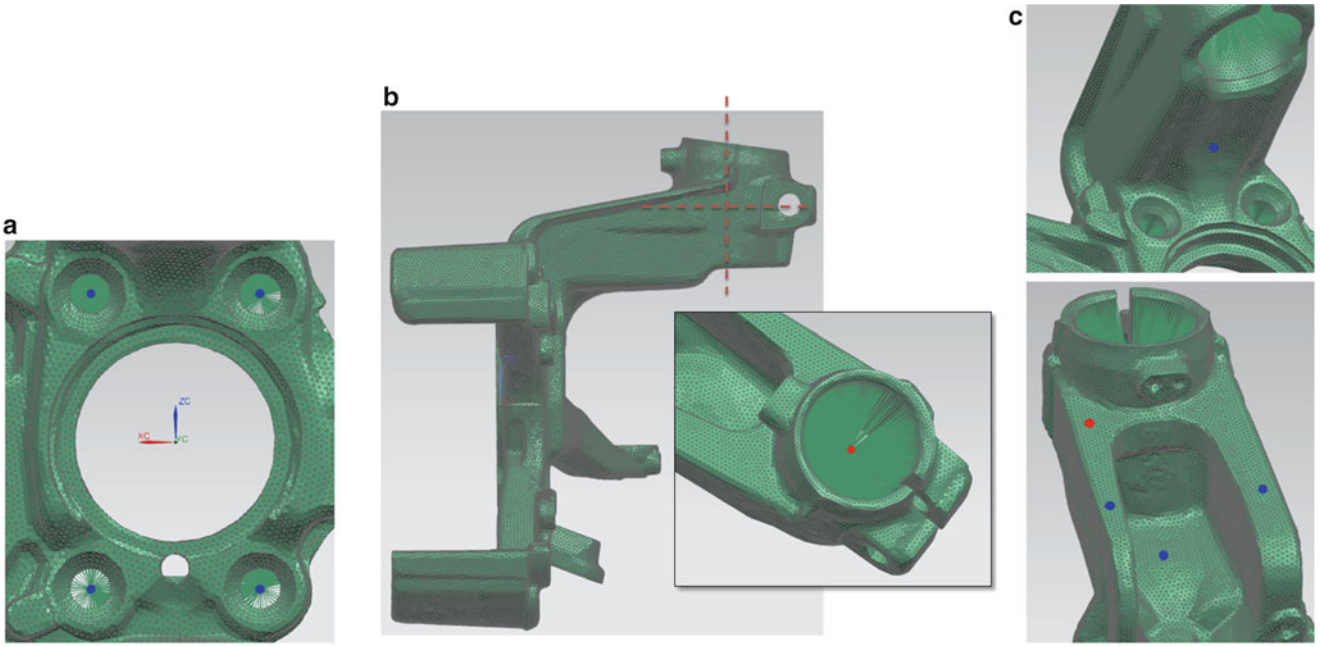

Fig. 35.2 Virtual exercise configuration (**a**) Constraints location; (**b**) Input location; (**c**) Output locations

of the associated covariance matrix $\mathbf{Q}_u$ have to be chosen. The values should be sufficiently large in order not to bound the amplitude of the estimated inputs. Finally, the initial state together with the associated initial error covariance matrix have to be set. In this work the initial state is assumed to be perfectly known so that the initial error covariance matrix can be set equal to zero.

Figures 35.3 and 35.4 show the results for the first estimation case where two force components are applied to the system. In this case four different strain measurements are considered; the locations of the four strain measurements are marked in blue in Fig. 35.2c. With this choice all the observability requirements described in Sect. 35.4 are satisfied. Three different sub-cases with different input forces amplitudes are considered. It can be observed that the estimation is always quite accurate except for the case where the input force in the y direction is much smaller compared to the one in the z direction (Fig. 35.4b). The stiffness of the model is much higher in the y direction and this affects the estimation accuracy. Furthermore sometimes some delay can be observed in the estimated input (Fig. 35.3).

Figures 35.5 and 35.6 show again the results for the first estimation case where two input components are estimated. This time a different set of measurements is used: two strain measurements and two acceleration measurements. The latter correspond to the accelerations in the y and z directions of the point marked in red in Fig. 35.2c. The observability requirements are again satisfied and this time the results show that the estimation is always accurate, even in the case where a small input force is applied in direction y, cf. Fig. 35.6b. Furthermore the algorithm does not introduce any delay in the estimated signals.

Finally Fig. 35.7 shows the results for the second estimation case, where three different force components are applied to the system. Only the sub-case where small force components are applied in direction x and y is considered, since it represents the most challenging situation. Here three strain measurements and three acceleration measurements corresponding to the acceleration along the three global directions of the red point of Fig. 35.2c are considered. With this set of measurements the observability requirements are again satisfied and all the input forces are well-estimated.

35.6 Conclusions

This paper addressed the problem of multiple force estimation on an automotive suspension component. Many techniques for solving the problem of input identification for mechanical systems have been developed in the past, both in the time and in the frequency domain and consisting of deterministic or stochastic approaches. In this work an augmented linear Kalman filter has been employed to solve the problem. It constitutes a combined deterministic and stochastic approach that leads to the simultaneous estimation of the states and of the inputs of a system, by combining a model of the system together

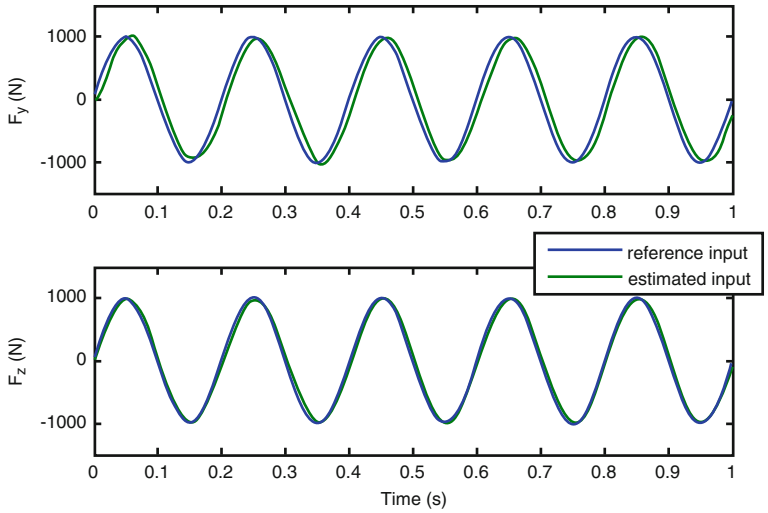

Fig. 35.3 Force estimation of two input components of the same amplitude, making use of 4 strain measurements

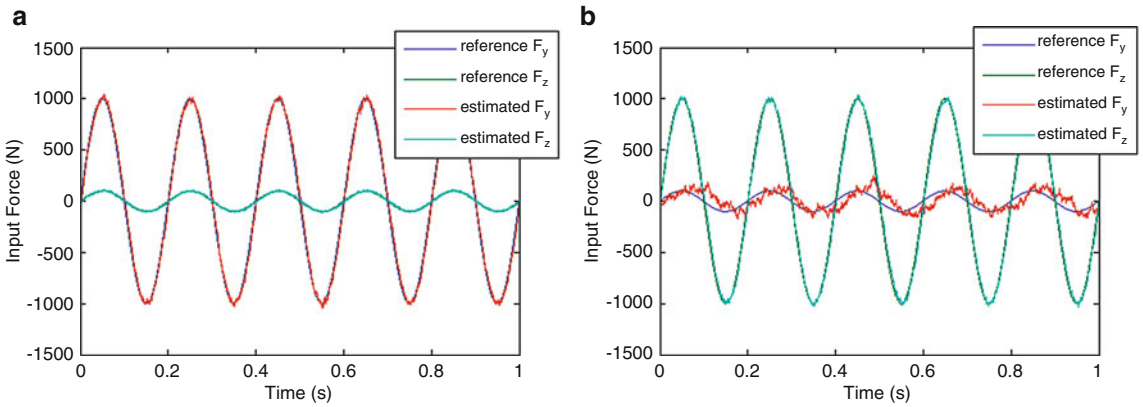

Fig. 35.4 Force estimation of two input components of different amplitudes, making use of 4 strain measurements (**a**) The input component along direction z is an order of magnitude lower than the one along direction y; (**b**) The input component along direction y is an order of magnitude lower than the one along direction z

with additional measurements. A reduced finite element model of the suspension component was used together with local acceleration and strain measurements. The derivation of the augmented linear Kalman filter and its application to a structural system were described. The proposed approach was then numerically validated for the case of multiple force estimation on a steering knuckle. It has been shown that, even though strain measurements are necessary in order to have an observable system, the estimation of low amplitude inputs along directions of high stiffness can be poor if only strain measurements are considered. In this case additional information can be provided by accelerations, leading to a better estimation accuracy.

Acknowledgements The authors gratefully acknowledge the European Commission for its support of the Marie Sklodowska Curie program through the ITN ANTARES project (GA 606817).

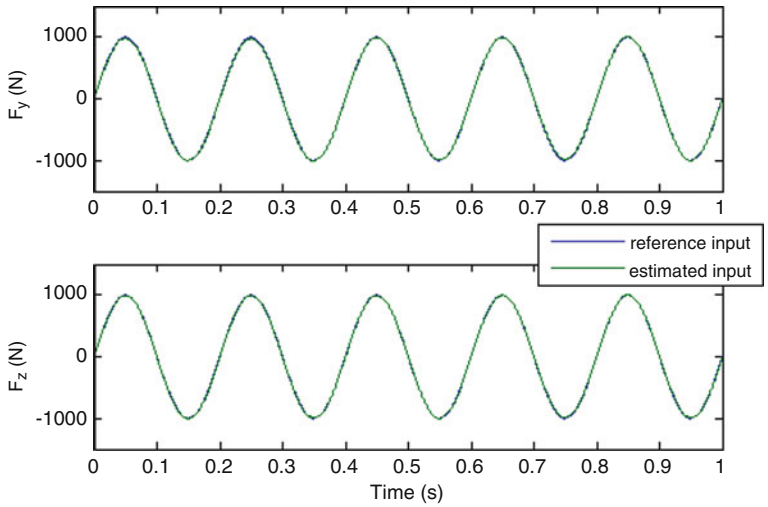

Fig. 35.5 Force estimation of two input components of the same amplitude, making use of 2 strain and 2 acceleration measurements

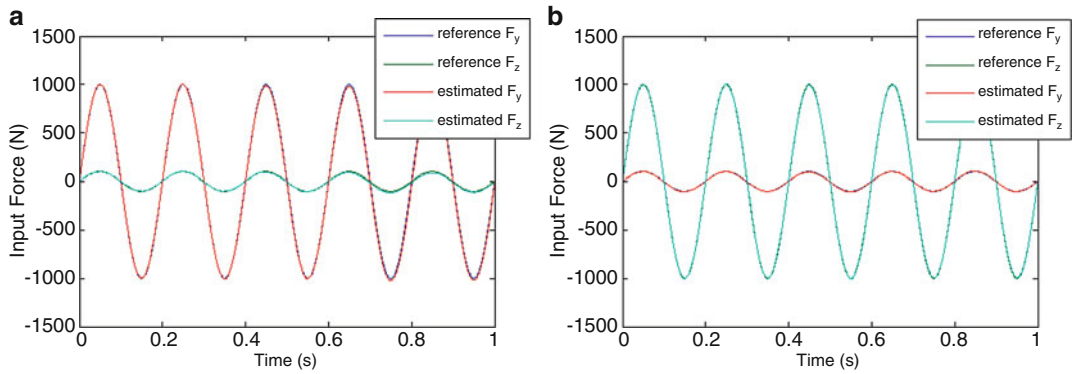

Fig. 35.6 Force estimation of two input components of different amplitudes, making use of 2 strain and 2 acceleration measurements. (**a**) The input component along direction z is an order of magnitude lower than the one along direction y; (**b**) The input component along direction y is an order of magnitude lower than the one along direction z

References

1. Klinkov, M., Fritzen, C.-P.: An updated comparison of the force reconstruction methods. Key Eng. Mater. **347**, 461–466 (2007)
2. Uhl, T.: The inverse identification problem and its technical application. Arch. Appl. Mech. **77**, 325–337 (2007)
3. Nordstrom, L.J.L., Nordberg, T.P.: A critical comparison of time domain load identification methods. In: International Conference on Motion and Vibration Control August (2002)
4. Hansen, P.C.: Analysis of discrete ill-posed problems by means of the L-curve. SIAM Rev. **34**(4), 561–580 (1992)
5. Steltzner, A.D., Kammer, D.C.: Input force estimation using an inverse structural filter. J. Vib. Acoust. **123**(4), 524–532 (2001)
6. Parloo, E., Verboven, P., Guillaume, P., Van Overmeire, M.: Force identification by means of in-operational modal models. J. Sound Vib. **262**(1), 161–173 (2003)
7. Blau, M.: Inverse force synthesis: state of the art and future research. In: InterNoise 2000 International Congress and Exhibition on Noise Control Engineering (August 2000)
8. Aucejo, M.: Structural source identification using a generalized Tikhonov regularization. J. Sound Vib. **333**(22), 5693–5707 (2014)
9. Rezayat, A., El-Kafafy, M., Maes, K., Lombaert, G., Vanlanduit, S., Guillaume, P.: Estimation of localized dynamic loads by means of sparse optimization. In: (IOMAC'15) 6th International Operational Modal Analysis Conference, Spain (2015)
10. Trujillo, D.M., Busby, H.R.: Practical Inverse Engineering. CRC Press, London (1997)
11. Uhl, T.: Identification of loads in mechanical structures-helicopter case study. Comput. Assist. Mech. Eng. Sci. **9**(1), 151–160 (2002)
12. Kalman, R.E.: A new approach to linear filtering and prediction problems. J. Basic Eng. **82**(1), 35–45 (1960)
13. Ma, C.-K., Tuan, P.-C., Lin, D.-C., Liu, C.-S.: A study of an inverse method for estimation of impulsive loads. Int. J. Syst. Sci. **29**(6), 663–672 (1998)
14. Gillijns, G., De Moor, B.: Unbiased minimum-variance input and state estimation for linear discrete-time systems. Automatica **43**, 111–116 (2007)
15. Hwang, J.-S., Kareem, A., Kim, W.-J.: Estimation of modal loads using structural response. J. Sound Vib. **326**(3–5), 522–539 (2009)

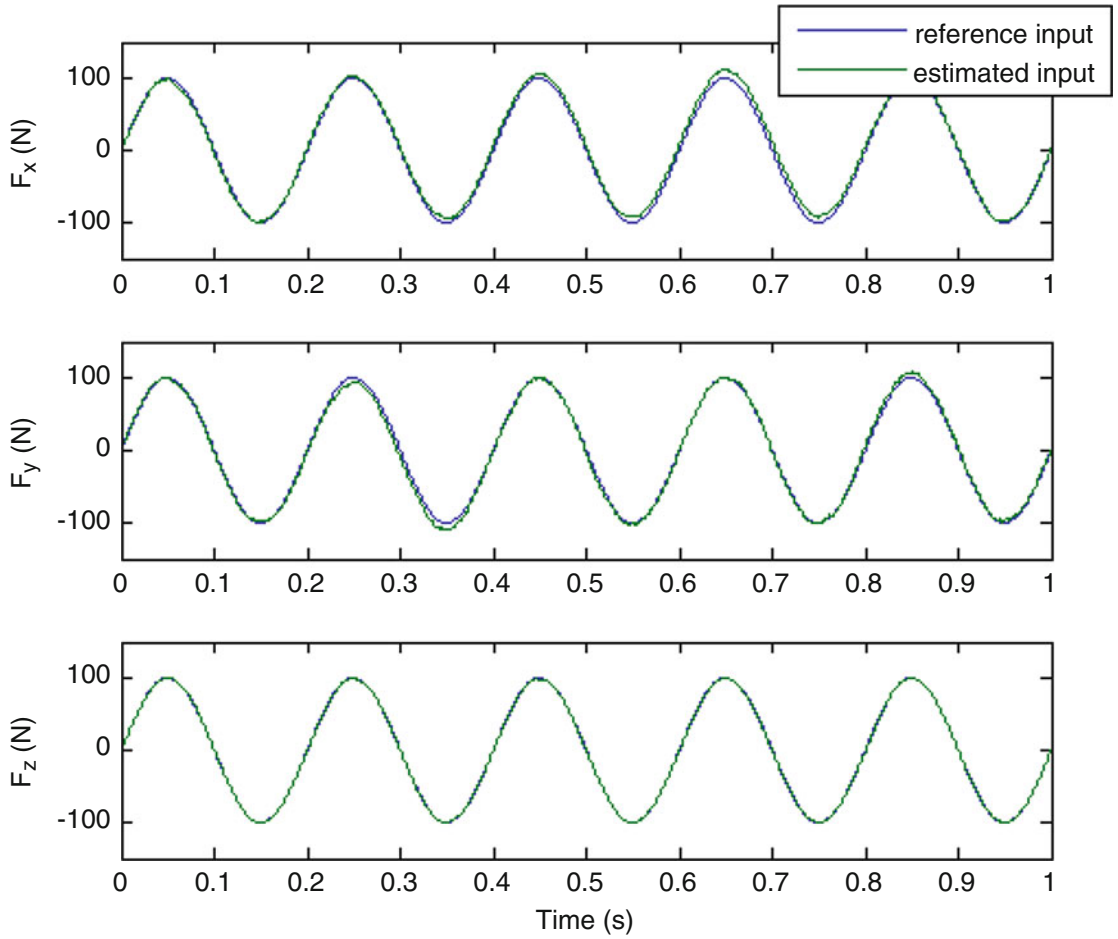

Fig. 35.7 Force estimation of three input components of different amplitudes (i.e., F_x and F_y significantly smaller than F_z), making use of 3 strain and 3 acceleration measurements

16. Friedland, B.: Treatment of bias in recursive filtering. IEEE Trans. Autom. Control **14**(4), 359–367 (1969)
17. Lourens, E., Reynders, E., De Roeck, G., Degrande, G., Lombaert, G.: An augmented Kalman filter for force identification in structural dynamics. Mech. Syst. Signal Process. **27**, 446–460 (2012)
18. Naets, F., Cuadrado, J., Desmet, W.: Stable force identification in structural dynamics using Kalman filtering and dummy-measurements. Mech. Syst. Signal Process. **50–51**, 235–248 (2015)
19. Naets, F., Croes, J., Desmet, W.: An online coupled state/input/parameter estimation approach for structural dynamics. Comput. Methods Appl. Mech. Eng. **283**, 1167–1188 (2015)
20. Simo, D.: Optimal State Estimation: Kalman, H_∞ and Nonlinear Approaches. Wiley, New York (2006)
21. Van Loan, C.F.: Computing integrals involving the matrix exponential. IEEE Trans. Autom. Control **23**(3), 395–404 (1978)
22. Zienkiewicz, O.C., Taylor, R.L.: The Finite Element Method. Butterworth Heinemann, Oxford (2000)
23. Besselink, B., Tabak, U., Lutowska, A., van de Wouw, N., Nijmeijer, H., Rixen, D. J., Hochstenbach, M.E., Schilders, W.H.A.: A comparison of model reduction techniques from structural dynamics, numerical mathematics and system and control. J. Sound Vib. **332**, 4403–4422 (2013)
24. Craig, R.R., Kurdila, A.J.: Fundamentals of Structural Dynamics. Wiley, New York (2006)
25. Ghosh, B.K., Rosenthal, J.: A generalized Popov-Belevitch-Hautus test of observability. IEEE Trans. Autom. Control **40**(1), 176–180 (1995)

Chapter 36
A Pretest Planning Method for Model Calibration for Nonlinear Systems

Yousheng Chen, Andreas Linderholt, Thomas Abrahamsson, Yuying Xia, and Michael I. Friswell

Abstract With increasing demands on more flexible and lighter engineering structures, it has been more common to take nonlinearity into account. Model calibration is an important procedure for nonlinear analysis in structural dynamics with many industrial applications. Pretest planning plays a key role in the previously proposed calibration method for nonlinear systems, which is based on multi-harmonic excitation and an effective optimization routine. This paper aims to improve the pretest planning strategy for the proposed calibration method. In this study, the Fisher information matrix (FIM), which is calculated from the gradients with respect to the chosen parameters with unknown values, is used for determining the locations, frequency range, and the amplitudes of the excitations as well as the sensor placements. This pretest planning based model calibration method is validated by a structure with clearance nonlinearity. Synthetic test data is used to simulate the test procedure. Model calibration and K-fold cross validation are conducted for the optimum configurations selected from the pretest planning as well as three other configurations. The calibration and cross validation results show that a more accurate estimation of parameters can be obtained by using test data from the optimum configuration.

Keywords Nonlinear model calibration • Pretest planning • Clearance • Multi-harmonic excitation • Fisher information matrix

36.1 Introduction

Model calibration of nonlinear systems has interested researchers in the field of structural dynamics in the past decades [1–3]. All mechanical systems display a certain degree of nonlinearity due to nonlinear material properties, large displacement, clearance, etc. In industry, linear finite element (FE) models are extensively used to represent the global behavior of mechanical systems, in which nonlinear effects are often neglected to simplify the model. When the test data shows significant nonlinearity, the prediction of a linear FE-model may become erroneous. In this case, it is essential to take nonlinearity into account. The nonlinearities are often local in structures. To present the dynamic behavior of structures with local nonlinearities, a common approach is to extend linear FE-models by added nonlinear elements. The nonlinear parameters often suffer from a large amount of uncertainty, which must be calibrated using experimental data. This procedure is called nonlinear FE-model calibration.

Pretest planning is a vital part of successful modal testing especially for a complex structure with a limited number of sensors and actuators. Finding the optimal sensor placement (OSP) is one of most important pretest steps, which has been extensively conducted in modal analysis. Many sensor placement techniques based on the information obtained from the nominal FE model have been developed [4–6]. The effective independence method (EFI), based on the Fisher information matrix (FIM), is one of the most popular methods to find the OSP. In [4], the FIM is defined as the product of the modal matrix and its transpose.

Y. Chen (✉) • A. Linderholt
Department of Mechanical Engineering, Linnaeus University, 35195 Växjö, Sweden
e-mail: yousheng.chen@lnu.se

T. Abrahamsson
Department of Applied Mechanics, Chalmers University of Technology, 41296 Göteborg, Sweden

Y. Xia
Department of Engineering, Design and Mathematics, University of the West of England, BS16 1QY Bristol, UK

M.I. Friswell
College of Engineering, Swansea University, SA1 8EN Swansea, UK

S. Atamturktur et al. (eds.), *Model Validation and Uncertainty Quantification, Volume 3*, Conference Proceedings of the Society for Experimental Mechanics Series, DOI 10.1007/978-3-319-29754-5_36

While much research has focused on how to best set-up and perform modal property identification, there has been little discussion on pretest planning for nonlinear system identification. In [7], the OSP algorithm, based on principal component analysis, has been applied for the detection of nonlinear structural behaviour. The measured responses of a nonlinear system depend not only on the placement of sensors and actuators but also on the excitation levels and the excitation frequency range. Therefore, they should be carefully selected to obtain the most important dynamic information.

In this paper, the previously proposed model calibration method [8] is improved by selecting an optimal configuration, involving location of the sensors and actuators, excitation levels and frequency ranges, ranked by the FIM which is calculated from the gradients with respect to the chosen parameters with unknown values. The model calibration method consists of three parts; pretest planning, multi-harmonic excitation and an efficient optimization routine. Pretest planning gives a strategy for measurements and forms an objective function for the optimization. The optimization is conducted by minimizing the difference between the numerical and experimental multi-harmonic nonlinear FRFs using a selected starting point. To calculate the steady-state response, the time domain method may be inefficient for a lightly damped system, therefore the frequency domain multi-harmonic balance (MHB) method [9–11] is used to calculate the numerical nonlinear FRFs. The improved model calibration method is validated using synthetic data from a numerical model with a clearance type nonlinearity.

36.2 Model Calibration Method

The previously proposed model calibration method [8], which requires pretest planning, uses a multi-harmonic excitation and an effective optimization routine, and is shown in Fig. 36.1. The method consists of three parts: pre-test planning, measurement and model calibration/validation. In pretest planning, the parameter identifiability is examined by use of the FIM. A test strategy for the measurement and the objective function for the optimization are achieved. Multi-harmonic frequency response test data are then generated using a multi-harmonic excitation. Finally, a parameter starting point, selected among the starting point candidates found through the Latin hypercube sampling method is used for calibration. The calibrated parameter setting is then used as the starting point for K-fold cross validation trainings.

36.2.1 Pretest Planning

Generally, the aim of pretest planning is to increase the likelihood of achieving valuable data in the test planned that maximizes the identifiability of the uncertain model parameters with respect to the experimental conditions. At this stage, the experimental data are not available and the nominal FE-model of the test object has to be used. Therefore, it is a good idea to use that nominal model in pretest planning to increase the possibility of creating a successful test outcome.

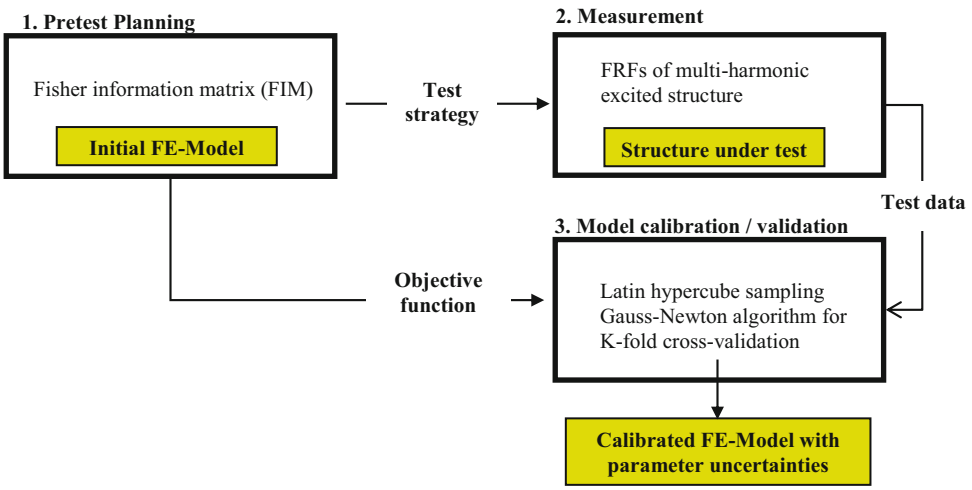

Fig. 36.1 An overview of the model calibration method

Due to the limited number of sensors and actuators, their configurations are main concerns in the pretest planning. For a nonlinear system, steady-state frequency response data depend on the excitation levels that should be carefully selected. It is computationally expensive to calculate or measure the nonlinear FRFs for a large frequency range and for the frequency range where the nonlinearity is not pronounced may be considered as uninformative to the nonlinear parameters. Therefore, it is desired to use a small and informative excitation frequency range for model calibration. In this paper, the pretest planning considers the positions, the excitation levels and the excitation frequency range for the excitation as well as the optimum sensor placement. The optimum configuration is determined by maximizing the determinant of the FIM.

Assume that the test data z_n can be predicted without bias with a parameterized model in its calibrated setting $\boldsymbol{p}^*$. In addition, assume a stationary, Gaussian residual $\boldsymbol{\varepsilon}_n$, with known standard deviation σ_n. Let the predicted data from the model be $\hat{z}_n$, then the test data can be presented as

$$z_n = \widehat{z}_n\left(\boldsymbol{p}^*\right) + \boldsymbol{\varepsilon}_n \tag{36.1}$$

The covariance matrix of the estimation error

$$\boldsymbol{R} = E\left[\left(z_n - \widehat{z}_n\right)\left(z_n - \widehat{z}_n\right)^{\mathrm{T}}\right] \tag{36.2}$$

should be minimized for good test data sets. The inverse parameter covariance lower bound known as the FIM, $\boldsymbol{F}$, can be expressed as

$$\boldsymbol{F} = \boldsymbol{R}^{-1} = \sum_{n=1}^{N} \sigma_n^{-2}\left[\frac{\partial}{\partial \boldsymbol{p}}\widehat{z}_n\left(\boldsymbol{p}\right)\right]\left[\frac{\partial}{\partial \boldsymbol{p}}\widehat{z}_n\left(\boldsymbol{p}\right)\right]^{\mathrm{T}} \tag{36.3}$$

The derivation of Eq. (36.3) can be found in [12]. The FIM, which is the inverse the covariance matrix of the estimation error, is useful in the study of data informativeness and parameter identifiability and it is used to rank the goodness of data sets.

36.2.2 FRFs of Multi-Harmonic Excited Structure

The governing equation of an N degrees of freedom nonlinear mechanical system can be expressed as

$$\boldsymbol{M}\ddot{\boldsymbol{q}} + \boldsymbol{V}\dot{\boldsymbol{q}} + \boldsymbol{K}\boldsymbol{q} + \boldsymbol{u}_{\mathrm{NL}}\left(\boldsymbol{q}, \dot{\boldsymbol{q}}\right) = \boldsymbol{u} \tag{36.4}$$

where $\boldsymbol{M}$, $\boldsymbol{K}$ and $\boldsymbol{V}$ are $N \times N$ mass, stiffness and damping matrices, $\boldsymbol{q}$, $\dot{\boldsymbol{q}}$, $\ddot{\boldsymbol{q}}$ are the nodal displacement, velocity and acceleration vectors, $\boldsymbol{u}_{\mathrm{NL}}$ denotes the nonlinear force vector and $\boldsymbol{u}$ is the external load vector.

The excitation force is designed to have harmonics of the fundamental frequency Ω, and can be expressed as

$$\boldsymbol{u}(t) = \sum_{j=1}^{h} \boldsymbol{U}_j e^{im_j \Omega t} \tag{36.5}$$

where $\boldsymbol{U}_j$ is a complex number, h is the number of harmonic components included in the excitation force and m_j denotes the multiple or divisor of the excitation frequency Ω; i.e., a sub- or super-harmonic. The periodic steady-state time response, if such exists, can be expressed with a series

$$\boldsymbol{q}(t) = \sum_{j=1}^{\infty} Q_j e^{im_j \Omega t} \tag{36.6}$$

where Q_j is the harmonic coefficients of the displacement. For a single degree of freedom system the multi-harmonic nonlinear FRF is defined as

$$H_j(\Omega) = \frac{Q_j(\Omega)}{U_j(\Omega)} \tag{36.7}$$

in which $H_1(\Omega)$ denotes the first-order nonlinear FRF with the fundamental frequency Ω and $H_j(\Omega)$ represents the j th order harmonic nonlinear FRF. These harmonic FRFs are calculated by the receptance based MHB method proposed in [10].

36.2.3 Model Calibration/Validation

The model calibration and validation are performed through optimization using Gauss-Newton algorithm. The Latin hypercube sampling method is used to select a limited number of starting point candidates which represent the parametric space plausibly. Then the candidate for which the objective function has the smallest value is used as a starting point for the optimization for the calibration.

36.2.3.1 Optimization Routine

The nonlinear model calibration minimizes the deviation between the analytical nonlinear multi-harmonic FRFs and the experimental counterparts. The objective function is defined as

$$\delta = \varepsilon^H W \varepsilon, \tag{36.8}$$

where W is a positive definite weighting factor matrix and ε is

$$\varepsilon = v_{\mathrm{H}}^{\mathrm{A}} - v_{\mathrm{H}}^{\mathrm{x}}, \tag{36.9}$$

where superscripts A denotes analytical and X denotes experimental and v_H is

$$v_H = \left[real\left(vect\left(H_1; H_2; \cdots; H_h\right)\right);\ imag\left(vect\left(H_1; H_2; \cdots; H_h\right)\right)\right]. \tag{36.10}$$

Here, *real* denotes the real part, *imag* the imaginary part, and H_h the h th order nonlinear FRF.

36.2.4 K-Fold Cross-Validation

A K-fold cross-validation is used to obtain an estimate of the parameter statistics after the model is calibrated. In the K-fold cross-validation, the available data set is partitioned into K equal size subsamples. In the extreme case, one subsample is used for validation while the remaining K-1 subsamples are used for calibration in K calibration runs. From these K calibration runs, K sets of calibrated parameter settings that minimize the calibration deviation metric for the K different partitions of the available data are obtained. These can then be used for statistical evaluation of the mean and covariance of the parameter estimates.

36.3 Case Study

36.3.1 Modelling of the Structure Under Test

The test rig used to study the method consists of a cantilever beam with a bump stop at its free end, see Fig. 36.2. The test structure is supported by a U-shaped steel frame, mainly made of square hollow tubes with an outer side length of 80 mm and a wall thickness of 6 mm. The cantilever beam is 593 mm long with a cross section of 14×14 mm^2 and the joint is 40 mm long with a cross section of 20×30 mm^2.

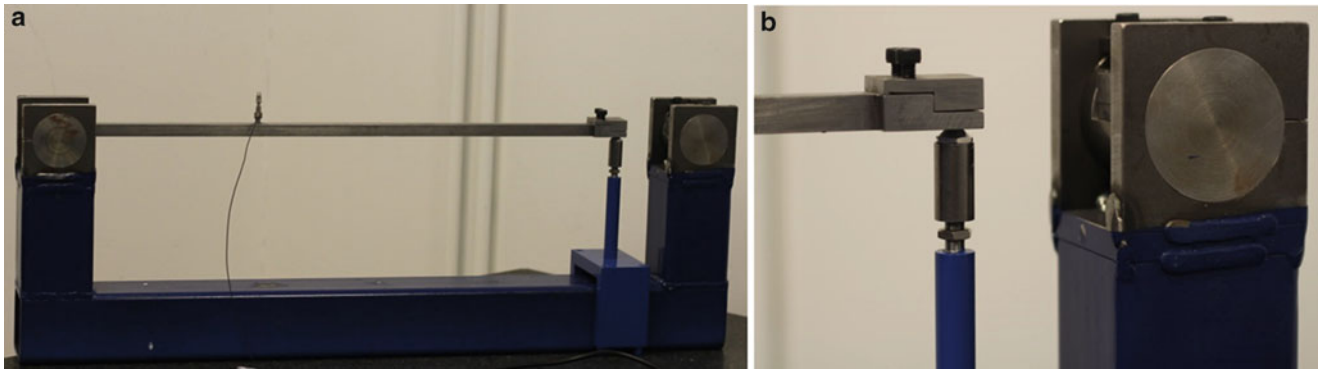

Fig. 36.2 (**a**) The test structure. (**b**) Closer perspective on the gap mechanism

Table 36.1 The parameter values used for the beam-joint structure

Young's modulus of the beam (GPa)	Young's modulus of the joint (GPa)	Density of the beam (kg/m^3)	Density of the joint (kg/m^3)
197	210	7620	7635

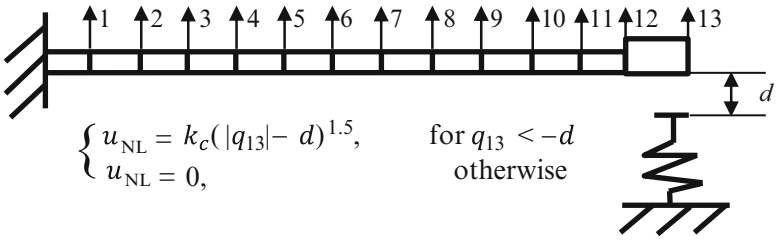

Fig. 36.3 The nominal FE-model of the structure under test

The cantilever beam is modelled by 12 equal size beam elements, while the joint structure is modelled by one beam element. The material properties, obtained from the calibration result shown in [8], used for the beam and the joint are shown in Table 36.1. The contact interface between the joint and the bump stop is represented by a Hertzian contact model with contact stiffness k_c. The numerical model is shown in Fig. 36.3. The contact stiffness k_c (parameter 1) and gap d (parameter 2) are considered as the two unknown parameters to be calibrated. The contact stiffness $k_c = 8 \times 10^4$ [N/m], and the gap $d = 8 \times 10^{-4}$ [m] are used in the nominal model. An example of the nonlinear multi-harmonic FRFs between response at degree-of-freedom (dof) 13 and a multi-harmonic external force that has the fundamental amplitude 2 N at dof 4, is shown in Fig. 36.4.

36.3.2 Pretest Planning Results

In this numerical example, the location of three sensors, the location of one actuator, three different excitation levels and one frequency range are selected from the candidate sets that are shown in Table 36.2. The first resonance of the underlying linear system appears in the first frequency range [11–50] Hz, while the second resonance is within the last set [131–170] Hz.

When an actuator is excited with three different excitation levels in a frequency range, the multi-harmonic FRFs, measured using three sensors, are considered as one data set. To select three sensor locations from seven candidates gives 35 combinations using the cluster sampling theory. Similarly, four combinations are provided by the candidates of the actuator positions, 35 combinations of the excitation levels and four combinations of frequency range. Combining these four terms (selections of the sensor locations, actuator location, excitation levels and frequency ranges) give 19,600 data sets in total. The FIM are calculated for each data set. The one with the largest determinant of the resulting FIM, which gives the smallest covariance matrix of the estimated parameters, are considered as the optimum configuration for the nonlinear model calibration. The optimum configuration is the number one configuration shown in Table 36.3.

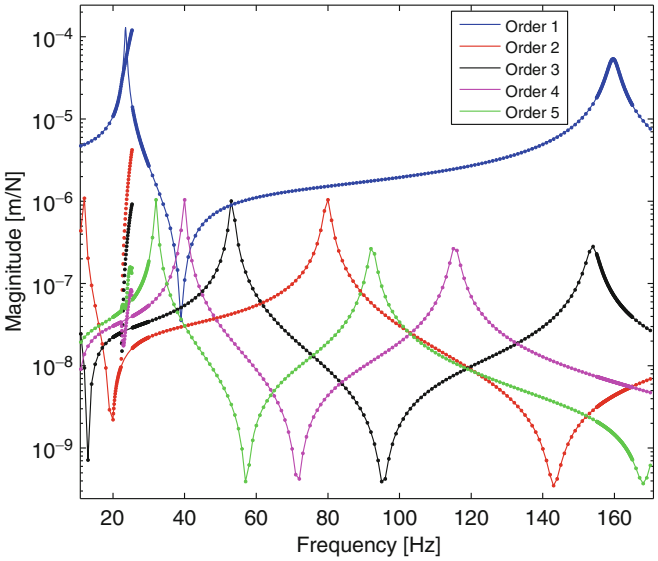

Fig. 36.4 An example of the multi-harmonic nonlinear FRFs compared with the underlying linear FRFs. The nonlinear FRFs are plotted by dots while the linear FRFs are plotted as solid lines. The magnitude of super harmonic FRFs are scaled with the ratio between the amplitude applied on the super harmonic and the fundamental term. The frequency axis is plotted with respect to the fundamental FRF. For the harmonic FRFs, the corresponding frequencies are equal to the frequencies shown in the figure multiplied by its order

Table 36.2 The candidate sets for the sensor locations, actuator positions, excitation levels and frequency ranges

Sensor locations (dofs)	Actuator positions (dofs)	Excitation levels	Frequency ranges
[2, 4, 6, 8, 10, 12, 13]	[2, 4, 6, 8]	[1, 1.5, 2, 2.5, 3, 4, 5] N	[11–50] Hz, [51–90] Hz, [91–130] Hz, [131–170] Hz

Table 36.3 The configurations used for the cross validation

Configurations	Sensor locations (dofs)	Actuator positions (dofs)	Excitation levels	Frequency ranges
1	[10, 12, 13]	4	[1.5, 2.5, 5] N	[11–50] Hz
2	[10, 12, 13]	4	[1, 2, 3] N	[11–50] Hz
3	[10, 12, 13]	4	[3, 4, 5] N	[11–50] Hz
4	[10, 12, 13]	4	[1, 2, 3] N	[131–170] Hz

Number 1 is the optimum configuration determined from the pretest planning

36.3.3 Synthetic Test Data

In this study, the nonlinear model calibration is illustrated using the FE-model representing the test setup shown in Fig. 36.2. Using the result from the pretest planning, a multi-harmonic stepped sine force excites the structure from 11 to 50 Hz for the fundamental harmonic, with steps of 1 Hz. Close to the system's resonance frequencies the excitation frequency steps are decreased to 0.01 Hz.

The excitation point is at the location of dof 4. The excitation force is designed to contain four super-harmonics together with the fundamental frequency. The magnitudes of these side harmonics are small compared to the fundamental frequency but large compared to the expected noise level [8]; the magnitude of the side harmonics is chosen as 2 % of the magnitude of the fundamental frequency. The multi-harmonic FRFs are obtained using the excitation level [1.5, 2.5, 5] N and the steady state responses are calculated at dofs [10 12 13].

To understand the effect of noise, model calibration is done for the synthetic test data polluted with three different noise levels; low, medium and high. The noise is added to the time response based on the response at the tip of the cantilever beam, for an excitation level of 1.5 N at 25 Hz. Gaussian noise is added with zero mean and standard deviation 0.1, 1 and 10 % of this base response. The calibration results are shown in Table 36.4.

To demonstrate that the accuracy of the estimated parameters is improved using the optimum configuration determined by the pretest planning, the results are compared to three alternative configurations. The configurations used to generate the synthetic test data are shown in Table 36.3.

Table 36.4 The calibration results for different noise levels are shown

	Calibrated parameters	
Noise levels	P_1 (contact stiffness)	P_2 (gap)
Low	1.00006	1.00007
Medium	1.00182	1.00316
High	0.99996	0.99717

The calibrated parameters are normalized with the true parameter values; one indicates a perfect match between the estimated parameter value and the corresponding true parameter value

Table 36.5 The mean value and the standard deviation of the ninefold cross validation for each configuration with different noise levels are nominalized using the true parameters

		Low noise level			Medium noise level			High noise level		
	Configuration	Mean	Error	Standard deviation	Mean	Error	Standard deviation	Mean	Error	Standard deviation
P_1	1	1.00006	0.006 %	0.00004	1.00183	0.183 %	0.00045	0.99997	0.003 %	0.00238
	2	1.00011	0.011 %	0.00006	1.00224	0.224 %	0.00116	1.01686	1.686 %	0.00489
	3	1.00001	0.001 %	0.00004	1.00087	0.087 %	0.00039	0.99697	0.303 %	0.00190
	4	–	–	–	–	–	–	–	–	–
P_2	1	1.00007	0.007 %	0.00010	1.00319	0.319 %	0.00095	0.99720	0.280 %	0.00512
	2	1.00010	0.010 %	0.00008	1.00512	0.512 %	0.00200	1.02544	2.544 %	0.00773
	3	1.00010	0.010 %	0.00011	1.00209	0.209 %	0.00086	0.99345	0.655 %	0.00719
	4	–	–	–	–	–	–	–	–	–

The error shown in the table is calculated by (mean value–true parameter)/true parameter × 100. '–' means that the parameters are unidentifiable

36.3.4 Calibration Results

The synthetic test data, multi-harmonic FRFs, are generated from the nominal model. It is assumed that the true parameter setting is unknown in the model calibration processes. Therefore, for the evaluation of optimization starting points, beta distributions are used for the contact stiffness (P_1) and the gap (P_2) with mean values equal to the corresponding values of the nominal model and the standard deviations are set to 20 % of the mean values. The Latin hypercube sampling method is used to select 100 parameter realizations which represent the parametric space plausibly. The multi-harmonic FRFs of these realizations are compared to the FRFs from the nominal model, here mimicking test data. Among the 100 candidate starting points, the point giving the smallest value of the objective function is used as the starting point for calibration. The calibrated parameter setting is then used as the starting point for K-fold cross validation trainings. The calibration and cross validation are done by using the Gauss–Newton optimization method.

36.3.5 Cross Validation Results

The data set is equally divided into nine subsamples, one subsample is used for validation, and the remaining eight subsamples are used to calibrate the model which results in nine runs. The cross validation results for these nine runs for different configurations and different noise levels are shown in Table 36.5 and Fig. 36.5.

From the calibration results shown in Table 36.4, the improved calibration method is able to identify unknown parameters from noisy test data with a good accuracy. The cross validation results show that the data from a badly chosen frequency range, such as the frequency range [131–170], in which the nonlinearity is not significant, is uninformative for the identification of the nonlinear parameters. With low and medium noise levels, different configurations give similar calibration results. However, with the high noise level, the optimum configuration gives much better results than other configurations.

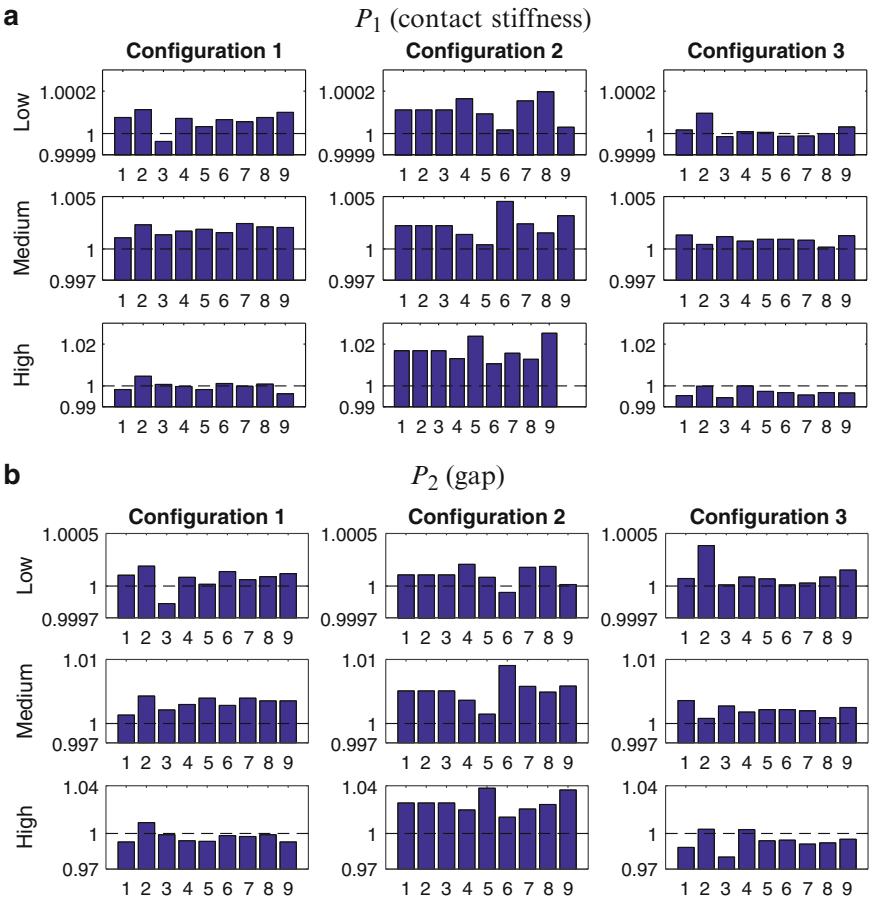

Fig. 36.5 The calibration results from the ninefold cross-validation. The nine estimated parameter realizations and their mean values and variances are normalized to the true parameter values; one indicates a perfect match between the estimated parameter value and the corresponding true parameter value. The blue bars represent the normalized estimated parameter value for each calibration

36.4 Conclusions

The previously proposed nonlinear model calibration method is improved by considering the location of sensors and actuators, the excitation levels and the frequency range in the pretest planning. The improved method is validated by performing model calibration and cross validation using synthetic data from a simulation model with clearance. The effect of noise is shown by comparing the cross validation results from the test data polluted with three different noise levels. It is shown that parameters become unidentifiable when a badly selected frequency range is used and the pretest based calibration method performs well even when the noise level is high.

References

1. Meyer, S., Link, M.: Modelling and updating of local non-linearities using frequency response residuals. Mech. Syst. Signal Process. **17**(1), 219–226 (2003)
2. Isasa, I., Hot, A., Cogan, S., Sadoulet-Reboul, E.: Model updating of locally non-linear systems based on multi-harmonic extended constitutive relation error. Mech. Syst. Signal Process. **25**, 2413–2425 (2011)
3. Kurta, M., Eritenb, M., McFarlandc, D., Bergmanc, L., Vakakis, A.: Methodology for model updating of mechanical components with local nonlinearities. J. Sound Vib. **357**(24), 331–348 (2015)
4. Kammer, D.C.: Sensor placement for on-orbit modal identification and correlation of large space structures. J. Guid. Control. Dyn. **14**(2), 251–259 (1991)
5. Papadimitriou, C., Beck, J.L.: Entropy-based optimal sensor location for structural model updating. J. Vib. Control. **6**(5), 781–800 (2000)
6. Penny, J.E.T., Friswell, M.I., Garvey, S.D.: Automatic choice of measurement locations for dynamic testing. AIAA J. **32**(2), 407–414 (1994)

7. Castro-Triguero, R., Friswell, M.I., Gallego Sevilla, R.: Optimal sensor placement for detection of non-linear structural behavior. In: Proceedings of the International Conference on Noise and Vibration Engineering (ISMA), Leuven (2014)
8. Yaghoubi, V., Chen, Y., Linderholt, A., Abrahamsson, T.: Locally non-linear model calibration using multi harmonic responses-applied on ecole de lyon non linear benchmark structure. In: Proceeding of the 31th the IMAC, Garden Grove (2013)
9. Cameron, T., Griffin, J.: An alternating frequency/time domain method for calculating the steady-state response of nonlinear dynamic systems. ASME J. Appl. Mech. **56**(1), 149–154 (1989)
10. Ren, Y., Beards, C.F.: A new receptance-based perturbative multi-harmonic balance method for the calculation of the steady state response of non-linear systems. J. Sound Vib. **172**(5), 593–604 (1994)
11. Ferreira, J.V., Ewins, D.J.: Algebraic nonlinear impedance equation using multi-harmonic describing function. In: Processing of the International Modal Analysis Conference, Orlando (1997)
12. Walter, E., Pronzato, L.: Identification of Parametric Models from Experimental Data. Springer, Heidelberg (1997)